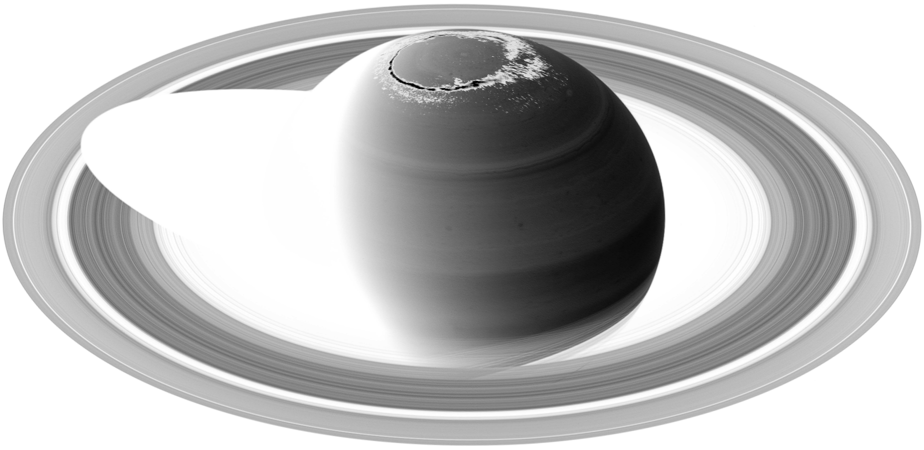

THE DYNAMICS OF SATURN'S ULTRAVIOLET AURORAE

ALEXANDER BADER

Supervised by
SARAH V. BADMAN and LICIA C. RAY

This thesis is submitted in partial fulfilment of the requirements
for the degree of Doctor of Philosophy

in the

Faculty of Science and Technology
Department of Physics

October 2020

Space & Planetary Physics | Lancaster University

ABSTRACT

THE DYNAMICS OF SATURN'S ULTRAVIOLET AURORAE

ALEXANDER BADER

Doctor of Philosophy

October 2020

Saturn's aurorae are highly dynamic, controlled from within Saturn's magnetosphere and by its interaction with the solar wind. This thesis investigates ultraviolet observations of these auroral emissions and corresponding in situ measurements of fields and particles, both mostly obtained by the CASSINI mission, in order to separate different components of the aurorae and determine their origin. The brightest emissions are found to be generated by recurring magnetotail reconnection, the occurrence of which is controlled by solar wind conditions and the phasing of Saturn's planetary period oscillation systems of rotating magnetic field perturbations and electric currents. The auroral signature resembles a series of bright patches emerging near local midnight and subcorotating with the planet's rotation. Underlying these is a steady auroral band which may be driven by flow shears in the outer magnetosphere and is modulated in intensity and location by the rotating planetary period oscillation systems, accompanied by a dim equatorward outer emission which is suggested to be related to wave scattering of electrons in the inner ring current. Observations further show various small-scale transients such as short-lived $\sim 1\,\mathrm{h}$ quasiperiodic flashes possibly indicative of magnetodisc reconnection occurring predominantly near dusk, or numerous fine arcs only visible in the highest resolution imagery obtained by CASSINI which may be related to interchange injection events. The relation between the source of auroral particles in the magnetosphere and the auroral emissions they generate upon impacting the atmosphere was investigated, with in situ measurements close above the aurorae revealing the presence of energetic field-aligned ion beams and conics as well as complex wave-particle interactions which may be responsible for their energization. While this thesis uncovers much unknown detail on the workings of Saturn's aurorae, many questions remain to be answered in future research.

DECLARATION

I hereby declare that this thesis titled

"The Dynamics of Saturn's Ultraviolet Aurorae"

is my own work, and has not been submitted in substantially the same form for the award of a higher degree elsewhere. Any sections of the thesis which have been published, or submitted for a higher degree elsewhere, are clearly identified. Parts of this thesis are the result of joint research; for these a statement indicating the nature of my contribution to that research is included, confirmed by both the supervisor(s) and all contributing authors of the materials accepted for publication.

Alexander Bader *Date*

List of Publications

Included in this thesis

A. Bader, S. V. Badman, J. Kinrade, S. W. H. Cowley, G. Provan and W. R. Pryor (2018)
"Statistical planetary period oscillation signatures in Saturn's UV auroral intensity"
Journal of Geophysical Research: Space Physics, *123*, 8459–8472.
doi:10.1029/2018JA025855

A. Bader, S. V. Badman, J. Kinrade, S. W. H. Cowley, G. Provan and W. R. Pryor (2019)
"Modulations of Saturn's UV auroral oval location by planetary period oscillations"
Journal of Geophysical Research: Space Physics, *124*, 952-970.
doi:10.1029/2018JA026117

A. Bader, S. V. Badman, Z. H. Yao, J. Kinrade and W. R. Pryor (2019)
"Observations of continuous quasiperiodic auroral pulsations on Saturn in high time-resolution UV auroral imagery"
Journal of Geophysical Research: Space Physics, *124*, 2451-2465.
doi:10.1029/2018JA026320

A. Bader, S. V. Badman, S. W. H. Cowley, Z. H. Yao, L. C. Ray, J. Kinrade, E. J. Bunce, G. Provan, T. J. Bradley, C. Tao, G. J. Hunt and W. R. Pryor (2019)
"The dynamics of Saturn's main aurorae"
Geophysical Research Letters, *46*, 10,283-10,294.
doi:10.1029/2019GL084620

A. Bader, S. V. Badman, L. C. Ray, C. Paranicas, C. T. S. Lorch, G. Clark, M. André, D. G. Mitchell, D. A. Constable, J. Kinrade, G. J. Hunt and W. R. Pryor (2020)
"Energetic particle signatures above Saturn's aurorae"
Journal of Geophysical Research: Space Physics, *125*, e2019JA027403.
doi:10.1029/2019JA027403

A. Bader, S. W. H. Cowley, S. V. Badman, L. C. Ray, J. Kinrade, B. Palmaerts and W. R. Pryor (2020)
"The morphology of Saturn's aurorae observed during the Cassini Grand Finale"
Geophysical Research Letters, *47*, e2019GL085800.
doi:10.1029/2019GL085800

Related

J. Kinrade, S. V. Badman, G. Provan, S. W. H. Cowley, L. Lamy and **A. Bader** (2018)
"Saturn's northern auroras and their modulation by rotating current systems during late northern spring in early 2014"
Journal of Geophysical Research: Space Physics, *123*, 6289-6306.
doi:10.1029/2018JA025426

A. Bader, G. Stenberg Wieser, M. André, M. Wieser, Y. Futaana, M. Persson, H. Nilsson and T. L. Zhang (2019)
"Proton temperature anisotropies in the plasma environment of Venus"
Journal of Geophysical Research: Space Physics, *124*, 3312-3330.
doi:10.1029/2019JA026619

J. Jasinski, C. S. Arridge, **A. Bader**, A. Smith, M. Felici, J. Kinrade, A. Coates, G. Jones, T. Nordheim, L. Gilbert, A. Azari, S. V. Badman, G. Provan, N. Sergis and N. Murphy (2019)
"Saturn's open-closed field line boundary: a Cassini electron survey at Saturn's magnetosphere"
Journal of Geophysical Research: Space Physics, *124*, 10,018-10,035.
doi:10.1029/2019JA027090

C. T. S. Lorch, L. C. Ray, C. S. Arridge, K. K. Khurana, C. J. Martin and **A. Bader** (2020)
"Local time asymmetries in Jupiter's magnetodisc currents"
Journal of Geophysical Research: Space Physics, *125*, e2019JA027455.
doi:10.1029/2019JA027455

J. Kinrade, S. V. Badman, C. Paranicas, D. G. Mitchell, **A. Bader**, R. L. Gray, C. S. Arridge, G. Provan, S. W. H. Cowley (2020)
"Tracking counterpart signatures in Saturn's auroras and ENA imagery during large-scale plasma injection events"
Journal of Geophysical Research: Space Physics, *125*, e2019JA027542.
doi:10.1029/2019JA027542

M.-T. Walach, G. J. Hunt, A. R. Fogg, **A. Bader** (2020)
"Autumn MIST 2019"
Astronomy & Geophysics, *61*, 4.26-4.28.
doi:10.1093/astrogeo/ataa056

C. Paranicas, M. F. Thomsen, P. Kollmann, A. Azari, **A. Bader**, S. V. Badman, M. Dumont, J. Kinrade, N. Krupp, E. Roussos (2020)
"Characterizing injection inflow speeds in Saturn's magnetosphere"
Journal of Geophysical Research: Space Physics, 125, e2020JA028299.
doi:10.1029/2020JA028299

A. Bader, J. Kinrade, S. V. Badman, C. Paranicas, D. A. Constable, D. G. Mitchell (in prep)
"A complete dataset of equatorial projections of Saturn's energetic neutral atom emissions observed by Cassini-INCA"
Journal of Geophysical Research: Space Physics.

J. Kinrade, **A. Bader**, S. V. Badman, C. Paranicas, D. G. Mitchell, C. S. Arridge, S. W. H. Cowley, G. Provan (in prep)
"The statistical morphology of Saturn's equatorial energetic neutral atom emissions"
Geophysical Research Letters.

G. Stenberg Wieser, M. André, N. Edberg, M. Persson, H. Gunell, **A. Bader**, Y. Futaana (in prep)
"Possible effects of ion heating caused by Alfvén waves at Venus"
Journal of Geophysical Research: Space Physics.

S. V. Badman, L. Lamy, W. R. Pryor, E. J. Bunce, R. Prangé, P. Zarka, B. Cecconi, J. D. Nichols, J. T. Clarke, G. J. Hunt, A. Radioti, J. Kinrade, **A. Bader**, W. S. Kurth, D. G. Mitchell, M. K. Dougherty (in prep)
"Interhemispheric asymmetries in Saturn's UV aurora"
Journal of Geophysical Research: Space Physics.

ACKNOWLEDGEMENTS

This thesis is not mine alone – it simply would not exist without the help of others who contributed to this work, each giving their time and energy to support me in their own valuable way. Below is a definitely incomplete list of people and organizations whose contributions I would like to highlight in specific.

◆

The honour of being named first here goes to Sarah and Licia, who never failed to fully support me even during periods of maternity leave and pandemic lockdown throughout this crazy PhD. Thank you for always having an open ear, for keeping the fun in science, for taking your time to patiently explain magnetospheric physics and for giving me the freedom to pursue whichever seemingly interesting results I stumbled across. Also, I'll be forever grateful for your help in defending myself and my work against reviewer 2 (one such occasion being exceptionally memorable).

◆

The SPP group and the good mood in the big shared office made me thoroughly enjoy my years at Lancaster. Thanks to everyone for making me feel welcome right away, for the daily crossword fun and interesting discussions about science, coding, politics and pretty much anything. Oh and for the cake! With special thanks to Joe for taming the PPOs with me (or attempting to, not sure about our success so far).

◆

There are also Stan Cowley, who at times adopted the role of an unofficial third supervisor, and Gabby Provan. Thank you for your detailed replies to my many emails full of (sometimes admittedly stupid) questions about PPOs and other things and your helpful comments on my paper drafts – your understanding and ability to explain the subject matter are really impressive.

◆

Our most recent work with INCA would have gone nowhere hadn't it been for Chris Paranicas and Don Mitchell who appear to know simply everything about this instrument and always quickly helped explaining weird features and figuring out the best way to process the data, thank you.

◆

My thanks also go to Sweden: to Gabriella and Martin for writing up my Master's project with me and for getting me interested in space physics and in doing a PhD to begin with; and to Mats for contributing to my work at both Venus and Saturn with his in-depth understanding of wave-particle interaction.

◆

Science would not be as awesome without good conferences. I therefore thank all organisers and sponsors for their efforts in keeping the community connected. Large meetings such as AGU and EGU as well as small meetings like NAM, MOP, MIST and Europlanet workshops were invaluable experiences for me, letting me see other parts of the world and meet many of my collaborators in person. All this was only made possible by generous funding from the *Lancaster University Faculty of Science and Technology*, the *Royal Astronomical Society*, the *European Space Agency* and the *Europlanet Society*.

◆

My workflow and productivity were greatly improved by important software such as *Python* and related packages (*matplotlib, numpy, pandas, rtree, scipy, shapely, spiceypy,...*), *Linux/Ubuntu*, *Git*, LaTeX, *Zotero* and many others. All of these are maintained by incredibly dedicated open source communities who have my utmost respect for their contributions to our society.

◆

On a more personal level, I'd like to thank my friends who, despite typically living at least hundreds of kilometers away, always have an open ear for me if needed. These notably include my mountain buddy Alex who lived through the joys and horrors of a Bachelor's degree in physics with me and my SpaceMaster friends Angel, Angèle and Anjana among others with whom I conquered the crazy life in Kiruna. Not to forget the hiking crew of course, whose last adventure was way too long ago!

◆

I count myself lucky to have a fantastic family who always has my back and supports me no matter what. From evening videochat sessions to home visits, from online gaming to hiking in the Greek summer heat together, I thank you for always supporting and encouraging me and for giving me opportunities to escape from the daily routine and reenergize whenever needed. Danke für alles und hab euch lieb!

◆

Lastly, Selina. My daily sunshine from near and far, my soulmate, and the kindest and most compassionate person I know. Thank you for your endless support, for encouraging me and for always believing in me. Thank you for fighting against the dark clouds without ever giving up – you are the strongest person in the world. Because of you I cherish every single moment, and I feel honoured to share this life with you. Ik zie u heel graag!

CONTENTS

APPENDICES

List of Figures

List of Tables

List of Acronyms

CAPS Cassini Plasma Spectrometer
CCD charge-coupled device
CHEMS Charge Energy Mass Spectrometer
CIR corotating interaction region
CODACON coded anode array converter
CRAND comic ray albedo neutron decay
DOY day of year
ENA energetic neutral atom
ESA European Space Agency
EUV extreme ultraviolet
FAC field-aligned current
FOV field of view
FUV far ultraviolet
HST Hubble Space Telescope
INCA Ion and Neutral Camera
IMF interplanetary magnetic field
IR infrared
ISS Imaging Science Subsystem
JPL Jet Propulsion Laboratory
KH Kelvin-Helmholtz
LEMMS Low-Energy Magnetospheric Measurement System
LT local time
MAG Cassini Magnetometer
MAMA multianode microchannel array
MCP multichannel plate
MHD magnetohydrodynamic
MIMI Magnetosphere Imaging Instrument
NASA National Aeronautics and Space Administration
OCB open-closed field line boundary
PPO planetary period oscillation
RPWS Radio and Plasma Wave Spectrometer
RTG radioisotope thermoelectric generator
SKR Saturn kilometric radiation

STIS	Space Telescope Imaging Spectrograph
SZA	solar zenith angle
UTC	Coordinated Universal Time
UV	ultraviolet
UVIS	Ultraviolet Imaging Spectrograph

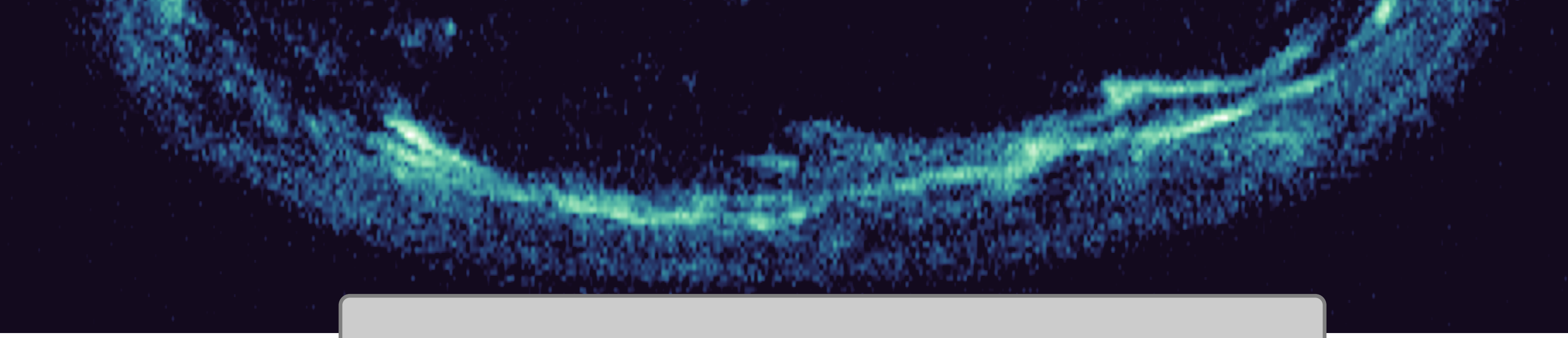

PREFACE

Colourful aurorae appearing in the terrestrial skies have been known to humankind for a long time, as evidenced by plenty of associated myths of a just as colourful nature. While in modern times named after the Roman goddess of dawn, AURORA, many different cultures have found a variety of names and explanations for this stunning phenomenon – spanning from battles between dragons in East Asian lore to a fast running firefox whose tail caused sparks lighting up the sky in Finnish mythology.

On a more scientific note, descriptive accounts of aurorae are known since the Greek and Roman natural philosophers. Suggested explanations of their origin however included a fair amount of guesswork for many more centuries, until Scandinavian scientists slowly began to unravel the relationship between this colourful light display and the Earth's magnetic field back in the 1800s. The foundation for our modern understanding of the terrestrial auroras has subsequently been lain by KRISTIAN BIRKELAND who formulated the first theories of atmospheric electric currents exciting atmospheric particles to emit visible light.

It was only recently that humankind's technological advance provided us access to space-based observations, with modern spacecraft orbiting our planet and others in the solar system to return to us ever increasing amounts of data on small-scale and large-scale conditions in various planetary magnetospheres. This led to the discovery of aurorae on other planets, from the rather diffuse emissions on Mars and Venus to the bright and dynamic light spectacles at Jupiter and Saturn.

Until the arrival of the CASSINI spacecraft at Saturn, little was known of the planet's auroral displays. Observations were limited to some spectral measurements obtained during the VOYAGER flybys and sparse imagery from the HUBBLE SPACE TELESCOPE (HST), making it challenging to gain significant insight into auroral dynamics or generation mechanisms. This changed drastically once CASSINI's ULTRAVIOLET IMAGING SPECTROGRAPH (UVIS) began to return entire sequences of crisp images from a variety of different perspectives, allowing us to observe the temporal evolution of the auroral morphology while also investigating parameters of the magnetospheric environment related to its generation.

This thesis summarizes a thorough investigation of this dataset of auroral imagery, aided by other in situ and remote sensing measurements of the CASSINI spacecraft and auroral observations of the HST. After a short introduction to space plasmas and the heliosphere in chapter 1, the current understanding of Saturn's magnetosphere and aurorae is presented in chapter 2. Chapter 3 gives an overview over the instrumentation and methodology used in this thesis. Studies describing the insights gleaned from the detailed scientific analyses performed over the course of this doctorate have been published in different journals and can be found attached in chapters 4 to 9. The results are summarized and discussed in the final chapter 10.

A. BADER performed all analysis work and drafted all publications contained in this thesis under guidance of S. V. BADMAN and L. C. RAY. Co-contributors both from LANCASTER UNIVERSITY and other research institutions assisted this work by providing further expertise on specific topics surrounding giant planet magnetospheres and aurorae, by sharing raw and processed data from the CASSINI mission for use in the analyses presented, and by providing invaluable knowledge about capabilities, limitations and quirks of the instruments collecting these data to allow for their proper use and interpretation.

This thesis is written in an alternative format. While most parts follow the traditional style, chapters which would normally lay out the scientific analyses and discuss their results have been replaced with peer-reviewed research articles which are included in their originally published form. Each publication can as such be considered its own well-contained science chapter, followed by the final chapter 10 in which the results are combined and discussed.

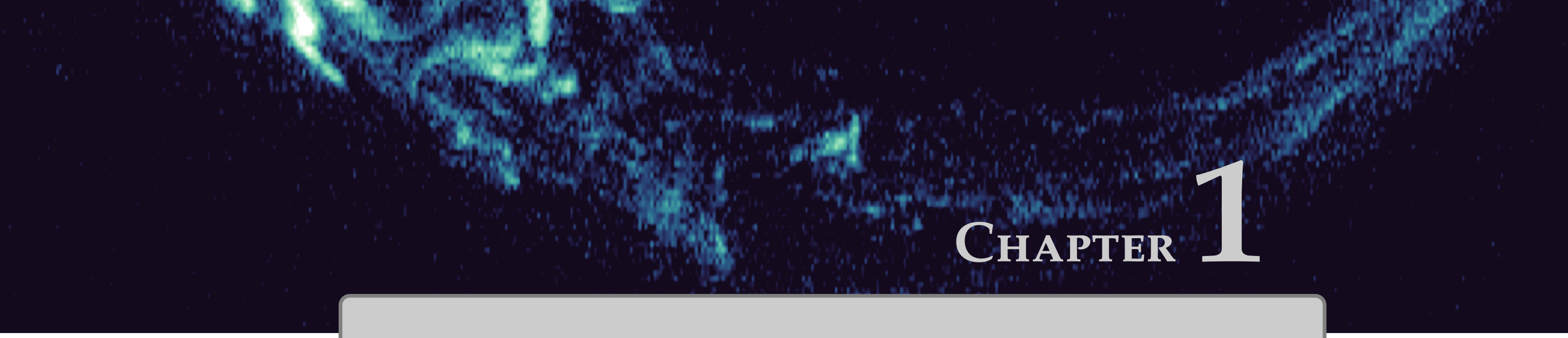

CHAPTER 1

INTRODUCTION

1.1 SPACE PLASMAS

The Plasma State

Plasma is one of the four fundamental states of matter, the others being solid, liquid and gas. In the plasma state, atoms are at least partly dissociated into their positive and negative components, i.e., ions and electrons. As charge is conserved, plasma is electrically "quasi-neutral" on the whole.

The interactions between single charged particles within an ideal plasma are determined by electromagnetic forces acting between them. The spatial scale over which one ion can influence its surroundings, limited by collective shielding of its potential by nearby electrons, is given by the Debye length,

$$\lambda_D = \sqrt{\frac{\varepsilon_0 k_B T_e}{n_e e^2}}. \tag{1.1}$$

Hereby ε_0 is the permittivity of free space and k_B is Boltzmann's constant, while T_e, n_e and e are the electron temperature, density and charge, respectively. Shielding of a plasma ion can only occur if the number of electrons within the Debye sphere, a sphere of radius λ_D around the considered ion, is sufficiently large. This is given when

$$N_D = \frac{4\pi}{3} n_e \lambda_D^3 \gg 1, \tag{1.2}$$

which is essentially the case for plasma at high temperatures and low densities and certainly true for solar wind and magnetospheric plasmas considered in this thesis.

Plasma does not need to be fully ionized in order to behave like an ideal plasma, but may also contain neutral particles. It is only required that the collision frequency between charged and neutral constituents is lower than the plasma frequency,

$$\omega_{pe} = \sqrt{\frac{n_e e^2}{m_e \varepsilon_0}}, \tag{1.3}$$

which describes the natural oscillation frequency of electrons of mass m_e about the ions in a quasi-neutral plasma.

As plasma predominantly consists of charged particles and is assumed collisionless due to the typically low number density, its behaviour is governed by electric and magnetic fields, **E** and **B**. These are described by Maxwell's equations,

$$\nabla \cdot \mathbf{E} = \frac{\rho_q}{\varepsilon_0} \tag{1.4}$$

$$\nabla \cdot \mathbf{B} = 0 \tag{1.5}$$

$$\nabla \times \mathbf{E} = -\frac{\partial \mathbf{B}}{\partial t} \tag{1.6}$$

$$\nabla \times \mathbf{B} = \mu_0 \left(\mathbf{j} + \varepsilon_0 \frac{\partial \mathbf{E}}{\partial t} \right), \tag{1.7}$$

with ρ_q as the charge density, μ_0 as the permeability of free space and **j** as the current density. Hereby equations (1.4) and (1.5) are Poisson's law and Gauss' law for magnetic fields, (1.6) is the Maxwell-Faraday equation and (1.7) is the Ampère-Maxwell law.

Single Particle Motion

In this section the motion of individual charged particles in the presence of electric and magnetic fields will be described, unaffected by interactions with surrounding particles like in a real plasma. A single particle with charge q and velocity **v** in an electromagnetic field will experience the Lorentz force,

$$\mathbf{F} = m \frac{d\mathbf{v}}{dt} = q \left(\mathbf{E} + \mathbf{v} \times \mathbf{B} \right). \tag{1.8}$$

In presence of a uniform magnetic field and absence of an electric field, the resulting motion reduces to a simple gyration about the magnetic field lines whose direction depends on the sign of the particle's charge. The angular frequency of this motion is known as gyrofrequency,

$$\omega_g = \frac{|q| B}{m}, \tag{1.9}$$

with B as the magnetic field strength, while the center of the gyration is known as the guiding center. The kinetic energy of the particle remains constant during the gyration, as the Lorentz force acts perpendicular to the particle's direction of motion,

$$\frac{d}{dt}\left(\frac{1}{2}m\mathbf{v}^2\right) = m\mathbf{v}\frac{d\mathbf{v}}{dt} = q\mathbf{v}\cdot(\mathbf{v}\times\mathbf{B}) = 0. \tag{1.10}$$

The velocity vector $\mathbf{v}$ is hereby always oriented perpendicular to the magnetic field, such that $\mathbf{v} = \mathbf{v}_\perp$.

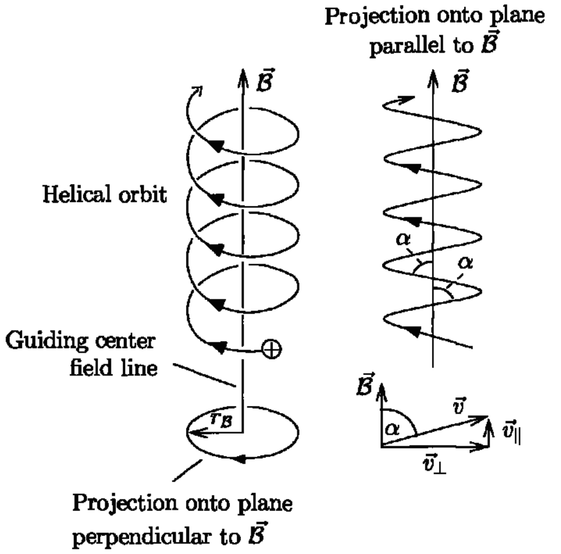

FIGURE 1.1: *Illustration of a charged particle's helical motion in a homogeneous magnetic field. Modified from Prölss [2004].*

If the particle has an additional velocity component $\mathbf{v}_\parallel$ parallel to the magnetic field, the total velocity is given by $\mathbf{v} = \mathbf{v}_\perp + \mathbf{v}_\parallel$ and the particle gyrates around the field lines while moving along them, describing a helical path such as shown in Figure 1.1. The angle at which it moves with respect to the magnetic field,

$$\alpha = \arctan\left(\frac{\mathbf{v}_\perp}{\mathbf{v}_\parallel}\right), \tag{1.11}$$

is called pitch angle. Values of $\alpha = 0°$ and $\alpha = 180°$ then describe particles moving parallel and antiparallel, respectively, to the background magnetic field (i.e., field-aligned), while $\alpha = 90°$ corresponds to pure gyration.

The motion of individual charged particles becomes more complicated in the presence of electric fields or other nonelectromagnetic forces. Any additional force $\mathbf{F}$ will result in a drift motion of the particle's guiding center, perpendicular to both $\mathbf{B}$ and $\mathbf{F}$ itself. The drift velocity $\mathbf{v_D}$ of the charged particle is given by

$$\mathbf{v_D} = \frac{\mathbf{F}\times\mathbf{B}}{qB^2}. \tag{1.12}$$

For an electric field **E** perpendicular to **B**, the additional force experienced by a charged particle is $\mathbf{F_E} = q\mathbf{E}$ such that

$$\mathbf{v_D} = \frac{\mathbf{E} \times \mathbf{B}}{B^2}. \tag{1.13}$$

We find that the drift velocity is in this case independent of both charge and mass of the particle, such that electrons and ions will drift in the same direction with a common velocity and no currents are induced; this is known as the "$\mathbf{E} \times \mathbf{B}$ drift".

Other forces typically acting on charged particles in planetary magnetospheres are related to the gradient and curvature of the magnetic field and to gravity and polarization, i.e.,

$$\mathbf{F}_\nabla = -\mu \nabla B \tag{1.14}$$

$$\mathbf{F_C} = m v_\parallel^2 \frac{\mathbf{R_C}}{R_C^2} \tag{1.15}$$

$$\mathbf{F_G} = -m\mathbf{g} \tag{1.16}$$

$$\mathbf{F_P} = -m\frac{d\mathbf{E}}{dt}, \tag{1.17}$$

with $\mathbf{R_C}$ as the local radius of magnetic field curvature and **g** as the gravitational acceleration. The gradient force is dependent on the magnetic moment,

$$\mu = \frac{m v_\perp^2}{2B} = \frac{W_\perp}{B}, \tag{1.18}$$

with $W_\perp$ as the kinetic energy associated with the perpendicular gyration. The magnetic moment is a characteristic constant also known as the first adiabatic invariant, as it is conserved if changes in the magnetic field are small compared to the time scale of the gyromotion.

As a charged particle moves slowly from a low into a high magnetic field strength region, its perpendicular velocity will increase to conserve its magnetic moment. With the particle's total energy $W = W_\parallel + W_\perp$ being unchanged in the absence of parallel electric fields, this can only occur through a reduction of its parallel velocity. The motion along the magnetic field line hence slows down as the magnetic field becomes stronger, up to the point where $\mathbf{v}_{\|} = 0$ and all kinetic energy is associated with the perpendicular gyration with a pitch angle of $\alpha = 90°$. As the mirror force $\mathbf{F}_{\nabla}$ continues acting on the particle regardless of its parallel velocity $\mathbf{v}_{\|}$, it is reflected back into regions of lower magnetic field, or "mirrored".

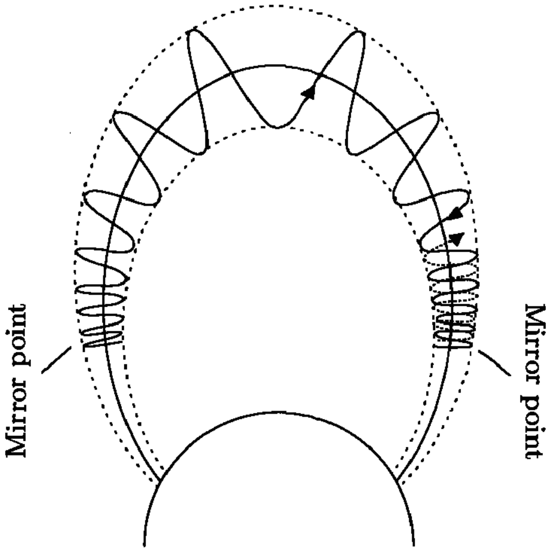

FIGURE 1.2: *Schematic of a charged particle's bounce motion in a planetary magnetic field, confined by magnetic mirrors at either end. Modified from Prölss [2004].*

Pitch angle and magnetic field strength along the particle's trajectory are hereby related through

$$\frac{B}{\sin^2(\alpha)} = \text{const.}, \tag{1.19}$$

such that the field strength at the mirror point ($\sin^2(\alpha) = 1$) can easily be determined with knowledge of a particle's pitch angle at a location of known magnetic field strength. For a dipole field such as found in planetary magnetospheres, there are two mirror points on each field line, essentially forming a magnetic bottle and trapping charged particles which bounce between them such as shown in Figure 1.2. However, depending on the initial/equatorial pitch angle a particle may not reach a region of large enough field strength to mirror before entering the atmosphere where it loses its energy in collisions with atmospheric neutrals and causes aurorae. At a point along the magnetic field line where the magnetic field strength is B, all particles with a pitch angle smaller than the loss cone angle

$$\alpha_{LC} = \arcsin\left(\sqrt{\frac{B}{B_{max}}}\right) \tag{1.20}$$

are lost to the atmosphere. Here B_{max} denotes the magnetic field strength just above the atmosphere.

Kinetic Theory and Phase Space

A macroscopic plasma, essentially a collection of particles, is difficult to describe in terms of the single particle behaviour detailed above. It is much easier to characterize the state of a plasma in terms of phase space density, i.e. by counting the number of particles located at a certain point in configuration space $\mathbf{r} = \begin{pmatrix} x \\ y \\ z \end{pmatrix}$ which have a velocity $\mathbf{v} = \begin{pmatrix} v_x \\ v_y \\ v_z \end{pmatrix}$. The phase space density for a collection of particles i located at $\mathbf{r}_i$ with velocity $\mathbf{v}_i$, respectively, is given by

$$f(\mathbf{r}, \mathbf{v}, t) = \sum_i \delta\big(\mathbf{r} - \mathbf{r}_i(t)\big)\delta\big(\mathbf{v} - \mathbf{v}_i(t)\big), \tag{1.21}$$

with $\delta(\mathbf{r}-\mathbf{r}_i) = \delta(x-x_i)\delta(y-y_i)\delta(z-z_i)$ and $\delta(\mathbf{v}-\mathbf{v}_i)$, similarly, as the three-dimensional Dirac delta functions.

This description allows the derivation of ensemble properties by calculating the moments of the distribution. Hereby the first moment gives the number density,

$$n(\mathbf{r}, t) = \int f(\mathbf{r}, \mathbf{v}, t) d\mathbf{v}, \tag{1.22}$$

and the second moment the bulk velocity,

$$u(\mathbf{r}, t) = \frac{1}{n(\mathbf{r}, t)} \int \mathbf{v} f(\mathbf{r}, \mathbf{v}, t) d\mathbf{v}, \tag{1.23}$$

while the third moment relates to the kinetic energy,

$$\langle \frac{1}{2} m \mathbf{v}^2 \rangle = \frac{1}{n(\mathbf{r}, t)} \int \frac{1}{2} m \mathbf{v}^2 f(\mathbf{r}, \mathbf{v}, t) d\mathbf{v}. \tag{1.24}$$

Phase space distributions cannot be directly measured, but can be inferred from the differential particle flux $J(W, \Omega, \mathbf{r}, t)$ within an energy band dW about W and within a solid angle $d\Omega$ observed at position $\mathbf{r}$ and at time t; this is the quantity typically measured by spacecraft-borne particle detectors. It is clear that the number density of particles depends on the phase space density as

$$dn = f(\mathbf{r}, \mathbf{v}, t) d\mathbf{v}, \tag{1.25}$$

or

$$dn = f(\mathbf{r}, \mathbf{v}, t) v^2 dv \; d\varphi \; \sin\vartheta d\vartheta = f(\mathbf{r}, \mathbf{v}, t) v^2 dv d\Omega \tag{1.26}$$

in spherical coordinates. Multiplying this quantity by v provides the differential flux, such that

$$J(W, \Omega, \mathbf{r}, t) dW d\Omega = f(\mathbf{r}, \mathbf{v}, t) v^3 dv d\Omega. \tag{1.27}$$

Finally, simplifying this expression using $dW = mvdv$ yields

$$f(\mathbf{r}, \mathbf{v}, t) = \frac{m^2}{2W} J(W, \Omega, \mathbf{r}, t), \tag{1.28}$$

a straightforward relation between differential particle flux and phase space distribution function.

Magnetohydrodynamics

In the theoretical concept of magnetohydrodynamics (MHD), the collective behaviour of charged particles in a plasma is described by treating plasma as a conducting fluid. This framework is applicable if the gyroperiod of the plasma constituents is smaller than the characteristic time scale of changes in the fluid and the scale size of the plasma significantly exceeds the charged particles' gyroradius. Similar to unmagnetised fluids, mass and momentum are conserved and viscous and pressure forces act on the particles; furthermore, charge conservation applies and the Lorentz force acts within a conducting plasma.

In MHD, the macroscopic plasma properties are described by the mass density, ρ_m, the bulk velocity, $\mathbf{u}$, and the pressure, P. We assume a plasma which is quasineutral within the characteristic length and time scales, such that $n_e \approx n_i = n$. The continuity equation, describing the conservation of mass, is then

$$\frac{\partial \rho_m}{\partial t} + \nabla \cdot (\rho_m \mathbf{u}) = 0 \tag{1.29}$$

while the momentum conservation equation is given by

$$\rho_m \left(\frac{\partial \mathbf{u}}{\partial t} + (\mathbf{u} \cdot \nabla)\mathbf{u} \right) = -\nabla P + \mathbf{j} \times \mathbf{B} + \rho_m \mathbf{g}. \tag{1.30}$$

The first two terms on the right hand-side of equation (1.30) describe the effects of a thermal pressure gradient and the magnetic forces, respectively. We can find another expression for the second term by taking the cross product of Ampère's law (1.7) with **B**, giving

$$\mathbf{j} \times \mathbf{B} = -\nabla \left(\frac{B^2}{2\mu_0} \right) + \frac{1}{\mu_0} (\mathbf{B} \cdot \nabla)\mathbf{B}. \tag{1.31}$$

Here $p_B = \frac{B^2}{2\mu_0}$ can be identified as the magnetic pressure, such that the first term on the right hand-side becomes the magnetic pressure force similar to the thermal pressure force in equation (1.30). The second term describes the magnetic tension force, acting as a restoring force in response to the deformation of the magnetic field. These equations are accompanied by the simplified Ohm's law,

$$\mathbf{j} = \sigma(\mathbf{E} + \mathbf{u} \times \mathbf{B}) \tag{1.32}$$

which describes the relationship between the electric field and the current density with σ as the conductivity.

Combining Ohm's law (1.32) with Faraday's law (1.6) and Ampère's law (1.7) yields the induction equation describing the temporal change of the magnetic field,

$$\frac{\partial \mathbf{B}}{\partial t} = \nabla \times (\mathbf{u} \times \mathbf{B}) + \frac{1}{\mu_0 \sigma} \nabla^2 \mathbf{B}. \tag{1.33}$$

The terms on the right hand-side are hereby the convective and diffusive terms, respectively. Their ratio is also known as the Reynolds number, which indicates the relative importance of convection and diffusion to the evolution of the magnetic field. It is given by

$$R_m = \frac{|\nabla \times (\mathbf{u} \times \mathbf{B})|}{|\nabla^2 \mathbf{B}/\mu_0\sigma|} = \mu_0 \sigma u L, \tag{1.34}$$

where u is the characteristic perpendicular velocity of the plasma and L the length scale of variations in $\mathbf{B}$. In typical collisionless space plasmas with $\sigma \sim \infty$ and very large L, we find $R_m \gg 1$ indicating that convection dominates over diffusion. This means that the motion of the plasma and the magnetic field are connected to one another; the magnetic flux is "frozen in" to the fluid. As a result of this, particles initially located on the same field line will remain "attached" to it as the plasma convects through space.

However, this frozen-in flux approximation breaks down in the process of magnetic reconnection where oppositely directed magnetic fields neighbouring another mix and the field topology is reconfigured. The change in magnetic field across the boundary between two such magnetic fields results in a current flowing within the boundary, forming the current sheet. Compressed by thermal and magnetic pressure, this current sheet becomes thinner, decreasing the characteristic length scale and hence also the Reynolds number until the diffusion term dominates the convection term in equation (1.33). The frozen-in flux approximation is broken, and the magnetic field can diffuse from both sides into the current sheet where the oppositely directed field lines essentially break up and reconnect with one another before being ejected from the diffusion region due to magnetic tension forces. The reconnection site in the center of the diffusion region is free of any magnetic field and also known as "X-line". A two-dimensional schematic illustrating the theoretical Sweet-Parker geometry of this process [*Parker*, 1957; *Sweet*, 1958] is shown in Figure 1.3.

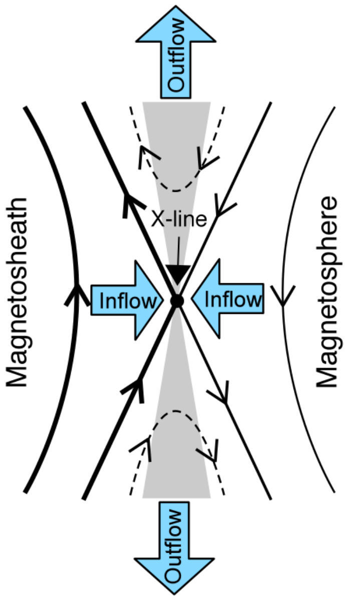

FIGURE 1.3: *Schematic showing the magnetic reconnection process between the interplanetary magnetic field and magnetospheric field lines, the current sheet highlighted in grey. Modified from Masters et al. [2012].*

Field-aligned Currents

Electrical currents are essential for facilitating various coupling mechanisms in planetary magnetospheres, such as momentum coupling through the Lorentz force and electric coupling through induction. Field-aligned currents (FACs) in specific couple the magnetosphere to the ionosphere and are closely related to the generation of auroral emissions.

The deep physical connection between electrical currents and plasma motion precludes a clear identification of cause and effect, but it may be useful to view currents as the effect of plasma motions distorting the magnetic field. From this perspective, the generation of currents can be described by combining Faraday's law (1.6) and Ampère's law (1.7), neglecting the displacement current in order to exclude high-frequency waves. With the electric field in a fixed frame of reference dominated by $-\mathbf{v} \times \mathbf{B}$, one obtains

$$\frac{\partial \mathbf{j}}{\partial t} = -\frac{1}{\mu_0} \nabla \times [\mathbf{B}(\nabla \cdot \mathbf{v}) + (\mathbf{v} \cdot \nabla)\mathbf{B} - (\mathbf{B} \cdot \nabla)\mathbf{v}] \tag{1.35}$$

as a general description. Considering small perturbations of an initially uniform magnetic field, an FAC can be obtained from the first order terms of (1.35) as

$$\frac{\partial \mathbf{j}_{\|}}{\partial t} = \frac{1}{\mu_0} (\mathbf{B} \cdot \nabla)\Omega_{\|} \tag{1.36}$$

with $\Omega_{\|}$ as the field-aligned component of the flow vorticity $\Omega = \nabla \times \mathbf{v}$. This means that field-aligned currents (FACs) can for example be formed by a clockwise twisting of a magnetic flux tube which decreases in the direction of the magnetic field [*Paschmann et al.*, 2003]. A discussion of the generation of FACs specifically in the context of magnetosphere-ionosphere coupling at Saturn can be found in section 2.2.

Plasma Waves and Wave-Particle Interactions

In the typically collisionless space plasmas, waves play an important role for the transfer of energy between different spatial regimes, particles and fields. On Earth we are used to waves occurring in neutral fluids such as air and water, where pressure perturbations excite compressional sound waves. In space plasmas however, the dynamics are additionally connected to electromagnetic fields – space plasmas can hence support a variety of waves with very different properties. In a magnetized plasma waves can propagate *parallel* or *perpendicular* to the magnetic field, the electric field perturbation they excite can occur *longitudinal* or *transverse* to their wave vector **k**, and they may be of an *electromagnetic* or *electrostatic* nature depending on whether they involve a perturbation of the magnetic field or not.

In a warm MHD plasma three different electromagnetic wave modes can be found. One of these is the transverse *shear Alfvén* mode whose waves propagate parallel or oblique to the magnetic field with a phase velocity $v_p = v_A \cos\theta$, where θ is the angle between **k** and **B** and

$$v_A = \frac{B}{\sqrt{\mu_0 \rho_m}} \tag{1.37}$$

is the so called Alfvén velocity. The magnetic field perturbations associated with shear Alfvén waves are perpendicular to both **B** and **k**, with magnetic tension acting as the restoring force. This wave mode has no effect on the plasma density/pressure or magnetic field magnitude and is hence dispersionless, but it may act to accelerate auroral particles if the time and length scales of the waves are similar to the basic scales of the plasma [e.g., *Saur et al.*, 2018]. The two other wave modes are the longitudinal *fast magnetosonic* and *slow magnetosonic* modes which carry changes of plasma and magnetic pressure and plasma density.

Other wave modes associated with ion oscillations are *electrostatic ion cyclotron* waves, low-frequency waves which are most intense near the ion gyrofrequencies and their harmonics, and (electrostatic) *ion acoustic waves* which are typically broadband with frequencies up to the ion plasma frequency. Both are longitudinal wave modes, propagating nearly perpendicular and parallel to the magnetic field, respectively. They are typically observed in ion pickup regions and on auroral field lines where field-aligned ion beams are present and energy transfer between waves and local auroral particles may occur [e.g., *Kindel and Kennel*, 1971; *Kintner et al.*, 1979; *André et al.*, 1987; *Wahlund et al.*, 1994].

Auroral hiss emissions are broadband whistler mode waves at frequencies below the electron gyrofrequency ($\sim$ 10s – 100s kHz at Saturn) which are right-hand polarized and propagate within a cone angle relative to the magnetic field. They are also observed on auroral field lines at Earth, Jupiter and Saturn, where they are thought to interact with field-aligned electron beams leading to electron scattering and acceleration [e.g., *Maggs*, 1976; *Gurnett et al.*, 1983; *Kopf et al.*, 2010; *Tetrick et al.*, 2017; *Elliott et al.*, 2018].

Another signature of wave-particle interactions is the occurrence of auroral radio emissions, known as auroral kilometric radiation at Earth, Jovian hectometric radiation at Jupiter and Saturn kilometric radiation (SKR) at Saturn. They are thought to be generated through the cyclotron maser instability, driven by antiplanetward beams of accelerated electrons in an environment of low-density magnetized plasma such as present in auroral regions, and are observed at frequencies above the local electron gyrofrequency. Remote observation of these auroral radio emissions can provide global insight into auroral and magnetospheric dynamics [e.g., *Wu*, 1985; *Zarka*, 1998; *Louarn et al.*, 2017; *Lamy et al.*, 2018b].

1.2 THE HELIOSPHERE

At the center of the solar system, the Sun produces a large amount of energy through fusion of Hydrogen in its core where pressure and temperature are sufficiently high. The so generated energy is transported to the surface and heats the solar corona, essentially the Sun's atmosphere. The high gas pressure arising in this region continuously pushes magnetised coronal plasma away from the Sun, driving the solar wind [*Parker*, 1958]. The solar wind flow accelerates up to $\sim 400 - 800\,\mathrm{km/s}$ within a few solar radii, after which it travels radially outward with relatively constant velocity. It eventually breaks down as it reaches the termination shock, marking the transition from the heliosphere into the heliosheath, beyond which the heliopause is the only separation between the solar system and interplanetary space [e.g., *Krimigis et al.*, 2019]. The shape of the heliosphere is still uncertain, but recent measurements from the VOYAGER and CASSINI spacecraft suggest that it is of bubble-like shape instead of the previously proposed magnetosphere-like shape with an extended tail shaped by the interstellar flow [e.g., *Dialynas et al.*, 2017]. An illustration of this is shown in Figure 1.4.

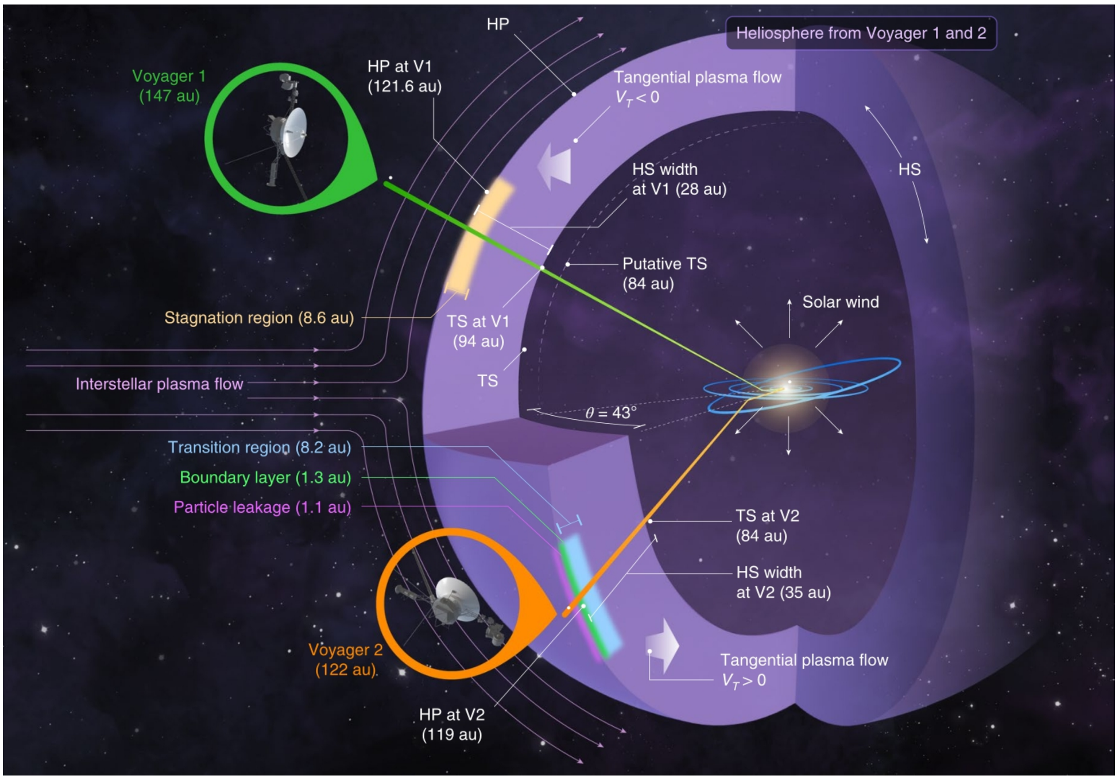

FIGURE 1.4: *Concept of the bubble-like heliosphere based on* VOYAGER *1 and 2 observations. The trajectories of the two spacecraft are indicated in green and orange; from their departure in the inner solar system passing the termination shock (TS), heliosheath (HS) and heliopause (HP) out of the heliosphere. Taken from Krimigis et al. [2019].*

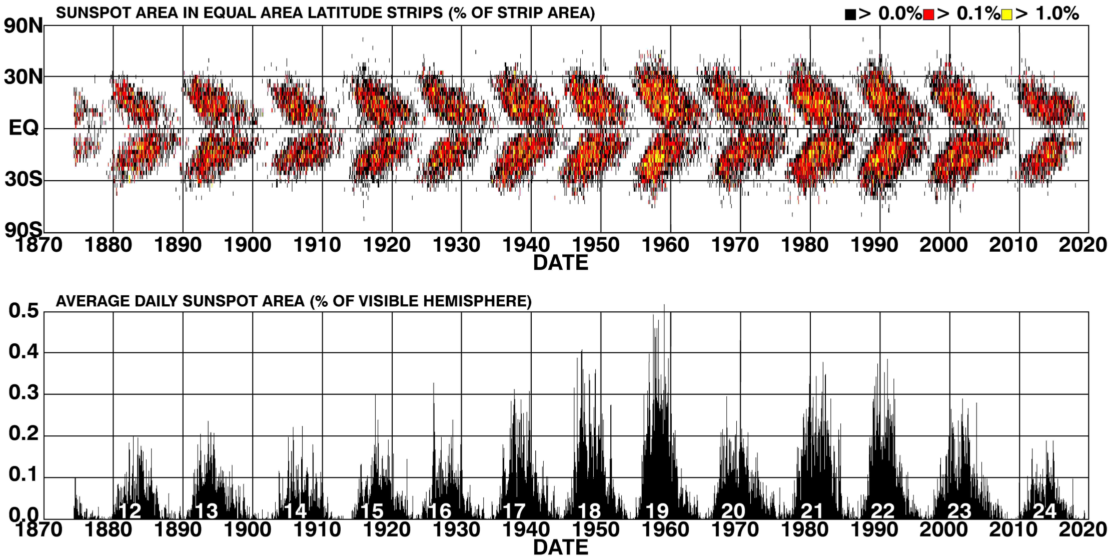

Figure 1.5: *The occurrence of sunspots over time. The top panel shows their latitudinal distribution and the bottom panel shows their total area. Image credit: NASA / David Hathaway.*

The Sun has a roughly dipolar magnetic field which is thought to be generated by the convection of plasma in the solar interior, acting as a dynamo. Its polarity periodically reverses every ~ 11 years, with solar activity decreasing and increasing over the course of this so called solar cycle. One indicator of solar activity is the occurrence of dark spots on the Sun's surface which mark cooler regions featuring intense magnetic field strengths. They are known as sunspots and are typically the origin of transient energetic phenomena such as solar flares and coronal mass ejections. Both sunspot number and location vary characteristically over the course of a solar cycle, as shown in Figure 1.5. Periods of low solar activity are marked by the near absence of sunspots; sunspots appear at higher latitudes in the inclining phase and at lower latitudes in the declining phase of the solar cycle.

The solar wind plasma is characterized by high conductivities and large length scales, such that the frozen-in flux approximation is satisfied. This means that plasma ejected from the Sun carries with it the Sun's internal magnetic field, then known as interplanetary magnetic field (IMF). With the Sun rotating at a period of ~ 24.5 days at the equator [*Snodgrass and Ulrich*, 1990], the IMF is coiled into a spiral-like configuration

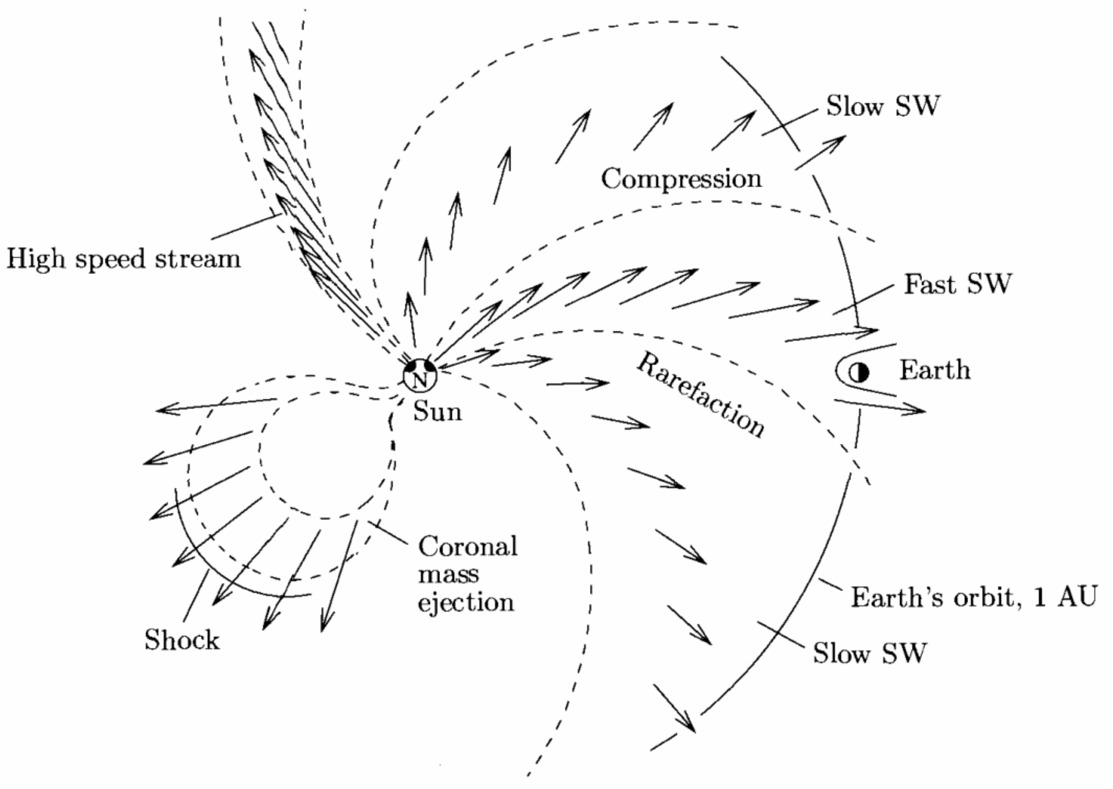

FIGURE 1.6: *Structure of the solar wind in the ecliptic, viewed from above the Sun. Dashed lines illustrate the shape of the Parker spiral. Taken from Prölss [2004].*

as the footpoint of a magnetic flux tube rotates while the associated solar wind plasma moves radially outward. This is known as the Parker spiral [*Parker*, 1958] and illustrated in Figure 1.6. The spiral angle of the magnetic field, defined as arctan(B_{tan}/B_{rad}) with B_{tan} and B_{rad} as the tangential and radial IMF components, respectively, increases with distance from the Sun. While the field is almost radial near the Sun with a Parker spiral angle of $\sim 0°$, the angle is typically $\sim 45°$ at Earth and $\sim 87°$ at Saturn [*Jackman et al.*, 2008b]. However, this simplified description does not account for the variable tilt of the Sun's magnetic dipole field relative to its rotation axis or for the complex field structure observed during solar maximum.

The solar wind is typically found to exhibit a bimodal velocity structure. Slow solar wind, of the same composition as the solar corona and emerging from the solar equatorial region, has a typical velocity of $\sim 400\,\text{km/s}$ at the Earth orbit. Fast solar wind is of photospheric composition, is thought to originate from coronal holes and has a velocity of ~ 750 km/s. Fast solar wind may "catch up" to slow solar wind, forming a large scale compression also known as corotating interaction region (CIR), also illustrated in Figure 1.6. A CIR is typically preceded by a forward shock in the slow solar wind and followed by a reverse shock and a rarefaction region.

Chapter 2

Saturn's Magnetosphere

2.1 The Magnetospheric Structure of Saturn

Saturn's magnetosphere is the second largest magnetosphere in our solar system. After several flyby missions, Cassini was the first and until now only spacecraft orbiting Saturn (2004-2017) and performing extensive observations of its plasma environment.

The magnetosphere, an illustration of which is shown in Figure 2.1, is formed as the solar wind is countered by Saturn's intrinsic magnetic field and locally produced plasma, representing an obstacle in the steady solar wind flow. The solar wind plasma is slowed down and diverted around the magnetosphere, separated from Saturn's

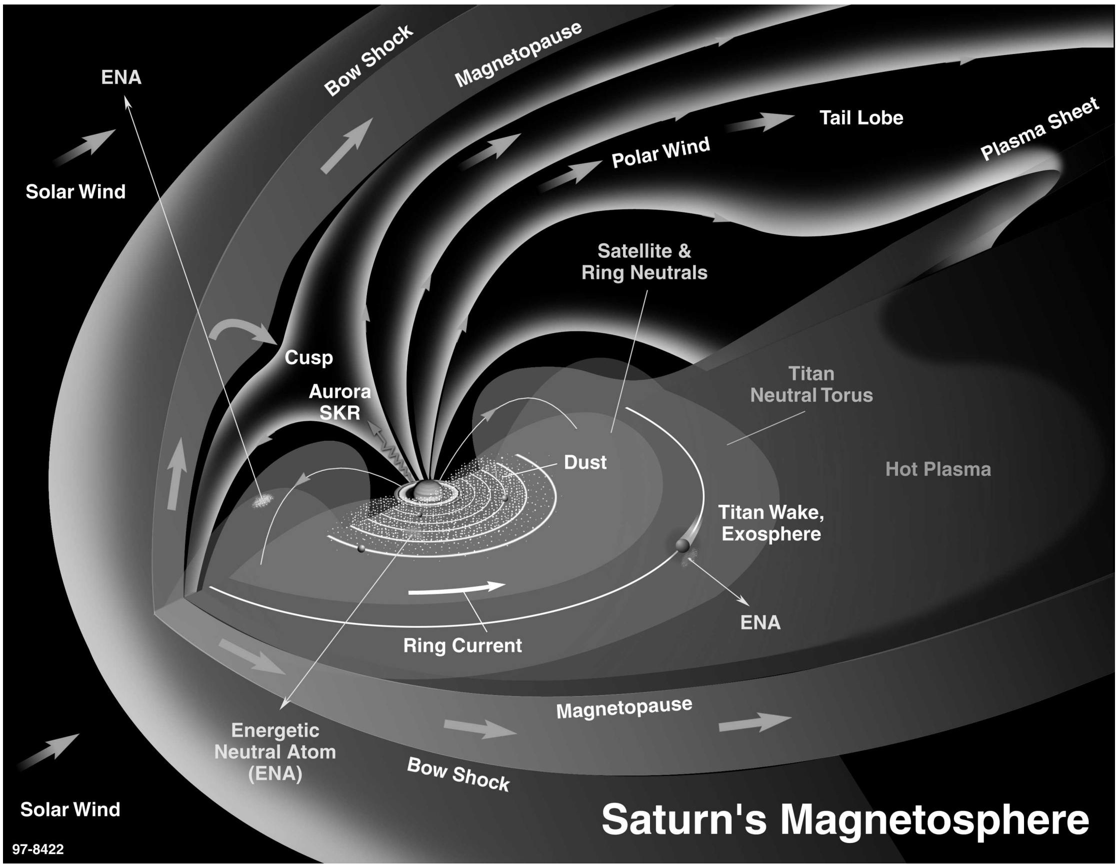

Figure 2.1: *Detailed illustration of the global configuration of Saturn's magnetosphere. Image credit: NASA/JPL.*

magnetospheric plasma by the magnetopause. Magnetospheric neutrals and plasma are largely provided by the moon Enceladus with its numerous geysers, releasing water vapor and ice into Saturn's inner magnetosphere. Outside of Enceladus' orbit, in the middle magnetosphere, the ejected material mass- and momentum-loads the system and the plasma angular velocity begins to depart from rigid corotation. This region also includes the ring current. The subcorotating plasma takes the shape of a magnetodisc, stretching the magnetic field in the equatorial plane. The outer magnetosphere, beyond Titan's orbit, is dominated by highly stretched field lines and a thin hinged magnetodisc. Quasi-periodic magnetotail reconnection of the nightside magnetodisc is thought to control the plasma outflow, balancing the plasma loading from Enceladus. This section reviews the current understanding of the structure of Saturn's magnetosphere and details its most relevant components.

The Internal Magnetic Field

Saturn's magnetic field was first investigated during the Pioneer 11 flyby in 1979 [*Smith et al.*, 1980a; *Acuña et al.*, 1980], and soon after during the two Voyager flybys in 1980/1981 [*Connerney et al.*, 1982]. These observations showed a close alignment between the dipolar magnetic field and the planet's spin axis as well as a significant quadrupole moment, describing a northward shift of the magnetic equator from the planetary equator.

With the arrival of Cassini at Saturn, the magnetic field could be characterized more accurately - data obtained during the Grand Finale phase of the Cassini mission revealed a dipole tilt $< 0.0095°$ and a $0.0466\,R_S = 2808$ km northward shift of the magnetic dipole [*Dougherty et al.*, 2018]. There is no evidence of longitudinal variation in the field [*Cao et al.*, 2011], preventing an accurate determination of the planet's rotation rate.

The perfect axisymmetry of Saturn's internal magnetic field is puzzling, as Cowling's theorem precludes the generation of an axisymmetric field through a dynamo process [*Cowling*, 1933]. A widely accepted explanation for this non-conformity proposes that nonaxisymmetric magnetic moments are electromagnetically shielded by differential rotation in an electrically conducting layer above the deep dynamo region [*Stevenson*, 1980, 1982]. Cassini's Grand Finale measurements revealed latitudinally banded magnetic fields, supporting this theory [*Dougherty et al.*, 2018].

Saturn's internal field **B** outside of the dynamo region is modelled as the gradient of a magnetic scalar potential V,

$$\mathbf{B} = -\nabla V, \tag{2.1}$$

assuming that the field is approximately curl-free (i.e., the effects of external current systems are negligible). This potential is then

$$V(r,\theta,\phi) = \sum_{n=1}^{\infty} \sum_{m=0}^{n} R_\mathrm{S} \left(\frac{R_\mathrm{S}}{r}\right)^{n+1} P_n^m(\cos\theta) \left[g_n^m \cos(m\phi) + h_n^m \sin(m\phi)\right], \tag{2.2}$$

with R_S as the radius of Saturn and r, θ and ϕ as the spherical planetocentric coordinates. $P_n^m(\cos\theta)$ are hereby Schmidt-normalised Legendre polynomials, while g_n^m and h_n^m are Gauss coefficients describing the contribution of each spherical mode to the field.

The values of n and m indicate the degree and order of the spherical harmonic field expansion, respectively. The Gauss coefficients of the most recent "CASSINI 11" field model are given in Table 2.1. In spherical planetocentric coordinates,

$$B_r = -\frac{\partial V}{\partial r}, \quad B_\theta = -\frac{1}{r}\frac{\partial V}{\partial \theta}, \quad B_\phi = -\frac{1}{r\sin\theta}\frac{\partial V}{\partial \phi} \tag{2.3}$$

gives the magnetic field components corresponding to the modelled potential $V(r,\theta,\phi)$.

Enceladus: The Main Source of Magnetospheric Plasma

Enceladus is a small moon (~ 500 km diameter) located in Saturn's inner magnetosphere at a radial distance of ~ 4 R_S. The first flybys performed by CASSINI in 2005 revealed significant cryovolcanic activity - dozens of distinct water-rich jets were found to erupt from the moon's southern polar terrain (see Fig. 2.2) where ice grains and water vapor are ejected from four prominent surface fractures, dubbed "tiger stripes" [e.g., *Dougherty et al.*, 2006; *Hansen et al.*, 2006; *Porco et al.*, 2006]. The cause of Enceladus' dynamic outgassing is thought to be the tidal deformation and energy dissipation arising from its orbital resonance with the moon Dione, upholding the eccentricity of Enceladus' orbit and causing diurnal variations in the magnitude and direction of the tidal distortion.

This energy input likely maintains a global or regional subsurface ocean, providing ejecta and enhancing the tidal stresses imposed on the moon's icy shell [e.g., *Hedman et al.*, 2013; *Porco et al.*, 2014; *Patthoff et al.*, 2019].

The atmospheric plumes are dominated by water and contain significant amounts of carbon dioxide, an unidentified species with a mass-to-charge ratio of 28 (either carbon monoxide or molecular nitrogen), and methane [*Waite et al.*, 2006]. The total mass flux is estimated at ∼ 200 kg/s for water vapor [*Hansen et al.*, 2011] and ∼ 50 kg for water ice [*Ingersoll and Ewald*, 2011], although the emission rates were found to be highly variable over time [e.g., *Saur et al.*, 2008; *Smith et al.*, 2010] and the solid-to-gas ratio varies between different geysers [*Hedman et al.*, 2018]. The ejected particles easily escape Enceladus' weak gravitational field and populate a neutral torus [*Johnson et al.*, 2006] and Saturn's E-ring [*Spahn et al.*, 2006; *Mitchell et al.*, 2015a].

TABLE 2.1: *Gauss coefficients of the* CASSINI *11 internal magnetic field model, derived from* CASSINI *Grand Finale magnetic field measurements [Dougherty et al., 2018]*

	Value (nT)	Uncertainty (nT)
g_1^0	21140.2	1.0
g_2^0	1581.1	1.2
g_3^0	2260.1	3.2
g_4^0	91.1	4.2
g_5^0	12.6	7.1
g_6^0	17.2	8.2
g_7^0	-59.6	8.1
g_8^0	-10.5	8.7
g_9^0	-12.9	6.3
g_{10}^0	15.0	7.0
g_{11}^0	18.2	7.1

Only a minority of the produced neutrals will eventually be ionized. Neutrals can be directly ionized by either electron impact ionization or photoionization, adding new ions and mass-loading the plasma environment. Charge exchange (neutral-ion collisions) on the other hand keeps the ion population constant and instead momentum-loads the system as the newly ionized particles are generally moving slower than the surrounding plasma [e.g., *Blanc et al.*, 2015] and the neutrals created in this process escape the magnetic field unimpeded as energetic neutral atoms (ENAs). The fraction of neutrals which is converted into plasma ranges between 17 – 38% [e.g., *Jurac and Richardson*, 2005; *Cassidy and Johnson*, 2010]; Enceladus hence provides plasma at a rate of 12 – 250 kg/s [*Bagenal and Delamere*, 2011] if a neutral production rate of 70 – 750 kg/s [*Smith et al.*, 2010] is

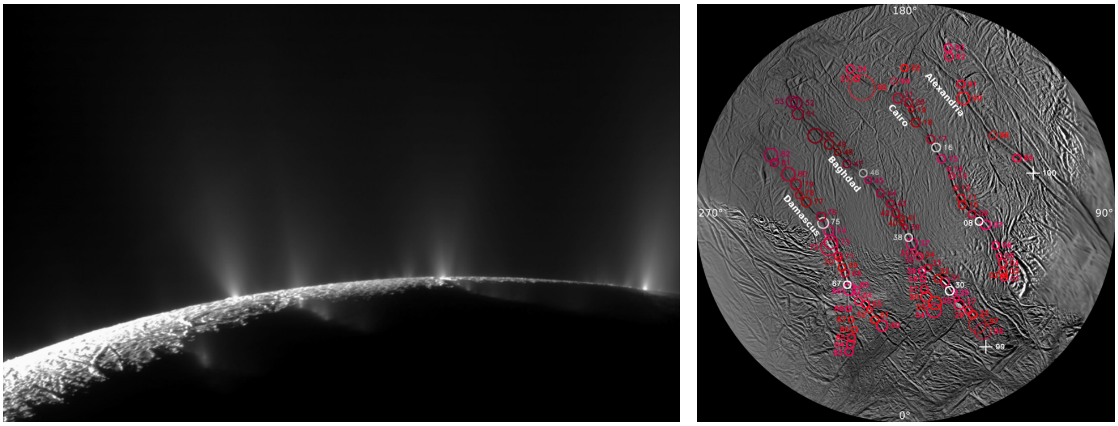

Figure 2.2: *Water plumes on Enceladus. (Left) Mosaic of* Cassini*'s ISS images of the south polar terrain, at a resolution of* $\sim 80\,\mathrm{m/pixel}$ *and (right) Basemap of the south polar terrain, showing the "tiger stripes". Observed jet sources are marked with colored circles. Modified from Porco et al. [2014].*

assumed.

Radiation Belts

Saturn's inner and middle magnetosphere is dominated by ion and electron radiation belts (see Figure 2.3) which have first been observed during the Pioneer 11 flyby [*Fillius and Ip*, 1980]. The main radiation belts extend from the outer edge of the F-ring (2.3 R_S) to roughly the orbit of the moon Tethys (4.9 R_S); they are clearly separated from one another by the major moon orbits (Janus at 2.5 R_S, Mimas at 3.1 R_S, and Enceladus at 4.0 R_S) as the moons remove charged particles while they orbit close to the equatorial plane [e.g., *Krupp et al.*, 2009; *Roussos et al.*, 2011]. Due to this separation, the main radiation belts are very stable as they are to some degree protected by external dynamics. However, between the orbits of Tethys and Dione (6.4 R_S) an additional transient radiation belt has been observed to appear in response to interplanetary events caused by solar eruptions [*Roussos et al.*, 2008].

The formation process of Saturn's ion radiation belts is not entirely understood. At least the high energy part of the ion distribution in the main belts and the small but energetic D-ring radiation belt [*Roussos et al.*, 2018] are thought to originate from the comic ray albedo neutron decay (CRAND) process [*Kollmann et al.*, 2013] - galactic cosmic

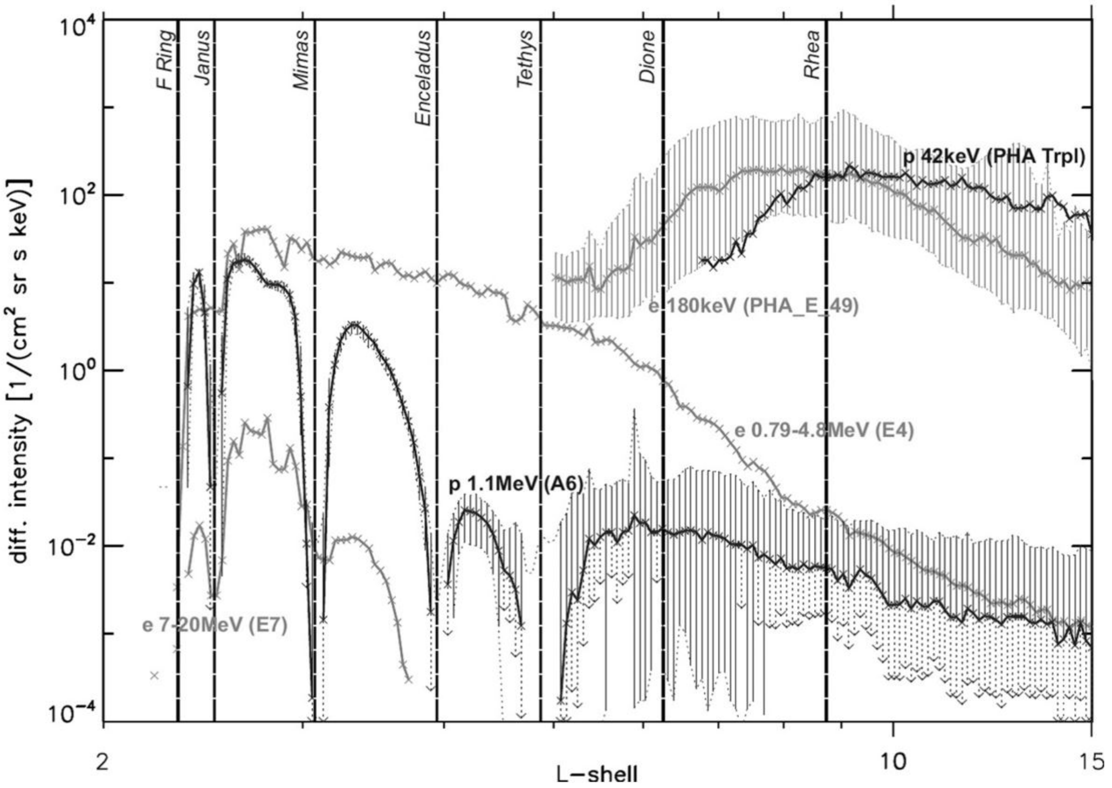

FIGURE 2.3: *Differential intensities of energetic protons (black, labelled with "p") and electrons (grey, labelled with "e") versus L-shell. The intensities shown are median averages from the entire CASSINI mission, obtained from the CASSINI MIMI instrument during times when CASSINI passed the equatorial region. The energy ranges and instrument channels considered are given next to the graphs. Taken from Krupp et al. [2018].*

rays impact material in Saturn's atmosphere, moons and rings, and cause energetic secondary neutrons to be emitted into space, which then decay into protons and electrons populating the radiation belts. This is supported by observations showing that the proton radiation belt intensity follows the solar cycle [*Roussos et al.*, 2011], as the access of galactic cosmic rays to Saturn's magnetosphere and hence also the CRAND process are directly related to solar activity. Recent modelling also proposed in-situ acceleration through wave-particle interaction as a possible source of trapped electron radiation belts [*Woodfield et al.*, 2018].

Ring Current

Outside of about 6 R_S, Saturn's magnetic field configuration starts to become more stretched due to the existence of an azimuthal ring current. This has been observed in magnetic field and particle data from the Pioneer 11 and Voyager flybys [e.g., *Smith et al.*, 1980b; *Connerney et al.*, 1981; *Ness et al.*, 1981, 1982; *Krimigis et al.*, 1983] and was investigated in more detail during the Cassini era [e.g., *Bunce et al.*, 2007, 2008b; *Kellett et al.*, 2010, 2011; *Sergis et al.*, 2010].

The ring current is carried by magnetospheric ions and electrons drifting azimuthally around the planet at different speeds and in different directions depending on their charge. In Saturn's rapidly rotating nonuniform magnetospheric field, this drift occurs due to the single particle curvature drift and the inertia drift associated with plasma corotation with the planet. The magnetic perturbation field induced by this current points northward at the inner edge of the ring current and southward at the outer edge. This reduces the magnetic field close to the planet but increases it in the outer magnetosphere, essentially stretching the planetary magnetic field lines away from the planet in the equatorial plane [e.g., *Gombosi et al.*, 2009; *Sergis et al.*, 2018]. The ring current statistically carries 9.2 ± 1.0 MA in total and maximizes at a radial distance of $\sim 9.5\,R_S$, although it can extend from $\sim 3-20\,R_S$ with an estimated half-thickness of $\sim 1.5\,R_S$ [*Carbary et al.*, 2012].

It is worth pointing out that the ring current is highly dynamic and often asymmetric. Imaging of ENAs, which allows for remote observations of the global equatorial ring current from above or below the planet, revealed that the ring current frequently exhibits distinct and persistent azimuthal intensity variations [e.g., *Krimigis et al.*, 2007; *Carbary et al.*, 2008b]. Furthermore, the asymmetric ring current has been shown to be enhanced in a periodic manner at roughly the planetary rotation period [e.g., *Paranicas et al.*, 2005; *Carbary et al.*, 2008a; *Mitchell et al.*, 2009a].

Magnetodisc and Magnetotail

In the outer magnetosphere, the magnetic field is distorted into a non-dipolar current sheet configuration as the magnetic tension cannot maintain balance with the outward

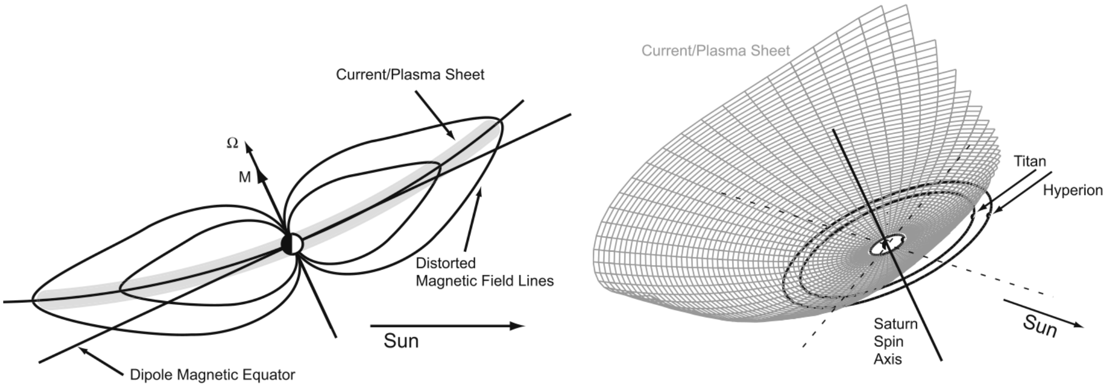

Figure 2.4: *Schematic illustrating the distortion of Saturn's magnetodisc. (Left) View of the noon-midnight meridian and (right) three-dimensional illustration of the bowl-shaped current sheet. Taken from Arridge et al. [2008a].*

plasma pressure and centrifugal forces. Newly added plasma, centrifugally confined to the equatorial region, is driven outward and the plasma corotation with the planet breaks down. Consequently, the closed magnetic field lines become highly stretched and bent back azimuthally due to the increasing subcorotation of the plasma populations in the outer magnetosphere, forming the magnetodisc [e.g., *Vasyliūnas*, 1983; *Arridge et al.*, 2008b]. Due to the steady flow of the solar wind, the magnetodisc is displaced from the rotational equator such that it takes the shape of a bowl [*Arridge et al.*, 2008a], as is illustrated in Figure 2.4.

The extent of the magnetodisc is on the dayside limited by the magnetopause standoff distance, as the solar wind pressure counters the outward centrifugal forces acting on the plasma in the magnetodisc current sheet. The location of Saturn's magnetopause was found to be highly variable depending on both the internal plasma pressure and the solar wind conditions, varying by several Saturn radii around roughly 25 R_S [e.g., *Arridge et al.*, 2006; *Achilleos et al.*, 2008; *Pilkington et al.*, 2015]. On the nightside however, solar wind drag acts to elongate the already stretched magnetosphere to much larger distances from Saturn, forming the magnetotail. The magnetic field lines become parallel, pointing radially outward above the current sheet and radially inward below. Outside the current sheet are the lobes, containing the open flux of the system - magnetic field lines connected to Saturn's ionosphere on one end and to the solar wind magnetic field on the other [e.g., *Gombosi et al.*, 2009].

2.2 THE DYNAMICS OF SATURN'S MAGNETOSPHERE

Global Transport of Mass and Energy

Most plasma in Saturn's magnetosphere is provided by the moon Enceladus in the inner magnetosphere and lost downtail through magnetic reconnection and the associated plasmoid ejections in the magnetotail. The processes responsible for the transport of plasma between these stages are diverse and the topic of ongoing investigation.

From its origin near Enceladus's orbit, plasma is transported through the magnetosphere mainly by radial interchange. "Fingers" of hot and tenuous plasma from the middle magnetosphere are hereby injected into the rather cold and dense plasma of the inner magnetosphere, driven by the centrifugal interchange instability [e.g., *Gold*, 1959; *Southwood and Kivelson*, 1987; *Thomsen*, 2013]. These injections are relatively small with a width of $\sim 1\,\mathrm{R_S}$ and are observed at radial distances between $6-10\,\mathrm{R_S}$, occurring roughly once per day [e.g., *Hill et al.*, 2005; *Chen and Hill*, 2008]. No clear ordering in local time (LT) has been observed, although some studies suggest that such events may occur more frequently at the nightside [*Kennelly et al.*, 2013; *Azari et al.*, 2019].

A second class of injections, unfortunately indistinguishable by name, can be observed at somewhat larger radial distances of $15-20\,\mathrm{R_S}$. These events occur less frequently, but they are larger and more persistent and involve more energetic plasma populations [e.g., *Mauk et al.*, 2005; *Paranicas et al.*, 2007; *Carbary et al.*, 2008c]. After their appearance typically at Saturn's nightside, their ENA signatures can extend across several Saturn radii and several hours LT and are observed to rotate around the planet, sometimes more than once, before dispersing [e.g., *Mitchell et al.*, 2009a; *Kinrade et al.*, 2020]. They appear to be associated with magnetotail activity and are hence likely related to dynamics further out in the magnetosphere.

Large-scale magnetic flux circulation in Saturn's middle and outer magnetosphere is driven by two main sources: the antisunward flow of the solar wind and the rapid rotation of the planet itself. The former drives the Dungey cycle, which is the main

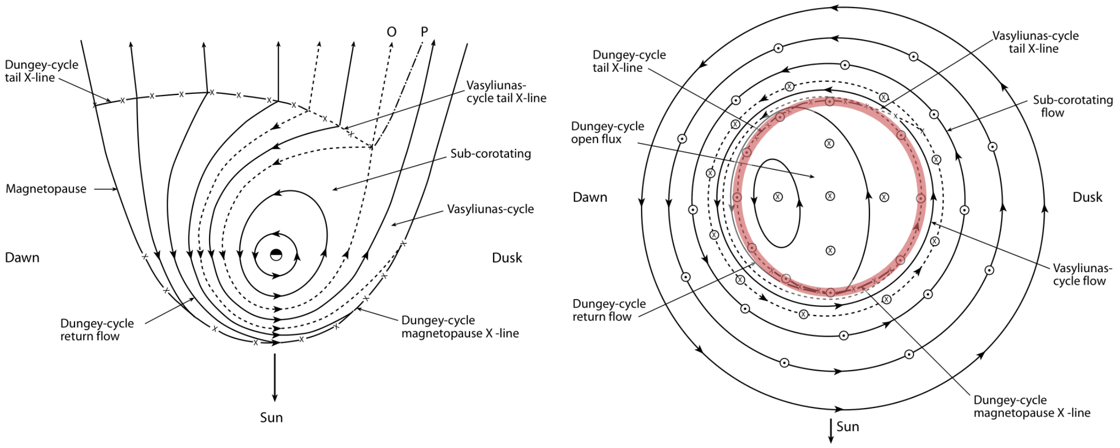

Figure 2.5: *Sketches of (left) plasma flows in Saturn's equatorial magnetosphere and (right) plasma flows and field aligned currents in Saturn's polar ionospheres. Both sketches describe the system seen from above the north pole and with the Sun toward the bottom. Plasma flows are indicated with solid arrowed lines, while boundaries between different flow regimes are shown with dashed lines. The red circle marks the location of the auroral oval and the OCB. Upward and downward current regions are indicated with circled dots and crosses, respectively. Modified from Cowley et al. [2004b].*

transport mechanism at Earth [*Dungey*, 1961]; the latter powers the Vasyliūnas cycle, dominating the Jovian magnetosphere [*Vasyliūnas*, 1983].

In the Dungey cycle process [*Dungey*, 1961], magnetospheric flux tubes reconnect with the oppositely directed IMF at the dayside magnetopause, creating open flux tubes whose ends are locked in the solar wind. These are dragged over the polar caps by the solar wind flow, stretching them and depositing them in the long magnetotail. Meanwhile, the flux tubes' ionospheric ends move into the polar cap to join preexisting regions of open flux and eventually are carried into the nightside as additional open flux is added to the dayside and eroded from the nightside polar cap. The magnetic field, directed oppositely on the two sides of the magnetotail current sheet, can then reconnect again. This leads to magnetic flux and plasma being ejected downtail, while the newly closed magnetospheric flux tubes contract toward the planet into a more dipolar configuration due to magnetic tension ("magnetic dipolarization"). The flux tubes, now empty of magnetic flux, then flow back to the dayside to begin the described process anew.

The Dungey cycle is the main process of flux circulation at Earth, but it is of much smaller importance for the rotating giant planet magnetospheres of Jupiter and Saturn.

With a magnetic field strength ten times larger than that of Earth, a magnetosphere nearly a hundred times as voluminous as Earth's and a rotation period of less than ten hours, especially Jupiter's magnetosphere is almost entirely controlled by its internal dynamics [*Brice and Ioannidis*, 1970].

Global plasma circulation is here described with the Vasyliūnas cycle [*Vasyliūnas*, 1983]: Magnetospheric plasma is added internally by ionization of cryovolcanic ejecta from the moon Io [e.g., *Thomas et al.*, 2004, and references therein]. This continuous mass and momentum loading stretches the magnetic field into a disc shape, facilitating reconnection through the thin equatorial current sheet as a result of rotational stresses and the related plasma instabilities [*Kivelson and Southwood*, 2005]. Plasma is released, the magnetic field dipolarizes and the remaining plasma continues to subcorotate. As the solar wind limits the outward expansion of the magnetosphere at the dayside, the magnetodisc is considered thicker than in the magnetotail - Vasyliūnas-type reconnection is therefore suggested to occur mainly at the nightside. However, recent investigations at Saturn have proposed this process to be active at all local times [*Delamere et al.*, 2015] and in-situ signatures of dayside magnetodisc reconnection have also been observed [*Guo et al.*, 2018a,b].

Saturn's magnetosphere is thought to be controlled by a combination of these two processes [*Cowley et al.*, 2004a,b]; their relative importance varies depending on, e.g., solar wind conditions and the internal plasma loading rate. It has been suggested that Dungey cycle reconnection voltages are comparable to Vasyliūnas cycle voltages under strong solar wind driving [*Jackman and Cowley*, 2006], but less significant during periods of low to average solar wind activity [*Badman and Cowley*, 2007]. Figure 2.5 shows sketches of the expected plasma flows in Saturn's equatorial magnetosphere and polar ionospheres resulting from a combination of the Dungey and Vasyliūnas cycles. Both are associated with their own ionospheric flow regions; the Dungey cycle dominating the polar cap region and the Vasyliūnas cycle controlling the corotating plasma flow just equatorward of the open-closed field line boundary (OCB).

As a result, the polar cap ionosphere is found to rotate at angular velocities of only $\sim 30 - 50\%$ of rigid corotation [e.g., *Stallard et al.*, 2004], transferring angular momentum to the tail by twisting the tail lobe field lines [*Isbell et al.*, 1984]. With the closed magnetosphere just equatorward of the OCB rotating much more rapidly, a shear in ionospheric plasma flows is maintained which is thought to set up a system of FACs driving Saturn's main aurorae [e.g., *Cowley et al.*, 2004a; *Stallard et al.*, 2007b; *Talboys et al.*, 2009b; *Hunt et al.*, 2014; *Bradley et al.*, 2018b].

Corotation Breakdown and Magnetosphere-Ionosphere Coupling

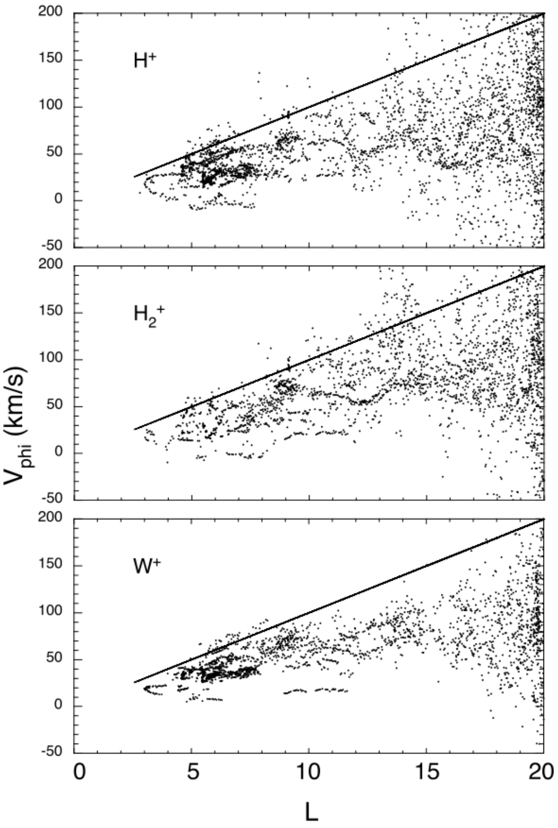

Figure 2.6: *Azimuthal flow speeds for three different ion species versus L shell; the values were derived from Cassini CAPS measurements close to the equatorial plane. Solid lines indicate rigid corotation. Taken from Thomsen et al. [2010].*

Most plasma is confined close to the magnetic equator by the centrifugal force, forming the magnetodisc [e.g., *Persoon et al.*, 2006]; especially heavier ions are concentrated at very low latitudes [e.g., *Thomsen et al.*, 2010; *Persoon et al.*, 2013]. The confined plasma largely flows in the direction of corotation [e.g., *Thomsen et al.*, 2010, 2014; *Livi et al.*, 2014], but the flow speeds are generally below rigid corotation speed as shown in Figure 2.6. Full corotation is observed until ~3.3 R_S, while the plasma begins to lag the planet's angular velocity further outward [e.g., *Wilson et al.*, 2009]. The subcorotation of the plasma relative to the neutral atmosphere is a direct consequence of mass and momentum loading and the outward transport of plasma under conservation of angular momentum [e.g., *Hill*, 1979; *Pontius and Hill*, 2009].

The angular flow shear arising from this differential plasma corotation sets up a current system which acts to transfer angular momentum from the planet to the surrounding magnetospheric plasma. A brief description will be given below, but the reader is referred to other works for more detailed discussions on this topic [e.g., *Hill*, 1979, 2001; *Cowley and Bunce*, 2001, 2003; *Ray et al.*, 2010, 2014; *Ray and Ergun*, 2012; *Vasyliūnas*, 2016; *Ray*, 2018].

Newly ionized plasma orbits Saturn at the Keplerian velocity, which is lower than rigid subcorotation. Upon its ionization, the bulk flow speed of the local plasma population hence decreases and a motional electric field is generated. In the corotating frame, this field points radially in toward the planet (E_M in Figure 2.7); in the ionosphere, this relates to an equatorward pointing latitudinal field (E_I).

The ionospheric field is associated with latitudinal Pedersen currents, which are fed by FACs diverging into the magnetodisc. The upward current is hereby carried by electrons precipitating into the ionosphere; most assuredly generating the steady main aurorae at Jupiter [e.g., *Cowley and Bunce*, 2001] but likely too weak to produce auroral emissions at Saturn [*Cowley and Bunce*, 2003].

The current circuit is closed by electrons flowing radially outward in the magnetodisc [e.g., *Martin and Arridge*, 2019] and back into the ionosphere along the magnetic field. Radial currents in the magnetodisc are associated with a **J** × **B** force which, for the case of outward directed currents, acts to accelerate the subcorotating plasma. The angular momentum for this azimuthal acceleration is supplied from the planet's rotation, transferred into the ionosphere through ion-neutral collisions and from there into the magnetosphere through the magnetosphere-ionosphere coupling current system described here. However, this current system is not able to enforce rigid corotation throughout the magnetosphere as it is limited by, e.g., the conductance of the ionosphere and the density of current carriers along the magnetic field lines [e.g., *Ray and Ergun*, 2012; *Ray*, 2018].

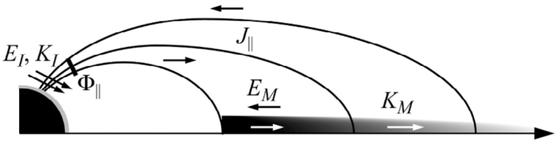

FIGURE 2.7: *Diagram of the magnetosphere-ionosphere coupling currents and fields.* E_I *and* E_M *are the perpendicular electric fields in the ionosphere and magnetosphere, respectively.* K_I *denotes the ionospheric Pedersen current and* K_M *the radial current in the magnetodisc. The field-aligned potential between the ionosphere and magnetosphere is given by* $\Phi_\parallel$*, the FACs by* $J_\parallel$*. Modified from Ray et al. [2010].*

Rotational Modulation

SKR measurements from the first Saturn flybys of Voyager 1 and 2 revealed periodic oscillations which were assumed to represent the planetary rotation period [*Desch and Kaiser*, 1981]. However, further observations unexpectedly showed the SKR period to vary by ~ 1° over several years [*Galopeau and Lecacheux*, 2000]; and the first Cassini SKR observations indeed verified a shift in the period from ~ 10.66 h to ~ 10.76 h [*Gurnett*, 2005]. The puzzling appearance of a secondary period [*Kurth et al.*, 2008] later led to the discovery of separate periods corresponding to SKR sources in the northern and southern hemisphere, respectively [*Gurnett et al.*, 2009a]. These can be separated by the circular polarization of the extraordinary mode emission, with left-hand-polarized SKR being generated in the southern and right-hand-polarized SKR in the northern hemisphere [e.g., *Lamy et al.*, 2008]. Both the northern and the southern period vary slowly over time (see Figure 2.9); at Cassini's arrival the two were clearly separated, but with the approach of Saturn's equinox they became more similar and eventually seemed to merge [*Gurnett et al.*, 2010], suggesting a seasonally dependent driver [*Brooks et al.*, 2019].

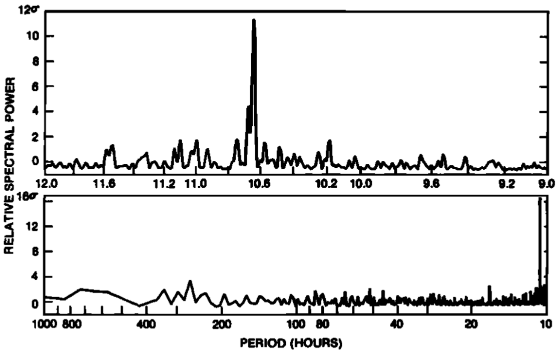

Figure 2.8: *Power spectra of Voyager SKR time series, (top) high-resolution and (bottom) low-resolution. Taken from Desch and Kaiser [1981].*

These so-called planetary period oscillation (PPO) periodicities and their evolution through time can also be tracked using magnetic field measurements from within Saturn's magnetosphere [e.g., *Espinosa and Dougherty*, 2000; *Giampieri et al.*, 2006]. The specific phase relation between the magnetic components hereby precludes that the periodicities may be generated by a tilted magnetic dipole [*Espinosa et al.*, 2003]; instead, magnetic perturbation fields were found to model the magnetic PPO perturbations rather closely.

Both the northern and southern PPO systems are associated with one perturbation field each, dominant in their respective polar hemisphere but double-modulating the magnetic field in the equatorial plane. Their perturbation dipoles are hereby oriented perpendicular to Saturn's rotation axis and rotate with their respective PPO period; they are associated with a complex array of FACs [e.g., *Southwood and Kivelson*, 2007; *Andrews et al.*, 2008, 2010a,b, 2012; *Provan et al.*, 2009a, 2011; *Southwood and Cowley*, 2014; *Hunt et al.*, 2014, 2015; *Bradley et al.*, 2018b].

The origin of Saturn's periodicities is a matter of ongoing investigation. Global MHD simulations could model the observed double modulation of the magnetosphere with vortical flow structures in Saturn's polar ionospheres as a driver [*Jia and Kivelson*, 2012; *Jia et al.*, 2012; *Kivelson and Jia*, 2014]. The proposed system is powered by double vortices in the polar caps which rotate at the observed PPO periods; the FACs associated with the PPO systems were shown to flow in the right sense to communicate the related modulations out into the magnetosphere [e.g., *Hunt et al.*, 2014; *Southwood and Cowley*, 2014]. The PPO-associated FACs close partly in the equatorial plane and partly in the opposite hemisphere, pervading the entire magnetosphere [e.g., *Southwood and Kivelson*, 2007, 2009; *Hunt et al.*, 2015; *Bradley et al.*, 2018b]. A sketch of PPO-related magnetic field perturbations and electric currents in accordance with the currently accepted model is shown in Figure 2.10. However, it is unclear how these ionospheric flow patterns could be generated - although it is likely that the driver may be unconnected with magnetospheric processes and instead be found in the neutral thermosphere or stratosphere [e.g., *Smith*, 2011, 2014; *Stallard et al.*, 2018].

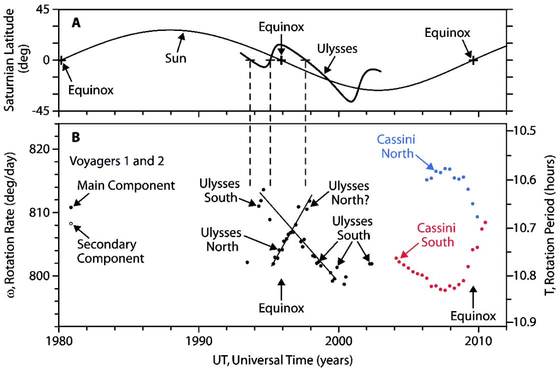

Figure 2.9: *(a) Saturnian latitudes of the Sun and Ulysses, (b) SKR periods over time as measured by the Voyager 1 and 2, Ulysses and Cassini spacecraft. Modified from Gurnett et al. [2010].*

The effects of this periodic modulation prevail in virtually all measurements within Saturn's magnetosphere. As already mentioned, rotational modulation is observed in magnetic field measurements [e.g., *Espinosa and Dougherty*, 2000; *Espinosa et al.*, 2003; *Andrews et al.*, 2008, 2010b,a, 2012; *Provan et al.*, 2009a, 2011, 2013, 2014, 2015, 2016, 2018]

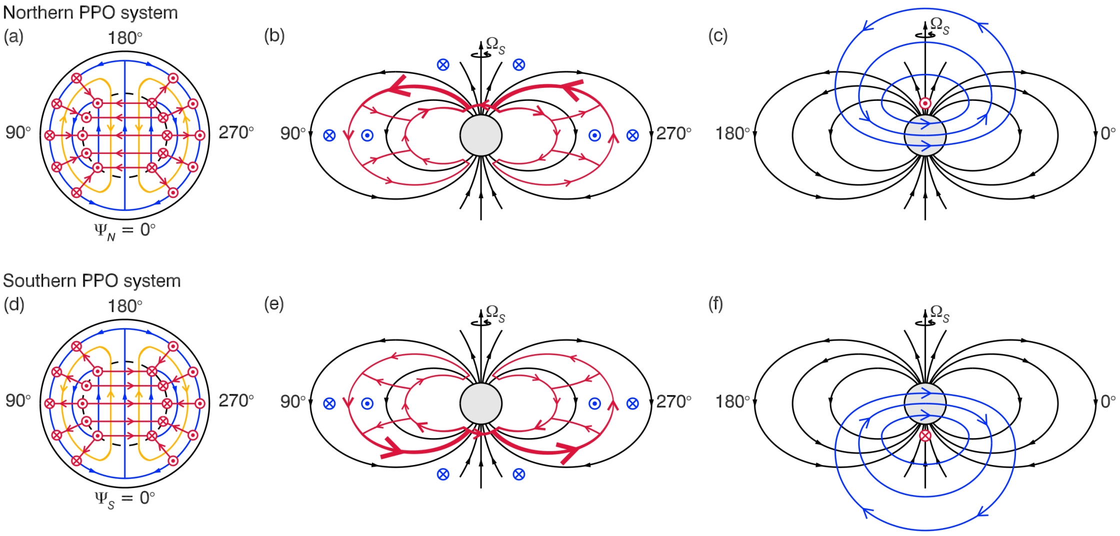

Figure 2.10: *PPO-related magnetic field perturbations and electric currents of the (a-c) northern and (d-f) southern PPO systems. Red arrowed lines and symbols show electric currents and blue arrowed lines and symbols magnetic fields, with circled dots and crosses indicating vectors pointing out of and into the plane of the figure, respectively. (a) View onto Saturn's northern polar ionosphere and (d) view from north "through" the planet into the southern ionosphere, yellow arrowed lines indicating the atmospheric/ionospheric flow patterns thought to generate PPOs. (b,e) Fields and currents in the* $\Psi_{N,S} = 90° — 270°$ *meridian plane and (c,f) fields and currents in the* $\Psi_{N,S} = 0° — 180°$ *meridian plane. Detailed descriptions of PPO phase angles and longitude systems are given in section 3.7. The background magnetic field is indicated in black. Modified from Provan et al. [2018].*

as well SKR variations [e.g., *Lamy*, 2011; *Lamy et al.*, 2013; *Ye et al.*, 2016]. The FACs flowing on auroral field lines connect the entire magnetosphere with the supposed atmospheric drivers in Saturn's polar ionospheres, and hence show clear PPO periodicities as well [e.g., *Hunt et al.*, 2014, 2015, 2016, 2018a,b; *Bradley et al.*, 2018b]. The PPO-associated variation of the current density on these field lines manifests as a periodic modulation of the auroral intensity [e.g., *Nichols et al.*, 2010a; *Badman et al.*, 2012b; *Nichols et al.*, 2016; *Bader et al.*, 2018] and of the latitude of the main emission in phase with the PPO modulation [e.g., *Provan et al.*, 2009b; *Nichols et al.*, 2010b, 2016; *Bader et al.*, 2019b]. The oscillations introduced by these rotating current systems propagate through the entire magnetosphere, such that the nightside plasma sheet can be observed to flap about the magnetic equator and periodically vary in thickness [e.g., *Arridge et al.*, 2011; *Provan et al.*, 2012; *Cowley and Provan*, 2017; *Thomsen et al.*, 2017; *Sorba et al.*, 2018]. At its thinnest, the plasma sheet is found more conducive to reconnection; plasmoid release and magnetic dipolarizations are hence more probable at certain PPO phases [e.g., *Jackman et al.*, 2016; *Cowley and Provan*, 2017; *Bradley et al.*, 2018a; *Bader et al.*, 2019a]. These global magnetospheric periodicities also emerge in the variation of the magnetopause location [*Clarke et al.*, 2010a], the bow shock location [*Clarke et al.*, 2010b] and the OCB [*Jasinski et al.*, 2019]. Finally, comparable periodicities are observed in all kinds of measurements of charged particles and ENAs [e.g., *Paranicas et al.*, 2005; *Carbary et al.*, 2008a, 2011; *Carbary*, 2017] and even in the structure of Saturn's rings [*Chancia et al.*, 2019].

2.3 SATURN'S ULTRAVIOLET AURORAE - AN OVERVIEW

Auroral Acceleration

As touched upon in the previous sections, the magnetosphere is coupled to the ionosphere by different systems of FACs on both global and local scales. These currents are largely carried by upgoing cold ionospheric electrons in downward current regions and by precipitating hot magnetospheric electrons in upward current regions. However, the current density which can be carried by thermal electrons is limited by the electron density in high latitudes, such that the carriers may need to be accelerated to maintain current continuity and charge neutrality [e.g., *Paschmann et al.*, 2003; *Ray and Ergun*, 2012].

The auroral acceleration region, located above the auroral ionosphere, is characterized by a multitude of small-scale processes which are not well understood and a topic of intensive research. Most of our knowledge of the processes involved is based on the terrestrial aurorae, although the JUNO spacecraft recently revealed the first details of Jupiter's auroral acceleration region which may be similar to Saturn's.

At Earth, auroral electrons are accelerated into the ionosphere by static electric fields parallel to the magnetic field [e.g., *Knight*, 1973; *Carlson et al.*, 1998b; *Ergun et al.*, 1998; *McFadden et al.*, 1999; *Marklund et al.*, 2001] such that precipitating electron populations are observed to be monoenergetic [*McIlwain*, 1960; *Evans*, 1968]. It is not clear how these fields are generated and maintained or what determines their spatial and temporal variability. The energetic environment above the auroral region is conducive to wave-particle interaction processes in which plasma waves are generated through instabilities in the typically beam-like particle distributions and, vice versa, charged particles are energized through coupling with waves [e.g., *Kintner et al.*, 1979; *Okuda and Ashour-Abdalla*, 1981; *Vago et al.*, 1992; *Chang*, 1993; *André*, 1997; *Shen et al.*, 2018].

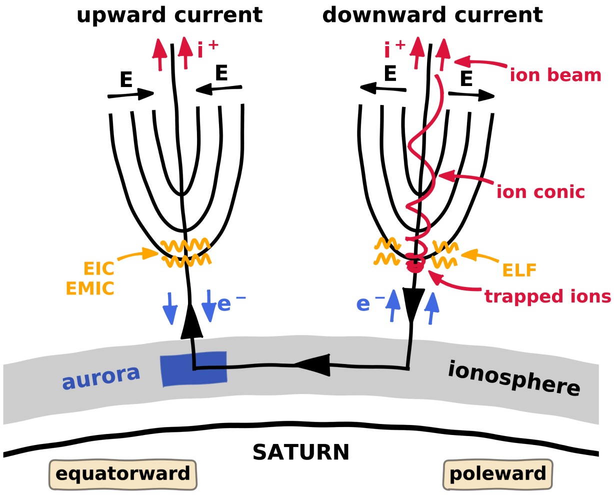

Figure 2.11: *Conceptual sketch of neighbouring upward and downward current regions in Saturn's auroral acceleration region. Also published in Bader et al. [2020a].*

Before the arrival of Juno at Jupiter, the Jovian auroral acceleration process was expected to be of a similar nature albeit operating at much higher energies [e.g., *Ray et al.*, 2010, 2012; *Cowley et al.*, 2017]. While strong parallel electric fields and coherent particle acceleration can be observed [*Clark et al.*, 2017a, 2018; *Ebert et al.*, 2017; *Mauk et al.*, 2018; *Paranicas et al.*, 2018], broadband acceleration likely caused by plasma waves seems to be the dominant mechanism through which auroral particles are energized [*Allegrini et al.*, 2017; *Mauk et al.*, 2017a,b]. Recent studies suggest that Alfvén waves may be the main source of energy for these processes [*Saur et al.*, 2018; *Gershman et al.*, 2019].

The situation is even less clear at Saturn, with Cassini's orbit geometry severely limiting our ability to study the acceleration region. However, energetic electron and ion beams were observed above the aurorae, suggesting powerful energization processes to take place [*Saur et al.*, 2006; *Mitchell et al.*, 2009b; *Badman et al.*, 2012a]. In situ measurements remained inaccessible until the end of the mission when two low-altitude auroral crossings revealed some more detail highlighting the complexity of energization mechanisms. While no Alfvén wave activity was observed, the accelerated particle populations appeared to be broadband like observed at Jupiter [*Bader et al.*, 2020a].

Generation of Auroral Emissions

Energetic electrons, constituting the majority of auroral precipitation into Saturn's hydrogen-dominated atmosphere, interact with atmospheric neutrals through both elastic scattering and inelastic collisions including ionization, excitation and dissociation [e.g., *Galand et al.*, 2011]. These interactions eventually lead to the generation of optical emissions in different wavebands ranging from the infrared (IR) through the visible and into the ultraviolet (UV) wavelengths. Figure 2.12 shows a simplified flowchart describing the different processes involved in the generation of these.

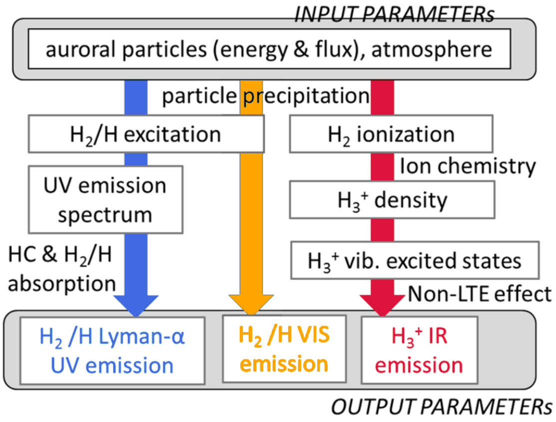

Figure 2.12: *Flowchart of different auroral emission processes driven by auroral particle precipitation into a hydrogen-dominated atmosphere. Modified from Badman et al. [2015].*

A significant fraction of the energy brought into Saturn's upper atmosphere by primary auroral electrons is lost in inelastic collisions with neutral H_2 molecules resulting in ionization. This produces secondary electrons, which can again interact with the neutral atmosphere to either ionize other H_2 molecules or excite them into upper electronic levels. The de-excitation of excited molecules to the ground electronic level then produces photons in the visible and UV wavebands, which are observable as auroral emission. The emission is hereby dominated by the H_2 Lyman and Werner bands and the H_2 continuum in the $800 - 1800$ Å wavelength range as well as the H Lyman atomic lines (Lyman-α at 1216 Å); excited H atoms are thought to be produced by dissociative excitation of H_2 [e.g., *Gustin et al.*, 2009, 2012, 2017; *Stallard et al.*, 2018]. Saturn's atmosphere contains a hydrocarbon layer, dominated by methane (CH_4), which causes a partial absorption of the UV auroral emission as the auroral photons travel away from the planet, depending on their energy and the length of their path through this layer. The auroral spectrum observed outside of the atmosphere hence contains information about the penetration depth and initial energy of the precipitating electron population [e.g., *Gustin et al.*, 2012, 2013].

IR auroral emission is radiated by H_3^+, which is created through chemical reaction of the H_2^+ ions produced by electron impact ionization with the neutral hydrogen atmosphere,

$$H_2 + H_2^+ \rightarrow H_3^+ + H. \tag{2.4}$$

The newly created H_3^+ ions are quickly thermalized within the neutral atmosphere [*Tao et al.*, 2011], leading to their excitation and subsequent de-excitation through radiation in the IR, forming specific emission lines. Due to its short lifetime of ~500 s, H_3^+ density is closely related to the local ionization rate such that the morphology of UV and IR aurorae are generally comparable [e.g., *Melin et al.*, 2011, 2016; *Lamy et al.*, 2013], with differences mainly arising due to the strong dependence of H_3^+ emission on atmospheric temperature [e.g., *Miller et al.*, 2013].

Auroral Signatures and Morphology

Part of this section was published as introduction in Publication VI.

Saturn's UV aurorae consist of various components located around the planet's poles. Some of these components are rather static and long-lived, while others are more transient indicating explosive energy release somewhere along the associated magnetic field lines. The current understanding of the great variety of observable signatures and their possible origins has previously been reviewed by, e.g., *Badman et al.* [2015] and *Grodent* [2015] and will be summarized and slightly updated here. Figure 2.13 shows examples of most of the features which will be described in the following paragraphs; all images are taken from the rich dataset obtained with the CASSINI UVIS detector. The choice of images is limited to CASSINI's high-latitude orbits in 2008 and its *Grand Finale mission* in 2017, when auroral imaging provided the highest spatial resolution.

MAIN EMISSION: Appropriate to it dominating the overall auroral morphology, the so called "main auroral oval" or "main emission" is the first structure characterized here. Panel 2.13e shows a full view of Saturn's typical UV aurorae, with the main emission forming an incomplete relatively circular bright band around the pole. Located at typically 15 – 20° colatitude from either pole [e.g., *Carbary*, 2012; *Bader et al.*, 2019b], the main emission is colocated with the infrared main aurorae [e.g., *Melin et al.*, 2011;

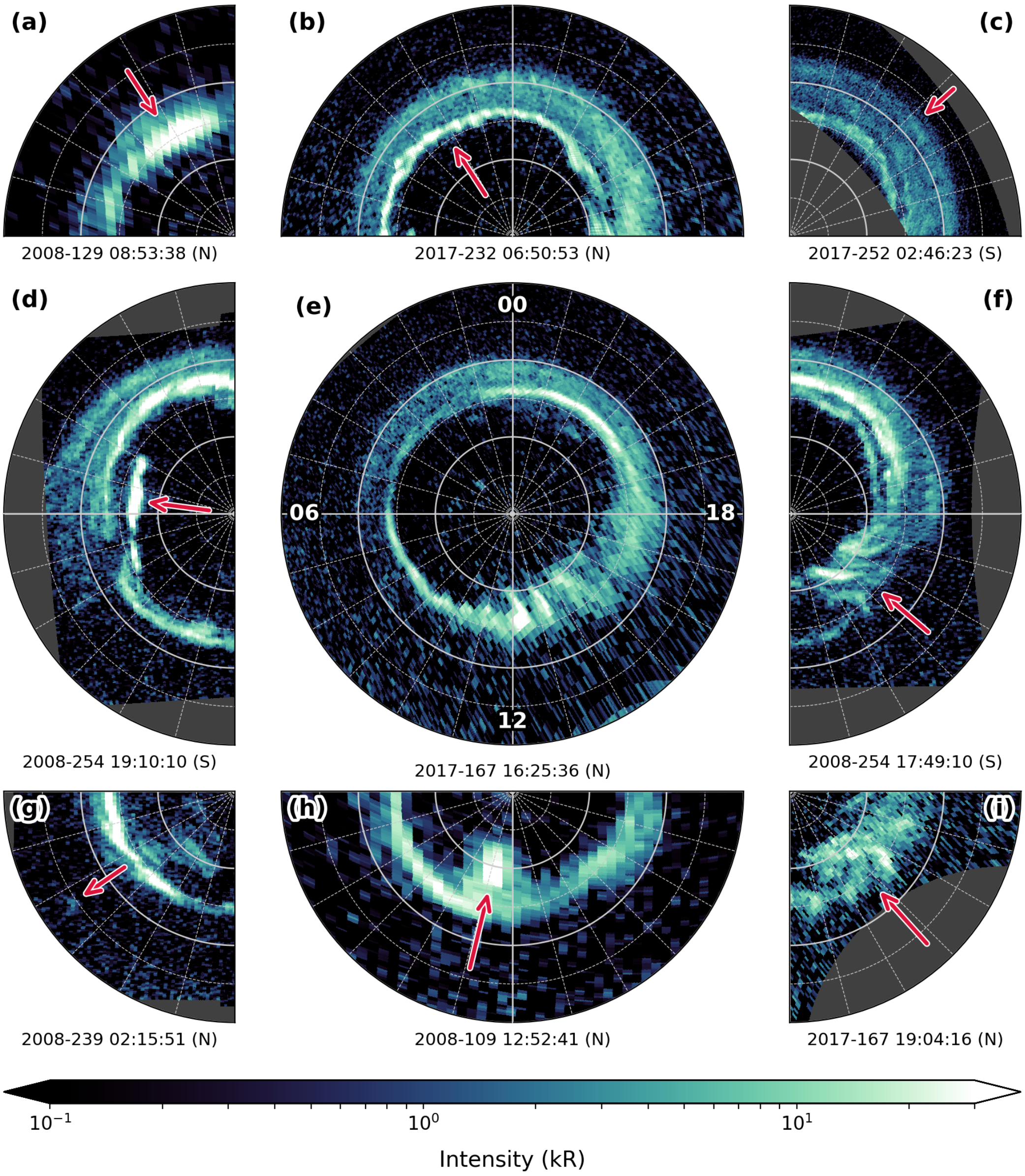

Figure 2.13: *Examples of typical signatures in Saturn's UV aurorae from* Cassini*'s UVIS instrument. The view is from above the north pole, down onto the northern or "through" the planet into the southern polar region. Local noon (12 LT) is at the bottom and midnight at the top as indicated in the center panel. Grey concentric rings mark colatitude from the pole in steps of 5°, radial lines mark LT in steps of 1 h. The timestamp and hemisphere of the observation are noted below each panel. The center panel (e) shows the typical morphology of Saturn's ring-shaped main emission with some spread near dusk. The surrounding panels highlight auroral signatures which are discussed in the text: (a) injection, (b) auroral beads, (c) outer emission, (d) poleward arc, (f) bifurcations, (g) Enceladus footprint, (h) cusp spot and (i) "bunch of grapes".*

Badman et al., 2011a,b] and expected to map to equatorial distances beyond the middle ring current [e.g., *Belenkaya et al.*, 2014]. The exact mechanism causing the acceleration of electrons into Saturn's polar ionospheres and thus generating the aurorae is unclear, but it is presumed that azimuthal flow shears between plasma populations subcorotating at different angular velocities in the outer magnetosphere may provide the required electric fields driving the observed auroral FACs [e.g., *Cowley et al.*, 2004a; *Stallard et al.*, 2007b; *Talboys et al.*, 2009b; *Hunt et al.*, 2014; *Bradley et al.*, 2018b].

The auroral brightness varies with LT, which may partly be due to the interaction of Saturn's magnetosphere with the solar wind flow. Both a static flow shear between the solar wind and magnetospheric plasma populations [e.g., *Cowley et al.*, 2004b] and viscous interaction through Kelvin-Helmholtz (KH) waves [e.g., *Delamere and Bagenal*, 2010; *Delamere et al.*, 2013] could cause asymmetries arising between the dawn and dusk aurorae. Further dynamic asymmetries are known to be imposed by the rotating patterns of FACs imposed by the two PPO current systems [e.g., *Hunt et al.*, 2014; *Bader et al.*, 2018].

As visible in some of the examples shown in Figure 2.13, the main emission usually does not assume a fully closed circular shape, but consists of multiple structures subcorotating with the planet [e.g., *Grodent et al.*, 2005]. It is thereby not centered on Saturn's magnetic/spin pole, but slightly displaced toward the midnight-dawn direction due to the compression of the dayside magnetosphere by the solar wind; the location of the oval is modulated about this average position by the rotating PPO current systems [e.g., *Nichols et al.*, 2008, 2016; *Bader et al.*, 2019b]. The size of the main oval is dependent on the amount of open magnetic flux contained within the polar cap and magnetotail lobes [e.g., *Belenkaya et al.*, 2007]; it changes if there is an imbalance between open flux creation at the dayside magnetopause and open flux closure in the magnetotail [e.g., *Badman et al.*, 2005, 2014; *Cowley et al.*, 2005]. The frequently observed spiral shape of the main emission could be caused by this change in open flux content from the day- or nightside combined with the planet's rotation [*Cowley et al.*, 2005], although partial ring current structures in the equatorial plane may similarly result in a broken spiral-shaped main emission as found at Earth [*Gkioulidou et al.*, 2009]. Furthermore, increased solar activity has been found to relate to a smaller auroral oval size [*Bader et al.*, 2019b]. Due to the significant quadrupole moment of Saturn's internal magnetic field, effectively an offset of the internal dipole field toward the northern hemisphere, the southern oval is typically larger than the northern one [e.g., *Carbary*, 2012; *Bader et al.*, 2019b].

The structure of the main emission is highly variable. The dawn side generally features a thin well-defined arc, while the aurorae cover a wider swath post-noon. In either of those regions the arc can include interesting substructures such as "auroral beads" (see Fig. 2.13b), multiple detached and consecutive auroral spots located along the main emission which may be related to shear flow-ballooning instabilities [*Radioti et al.*, 2019]. Similar small isolated features are sometimes observed in the dayside aurora (see Fig. 2.13i); *Grodent et al.* [2011] termed this the "bunch of grapes" configuration and proposed FACs driven by nonuniform plasma flow in the equatorial plane and vortices triggered by magnetopause KH waves as possible drivers.

OUTER EMISSION: Equatorward of the main aurorae a rather permanent band of emission can often be observed, the so called "outer emission" (visible in Fig. 2.13b-f, highlighted in Fig. 2.13c). While it was first observed in HST imagery [*Grodent et al.*, 2005, 2010; *Lamy et al.*, 2018a], detections with the HST are quite limited as the relatively faint outer emission is usually above the detection threshold only on the nightside. The CASSINI UVIS detector provided many more observations [e.g., *Radioti et al.*, 2017b; *Bader et al.*, 2020b]. It is believed to be caused by suprathermal electrons between 7-10 R_S [*Schippers et al.*, 2008] which may reach the ionosphere through pitch angle scattering by plasma waves [*Grodent et al.*, 2010; *Grodent*, 2015; *Tripathi et al.*, 2018].

ENCELADUS FOOTPRINT: At Jupiter, the footprints of the moons Io, Europa and Ganymede are frequently visible in the UV aurora [e.g., *Clarke et al.*, 2002], generated as the slowly orbiting moons perturb the rapidly corotating plasma in the equatorial magnetodisc. This induces Alfvén waves propagating along the magnetic field line, which in turn cause electrons to precipitate into the ionosphere [e.g., *Kivelson*, 2004]. A similar interaction happens in the vicinity of the moon Enceladus at Saturn, but the signature is very weak and barely detectable - only on 26 August 2008 could Enceladus' faint auroral footprint be observed with the CASSINI UVIS detector (*Pryor et al.* [2011], see Fig. 2.13g). Through the three images in which the spot could be observed, the brightness varied by a factor of about three - most likely reflecting variations in Enceladus' water plume activity.

Dayside Transients: The dayside aurorae frequently feature transient brightenings which may be indicative of the interaction between Saturn's dayside magnetosphere and the solar wind. Even before the arrival of the Cassini spacecraft, HST images revealed the irregular appearance of a bright spot slightly poleward of the main aurorae near noon [*Gérard et al.*, 2004, 2005]. An example from the UVIS dataset is shown in panel 2.13h. This feature may be related to magnetic reconnection of the magnetospheric lobe at high latitudes [*Bunce et al.*, 2005a; *Kinrade et al.*, 2017], similar to the lobe cusp spot observed at Earth [*Milan et al.*, 2000; *Fuselier et al.*, 2002], and is often termed the "cusp spot". This spot can at times be observed to pulsate [*Palmaerts et al.*, 2016a], which could indicate that the lobe reconnection events generating it occur in a pulsed fashion as proposed earlier by *Bunce et al.* [2005a]. Closely related to this signature is the appearance of bifurcations in the post-noon sector (see Fig. 2.13f), which take the shape of parallel arcs protruding into the polar cap. These seem to frequently develop after a cusp spot is observed, and may be a signature of multiple magnetic reconnection events at the low-latitude magnetopause [e.g., *Radioti et al.*, 2011, 2013; *Badman et al.*, 2013].

Dawn brightenings: Magnetotail reconnection is the main process through which plasma can be released from Saturn's magnetosphere, and is hence observed rather frequently [e.g., *Bunce et al.*, 2005b; *Jackman et al.*, 2007, 2008a, 2011; *Thomsen et al.*, 2015a; *Smith et al.*, 2016]. Following a reconnection event and the associated release of a plasmoid, the newly closed field lines are rapidly accelerated back toward Saturn. This is thought to cause a sudden brightening of the nightside aurorae, which subsequently subcorotates into dawn LTs before slowly dispersing [e.g., *Mitchell et al.*, 2009a; *Jackman et al.*, 2013]. Possible differences between Dungey cycle and Vasyliūnas cycle-related reconnection events are not entirely clear, but poleward arcs and possibly also bright patches at colatitudes near the main auroral oval (see panels 2.13d and 2.13a, respectively) may be associated with plasmoid release in context of the Vasyliūnas cycle [e.g., *Radioti et al.*, 2016]. These features are observed on planetary rotation time scales [*Bader et al.*,

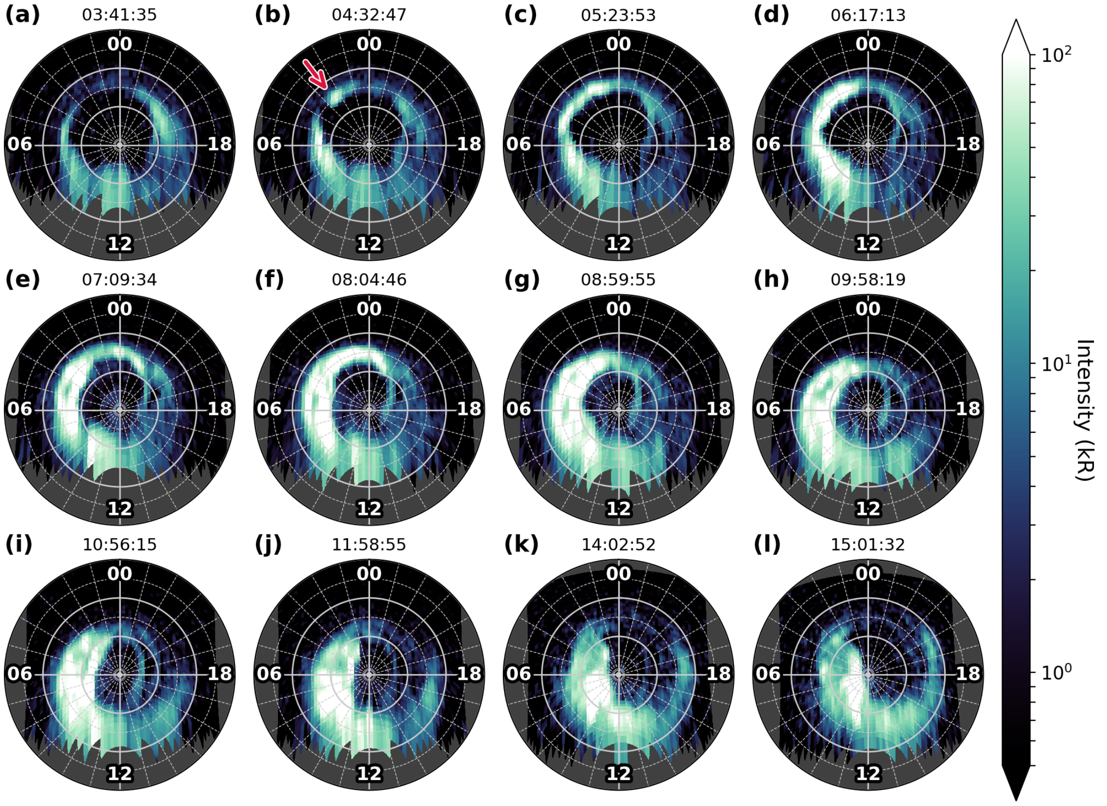

FIGURE 2.14: *UVIS example sequence from 2017-257 showing the sudden commencement (red arrow) and following evolution of an auroral storm at dawn. Noon is again toward the bottom and dusk to the right, the start of each exposure is given on top of each panel. Note that the color scale is extended to an upper limit of 100 kR compared to the previous figure.*

2019a]. Dungey-cycle reconnection on the other hand is likely associated with so called "dawn storms" - strong aurorae which, starting from the nightside, quickly cover the entire dawn half of the polar region and extend up to the pole (see Fig. 2.14). These are likely triggered by solar wind compressions or changes in the IMF direction, typically last for more than one Saturn rotation and are observed comparably infrequent on solar rotation time scales [e.g., *Badman et al.*, 2005; *Clarke et al.*, 2009; *Kidder et al.*, 2012; *Meredith et al.*, 2014b; *Nichols et al.*, 2014; *Palmaerts et al.*, 2018]. These brightenings at dawn have been shown to affect the statistical LT brightness distribution of Saturn's aurorae much more than any static asymmetries imposed by, e.g., the solar wind flow [*Bader et al.*, 2019a].

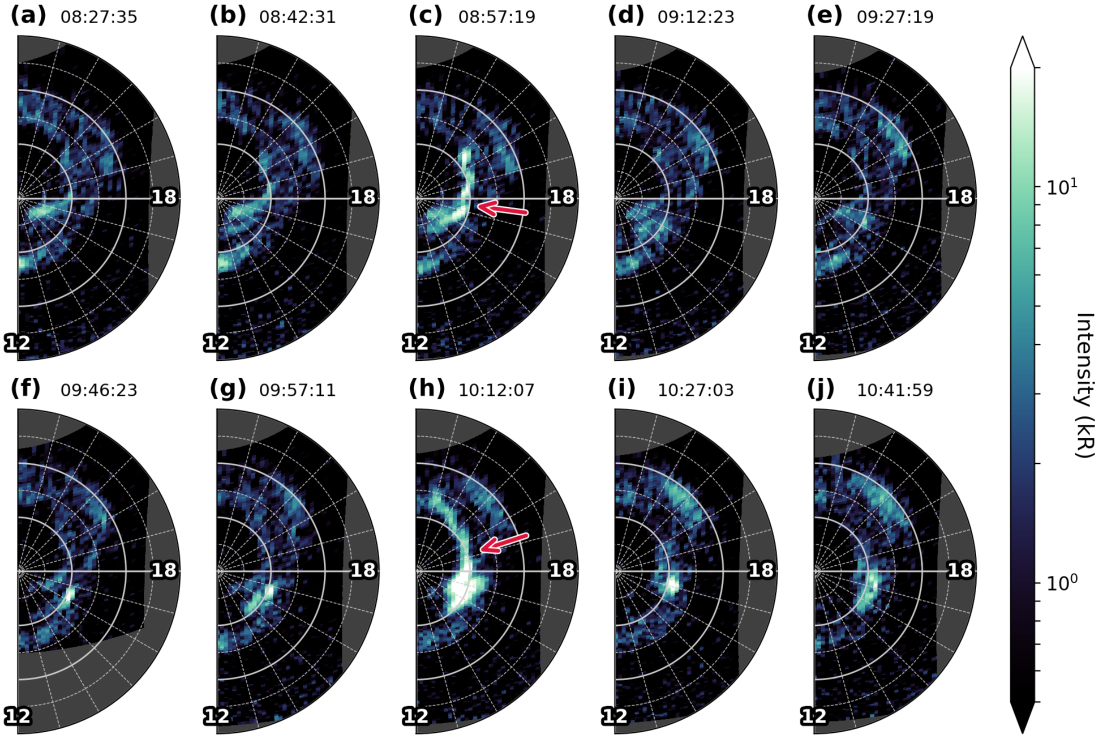

Figure 2.15: *Example sequence from 2008-195 showing the appearance of short-lived bright auroral flashes near dusk (c,h), taken by the UVIS instrument. Noon is again toward the bottom and dusk to the right, the start of each exposure is given on top of each panel.*

Transient auroral flashes: The last auroral signature considered here is the appearance of short-lived localized auroral brightenings predominantly at dusk LTs as shown in Fig. 2.15. First observed as single events in HST imagery [*Radioti et al.*, 2009a], they were suggested to be related to energetic particle injections or magnetic reconnection processes. A later study proposed these features to be located on field lines newly opened by dayside reconnection, consistent with the strict north-south non-asymmetries observed [*Meredith et al.*, 2013]. Recently, *Bader et al.* [2019c] revealed the continuous and roughly 1-hour quasiperiodic occurrence of these brightenings in phase with intensifications of electron flux and auroral hiss as well as with sawtooth-shaped signatures in magnetic field measurements. An internal driver is suggested, such as small-scale magnetodisc reconnection thought to occur predominantly near dusk. However, the origin of the relatively stable periodicity of these auroral flashes remains unknown.

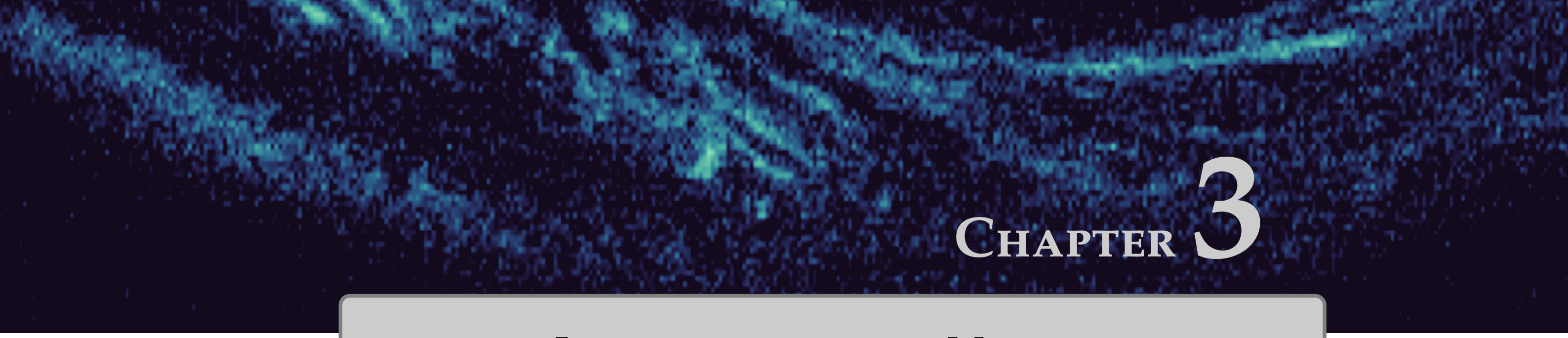

Chapter 3

Instrumentation and Methods

3.1 The Cassini-Huygens Mission

The Cassini-Huygens mission was a flagship-class planetary science mission to the Saturnian system, a collaboration between the National Aeronautics and Space Administration (NASA), the European Space Agency (ESA), and the Agenzia Spaziale Italiana (ASI). The project comprised both NASA's Cassini orbiter and ESA's Huygens probe, which entered the atmosphere of Saturn's biggest moon Titan and descended to its surface via parachute.

Following its launch in October 1997, the spacecraft performed flybys of Venus, Earth, and Jupiter in order to gain enough momentum to reach Saturn. Cassini-Huygens was inserted into Saturn orbit on the 1st of July 2004 after more than six years of cruise time through the solar system. The primary mission was completed in 2008, and several mission extensions ensured continued scientific investigations during the *Equinox mission* (until September 2010), *Solstice mission* (until April 2017), and the *Grand Finale mission* (until September 2017). On the 15th of September 2017, the extraordinarily productive project ended with Cassini's controlled plunge into Saturn's atmosphere.

A schematic of the Cassini spacecraft is shown in Figure 3.1. Cassini was a three-axis stabilized robotic spacecraft powered by three radioisotope thermoelectric generators (RTGs). With a launch mass of nearly 6 tonnes, it was one of the largest interplanetary spacecraft ever built. The Cassini probe was equipped with twelve interrelating science instruments that addressed many major scientific questions about the Saturn system. The remote sensing pallet comprised the following instruments used mainly for optical imaging in different wavelength ranges:

- **CIRS** (Composite Infrared Spectrometer) measured infrared emissions from atmospheres, rings and surfaces and analyzed their temperature and composition [*Flasar et al.*, 2004]

- **ISS** (Imaging Science Subsystem) was a camera system operating in the visual and

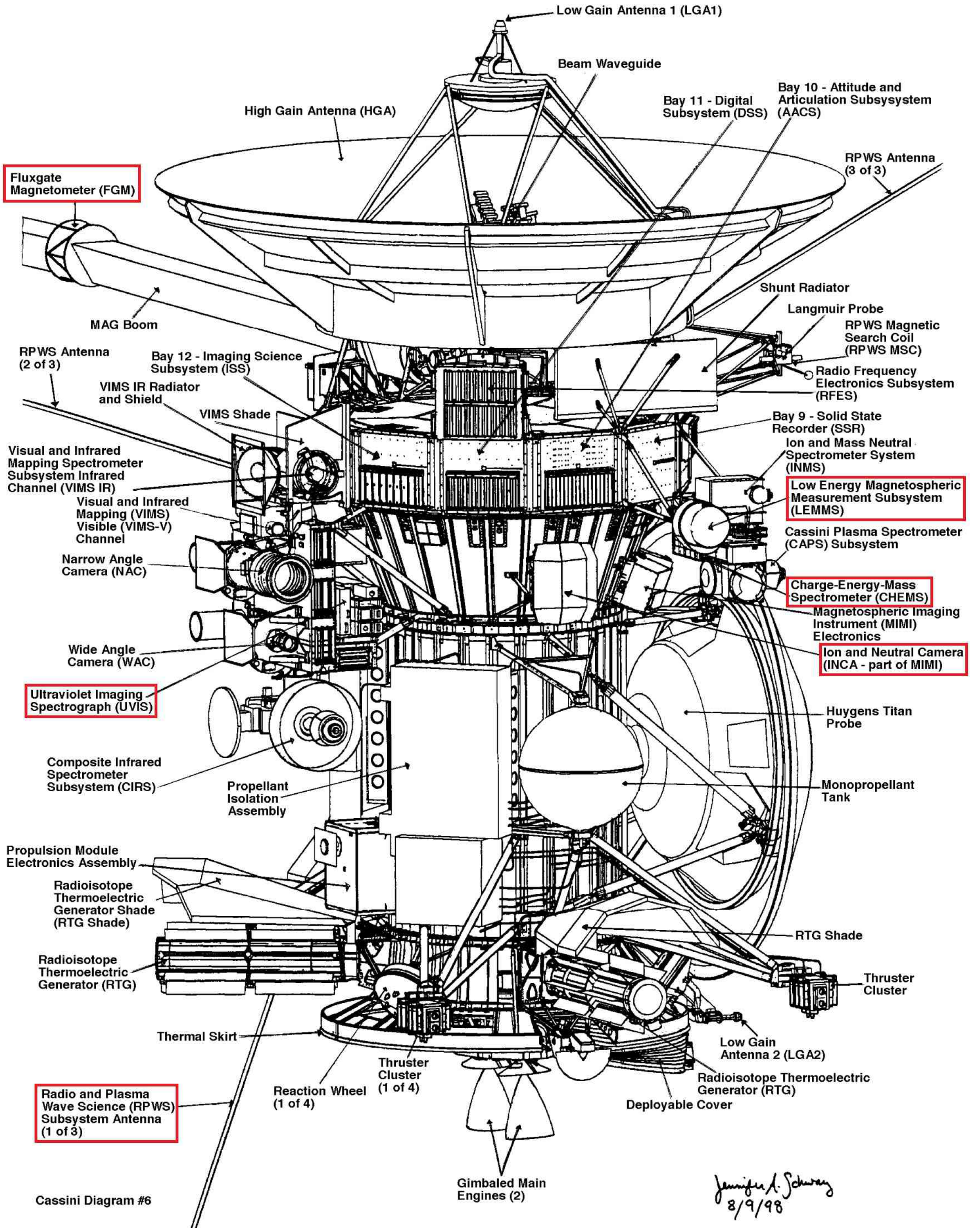

Figure 3.1: *Schematic of the Cassini-Huygens mission, most of the key components are labelled. Instruments of specific interest in the context of this thesis are highlighted in red. Image credit: NASA/JPL.*

infrared wavelength range and photographing Saturn, its rings and its moons [*Porco et al.*, 2004]

- **UVIS** (ULTRAVIOLET IMAGING SPECTROGRAPH) imaged Saturn's rings and auroral emissions [*Esposito et al.*, 2004]
- **VIMS** (VISIBLE AND INFRARED MAPPING SPECTROMETER) mapped the surface spatial distribution of mineral and chemical features of different targets in high spectral resolution [*Brown et al.*, 2004]

A second group of instruments was dedicated to studying dust and plasma in the environment of Saturn:

- **CAPS** (CASSINI PLASMA SPECTROMETER) measured the properties of ion and electron populations in Saturn's plasma environment [*Young et al.*, 2004]
- **CDA** (COSMIC DUST ANALYZER) investigated the properties of small ice and dust particles [*Srama et al.*, 2004]
- **INMS** (ION AND NEUTRAL MASS SPECTROMETER) determined the composition and structure of ions and neutrals in the moons' environments and the magnetosphere of Saturn [*Waite et al.*, 2004]
- **MAG** (CASSINI MAGNETOMETER) measured the magnetic field properties of Saturn's environment [*Dougherty et al.*, 2004]
- **MIMI** (MAGNETOSPHERE IMAGING INSTRUMENT) measured the properties of high-energy ions and electrons and imaged energetic particles in Saturn's magnetosphere [*Krimigis et al.*, 2004]
- **RPWS** (RADIO AND PLASMA WAVE SPECTROMETER) determined electrical and magnetic fields and perturbations in Saturn's plasma environment [*Gurnett et al.*, 2004]

Lastly, two radio wave instruments were part of the payload:

- **Cassini Radar** mapped the surface of Titan [*Elachi et al.*, 2004]

- **RSS** (Radio Science Subsystem) conducted radio measurements of atmospheric and ionospheric properties as well as of the masses of objects in the Saturn system using NASA's Deep Space Network ground antennas [*Kliore et al.*, 2004]

Instruments of interest to the reader of this thesis are highlighted in red in Figure 3.1. UVIS, which the majority of the results presented here are based on, is described in more detail in the following section.

3.2 Cassini's Ultraviolet Imaging Spectrograph

UVIS was a spectral imaging instrument in the UV wavelength range and was comprised of two moderate-resolution telescope-spectrographs operating in the wavelength ranges 56 to 118 nm (extreme ultraviolet, or EUV) and 110 to 190 nm (far ultraviolet, or FUV), a high speed photometer, and a hydrogen deuterium absorption cell. Figure 3.2 shows the assembly of the different components.

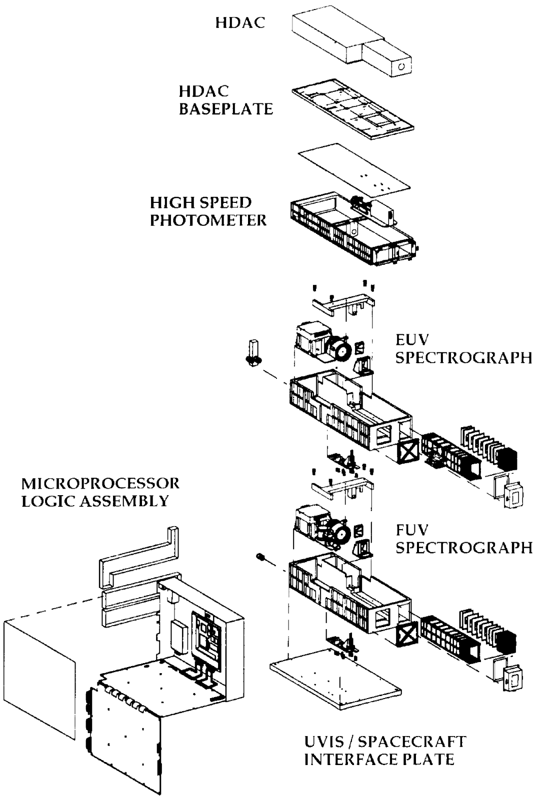

Figure 3.2: *Schematic of the UVIS instrument, with the different sensors labelled. Image taken from Esposito et al. [2004]*

The UVIS instrument had a broad range of scientific objectives. It proved a useful tool for determining the atmospheric and cloud properties and composition, and for analysing the atmospheric circulation and physics of Titan and Saturn. Using stellar occultation and spectroscopy, UVIS contributed greatly to the investigation of the configuration and composition of Saturn's rings and their interrelation with Saturn's satellites. Furthermore, UVIS data helped unravelling the characteristics of Saturn's icy moons.

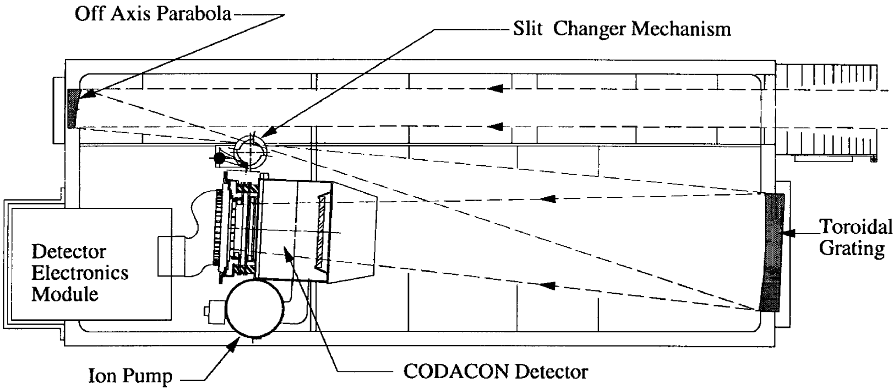

Figure 3.3: *Schematic of the UVIS FUV sensor. Image taken from Esposito et al. [2004]*

Of a greater importance to this thesis however are the capabilities of UVIS in observing Saturn's UV auroral emissions, as the far ultraviolet (FUV) channel covers the wavelength range in which much of the UV auroral emission falls. The signal in the FUV's spectral range is dominated by the H_2 Lyman and Werner bands and includes the H Lyman-α line; the FUV sensor is therefore perfectly suited to capture the bulk of Saturn's auroral emissions.

The FUV telescope-spectrograph, a schematic of which is shown in Figure 3.3, has an aperture of $20 \times 20\,\mathrm{mm}^2$. The incident light first reaches an off-axis parabolic mirror and is deflected through an interchangeable entrance slit of width 75/150/800 μm, providing a field of view (FOV) of $0.75/1.5/8 \times 64\,\mathrm{mrad}^2$, onto a toroidal grating. The grating has a 300 mm horizontal radius of curvature and acts as a spectrometer. Both the mirror and the grating are coated with Al and MgF_2. Finally, the diffracted light falls onto a two-dimensional coded anode array converter (CODACON) detector. This detector plate counts and locates impinging photons with a resolution of 64 spatial pixels × 1024 spectral pixels. At one instance in time, the FUV sensor can therefore image a line of 64 pixels at its full spectral resolution of 1024 frequency bins between 110 and 190 nm.

All intensities measured by the detector need to be corrected in several steps. While the sensitivity of the CODACON has been measured in a laboratory environment before the launch of Cassini, it was observed to change as a function of wavelength and time such that continuous in-flight re-calibrations were necessary. This was achieved by observing the star Spica on a regular basis and adjusting calibrations following an exponential decay of sensitivity. After accounting for the detector sensitivity, the constant background caused by the RTGs has to be subtracted from the data. Lastly, anomalous CODACON pixels have to be invalidated and the missing data interpolated.

Observations of auroral emissions on giant planets may also be considerably affected by hydrocarbon absorption, skewing the detectable emission. However, with some knowledge of the ionospheric composition it is possible to infer the total unabsorbed H_2 emission intensity in the UV range ($70 - 170\,\mathrm{nm}$) from the observed UVIS spectra. For this reason, all UVIS data used in this thesis is integrated between $155 - 162\,\mathrm{nm}$ and multiplied by a factor 8.1 as described in *Gustin et al.* [2016, 2017]. A single UVIS exposure is thereby reduced to a row of 64 pixel intensities of the total unabsorbed H_2 emission in the UV, without any spectral information remaining.

Combination of Auroral Images

In order to obtain two-dimensional images, the spacecraft was slewed such that the UVIS slit sweeped across the auroral region. Combining consecutive slit exposures yields a pseudo-image – named such because different parts of the image have been recorded at different times and not over the same period such as for "real" images.

Each image is projected onto a $0.5° \times 0.25°$ (lon × lat) planetocentric polar grid at an altitude of 1100 km above Saturn's 1 bar level ($R_E = 60,268\,\mathrm{km}$, $R_P = 54,364\,\mathrm{km}$) where the auroral emission profile was observed to maximize [*Gérard et al.*, 2009]. Figure 3.4a shows an example dataset from 2016 DOY 278. The data has been calibrated and spectrally integrated as described above, such that only two dimensions remain (1151 slit exposures × 64 pixels). Shown here is the emission rate in kR observed by each pixel during each exposure (color scale shown in Fig. 3.4b), with the consecutive slit exposures arranged from the top downwards. Note that the two outermost pixels on both sides of the slit are unused – they have shown anomalous signals and were therefore excluded in most auroral observations. In this example, UVIS scanned over the auroral emission three times, imaging different parts of the auroral oval. After each scan, marked with a blue-dashed frame, CASSINI quickly slewed back across the auroral oval to prepare for the following scan. These sections, marked with red-dashed frames, are excluded

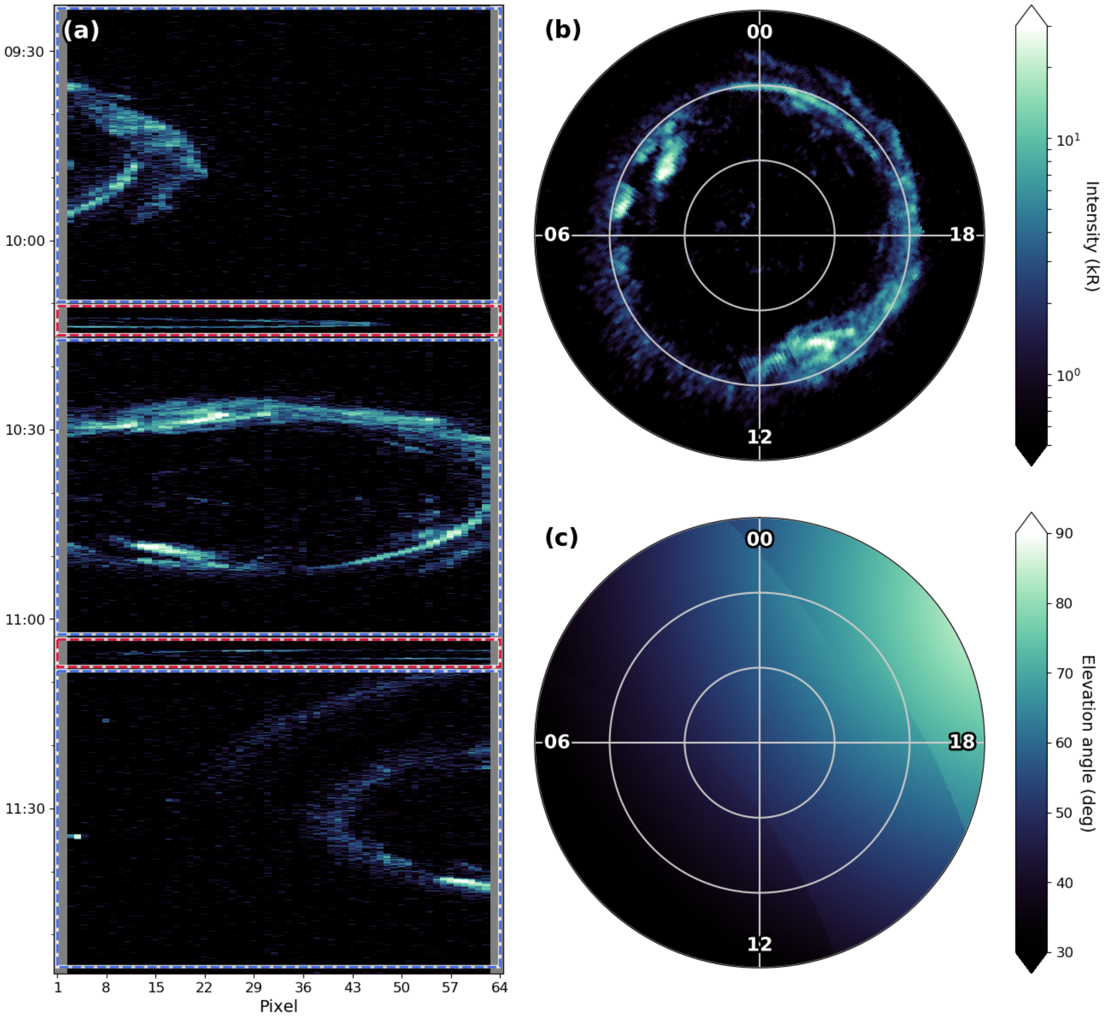

FIGURE 3.4: *UVIS polar projection procedure. (a) Calibrated and spectrally integrated dataset from 2016 DOY 278, 09:22-11:56 UTC (southern hemisphere), with UTC time on the vertical axis and the 64 UVIS pixels on the horizontal. All single slit exposures are simply arranged below one another, the integrated emission rate of each pixel shown in a logarithmic color scale (same scale as in panel b). Blue and red boxes frame the sections of the original dataset which were eventually projected or discarded, respectively. (b) Polar projection resulting from this dataset, with the same color scale. The view is from above the northern pole, observing the southern hemisphere through the planet. Local midnight is on the top, the Sun / local noon is at the bottom. Concentric grid rings mark the colatitude from the pole in steps of 10°. (c) CASSINI's elevation angle above the horizon as seen from each grid bin.*

from the projection procedure due to the high attitude uncertainty and the lower spatial resolution during the quick attitude change. All data within the blue-dashed frames is then polar projected onto a planetocentric grid. This is done using Cassini SPICE pointing information available on the NASA Planetary Data System to determine the exact viewing direction of each pixel (boresight and corners) and its intersection with the aurorae's ionospheric layer. The polar projection of the example dataset from Fig. 3.4a is shown in Figure 3.4b. Panel 3.4c shows Cassini's elevation angle above the horizon at the location of each longitude-latitude grid bin.

It is important to note that this projection does not conserve photon counts, which means that auroral emission powers can only be obtained with knowledge of the spacecraft viewing geometry. A detailed analysis of this problem is given in appendix A.

Dayglow Removal

Depending on the hemisphere and season at Saturn, some auroral images obtained by UVIS may be contaminated with dayglow. The choice of UV wavelength range used to derive the UV brightness as described in the previous section mitigates this effect to some degree, but some contamination remains nevertheless. This dayglow is visible as a clear gradient in background brightness, increasing from midnight to noon. If the radiant flux, or "auroral power", is to be integrated from such images (see appendix A) or absolute brightness values are to be compared, it may be necessary to remove this background in order to obtain reliable values.

Figure 3.5 demonstrates a simple algorithm which proved to reliably remove dayglow from UVIS images. Using all UVIS images of the same hemisphere obtained during a ±3 h window centered on the image which is to be corrected, we determine a distribution of SZA versus background brightness. This is achieved by collecting all pixels situated at colatitudes $> 23°$ (red-dashed line in Figure 3.5a) – covering only regions well equatorward of the statistical equatorward boundary of auroral emissions [e.g., *Badman et al.*, 2006; *Carbary*, 2012; *Nichols et al.*, 2016; *Kinrade et al.*, 2018; *Bader et al.*, 2019b]. By median-filtering the SZA-brightness distribution with a box 10° wide in SZA, we obtain a smooth, rather linear relation (see Fig. 3.5b) which is used to model the background

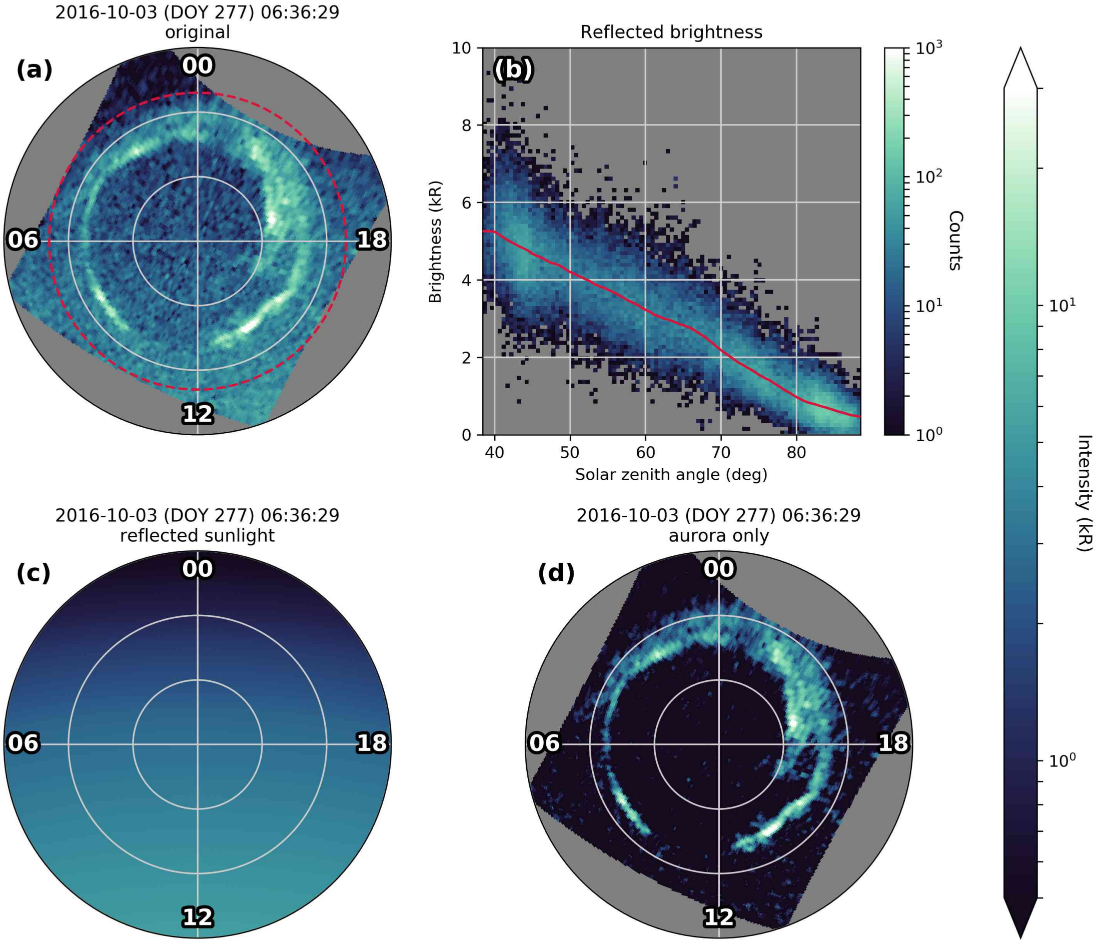

Figure 3.5: *Demonstration of an algorithm removing dayglow from UVIS images. (a) Polar-projected UVIS image from 2016 DOY 277, looking down onto the northern pole with midnight towards the top. Shown is the total unabsorbed* H_2 *emission intensity of Saturn's northern aurorae with a logarithmic color scale as defined with the large colorbar to the right. Concentric rings mark the colatitude from the northern pole in steps of* 10°. *All data outside of the red-dashed line at* 23° *colatitude is considered background emission and used for estimating the brightness of dayglow. (b) SZA versus brightness histogram of all background pixels of all images within a* ±3 h *window around this observation, with the median overlaid in red. (c) Brightness map of dayglow derived from the median of the distribution in (b). (d) The original image with the derived background brightness (c) subtracted.*

of dayglow for the entire region covered by the UVIS image (Fig. 3.5c). This modelled background brightness is subtracted from the original image, leaving only true auroral emissions (Fig. 3.5d).

3.3 THE CASSINI MAGNETOMETER

The CASSINI orbiter was equipped with two magnetometers: a fluxgate magnetometer and a vector helium magnetometer, both mounted on the magnetometer beam at different distances to allow for proper subtraction of the spacecraft's magnetic field contribution [*Dougherty et al.*, 2004]. However, the vector helium magnetometer failed soon after CASSINI's arrival at Saturn, leaving only the fluxgate magnetometer and necessitating more complex calibration and data cleaning procedures.

The fluxgate magnetometer consisted of three single-axis ring core fluxgate sensors mounted orthogonally to each other, allowing the measurements of the magnetic field in three dimensions. A drive coil, wound around the high permeability ring core, generated a modulated magnetic field driving the core into saturation with alternating polarity at a frequency of $\sim 15\,\mathrm{kHz}$. A second coil around the ring core then measured changes in the symmetry of the core's saturation as voltage changes which were analysed by the on-board electronics.

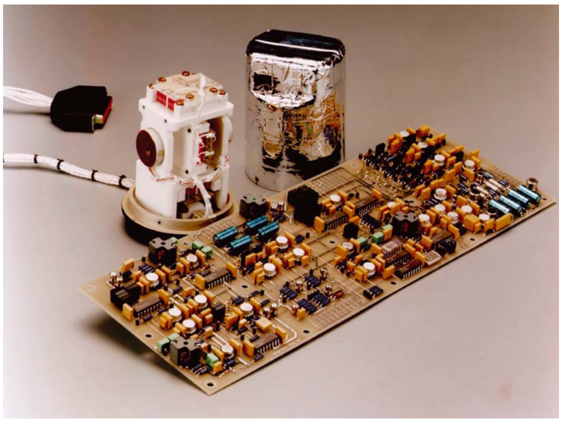

FIGURE 3.6: *Photo of CASSINI's fluxgate magnetometer and its electronics board. Taken from Dougherty et al. [2004].*

The magnetometer operated in four dynamic ranges, allowing magnetic field observations up to $\pm 44,000\,\mathrm{nT}$ at $5.4\,\mathrm{nT}$ resolution. Smaller dynamic ranges allowed for better resolutions, reaching down to $4.9\,\mathrm{pT}$ in the $\pm 40\,\mathrm{nT}$ range. The time resolution at which magnetic field vectors were downlinked to Earth was typically 32 measurements per second.

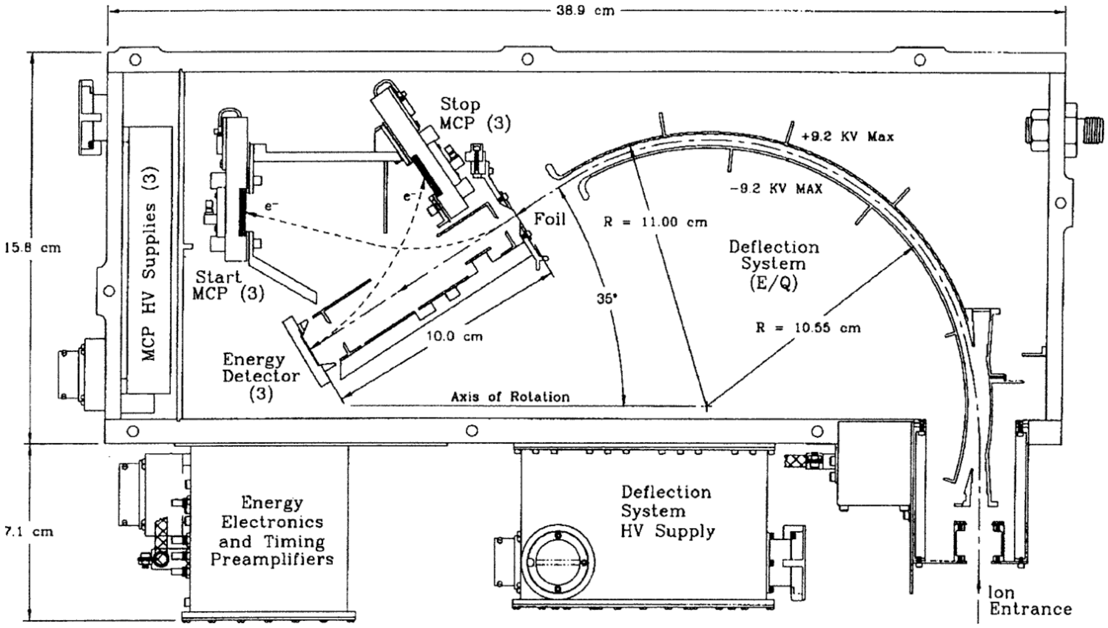

Figure 3.7: *Schematic of the MIMI-CHEMS detector. Taken from Krimigis et al. [2004].*

3.4 Cassini's Magnetosphere Imaging Instrument

Cassini's Magnetosphere Imaging Instrument (MIMI) was an instrument package designed for performing in situ measurements of neutral and charged particles as well as global imaging of Saturn's magnetosphere [*Krimigis et al.*, 2004]. Its three detector systems will be introduced below.

Charge Energy Mass Spectrometer

The Charge Energy Mass Spectrometer (CHEMS) was designed to measure the three-dimensional distribution of suprathermal ion populations in Saturn's magnetosphere. It consisted of three telescopes placed around the spacecraft body, resulting in a nearly full 4π steradian FOV when Cassini was spinning.

Each telescope was equipped with an electrostatic analyser followed by a time of flight detection system and a solid state detector. This allowed CHEMS to determine an incoming particle's energy per charge, speed of motion and residual energy, respectively – providing knowledge of its mass, charge state and energy. A sketch of one detector is shown in Figure 3.7. CHEMS was capable of measuring ions with energy per charge

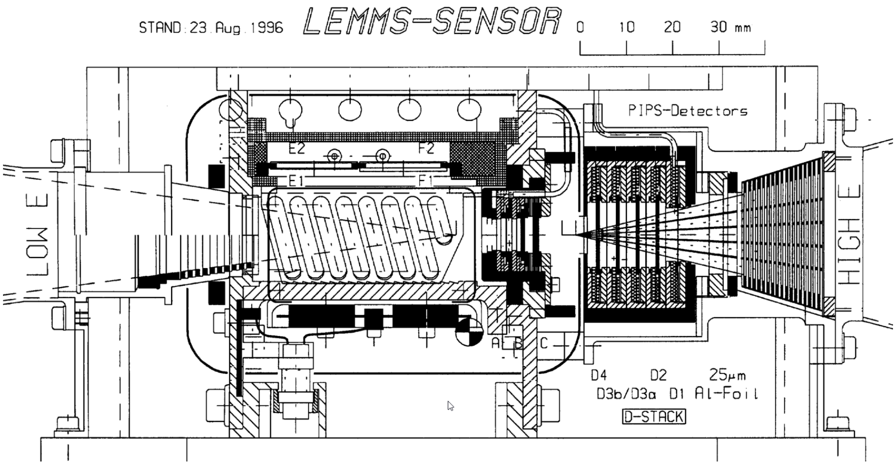

Figure 3.8: *Schematic of the MIMI-LEMMS detector head. Taken from Krimigis et al. [2004].*

between 3 – 220 keV and ion species as heavy as Fe.

Low-Energy Magnetospheric Measurement System

The Low-Energy Magnetospheric Measurement System (LEMMS) was a two-ended telescope used for measuring ions with energies > 30 keV and electrons with energies between 15 keV and 1 MeV. Each telescope end was equipped with solid state detectors, with one telescope end designed to cover the lower and the other covering the higher end of the measurable energy ranges. The entire telescope was heavily shielded against penetrating particles and mounted on a rotating platform to maximize its pitch angle coverage in combination with spacecraft rolling. However, the rotation mechanism unfortunately malfunctioned partway through Cassini's Saturn tour, such that for the rest of the mission only specific viewing directions could be observed.

In the low energy end of the telescope, electrons were separated from ions and deflected by a static inhomogeneous magnetic field to hit different side-facing detectors while ions proceeded to detectors at the end of the telescope. The electron and ion signals were processed by a pulse height analyser to provide 64-channel energy spectra. The high energy end of the telescope was equipped with a stack of solid state detectors which measured the energy loss of energetic electrons and ions along their trajectory through the detector stack.

Ion and Neutral Camera

MIMI's Ion and Neutral Camera (INCA) was a time of flight sensor capable of detecting both ions and ENAs with energies from 7 keV/nucleon to 3 MeV/nucleon. It could provide information on the mass of each detected particle as well as its direction of motion and energy.

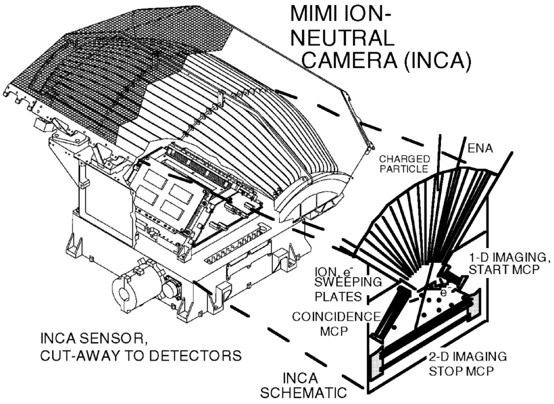

Figure 3.9: *Schematic of MIMI-INCA. Taken from Krimigis et al. [2004].*

With an instantaneous FOV of 120° × 90° and an angular resolution of up to 64 × 64 pixels, it was able to either resolve a significant part of the local ion pitch angle distribution or to provide remote imagery of the global distribution of energetic ions using a technique known as ENA imaging [e.g., *Roelof*, 1987]. Switching between these two modes was done by changing the potential applied to the collimator plates ("Ion, e^- sweeping plates" in Figure 3.9) to either allow charged particles to pass into the detector or let them instead be deflected into the collimator walls.

The time of flight detector was triggered when incoming particles penetrated the thin start foil – secondary electrons were produced which entered the start multichannel plate (MCP) to provide the start time. The original incident particle traveled further through the instrument until it encountered a second foil, located in front of the stop MCP. Again, secondary electrons were produced and entered the MCP, registering the stop time. The mass of an incident particle was determined by the pulse height of the MCP signal, as the number of secondary electrons produced increases with the particle mass. The pulse height was sufficient to distinguish between the two most common neutrals in Saturn's magnetosphere, hydrogen and oxygen, but further mass discrimination was not feasible.

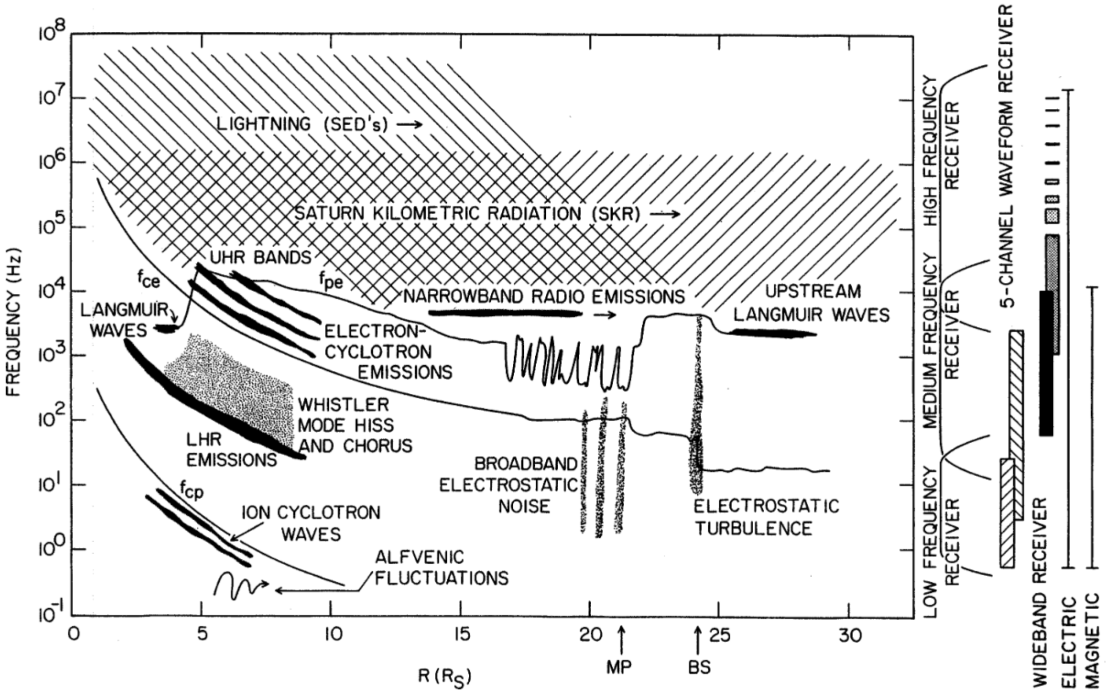

Figure 3.10: *Sketch of radio and plasma wave features observable in Saturn's magnetosphere. Taken from Gurnett et al. [2004].*

3.5 The Cassini Radio and Plasma Wave Spectrometer

The Radio and Plasma Wave Spectrometer (RPWS) was used to study radio emissions and plasma waves in Saturn's magnetosphere [*Gurnett et al.*, 2004]. A sketch of the different radio and plasma wave features known to occur is shown in Figure 3.10.

It was equipped with three nearly orthogonal electric field antennas measuring electric fields at frequencies between 1 Hz and 16 MHz, three orthogonal search coil magnetic antennas measuring magnetic fields at frequencies between 1 Hz and 12 kHz as well as a Langmuir probe used for determining the electron density and temperature.

A number of different receiver systems was used to analyse the antenna signals. The high frequency, medium frequency and low frequency receiver together covered a frequency range from 1 Hz to 16 MHz, while a five-channel waveform receiver could process observations from up to five antennas simultaneously in different spectral ranges. A wideband receiver completed the set of receivers, making RPWS the most advanced radio spectrometer to investigate Saturn's magnetosphere to date.

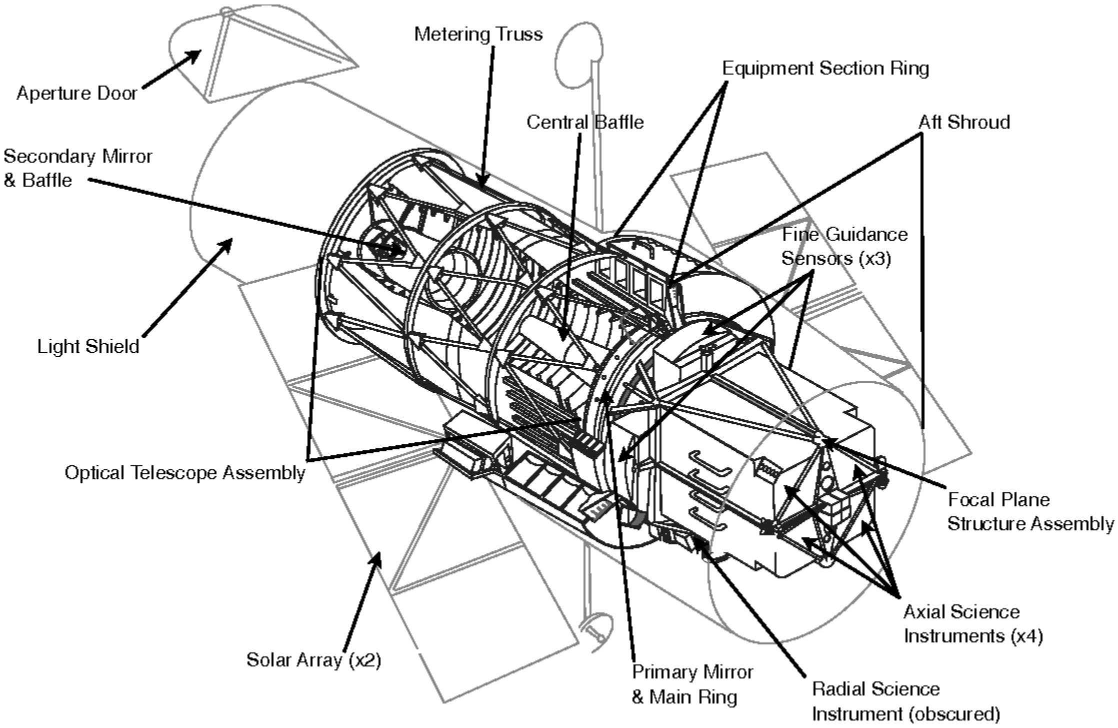

Figure 3.11: *Schematic highlighting the HST's main components. The imaging instruments used for auroral observation campaigns are indicated as "Axial Science Instruments" at the rear of the telescope. Image taken from [Lallo, 2012].*

3.6 The Hubble Space Telescope

The Hubble Space Telescope (HST) is a 2.4 m reflecting telescope observing in the near-UV, visible, and near-IR bands, built by the NASA and operated in a coordinated programme together with the ESA. It was placed into orbit in 1990 and remains in operation, providing scientific data of immense importance to the astronomical community. It is positioned in a geocentric low Earth orbit at an altitude of about 540 km, allowing observations unimpeded by atmospheric effects.

A basic schematic of the HST is shown in Figure 3.11. The optical assembly constitutes the biggest part of the spacecraft, with the scientific instruments located towards the rear. Currently there are four instruments in operation:

- **ACS** (Advanced Camera for Surveys) is a highly versatile imaging instrument operating between the near-UV and near-IR bands

- **COS** (Cosmic Origins Spectrograph) performs UV spectroscopy of faint point sources
- **STIS** (Space Telescope Imaging Spectrograph) is mainly used for imaging and spectrography in the UV spectrum and is the main instrument used for observing aurorae on the outer planets
- **WFC3** (Wide Field Camera 3) is designed for imaging in the visible spectrum

Most auroral observations from Saturn used in this thesis were taken by the Space Telescope Imaging Spectrograph (STIS), described in detail in *Woodgate et al.* [1998]. It was installed on HST in 1997 and is still in operation. Its optics are designed to correct for the spherical aberration of HST's primary mirror before the beam of light entering the instrument is directed according to the observation mode and detector required. After passing either gratings for the spectroscopy modes or apertures for the imaging modes, the beam eventually hits one of STIS' three detectors: two multianode microchannel array (MAMA) detectors for the UV and a charge-coupled device (CCD) for the visible bands. Auroral emissions at Saturn maximize in the FUV wavelength range, which is covered by one of the MAMA detectors designed for observations within $115 - 170\,\mathrm{nm}$. Incident photons produce electrons as they hit the CsI photocathode, which are accelerated into an MCP where the charge is detected by an anode array. The MAMA detector is hence able to record the time and position on the detector of each incident photon (time tag mode) or simply integrate the signal to an image over a fixed exposure time. For auroral observations, a SrF_2 filter (bandpass $125 - 190\,\mathrm{nm}$) is often used to block the H Lyman-α line (121 nm) in order to remove potential geocoronal contamination.

All HST images were background subtracted, corrected for geometric distortion and projected onto a planetocentric polar grid [*Clarke et al.*, 2009]. A comparison between a raw HST image and its projection is shown in Figure 3.12.

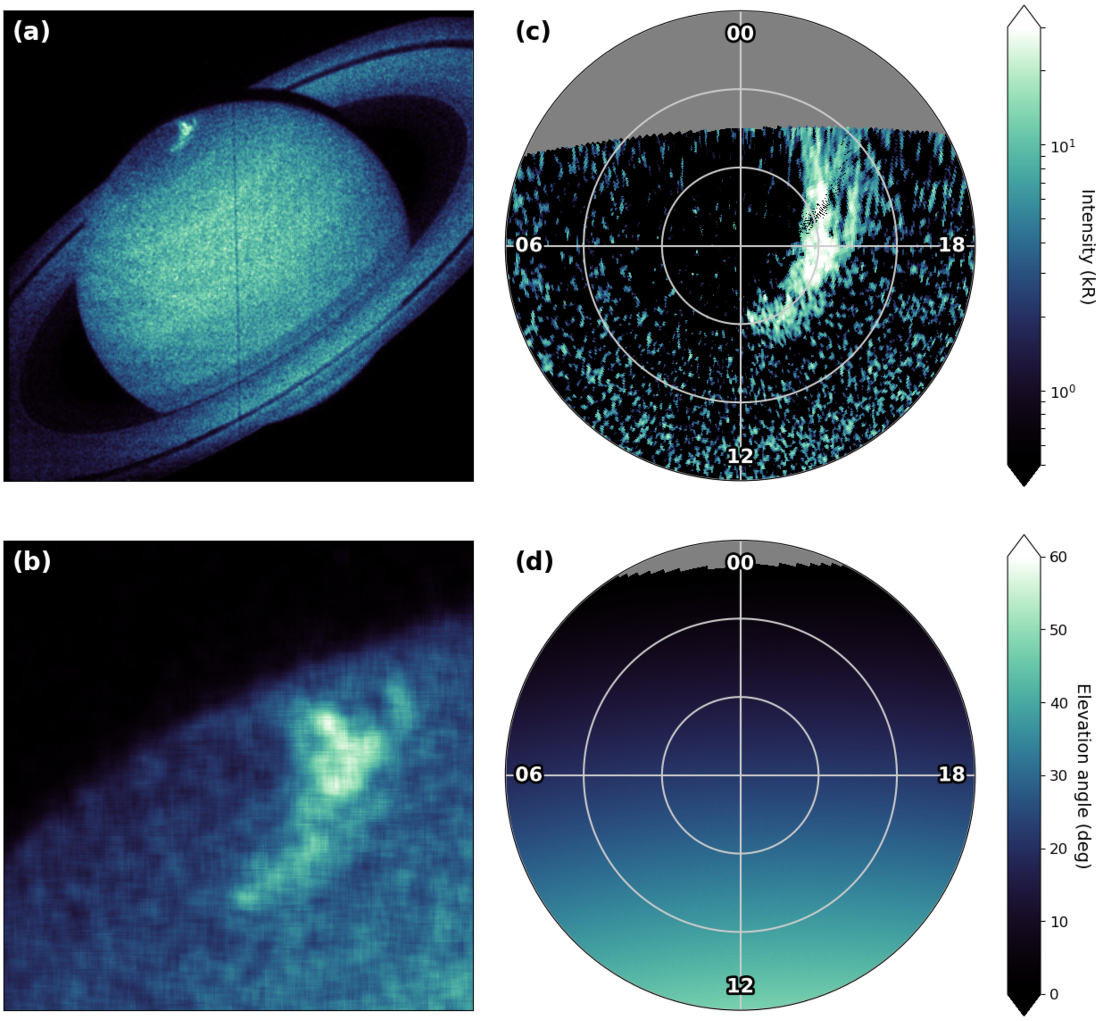

FIGURE 3.12: *HST polar projection procedure. (a) HST STIS image from 2014 DOY 100, 02:29 Saturn UTC (northern hemisphere). The original photon count rate per pixel, smoothed with a 11 × 11 pixel^2 box, is shown in an arbitrary color scale. (b) Detail of the same image, highlighting the auroral region. (c) Background-subtracted polar projection resulting from this image, the emission rate color-coded. The view is from above the northern pole, with local midnight on the top and the Sun / local noon at the bottom. Concentric grid rings mark the colatitude from the pole in steps of 10°. (d) HST's elevation angle above the horizon as seen from each grid bin.*

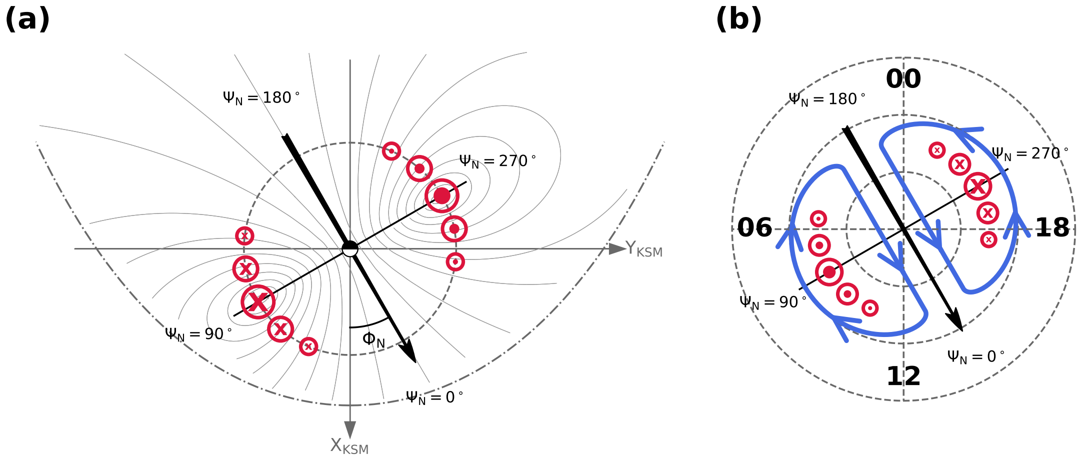

Figure 3.13: *Sketch showing the northern PPO system as seen from above the northern hemisphere. (a) Saturn's equatorial magnetosphere, with noon towards the bottom and dusk towards the right. The magnetopause is indicated with a grey dash-dotted line, following the model of Arridge et al. [2006] with $p_{\mathrm{dyn}} = 0.05\,\mathrm{nPa}$. The inner grey dashed circle marks the approximate location where the main PPO-related FACs pass through the equatorial plane at $\sim 15R_{\mathrm{S}}$. At the instant shown, the northern PPO phase is $\Phi_{\mathrm{N}}(t) = 30°$, a black arrow marking the orientation of the associated equatorial model perturbation dipole. The magnetic perturbation field lines of the northern PPO system are shown as solid grey lines, following, e.g., Provan et al. [2009b] and Andrews et al. [2010b]. The principal meridians of the PPO phase function are shown by the black arrow and its perpendicular, the phase values Ψ_{N} increasing clockwise as indicated. The direction of FACs passing the equatorial plane due to the perturbation field is marked in red, with circled crosses indicating a flow into and circled dots a flow out of the plane of the figure. (b) The corresponding view of Saturn's northern ionosphere as seen from above the north pole, again with noon towards the bottom. Bold numbers around the edge of the panel indicate the LT, dashed circles mark the northern colatitude from the pole in $10°$ steps. The orientation of the model perturbation dipole and the PPO principal meridians are marked in black as in panel (a). Ionospheric upward (downward) FAC regions at auroral latitudes are indicated with red circled dots (crosses). Blue lines and arrows sketch the driving neutral atmospheric and ionospheric flows in the northern hemisphere [Jia et al., 2012; Jia and Kivelson, 2012; Hunt et al., 2014, 2015].*

3.7 Planetary Period Oscillation Longitude Systems

This section describes longitude systems which are based on PPO magnetic field periodicities. The momentary orientation of each PPO system is hereby defined by the PPO dipole phase angle $\Phi_{\mathrm{N,S}}(t)$, which describes the azimuthal angle at time t at which the northern/southern PPO-related equatorial magnetic perturbation fields point radially outward from the planet. $\Phi_{\mathrm{N,S}}(t)$ is hereby measured from noon and in the direction of Saturn's rotation. Figure 3.13 shows the northern PPO system at $\Phi_{\mathrm{N}}(t) = 30°$, a black arrow indicating the PPO perturbation dipole in the equatorial plane.

The PPO phases $\Psi_{\mathrm{N,S}}(\varphi, t)$ then provide longitude systems rotating with the PPO dipoles. They are defined as

$$\Psi_{\mathrm{N,S}}(\varphi, t) = \Phi_{\mathrm{N,S}} - \varphi \tag{3.1}$$

with φ being the azimuthal angle of any spatial point measured from local noon. In Fig. 3.13, four Ψ_{N} longitudes are marked in black.

PPO-associated FACs are always located at the same PPO phase. The FACs related to the northern PPO system are indicated in red in Fig. 3.13, with 3.13a showing the currents (partly) passing through the equatorial plane from the northern to the southern hemisphere (circled red crosses) and in the opposite direction (circled red dots) - roughly half of the PPO-associated currents diverge from the field-aligned direction and close in the equatorial plane [*Bradley et al.*, 2018b]. Figure 3.13b shows the footpoints of these currents in Saturn's northern polar ionosphere, upward (downward) currents being indicated with red circled dots (crosses). The atmospheric/ionospheric vortical flow pattern thought to generate the northern PPO perturbations are shown in blue. The southern PPO system, generated by oppositely directed atmospheric/ionospheric flows in the southern hemisphere, effects the same pattern of FACs in the northern hemisphere in its own longitude system (see Figure 3.14).

The PPO dipole phase angles $\Phi_{\mathrm{N,S}}(t)$ used in this study were derived from sinusoidal fits to Cassini magnetic field data as thoroughly described in, e.g., [*Andrews et al.*, 2012; *Provan et al.*, 2013, 2014, 2015, 2016, 2018].

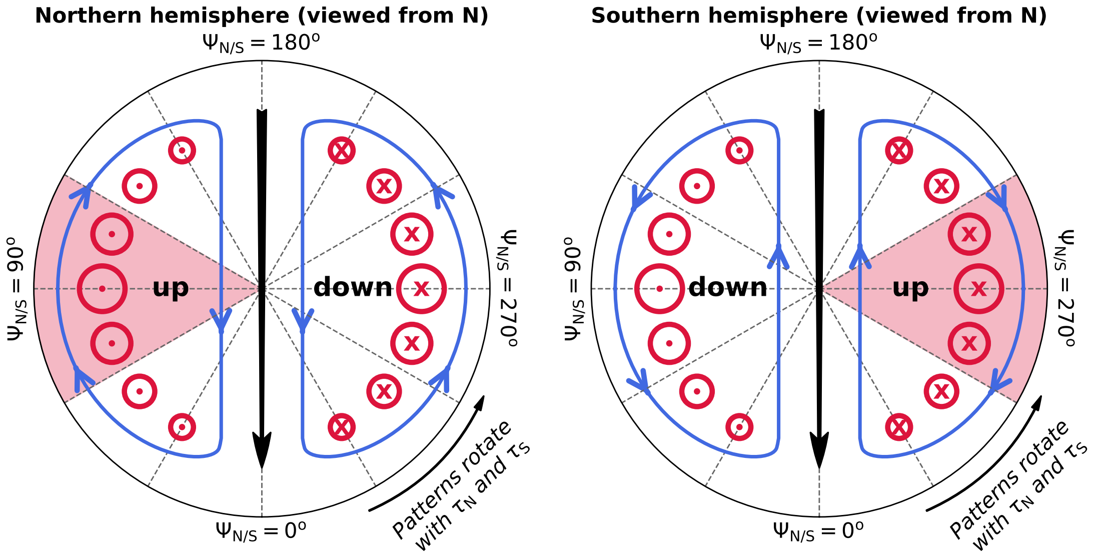

FIGURE 3.14: *PPO-related rotating FAC patterns in Saturn's polar ionospheres, shown in PPO longitude systems. (Left) PPO-associated FACs in the northern polar ionosphere. Red-circled dots (crosses) mark FACs flowing out of (into) the figure plane, corresponding to upward (downward) currents relative to Saturn's surface. The section highlighted in red marks where an intensification of the aurorae is expected. The atmospheric/ionospheric flow pattern in northern hemisphere, driving the northern PPO perturbations, is drawn in blue. (right) Corresponding sketch for the southern hemisphere, looking through the planet from the north. Circled dots (crosses) mark downward (upward) currents now, and blue lines and arrows mark the atmospheric/ionospheric flows in the southern hemisphere which drive the southern PPO system.*

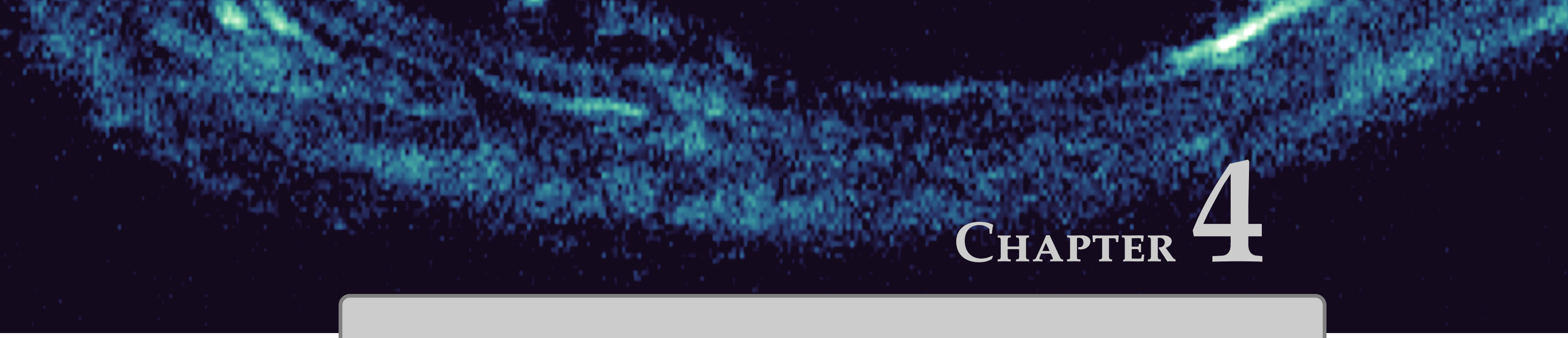

CHAPTER 4

PUBLICATION I

Statistical planetary period oscillation signatures in Saturn's UV auroral intensity

A. BADER, S. V. BADMAN, J. KINRADE, S. W. H. COWLEY, G. PROVAN AND W. R. PRYOR (2018)

Journal of Geophysical Research: Space Physics, *123*, 8459–8472

doi:10.1029/2018JA025855

AUTHOR CONTRIBUTION STATEMENT AB led the study, performed the data reduction and analysis and authored the initial draft. SVB provided guidance throughout the project. JK supported the data analysis. SWHC and GP provided expertise on PPOs in Saturn's magnetosphere. GP provided PPO phase data for the analysis. WRP provided technical support for UVIS data. All authors contributed to the interpretation of the results and were involved in review and editing of the paper until publication.

This authorship statement was approved by all collaborating research groups.

Journal of Geophysical Research: Space Physics

RESEARCH ARTICLE
10.1029/2018JA025855

Key Points:

- Saturn's UV auroral intensities are modulated in phase with rotating current systems through all local times and in both hemispheres
- The intensity modulation in each hemisphere is controlled by the superposition of currents originating in both hemispheres
- This marks the first unambiguous evidence of planetary period oscillation-associated field-aligned current flow effects in auroral data

Correspondence to:
A. Bader,
a.bader@lancaster.ac.uk

Citation:
Bader, A., Badman, S. V., Kinrade, J., Cowley, S. W. H., Provan, G., & Pryor, W. R. (2018). Statistical planetary period oscillation signatures in Saturn's UV auroral intensity. *Journal of Geophysical Research: Space Physics*, *123*, 8459–8472. https://doi.org/10.1029/2018JA025855

Received 2 JUL 2018
Accepted 26 SEP 2018
Accepted article online 3 OCT 2018
Published online 29 OCT 2018

Statistical Planetary Period Oscillation Signatures in Saturn's UV Auroral Intensity

A. Bader[1], **S. V. Badman**[1], **J. Kinrade**[1], **S. W. H. Cowley**[2], **G. Provan**[2], **and W. R. Pryor**[3]

[1]Department of Physics, Lancaster University, Lancaster, UK, [2]Department of Physics and Astronomy, University of Leicester, Leicester, UK, [3]Science Department, Central Arizona College, Coolidge, AZ, USA

Abstract Saturn's auroral emissions are a good measure of field-aligned current (FAC) systems in the planet's magnetospheric environment. Previous studies based on magnetic field data have identified current systems rotating with the planetary period oscillations (PPOs) in both hemispheres, superimposed onto the local time-invariant current system producing the main auroral emission. In this study we analyze the statistical behavior of Saturn's ultraviolet auroral emissions over the full Cassini mission using all suitable Cassini-UVIS images acquired between 2007 and 2017. We examine auroral intensities by organizing the data by the two PPO coordinate systems. Strong statistical intensifications are observed close to the expected locations of upward FACs in both hemispheres, clearly supporting the main assumptions of the present theoretical model. We furthermore find clear signatures of modulation due to interhemispheric current closure from the PPO system in the opposite hemisphere, although with a weaker modulation amplitude. The auroral intensity in the northern hemisphere is shown to be modulated by a superposition of the FACs associated with both PPO systems, as the modulation phase and amplitude varies as expected for different relative orientations (beat phases) of the two PPO systems.

1. Introduction

Saturn's ring of main auroral emission is located approximately at the open-closed field line boundary (e.g., Cowley et al., 2004). This region maps magnetically to the outer magnetosphere where flow shears between hot plasma populations, subcorotating at different angular speeds with Saturn's planetary rotation, are the largest (e.g., Belenkaya et al., 2014; Hunt et al., 2014). These flow shears are thought to set up a system of field-aligned currents (FACs), of which the upward component is carried by downward electrons precipitating onto the upper atmosphere. The electron impact excitation of hydrogen then generates auroral emissions in a range of wavelengths spanning IR, visible, and UV bands. The same accelerated electron populations are thought to generate the Saturn Kilometric Radio (SKR) emissions through the cyclotron maser instability (e.g., Galopeau et al., 1989).

This largely local time (LT)-fixed FAC system is controlled by internal plasma production and flow as described by the Vasyliunas cycle and by the interaction of Saturn's magnetosphere with the solar wind (e.g., Belenkaya et al., 2011; Cowley et al., 2004, and references therein). How exactly the factors internal and external to Saturn's magnetosphere contribute to the observed LT asymmetries as observed, for example, in ultraviolet and infrared auroral emissions (e.g., Badman, Andrews, et al., 2012; Kinrade et al., 2018; Lamy et al., 2018) remains unsolved. However, it is presumed that the Dungey cycle reconnection near the high-latitude magnetopause occurs mostly in the prenoon sector, leading to larger auroral intensities in this LT regime. This is thought to happen due to a blockage near noon, preventing empty flux tubes returning from the nightside from crossing into the postnoon sector. As the flux tubes can only flow past noon once reconnection has been triggered, auroral emissions could largely be confined to the prenoon sector (Radioti et al., 2017; Southwood & Chané, 2016).

The Kronian aurora is furthermore characterized by many different transient features on both the dayside and nightside of Saturn. These are usually associated with magnetic reconnection events in the magnetotail, the dayside magnetopause, and the cusp (e.g., Badman et al., 2013; Jackman et al., 2013; Meredith et al., 2013). It is also assumed that plasma wave activity, possibly induced by the noon blockage of the plasma return flow, might be responsible for transient brightenings (Yao et al., 2017). Recently, Guo et al. (2018) furthermore observed signatures of near-noon reconnection within Saturn's magnetodisk. These findings indicate that transient dayside emissions might not only be controlled by solar wind interaction as previously thought but also by the internally controlled Vasyliunas cycle plasma flow.

Furthermore, auroras on Saturn are expected to be modulated by the planetary period oscillations (PPOs). These are periodicities close to Saturn's rotation period which can be observed frequently in all particle, field, and radio wave measurements around Saturn (e.g., Carbary & Mitchell, 2013, and references therein). Possible driving mechanisms for this phenomenon could be a vortical flow structure in the ionosphere of Saturn (e.g., Jia & Kivelson, 2012; Jia et al., 2012) or the plasma pressure of periodically injected energetic particles (Brandt et al., 2010). The PPO behavior can be modeled rather well by two magnetic perturbation fields, one located in each hemisphere and independently rotating in the direction of planetary rotation in both hemispheres at close to the planetary rotation rate—thereby generating a rotating system of FACs superimposed on the LT fixed system thought responsible for the main auroral emission (e.g., Andrews et al., 2010; Provan et al., 2016). These rotating FAC systems were found to produce upward and downward FAC regions mapping to the main auroral oval—modulating the intensity and location of the auroral oval in a sinusoidal manner (Hunt et al., 2014, 2015, 2016).

It has so far been challenging to study the PPO-induced modulation of the Kronian aurora to a significant extent, as this continuous modulation is superimposed on LT asymmetries in the auroral emission pattern, as well as with transient effects like solar wind compressions and sudden reconnection events. First studies investigating a possible intensity modulation of auroral emissions due to the PPO-induced FAC systems' phases have been performed but often produced inconsistent results. A physical association of the UV aurora and SKR emissions has been observed in preequinox HST data (Nichols, Cecconi, et al., 2010). Nichols et al. (2016), using HST imagery from 2011 to 2013, found some modulation of the observed UV intensities in both hemispheres—but as this study was performed on a comparably small dataset with incomplete PPO phase coverage, no hard conclusions could be drawn. An earlier study by Carbary (2013) used Cassini UVIS imagery from 2006 to 2009 to investigate rotational modulation of Saturn's auroral intensities with respect to SKR phase, but observed clear dependencies only for the southern hemisphere. Lastly, Badman, Andrews, et al. (2012) observed rotational modulation of infrared emissions in Cassini VIMS data between 2006 and 2009, although out of phase with the expected auroral response.

In this study, we expand on the previous investigations of auroral modulation due to PPO influences. Section 2 presents a short background on the ongoing investigations of PPO and the reference frames used in this study. Drawing on the full Cassini UVIS data set covering the time span from 2007 to 2017, described in section 3, we are able to statistically investigate auroral intensity modulations in great detail. The results of this analysis are presented in section 4. Finally, we summarize and discuss our findings and their implications for present theoretical models in section 5.

2. The PPO Systems and Their Reference Frames

With the arrival of Cassini at Saturn, it became clear that most magnetospheric data exhibit oscillatory signatures at rates close to Saturn's rotation rate. After Kurth et al. (2008) had found two distinct SKR rotation periods, Gurnett et al. (2009) suggested that these emanate from the two polar hemispheres of Saturn. Extensive studies showed that in the northern (southern) polar cap regions, only magnetic field oscillations due to the northern (southern) PPO system are observed (Andrews et al., 2012), but in the equatorial regions, a superposition of both systems' oscillations is found (Provan et al., 2011). Provan et al. (2018) observed southern oscillations in the northern hemisphere on the proximal and F-ring orbits. Such interhemispheric coupling is believed to be observed on these orbits due to the trajectory of Cassini, where the spacecraft moves very close to the FAC regions. The relative amplitude of the two systems has been found to vary over time (Provan et al., 2013), which can largely be attributed to seasonal effects (Provan et al., 2015) and, to some degree, changes in the upstream solar wind properties (Zarka et al., 2007). From mid-2013 to mid-2014, the two PPO systems have been shown to rotate in coalescence, locked nearly in relative antiphase (Provan et al., 2016).

Both PPO systems are thought to be associated with a system of rotating current systems, with currents flowing into one side of the ionosphere along the magnetic field, crossing the polar cap as ionospheric Pedersen currents and returning outward into the magnetosphere as FACs on the other side. Current closure is expected to occur partly in the equatorial plane in the outer magnetosphere and partly in the opposite hemisphere. In each hemisphere's ionosphere, currents associated with either PPO system flow on the same field lines and are therefore not latitudinally separated (e.g., Bradley et al., 2018; Hunt et al., 2015). A comprehensive and illus-

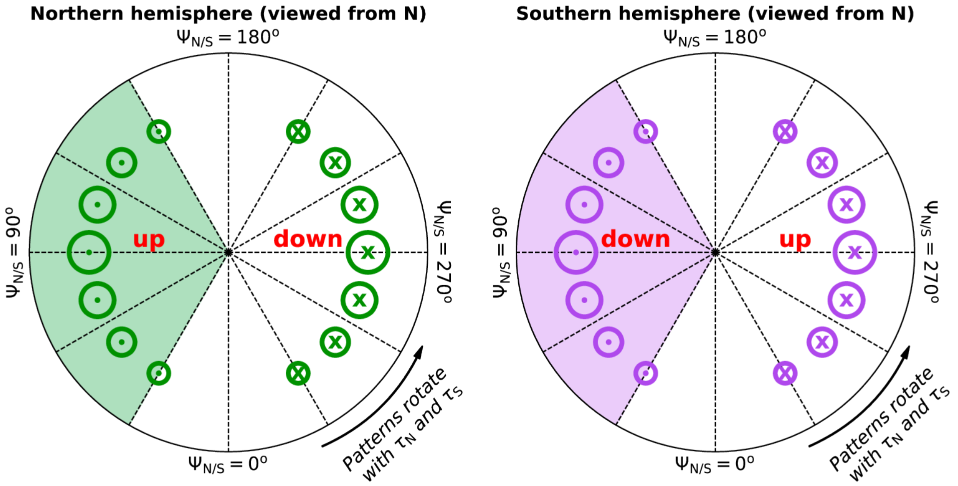

Figure 1. Sketch of the PPO-related rotating FAC patterns in Saturn's polar ionosphere. To the left (right), the northern (southern) polar region is shown as viewed from above the north pole. With the near-equatorial PPO perturbation fields directed toward the bottom of the figure, $\Psi_{N/S}$ increases in clockwise direction. Green/purple-circled crosses and dots represent FACs flowing into and out of the plane of the diagram, respectively. For example, in the northern hemisphere, upward FACs and therefore increased auroral intensities are expected at around $\Psi_N = 90°$ and at around $\Psi_S = 90°$. The relative orientation of the two PPO systems determines whether their associated upward FAC regions are colocated or not. PPO = planetary period oscillation; FAC = field-aligned current.

trated description of these current systems is given in, for example, Hunt et al. (2015). Both these PPO systems can be modeled with horizontally orientated dipole fields and rotate azimuthally in the direction of planetary rotation with their respective PPO rotation rates $\tau_{N/S}$. The orientation of each system is hereby defined by the counterclockwise azimuthal angle of the equatorial perturbation field $\Phi_{N/S}(t)$. This angle is referenced to local noon, increases in the direction of planetary rotation, and is often referred to as PPO dipole angle or phase angle.

For locating an auroral feature in this rotating frame, a PPO "longitude" system can then be defined with $\Psi_{N/S}(\varphi, t) = \Phi_{N/S}(t) - \varphi$ with φ as the LT-referenced planetary longitude. The location of a feature is therefore referenced to the PPO system's dipole orientation $\Phi_{N/S}(t)$ at a specific time t. An auroral feature rotating with the same speed as the PPO dipole, for example, would therefore have a constant $\Psi_{N/S}$ value.

From the PPO model initially proposed by Andrews et al. (2010) and more recently described by Hunt et al. (2015), it is clear that the associated FACs will have different strengths and flow directions at different $\Psi_{N/S}$. The expected FAC patterns are sketched in Figure 1. In the northern hemisphere, the upward FACs are expected to maximize close to $\Psi_N = 90°$ for the northern (primary) PPO system, with the downward currents maximizing around $\Psi_N = 270°$. Interhemispheric currents from the southern (secondary) PPO system closing the northern hemisphere are thought to cause the same FAC pattern, with upward currents maximizing near $\Psi_S = 90°$ and downward FACs peaking around $\Psi_S = 270°$. Conversely, upward FACs are expected to maximize close to $\Psi_{S/N} = 270°$ and downward FACs near $\Psi_{S/N} = 90°$ in the southern hemisphere (Hunt et al., 2015). With auroral brightness being directly related to upward currents associated with downward-precipitating electrons, we therefore expect to observe relatively higher auroral intensities at $\Psi_{N/S} = 90°$ for the northern hemisphere and $\Psi_{N/S} = 270°$ for the southern hemisphere and relatively lower intensities on the other side of the polar cap.

The relative strength of the current systems associated with the primary and secondary PPO systems changes with season (Provan et al., 2013). Over the course of the Cassini mission, the two PPO systems switched dominance several times, with often one system being stronger than the other by a factor 2 or larger. In case of equal strengths, we expect the primary PPO system to dominate the rotational modulation of the UV auroral intensity in each hemisphere, since the secondary system's currents are partly closed in the equatorial plane. Bradley et al. (2018) found that about half the current associated with each PPO system is closed in the equatorial plane, while the remaining half closes in the opposite hemisphere—the FACs in each hemisphere are therefore expected to be modulated twice as strongly by the primary than by the secondary PPO system. If however the strengths of the two PPO systems differ significantly, the currents associated with the dominating system and crossing over into the other hemisphere might be as strong or even stronger than the currents associated with the (primary) PPO system in that hemisphere. For a more detailed description, the reader is referred to, for example, Nichols et al. (2016).

3. Data Set

3.1. General

This study is based on the complete data set of auroral imagery obtained by the Cassini UVIS spectrographic imager (Esposito et al., 2004) between orbit insertion on 1 July 2004 and end of mission on 15 September 2017. The UVIS instrument consists of two telescope-spectrographs covering the wavelength ranges 56–118 nm (extreme ultraviolet) and 110–190 nm (far ultraviolet or FUV). All observations used in this study have been taken with the FUV channel.

The UVIS FUV sensor consists of 64 × 1,024 pixels, providing 64 spatially distinct spectra arranged along a single line. Each of the 64 spatial pixels has an angular resolution of 1.0 × 1.5 mrad. A two-dimensional pseudo-image is obtained by slowly slewing the spacecraft such that the detector sweeps over the area of interest. Depending on the apparent size of the auroral oval from the spacecraft's point of view, repeated sweeps may be necessary to attain full coverage of the auroral region. Latitude-longitude grids of each image are calculated by projecting each pixel onto an ellipsoid located at an altitude of 1,100 km above Saturn's 1 bar level ($R_E = 60,268$ km, $R_P = 54,364$ km)—the altitude at which auroral emissions are thought to be generated (Gérard et al., 2009). This is performed using Cassini SPICE pointing information available on the Planetary Data System.

During one exposure, each spatial pixel provides an intensity spectrum with a resolution of up to 1,024 spectral bins equally spread over the 110–190-nm range. In order to obtain the total unabsorbed H_2 emission in the 70–170-nm range, we first determine the brightness in the 155–162-nm range from the measured spectra. Multiplying the resulting intensity by the factor 8.1 then gives the unabsorbed H_2 emission intensity over the whole UV wavelength range (Gustin et al., 2016, 2017).

After discarding images with poor coverage of the auroral region and unsuitable viewing geometries, we are left with 4,192 images suitable for our analysis. From mid-2013 to mid-2014, the northern and southern PPO systems were rotating at the same rate, locked in near antiphase (Provan et al., 2016). Images taken during this interval would therefore introduce a strong statistical bias, as the two phase systems are not quasi-independent anymore. We therefore exclude all imagery taken during this time from our data set, leaving us with 2,777 images—still a much larger set than used in comparable previous studies.

The PPO phase for each UVIS image was determined using the most recent PPO model described in Provan et al. (2018). The initial determination of the PPO phase values employed in this study includes some inherent uncertainty due to the use of sliding windows with a size of several months, but the errors are relatively small and well described in the corresponding publications (e.g., Provan et al., 2016, 2018).

Additional inaccuracies are introduced due to the exposure time of UVIS UV imagery. High-resolution scans can take up to 3 hr—during this period, the PPO phase $\Phi_{N/S}(t)$ will have changed by more than 90°. Different pixels covering the auroral oval have likely been measured at different PPO phase angles, and the PPO phase used in our calculations might in some extreme cases be in error by up to 45° (the center time of the UVIS exposure is used to define its corresponding PPO orientations). These are rather rare cases, however—the mean exposure time of all imagery used is below 1,000 s, resulting in a PPO phase angle change of less than 10° throughout the exposure of a typical image. With a large enough data set like ours, we therefore expect these effects to largely average out.

3.2. Temporal and PPO-Phase Sampling

As most UVIS imagery has not been collected continuously but only in campaign-style whenever Cassini's orbital position was favorable and there was a justifiable scientific interest, the temporal coverage of the data set is very uneven. Figure 2 shows the number of images per year used in this study for both hemispheres. The number of images varies strongly throughout the mission, with, for example, only ~20 images from 2009 but close to 1,000 from the second half of 2014 for the northern hemisphere (imagery between 2014-0 and 2014-180 having been excluded due to the PPO phase lock as indicated in section 3.1). During the years 2010–2012, no UVIS images are available as Cassini's orbit was positioned mostly in the equatorial plane, and Saturn's polar regions were simply not visible to the instrument. Overall, we therefore cannot take into account

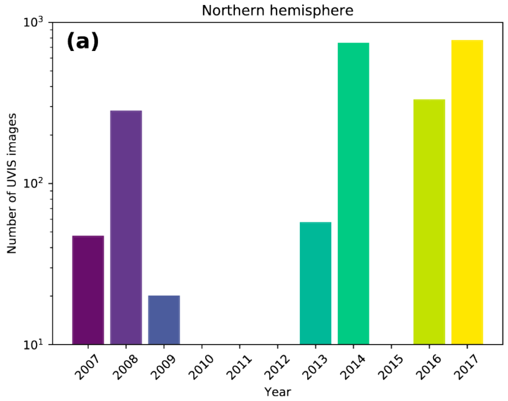

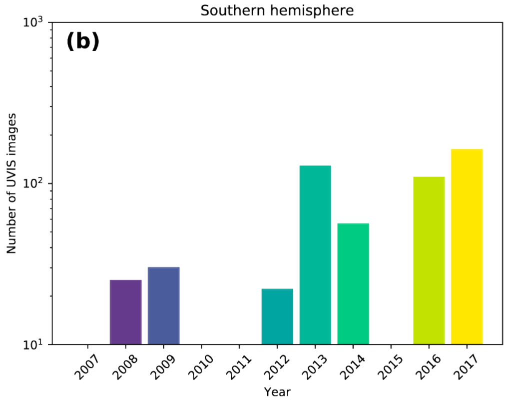

Figure 2. Number of UVIS images available for this study, (a) for the northern and (b) for the southern hemisphere. Note the logarithmic scale of the *y* axis. The temporal sampling is clearly quite uneven, with the years 2009–2012 providing barely any auroral imagery useful for our purpose.

temporal changes in relative PPO strengths and rotation rates between the two perturbation fields in any significant manner, apart from excluding the statistically biased data from mid-2013 to mid-2014 coalescence period as noted above. Note the unequal coverage between the northern and southern hemispheres—our data set encompasses 2,245 images in the north and 532 in the south.

Figure 3 shows the distribution of the used images across different PPO phase angles $\Phi_N(t)$ and $\Phi_S(t)$. As uneven as the temporal coverage may be, the full range of PPO phase angles has been sampled quite evenly

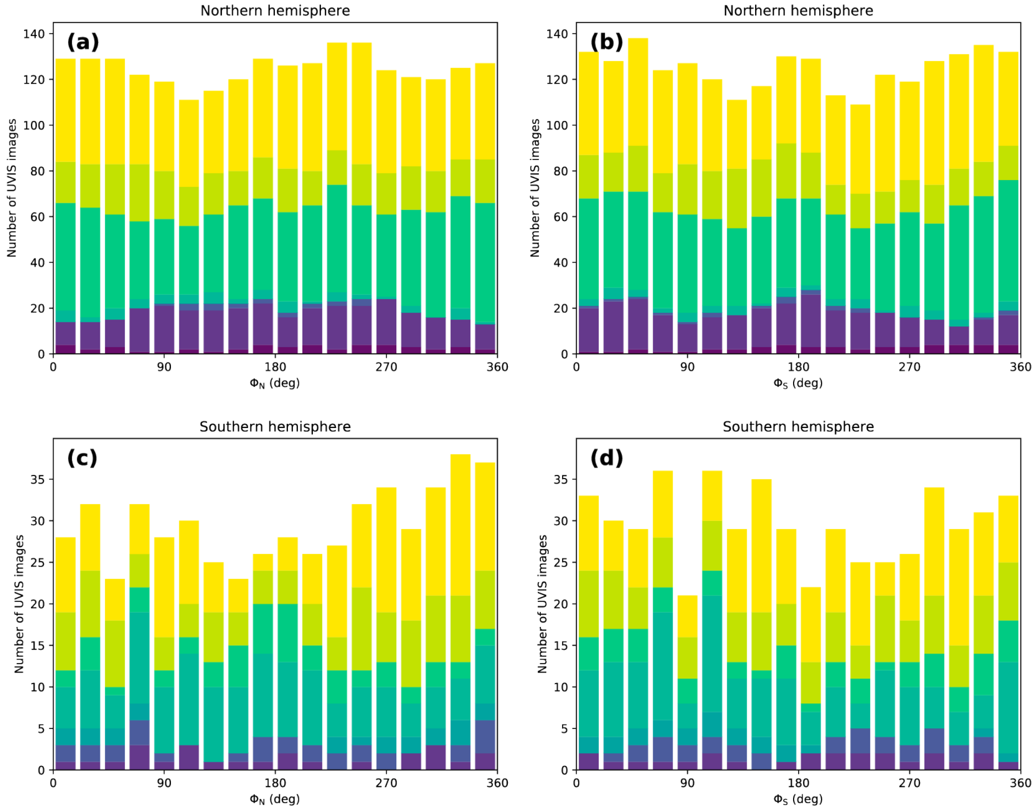

Figure 3. Coverage of planetary period oscillation phase angles $\Phi_{N/S}$ in both hemispheres; same data set as shown in Figure 2. (a) and (b) show the number of UVIS images per planetary period oscillation phase angle Φ_N and Φ_S bin, respectively. (c) and (d) show the same statistics for the southern hemisphere. The color scale in all plots corresponds to the year-coloring in Figure 2. Note the different vertical scaling between the top and bottom plots.

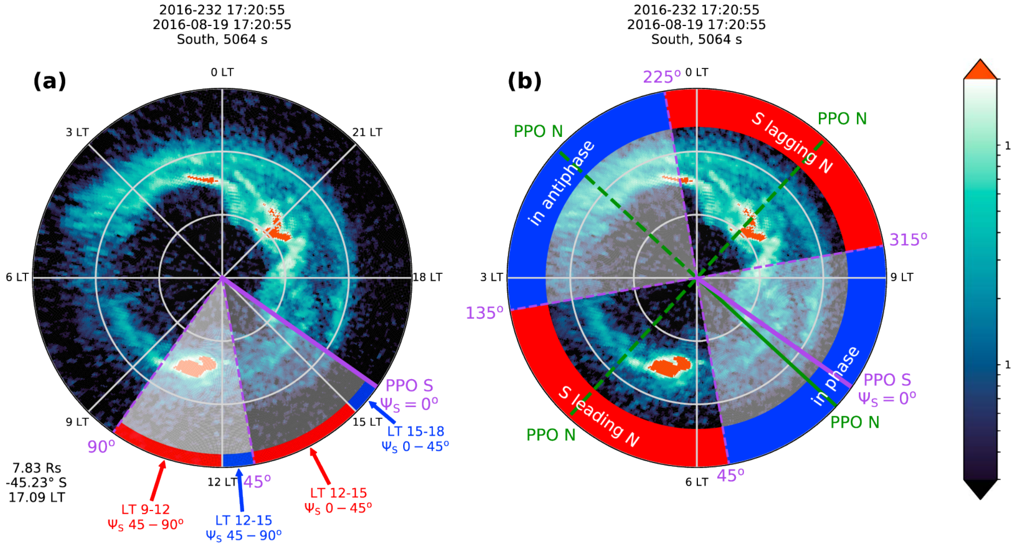

Figure 4. Example UVIS image of the southern hemisphere from 2016-232 on which the binning procedures are visualized. The view is from the above the north pole, looking "through" the planet into the southern hemisphere; the Sun/noon is toward the bottom of the figure. Concentric rings around the pole mark 10° colatitude steps. Information about Cassini's location (radius, latitude, and LT) is given in the bottom left corner; time stamp, hemisphere, and exposure time are given on top. Note the logarithmic intensity scale. (a) shows a 3-hr LT grid superimposed on the original image, with two exemplary PPO bins (45° bin size) overlaid in shades of white (the actual bin size used for this study is 4/3 h, and 20°, respectively. The orientation of the southern PPO system for this time period is indicated by a bold purple line, by definition coinciding with $\Psi = 0°$. The superposition of the LT and PPO bin grids creates a pattern of LT-PPO bins of alternating sizes; marked in blue and red and annotated accordingly. (b) defines the beat phases of the two PPO systems. Red and blue sections mark which beat phase this image would correspond to depending on the orientation of the northern PPO system. The actual orientation of the northern PPO system for this time stamp is marked in green, this image would therefore be assigned the beat phase *in phase*. Note that the beat phase does not depend on which hemisphere one considers, it is well defined only by comparing the orientations of the two PPO systems. PPO = planetary period oscillation; LT = local time.

in the northern hemisphere due to the large number of images. The coverage in the south is more uneven, but all PPO phases have been sampled a number of times.

4. Analysis

When analyzing the modulation of the auroral intensity due to the two rotating PPO systems, one has to take into account the clear LT differences which the Kronian aurora statistically exhibits (e.g., Grodent et al., 2005). In order to separate LT and PPO modulation as well as possible, we analyze the auroral intensity in an LT-PPO phase space—similar to previous studies using HST and Cassini VIMS data (Badman, Achilleos, et al., 2012; Nichols et al., 2016). The binning algorithm employed in this study is illustrated in Figure 4a. Each image is sectioned in longitude according to a combination of equally sized LT and PPO $\Psi_{N/S}$ binning grids. We choose bin sizes of $\Delta LT = 4/3$ hr and $\Delta\Psi_{N/S} = 20°$, respectively, resulting in 18 LT and 18 PPO "magnetic longitude", $\Psi_{N/S}$, bins. Note that superposing these two grids leads to the image being sectioned in 36 sections of alternating size as shown in Figure 4a. Each section is averaged in longitude before its intensity maximum is determined; all these maxima of all relevant images are then sorted into LT-PPO bins. The average intensity maximum in each LT-PPO bin is then calculated by taking a mean of all values in the corresponding bin.

The LT-PPO intensity histograms for the northern hemisphere are shown in Figure 5. Both histograms are based on the same set of 2,245 UVIS images of the northern aurora. A first look at the LT histogram on the top of both plots shows the typical LT distribution of the Kronian auroral intensity, with a clear peak near dawn and a small bump between dusk and midnight. This agrees with previous studies of both the UV (e.g., Kinrade et al., 2018; Nichols et al., 2016) and IR auroral emissions (Badman, Andrews, et al., 2012). The secondary emission peak behind dusk could be associated with periodic auroral spots caused by magnetopause reconnection or Kelvin-Helmholtz waves (e.g., Mitchell et al., 2016).

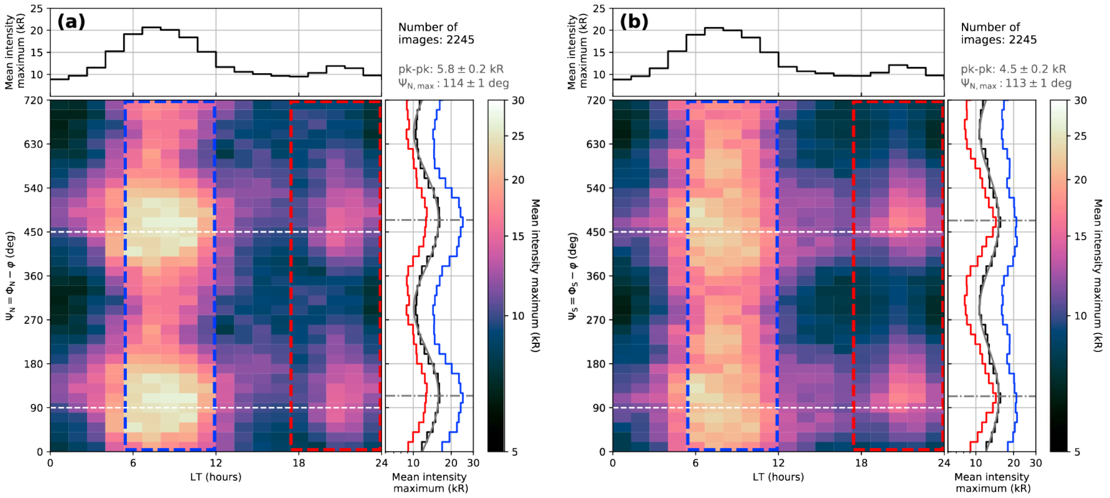

Figure 5. Mean of northern UV auroral intensity maxima per local time (4/3-hr bin size) and PPO phase $\Psi_{N/S} = \Phi_{N/S} - \varphi$ (20° bin size), shown in a logarithmic color scale. (a) Northern hemisphere auroral intensity ordered by the northern PPO system and (b) northern hemisphere auroral intensity ordered by the southern PPO system. Two Ψ phase cycles are plotted for clarity; the expected locations of maximum upward current are indicated by white-dashed lines. On the top and to the side of each 2-D histogram, the averages of the mean intensity maxima over the $\Psi_{N/S}$ and LT dimensions are shown in black, respectively. Separate histograms showing the PPO intensity modulation in the dawn-noon (blue) and dusk-midnight (red) regions are calculated from the accordingly marked parts of the histogram and shown to the right side (note the logarithmic intensity scale). The histogram over the full LT range (black) has been fitted with a simple sine (gray). Its maxima are marked with vertical dash-dotted lines; its peak-to-peak (pk-pk) amplitude and the Ψ_N angle with the highest intensity are given in the top right corner of each figure.

More interestingly, the northern auroral intensity shows a clear modulation in terms of both Ψ_N and Ψ_S. In Figure 5a, showing the auroral intensity ordered by LT and Ψ_N, the mean auroral intensity maximum varies with a peak-to-peak amplitude of about 5.8 kR. We find the sinusoidal fit on the histogram to maximize at $\Psi_N = 114°$, slightly lagging behind the expected location where maximum upward FAC is expected to occur, at $\Psi_N \approx 90°$ (e.g., Andrews et al., 2010; Hunt et al., 2014). This intensity modulation is however significantly higher and more ordered than observed in previous studies (Badman, Achilleos, et al., 2012; Nichols et al., 2016). The modulations are most intense near dawn (blue box/histogram) but clearly also present between dusk and midnight (red box/histogram). The phase of the modulation is largely consistent through LT and fits reasonably well to the regions of FACs identified by Hunt et al. (2014) using Cassini MAG data.

The northern auroral response associated with interhemispheric current closure of the southern PPO system, shown in Figure 5b, is very similar to the modulation imposed by the primary system. The peak-to-peak intensity modulation amplitude is approximately 4.5 kR, slightly smaller than what we observe for the primary system, and the peaks themselves seem less pronounced in Ψ_S. The intensity maxima are again located close to their expected location at $\Psi_S \approx 90°$ throughout all LTs, with the highest intensities occurring at $\Psi_S = 113°$.

In the southern hemisphere, considerably fewer UVIS images were available for this analysis—only 532 images, about 24% of what were used from the northern hemisphere. The corresponding histograms are shown in Figure 6. Nevertheless, modulations both due to the primary (Figure 6b) and secondary (Figure 6a) PPO system are clearly visible and mostly consistent with what was observed in the north. Again, intensity maxima in the primary (secondary) PPO system are found at $\Psi_S = 299°$ ($\Psi_N = 317°$) close to their expected locations at $\Psi_{N/S} \approx 270°$, and the amplitude of the modulation is slightly higher for the primary PPO system (5.6 kR) than for the secondary one (4.2 kR). It does seem that the modulation phase is slightly shifted between the dawn-noon and dusk-midnight sectors, although this might well be an effect due to the much smaller size of the data set compared to the northern hemisphere.

A feature shared between all the histograms shown however is the shift of the intensity peak in $\Psi_{N/S}$ relative to where the largest FACs are expected from the initial model deduced by Andrews et al. (2010), sketched in Figure 1. In both hemispheres and for both the primary and secondary PPO modulation, the intensity peak is consistently observed at larger $\Psi_{N/S}$ than expected from this model. The offset is in the range of $\Psi_{max} - \Psi_{N/S} \approx 25-50°$ in most histograms, such that the intensity maximum is always lagging behind the expected FAC maximum. Supporting this offset, Hunt et al. (2014) observed the magnetic signatures of the parallel upward

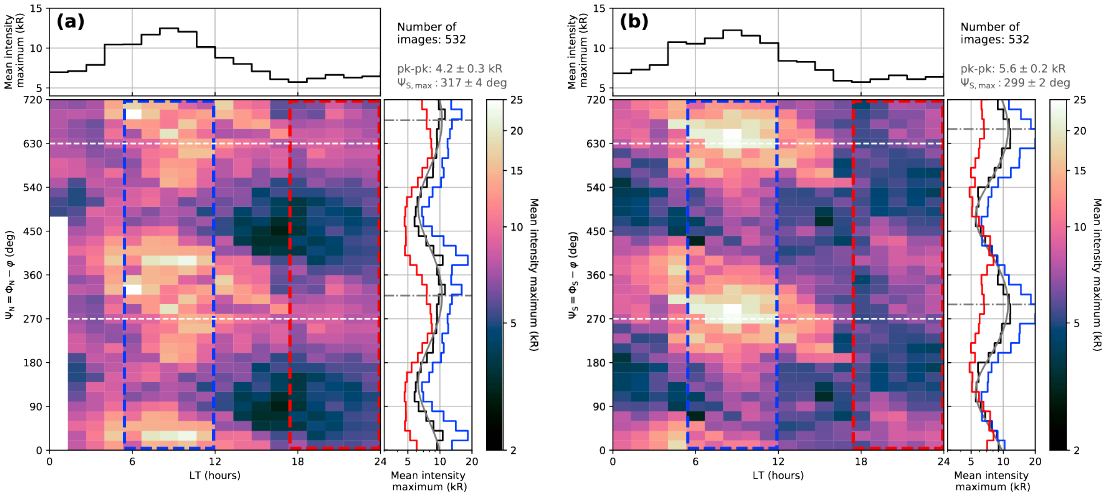

Figure 6. Mean of southern UV auroral intensity maxima per local time and PPO phase $\Psi_{N/S} = \Phi_{N/S} - \varphi$, in the same format as Figure 5. (a) Southern hemisphere auroral intensity ordered by the northern PPO system and (b) southern hemisphere auroral intensity ordered by the southern PPO system. Note the different intensity scales compared to Figure 5. PPO = planetary period oscillation.

current density of the main current sheet in the southern hemisphere to maximize at roughly $\Psi_S \approx 300°$, perfectly fitting to the intensity maximum in Figure 6b. In the northern hemisphere, the exact phase Ψ_N at which the upward current density maximizes was not determined (Hunt et al., 2015)—assuming a similar lag as in the southern hemisphere, the upward current can be expected to maximize at $\Psi_S \approx 120°$, coinciding very closely with the location of the observed UV intensity maximum we find (Figure 5a). It is unclear how this lag between the expected (Andrews et al., 2010) and observed FAC maxima, seen in both the magnetic field data (Hunt et al., 2014) and auroral emissions, can be explained.

We also want to note here that the auroral intensifications we observe in Figures 5 and 6 are not necessarily caused directly by PPO-associated FAC maxima rotating around the planet. PPO modulations pervade the entire magnetosphere and therefore entail a whole host of magnetospheric dynamics which could influence the auroral intensity in a periodic manner. The most obvious or best explored process in this context might be magnetotail reconnection, the occurrence of which is ordered by PPO phase (Jackman et al., 2016). Magnetotail reconnection events have been shown to occur preferentially at $\Psi_N \approx 0/360°$ and at $\Psi_S \approx 90°$, that is, they happen preferentially ~90° ahead in phase of the peak in the upward current for both PPO systems. With magnetotail reconnection generally causing short-lived and localized intense auroral features (Jackman et al., 2013), we would also observe statistical brightenings of the UV aurora at certain PPO phases—depending on the reconnection site as well as the lifetime and corotation speed of the associated auroral feature.

We have no means of separating direct PPO FAC-related auroral intensifications from indirect ones caused by PPO-modulated magnetospheric dynamics, and the impact of indirectly caused intensifications on our results cannot be judged reliably. The size of the data set and the typically rather low exposure time of the UVIS images compared to the occurrence rate of tail reconnection may seem to indicate that the fraction of images in which associated auroral emissions are observed is rather small—but depending on their lifetime, these auroral features might (sub)corotate for a significant time and, for example, lead to an auroral intensification when passing through dawn, "compromising" whole imaging sequences with indirect auroral brightenings.

The large number of UV images in the north additionally provides us with the chance to further investigate interactions between the primary and secondary PPO systems. In order to look at the interhemispheric interactions in more detail, we split the data set in four groups according to the relative orientation of the two PPO systems, the *beat phase*. Each image is binned into *in phase*, *in antiphase*, *S leading N*, and *S lagging N* beat phase bins as demonstrated in Figure 4b.

Depending on the beat phase, one can expect some overlaps between the FACs of both PPO systems, enhancing or attenuating the overall FACs flowing at certain $\Psi_{N/S}$. A sketch illustrating the anticipated behavior in the northern hemisphere is shown in Figure 7. Note that the latitudinal offsets of the current regions shown are

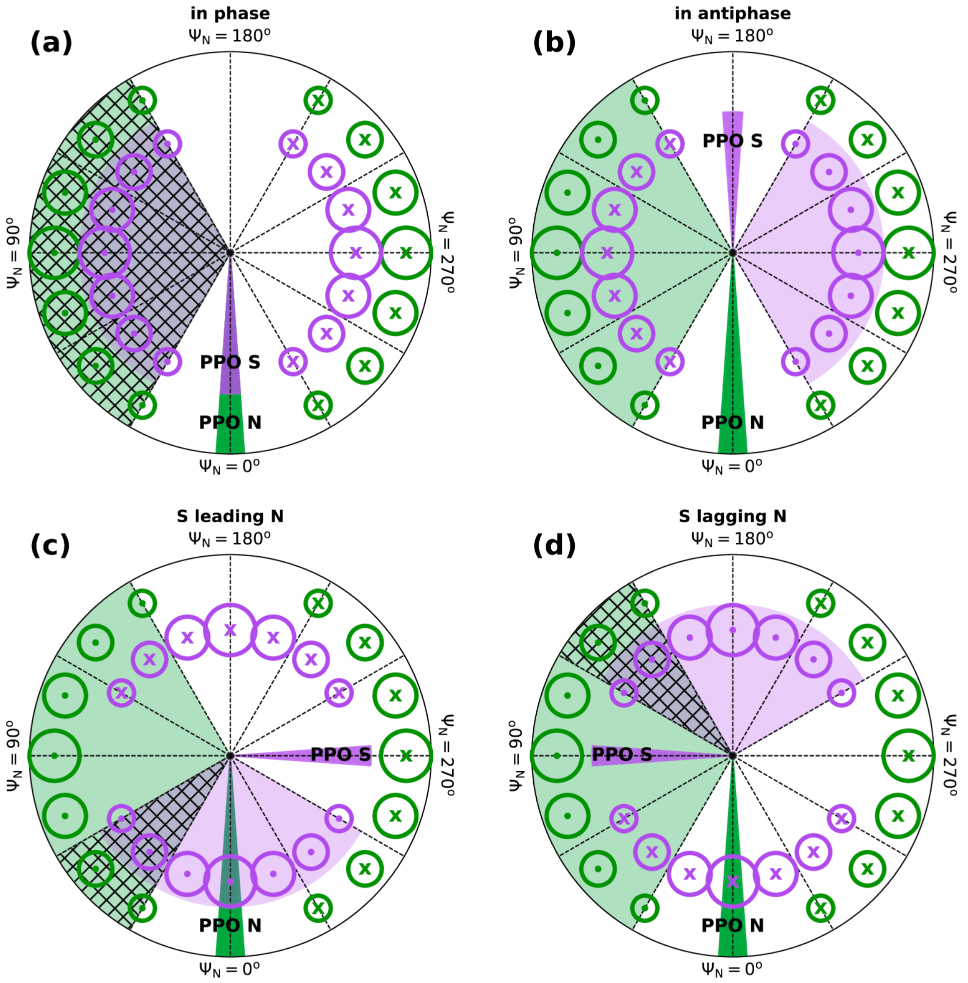

Figure 7. Sketch of expected FAC flows in the northern hemisphere for different beat phases. The view is onto the north pole, with the observer rotating with the primary PPO system (PPO north, in green). The northern PPO perturbation field is directed toward the bottom of each plot, with "magnetic longitude" Ψ_N increasing in clockwise direction. The relative orientation of the secondary PPO system (PPO south) is marked in purple. Circles with dots represent upward FACs, while circles with crosses indicate downward FACs; both colored according to the PPO system they are associated with. The radial/latitudinal offset of the FAC markers for both systems is only for clarity; in reality, both systems' FAC regions map to similar latitudes (e.g., Hunt et al., 2015). Regions where both systems' upward FACs overlap are highlighted with hatching. (a) shows how the upward FACs of the two PPO systems overlap around $\Psi_N = 90°$ if they are beating *in phase*, increasing the overall current density and leading to an enhancement of the intensity modulation expected due to the primary PPO system. At the same time, downward currents on the other side of the pole overlap. (b) In antiphase, the primary PPO upward FAC region coincides with the secondary PPO downward FAC region and vice versa; attenuating the modulation of auroral intensity due to the primary PPO system. (c) and (d) show overlaps between the two rotating FAC systems for the intermediate beat phases *S leading N* and *S lagging N*. The overlaps are thought to create regions of enhanced upward FACs offset to smaller/larger Ψ_N angles than expected if only primary PPO modulation was present. PPO = planetary period oscillation; FAC = field-aligned current.

only for clarity and have no physical background (the reader shall be reminded that FACs associated with both the primary and secondary PPO system flow on the same field lines, i.e., map to the same latitude; ; Bradley et al., 2018; Hunt et al., 2015). If both PPO systems are aligned *in phase* (Figure 7a), an increase in the FAC modulation due to the primary PPO system can be expected, while in the case of antiparallel orientation (*in antiphase* Figure 7b), the modulation should be attenuated by a factor depending on the relative strength of the two current systems at that time. For the intermediate beat phases (Figures 7c and 7d), shifts of the peak upward FAC regions caused by primary PPO modulation to lower (higher) Ψ_N are expected for PPO S leading (lagging) PPO N.

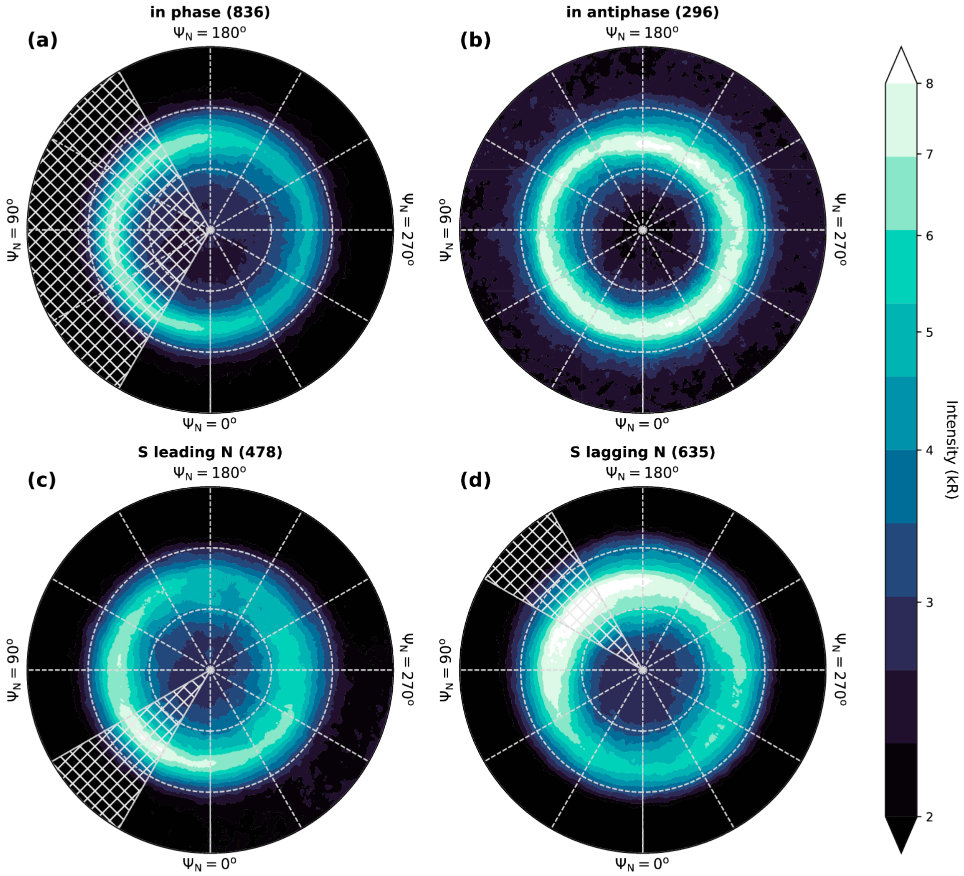

Figure 8. Contour plots of the median northern auroral intensity in the PPO north frame, for the four different beat phases. The format is the same as in Figure 7, with (a) the mean of all images taken while the two PPO systems were in phase and (b) for the *in antiphase* case. (c) and (d) show the mean auroral intensity for the *S leading N* and *S lagging N* beat phases, respectively. The white-hatched regions are very rough estimates of where the upward current regions of the northern (primary) and southern (secondary) PPO systems overlap and the UV auroral emission is expected to increase, as explained in Figure 7 and the accompanying text. Numbers in parentheses correspond to the number of UVIS images on which each median image is based. PPO = planetary period oscillation.

Figure 8 shows the average auroral emissions observed in the northern hemisphere. Each plot shows the mean of all UVIS images of the northern auroral oval and used in this study which were obtained when the two PPO systems were orientated *in phase*, *in antiphase*, and so on. If both PPO systems are aligned *in phase* (see Figure 8a), we find a clear increase of the auroral emission strength close to $\Psi_N = 90°$; directly opposite, we observe a strong depression in the emission strength near $\Psi_N = 270°$. This whole pattern is, as already observed previously, tilted to slightly larger Ψ_N than expected.

Figure 8b shows that the auroral emissions are considerably less ordered in the northern PPO frame if the northern and southern PPO systems are orientated in relative *antiphase*. While we expect the intensity maximum to be lower than for the *in phase* case, this cannot be observed. Instead, the emission is mostly unordered in Ψ_N, and the mean overall intensity seems to be higher compared to when the two PPO systems are *in phase*. It is to note however that the set of images on which Figure 8b is based is less than half the size of the set corresponding to Figure 8a. And while the number of images may still seem quite large, it is worth mentioning again that these are by no means continuous data sets. Of the 296 UVIS images used in Figure 8b, 73 have been acquired on 2014 DOY 289-290 and 56 on 2008 DOY 201. This strong grouping of images is on one hand fortunate, as it allows us to track several planetary rotations and directly investigate PPO-related modulations under near constant magnetospheric conditions. On the other hand, this obviously introduces a clear bias toward effects external to PPO such as different solar wind input between different image groups, and the absolute intensities between the different beat phase averages are therefore not really comparable.

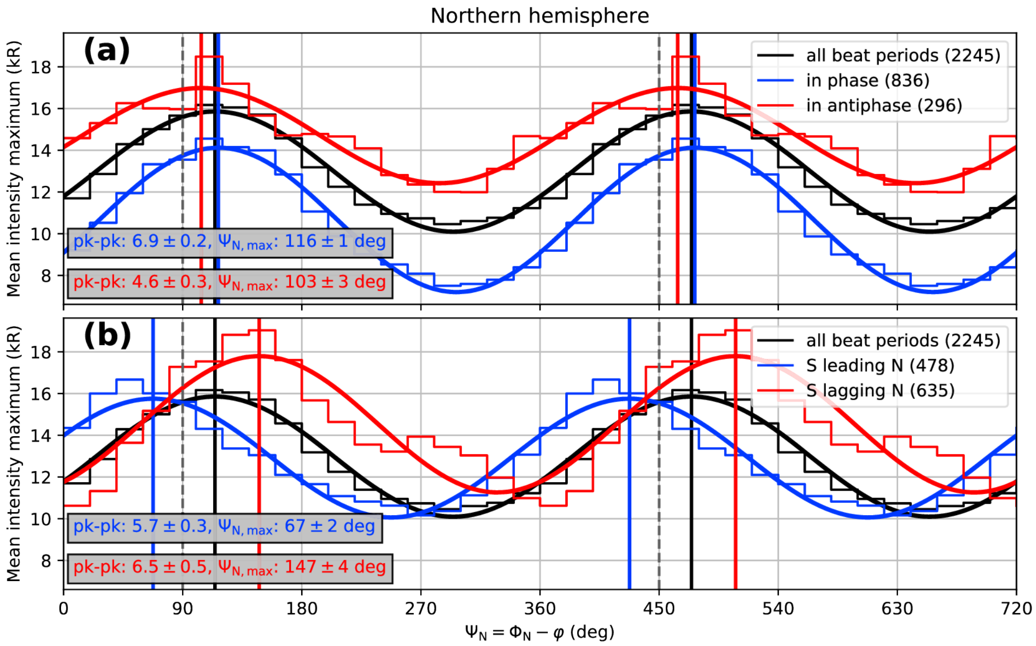

Figure 9. Comparison of Ψ_N versus mean intensity maximum histograms for different PPO beat phases for auroral observations in the northern hemisphere, ordered by the northern PPO system. Again, two Ψ_N cycles are shown for clarity. (a) compares the overall intensity modulation (black) with the modulations observable when the northern and southern PPO systems are in phase (blue) and when they are in antiphase (red). Numbers in parentheses show the number of UVIS images included in each subset. Note that the black line plot is identical to the black plot in the right side histogram in Figure 5a. The three histograms have been fitted with a simple sinusoid to clarify similarities and differences in modulation phase and amplitude. The fits' peak-to-peak modulation amplitudes and phases are given in boxes in the bottom left corner. The locations where maximum upward FACs are expected are marked with vertical-dashed lines. (b) is of the same format, comparing the northern auroral intensity modulations when the southern PPO system is leading (blue) or lagging (red) the northern PPO system with respect to the direction of planetary rotation. PPO = planetary period oscillation; pk-pk = peak-to-peak.

In Figures 8c and 8d, we see the observed auroral maximum in the northern PPO frame to be clearly displaced from its average location at about $\Psi_N = 90°$. As the hatched regions indicate, the displacement follows the direction predicted by the simple model of overlapping currents described in Figure 7. Please be aware that the hatched regions are only an approximation to guide the eye, and their width and location are by no means exact or based on any observations or calculations.

We now perform the same intensity analysis as shown previously (e.g., Figure 5) but this time, for a separate data set for each beat phase. Here we focus on analyzing the auroral intensity modulation in the northern hemisphere due to the northern PPO system (i.e., we calculate histograms identical to the one shown in Figure 5a with beat phase subsets of the full data set). For brevity, the full histograms are not shown—we only compare the LT-averaged histograms such as found, for example, on the side of Figure 5a. A comparison of these histograms for the different beat phases is shown in Figure 9. Figure 9a compares the averaged auroral intensity maximum of the *in phase* and *in antiphase* beat phases to the overall intensity histogram shown in Figure 5a. For clarity, all histograms have been fitted with a simple sinusoid. It is clear that the phase of the primary PPO-induced modulation does not shift noticeably, but the amplitude of the modulation is enhanced if both PPO systems beat *in phase* compared to when they are in relative *antiphase*. The modulation amplitude for the latter case is comparable to the overall modulation amplitude drawn in black. The intensity baselines of the colored curves are significantly offset, with the *in phase* intensities oscillating about an average intensity maximum of approximately 10 kR and the *in antiphase* curve being centered on approximately 15 kR. This difference might well be explained by the comparably small number of *in antiphase* images, making the overall histogram visibly noisy and possibly introducing a bias toward certain time periods, solar wind conditions or other non-PPO related effects.

Figure 9b compares the two intermediate beat phases with the overall average. In both cases, the modulation amplitude is largely comparable to the overall modulation amplitude. The slight differences in modulation amplitude may again be accounted for by the differing number of UVIS images going into each histogram, together with a possible bias due to varying image resolutions. However, the important detail in this figure is the phase shift of the two histograms compared to the overall average. As sketched in Figures 7c and 7d, we expect the auroral intensity peak to move to smaller Ψ_N if the southern PPO system is leading the northern (primary) one and to larger Ψ_N values for the opposite case—consistent with what we observe in Figure 9b.

5. Summary and Discussion

Following previous studies investigating PPO-modulation of Saturn's auroral emissions using HST UV imagery (Nichols et al., 2008, 2016; Nichols, Cowley, et al., 2010) and Cassini VIMS IR imagery (Badman, Andrews, et al., 2012), we employed the full Cassini UVIS data set to analyze the rotational modulation of Saturn's northern and southern UV aurora between 2007 and 2017. In order to avoid introducing a statistical bias due to the phase lock of the northern and southern PPO systems in near antiphase between mid-2013 and mid-2014, no data from this time window are included. This left us with 2,777 UVIS images which were used to qualitatively and quantitatively investigate modulations of the auroral intensity, due to the two PPO systems.

In both hemispheres, the auroral intensity was found to be strongly modulated by the primary PPO system (i.e., the system originating in the same hemisphere). The UV intensity generally maximizes close to $\Psi_N = 90°$ in the northern hemisphere and $\Psi_S = 270°$ in the southern hemisphere—coinciding with regions where upward FAC signatures have been observed (Andrews et al., 2010; Hunt et al., 2014). Concurrently, the intensities minimize on the opposite side of the pole where downward FACs have been observed. These intensity modulations are persistent throughout LT, albeit with varying modulation amplitudes in the dawn-noon and dusk-midnight regions.

Similarly, we observe clear UV auroral intensity modulations caused by the secondary PPO system (i.e., the system located in the opposite hemisphere) in both hemispheres. Again, intensity maxima (minima) are found close to where upward (downward) FAC currents associated with the secondary PPO systems have been observed to maximize (Bradley et al., 2018; Hunt et al., 2015)—with intensity maxima in the northern (southern) hemisphere occurring at about $\Psi_S = 90°$ ($\Psi_N = 270°$). Our observations are therefore clearly consistent with the present model of interhemispheric closure of PPO-associated currents (Bradley et al., 2018; Hunt et al., 2015). It seems as though the intensity modulation of the auroral emissions is slightly weaker for the secondary PPO systems than for the primary ones—indicating that not all PPO-associated currents close in the opposite hemisphere. Instead, this confirms that current closure must partly occur in the equatorial region just as observed by Bradley et al. (2018).

Interestingly, in both hemispheres and for both primary and secondary PPO modulations, the observed modulation of the UV auroral intensity is slightly phase shifted with respect to the sinusoidal modulation of FAC currents proposed by, for example, Hunt et al. (2014, 2015). This phase shift corresponds to an angular displacement of about 30–45° by which the observed auroral maxima and minima lag behind their expected locations. While we cannot readily explain this observation, we note that Hunt et al. (2014) found the upward FACs associated with the primary PPO system in the southern hemisphere to maximize at around $\Psi_S = 300°$—lagging the model expectation by about 30° as well. However, this analysis could be performed neither for the northern hemisphere or for interhemispheric modulations due to the complexity of the data set. Relying on this one analysis though, we can assume that the FAC and UV emission maxima are colocated and altogether lagging the model proposed by Andrews et al. (2010; see their Figure 12). Furthermore, it is worth pointing out that the FACs they observed in the equatorial plane are by no means as clearly organized as this first-order model assumes—the lag we observe in the UV auroral intensity is therefore well within the prediction error of this model.

A more in-depth analysis of the intensity modulation of the northern UV aurora during different relative orientations of the two PPO systems (beat phases) shows the expected higher (lower) modulation amplitude when the two systems are in phase (in antiphase); the expected phase shift of the modulation during times when the southern PPO system is leading/lagging the northern PPO system is also clearly observable. This serves as further proof that both the FACs associated with the primary and secondary PPO systems flow on the same field lines and that the auroral intensity depends on the combined current density of the two.

Overall, the UV auroral intensity observations analyzed in this study clearly support observations of FAC flows in both hemispheres. Despite some offsets between the locations of FAC maxima proposed by the initial simple model by Andrews et al. (2010) and the intensity maxima observed in auroral emissions, the results of this investigation provide the best overall evidence to date in auroral data for the application of the present simple PPO model (e.g., Andrews et al., 2010; Bradley et al., 2018; Hunt et al., 2014, 2015). This highlights the importance of continuous auroral observations for tracking PPO-related features on Saturn, as large data sets are required to successfully perform the necessary statistical analyses.

Acknowledgments
UVIS data are available from the NASA Planetary Data System (https://pds.jpl.nasa.gov). All PPO phase data (2004–2017) are available on the University of Leicester Research Archive (http://hdl.handle.net/2381/42436). A. B. was funded by a Lancaster University FST studentship. J. K. and S. V. B. were supported by STFC grant ST/M001059/1. S. V. B. was also supported by an STFC Ernest Rutherford Fellowship ST/M005534/1. Work at the University of Leicester was supported by STFC Consolidated Grant ST/N000692/1. W. R. P. acknowledges support from the NASA JPL Cassini Project and Central Arizona College.

References

Andrews, D. J., Cowley, S. W. H., Dougherty, M. K., Lamy, L., Provan, G., & Southwood, D. J. (2012). Planetary period oscillations in Saturn's magnetosphere: Evolution of magnetic oscillation properties from southern summer to post-equinox. *Journal of Geophysical Research*, *117*, A04224. https://doi.org/10.1029/2011JA017444

Andrews, D. J., Cowley, S. W. H., Dougherty, M. K., & Provan, G. (2010). Magnetic field oscillations near the planetary period in Saturn's equatorial magnetosphere: Variation of amplitude and phase with radial distance and local time. *Journal of Geophysical Research*, *115*, A04212. https://doi.org/10.1029/2009JA014729

Badman, S. V., Achilleos, N., Arridge, C. S., Baines, K. H., Brown, R. H., Bunce, E. J., et al. (2012). Cassini observations of ion and electron beams at Saturn and their relationship to infrared auroral arcs. *Journal of Geophysical Research*, *117*, A01211. https://doi.org/10.1029/2011JA017222

Badman, S. V., Andrews, D. J., Cowley, S. W. H., Lamy, L., Provan, G., Tao, C., et al. (2012). Rotational modulation and local time dependence of Saturn's infrared H_3^+ auroral intensity. *Journal of Geophysical Research*, *117*, A09228. https://doi.org/10.1029/2012JA017990

Badman, S., Masters, A., Hasegawa, H., Fujimoto, M., Radioti, A., Grodent, D., et al. (2013). Bursty magnetic reconnection at Saturn's magnetopause. *Geophysical Research Letters*, *40*, 1027–1031. https://doi.org/10.1002/grl.50199

Belenkaya, E. S., Cowley, S. W. H., Meredith, C. J., Nichols, J. D., Kalegaev, V. V., Alexeev, I. I., et al. (2014). Magnetospheric magnetic field modelling for the 2011 and 2012 HST Saturn aurora campaigns—Implications for auroral source regions. *Annales Geophysicae*, *32*(6), 689–704. https://doi.org/10.5194/angeo-32-689-2014

Belenkaya, E. S., Cowley, S. W. H., Nichols, J. D., Blokhina, M. S., & Kalegaev, V. V. (2011). Magnetospheric mapping of the dayside UV auroral oval at Saturn using simultaneous HST images, Cassini IMF data, and a global magnetic field model. *Annales Geophysicae*, *29*(7), 1233–1246. https://doi.org/10.5194/angeo-29-1233-2011

Bradley, T. J., Cowley, S. W. H., Provan, G., Hunt, G. J., Bunce, E. J., Wharton, S. J., et al. (2018). Field-aligned currents in Saturn's nightside magnetosphere: Subcorotation and planetary period oscillation components during northern spring. *Journal of Geophysical Research: Space Physics*, *123*, 3602–3636. https://doi.org/10.1029/2017JA024885

Brandt, P. C., Khurana, K. K., Mitchell, D. G., Sergis, N., Dialynas, K., Carbary, J. F., et al. (2010). Saturn's periodic magnetic field perturbations caused by a rotating partial ring current. *Geophysical Research Letters*, *37*, L22103. https://doi.org/10.1029/2010GL045285

Carbary, J. F. (2013). Longitude dependences of Saturn's ultraviolet aurora. *Geophysical Research Letters*, *40*, 1902–1906. https://doi.org/10.1002/grl.50430

Carbary, J. F., & Mitchell, D. G. (2013). Periodicities in Saturn's magnetosphere. *Reviews of Geophysics*, *51*, 1–30. https://doi.org/10.1002/rog.20006

Cowley, S. W. H., Bunce, E. J., & Prangé, R. (2004). Saturn's polar ionospheric flows and their relation to the main auroral oval. *Annales Geophysicae*, *22*(4), 1379–1394. https://doi.org/10.5194/angeo-22-1379-2004

Esposito, L. W., Barth, C. A., Colwell, J. E., Lawrence, G. M., McClintock, W. E., Stewart, A. I. F., et al. (2004). The Cassini ultraviolet imaging spectrograph investigation. *Space Science Reviews*, *115*(1–4), 299–361. https://doi.org/10.1007/s11214-004-1455-8

Galopeau, P., Zarka, P., & Le Queau, D. (1989). Theoretical model of Saturn's kilometric radiation spectrum. *Journal of Geophysical Research*, *94*(A7), 8739–8755. https://doi.org/10.1029/JA094iA07p08739

Gérard, J.-C., Bonfond, B., Gustin, J., Grodent, D., Clarke, J. T., Bisikalo, D., & Shematovich, V. (2009). Altitude of Saturn's aurora and its implications for the characteristic energy of precipitated electrons. *Geophysical Research Letters*, *36*, L02202. https://doi.org/10.1029/2008GL036554

Grodent, D., Gérard, J.-C., Cowley, S. W. H., Bunce, E. J., & Clarke, J. T. (2005). Variable morphology of Saturn's southern ultraviolet aurora. *Journal of Geophysical Research*, *110*, A07215. https://doi.org/10.1029/2004JA010983

Guo, R. L., Yao, Z. H., Wei, Y., Ray, L. C., Rae, I. J., Arridge, C. S., et al. (2018). Rotationally driven magnetic reconnection in Saturn's dayside. *Nature Astronomy*, *2*(8), 640–645. https://doi.org/10.1038/s41550-018-0461-9

Gurnett, D. A., Lecacheux, A., Kurth, W. S., Persoon, A. M., Groene, J. B., Lamy, L., et al. (2009). Discovery of a north-south asymmetry in Saturn's radio rotation period. *Geophysical Research Letters*, *36*, L16102. https://doi.org/10.1029/2009GL039621

Gustin, J., Grodent, D., Radioti, A., Pryor, W., Lamy, L., & Ajello, J. (2017). Statistical study of Saturn's auroral electron properties with Cassini/UVIS FUV spectral images. *Icarus*, *284*, 264–283. https://doi.org/10.1016/j.icarus.2016.11.017

Gustin, J., Grodent, D., Ray, L., Bonfond, B., Bunce, E., Nichols, J., & Ozak, N. (2016). Characteristics of north Jovian aurora from STIS FUV spectral images. *Icarus*, *268*, 215–241. https://doi.org/10.1016/j.icarus.2015.12.048

Hunt, G. J., Cowley, S. W. H., Provan, G., Bunce, E. J., Alexeev, I. I., Belenkaya, E. S., et al. (2014). Field-aligned currents in Saturn's southern nightside magnetosphere: Subcorotation and planetary period oscillation components. *Journal of Geophysical Research: Space Physics*, *119*, 9847–9899. https://doi.org/10.1002/2014JA020506

Hunt, G. J., Cowley, S. W. H., Provan, G., Bunce, E. J., Alexeev, I. I., Belenkaya, E. S., et al. (2015). Field-aligned currents in Saturn's northern nightside magnetosphere: Evidence for interhemispheric current flow associated with planetary period oscillations. *Journal of Geophysical Research: Space Physics*, *120*, 7552–7584. https://doi.org/10.1002/2015JA021454

Hunt, G. J., Cowley, S. W. H., Provan, G., Bunce, E. J., Alexeev, I. I., Belenkaya, E. S., et al. (2016). Field-aligned currents in Saturn's magnetosphere: Local time dependence of southern summer currents in the dawn sector between midnight and noon. *Journal of Geophysical Research: Space Physics*, *121*, 7785–7804. https://doi.org/10.1002/2016JA022712

Jackman, C. M., Achilleos, N., Cowley, S. W., Bunce, E. J., Radioti, A., Grodent, D., et al. (2013). Auroral counterpart of magnetic field dipolarizations in Saturn's tail. *Planetary and Space Science*, *82-83*, 34–42. https://doi.org/10.1016/j.pss.2013.03.010

Jackman, C. M., Provan, G., & Cowley, S. W. H. (2016). Reconnection events in Saturn's magnetotail: Dependence of plasmoid occurrence on planetary period oscillation phase. *Journal of Geophysical Research: Space Physics*, *121*, 2922–2934. https://doi.org/10.1002/2015JA021985

Jia, X., & Kivelson, M. G. (2012). Driving Saturn's magnetospheric periodicities from the upper atmosphere/ionosphere: Magnetotail response to dual sources. *Journal of Geophysical Research*, *117*, A11219. https://doi.org/10.1029/2012JA018183

Jia, X., Kivelson, M. G., & Gombosi, T. I. (2012). Driving Saturn's magnetospheric periodicities from the upper atmosphere/ionosphere. *Journal of Geophysical Research*, *117*, A04215. https://doi.org/10.1029/2011JA017367

Kinrade, J., Badman, S. V., Provan, G., Cowley, S. W. H., Lamy, L., & Bader, A. (2018). Saturn's northern auroras and their modulation by rotating current systems during late northern spring in early 2014. *Journal of Geophysical Research: Space Physics*, *123*, 6289–6306. https://doi.org/10.1029/2018JA025426

Kurth, W. S., Averkamp, T. F., Gurnett, D. A., Groene, J. B., & Lecacheux, A. (2008). An update to a Saturnian longitude system based on kilometric radio emissions. *Journal of Geophysical Research*, *113*, A05222. https://doi.org/10.1029/2007JA012861

Lamy, L., Prangé, R., Tao, C., Kim, T., Badman, S. V., Zarka, P., et al. (2018). Saturn's northern aurorae at solstice from HST observations coordinated with Cassini's grand finale. *Geophysical Research Letters*, *45*. https://doi.org/10.1029/2018GL078211

Meredith, C. J., Cowley, S. W. H., Hansen, K. C., Nichols, J. D., & Yeoman, T. K. (2013). Simultaneous conjugate observations of small-scale structures in Saturn's dayside ultraviolet auroras: Implications for physical origins. *Journal of Geophysical Research: Space Physics*, *118*, 2244–2266. https://doi.org/10.1002/jgra.50270

Mitchell, D., Carbary, J., Bunce, E., Radioti, A., Badman, S., Pryor, W., et al. (2016). Recurrent pulsations in Saturn's high latitude magnetosphere. *Icarus*, *263*, 94–100. https://doi.org/10.1016/j.icarus.2014.10.028

Nichols, J. D., Badman, S. V., Bunce, E. J., Clarke, J. T., Cowley, S. W. H., Hunt, G. J., & Provan, G. (2016). Saturn's northern auroras as observed using the Hubble Space Telescope. *Icarus*, *263*, 17–31. https://doi.org/10.1016/j.icarus.2015.09.008

Nichols, J. D., Cecconi, B., Clarke, J. T., Cowley, S. W. H., Gérard, J.-C., Grocott, A., et al. (2010). Variation of Saturn's UV aurora with SKR phase. *Geophysical Research Letters*, *37*, L15102. https://doi.org/10.1029/2010GL044057

Nichols, J. D., Clarke, J. T., Cowley, S. W. H., Duval, J., Farmer, A. J., Gérard, J.-C., et al. (2008). Oscillation of Saturn's southern auroral oval. *Journal of Geophysical Research*, *113*, A11205. https://doi.org/10.1029/2008JA013444

Nichols, J. D., Cowley, S. W. H., & Lamy, L. (2010). Dawn-dusk oscillation of Saturn's conjugate auroral ovals. *Geophysical Research Letters*, *37*, L24101. https://doi.org/10.1029/2010GL045818

Provan, G., Andrews, D. J., Cecconi, B., Cowley, S. W. H., Dougherty, M. K., Lamy, L., & Zarka, P. M. (2011). Magnetospheric period magnetic field oscillations at Saturn: Equatorial phase "jitter" produced by superposition of southern and northern period oscillations. *Journal of Geophysical Research*, *116*, A04225. https://doi.org/10.1029/2010JA016213

Provan, G., Cowley, S. W. H., Bradley, T. J., Bunce, E. J., Hunt, G. J., & Dougherty, M. K. (2018). Planetary period oscillations in Saturn's magnetosphere: Cassini magnetic field observations over the northern summer solstice interval. *Journal of Geophysical Research: Space Physics*, *123*, 3859–3899. https://doi.org/10.1029/2018JA025237

Provan, G., Cowley, S. W. H., Lamy, L., Bunce, E. J., Hunt, G. J., Zarka, P., & Dougherty, M. K. (2016). Planetary period oscillations in Saturn's magnetosphere: Coalescence and reversal of northern and southern periods in late northern spring. *Journal of Geophysical Research: Space Physics*, *121*, 9829–9862. https://doi.org/10.1002/2016JA023056

Provan, G., Cowley, S. W. H., Sandhu, J., Andrews, D. J., & Dougherty, M. K. (2013). Planetary period magnetic field oscillations in Saturn's magnetosphere: Postequinox abrupt nonmonotonic transitions to northern system dominance. *Journal of Geophysical Research: Space Physics*, *118*, 3243–3264. https://doi.org/10.1002/jgra.50186

Provan, G., Tao, C., Cowley, S. W. H., Dougherty, M. K., & Coates, A. J. (2015). Planetary period oscillations in Saturn's magnetosphere: Examining the relationship between abrupt changes in behavior and solar wind-induced magnetospheric compressions and expansions. *Journal of Geophysical Research: Space Physics*, *120*, 9524–9544. https://doi.org/10.1002/2015JA021642

Radioti, A., Grodent, D., Gérard, J.-C., Southwood, D. J., Chané, E., Bonfond, B., & Pryor, W. (2017). Stagnation of Saturn's auroral emission at noon. *Journal of Geophysical Research: Space Physics*, *122*, 6078–6087. https://doi.org/10.1002/2016JA023820

Southwood, D. J., & Chané, E. (2016). High-latitude circulation in giant planet magnetospheres. *Journal of Geophysical Research: Space Physics*, *121*, 5394–5403. https://doi.org/10.1002/2015JA022310

Yao, Z. H., Radioti, A., Rae, I. J., Liu, J., Grodent, D., Ray, L. C., et al. (2017). Mechanisms of Saturn's near-noon transient aurora: In situ evidence from Cassini measurements. *Geophysical Research Letters*, *44*, 11,217–11,228. https://doi.org/10.1002/2017GL075108

Zarka, P., Lamy, L., Cecconi, B., Prangé, R., & Rucker, H. O. (2007). Modulation of Saturn's radio clock by solar wind speed. *Nature*, *450*(7167), 265–267. https://doi.org/10.1038/nature06237

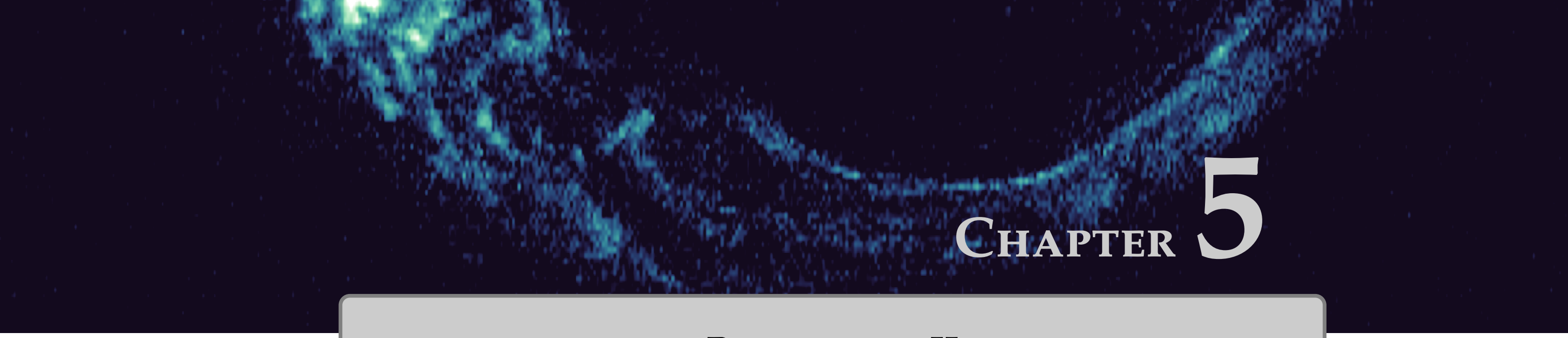

CHAPTER 5

PUBLICATION II

Modulations of Saturn's UV auroral oval location by planetary period oscillations

A. BADER, S. V. BADMAN, J. KINRADE, S. W. H. COWLEY, G. PROVAN AND W. R. PRYOR (2019)

Journal of Geophysical Research: Space Physics, *124*, 952-970

doi:10.1029/2018JA026117

AUTHOR CONTRIBUTION STATEMENT AB led the study, performed the data reduction and analysis and authored the initial draft. SVB provided guidance throughout the project. JK supported the data analysis. SWHC and GP provided expertise on PPOs in Saturn's magnetosphere. GP provided PPO phase data for the analysis. WRP provided technical support for UVIS data. All authors contributed to the interpretation of the results and were involved in review and editing of the paper until publication.

This authorship statement was approved by all collaborating research groups.

Supplementary information for this publication can be found in appendix B.

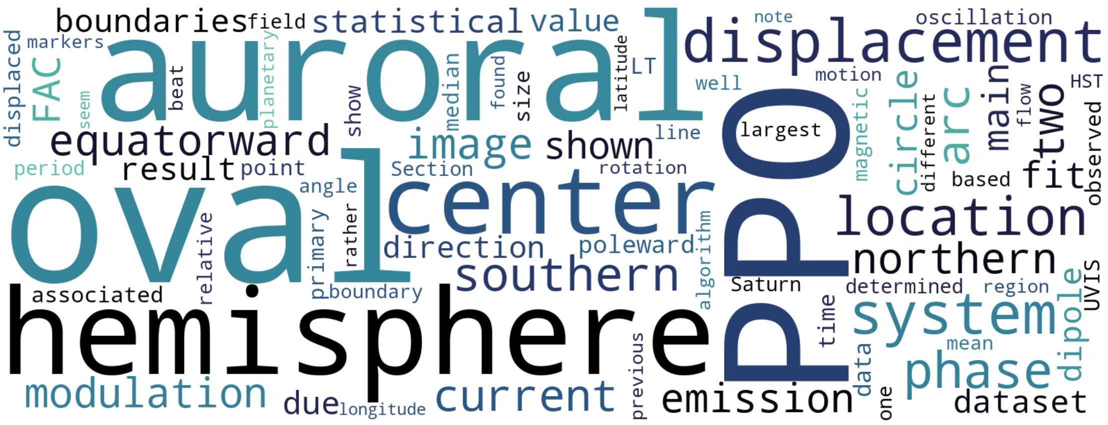

JGR Space Physics

RESEARCH ARTICLE

10.1029/2018JA026117

Key Points:
- The UV main auroral oval is displaced from its statistical location due to PPO field-aligned currents
- The northern oval is displaced nearly parallel to northern PPO dipole, the southern oval nearly antiparallel to southern PPO dipole
- Varying spatial oscillations for different PPO beat phases indicate interhemispheric PPO modulations

Supporting Information:
- Supporting Information S1
- Text S1

Correspondence to:
A. Bader,
a.bader@lancaster.ac.uk

Citation:
Bader, A., Badman, S. V., Kinrade, J., Cowley, S. W. H., Provan, G., & Pryor, W. (2019). Modulations of Saturn's UV auroral oval location by planetary period oscillations. *Journal of Geophysical Research: Space Physics*, *124*, 952–970. https://doi.org/10.1029/2018JA026117

Received 20 SEP 2018
Accepted 19 JAN 2019
Accepted article online 29 JAN 2019
Published online 4 FEB 2019

The copyright line for this article was changed on 1 APR 2019 after original online publication.

Modulations of Saturn's UV Auroral Oval Location by Planetary Period Oscillations

A. Bader[1], S.V. Badman[1], J. Kinrade[1], S.W.H. Cowley[2], G. Provan[2], and W. Pryor[3]

[1]Department of Physics, Lancaster University, Lancaster, UK, [2]Department of Physics and Astronomy, University of Leicester, Leicester, UK, [3]Science Department, Central Arizona College, Coolidge, AZ, USA

Abstract It is well known that Saturn's magnetospheric dynamics are greatly influenced by the so-called planetary period oscillations (PPOs). Based on Cassini Ultraviolet Imaging Spectrograph (UVIS) imagery, it has been shown previously that the UV auroral intensity is clearly modulated in phase with rotating field-aligned current (FAC) systems associated with the PPOs. Here we expand upon this investigation by using the same data set to examine the PPO-induced spatial modulation of the main auroral oval. We present a robust algorithm used for determining the location of the main emission in Cassini-UVIS images. The location markers obtained are then used to calculate the statistical location of the auroral oval and its periodic displacement due to the PPO FACs and the related ionospheric flows. We find that the largest equatorward displacement of the main arc lags behind the PPO-dependent statistical brightening of the UV aurora by roughly 45–90° in both hemispheres and is not colocated with it as the present model based on magnetometer observations suggests. We furthermore find the center of the auroral oval by fitting circles to the main emission and analyze its elliptic motion as the entire oval is displaced in phase with the PPO phases. It is demonstrated that the periodic displacements of both the auroral oval arc and its center are larger when the two PPO systems rotate in relative antiphase than when they are in phase, clearly indicating that interhemispheric PPO FAC closure modulates not only the intensity but also the location of the main UV auroral emission.

1. Introduction

Even though Saturn's magnetic dipole tilt relative to its rotational axis is negligibly small (Burton et al., 2010; Dougherty et al., 2018), the surrounding magnetosphere is permeated with periodic phenomena occurring mostly at periods close to the planetary rotation period of ~ 10.5 hr. These features are effects of the so-called planetary period oscillations (PPOs) modulating, i.a., magnetic fields, particle populations, plasma waves, and radio emissions detected around Saturn (e.g., Andrews, Cowley, et al., 2010; Arridge et al., 2011; Carbary, 2017; Carbary & Mitchell, 2013; Cowley & Provan, 2017; Lamy, 2011; Ye et al., 2016). These periodic modulations have been shown to exhibit two close but distinct periods, each of which are associated with one of the two polar hemispheres (e.g., Andrews, Coates, et al., 2010; Gurnett et al., 2009). The origin of these periodic phenomena is therefore thought to be vortical flow structures in Saturn's polar ionospheres (e.g., Jia & Kivelson, 2012; Jia et al., 2012).

Saturn's auroral emission is a good proxy for the global state of the surrounding magnetosphere. The main emission is generated by flow shears between different plasma populations in the outer magnetosphere—subcorotating with the planet at different angular speeds, this sets up a system of field-aligned currents (FACs) causing electrons to precipitate into the polar upper atmosphere (e.g., Badman et al., 2015; Belenkaya et al., 2014; Hunt et al., 2014). Superimposed on this local time (LT)-fixed FAC system are the two rotating FAC systems, associated with one PPO system each (e.g., Andrews, Coates, et al., 2010; Provan et al., 2016). These FAC systems independently rotate at close to the planetary rotation rate in both polar hemispheres, modulating the currents responsible for the generation of auroral emission in their local as well as in the opposite hemisphere (e.g., Bradley et al., 2018; Hunt et al., 2014, 2015, 2016).

These modulations are expected to manifest as periodicities in the auroral emissions. It has, for example, been shown that the auroral brightness exhibits a rotational modulation (Sandel et al., 1982), which is in phase with the rotation of the two PPO systems as expected from Saturn kilometric radiation (SKR) and FAC measurements (Bader et al., 2018; Nichols, Cecconi, et al., 2010). Each hemisphere's auroral intensity exhibits dual modulation controlled by the superposition of the primary (same hemisphere) and secondary (opposite hemisphere) PPO systems' FACs.

Several studies based on limited Hubble Space Telescope (HST) data sets have investigated the motion of the auroral oval by analyzing the displacement of the oval's boundaries and centers in relation to periodicities in SKR emissions and magnetic field data (Nichols et al., 2016; Nichols, Cecconi, et al., 2010; Nichols et al., 2008; Nichols, Cowley, & Lamy, 2010; Provan et al., 2009). Correlations between SKR and auroral emissions are expected as the ionospheric footprints of observed SKR sources are colocated with the UV aurora and both are associated with accelerated electrons at high latitudes (Lamy et al., 2009). Analyzing HST images from 2007–2008, Nichols et al. (2008) found clear evidence of an oscillatory motion of the auroral oval with a period close to the planetary rotation, and Provan et al. (2009) showed that the southern oval is generally tilted away from the southern hemisphere's magnetic perturbation field. These findings could be confirmed with 2011–2013 HST data (Nichols et al., 2016), but not with the 2014 HST data set (Kinrade et al., 2018). However, many images in the latter data set did not exhibit a dawn arc, preventing reliable circle fits and cutting down the usable data set such that the PPO phase coverage was rather limited.

The strength of these auroral modulations is expected to depend on the relative strength of the two PPO-associated current systems. In the case of equal modulation amplitudes, about half the current of each system closes in the equatorial region and half in the opposite hemisphere (Bradley et al., 2018). It can therefore be assumed that in each hemisphere the primary system's FACs are twice as strong as the secondary system's. In this case, the primary PPO modulation would dominate. However, the relative strength of the two systems has been shown to change over time (e.g., Provan et al., 2013). With one system frequently dominating the other by a factor 2 or larger, the auroral modulation might well be controlled by the secondary PPO system depending on time and hemisphere.

Using a large set of Cassini UVIS data, we want to expand on previous studies by analyzing the statistical location and displacement of Saturn's UV aurora due to PPO current modulation. In section 2 we present a new algorithm for automatically determining the location of Saturn's main emission auroral arcs, describe how the auroral oval is fitted with a circle based on the location markers determined in the previous step and characterize the data set used. Drawing on all appropriate Cassini UVIS data, we determine the statistical location of the main auroral oval in section 3.1, estimate the seasonal and solar cycle influence on this statistical location (section 3.2), and investigate how the main emission is displaced due to PPO modulations (section 3.3). Lastly, we analyze the PPO-induced oscillatory motion of the auroral oval in section 3.4 by employing circle fits of the auroral oval. Section 4 summarizes and discusses our findings and conclusions.

2. Data Set and Analysis Methods

The data set employed in this study is initially identical to the one used in Bader et al. (2018)—containing all auroral imagery obtained with the FUV channel (far ultraviolet, 110–190 nm) of the UVIS spectrographic imager (Esposito et al., 2004) during the whole Cassini Saturn tour between July 2004 and September 2017. For a more detailed overview describing the instrumentation and the projection and integration methods we refer the reader to Bader et al. (2018).

2.1. Determining the Location of the Auroral Oval

The poleward and equatorward boundaries of Saturn's auroral oval have been determined in several previous studies based on HST auroral imagery. Starting with Badman et al. (2006), these boundaries were usually determined by the full-width half-maximum (FWHM) (co)latitudes of the auroral brightness distribution. This technique was later improved by Nichols et al. (2016), who first fitted Gaussians to the latitudinal brightness distribution before calculating the FWHM values representing the poleward and equatorward boundaries of the oval.

However, in combination with the quite different UVIS auroral imagery this method proved to be unreliable and too rigid to capture the dynamic morphologies observed. Hot pixels and poleward injections can easily throw off the resulting main emission boundaries, and the highly variable viewing geometries with often large pixel sizes frequently produce jagged boundaries following the pixel outline. It is furthermore not possible to remove "wrong" data points manually simply due to the size of the data set. Overall, the boundary points determined using the de facto standard method often did not fit to what would be selected by eye and

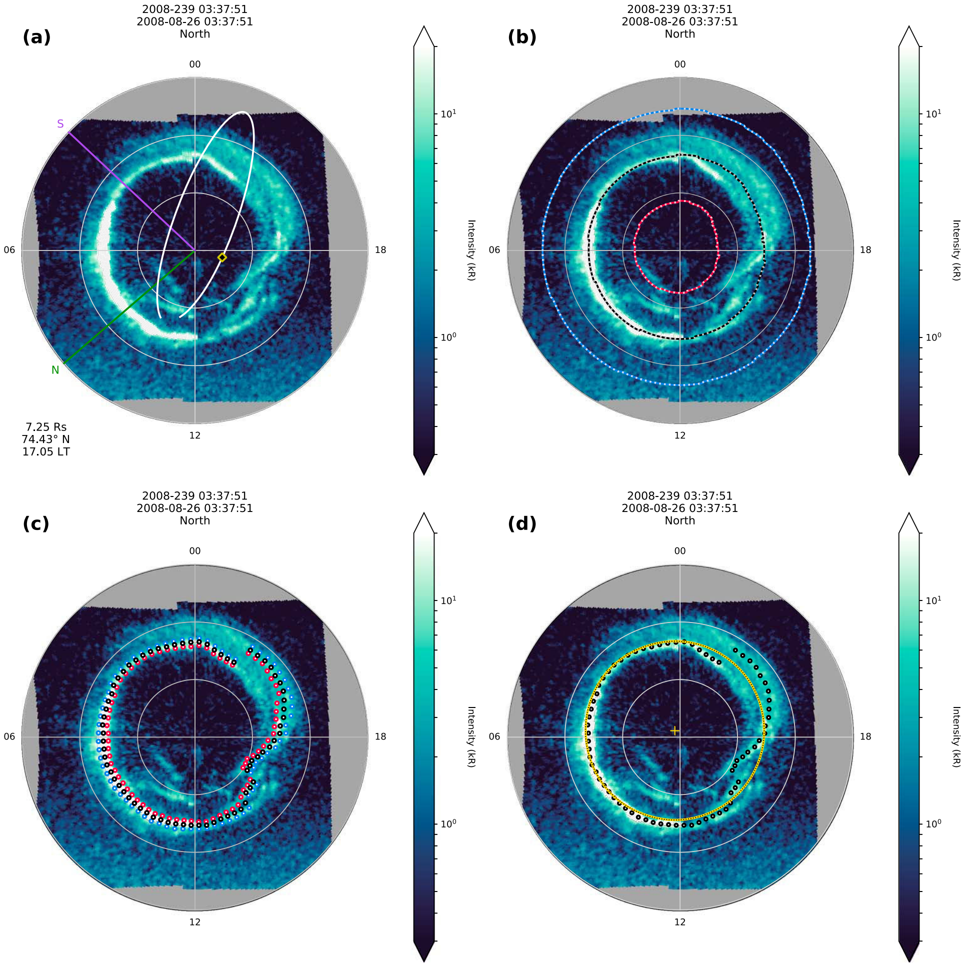

Figure 1. Ultraviolet Imaging Spectrograph (UVIS) image of the northern hemisphere from 2008 DOY 239 at 03:37. The gray grid is spaced in 90° longitude and 10° colatitude. The UV auroral intensity is shown with a logarithmic color scale. (a) Cassini's magnetic footprint is indicated with a yellow-and-black diamond, its trajectory ±2 days drawn in white. Green and purple lines show the orientation of the two PPO systems' perturbation dipoles at the time of the image. Positional data for Cassini in KRTP coordinates is given on the bottom left. (b) The initial guess of the auroral oval location is marked with a black-and-white line. The poleward and equatorward limits of the extracted region are marked with a red and blue line, respectively. (c) The arc center locations are shown with black markers, and the poleward and equatorward boundaries with red and blue markers, respectively. (d) The yellow circle represents the best fit circle to the given center points (black markers), the circle center being marked with a small yellow cross close to the planet's pole. DOY = day of year; LT = local time.

cleaning the results by hand was not feasible. We therefore developed a quite different method of detecting the location of the auroral oval and its boundaries, based on basic image processing and filtering algorithms.

Figure 1a shows an example UVIS image, which will be used here to explain the processing stages involved. As a first step, we calculate an initial guess of the main emission's location. Since Saturn's auroral "oval" is nearly circular and centered around the pole, we simply bin the original intensity distribution into 0.5° longitude (2-min LT) bins and determine at which colatitude the brightness maximizes. Running a simple median box filter of size 60° in longitude (4-hr LT) over this series of colatitude values gets rid of outliers, fills some missing values, and provides a satisfying first guess of where we expect the auroral oval to be located. In Figure 1b, this initial guess is indicated with a black-and-white rather circular line.

Next we "extract" a part of the image for further processing—following the initial guess line, we keep all data within a great-circle distance of 8° of the guess and discard the rest. For each point of the initial guess (0.5° longitude/2-min LT binning), the perpendicular to the guess line is calculated using neighboring points.

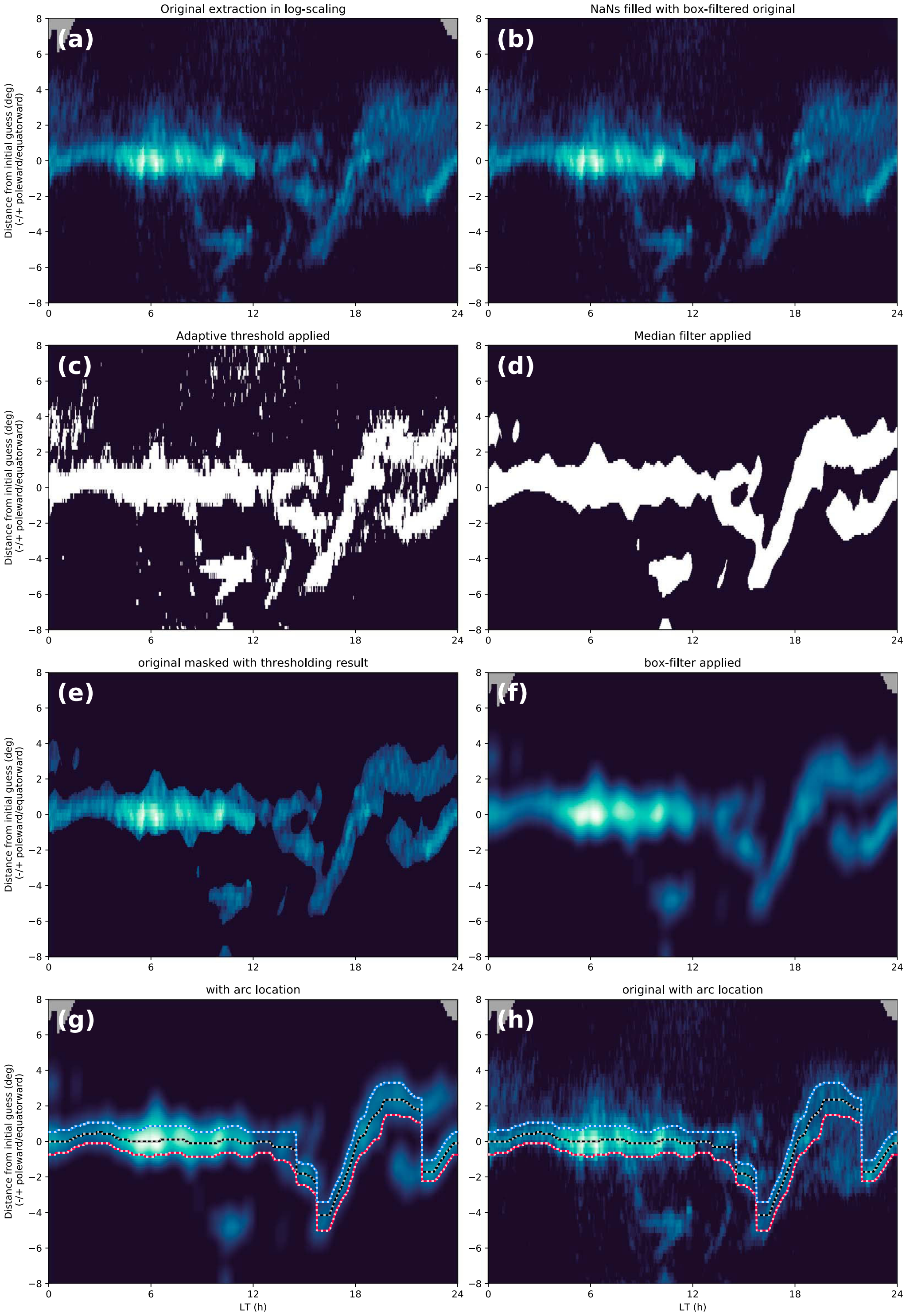

Figure 2. Extracted region of the original image, with local time (LT) along the *x* axis and pseudolatitude along the *y* axis (negative values indicating a poleward direction). The processing steps involved are explained in the text.

Along this perpendicular, we note the brightness of the original image in 150 equal steps. This results in a brightness grid of 720 longitudes/LTs (0° to 360°, 0 to 24 LT) and 150 "pseudolatitudes" (−8° to 8° great-circle distance from the guess line). The poleward and equatorward limits of the extracted region are shown in red and blue, respectively, in Figure 1b.

The extracted region with its original brightness distribution is shown in Figure 2a. Depending on the quality of the initial guess, the auroral oval should be somewhat horizontally in the center of the image. This extracting and "stratifying" of a subimage from the original is necessary so that we can apply asymmetric filters later on, for example, smoothing operations with a box wide in pseudolatitude but narrow in LT.

Note the small sections with invalid values in the top left and right corners—as these occur quite frequently and are not supported by most image processing algorithms, they need to be filled. In this case we calculate a filler image by replacing the missing values with zeros, mean filtering it with a 12 hr × 8° (LT × pseudolatitude) box filter and scaling it such that the maximum values of the original and the filler image are the same. The original's missing values are then filled with the corresponding values of the filler array. This way we smooth the transition between valid and invalid values in dimmer regions such as to avoid false detections at a later stage. Figure 2b shows the original with missing values filled in as described.

Now we use an adaptive thresholding algorithm as a basic means of feature detection. We choose a window size of 151 × 151 pixels (median filter boxes need to have uneven side lengths), or about 5 hr × 16° (LT × pseudolatitude). This window covers the whole pseudolatitude range so that in most cases only the main emission with its generally clear brightness peak is picked out as a feature. The rather limited LT size ensures that there is not too much smearing in this direction. The threshold value is a sum of all values in the window, weighted with a Gaussian distribution according to the pixel distance from the window center. The result of this adaptive thresholding is shown in Figure 2c. A simple median filter of size 15 × 15 pixels, or 0.5 hr × 1.6°, cleans the result of small patches and joins nearby detections (see Figure 2d).

Figure 2e shows the original extraction multiplied with the patch detection result, Figure 2d. We mean filter this result with a 20×15 pixel, or 40 min × 1.6°, window such as to smooth out the noise of the original UVIS pixels and to create a smooth transition between regions corresponding to detections and non-detections of patches (see Figure 2f). The boundaries and arc center location of the auroral oval are then obtained by determining the FWHM boundaries and the maximum, respectively, along pseudolatitude for every LT bin. Median filtering the obtained values with a 40-min LT window yields our final result, shown in Figures 2g and 2h plotted onto the processed and original extracted images, respectively. Lastly, we bin and median average the pseudolatitudes into 72 longitude/LT bins of size 5°/20min LT and retransform them into true colatitudes. By removing points which deviate from the mean of the set by more than 3 times the standard deviation, we exclude all poleward and equatorward patches which are definitely not related to the main emission. These final poleward and equatorward boundaries and the arc center locations of the auroral oval as determined by the described algorithm are shown in Figure 1c, overplotted on the original image.

We note here that the given window sizes are partly justified by logical reasoning as described in the previous paragraphs, but sometimes also simply chosen by trial-and-error such that the algorithm is as robust as possible and that the calculated oval locations fit best to what would be chosen visually. While the calculated arc center (co)latitudes of the auroral oval are unaffected by this, we expect the poleward and equatorward boundaries to be influenced by the window size of the mean filter applied between Figures 2e and 2f. These boundaries are consistent within this data set and study, but we advise caution when applying these values and their difference (the width of the auroral arc) to results of previous studies.

2.2. Circle Fitting

In order to track the motion of the auroral oval's center, we utilize the points determined with the presented algorithm and fit a circle to them. We use the arc center colatitude markers of the auroral oval and find the circle center point close to the pole which minimizes the average radial distance of all markers to it using a simple least squares minimization. Note that previous studies (Kinrade et al., 2018; Nichols et al., 2008, 2016) have used the equatorward boundary of the auroral oval instead of the arc center in order to avoid taking into account poleward emissions. However, as our detection method suppresses the detection of poleward emission, we prefer to use the center of the arc such as to not introduce an additional error due to the varying width of the auroral oval. Figure 1d shows the same image as before, this time with only the arc center colatitude markers of the auroral oval shown with their corresponding circle fit. The error of the

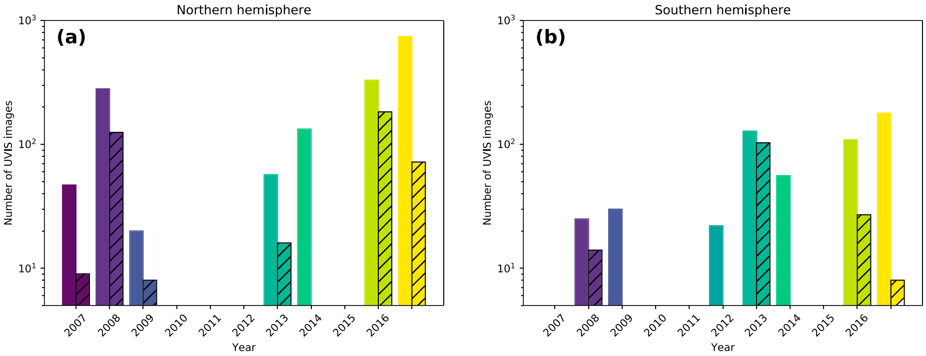

Figure 3. Number of Ultraviolet Imaging Spectrograph (UVIS) images per year available for this study, (a) for the northern and (b) for the southern hemispheres, outside of the planetary period oscillation coalescence period. Shown is the number of images providing boundary and arc center points (nonhatched bars) and the number of images on which circle fits were successful (hatched bars). Note the logarithmic scale of the *y* axis.

circle center is assumed to be equal to the average distance of the fit markers to the final optimal fit circle. We do not take into account any errors arising from the image projection, as we exclude uncertain projections beforehand (see section 2.3).

Several constraints had to be put in place in order to avoid poor circle fits. We require that at least 36 out of the possible 72 boundary points should be defined, and the available points have to be spread such that there are more than 3 in at least three of the four quadrants (dawn, noon, dusk, and midnight). This way we prevent fitting when the circle is unconstrained to one side.

Due to the inconsistency of the data set it was nevertheless necessary to sort the remaining successful fits manually—discarding several observation days with unusually low auroral activity and no main emission arcs, as well as observations with bad viewing geometries, where the main emission was partly observed close to the terminator and its colatitude is associated with a large projection error.

We also tried fitting the data with an ellipse instead of a circle. However, the results were not noticeably impacted by this, and the number of usable images was reduced because any ellipse fitting algorithm is generally less robust against, for example, missing values than a circle fitting algorithm due to its increased degrees of freedom. Hence we favored simple circle fits to improve statistics.

2.3. Data Set Selection

The existing set of 4,192 images is downselected in order to exclude images taken when Cassini was more than 40 R_S from the planet (when the pixel size begins to exceed the typical width of the auroral oval). For an image to be considered suitable for our analysis, we also require Cassini to be located at latitudes at least 30° above/below the equatorial plane such that the projection error is limited (i.e., the auroral oval was not observed too close to the planetary limb). This leaves 2,613 images (1,990 in northern hemisphere; 623 in the southern hemisphere) available for the calculation of the statistical location and boundaries of the auroral oval. For investigating PPO-related features this data set reduces to 2,160 (1,611 in the northern hemisphere; 549 in the southern hemisphere) images, as some images fall into the coalescence period when the two PPO systems were rotating locked in antiphase between mid-2013 and mid-2014. In this time period, the two PPO phases were not statistically independent anymore, and the analysis of the auroral oval center's motion which we undertake in this study is not justifiable. Of the remaining images, 574 (416 in the northern hemisphere; 158 in the southern hemisphere) exhibited a clear enough main emission oval with good enough LT coverage to be fitted with a circle. These have been chosen manually as described in section 2.2.

The temporal distribution of these sets of images is shown in Figure 3. We note that there are several years during which no data suitable for locating the auroral oval are available, for example, during Cassini's equatorial orbits in the years 2009–2012.

2.4. PPO Phases

Each of the two rotating PPO systems is associated with a system of electrical currents, flowing as a downward FAC into one side of the ionosphere. The current then crosses the polar cap as a Pedersen current before returning out into the magnetosphere as an upward FAC on the opposite side of the polar cap

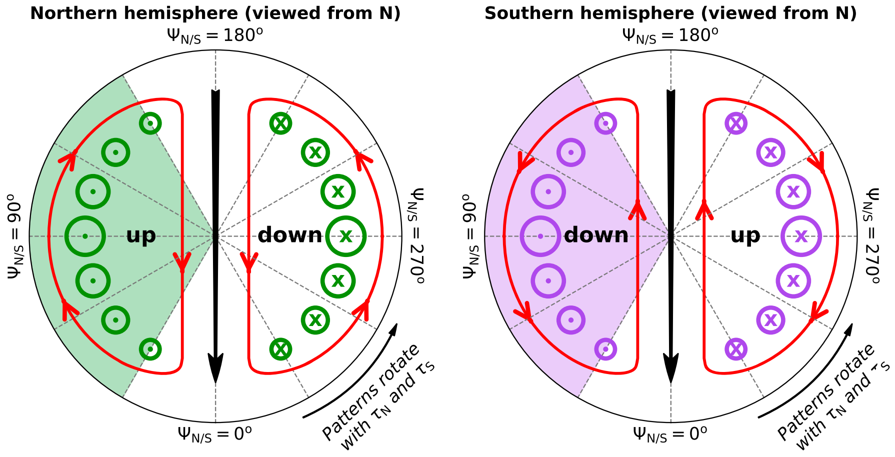

Figure 4. Planetary period oscillation (PPO)-related rotating field-aligned current (FAC) patterns in Saturn's polar ionosphere. To the left (right), the northern (southern) polar region is shown as seen from above the north pole. The near-equatorial magnetic PPO perturbation dipoles are directed toward the bottom of the figure and indicated with black arrows. $\Psi_{N/S}$ increases in clockwise direction. Green/purple circled crosses and dots represent FACs flowing into and out of the diagram plane, respectively. For example, in the northern hemisphere, upward FACs and therefore increased auroral intensities are expected at around $\Psi_N = 90°$ for the primary system and at around $\Psi_S = 90°$ for the secondary system. The relative orientation of the two PPO systems determines whether their associated upward FAC regions are colocated or not. Red lines and arrows sketch the driving neutral atmospheric and ionospheric flows in the respective hemisphere. Adapted from Bader et al. (2018) and Provan et al. (2018).

(e.g., Hunt et al., 2014, 2015). This current circuit closes partly in the equatorial region, and partly in the other hemisphere where it enters the ionosphere, crosses the polar cap, and exits into the magnetosphere in a similar fashion. The currents associated with the two PPO systems flow on the same field lines and are not latitudinally separated (e.g., Bader et al., 2018; Bradley et al., 2018). A good sketch of the PPO systems and their associated currents is given in, for example, Provan et al. (2018, Figure 1).

Each PPO current system has an associated magnetic dipole moment directed transverse to the planetary dipole moment, which rotates in the azimuthal direction in the sense of planetary rotation with its respective PPO rotation period $\tau_{N/S}$. We define the instantaneous orientation of each system by the azimuthal angle of the perturbation field's dipole vector $\Phi_{N/S}(t)$. This angle increases eastward (in the direction of planetary rotation), is referenced to local noon, and is frequently referred to as PPO dipole angle or phase angle.

We also define PPO dipole-fixed frames in order to position auroral features with respect to the PPO perturbation fields. The so-called "magnetic longitude" of a certain location in the LT frame at a certain point in time is given by $\Psi_{N/S}(\varphi, t) = \Phi_{N/S}(t) - \varphi$ with φ as the noon-referenced planetary longitude, such that $\Psi_{N/S} = 0°$ is aligned with the transverse dipole of the respective perturbation system. As this describes the rest frame of the PPO rotation, all PPO-associated FACs are located at constant values of $\Psi_{N/S}$.

Figure 4 shows where upward and downward FACs are expected to be located in the two hemispheres in the respective magnetic longitude frames (e.g., Andrews, Coates, et al., 2010; Hunt et al., 2015). In each hemisphere, the FAC patterns associated with the primary and secondary systems are the same. However, they rotate at different rates τ_N and τ_S together with the northern and southern PPO perturbation dipoles such that there is an arbitrary angle between the dipoles; the FAC patterns therefore may or may not overlap (see also Bader et al., 2018, Figure 7, and Provan et al., 2016, Figure 10). The upward FACs in the northern hemisphere were found to maximize around $\Psi_N \approx 90°$ for the northern/primary PPO system, with the downward currents peaking near $\Psi_N \approx 270°$. Interhemispheric currents from the southern/secondary PPO system closing in the northern hemisphere are thought to cause the same FAC pattern, with upward (downward) currents maximizing at $\Psi_S \approx 90°$ ($\Psi_S \approx 270°$). Conversely, upward (downward) currents in the southern hemisphere maximize close to $\Psi_{S/N} \approx 270°$ ($\Psi_{S/N} \approx 90°$). Note that auroral emissions occur in regions with upward currents, i.e. due to precipitating electrons.

The PPO phases for all UVIS images were determined using the empirical PPO model described in Provan et al. (2018), which encompasses magnetic field measurements from the full Cassini mission. Their phases

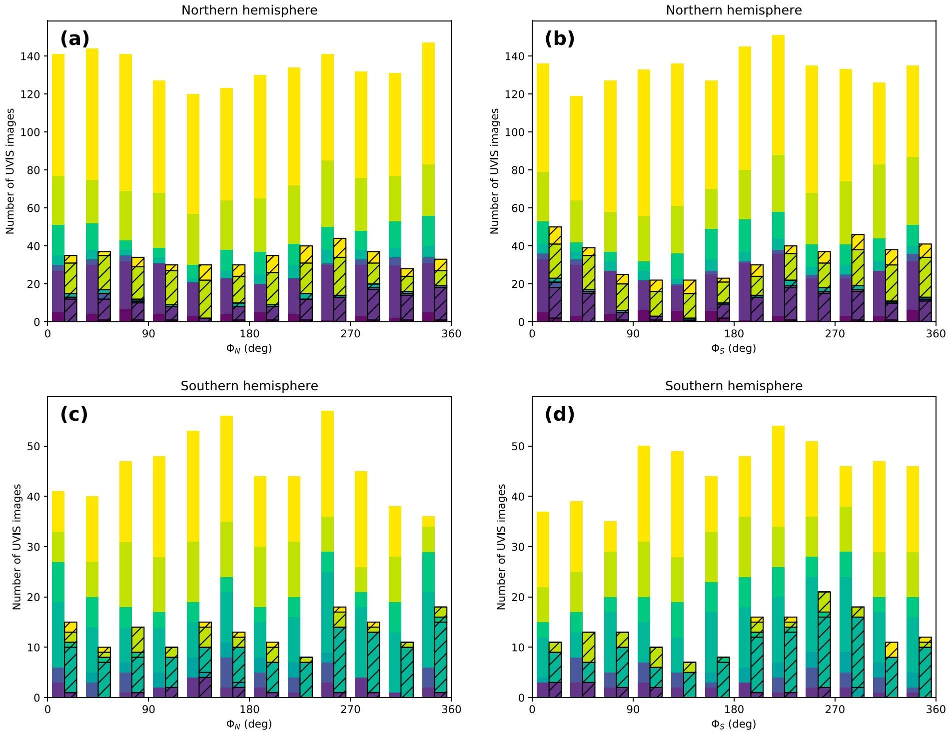

Figure 5. Coverage of PPO phase angles $\Phi_{N/S}$ in both hemispheres using the same data set as shown in Figure 3. Panels (a) and (b) show the number of Ultraviolet Imaging Spectrograph (UVIS) images per 30° PPO phase angle Φ_N and Φ_S bin, respectively. Panels (c) and (d) show the same statistics for the southern hemisphere. The color scale in all plots corresponds to the year coloring in Figure 3. Nonhatched bars show the number of images providing boundary and arc center points, hatched bars the number of images with successful circle fits. Note the different vertical scaling between the top and bottom plots. PPO = planetary period oscillation.

include some uncertainty due to the use of sliding windows with sizes of up to several months, but the phase errors are relatively small and well described in the corresponding studies (e.g., Provan et al., 2016, 2018). Additional inaccuracies might arise based on the exposure time of the UVIS images, which can be up to 3 hr long. However, as shown in Bader et al. (2018), the mean error due to exposure time is expected to be less than 10°.

Figure 5 shows the distribution of the images in our data set across different PPO phase angles $\Phi_N(t)$ and $\Phi_S(t)$. The whole range of PPO phase angles has been sampled rather evenly in both hemispheres, more evenly in the north than in the south due to the different size of the data sets. In the northern (southern) hemisphere, in each PPO phase bin with size 30° there are at least ~ 120 (~ 35) images with location markers and boundary points available, and ~ 20 (~ 5) images with successful circle fits.

3. Analysis and Discussion

3.1. Statistical Auroral Oval Location

Several studies have determined the statistical location of the auroral oval based on HST (e.g., Badman et al., 2006; Kinrade et al., 2018; Nichols et al., 2016) and UVIS imagery (Carbary, 2012). Here we want to update these results with all suitable UVIS data, the largest data set used to date for this purpose, including statistics for the full nightside unlike most HST data.

Our poleward and equatorward boundary points and arc center locations are available in 5° longitude/20-min LT steps. We find the statistical boundaries and arc centers by median averaging all available points in each longitude bin. The error is determined using the median absolute deviation on the respective data subsets. Figures 6a and 6b show the resulting statistical arc center in black, and the statistical poleward and equatorward boundaries in red and blue, respectively. The values with their associated uncertainties are also given in Table 1.

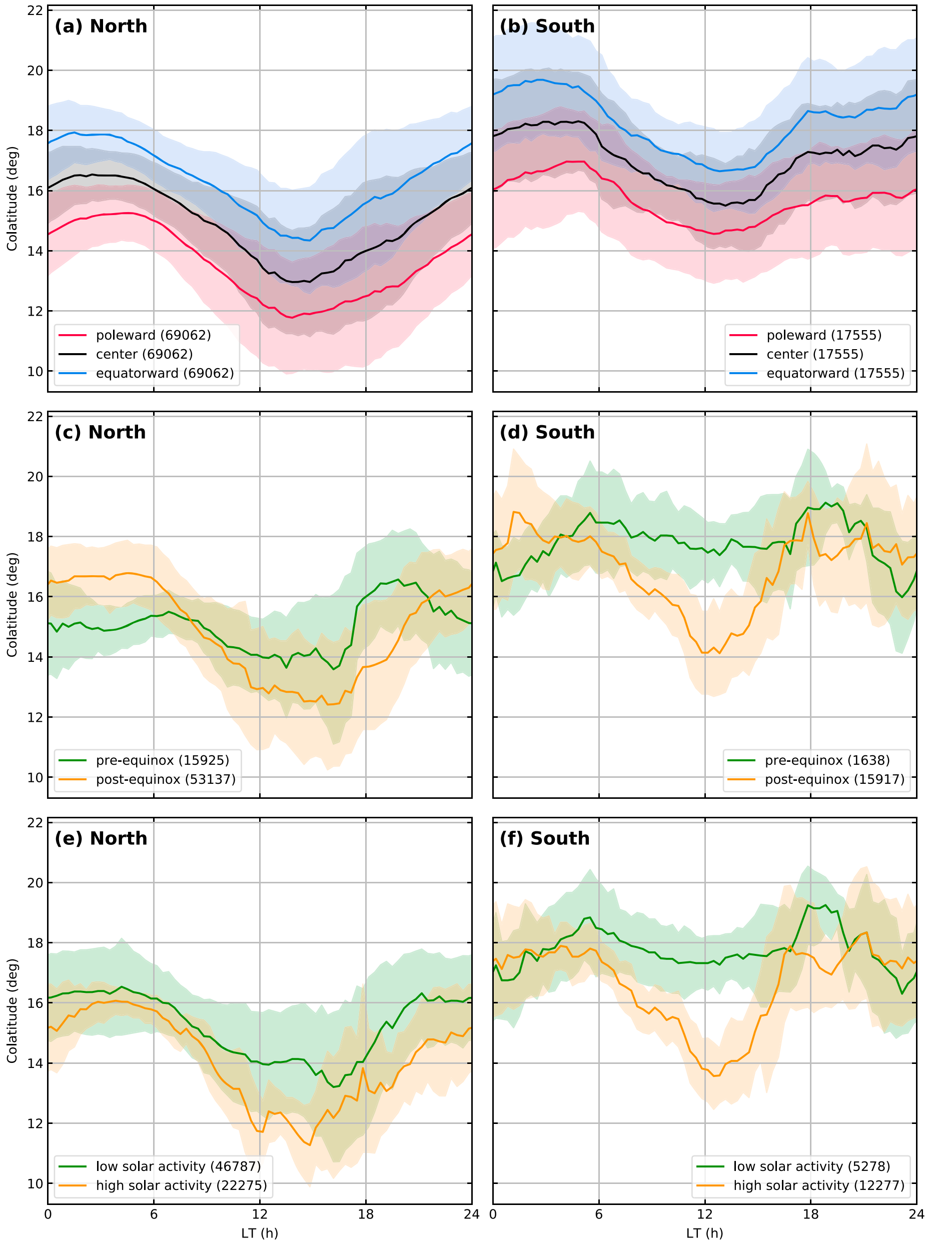

Figure 6. (a, b) Median poleward (red) and equatorward (blue) boundaries and arc centers (black) of Saturn's northern and southern auroral ovals in a local time (LT) frame. Median absolute deviation (MAD) uncertainties are indicated with shaded envelopes; numbers in brackets represent the number of boundary points/arc center points on which each graph is based (one image with full LT coverage yielding 72 points). (c, d) The northern/southern oval's median arc center and its MAD calculated from all imagery obtained before (green) and after equinox (yellow) in 2009. (e, f) The northern/southern oval's median arc center and its MAD calculated from all imagery obtained during low solar activity periods (2007–2009 and 2016–2017, green) and high solar activity periods (2012–2014, yellow).

The boundaries we determined in this study generally agree with the previous investigations. We can confirm that the auroras in both hemispheres are found most equatorward between midnight (0 LT) and dawn (6 LT) LTs and that it is most poleward in the postnoon sector (12–18 LT). The southern auroral oval is found to be more extended than the northern one due to the presence of a significant axial quadrupole component in Saturn's magnetic field, corresponding to a northward shift of the magnetic dipole (e.g., Dougherty et al., 2018).

Table 1
Statistical Location of Saturn's Auroral Oval for All Local Times

	North						South					
φ_{LT} (LT)	θ_p	$\Delta\theta_p$	θ_c	$\Delta\theta_c$	θ_e	$\Delta\theta_e$	θ_p	$\Delta\theta_p$	θ_c	$\Delta\theta_c$	θ_e	$\Delta\theta_e$
5 (00:20)	14.6	1.3	16.2	1.1	17.7	1.2	16.1	1.9	17.9	1.8	19.3	1.9
15 (01:00)	14.9	1.2	16.4	1.1	17.8	1.1	16.4	1.9	18.1	1.7	19.5	1.9
25 (01:40)	15.0	1.1	16.5	1.0	17.9	1.0	16.5	1.8	18.2	1.8	19.6	1.9
35 (02:20)	15.1	1.0	16.5	0.9	17.9	1.0	16.6	1.8	18.2	1.8	19.6	1.9
45 (03:00)	15.2	1.0	16.5	0.8	17.9	0.9	16.7	1.9	18.3	1.8	19.7	1.8
55 (03:40)	15.2	0.9	16.5	0.8	17.8	0.8	16.8	1.9	18.2	1.8	19.6	1.8
65 (04:20)	15.2	0.9	16.4	0.8	17.7	0.8	17.0	1.7	18.3	1.7	19.5	1.7
75 (05:00)	15.2	0.9	16.3	0.8	17.5	0.8	17.0	1.7	18.3	1.6	19.4	1.7
85 (05:40)	15.1	1.0	16.2	0.9	17.3	0.8	16.7	1.7	18.0	1.7	19.1	1.7
95 (06:20)	14.9	1.0	15.9	0.9	17.0	0.8	16.4	1.8	17.4	1.7	18.6	1.6
105 (07:00)	14.6	1.0	15.7	0.9	16.8	0.9	16.2	1.8	17.1	1.7	18.2	1.4
115 (07:40)	14.3	1.2	15.5	1.0	16.6	0.9	15.7	1.7	16.9	1.5	17.9	1.2
125 (08:20)	14.0	1.3	15.2	1.1	16.4	0.9	15.4	1.7	16.6	1.3	17.8	1.2
135 (09:00)	13.7	1.5	15.0	1.2	16.3	1.0	15.3	1.6	16.5	1.1	17.6	1.2
145 (09:40)	13.4	1.6	14.8	1.3	16.0	1.2	15.0	1.5	16.3	1.1	17.3	1.1
155 (10:20)	13.0	1.7	14.5	1.4	15.8	1.3	14.9	1.5	16.1	1.1	17.2	1.0
165 (11:00)	12.7	1.8	14.1	1.6	15.4	1.4	14.8	1.5	16.0	1.2	17.1	1.2
175 (11:40)	12.5	1.9	13.8	1.7	15.2	1.5	14.7	1.6	15.7	1.4	16.9	1.3
185 (12:20)	12.1	1.9	13.3	1.8	14.8	1.5	14.6	1.6	15.6	1.5	16.7	1.4
195 (13:00)	12.0	1.9	13.2	1.8	14.6	1.6	14.6	1.6	15.5	1.4	16.7	1.3
205 (13:40)	11.8	1.9	13.0	1.7	14.5	1.6	14.7	1.6	15.6	1.5	16.7	1.3
215 (14:20)	11.9	1.8	13.0	1.8	14.4	1.7	14.7	1.7	15.6	1.6	16.7	1.4
225 (15:00)	11.9	1.9	13.0	1.8	14.4	1.8	14.9	1.7	15.8	1.7	16.9	1.5
235 (15:40)	12.0	2.0	13.3	2.0	14.7	1.9	15.1	1.7	16.2	1.7	17.3	1.6
245 (16:20)	12.1	2.1	13.4	2.1	14.8	2.0	15.3	1.7	16.6	1.7	17.6	1.6
255 (17:00)	12.3	2.1	13.7	2.1	15.1	2.2	15.4	1.7	16.9	1.6	18.1	1.6
265 (17:40)	12.4	2.3	13.9	2.2	15.4	2.2	15.5	1.8	17.2	1.6	18.5	1.8
275 (18:20)	12.6	2.3	14.1	2.3	15.7	2.2	15.7	1.8	17.2	1.6	18.6	1.7
285 (19:00)	12.7	2.2	14.2	2.2	15.8	2.2	15.8	1.7	17.3	1.5	18.6	1.7
295 (19:40)	12.8	2.0	14.4	2.1	16.0	2.0	15.7	1.7	17.3	1.6	18.4	1.5
305 (20:20)	13.0	1.9	14.7	1.9	16.3	1.8	15.7	1.8	17.2	1.7	18.4	1.7
315 (21:00)	13.4	1.8	15.0	1.7	16.6	1.7	15.8	1.8	17.3	1.7	18.6	1.7
325 (21:40)	13.6	1.7	15.3	1.5	16.8	1.5	15.9	1.8	17.5	1.7	18.7	1.9
335 (22:20)	13.9	1.6	15.5	1.4	17.0	1.4	15.9	1.9	17.4	1.9	18.7	2.0
345 (23:00)	14.2	1.5	15.8	1.3	17.2	1.4	15.8	1.9	17.4	1.8	18.8	1.9
355 (23:40)	14.4	1.5	16.0	1.2	17.4	1.3	15.9	1.9	17.8	1.9	19.1	1.9

Note. We present the median poleward and equatorward boundaries as well as the statistical center colatitudes θ together with their median absolute deviations $\Delta\theta$, indicated with subscripts p, e, and c, respectively. All values are given in degrees colatitude from the corresponding pole. LT = local time.

While we find the largest equatorward extent of the equatorward boundaries to be 17.9° (19.7°) for the northern (southern) hemisphere, Nichols et al. (2016) determined values of 17.7° (18.3°) for the same. The difference is only small and can likely be explained by the different detection methods, and with different definitions of the boundary itself. While in previous studies the boundary is solely determined by the FWHM of the brightness distribution in each longitude sector, our results depend on more parameters. The raw brightness is still the most determining factor, but the extent of the corresponding patch detected with adaptive thresholding clearly also has an impact on where exactly the boundary is eventually placed. Lastly, the window size of the box filter applied between Figures 2e and 2f influences the final processed intensity distribution from which the FWHM boundaries are calculated. However, this window size was deliberately chosen very small to minimize this effect.

In comparison with Carbary (2012), who found the corresponding equatorward peaks of the equatorward boundaries at approximately 18° (20°), we can confidently conclude that the boundary detection method newly presented in this paper seems to complement the previous analysis methods.

The statistically most poleward extent of the poleward boundaries was 11.8° (14.6°) for the northern (southern) hemisphere, Nichols et al. (2016) determined values of 5.9° (9.9°) for the same. Carbary's (2012) poleward boundaries reach minimum values of approximately 9° (8°). This clearly shows one of the limitations of the previously employed methods for the determination of boundaries: frequent observations of transient polar emissions attributed to dayside and cusp reconnection (e.g., Badman et al., 2013; Gérard et al., 2005; Kinrade et al., 2017; Meredith et al., 2014; Radioti et al., 2011). As these can be rather bright, they are easily picked out as "main emission" using simple FWHM or Gaussian fits on the raw brightness distribution. Our new algorithm instead employs several (median) filtering steps to minimize the impact of small poleward or equatorward features; therefore, the statistical location of the main auroral oval as determined in this study exhibits a smaller poleward displacement in the corresponding local time region. Of course, larger poleward features will still be detected—posing the question of which part of the auroral emission in this local time sector is even considered the "main emission."

3.2. Seasonal and Solar Cycle Variation of the Auroral Oval Location

Before investigating PPO-induced modulations of the auroral oval position, we consider possible seasonal and solar cycle-related changes. Figures 6c and 6d show the statistical arc centers of the northern and southern auroral for the time intervals before 2010 (green) and after 2010 (yellow). They are calculated in the same way as the statistical arc centers shown in Figures 6a and 6b, only based on the pre-2010 and post-2010 subsets of the complete data set. With equinox having occurred in August 2009, this division effectively separates the data into preequinox (southern summer) and postequinox (northern summer) sets since no usable imagery was available in 2010–2011 (see Figure 3). Figures 6e and 6f show the statistical arc centers for periods of low solar activity (2007–2009 and 2016–2017, green) and high solar activity (2012–2014, yellow), calculated in the same fashion as the seasonal auroral oval locations in Figures 6c and 6d.

Splitting the data set according to season (Figures 6c and 6d), we find a similar behavior for the northern and the southern hemispheres. In both, the auroral oval seems to be located more poleward around noon and more equatorward around midnight in the postequinox data compared to the preequinox locations. Generally, the oval appears to be more centered on Saturn's spin pole during the preequinox period. This does not correspond to a seasonal effect, for which one would expect the hemispheres to act oppositely and not in the same way as seen here—i.e. one would expect a "summer-shaped" and a "winter-shaped" oval switching between the hemispheres. The effect we see here, apparent or real but certainly significant, therefore cannot be directly related to the angle of attack of the solar wind onto the Kronian magnetosphere.

We therefore consider solar activity as a possible influence and investigate how the oval center location differs between high and low solar activity periods (Figures 6e and 6f). We clearly see that the auroral oval is quite consistently smaller (more poleward at most LTs) during high solar activity than during low solar activity, the largest difference between the two occurring at noon for both hemispheres. This effect could be a sign of increased magnetopause and cusp reconnection rates during high solar activity, effecting poleward auroral signatures to occur more frequently, as well as more prevalent tail reconnection closing thereby "accumulated" open flux more quickly than during low solar activity (see, e.g., Badman et al., 2005, 2014).

Close similarities between Figures 6d and 6f for the southern hemisphere arise due to the similarity of the data sets used. This is because all preequinox data are from low solar activity periods, and about 75% of postequinox data corresponds to high solar activity periods—the "seasonal" modulations observed in Figure 6d are hence most likely solar activity related and not truly seasonal. By extension, the same reasoning lets us assume that the northern hemispheric "seasonal" changes in Figure 6c might largely be explained with biases toward certain solar activity periods. These inevitably result from the uneven temporal and spatial sampling of our data set (see Figure 3).

We therefore conclude that there is a consistent solar activity-related modulation of the statistical oval location but cannot find conclusive evidence of a seasonal effect. We note, however, that some auroral features have indeed been shown to be directly controlled by the interaction of Saturn's magnetosphere with the

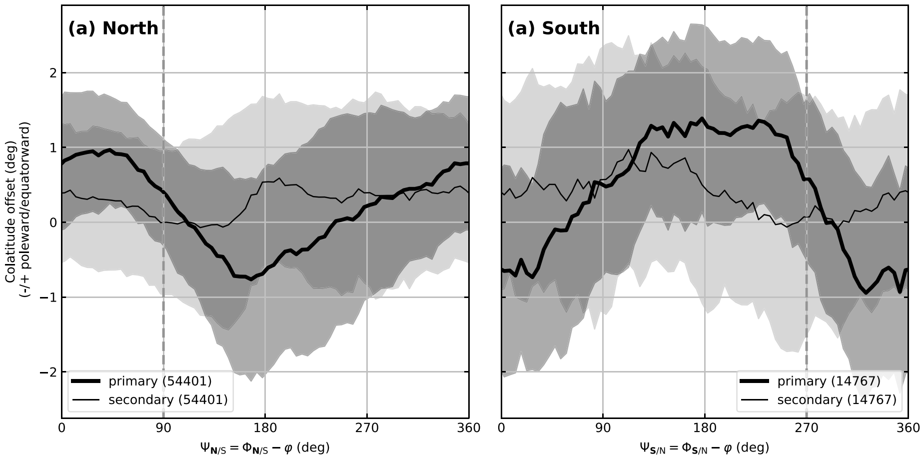

Figure 7. Median latitudinal displacement of the auroral oval's arc center location from its median position depending on planetary period oscillation (PPO) magnetic longitude $\Psi_{N/S}$ for the (a) northern and (b) southern hemispheres. The thick line marks the displacement ordered by the primary PPO system (i.e., the system located in the same hemisphere, respectively), and the thin line the displacement ordered by the secondary PPO system (i.e., the system located in the opposite hemisphere, respectively). Shaded envelopes mark the median absolute deviation uncertainties. Vertical dashed lines mark the expected location of maximum upward field-aligned currents. Numbers in brackets give the number of boundary points/arc center points each graph is based on.

solar wind; both cusp emissions (e.g., Bunce et al., 2005; Gérard et al., 2005; Kinrade et al., 2017; Palmaerts et al., 2016) and magnetopause reconnection (e.g., Badman et al., 2013; Radioti et al., 2013) were observed to be modulated by the solar wind conditions and might hence vary not only with solar activity but also with season. These features are however of a transient nature and often comparably small; they are therefore partly excluded from this analysis due the filtering procedures applied in the arc detection algorithm presented here.

3.3. Statistical Oval Displacement With PPO Phase

In order to investigate the displacement of the auroral oval caused by the two PPO systems, we examine the boundary and arc center markers which have been calculated as presented in section 2.1. Instead of simply rotating all images with their markers into the PPO frames, we first take into account the underlying local time patterns determined in section 3.1. We therefore first calculate the difference between each image's arc center markers and the statistical centers of the auroral oval in the corresponding hemisphere, using the "low solar activity" or "high solar activity" center locations shown in Figure 6 depending on when the image was obtained. The resulting displacements are then rotated into the two PPO frames. Statistical offsets are obtained by median averaging the resulting set of displacement values, and errors are again calculated using median absolute deviation. We did not observe clear changes in the statistical PPO-induced latitudinal offsets depending on whether the overall statistical center locations or the statistical locations separated by season or solar activity were used as a baseline.

The median displacements of the auroral oval's arc centers from their statistical location are shown in Figure 7, for both hemispheres, and ordered by both the north and south PPO systems. Clear modulations due to the primary PPO systems are visible in both hemispheres (Figures 7a and 7b, bold lines). Interhemispheric current closure of the secondary PPO systems, however, does not seem to have a noticeable impact on the arc center locations of the auroral oval (Figures 7a and 7b, thin lines), as the statistical displacements are comparably small and barely ordered. The median offsets of the boundaries from their median location due to the primary PPO systems vary between roughly ±1° colatitude for the northern oval, and slightly more for the southern for both the northern and the southern auroral oval.

In both hemispheres we observe noticeable modulation induced by the primary PPO systems (Figure 7, bold lines). The modulation seems to be notably sawtoothed and shifted by ~ 180° between the two hemispheres. Based on Cassini MAG results from the southern hemisphere, we would expect the largest equatorward displacement in the northern hemisphere (Figure 7a, bold line) to occur near $\Psi_N \approx 90°$ (Hunt et al., 2014, 2015). We observe a peak at around $\Psi_N \approx 45°$, agreeing fairly well although with a non-negligible offset.

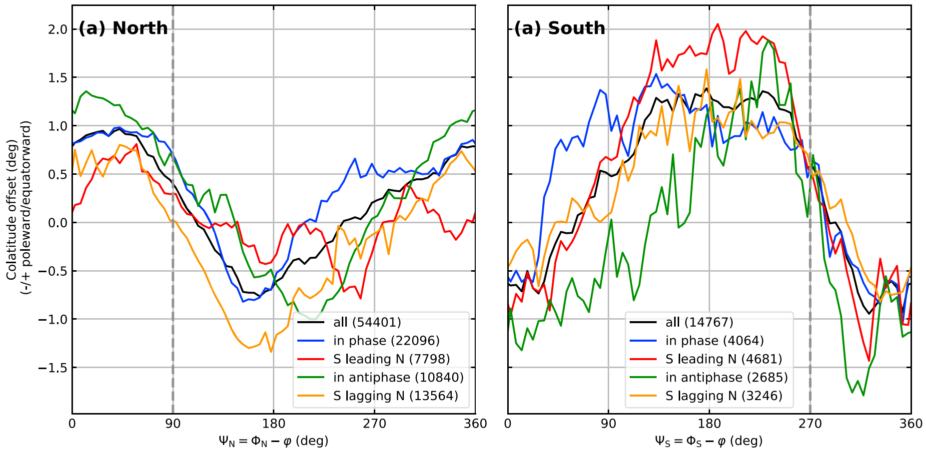

Figure 8. Median latitudinal displacement of the auroral oval’s arc center location from its median position. Panel (a) shows the displacements in the northern hemisphere ordered by Ψ_N, (b) the displacements in the southern hemisphere ordered by Ψ_S. Otherwise the same format as Figure 7.

The modulation of the southern boundaries due to southern PPO (Figure 7b, bold line) shows a broad region of enhanced equatorward displacement. The largest equatorward offset from the median oval location is observed at about $\Psi_S = 225°$. This agrees rather well with Hunt et al.’s (2014) direct observations of FAC regions in the postmidnight sector, in that they observed the largest equatorward displacement of the FAC current sheets thought to generate auroral emission close to $\Psi_S \approx 270°$.

We note, however, that in both hemispheres we observe offsets between the peak (equatorward) displacements and their expected $\Psi_{N/S}$ location. These offsets are consistent in both hemispheres, with the largest equatorward displacements occurring about 45° ahead of where most equatorwardly displaced FACs were found (Hunt et al., 2014). Considering that the auroral intensity maximum has been shown to be lagging its expected location by some 30° (Bader et al., 2018), we conclude that the largest equatorward displacement of the auroral oval is not colocated with the auroral intensity maximum. This actually agrees with direct FAC observations (Hunt et al., 2014), which showed that the upward FAC density maximum of the major FAC sheet lags its largest equatorward displacement by roughly 45° in the southern hemisphere.

The larger size of this data set further allows us to take a closer look at possible interhemispheric PPO modulations of the auroral oval's latitudes. As shown in Figure 7, there is no clear and ordered modulation visible when directly considering the arc center displacements in terms of their secondary PPO system. As an indirect means of picking out secondary PPO modulations, we instead examine how the modulation caused by the primary PPO system changes with beat phase, i.e., the relative orientation of the two systems.

Each image has an associated northern and southern PPO phase, and therefore an associated beat phase depending on the relative orientation of the two PPO systems' magnetic perturbation dipoles. We bin our data set into four groups: *in phase* including all images where the two PPO dipoles were in parallel (0° ± 45°) orientation, and *in antiphase* where the two dipoles were antiparallel (180° ± 45°) relative to one another. The two intermediate beat phases, also of 90° bin size, are *S leading N* and *S lagging N*, depending on whether the southern dipole is leading or lagging the northern one with respect to the direction of planetary rotation.

We then calculate the same statistical displacements as shown by the bold graphs in Figure 7 separately for the different beat phase bins. The resulting statistical auroral oval arc center displacements are shown in Figure 8. Note that the results for the southern hemisphere are rather noisy, as there are significantly fewer boundary points included than from the northern hemisphere.

There are clearly some differences between the beat phases. The overall statistical displacements from Figure 7 are shown in black for reference, and the colored beat phase graphs of Figure 8 follow the overall result rather closely. There seem to be some slight phase-shifts, but they do not show any obvious ordering and aren't consistent through both hemispheres.

Yet, looking at the modulation amplitudes, we observe that in both hemispheres the boundary displacements are largest when the two PPO systems are *in antiphase*, and comparably small when they are *in phase*.

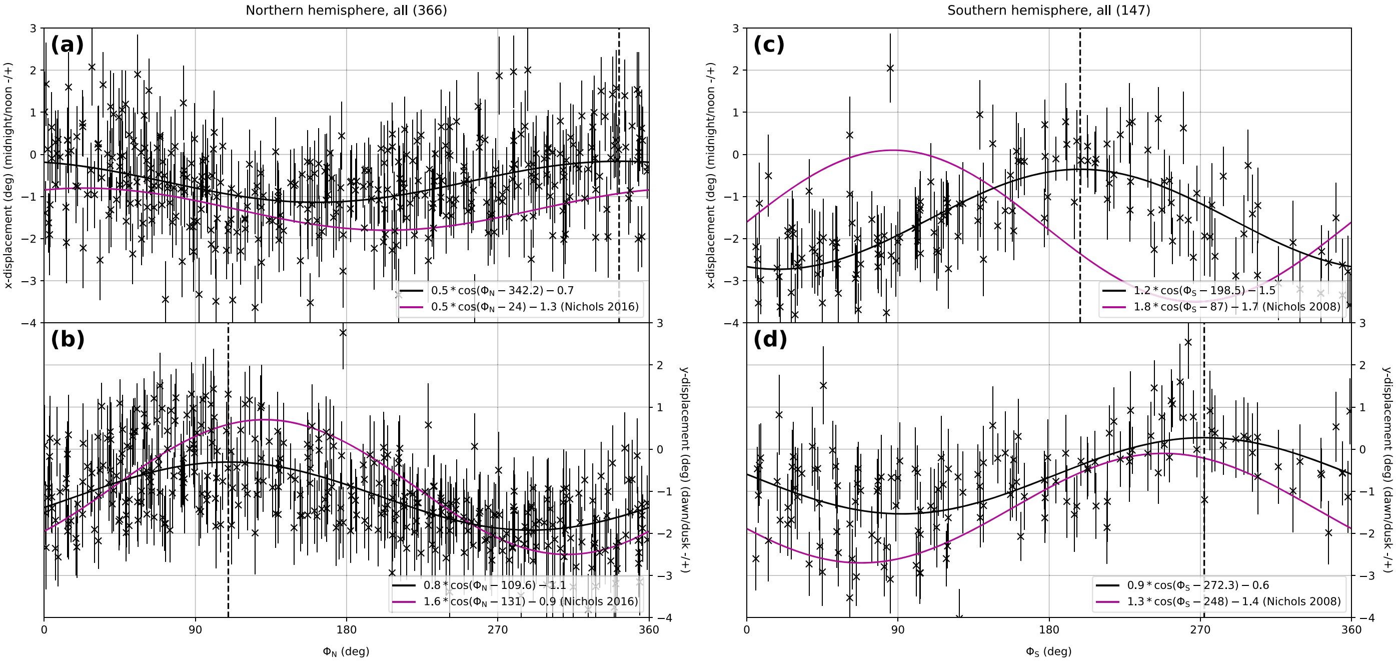

Figure 9. Displacements of the circle-fitted center locations of the northern and southern auroral ovals depending on the phase angle Φ_N and Φ_S, respectively (primary PPO system). (a) Northern hemisphere displacements in the midnight-noon direction and (b) northern hemisphere displacements along the dawn-dusk axis. (c) Southern hemisphere displacements in the midnight-noon direction and (d) southern hemisphere displacements along the dawn-dusk axis. A black line shows the best cosine fit to our data; the fit parameters are given on the bottom right. The number of images/data points is given in parentheses on top. Purple lines show the corresponding fits from Nichols et al. (2008, 2016).

This agrees with the standard picture of the fields and driving atmospheric flows in the two PPO systems as indicated with red lines and arrows in Figure 4 (e.g., Hunt et al., 2014; Jia & Kivelson, 2012; Jia et al., 2012)—showing directly that when the two PPO systems are *in phase*, the ionospheric/atmospheric flows in the two hemispheres are reduced, given that one hemisphere acts to impose its sense of flow on the other. A reduced flow then would imply reduced boundary displacements. This conclusion may seem at odds with having enhanced ionospheric currents flowing under that condition, but one has to note that the ionospheric current depends on the difference in velocity of the neutral and ionized components (i.e., $j = \sigma E^{'}$, where $E^{'}$ is the electric field in the rest frame of the neutrals, proportional to the difference in plasma and neutral velocity). While the absolute velocities are reduced, the difference is increased, and hence so is the current.

3.4. Oval Center Motion

Wherever possible, we fitted circles to the detected auroral oval arc centers as described in section 2.2. We take the center point of each of these fits to be the center of the auroral oval, or "oval center," and examine its motion relative to the respective primary PPO system in both hemispheres.

The oscillation of the oval center is then analyzed similarly to previous studies where circles were fitted to HST data (Nichols et al., 2008, 2016; Nichols, Cowley, & Lamy, 2010). The longitude-latitude position of each center point is converted into Cartesian coordinates describing the displacement from the planet's pole along the midnight-noon and dawn-dusk axes, in units of degrees. These displacements depending on the PPO phase angles $\Phi_{N/S}$ are shown in Figure 9 for both the northern and southern hemispheres. The clearly visible modulation was fitted with cosine functions similar to previous studies (Nichols et al., 2008, 2016).

In the northern hemisphere, our results clearly agree with recent observations based on 2011–2013 HST imagery (Nichols et al., 2016)—both fits are largely in phase (within 45°), although the amplitudes differ significantly in the y/dawn-dusk direction. As the data points in Figures 9a and 9b show, the circle fitting procedure is associated with significant errors. In addition, the oscillation is likely variable throughout time as well, depending on the relative strengths of the two PPO systems. It is apt to note that the oscillation we examine has an amplitude of the order 1°, which is at the limit of the HST resolution due to the large

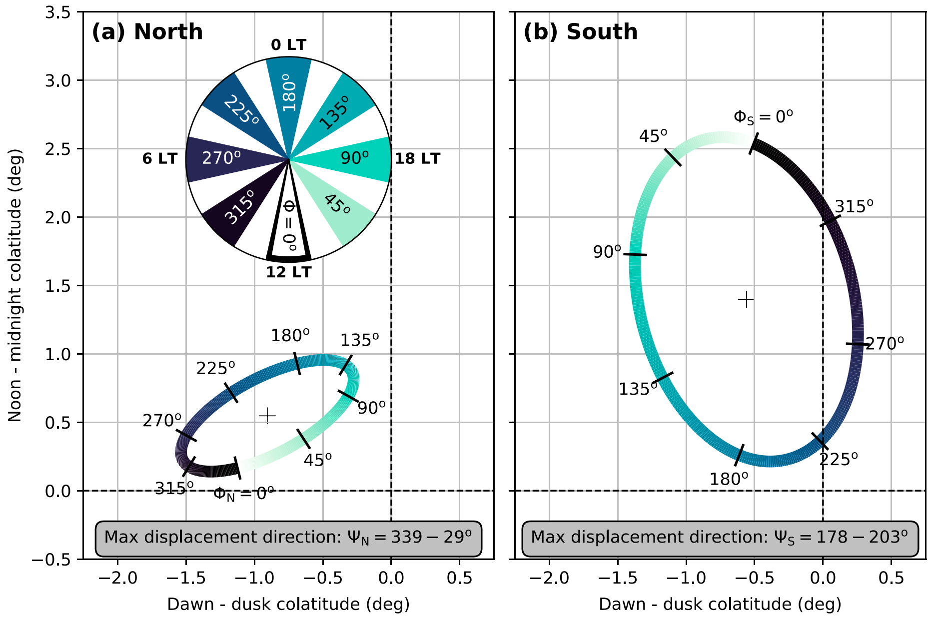

Figure 10. Fitted motion of the auroral oval center as derived from Figure 9. The view is from above the north pole, (a) onto the northern polar cap and (b) through the planet into the southern polar cap, with local noon toward the bottom of the figure and dawn to the left. A location is defined by its colatitudinal displacement from the pole along the dawn-dusk and noon-midnight axes. The pole is located at the intersection of the vertical and horizontal dashed lines. The fitted elliptic motion of the auroral oval center through one planetary period oscillation (PPO) rotation is displayed with a color scale, an inset reminds the reader of the corresponding orientation of the PPO dipoles (same view as the main plots, looking from above the north pole with noon toward the bottom). The mean position of the auroral oval's center is indicated with a black cross in the center of each ellipse. The range of $\Psi_{N/S}$ describing the offset angle between the PPO dipole direction and the direction in which the center of the auroral oval is displaced relative to its mean position over a full PPO rotation is given in a box at the bottom of each plot.

distance of Saturn from Earth, and most of the UVIS data set does not provide a better resolution either. Altogether, this difference in amplitude is likely to be accounted for by all these limitations.

The results for the southern hemisphere (cf. Nichols et al., 2008) are less clear (see Figures 9c and 9d). While both data sets agree rather well concerning phase and amplitude of the dawn-dusk modulation, the midnight-noon center displacements are phase offset by more than 90°. A reason for this might be that the center displacements along this axis are inherently uncertain in HST data, as generally only a partial auroral oval can be observed from Earth and the circle fits are unconstrained on the nightside. In addition, the Nichols et al. (2008) data set is considerably smaller than ours.

To better visualize the motion of the auroral oval, the trajectory described by the cosine fits on the oval center displacements is shown in Figure 10 for both hemispheres. The two fits combined result in a motion following the shape of a Lissajous ellipse (see Nichols et al., 2008, and references therein). In both hemispheres the mean location of the auroral oval centers is displaced from the pole toward the nightside, likely due to solar wind pressure (Badman et al., 2006; Nichols et al., 2008). We also observe a dawnward displacement of the mean center location, agreeing with Nichols et al. (2008, 2016) and Kinrade et al. (2018). The center oscillation seems to be more pronounced in the south, likely due the northward offset of Saturn's magnetic dipole increasing both the size and visible spatial oscillation of the oval. The “center trajectory” in the southern hemisphere appears to be much more circular than in the north, where it is quite elliptical with the semimajor axis oriented in approximately azimuthal direction.

The relative orientation of the PPO systems over one rotation period is indicated by a color map imposed on the elliptic trajectories. The location of the oval's center for $\Phi_{N/S} = 0°$ is implied by the brightest color, darkening with increasing PPO phase angle up to $\Phi_{N/S} = 360°$, shown in black. As observed previously, the motion of the auroral oval's center follows the counterclockwise (seen from above the north pole) direction of planetary rotation/PPO system rotation.

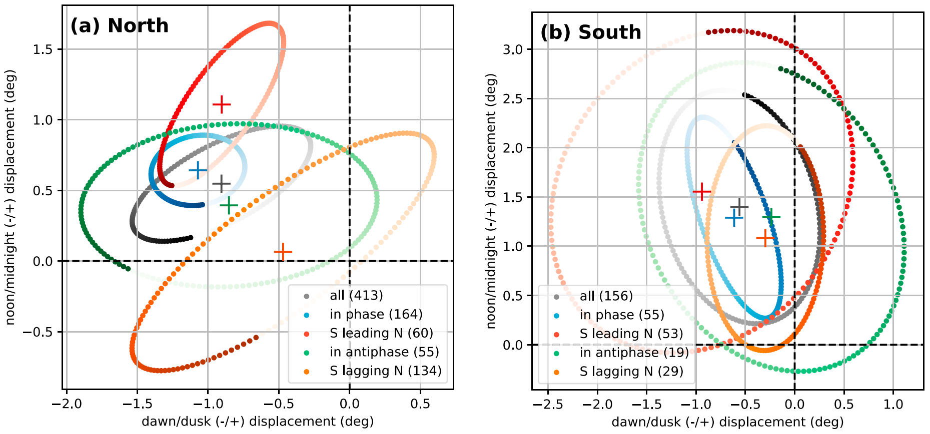

Figure 11. Oval center trajectories for the different beat phases overlaid over the average (white-to-black trajectory). Panel (a) shows the trajectories in the northern hemisphere and (b) in the southern hemisphere. The format is the same as in Figure 10. The brightest marker of each trajectory corresponds to the location of the oval center at $\Phi_{N/S} = 0$; the color darkens with increasing $\Phi_{N/S}$ angles. Numbers in parentheses show the number of Ultraviolet Imaging Spectrograph (UVIS) images/circle fits each ellipse trace is based on.

In order to allow for some comparison with the boundary displacements from section 3.1, we also calculate the magnetic longitude $\Psi_{N/S}$ toward which the oval's centers are displaced relative to the mean location of the oval's center (indicated by the cross in the center of each ellipse). This is done by comparing the angle between a position on the oval center displacement trajectory, the mean oval center location and the noon direction with the PPO angle corresponding to this particular displacement. The range of $\Psi_{N/S}$ we obtain this way depends on the eccentricity of the ellipse and the offset of the mean oval center location from the pole—for a circular motion of the oval center about the pole, $\Psi_{N/S}$ of the displacement direction will be constant throughout a PPO phase cycle, while for a more elliptical trajectory $\Psi_{N/S}$ will change within a certain range. The $\Psi_{N/S}$ angles toward which the oval's centers are displaced in each hemisphere are given in the bottom right corner of both Figures 10a and 10b.

We find that in the northern hemisphere, the center of the auroral oval is generally displaced more or less in the direction of the primary PPO dipole. With the oval centers being displaced toward $\Psi_N = 339–29°$ relative to the mean location of the oval center, this fits reasonably well with our observations of the main oval arc displacements—the maximum equatorward displacement from the median arc position having been observed at $\Psi_N \approx 45°$. The oscillation of the southern auroral oval seems to be such that the oval's center is generally displaced away from the primary PPO dipole direction Φ_S as already observed by Provan et al. (2009), found at slightly larger magnetic longitudes $\Psi_S = 178–203°$ than the exact opposite of the dipole direction. Again, this agrees rather well with the maximum equatorward displacement of the oval arcs, which we observed at around $\Psi_S \approx 225°$. Seeing that the displacement directions of the oval center with respect to PPO phase are consistent between the two hemispheres, we assume that our fits from Figure 9 are reasonable.

As for the statistical displacement of the auroral arc centers in section 3.3, we separate our available data points into four beat phase bins (*in phase*, *in antiphase*, *S lagging N*, and *S leading N*) and perform the same analysis as shown in Figures 9 and 10. The oscillations of the circle centers are shown in Figure 11. We do not show the cosine fits on the dawn-dusk and midnight-noon displacements here and instead refer the reader to the supporting information available for this paper. Of course, due to the sometimes very limited number of points (e.g., only 19 center locations for the *in antiphase* beat period in the southern hemisphere) some of these fits are not very reliable and the results should be taken with caution.

We find that for all beat phases, the oval centers always oscillate about a mean location displaced toward the midnight-dawn side; furthermore, all ellipse traces follow the direction of planetary rotation. This can be taken as a sort of "sanity check" concerning the sometimes rather unconstrained cosine fits. The shape of the ellipse trajectories that the oval center follows seems to stay fairly constant through the beat phases as well, as does the displacement direction relative to the respective primary PPO system in each hemisphere.

The amplitude of the oval center motion in both hemispheres seems to be much larger when the two PPO systems are *in antiphase* (green) than when they are *in phase* (blue). This agrees well with what we observed in section 3.3, where we found that the main emission arcs are displaced furthest from their statistical location under the same conditions. This observed arc displacement can therefore be explained by an enhanced auroral oval oscillation and we can quite safely rule out a contraction/an expansion of the main emission oval when the two PPO systems are *in phase*/*antiphase*.

We furthermore observe that the oval center oscillation in the northern hemisphere is more pronounced when the southern PPO system is *lagging* the northern one (yellow) than it is in the opposite case (*S leading N*, red). For the southern hemisphere, this behavior is inverted—so the oscillation seems to be more pronounced when the primary PPO system is leading the secondary one.

4. Summary

In continuation of the recent investigation of PPO-induced UV auroral intensity modulations based on all available Cassini UVIS data with exception of the mid-2013 to mid-2014 coalescence period (Bader et al., 2018), we now used a subset of the same data set to determine the spatial modulation of the main auroral emission.

We extract the central location of the main emission arc and its poleward and equatorward boundaries from each UVIS image using a newly developed algorithm based on adaptive thresholding and filtering methods. Using the set of location points obtained, we calculate the statistical location of the auroral oval and its boundaries in a local time frame. The results agree fairly well with previous results based on HST and UVIS data (e.g., Badman et al., 2006; Kinrade et al., 2018; Nichols et al., 2016) and show the same pattern characterized by a rather circular shaped oval displaced toward the midnight-dawn direction, with a more poleward location in the postnoon sector presumably due to transient poleward features caused by magnetopause and cusp reconnection. We find no significant seasonal variation of the statistical oval location, but observe the auroral oval to be more contracted during high solar activity periods in agreement with earlier investigations of the open flux content (Badman et al., 2005, 2014).

After subtracting the statistical location from all location markers, the average displacement of the auroral oval from its median location could be determined in a PPO-fixed frame. In both hemispheres, the most equatorward displacement of the auroral oval arc is observed roughly 45° ahead of the region where the highest upward current is expected ($\Psi_N \approx 90°$ in the northern, $\Psi_S \approx 270°$ in the southern hemisphere). Considering that the UV auroral intensity was shown to peak about 30° behind this model maximum (Bader et al., 2018), we have to conclude that the largest equatorward displacement of the auroral oval and its intensity maximum seem to be displaced significantly. We could not find direct evidence of oval arc displacements in phase with the respective secondary PPO systems. However, a beat phase analysis of these displacements revealed that the spatial modulation seems to be largest when the two PPO systems are oriented in relative antiphase, and somewhat smaller when they are in phase—possibly indicating interhemispheric modulations of the oval's location.

By fitting circles to the extracted auroral oval location markers, we also investigate the motion of the oval center with PPO phase. Our results largely verify previous investigations based on HST data (Nichols et al., 2008, 2016), with the exception of a $\approx 90°$ phase shift of the midnight-noon oscillation in the southern hemisphere. It is confirmed that the southern auroral oval oscillates with a significantly larger amplitude than the northern oval. In good agreement with our observations of auroral oval arc displacements we find that the oval center in the northern hemisphere is generally displaced roughly *in* the pointing direction of the northern PPO dipole, and in the southern hemisphere generally *away* from the pointing direction of the southern dipole.

We again conducted a beat phase analysis to evaluate possible interhemispheric PPO coupling and found that the oval center oscillation is more pronounced when the two PPO systems are in antiphase than when they are in phase—agreeing with the increased oval arc displacements. In accordance with the present model of PPO current flows (e.g., Hunt et al., 2014, 2015; Provan et al., 2018), the oval center oscillation is smallest in both hemispheres when the systems are in phase, as each system acts to impose its sense of flow on the other—reducing the absolute ionospheric flow velocities and thereby reducing the displacement of the auroral oval. We note, however, that separating the data sets into beat phases greatly worsens the statistical properties and limits the credibility of these findings. While the results may be fairly consistent between the two hemispheres, many features remain unexplained.

It is obvious that the coupling between the two PPO systems significantly influences the modulations of the UV aurora and likely the entire magnetospheric environment—considering the two PPO systems in isolation does not provide the full picture.

Acknowledgments
UVIS data are available from the NASA Planetary Data System (https://pds.jpl.nasa.gov). All PPO phase data (2004–2017) are available in the University of Leicester Research Archive (http://hdl.handle.net/2381/42436). A. B. was funded by a Lancaster University FST studentship. J. K. and S. V. B. were supported by STFC grant ST/M001059/1. S. V. B. was also supported by an STFC Ernest Rutherford Fellowship ST/M005534/1. Work at the University of Leicester was supported by STFC Consolidated Grant ST/N000692/1.

References

Andrews, D. J., Coates, A. J., Cowley, S. W. H., Dougherty, M. K., Lamy, L., Provan, G., & Zarka, P. (2010). Magnetospheric period oscillations at Saturn: Comparison of equatorial and high-latitude magnetic field periods with north and south Saturn kilometric radiation periods. *Journal of Geophysical Research*, *115*, A12252. https://doi.org/10.1029/2010JA015666

Andrews, D. J., Cowley, S. W. H., Dougherty, M. K., & Provan, G. (2010). Magnetic field oscillations near the planetary period in Saturn's equatorial magnetosphere: Variation of amplitude and phase with radial distance and local time. *Journal of Geophysical Research*, *115*, A04212. https://doi.org/10.1029/2009JA014729

Arridge, C. S., André, N., Khurana, K. K., Russell, C. T., Cowley, S. W. H., Provan, G., et al. (2011). Periodic motion of Saturn's nightside plasma sheet. *Journal of Geophysical Research*, *116*, A11205. https://doi.org/10.1029/2011JA016827

Bader, A., Badman, S. V., Kinrade, J., Cowley, S. W. H., Provan, G., & Pryor, W. R. (2018). Statistical planetary period oscillation signatures in Saturn's UV auroral intensity. *Journal of Geophysical Research: Space Physics*, *123*, 8459–8472. https://doi.org/10.1029/2018JA025855

Badman, S. V., Branduardi-Raymont, G., Galand, M., Hess, S. L. G., Krupp, N., Lamy, L., et al. (2015). Auroral processes at the giant planets: Energy deposition, emission mechanisms, morphology and spectra. *Space Science Reviews*, *187*(1-4), 99–179. https://doi.org/10.1007/s11214-014-0042-x

Badman, S. V., Bunce, E. J., Clarke, J. T., Cowley, S. W. H., Gérard, J.-C., Grodent, D., & Milan, S. E. (2005). Open flux estimates in Saturn's magnetosphere during the January 2004 Cassini-HST campaign, and implications for reconnection rates. *Journal of Geophysical Research*, *110*, A11216. https://doi.org/10.1029/2005JA011240

Badman, S. V., Cowley, S. W. H., Gérard, J.-C., & Grodent, D. (2006). A statistical analysis of the location and width of Saturn's southern auroras. *Annales Geophysicae*, *24*(12), 3533–3545. https://doi.org/10.5194/angeo-24-3533-2006

Badman, S. V., Jackman, C. M., Nichols, J. D., Clarke, J. T., & Gérard, J.-C. (2014). Open flux in Saturn's magnetosphere. *Icarus*, *231*, 137–145. https://doi.org/10.1016/j.icarus.2013.12.004

Badman, S. V., Masters, A., Hasegawa, H., Fujimoto, M., Radioti, A., Grodent, D., et al. (2013). Bursty magnetic reconnection at Saturn's magnetopause. *Geophysical Research Letters*, *40*, 1027–1031. https://doi.org/10.1002/grl.50199

Belenkaya, E. S., Cowley, S. W. H., Meredith, C. J., Nichols, J. D., Kalegaev, V. V., Alexeev, I. I., et al. (2014). Magnetospheric magnetic field modelling for the 2011 and 2012 HST Saturn aurora campaigns—Implications for auroral source regions. *Annales Geophysicae*, *32*(6), 689–704. https://doi.org/10.5194/angeo-32-689-2014

Bradley, T. J., Cowley, S. W. H., Provan, G., Hunt, G. J., Bunce, E. J., Wharton, S. J., et al. (2018). Field-aligned currents in Saturn's nightside magnetosphere: Subcorotation and planetary period oscillation components during northern spring. *Journal of Geophysical Research: Space Physics*, *123*, 3602–3636. https://doi.org/10.1029/2017JA024885

Bunce, E. J., Cowley, S. W. H., & Milan, S. E. (2005). Interplanetary magnetic field control of Saturn's polar cusp aurora. *Annales Geophysicae*, *23*(4), 1405–1431. https://doi.org/10.5194/angeo-23-1405-2005

Burton, M. E., Dougherty, M. K., & Russell, C. T. (2010). Saturn's internal planetary magnetic field. *Geophysical Research Letters*, *37*, L24105. https://doi.org/10.1029/2010GL045148

Carbary, J. F. (2012). The morphology of Saturn's ultraviolet aurora. *Journal of Geophysical Research*, *117*, A06210. https://doi.org/10.1029/2012JA017670

Carbary, J. F. (2017). Update on Saturn's energetic electron periodicities. *Journal of Geophysical Research: Space Physics*, *122*, 156–165. https://doi.org/10.1002/2016JA023405

Carbary, J. F., & Mitchell, D. G. (2013). Periodicities in Saturn's magnetosphere. *Reviews of Geophysics*, *51*, 1–30. https://doi.org/10.1002/rog.20006

Cowley, S. W. H., & Provan, G. (2017). Planetary period modulations of Saturn's magnetotail current sheet during northern spring: Observations and modeling. *Journal of Geophysical Research: Space Physics*, *122*, 6049–6077. https://doi.org/10.1002/2017JA023993

Dougherty, M. K., Cao, H., Khurana, K. K., Hunt, G. J., Provan, G., Kellock, S., et al. (2018). Saturn's magnetic field revealed by the Cassini Grand Finale. *Science*, *362*(6410), eaat5434. https://doi.org/10.1126/science.aat5434

Esposito, L. W., Barth, C. A., Colwell, J. E., Lawrence, G. M., McClintock, W. E., Stewart, A. I. F., et al. (2004). The Cassini Ultraviolet Imaging Spectrograph investigation. *Space Science Reviews*, *115*(1-4), 299–361. https://doi.org/10.1007/s11214-004-1455-8

Gérard, J.-C., Bunce, E. J., Grodent, D., Cowley, S. W. H., Clarke, J. T., & Badman, S. V. (2005). Signature of Saturn's auroral cusp: Simultaneous Hubble Space Telescope FUV observations and upstream solar wind monitoring. *Journal of Geophysical Research*, *110*, A11201. https://doi.org/10.1029/2005JA011094

Gurnett, D. A., Persoon, A. M., Groene, J. B., Kopf, A. J., Hospodarsky, G. B., & Kurth, W. S. (2009). A north-south difference in the rotation rate of auroral hiss at Saturn: Comparison to Saturn's kilometric radio emission. *Geophysical Research Letters*, *36*, L21108. https://doi.org/10.1029/2009GL040774

Hunt, G. J., Cowley, S. W. H., Provan, G., Bunce, E. J., Alexeev, I. I., Belenkaya, E. S., et al. (2014). Field-aligned currents in Saturn's southern nightside magnetosphere: Subcorotation and planetary period oscillation components. *Journal of Geophysical Research: Space Physics*, *119*, 9847–9899. https://doi.org/10.1002/2014JA020506

Hunt, G. J., Cowley, S. W. H., Provan, G., Bunce, E. J., Alexeev, I. I., Belenkaya, E. S., et al. (2015). Field-aligned currents in Saturn's northern nightside magnetosphere: Evidence for interhemispheric current flow associated with planetary period oscillations. *Journal of Geophysical Research: Space Physics*, *120*, 7552–7584. https://doi.org/10.1002/2015JA021454

Hunt, G. J., Cowley, S. W. H., Provan, G., Bunce, E. J., Alexeev, I. I., Belenkaya, E. S., et al. (2016). Field-aligned currents in Saturn's magnetosphere: Local time dependence of southern summer currents in the dawn sector between midnight and noon. *Journal of Geophysical Research: Space Physics*, *121*, 7785–7804. https://doi.org/10.1002/2016JA022712

Jia, X., & Kivelson, M. G. (2012). Driving Saturn's magnetospheric periodicities from the upper atmosphere/ionosphere: Magnetotail response to dual sources. *Journal of Geophysical Research*, *117*, A11219. https://doi.org/10.1029/2012JA018183

Jia, X., Kivelson, M. G., & Gombosi, T. I. (2012). Driving Saturn's magnetospheric periodicities from the upper atmosphere/ionosphere. *Journal of Geophysical Research*, *117*, A04215. https://doi.org/10.1029/2011JA017367

Kinrade, J., Badman, S. V., Bunce, E. J., Tao, C., Provan, G., Cowley, S. W. H., et al. (2017). An isolated, bright cusp aurora at Saturn. *Journal of Geophysical Research: Space Physics*, *122*, 6121–6138. https://doi.org/10.1002/2016JA023792

Kinrade, J., Badman, S. V., Provan, G., Cowley, S. W. H., Lamy, L., & Bader, A. (2018). Saturn's northern auroras and their modulation by rotating current systems during late northern spring in early 2014. *Journal of Geophysical Research: Space Physics*, *123*, 6289–6306. https://doi.org/10.1029/2018JA025426

Lamy, L. (2011). Variability of southern and northern periodicities of Saturn kilometric radiation. In H. O. Rucker, W. S. Kurth, P. Louarn, & G. Fischer (Eds.), *Planetary radio emissions VII* (pp. 39–50). Vienna: Austrian Academy of Sciences Press.

Lamy, L., Cecconi, B., Prangé, R., Zarka, P., Nichols, J. D., & Clarke, J. T. (2009). An auroral oval at the footprint of Saturn's kilometric radio sources, colocated with the UV aurorae. *Journal of Geophysical Research*, *114*, A10212. https://doi.org/10.1029/2009JA014401

Meredith, C. J., Alexeev, I. I., Badman, S. V., Belenkaya, E. S., Cowley, S. W. H., Dougherty, M. K., et al. (2014). Saturn's dayside ultraviolet auroras: Evidence for morphological dependence on the direction of the upstream interplanetary magnetic field. *Journal of Geophysical Research: Space Physics*, *119*, 1994–2008. https://doi.org/10.1002/2013JA019598

Nichols, J. D., Badman, S. V., Bunce, E. J., Clarke, J. T., Cowley, S. W. H., Hunt, G. J., & Provan, G. (2016). Saturn's northern auroras as observed using the Hubble Space Telescope. *Icarus*, *263*, 17–31. https://doi.org/10.1016/j.icarus.2015.09.008

Nichols, J. D., Cecconi, B., Clarke, J. T., Cowley, S. W. H., Gérard, J.-C., Grocott, A., et al. (2010). Variation of Saturn's UV aurora with SKR phase. *Geophysical Research Letters*, *37*, L15102. https://doi.org/10.1029/2010GL044057

Nichols, J. D., Clarke, J. T., Cowley, S. W. H., Duval, J., Farmer, A. J., Gérard, J.-C., et al. (2008). Oscillation of Saturn's southern auroral oval. *Journal of Geophysical Research*, *113*, A11205. https://doi.org/10.1029/2008JA013444

Nichols, J. D., Cowley, S. W. H., & Lamy, L. (2010). Dawn-dusk oscillation of Saturn's conjugate auroral ovals. *Geophysical Research Letters*, *37*, L24101. https://doi.org/10.1029/2010GL045818

Palmaerts, B., Radioti, A., Roussos, E., Grodent, D., Gérard, J.-C., Krupp, N., & Mitchell, D. G. (2016). Pulsations of the polar cusp aurora at Saturn. *Journal of Geophysical Research: Space Physics*, *121*, 11,952–11,963. https://doi.org/10.1002/2016JA023497

Provan, G., Cowley, S. W. H., Bradley, T. J., Bunce, E. J., Hunt, G. J., & Dougherty, M. K. (2018). Planetary period oscillations in Saturn's magnetosphere: Cassini magnetic field observations over the northern summer solstice interval. *Journal of Geophysical Research: Space Physics*, *123*, 3859–3899. https://doi.org/10.1029/2018JA025237

Provan, G., Cowley, S. W. H., Lamy, L., Bunce, E. J., Hunt, G. J., Zarka, P., & Dougherty, M. K. (2016). Planetary period oscillations in Saturn's magnetosphere: Coalescence and reversal of northern and southern periods in late northern spring. *Journal of Geophysical Research: Space Physics*, *121*, 9829–9862. https://doi.org/10.1002/2016JA023056

Provan, G., Cowley, S. W. H., & Nichols, J. D. (2009). Phase relation of oscillations near the planetary period of Saturn's auroral oval and the equatorial magnetospheric magnetic field. *Journal of Geophysical Research*, *114*, A04205. https://doi.org/10.1029/2008JA013988

Provan, G., Cowley, S. W. H., Sandhu, J., Andrews, D. J., & Dougherty, M. K. (2013). Planetary period magnetic field oscillations in Saturn's magnetosphere: Postequinox abrupt nonmonotonic transitions to northern system dominance. *Journal of Geophysical Research: Space Physics*, *118*, 3243–3264. https://doi.org/10.1002/jgra.50186

Radioti, A., Grodent, D., Gérard, J.-C., Bonfond, B., Gustin, J., Pryor, W., et al. (2013). Auroral signatures of multiple magnetopause reconnection at Saturn. *Geophysical Research Letters*, *40*, 4498–4502. https://doi.org/10.1002/grl.50889

Radioti, A., Grodent, D., Gérard, J.-C., Milan, S. E., Bonfond, B., Gustin, J., & Pryor, W. (2011). Bifurcations of the main auroral ring at Saturn: Ionospheric signatures of consecutive reconnection events at the magnetopause. *Journal of Geophysical Research*, *116*, A11209. https://doi.org/10.1029/2011JA016661

Sandel, B. R., Shemansky, D. E., Broadfoot, A. L., Holberg, J. B., Smith, G. R., Mcconnell, J. C., et al. (1982). Extreme ultraviolet observations from the Voyager 2 encounter with Saturn. *Science*, *215*(4532), 548–553. https://doi.org/10.1126/science.215.4532.548

Ye, S.-Y., Fischer, G., Kurth, W. S., Menietti, J. D., & Gurnett, D. A. (2016). Rotational modulation of Saturn's radio emissions after equinox. *Journal of Geophysical Research: Space Physics*, *121*, 11,714–11,728. https://doi.org/10.1002/2016JA023281

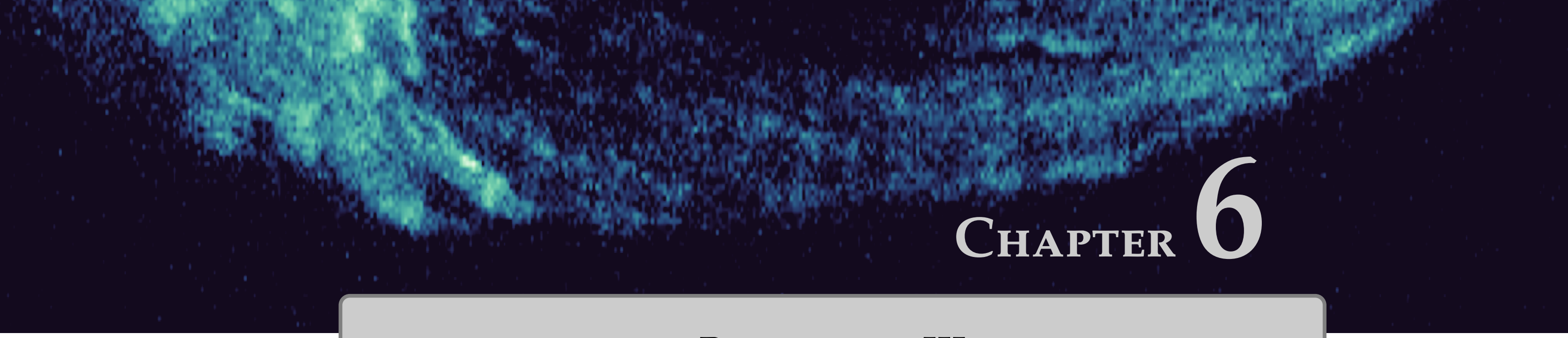

CHAPTER 6

PUBLICATION III

Observations of continuous quasiperiodic auroral pulsations on Saturn in high time-resolution UV auroral imagery

A. BADER, S. V. BADMAN, Z. H. YAO, J. KINRADE AND W. R. PRYOR (2019)
Journal of Geophysical Research: Space Physics, *124*, 2451-2465
doi:10.1029/2018JA026320

AUTHOR CONTRIBUTION STATEMENT AB conceived the study, performed the data reduction and analysis and authored the initial draft. SVB provided reduced HST data and guidance throughout the project. ZHY and JK provided various theoretical support. WRP provided technical support for UVIS data. All authors contributed to the interpretation of the results and were involved in review and editing of the paper until publication.

This authorship statement was approved by all collaborating research groups.

Supplementary information for this publication can be found in appendix B.

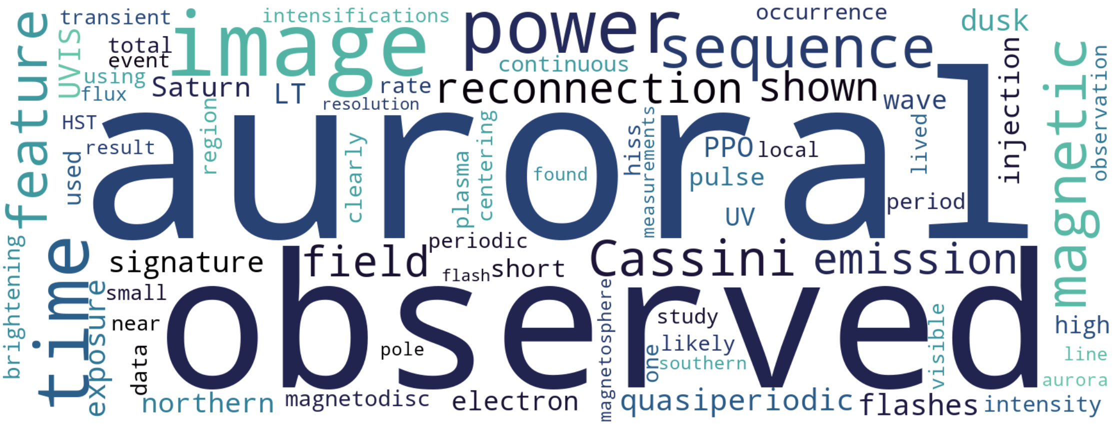

JGR Space Physics

RESEARCH ARTICLE
10.1029/2018JA026320

Observations of Continuous Quasiperiodic Auroral Pulsations on Saturn in High Time-Resolution UV Auroral Imagery

A. Bader[1], S. V. Badman[1], Z. H. Yao[2], J. Kinrade[1], and W. R. Pryor[3]

[1]Department of Physics, Lancaster University, Lancaster, UK, [2]Laboratoire de Physique Atmosphérique et Planétaire, Space sciences, Technologies and Astrophysics Research (STAR) Institute, Université de Liège, Liège, Belgium, [3]Science Department, Central Arizona College, Coolidge, USA

Key Points:
- Continuous 1-hr quasiperiodic flashes in Saturn's UV aurora are revealed in high time-resolution Cassini UVIS imagery
- The auroral flash locations and periodicities match well to quasiperiodic signatures observed recently in Cassini electron and radio data
- Small-scale magnetodisc reconnection predominantly occurring at dusk is suggested as a likely driver

Supporting Information:
- Text S1
- Figure S1
- Figure S2
- Figure S3
- Data Set S1

Correspondence to:
A. Bader,
a.bader@lancaster.ac.uk

Citation:
Bader, A., Badman, S. V., Yao, Z. H., Kinrade, J., & Pryor, W. R. (2019). Observations of continuous quasiperiodic auroral pulsations on Saturn in high time-resolution UV auroral imagery. *Journal of Geophysical Research: Space Physics*, *124*, 2451–2465. https://doi.org/10.1029/2018JA026320

Received 26 NOV 2018
Accepted 5 MAR 2019
Accepted article online 12 MAR 2019
Published online 3 APR 2019

Abstract Saturn's aurora represents the ionospheric response to plasma processes occurring in the planet's entire magnetosphere. Short-lived ~1-hr quasiperiodic high-energy electron injections, frequently observed in in situ particle and radio measurements, should therefore entail an associated flashing auroral signature. This study uses high time-resolution ultraviolet (UV) auroral imagery from the Cassini spacecraft to demonstrate the continuous occurrence of such flashes in Saturn's northern hemisphere and investigate their properties. We find that their recurrence periods of order 1 hr and preferential occurrence near dusk match well with previous observations of electron injections and related auroral hiss features. A large spread in UV auroral emission power, reaching more than 50% of the total auroral power, is observed independent of the flash locations. Based on an event observed both by the Hubble Space Telescope and the Cassini spacecraft, we propose that these auroral flashes are not associated with low-frequency waves and instead directly caused by recurrent small-scale magnetodisc reconnection on closed field lines. We suggest that such reconnection processes accelerate plasma planetward of the reconnection site toward the ionosphere inducing transient auroral spots while the magnetic field rapidly changes from a bent-back to a more dipolar configuration. This manifests as a sawtooth-shaped discontinuity observed in magnetic field data and indicates a release of magnetospheric energy through plasmoid release.

1. Introduction

The Cassini mission, in orbit around Saturn between 2004 and 2017, gradually revealed the high complexity of the Kronian magnetosphere. One of the many dynamical processes that yet remain to be understood is the occurrence of ~1-hr quasiperiodic features observed in a variety of magnetospheric measurements. The observed features include magnetic field fluctuations (Yates et al., 2016), signatures in ion and electron measurements (e.g., Badman et al., 2012; Mitchell et al., 2009; Palmaerts et al., 2016; Roussos et al., 2016), pulses in radio emissions/auroral hiss (e.g., Carbary et al., 2016; Mitchell et al., 2016), and periodic brightenings in Saturn's ultraviolet (UV) and visible auroral intensity (e.g., Dyudina et al., 2016; Mitchell et al., 2016; Palmaerts et al., 2016; Radioti et al., 2013). All these have been reported to occur periodically at a relatively fixed period of ~60 min, but their origin is still unclear.

Recent surveys have statistically investigated the occurrence of such short periodicities throughout the Kronian magnetosphere. Roussos et al. (2016) and Palmaerts et al. (2016) analyzed quasiperiodic injections of relativistic electrons and found that most events occurred at ~1-hr periodicities and outside of Titan's orbit (~20 R_S), spread through almost all the outer magnetosphere—although with a significant location bias toward dusk local times (LTs). Palmaerts et al. (2016) further observed strong radio bursts in the auroral hiss collocated with the electron injections and higher growth rates of the pulses at high latitudes, suggesting a high-latitude acceleration region. The observed location at which these injections take place points to magnetopause or Vasyliunas-cycle reconnection as possible trigger mechanisms (Roussos et al., 2016). Kelvin-Helmholtz waves are deemed unlikely to effectuate the observed LT disparity.

Based on radio measurements from the entire Cassini mission, Carbary et al. (2016) observed similarly increased occurrence rates of periodicities in plasma wave intensity near dusk and at high latitudes, although noting that this bias might be explained with higher auroral hiss observation rates in these regions. They

Table 1
Northern Hemisphere UVIS Image Sequences Used for This Study With UTC Start and Stop Time of Each Sequence, the Number of Images Included and Their Median Exposure Time T_{median}, the Number of Peaks Recorded, and the Peak Percentage of Auroral Power P_{max} Contributed by the Pulsing Emissions

Start time (UTC)	Stop time (UTC)	Images #	T_{median} (min)	Peaks #	P_{max} (%)
2008-04-18 09:43	2008-04-18 13:46	21	12.1	2	33.7
2008-05-08 07:59	2008-05-08 13:47	24	15.1	4	32.7
2008-07-13 03:50	2008-07-13 10:48	29	14.9	1	26.7
2008-07-19 03:26	2008-07-19 13:21	54	11.1	5	18.5
2014-03-20 01:07	2014-03-20 04:14	19	10.4	3	25.8
2014-03-28 09:45	2014-03-28 19:08	54	10.4	9	52.2
2014-05-10 02:25	2014-05-10 17:12	70	12.8	6	32.7
2014-05-25 05:08	2014-05-25 22:36	96	11.0	18	30.3
2014-05-27 04:16	2014-05-27 22:44	116	9.6	11	51.9
2014-05-29 04:16	2014-05-29 22:25	114	9.6	17	41.6
2014-05-30 17:01	2014-05-30 22:31	37	9.2	6	36.8
2014-05-31 17:01	2014-05-31 22:23	35	9.4	4	34.2
2014-06-01 16:54	2014-06-01 22:07	34	9.4	3	41.3
2014-06-02 17:34	2014-06-02 23:44	40	9.4	7	71.1
2014-06-03 17:34	2014-06-03 23:44	40	9.4	5	54.0
2014-06-05 07:45	2014-06-06 04:25	120	10.4	12	35.7
2014-06-07 14:56	2014-06-08 04:08	77	10.4	5	31.8
2014-06-09 10:48	2014-06-10 04:09	93	11.3	5	40.3
2014-06-10 15:49	2014-06-11 09:33	90	11.9	11	33.6
2014-09-05 11:52	2014-09-05 20:59	73	7.6	10	35.0
2014-09-13 06:07	2014-09-13 14:13	60	8.2	7	30.1
2014-10-16 16:18	2014-10-17 05:32	73	11.0	11	27.7
2014-11-06 23:08	2014-11-07 12:32	123	6.3	6	46.7
2014-11-23 12:39	2014-11-23 16:46	42	6.1	5	27.8
2014-11-27 19:56	2014-11-28 10:30	136	6.3	12	33.6
2014-12-01 01:28	2014-12-01 09:02	69	6.7	3	31.9
2016-06-25 02:05	2016-06-25 06:47	28	10.4	2	27.1
2016-09-06 22:05	2016-09-07 05:31	28	16.5	4	20.3
2016-09-29 17:49	2016-09-29 20:38	18	9.9	1	39.5
2016-09-30 09:17	2016-09-30 16:38	37	12.2	1	46.0
2016-10-01 11:49	2016-10-02 02:24	50	17.2	2	35.8
2016-10-29 02:32	2016-10-29 10:29	40	12.3	2	23.9
2017-01-14 16:57	2017-01-14 22:39	29	12.3	1	26.2
2017-03-20 03:36	2017-03-21 04:46	89	16.1	9	42.4
2017-04-02 15:51	2017-04-02 21:48	48	7.6	4	22.9
2017-04-18 05:39	2017-04-18 11:16	26	13.4	0	10.8

Note. UVIS = ultraviolet spectrographic imager.

suggest interhemispheric Alfven waves as a possible source, similar to Yates et al. (2016), who used magnetic field data to show that second harmonic standing Alfven waves could be responsible for the periodic phenomena observed. Yates et al. (2016) also observed the intensity of the quasiperiodic magnetic field oscillations to depend on the phase of the ~10.7-hr planetary period oscillation (PPO) and related this to PPO modulation of Cassini's distance from the magnetospheric current sheet.

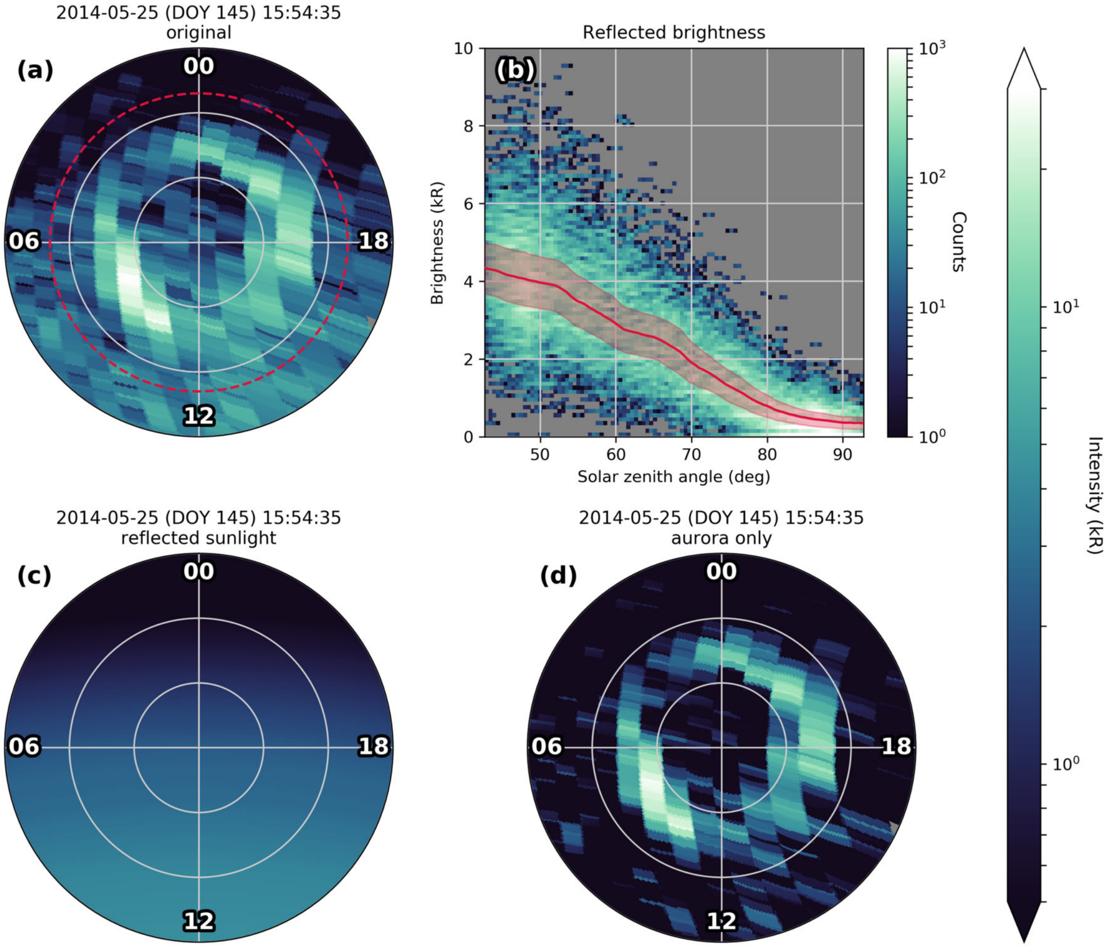

Figure 1. Removal of dayglow procedure. (a) Polar-projected UVIS image, looking down onto the northern pole with midnight toward the top. Concentric rings mark the colatitude from the northern pole in steps of 10°. The total unabsorbed H_2 emission intensity of Saturn's northern aurora is shown with a logarithmic color map as defined with the large color bar to the right. Pixels outside of the red-dashed line at 23° colatitude are considered background emission and used for estimating the brightness of dayglow. (b) Solar zenith angle versus brightness histogram of all background emission of all UVIS images within a ±3-hr window of this observation, with the filtered median shown in red and and the median absolute deviation shown with red shading. (c) Brightness map of dayglow derived from the median of the distribution in (b). (d) The original image with the derived dayglow brightness (c) subtracted. UVIS = Ultraviolet Imaging Spectrograph.

Several case studies have analyzed periodic brightenings of the high-latitude auroral oval (Mitchell et al., 2016) and transient auroral spots and bifurcated arcs on the duskside (Radioti et al., 2009, 2013), as well as pulsating cusp emissions (Palmaerts et al., 2016). Mitchell et al. (2016) demonstrated that these quasiperiodic auroral brightenings are in phase with auroral hiss and particle signatures, indicating a common generation process. Energetic neutral atom signatures of this process are expected but could so far not be observed, likely due to the spatial and time resolution of the Cassini Ion and Neutral Camera (INCA) (Krimigis et al., 2004) being too limited to capture these small-scale and short-lived features. All these studies favor magnetic reconnection processes as likely triggers, but the main question—how exactly these quasiperiodic fluctuations are generated and what determines their periodicity—remains unanswered.

In this study we investigate pulsations in the UV auroral intensity using large sets of to date mostly unused images from Cassini's Ultraviolet Imaging Spectrograph (UVIS) with the aim of shedding more light on possible driving mechanisms. In section 2 we present the data set used. Our analysis methods and results are explained in sections 3 and 4, respectively. We conclude this study in section 5.

2. Data Set

We use a selection of images from the Cassini UVIS spectrographic imager (Esposito et al., 2004), which intermittently observed Saturn's UV auroras between Cassini's orbit insertion on 1 July 2004 and end of mission on 15 September 2017. Auroral imagery was obtained by scanning the instrument's FUV slit (1.5 × 64 mrad, 110–190 nm) across the auroral region. Depending on the viewing geometry and the accumulation time for each slit exposure, the total exposure time for an image covering the full auroral oval can vary between 6 and 180 min. In this study we only use image sequences with more than 15 images taken in quick succession, with the median exposure time of the images included, T_{median}, smaller than 1,000 s $\approx$ 17 min. The highest single image exposure time used is 19.7 min. Taking only into account images from the northern hemisphere, this results in a set of 2,130 images spread over 36 sequences, with 14 sequences providing (near-)continuous observations of the auroral oval over more than one Saturn rotation ($\sim$ 10.66 hr). A list of the image sequences used is given in Table 1.

Each image was polar projected onto a 0.5° × 0.25° (lon × lat) planetocentric polar grid at an altitude of 1,100 km above Saturn's 1-bar level (with Saturn's equatorial and polar radii R_{SEQ} = 60,268 km and R_{SPO} = 54,364 km) where auroral emissions are thought to be generated (Gérard et al., 2009) using Cassini SPICE pointing information available on NASA's Planetary Data System. The intensity recorded by the UVIS FUV sensor is converted to the total unabsorbed H_2 emission intensity (70–170 nm) by multiplying the value measured in the 155- to 162-nm range by the factor 8.1 as empirically determined by Gustin et al. (2016, 2017) in order to minimize dayglow emission and hydrocarbon absorption effects.

Even so, some dayglow remains in most UVIS images; we remove it in order to obtain accurate auroral brightnesses and emission powers. This is done by determining the dayglow brightness dependence on solar zenith angle (SZA) using all UVIS images collected between ±3 hr of the image, which is being corrected (see Figure 1). We use all pixels equatorward of 23° colatitude from the pole-equatorward of the median equatorward boundary of Saturn's auroral oval and its median absolute deviation (Bader et al., 2019). We determine an SZA-brightness histogram (Figure 1b) and median-filter the data with a box 10° wide in SZA to obtain a smooth median brightness per SZA distribution, shown with a red line. This is used to model the dayglow background of an auroral image (Figure 1c), which is then subtracted from the original image such that only true auroral emissions remain (Figure 1d).

3. Method

A short example sequence of UVIS images is shown in Figure 2. The 25 images displayed have an exposure time of ~9 min each, adding up to ~4.5 hr of near-continuous observations. Quasiperiodic auroral flashes in the dusk region are visible in panels (b), (f), (l), (p), and (v) and marked with yellow arrows. A high time resolution for an extended period such as this can only be achieved if Cassini is located close to apoapsis above one of the poles, since only then the viewing geometry allows UVIS to successively sweep over the whole auroral oval with short scans for extended periods of time. This naturally implies a greatly reduced spatial resolution as is clearly visible in the images shown.

In order to mitigate this drawback, we will use the auroral power to track periodic transient auroral intensifications such as those shown in Figure 2. Since each pixel of the UVIS instrument represents an average of the brightness observed across the area it covers, an integration over a complete image or part of it should yield a value of the auroral power which is only marginally impacted by the low spatial resolution—only the relative weights of differently bright areas subtending the pixel can be modified as the polar projection is performed, skewing the calculated powers to some degree.

After correcting for dayglow as described above, we section each image into 36 LT bins and integrate their enclosed intensities between 0° and 30° colatitude from the pole to obtain an LT distribution of radiant fluxes, or "auroral powers"—noting that the column emission rates observed by each UVIS pixel need to be corrected for the angle under which the emitting surface (ionospheric layer) was observed such as to not overestimate the emission rate of regions observed under low elevation angles. By combining LT-power distributions of several images, we obtain a keogram. The one including all images from Figure 2 is shown in Figure 3a, with the total emission power P_{tot} below. The most prominent feature is a strong brightening occurring at about 11:00 UTC close to the midpoint of the sequence, and subcorotating through noon into dusk until the end of the sequence. This is likely a large-scale injection event triggered by tail reconnection (e.g., Mitchell et al., 2009).

However, we focus on the short-lived flashes shown in Figure 2—visible as bright vertical lines between roughly 15 and 21 LT. In order to separate these highly dynamic features from the more long-lived auroral

10.1029/2018JA026320

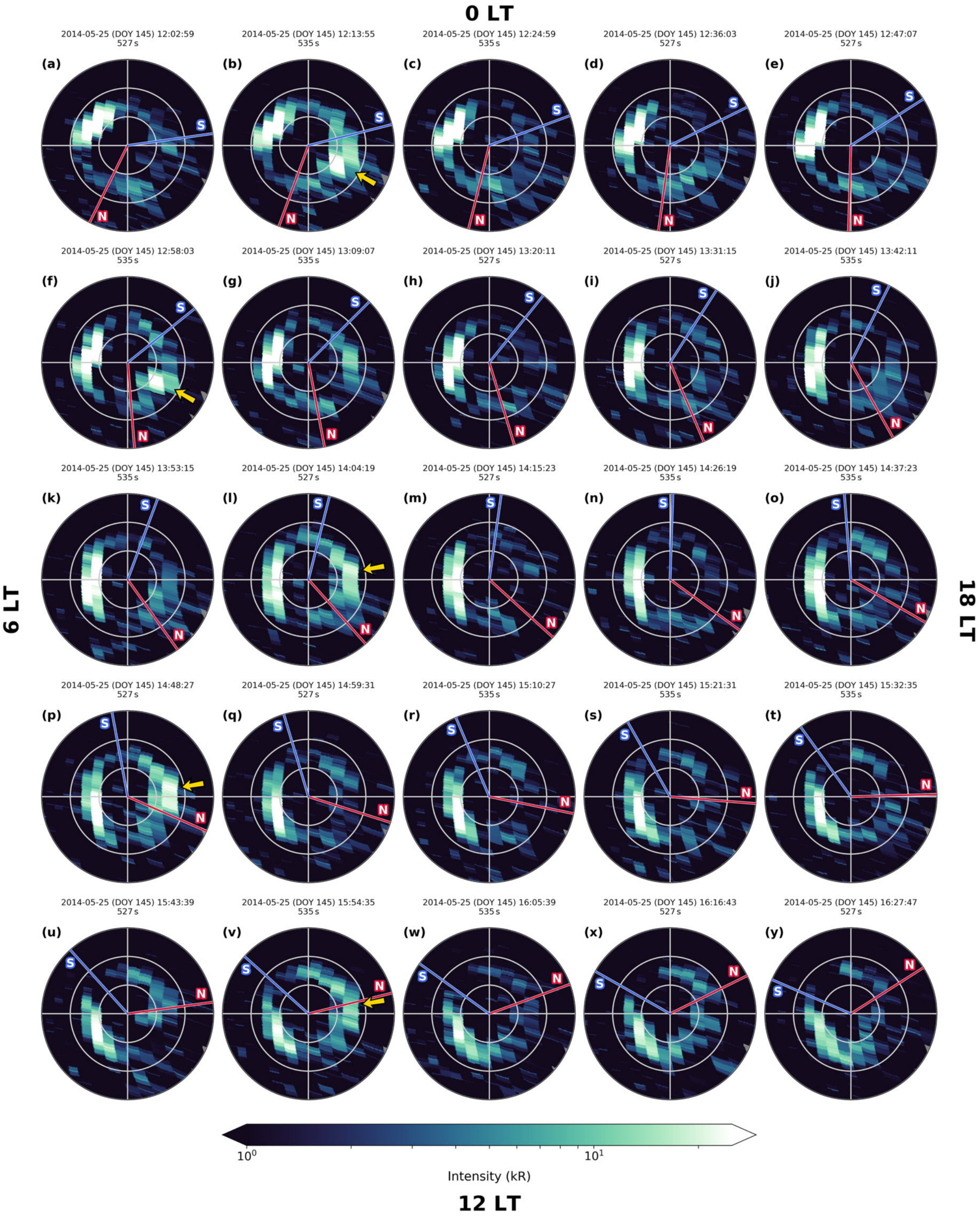

Figure 2. Example sequence of UVIS images from 25 May 2014 (DOY 145). Shown is the total unabsorbed H_2 emission intensity of Saturn's northern aurora with a logarithmic color scale, after the dayglow has been subtracted. The view is from above the north pole, such that the pole is in the center of each image with local midnight toward the top of the figure and local noon toward the bottom. Concentric rings mark the colatitude from the pole in 10° steps. The northern (southern) PPO system's orientation is indicated with red (blue) lines, which mark the pointing direction of the corresponding magnetic perturbation dipole (such that $\Phi_{N/S}$ is the counterclockwise angle between local noon and the marked line). The time at which a UVIS scan started is noted on top of each panel, together with the total exposure time of the corresponding sweep. Yellow arrows in panels (b), (f), (l), (p), and (v) indicate short-lived auroral intensifications at local dusk. LT = local time; UVIS = Ultraviolet Imaging Spectrograph.

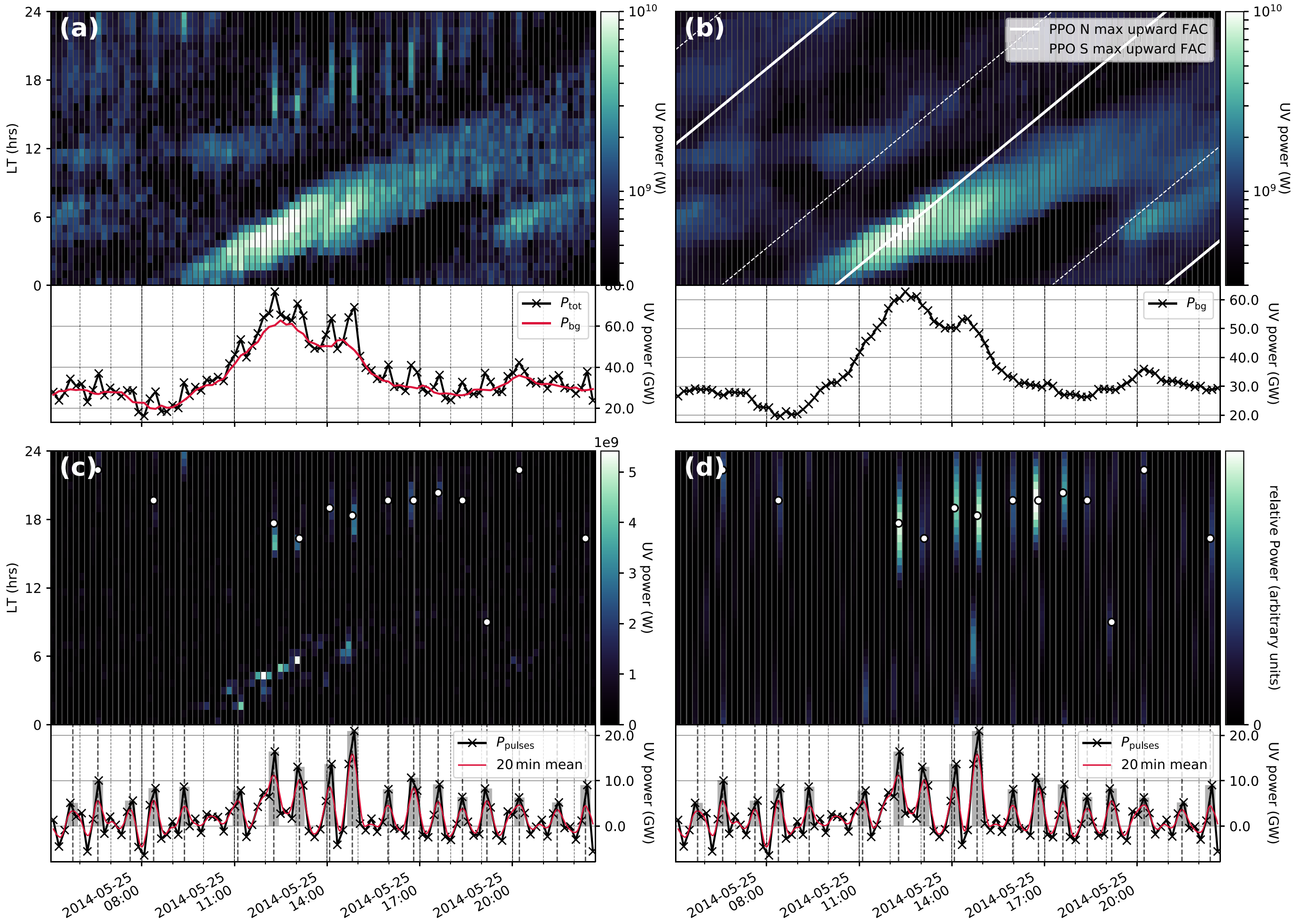

Figure 3. Ultraviolet (UV) power keogram from 25 May 2014 (DOY 145) based on 96 UVIS images, including but not limited to the sequence shown in Figure 2. (a) The original keogram, with each vertical stripe corresponding to the UV power of a single UVIS image integrated in 36 local time bins between 0° and 30° colatitude from the northern pole. The total UV power P_{tot} of each image (the sum of the keogram in vertical direction) is shown below with black crosses. Overlaid in red is the contribution of the auroral background to the total power, P_{bg}. (b) The median-filtered background. Diagonal white lines track the approximate location of upward field-aligned current maxima caused by the two planetary period oscillation (PPO) perturbation systems—the bold (dashed) line corresponding to the primary (secondary) PPO system located in the same (opposite) hemisphere (e.g., Andrews et al., 2010; Hunt et al., 2014; Provan et al., 2018). Below the keogram is P_{bg}, as already plotted in red in panel (a). (c) The difference between the previous panels (a) and (b), corresponding to the UV pulsing power with the background removed. Below again the sum of the keograms in black, P_{pulses}, with a 20-min boxcar average overlaid in red. Gray dashed vertical lines and bars mark the determined pulse locations and heights. The approximate local time (LT) location of these brightenings is marked with black-and-white circles in the keogram. (d) A filtered version of panel (c) as described in the text, used for determining the approximate LT location of the auroral flashes. Again, the black-and-white circles mark the LT location in the keogram. Below is a copy of the corresponding graph from panel (c), added for reference.

background of subcorotating patches, we create a median-filtered version of the keogram using a box of size 3,000 s × 30° (2-hr LT), tilting the box according to a subcorotation rate of 65% of Saturn's rotation to account for the relatively steady motion of Saturn's auroral emissions (Grodent, 2005). Subtracting the so calculated background (see Figure 3b, summed power P_{bg} below) from the original keogram yields a keogram of transient features, shown in Figure 3c. A time series of the UV power attributed to these pulsing features, P_{pulses}, is obtained by summing up all LT bins for each image/time step (black graph in Figure 3c); smoothing the result with a 20-min boxcar average (red graph in Figure 3c) reveals the quasiperiodic intensifications quite clearly.

Pulses are identified by finding all local maxima in the smoothed result with a prominence larger than 3 GW, an empirically determined limit. This value may seem rather small, but it is to note that the boxcar averaging significantly decreases the original peak height—most detected peaks have powers >5 GW on an

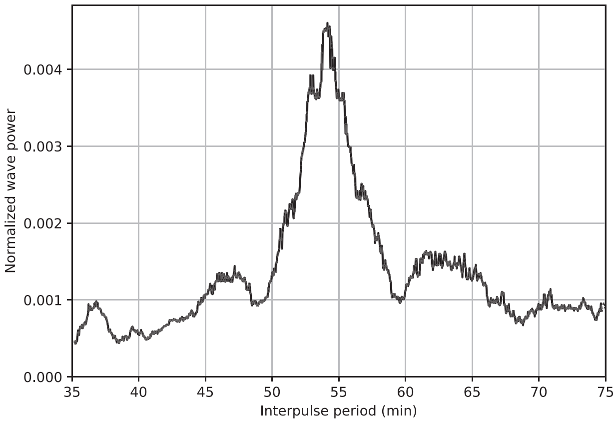

Figure 4. Lomb-Scargle periodogram of all P_{pulses} powers of all image sequences listed in Table 1.

auroral background of roughly 20–200 GW. The uncertainty of the total UV power can only be estimated based on the noise in the time series but is likely in the range of only 1–2 GW. The peak power is determined by the closest datapoint in P_{pulses}. We also try to find the approximate origin of each pulse using the keogram of transient features (Figure 3c). These auroral flashes are usually very short lived with a lifetime <10 min (Dyudina et al., 2016) - they are nearly never spread over 2 UVIS images with exposure times of ∼10 min - but rather wide in LT. Hence, we apply a median filter of size 600 s × 90° (6-hr LT) to highlight the pulses and exclude other features, followed by a same-sized mean filter to create smooth peaks. The resulting array is shown in Figure 3d; the maximum in LT corresponding to each pulse is highlighted with a black-and-white circle. If the maximum in this array corresponding to a pulse in UV power does not exceed 5 times the median absolute deviation of the array, the location determined in this step is deemed unreliable and discarded. Figures similar to Figure 3 for all analyzed sequences can be found in the supporting information.

4. Results and Discussion

4.1. Flash Powers and Periodicities

Table 1 summarizes the results for all sequences analyzed. We find quasiperiodic brightenings in all sequences, although with highly variable strengths: The largest instantaneous contribution of the pulsing features to the total emitted UV power per sequence, $P_{\text{max}} = \max(P_{\text{pulses}}/P_{\text{tot}})$, ranges between 10.8% and 71.1%, reaching up to 50% or more of the total auroral power emitted in several sequences. In many observations, the flashes hence seem to be more powerful than the remaining auroral emissions combined. We note that these values represent lower limits, since the lifetime of such auroral flashes is shorter than or comparable to the exposure time of the UVIS imagery used. As visible in Figure 2, one flash is usually fully scanned with only few single slit exposures (8 s each)—in this example, the UVIS slit was aligned roughly into the dawn-dusk direction and scanned from midnight to noon. With Cassini slewing with a constant angular velocity and the entire scan taking less than 10 min, the time during which the UVIS slit was pointed toward the flash direction is of order 1 min or less. The recorded power therefore likely corresponds to the rise or decay phases of a flash and is lower than its actual power maximum.

We determine the periodicity of these features by combining the P_{pulses} time series of all periods investigated here and calculating a Lomb-Scargle periodogram (see Figure 4). A wide peak in the periodogram indicates periodicities close to 54 min, with a noticeable spread a few minutes either direction, clearly indicating that these auroral flashes must be closely related to the quasiperiodic features observed in electron, radio, and magnetic field data in previous studies (e.g., Carbary et al., 2016; Mitchell et al., 2009; Mitchell et al., 2016; Palmaerts et al., 2016; Roussos et al., 2016; Yates et al., 2016).

As can be seen in Table 1 and the supporting information figures, we identify auroral flashes in nearly every investigated sequence. Due to UVIS' slit-scanning mechanism, it is likely that some flashes occur but are not recorded due to their lifetime being too short and the UVIS slit being pointed at a different location while a flash is active. We hence conclude that this auroral flashing seems to be quasi-continuous just as the energetic electron and auroral hiss intensifications observed previously.

4.2. Statistical Properties of Auroral Flashes

In the context of this study we could identify 214 auroral intensifications, 149 of which were prominent enough to be located in LT. We note that the determined LT positions are, due to the pixel size and the size of the flashes themselves, only approximate; we assume an error of ±1-hr LT. Figure 5 shows a statistical analysis of the properties of the auroral brightenings observed. We find that their power can reach more than 30 GW, although values ∼5–10 GW are most common. A histogram of periods between consecutive pulses (Figure 5b) reveals that intervals as low (high) as ∼30 min (∼70 min) are observed. While this spread might to some degree be accounted for by the still relatively low sampling frequency of the UVIS images, it certainly seems that the pulsing auroral features are, albeit continuous, not quite as periodic as related signatures in other data sets. We also observe a clear LT bias toward the dusk side (Figure 5c), in agreement with the

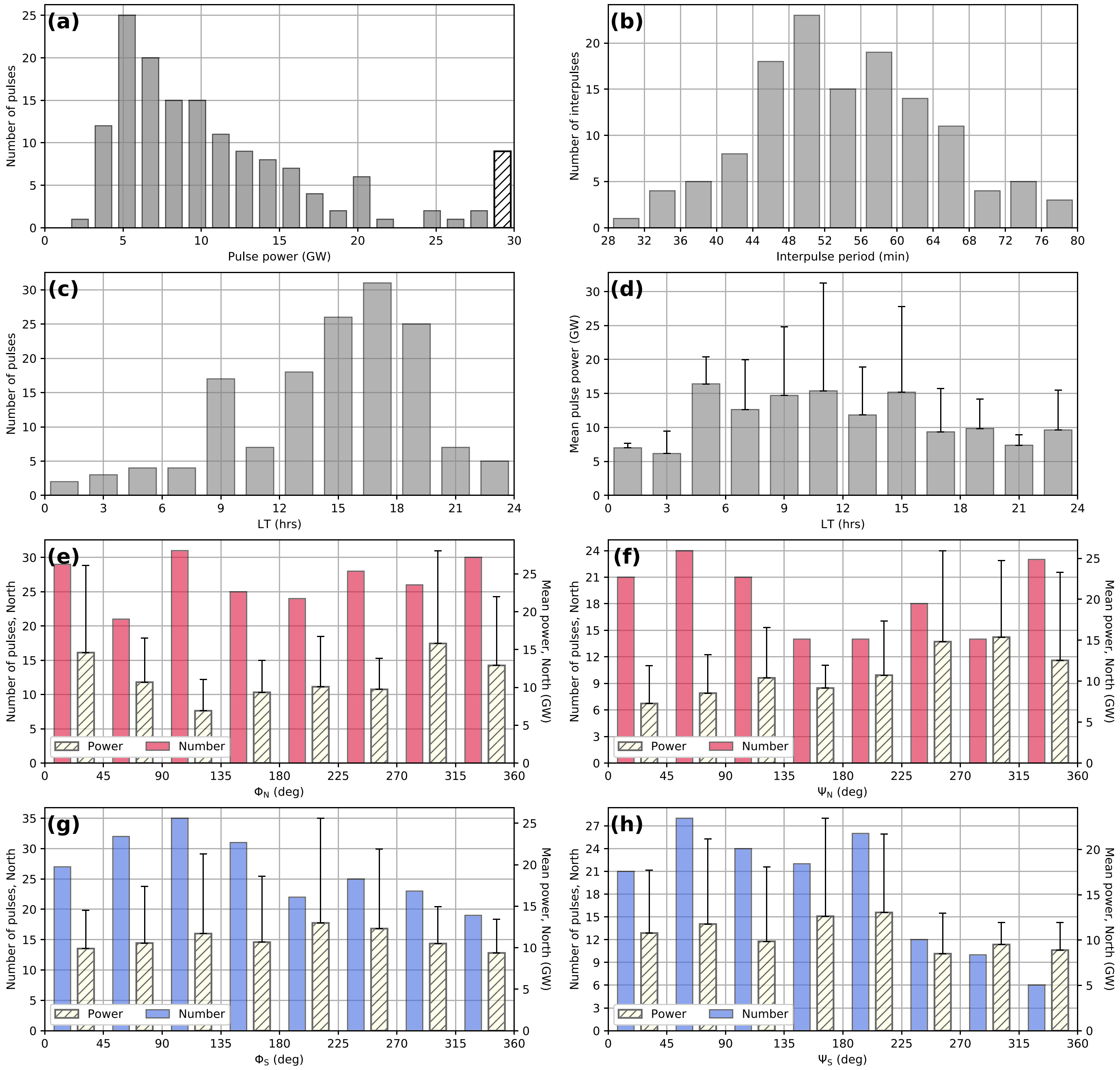

Figure 5. Basic statistics of the auroral flashes identified in this study. (a) Histogram of the flashes' peak UV powers, the hatched bar combines all those whose peak power was larger than the upper histogram limit. (b) Histogram of interpulse periods, (c) histogram of local time locations, and (d) mean UV flash power and associated error in each local time bin. (e) The occurrence, mean power, and errors of northern hemispheric auroral flashes depending on the northern planetary period oscillation (PPO) phase Φ_N and (f) the location of these intensifications in the corresponding PPO-fixed magnetic longitude frame Ψ_N. (g), (h) The occurrence, mean power, and errors of northern hemispheric auroral brightenings in the southern PPO system, Φ_S and Ψ_S, respectively.

location bias of electron and plasma wave events (Carbary et al., 2016; Palmaerts et al., 2016; Roussos et al., 2016). The mean power of the auroral pulses however is largely unchanged through all LTs (Figure 5d).

The occurrence rates and mean powers of northern hemispheric auroral flashes in different PPO frames (e.g., Andrews et al., 2010; Hunt et al., 2014) are shown in Figures 5e–5h. The angle $\Phi_{N/S}(t)$ represents hereby the instantaneous azimuthal angle between the transverse dipole of the northern/southern PPO

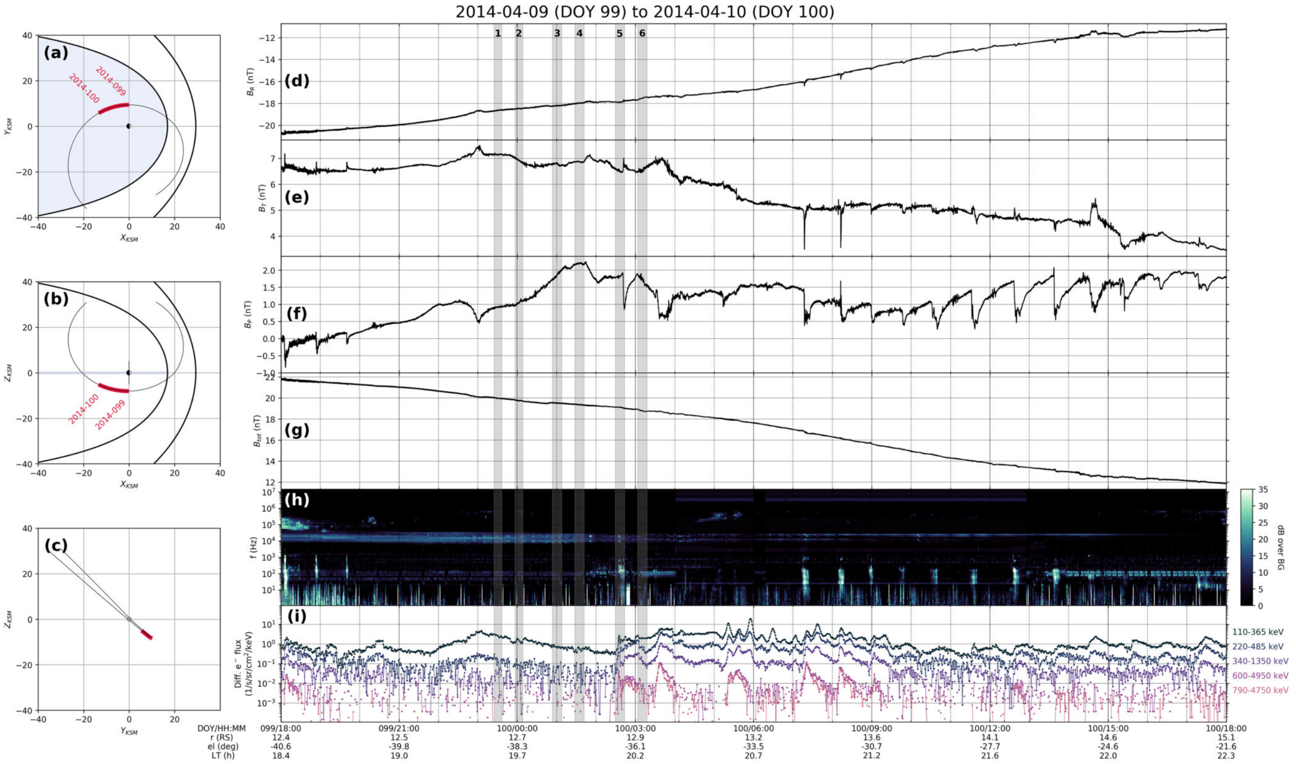

Figure 6. Cassini in situ data from 9 April 2014 (DOY 99) 18:00 to 10 April 2014 (DOY 100) 18:00. (a–c) The position of Cassini in Saturn-centered Kronocentric Solar Magnetospheric (KSM) coordinates. The orbit ±10 days is shown in black, with the red section indicating the time period whose data are shown in the following panels. The modeled magnetopause locations at solar wind pressures of 0.01 and 0.1 nPa (Arridge et al., 2006) are indicated with bold black lines. (d–f) Magnetic field measurements in Saturn-centered R-Theta-Phi coordinates. (g) The total magnetic field strength. (h) Radio and Plasma Wave Science (RPWS) electric field spectrogram. (i) High-energy electron fluxes of the Low-Energy Magnetospheric Measurement System (LEMMS) instrument. Gray-colored and numbered areas indicate when Hubble Space Telescope images were obtained. Cassini's orbital radius (r), latitude (el) and local time (LT) are noted on the bottom.

perturbation system and local noon; it increases eastward in direction of planetary rotation. $\Psi_{N/S}$ describes the rest frame of the northern/southern PPO rotation; it is defined such that $\Psi_{N/S} = 0°$ is aligned with the transverse perturbation dipole and $\Psi_{N/S}$ increases westward such that increasing values describe increasing rotational lags with respect to the dipole (see, e.g., Bader et al., 2018; Hunt et al., 2014). The PPO phases were determined using an empirical PPO model encompassing magnetic field measurements from the full Cassini mission (e.g., Provan et al., 2018). Since the mean duration of the sequences used is ~ 10.1 hr, we can assume even coverage throughout all PPO phases. As visible in the histograms, neither the occurrence rate nor the power of the quasiperiodic flashes are significantly affected by PPOs. This does not necessarily disagree with the wave packet structure observed by Yates et al. (2016), as they presumed this to be an effect of the varying distance between the magnetic dipole equator and the spacecraft. The observation of auroral features is not affected by this effect.

However, there seems to be a depression of pulse occurrences at around $\Psi_S \approx 230 - 360°$—but it is unclear why the flash occurrence in the northern hemisphere should depend more on the southern than on the northern PPO system. We note though that a large part of the data used in this study was obtained between mid-2013 and mid-2014, a period during which the northern and southern PPO systems were locked in near relative antiphase and their relative strengths were highly variable (Provan et al., 2016). A clear relationship between the auroral intensity and the PPO phases has been confirmed (Bader et al., 2018), but the situation has been shown to become more complex when the two periods converge (Kinrade et al., 2018).

4.3. Auroral Flash Evolution: Case Study

Figure 6 shows one day of Cassini in situ data obtained at the same time as several Hubble Space Telescope (HST) auroral images. The second half of the period shown is clearly dominated by ~1 hr quasiperiodic features in all instruments. The clearest signatures are visible in B_P, which is the azimuthal component of

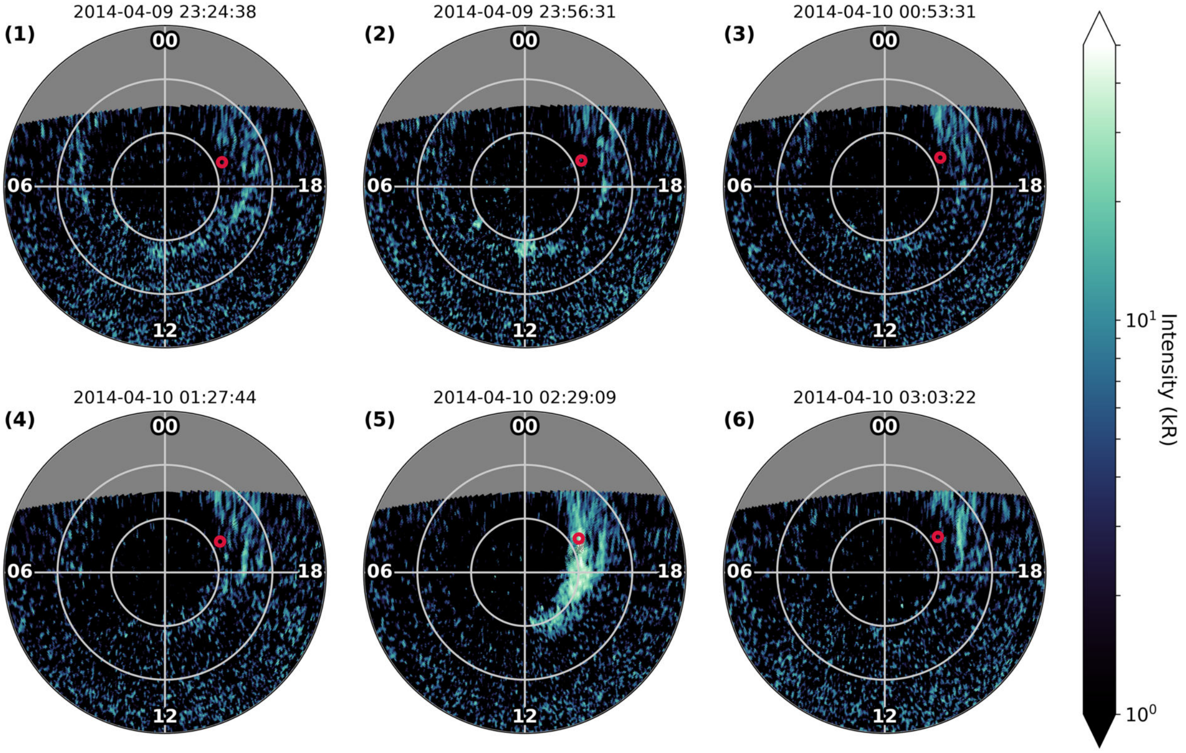

Figure 7. Hubble Space Telescope (HST) images of Saturn's northern hemisphere from 9 April 2014 to 10 April 2014 (DOY 99–100), numbered as in Figure 6. Exposure times range from 700 to 840 s. Cassini's ionospheric footprint was mapped using the Burton et al. (2010) model of the planetary field plus a contribution from the ring current modeled by Bunce et al. (2008) and is indicated with a red circle.

the R-Theta-Phi coordinate system used here and positive in the direction of planetary rotation. B_P follows a sawtooth-shape, exhibiting significant dropoffs roughly every hour. The other magnetic field components change accordingly such that the total magnetic field strength (see Figure 6g) shows no discontinuities, describing a simple rotation of the magnetic field vector. These features are very similar to those observed in Figure 1 of Palmaerts et al. (2016). As Cassini was located in the southern hemisphere well below the current sheet, these signatures correspond to a sudden change of the magnetic field from a bent-back to a more dipolar configuration, followed by a slow and steady change into the bent-back state. Coincident with these sharp features Cassini observed clearly enhanced auroral hiss (see Figure 6h) and increased energetic electron fluxes. All these signatures are also visible at the beginning of the sequence, and one signature was observed during the exposure of HST image 5.

The HST images corresponding to this sequence of in situ measurements are shown in Figure 7. These images were acquired by the HST Space Telescope Imaging Spectrograph (STIS), with the STIS FUV multi-anode microchannel array using the F25SrF2 long-pass filter with an exposure time of 840 s. This filter is a band-pass filter letting 125- to 190-nm wavelengths pass while blocking the H Lyman-α emission line at 121 nm. All exposures were background-subtracted and projected on a planetocentric polar grid (e.g., Clarke et al., 2009; Kinrade et al., 2017). This day clearly featured an exceptionally quiet aurora in the northern hemisphere, with none of the images including any dawn emission. The dominant feature is a transient brightening in image 5, coinciding exactly with the in situ signatures described above.

In Figure 8 we present a sequence of HST images showing the dynamic motion of this one auroral flash in detail. The sequence was obtained by splitting HST image 5, which was acquired in time-tag mode, into six subexposures of equal length. Figures 8a–8f shows the six subexposures in chronological order. With the flash just appearing in Figure 8a, we can follow its evolution for about 10 min—probably most of its expected lifetime. The detailed views of the smoothed auroral intensity (Figures 8g–8l) reveal that this auroral "flash" is rather a series of short, small-scale injections clustered together. Two of these injections are comparably long-lived and bright enough to be traced through several images; their central positions were determined

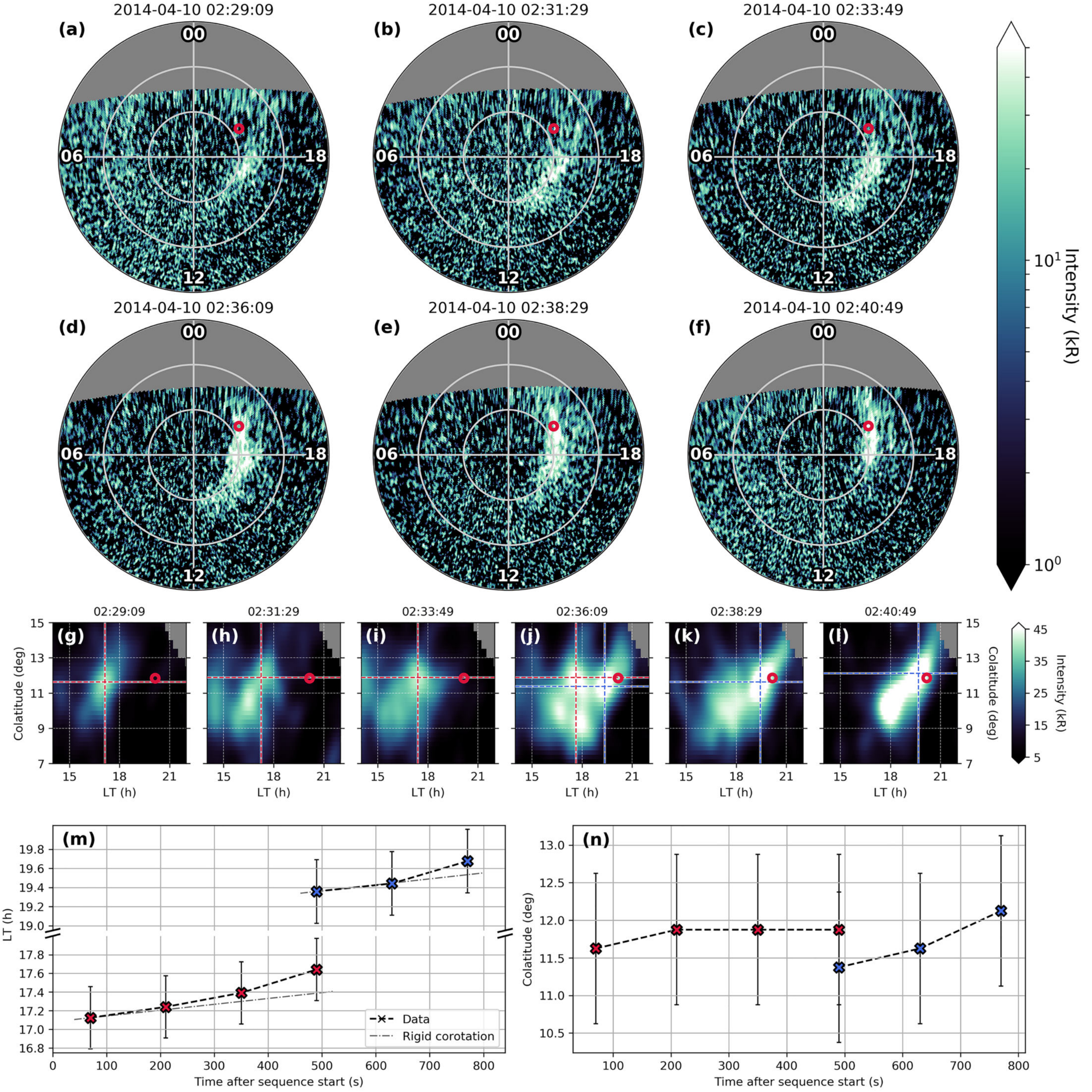

Figure 8. Time-tag Hubble Space Telescope image from 10 April 2014 03:44:20–03:58:20 (image number 5 in Figures 6 and 7) split into six subexposures of equal length. (a–f) The background-subtracted and polar-projected subexposures as seen from above the north pole, formatted as in Figure 2. Cassini's ionospheric footprint is indicated with a red circle. (g–l) Their section between 14–22 local time (LT) and 7–15° colatitude, smoothed with a 5 × 5/8° (lon × colat) Gaussian filter. The motion of two spots is traced through some images, with their local brightness maximum marked with red/blue dashed lines. (m) LT and (n) colatitude motion of the traced spots, colors corresponding to the previous panels, with their uncertainty shown with error bars (Grodent, 2005).

by their brightness maximum and are marked with red (blue) dashed lines in Figures 8g–8j (Figures 8j–8l). For their location, we assume an error of 1° in colatitude and 5° in longitude (20-min LT) based on the HST projection errors estimated by Grodent (2005).We observe that both injections move at least at full corotation speed (Figure 8m), with their azimuthal motion accelerating up to their last detection. At the same time, the first spot (red) is found to move equatorward between its first and second detection, after which is stays at the same colatitude (see Figure 8n). The second injection (blue) exhibits a somewhat clear equatorward motion. We note however that the (co)latitudinal motion observed measures less than 1°, with the projection grid of the original HST images being sized 0.25° in colatitude and the projection error being roughly 1° in this direction (Grodent, 2005); we therefore abstain from a quantitative analysis here and only conclude that the auroral features seem to stay at their colatitudinal location or move slightly equatorward but almost certainly do not move in a poleward direction.

4.4. Discussion

Previous investigations have referred to Alfvèn mode standing waves as a possible driving mechanism of periodic transient features in Saturn's aurora (Meredith et al., 2013), magnetic field data (Yates et al., 2016), and auroral hiss (Carbary et al., 2016). It has recently been shown that pulsating auroral emissions could also be connected to traveling Alfvèn waves inducing pulsating field-aligned currents (Yao et al., 2017), possibly generated through the Kelvin-Helmholtz instability (Masters et al., 2009) or perturbations at Saturn's plasma circulation blockage near noon (e.g., Southwood & Chané, 2016). However, the magnetic field signatures shown in Figure 6 do not seem to be wave related. The prominent sawtooth shape does not correspond to the characteristics of known ULF wave observations in Saturn's magnetosphere (e.g., Kleindienst et al., 2009; Russell et al., 2006), and the recurrence period of the discontinuities observed in B_P (Figure 6f) is less constant than would be expected for wave-like structures. The “interpulse period” between these features changes from significantly less than 1 hr at around 09:00 UT to over 1 hr at about 12:00 UT in the sequence shown in Figure 6, for example.

The auroral flash presented in Figure 8 was observed in the northern hemisphere, while coincident magnetic field, energetic electron, and auroral hiss perturbations were observed by Cassini, which was located south of the magnetodisc—suggesting that these quasiperiodic features occur on closed field lines. Furthermore, the auroral flash investigated in section 4.3 seems to move equatorward or stay at one latitude but clearly does not move in a poleward direction as would be expected if it was connected to open field lines. This conclusion is supported by an observation investigated by Jasinski et al. (2014), who observed the ~1 hr quasiperiodic whistler mode intensifications to disappear as Cassini crossed from the closed magnetosphere into the cusp region. Based on the at least rigid corotation of the transient brightenings investigated above, we propose that its clustered spots are attached to planetward sections of a series of reconnected magnetodisc flux tubes. As the bulk of the plasma is being released outward through Vasyliunas-cycle reconnection, the entropy of the formerly stretched and subcorotating flux tubes is lowered. This allows them to interchange in a planetward direction (e.g., Gold, 1959; Mitchell et al., 2015, and references therein) and results in an equatorward motion of the flux tube footprint. The observed dynamic corotation of the auroral spots clearly indicates that the attached flux tubes must be mostly empty of plasma, allowing the magnetic field to return from a bent-back into a steady dipolar configuration.

Delamere et al. (2015) analyzed current sheet crossings using Cassini magnetometer data and found a greatly increased number of possible magnetodisc reconnection sites near the dusk flank of Saturn. They conclude that a continuous “drizzle” of small and patchy reconnection events in this region is likely to contribute significantly to the continuous magnetic flux circulation in the magnetosphere—in line with earlier theoretical results (e.g., Bagenal, 2007; Bagenal & Delamere, 2011; Delamere & Bagenal, 2010, and references therein) and more recent investigations of magnetic turbulence in Saturn's plasma sheet (Kaminker et al., 2017; von Papen & Saur, 2016). This process is similar to small plasma bubbles breaking off the outer edge of Jupiter's magnetodisc and moving down the dusk flank as proposed by Kivelson and Southwood (2005). Furthermore, Guo, Yao, Wei, et al. (2018) and Guo, Yao, Sergis et al. (2018) recently found direct evidence of dayside magnetodisc reconnection and estimated the resulting energy flux in the reconnection region to be sufficient to power auroras. They also found ~1 hr quasiperiodic energetic electron enhancements during and after the reconnection event investigated. Furthermore, a recent study revealed multiple reconnection x-line configurations in the premidnight sector, likely indicating recurrent small-scale reconnection events at the dusk side (Smith et al., 2018). These results clearly support the mechanism suggested above, likely leading to predominant observations of auroral flashes, energetic electron injections (Palmaerts et al., 2016;

Roussos et al., 2016), and auroral hiss intensifications (Carbary et al., 2016) near dusk LTs due to increased magnetodisc reconnection rates.

However, it remains unclear why the observed intensifications on Saturn occur ~1-hr quasiperiodically. At Jupiter, Nichols et al. (2017) recently observed recurrent auroral brightenings in the dusk active region and showed that these features were more prominent during solar wind compressions, but also active during a solar wind rarefaction. However, the periodicities are observed to be of order ~3 min and therefore of higher frequency than those observed at Saturn in this study.

5. Summary

We have used 36 sequences of altogether more than 2,100 UVIS images with short exposure times <20 min to investigate quasiperiodic changes in UV auroral emission power. Continuous pulsing at periodicities ~1 hr could be observed in all sequences, suggesting a continuous process largely independent of the upstream solar wind conditions. The power of the auroral flashes was shown to be highly variable; several sequences include pulses accounting for more than 25% of the instantaneous UV auroral emission power, indicating a significant energy input into the Kronian ionosphere. Locatable auroral flashes exhibit a significant dawn-dusk asymmetry, clearly favoring occurrences at dusk in agreement with high-energy electron injections and auroral hiss intensifications (Carbary et al., 2016; Palmaerts et al., 2016; Roussos et al., 2016). However, the mean pulse power is globally similar within errors, suggesting a common acceleration process throughout all LTs activated by an LT-biased trigger. We investigated the evolution of one such short-lived auroral emission using HST imagery and the associated in situ measurements and found that it is better described as a patchy network of small injections with lifetimes <10 min. The injections were observed on the northern hemisphere, while corresponding magnetic field, energetic electron, and auroral hiss signatures were observed by Cassini in the southern hemisphere—suggesting that these features are a consequence of magnetodisc reconnection events followed by a planetward motion of the reconnected and largely empty flux tubes through the interchange instability. The dynamic corotation of the patches and the coincident sawtooth-shaped discontinuities in the azimuthal magnetic field component observed in this event are likely signatures of a rapid return of the magnetic field from a bent-back to a nearly dipolar configuration. Magnetodisc reconnection at Saturn has been observed near noon (Guo, Yao, Sergis, et al., 2018; Guo, Yao, Wei, et al., 2018) and is presumed to occur predominantly and continuously at dusk (e.g., Delamere et al., 2015; Kivelson & Southwood, 2005; Kaminker et al., 2017, and references therein), inducing auroral emissions like those investigated here and significantly contributing to magnetic flux circulation through a constant “drizzle” of small-scale reconnection and plasmoid release. What determines the reconnection rate and the distinct periodicity is still an open question.

Acknowledgments
All Cassini data are available from the NASA Planetary Data System (https://pds.jpl.nasa.gov). This work is based on observations made with the NASA/ESA Hubble Space Telescope (observation ID: GO13396), obtained at the Space Telescope Science Institute (STScI), which is operated by AURA, Inc., for NASA. The Hubble observations are available from the MAST (https://archive.stsci.edu/hst/) or APIS (https://apis.obspm.fr) repositories, supported by the STScI (http://www.stsci.edu/hst). The authors thank G. Provan and S. W. H. Cowley for providing the PPO phase data (2004–2017), which are available on the University of Leicester Research Archive (http://hdl.handle.net/2381/42436). A. B. was funded by a Lancaster University FST studentship. S. V. B. and J. K. were supported by STFC Grant ST/M001059/1. S. V. B. was also supported by an STFC Ernest Rutherford Fellowship ST/M005534/1. Z. Y. acknowledges financial support from the Belgian Federal Science Policy Office (BELSPO) via the PRODEX Programme of ESA.

References

Andrews, D. J., Cowley, S. W. H., Dougherty, M. K., & Provan, G. (2010). Magnetic field oscillations near the planetary period in Saturn's equatorial magnetosphere: Variation of amplitude and phase with radial distance and local time. *Journal of Geophysical Research*, *115*, A04212. https://doi.org/10.1029/2009JA014729

Arridge, C. S., Achilleos, N., Dougherty, M. K., Khurana, K. K., & Russell, C. T. (2006). Modeling the size and shape of Saturn's magnetopause with variable dynamic pressure. *Journal of Geophysical Research*, *111*, A11227. https://doi.org/10.1029/2005JA011574

Bader, A., Badman, S. V., Kinrade, J., Cowley, S. W. H., Provan, G., & Pryor, W. R. (2018). Statistical planetary period oscillation signatures in Saturn's UV auroral intensity. *Journal of Geophysical Research: Space Physics*, *123*, 8459–8472. https://doi.org/10.1029/2018JA025855

Bader, A., Badman, S. V., Kinrade, J., Cowley, S. W. H., Provan, G., & Pryor, W. (2019). Modulations of Saturn's UV auroral oval location by planetary period oscillations. *Journal of Geophysical Research: Space Physics*, *124*. https://doi.org/10.1029/2018JA026117

Badman, S. V., Achilleos, N., Arridge, C. S., Baines, K. H., Brown, R. H., Bunce, E. J., & Tao, C. (2012). Cassini observations of ion and electron beams at Saturn and their relationship to infrared auroral arcs. *Journal of Geophysical Research*, *117*, A01211. https://doi.org/10.1029/2011JA017222

Bagenal, F. (2007). The magnetosphere of Jupiter: Coupling the equator to the poles. *Journal of Atmospheric and Solar-Terrestrial Physics*, *69*(3), 387–402. https://doi.org/10.1016/j.jastp.2006.08.012

Bagenal, F., & Delamere, P. A. (2011). Flow of mass and energy in the magnetospheres of Jupiter and Saturn. *Journal of Geophysical Research*, *116*, A05209. https://doi.org/10.1029/2010JA016294

Bunce, E. J., Arridge, C. S., Cowley, S. W. H., & Dougherty, M. K. (2008). Magnetic field structure of Saturn's dayside magnetosphere and its mapping to the ionosphere: Results from ring current modeling. *Journal of Geophysical Research*, *113*, A02207. https://doi.org/10.1029/2007JA012538

Burton, M. E., Dougherty, M. K., & Russell, C. T. (2010). Saturn's internal planetary magnetic field. *Geophysical Research Letters*, *37*, L24105. https://doi.org/10.1029/2010GL045148

Carbary, J. F., Kurth, W. S., & Mitchell, D. G. (2016). Short periodicities in low-frequency plasma waves at Saturn: Short Periodicities at Saturn. *Journal of Geophysical Research: Space Physics*, *121*, 6562–6572. https://doi.org/10.1002/2016JA022732

Clarke, J. T., Nichols, J., Gérard, J. C., Grodent, D., Hansen, K. C., Kurth, W., & Cecconi, B. (2009). Response of Jupiter's and Saturn's auroral activity to the solar wind. *Journal of Geophysical Research*, *114*, A05210. https://doi.org/10.1029/2008JA013694

Delamere, P. A., & Bagenal, F. (2010). Solar wind interaction with Jupiter's magnetosphere. *Journal of Geophysical Research*, *115*, A10201. https://doi.org/10.1029/2010JA015347

Delamere, P. A., Otto, A., Ma, X., Bagenal, F., & Wilson, R. J. (2015). Magnetic flux circulation in the rotationally driven giant magnetospheres. *Journal of Geophysical Research: Space Physics*, *120*, 4229–4245. https://doi.org/10.1002/2015JA021036

Dyudina, U. A., Ingersoll, A. P., Ewald, S. P., & Wellington, D. (2016). Saturn's aurora observed by the Cassini camera at visible wavelengths. *Icarus*, *263*, 32–43. https://doi.org/10.1016/j.icarus.2015.05.022

Esposito, L. W., Barth, C. A., Colwell, J. E., Lawrence, G. M., McClintock, W. E., Stewart, A. I. F., & Yung, Y. L. (2004). The Cassini ultraviolet imaging spectrograph investigation. *Space Science Reviews*, *115*(1-4), 299–361. https://doi.org/10.1007/s11214-004-1455-8

Gérard, J. C., Bonfond, B., Gustin, J., Grodent, D., Clarke, J. T., Bisikalo, D., & Shematovich, V. (2009). Altitude of Saturn's aurora and its implications for the characteristic energy of precipitated electrons. *Geophysical Research Letters*, *36*, L02202. https://doi.org/10.1029/2008GL036554

Gold, T. (1959). Motions in the magnetosphere of the Earth. *Journal of Geophysical Research*, *64*(9), 1219–1224. https://doi.org/10.1029/JZ064i009p01219

Grodent, D. (2005). Variable morphology of Saturn's southern ultraviolet aurora. *Journal of Geophysical Research*, *110*, A07215. https://doi.org/10.1029/2004JA010983

Guo, R. L., Yao, Z. H., Sergis, N., Wei, Y., Mitchell, D., Roussos, E., & Wan, W. X. (2018). Reconnection acceleration in Saturn's dayside magnetodisk: A multicase study with Cassini. *The Astrophysical Journal*, *868*(2), L23. https://doi.org/10.3847/2041-8213/aaedab

Guo, R. L., Yao, Z. H., Wei, Y., Ray, L. C., Rae, I. J., Arridge, C. S., & Dougherty, M. K. (2018). Rotationally driven magnetic reconnection in Saturn's dayside. *Nature Astronomy*, *2*(8), 640–645. https://doi.org/10.1038/s41550-018-0461-9

Gustin, J., Grodent, D., Radioti, A., Pryor, W., Lamy, L., & Ajello, J. (2017). Statistical study of Saturn's auroral electron properties with Cassini/UVIS FUV spectral images. *Icarus*, *284*, 264–283. https://doi.org/10.1016/j.icarus.2016.11.017

Gustin, J., Grodent, D., Ray, L., Bonfond, B., Bunce, E., Nichols, J., & Ozak, N. (2016). Characteristics of north Jovian aurora from STIS FUV spectral images. *Icarus*, *268*, 215–241. https://doi.org/10.1016/j.icarus.2015.12.048

Hunt, G. J., Cowley, S. W. H., Provan, G., Bunce, E. J., Alexeev, I. I., Belenkaya, E. S., & Coates, A. J. (2014). Field-aligned currents in Saturn's southern nightside magnetosphere: Subcorotation and planetary period oscillation components. *Journal of Geophysical Research: Space Physics*, *119*, 9847–9899. https://doi.org/10.1002/2014JA020506

Jasinski, J. M., Arridge, C. S., Lamy, L., Leisner, J. S., Thomsen, M. F., Mitchell, D. G., & Waite, J. H. (2014). Cusp observation at Saturn's high-latitude magnetosphere by the Cassini spacecraft. *Geophysical Research Letters*, *41*, 1382–1388. https://doi.org/10.1002/2014GL059319

Kaminker, V., Delamere, P. A., Ng, C. S., Dennis, T., Otto, A., & Ma, X. (2017). Local time dependence of turbulent magnetic fields in Saturn's magnetodisc. *Journal of Geophysical Research: Space Physics*, *122*, 3972–3984. https://doi.org/10.1002/2016JA023834

Kinrade, J., Badman, S. V., Bunce, E. J., Tao, C., Provan, G., Cowley, S. W. H., & Dougherty, M. K. (2017). An isolated, bright cusp aurora at Saturn. *Journal of Geophysical Research: Space Physics*, *122*, 6121–6138. https://doi.org/10.1002/2016JA023792

Kinrade, J., Badman, S. V., Provan, G., Cowley, S. W. H., Lamy, L., & Bader, A. (2018). Saturn's northern auroras and their modulation by rotating current systems during late northern spring in early 2014. *Journal of Geophysical Research: Space Physics*, *123*, 6289–6306. https://doi.org/10.1029/2018JA025426

Kivelson, M. G., & Southwood, D. J. (2005). Dynamical consequences of two modes of centrifugal instability in Jupiter's outer magnetosphere. *Journal of Geophysical Research*, *110*, A12209. https://doi.org/10.1029/2005JA011176

Kleindienst, G., Glassmeier, K. H., Simon, S., Dougherty, M. K., & Krupp, N. (2009). Quasiperiodic ULF-pulsations in Saturn's magnetosphere. *Annales Geophysicae*, *27*(2), 885–894. https://doi.org/10.5194/angeo-27-885-2009

Krimigis, S. M., Mitchell, D. G., Hamilton, D. C., Livi, S., Dandouras, J., Jaskulek, S., & Williams, D. J. (2004). Magnetosphere Imaging Instrument (MIMI) on the Cassini Mission to Saturn/Titan. *Space Science Reviews*, *114*(1-4), 233–329. https://doi.org/10.1007/978-1-4020-2774-1_3

Masters, A., Achilleos, N., Bertucci, C., Dougherty, M., Kanani, S., Arridge, C., & Coates, A. (2009). Surface waves on Saturn's dawn flank magnetopause driven by the Kelvin-Helmholtz instability. *Planetary and Space Science*, *57*(14-15), 1769–1778. https://doi.org/10.1016/j.pss.2009.02.010

Meredith, C. J., Cowley, S. W. H., Hansen, K. C., Nichols, J. D., & Yeoman, T. K. (2013). Simultaneous conjugate observations of small-scale structures in Saturn's dayside ultraviolet auroras: Implications for physical origins. *Journal of Geophysical Research: Space Physics*, *118*, 2244–2266. https://doi.org/10.1002/jgra.50270

Mitchell, D. G., Brandt, P. C., Carbary, J. F., Kurth, W. S., Krimigis, S. M., Paranicas, C., & Pryor, W. R. (2015). Injection, interchange, and reconnection. In A. Keiling, C. M. Jackman, & P. A. Delamere (Eds.), *Energetic particle observations in Saturn's magnetosphere, Geophysical Monograph Series* (pp. 327–343). Hoboken, NJ: John Wiley & Sons, Inc. https://doi.org/10.1002/9781118842324.ch19

Mitchell, D. G., Carbary, J. F., Bunce, E. J., Radioti, A., Badman, S. V., Pryor, W. R., & Kurth, W. S. (2016). Recurrent pulsations in Saturn's high latitude magnetosphere. *Icarus*, *263*, 94–100. https://doi.org/10.1016/j.icarus.2014.10.028

Mitchell, D. G., Krimigis, S. M., Paranicas, C., Brandt, P. C., Carbary, J. F., Roelof, E. C., & Pryor, W. R. (2009). Recurrent energization of plasma in the midnight-to-dawn quadrant of Saturn's magnetosphere, and its relationship to auroral UV and radio emissions. *Planetary and Space Science*, *57*(14-15), 1732–1742. https://doi.org/10.1016/j.pss.2009.04.002

Mitchell, D. G., Kurth, W. S., Hospodarsky, G. B., Krupp, N., Saur, J., Mauk, B. H., & Hamilton, D. C. (2009). Ion conics and electron beams associated with auroral processes on Saturn. *Journal of Geophysical Research*, *114*, A02212. https://doi.org/10.1029/2008JA013621

Nichols, J. D., Badman, S. V., Bagenal, F., Bolton, S. J., Bonfond, B., Bunce, E. J., & Yoshikawa, I. (2017). Response of Jupiter's auroras to conditions in the interplanetary medium as measured by the Hubble Space Telescope and Juno. *Geophysical Research Letters*, *44*, 7643–7652. https://doi.org/10.1002/2017GL073029

Palmaerts, B., Radioti, A., Roussos, E., Grodent, D., Gérard, J. C., Krupp, N., & Mitchell, D. G. (2016). Pulsations of the polar cusp aurora at Saturn. *Journal of Geophysical Research: Space Physics*, *121*, 11,952–11,963. https://doi.org/10.1002/2016JA023497

Palmaerts, B., Roussos, E., Krupp, N., Kurth, W., Mitchell, D., & Yates, J. (2016). Statistical analysis and multi-instrument overview of the quasi-periodic 1-hour pulsations in Saturn's outer magnetosphere. *Icarus*, *271*, 1–18. https://doi.org/10.1016/j.icarus.2016.01.025

Provan, G., Cowley, S. W. H., Bradley, T. J., Bunce, E. J., Hunt, G. J., & Dougherty, M. K. (2018). Planetary period oscillations in Saturn's magnetosphere: Cassini magnetic field observations over the northern summer solstice interval. *Journal of Geophysical Research: Space Physics*, *123*, 3859–3899. https://doi.org/10.1029/2018JA025237

Provan, G., Cowley, S. W. H., Lamy, L., Bunce, E. J., Hunt, G. J., Zarka, P., & Dougherty, M. K. (2016). Planetary period oscillations in Saturn's magnetosphere: Coalescence and reversal of northern and southern periods in late northern spring. *Journal of Geophysical Research: Space Physics*, *121*, 9829–9862. https://doi.org/10.1002/2016JA023056

Radioti, A., Grodent, D., Gérard, J. C., Bonfond, B., Gustin, J., Pryor, W., & Arridge, C. S. (2013). Auroral signatures of multiple magnetopause reconnection at Saturn. *Geophysical Research Letters*, *40*, 4498–4502. https://doi.org/10.1002/grl.50889

Radioti, A., Grodent, D., Gérard, J. C., Roussos, E., Paranicas, C., Bonfond, B., & Clarke, J. T. (2009). Transient auroral features at Saturn: Signatures of energetic particle injections in the magnetosphere. *Journal of Geophysical Research*, *114*, A03201. https://doi.org/10.1029/2008JA013632

Roussos, E., Krupp, N., Mitchell, D., Paranicas, C., Krimigis, S., Andriopoulou, M., & Dougherty, M. (2016). Quasi-periodic injections of relativistic electrons in Saturn's outer magnetosphere. *Icarus*, *263*, 101–116. https://doi.org/10.1016/j.icarus.2015.04.017

Russell, C. T., Leisner, J. S., Arridge, C. S, Dougherty, M. K, & Blanco-Cano, X. (2006). Nature of magnetic fluctuations in Saturn's middle magnetosphere. *Journal of Geophysical Research*, *111*, A12205. https://doi.org/10.1029/2006JA011921

Smith, A. W., Jackman, C. M., Thomsen, M. F., Lamy, L., & Sergis, N. (2018). Multi-instrument investigation of the location of Saturn's magnetotail x-line. *Journal of Geophysical Research: Space Physics*, *123*, 5494–5505. https://doi.org/10.1029/2018JA025532

Southwood, D. J., & Chané, E. (2016). High-latitude circulation in giant planet magnetospheres. *Journal of Geophysical Research: Space Physics*, *121*, 5394–5403. https://doi.org/10.1002/2015JA022310

von Papen, M., & Saur, J. (2016). Longitudinal and local time asymmetries of magnetospheric turbulence in Saturn's plasma sheet. *Journal of Geophysical Research: Space Physics*, *121*, 4119–4134. https://doi.org/10.1002/2016JA022427

Yao, Z. H., Radioti, A., Rae, I. J., Liu, J., Grodent, D., Ray, L. C., & Palmaerts, B. (2017). Mechanisms of Saturn's near-noon transient aurora: In situ evidence from Cassini. *Geophysical Research Letters*, *44*, 11,217–11,228. https://doi.org/10.1002/2017GL075108

Yates, J. N., Southwood, D. J., Dougherty, M. K., Sulaiman, A. H., Masters, A., Cowley, S. W. H., & Coates, A. J. (2016). Saturn's quasiperiodic magnetohydrodynamic waves. *Geophysical Research Letters*, *43*, 11,102–11,111. https://doi.org/10.1002/2016GL071069

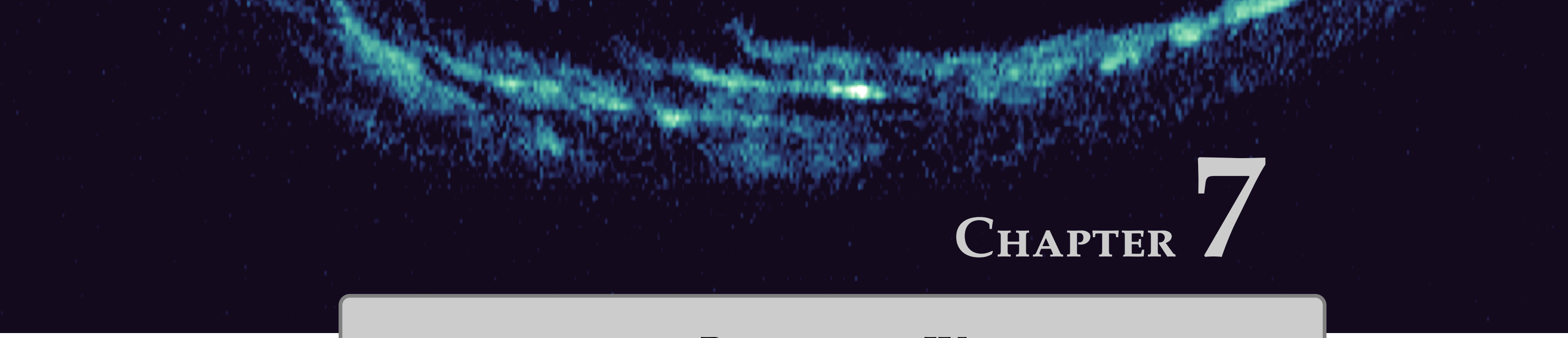

CHAPTER 7

PUBLICATION IV

The dynamics of Saturn's main aurorae

A. BADER, S. V. BADMAN, S. W. H. COWLEY, Z. H. YAO, L. C. RAY, J. KINRADE, E. J. BUNCE,
G. PROVAN, T. J. BRADLEY, C. TAO, G. J. HUNT AND W. R. PRYOR (2019)

Geophysical Research Letters, *46*, 10,283-10,294
doi:10.1029/2019GL084620

AUTHOR CONTRIBUTION STATEMENT AB conceived the study, performed the data reduction and analysis and authored the initial draft. SVB, SWHC and LCR provided guidance and expertise in magnetospheric physics. ZHY and JK provided various theoretical support. EJB, GP, TJB and GJH provided expertise on FACs and PPOs. GP further provided PPO phase data for the analysis. CT provided technical support for the solar wind propagation model. WRP provided technical support for UVIS data. All authors contributed to the interpretation of the results and were involved in review and editing of the paper until publication.

This authorship statement was approved by all collaborating research groups.

Supplementary information for this publication can be found in appendix B.

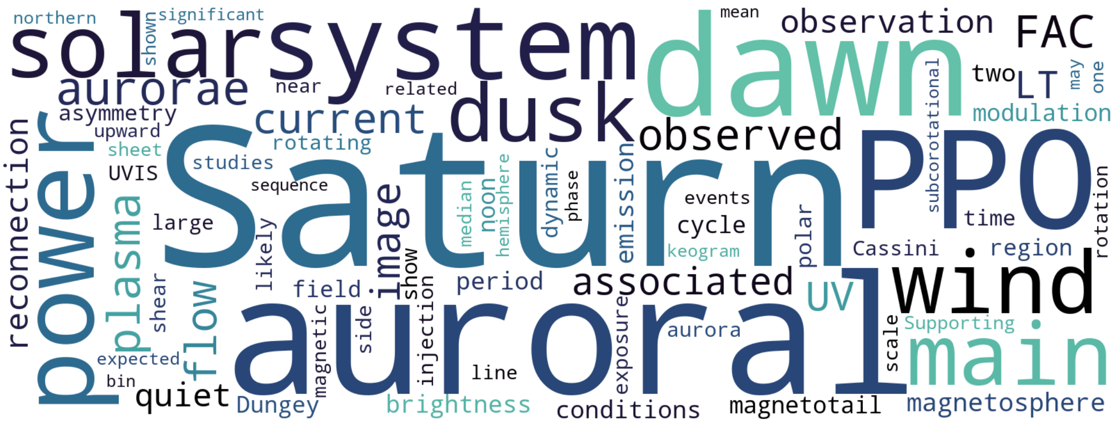

Geophysical Research Letters

RESEARCH LETTER
10.1029/2019GL084620

Key Points:
- A dawn-dusk asymmetry in Saturn's auroral emissions due to Dungey cycle activity is not observed under typical solar wind driving
- The previously observed statistical intensity maximum near dawn is the result of large-scale auroral plasma injections from Saturn's nightside
- The phasing of these auroral injections indicates that magnetotail reconnection seems to partly be governed by planetary period oscillations

Supporting Information:
- Supporting Information S1

Correspondence to:
A. Bader,
a.bader@lancaster.ac.uk

Citation:
Bader, A., Badman, S. V., Cowley, S. W. H., Yao, Z. H., Ray, L. C., Kinrade, J., et al. (2019), The dynamics of Saturn's main aurorae. *Geophysical Research Letters*, *46*, 10,283–10,294. https://doi.org/10.1029/2019GL084620

Received 29 MAY 2019
Accepted 29 AUG 2019

The Dynamics of Saturn's Main Aurorae

A. Bader[1], **S. V. Badman**[1], **S. W. H. Cowley**[2], **Z. H. Yao**[3], **L. C. Ray**[1], **J. Kinrade**[1], **E. J. Bunce**[2], **G. Provan**[2], **T. J. Bradley**[2], **C. Tao**[4,5], **G. J. Hunt**[6], and **W. R. Pryor**[7]

[1]Department of Physics, Lancaster University, , [2]Department of Physics and Astronomy, University of Leicester, Leicester, UK, [3]Laboratoire de Physique Atmosphérique et Planétaire, Space sciences, Technologies and Astrophysics Research (STAR) Institute, Université de Liège, Liège, Belgium, [4]National Institute of Information and Communications Technology, Koganei, Japan, [5]Department of Geophysics, Tohoku University, Sendai, Japan, [6]Blackett Laboratory, Imperial College London, London, UK, [7]Science Department, Central Arizona College, Coolidge, AZ, USA

Abstract Saturn's main aurorae are thought to be generated by plasma flow shears associated with a gradient in angular plasma velocity in the outer magnetosphere. Dungey cycle convection across the polar cap, in combination with rotational flow, may maximize (minimize) this flow shear at dawn (dusk) under strong solar wind driving. Using imagery from Cassini's Ultraviolet Imaging Spectrograph, we surprisingly find no related asymmetry in auroral power but demonstrate that the previously observed "dawn arc" is a signature of quasiperiodic auroral plasma injections commencing near dawn, which seem to be transient signatures of magnetotail reconnection and not part of the static main aurorae. We conclude that direct Dungey cycle driving in Saturn's magnetosphere is small compared to internal driving under usual conditions. Saturn's large-scale auroral dynamics hence seem predominantly controlled by internal plasma loading, with plasma release in the magnetotail being triggered both internally through planetary period oscillation effects and externally through solar wind compressions.

Plain Language Summary Saturn's main aurorae are thought to be generated as a result of sheared plasma flows near the boundary between the rapidly rotating magnetosphere of Saturn and interplanetary space. It is often assumed that the steady flow of the solar wind away from the Sun has an impact on this flow shear; due to the direction of Saturn's rotation the aurorae would then have to be brighter at the planet's dawnside than on its duskside, which was observed in previous studies. Here we analyze a large set of auroral images taken by Cassini's ultraviolet camera, but we cannot find any sign of such an asymmetry. This indicates that the impact of the solar wind on Saturn's aurorae must be smaller than previously thought and that they must instead mainly be controlled from within the system. This assumption is supported by our observations of bright auroral patches at dawn, which are likely a signature of plasma being released from Saturn's magnetosphere and appear at quite regular periods corresponding to Saturn's rotation period.

1. Introduction

Planetary aurorae appear throughout the solar system and illustrate many different plasma processes. Their origins are very different—while, for example, aurorae on Earth and Mars are almost entirely controlled by the solar wind (e.g., Brain et al., 2006; Milan et al., 2003; Walach et al., 2017), Jupiter's brightest aurorae are internally generated due to the breakdown of corotation in the middle magnetosphere (e.g., Cowley & Bunce, 2001; Hill, 2001; Southwood & Kivelson, 2001). While also being a fast-rotating gas giant like Jupiter, Saturn's corotation breakdown currents are thought to be too weak to produce auroral emissions (Cowley & Bunce, 2003). Instead, the flow shear associated with a strong gradient in angular plasma velocity between the outer closed magnetosphere and the open field region—caused by ion-neutral collisions in the ionosphere twisting the open field lines (Isbell et al., 1984; Milan et al., 2005)—was proposed as a possible driver generating the field-aligned currents (FACs) responsible for electron precipitation into Saturn's polar atmosphere, forming the "subcorotational system" (e.g., Cowley, Bunce & O'Rourke 2004; Cowley, Bunce & Prangé 2004; Cowley et al., 2005; Stallard et al., 2007; Vasyliūnas, 2016).

Under strong solar wind driving (increased solar wind velocity and density), active Dungey cycle reconnection between the interplanetary magnetic field and Saturn's magnetic field at the dayside magnetopause may prompt an antisunward flow in the slowly subcorotating polar open field region just like at Earth (Dungey, 1961). At dawn, this Dungey cycle convection across the polar cap—here oppositely directed to the subcorotating magnetospheric plasma flow—would act to enhance the (rotational) plasma flow shear associated with the generation of Saturn's main aurorae and hence also the auroral brightness. Conversely, strong solar wind driving should lead to a reduction of this plasma flow shear and the auroral brightness at dusk (e.g., Cowley, Bunce & Prangé 2004; Jackman & Cowley, 2006). Adding to this local time (LT) asymmetry, the Dungey and Vasyliunas cycle return flows are expected to pass from the magnetotail toward the dayside via dawn due to the rapid rotation of the magnetosphere (e.g., Cowley, Bunce & Prangé 2004; Vasyliūnas, 1983). However, the importance of Dungey cycle convection at Saturn is disputed as magnetopause reconnection may be inhibited across parts of the magnetopause (e.g., Desroche et al., 2013; Masters et al., 2012, 2014) and viscous interactions mediated by Kelvin-Helmholtz instabilities may instead be the main coupling mechanism between the solar wind and Saturn's magnetosphere (e.g., Delamere & Bagenal, 2010; Delamere et al., 2013).

Previous studies using auroral imagery obtained by the Hubble Space Telescope in the ultraviolet (UV) wavelength band (e.g., Kinrade et al., 2018; Lamy et al., 2009, 2018; Nichols et al., 2016) and by the Cassini spacecraft at infrared (IR) and UV wavelengths (e.g., Bader et al., 2018; Badman et al., 2011; Carbary, 2012) have statistically identified such a brightness asymmetry, seemingly confirming that Saturn's main aurorae are indeed significantly solar wind driven. However, most of these studies used rather small sets of single exposures lacking context and/or short observation series without good time resolution to obtain statistical averages, hence not taking into account the complicated dynamics of Saturn's aurora which had already been observed by the Voyager spacecraft (Sandel & Broadfoot, 1981; Sandel et al., 1982).

In this study we use extensive sets of auroral imagery obtained by the Cassini spacecraft to investigate the dynamics of Saturn's main aurorae and shed more light on its generation mechanisms. We present the data set and describe our analysis methods in section 2. In section 3 we analyze observations consistent with quiet auroral conditions to reveal the structure of subcorotationally driven main aurorae and their modulation by planetary period oscillations (PPOs), while in section 4 we describe the added complexity brought into the system by magnetotail dynamics, causing transient large-scale brightenings. We summarize our findings and propose an updated model of Saturn's main aurorae in section 5.

2. Data and Methods

NASA's Cassini spacecraft orbited Saturn for over 13 years, providing a rich set of auroral observations in the UV spectrum with its Ultraviolet Imaging Spectrograph (UVIS; Esposito et al., 2004). Here we investigate Saturn's auroral dynamics and therefore select observation windows where many images were taken in quick succession (exposure time <20 min) for several hours. This corresponds to auroral observations from high apoapsis where Cassini moved relatively slowly, preserving the same viewing geometry for long periods; and where the large distance from Saturn allowed UVIS to cover the entire auroral oval with a single slit scan, allowing for low exposure times. Nearly all available observations of this kind fall into 2014/2016/2017, and all are from Saturn's northern hemisphere.

2.1. Cassini-UVIS Imagery

The Cassini-UVIS instrument includes two telescope-spectrographs observing in the 56- to 118-nm (extreme ultraviolet) and 110- to 190-nm (far ultraviolet, or FUV) wavelength ranges; most of Saturn's auroral UV emissions are observed in the FUV band. The UVIS FUV slit has a field of view of 1.5 × 64 mrad, with 64 spatial pixels of size 1.5 × 1 mrad each arranged along a single line. Pseudo-images of the aurora are obtained by scanning this slit across the auroral region. Several successive scans may be necessary to cover the entire region of interest depending on Cassini's distance from Saturn, increasing the exposure time of auroral images. The total exposure time for a pseudo-image of the entire auroral oval can vary between 6 and 180 min.

Each image is polar projected onto a planetocentric polar grid with resolution 0.5° × 0.25° (lon × lat) at an altitude of 1,100 km above Saturn's 1-bar pressure surface (oblate spheroid with $R_{\mathrm{SEQ}} = 60{,}268$ km and $R_{\mathrm{SPO}} = 54{,}364$ km as equatorial and polar radii), the approximate altitude of Saturn's auroral emissions (Gérard et al., 2009). Cassini SPICE pointing information is used to perform the projection. The spectrum recorded by each pixel of the UVIS FUV sensor, observed in 1,024 spectral bins, is reduced to total unabsorbed H_2 emission intensity (70–170 nm) by multiplying the intensity measured in the 155- to 162-nm range by the factor 8.1 (Gustin et al., 2016, 2017). Using this method, dayglow emission and hydrocarbon absorption affect the estimated total unabsorbed H_2 intensity as little as possible. Even so, some dayglow is still apparent in most UVIS images; it is removed as previously described in Bader et al. (2019) in order to obtain accurate auroral brightnesses and emission powers.

Many of the images in this study have quite low spatial resolutions, with single pixels extending over up to 5° in colatitude or 1 hr in LT. However, this issue is circumvented by integrating over the auroral brightness to obtain the emitted radiant flux, or "auroral power," as laid out in the supporting information of this paper. A large instrument pixel covering a small bright auroral feature and its surroundings is dimmer than the actual brightness maximum of the observed emission—however, the pixel brightness corresponds to the average brightness of the area it subtends during the time of the exposure. Integrating over this area therefore gives a quite exact measure of the auroral power nevertheless. We reduce each image by integrating its auroral brightness between 8° and 22° colatitude in 36 LT bins and thereby obtain a distribution of auroral power per hour of LT. This latitudinal range fully includes the statistical position of the main aurorae and associated uncertainties (Bader et al., 2019). Arranging these integrated powers of all images along the horizontal axis—taking into account the start and stop times of each exposure—we obtain a keogram.

2.2. PPO Systems

Each of Saturn's hemispheres is associated with one PPO system, a complex array of FACs spanning the entire magnetosphere of Saturn (e.g., Andrews et al., 2010; Hunt et al., 2014; Provan et al., 2011; Southwood & Kivelson, 2007) likely associated with vortical flow structures in Saturn's polar ionospheres (e.g., Hunt et al., 2014; Jia & Kivelson, 2012; Jia et al., 2012; Southwood & Cowley, 2014). Their rotation at roughly the planetary period generates periodic signatures in all plasma properties and processes in Saturn's environment, the two systems exhibiting close but distinct periods that vary with time (e.g., Provan et al., 2013, 2016). Each PPO system is usually dominant in one hemisphere, but its associated system of FACs partly closes in the opposite hemisphere such that each hemisphere experiences a double modulation of, for example, auroral FACs by both the northern and southern PPO systems (e.g., Bader et al., 2018; Bradley et al., 2018; Hunt et al., 2015; Provan et al., 2018).

A sketch of the northern PPO system is shown in Figure S1 in the supporting information, with Figure S1a showing the magnetic field and electric currents in the equatorial plane and Figure S1b showing the electric currents and atmospheric/ionospheric flows in the northern polar ionosphere. The southern PPO system effects the same pattern of upward/downward FACs in the northern hemisphere as shown here for the northern system. Depending on the relative orientation between the two systems, their associated FACs can combine to intensify or negate one another. The orientation of the two PPO systems is described by the PPO phase angles $\Phi_{N,S}$, the counterclockwise azimuthal angle between the PPO magnetic perturbation dipoles in the equatorial plane and local noon. In this study we use the phase angles determined by Provan et al. (2016, 2018). PPO-fixed reference frames are defined using the phase values $\Psi_{N,S}$, giving the clockwise angle from the PPO dipole direction.

In the northern hemisphere, the PPO-associated upward FACs maximize at $\Psi_{N,S} = 90°$, with the downward FACs maximizing at $\Psi_{N,S} = 270°$ (e.g., Hunt et al., 2014). The modulation effect is hence largest when the two PPO systems are in phase, their perturbation dipoles parallel. In the keograms shown through this study and in the supporting information, $\Psi_{N,S} = 90°$ is marked with yellow lines.

The PPO-induced modulation of the equatorial current sheet thickness shows a different phasing; the current sheet being thinnest at $\Psi_N = 0°$ and $\Psi_S = 180°$ (Bradley et al., 2018; Cowley & Provan, 2017; Jackman et al., 2016). This modulation is therefore emphasized when the two PPO systems are in antiphase. In Figures 4 and S4, the two systems were within 45° of antiphase—orange dotted lines hence indicate the approximate location at which the PPO-related thinning of the current sheet is expected to be most pronounced.

3. Saturn's Quiet Main Aurora: Subcorotational and PPO Systems

In quiet and steady auroral conditions, the main aurorae should form a quasi-static ring of emission around both poles corresponding to the region of peak flow shear between the rapidly rotating magnetospheric

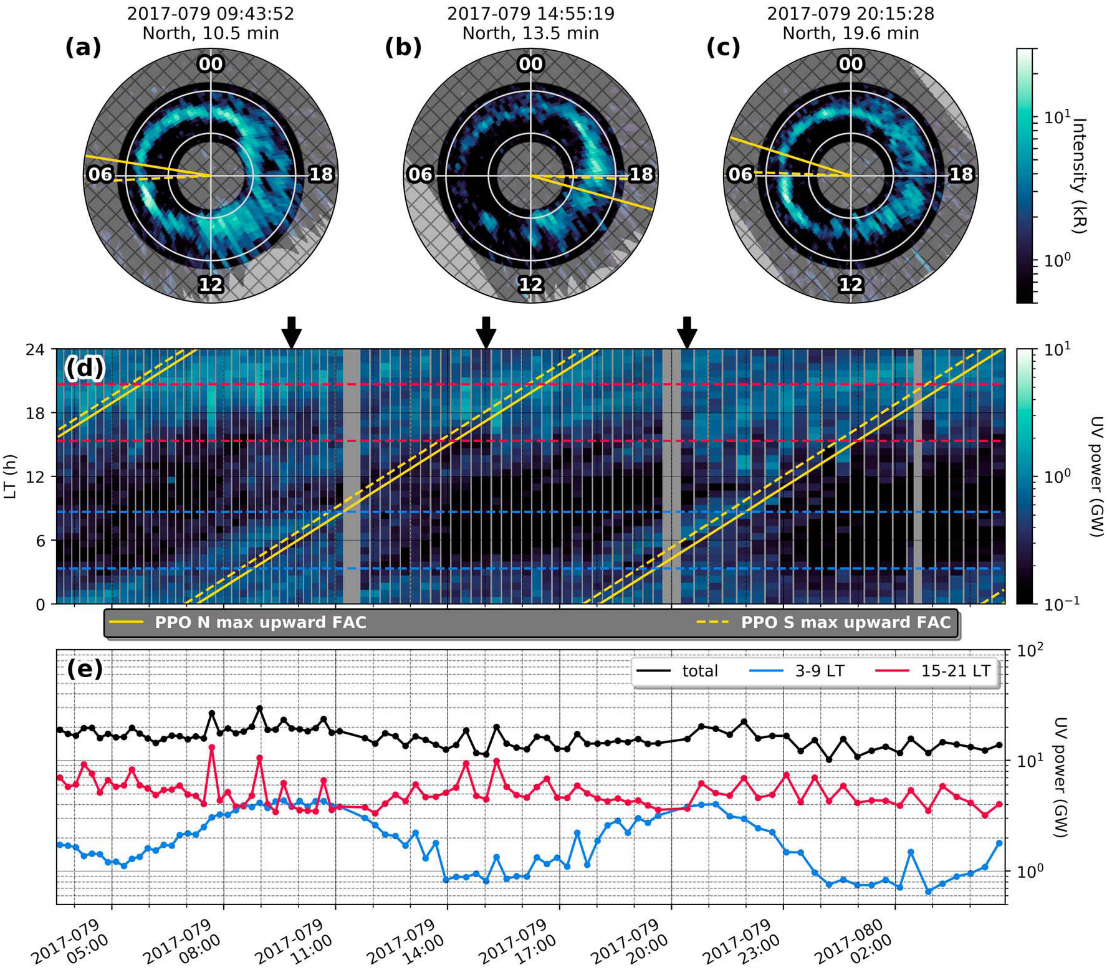

Figure 1. Ultraviolet (UV) auroral power keogram, quiet auroral conditions (2017 DOY 79–80). (a–c) Three UVIS images within this sequence, each about 5–6 hr apart. The view is from above the planet down onto the north pole, with noon/the Sun toward the bottom. White numbers around each image mark local time (LT), and gray concentric circles mark the northern colatitude in steps of 10°. The gray shaded and hatched regions (colatitudes >22° and <8°) were ignored for the integration of UV powers. The start and exposure time of each observation are given on top. Shown is the background-subtracted auroral brightness in kilo-Rayleigh; note the logarithmic scale. (d) UV power keogram of all images in this sequence; logarithmic power scale. The UV power between 8° and 22° colatitude was integrated in 36 LT bins for each image and is arranged by the image collection time such that UT increases to the right. Diagonal lines mark planetary period oscillation (PPO) upward field-aligned current regions propagating around the planet at their respective PPO rotation rate. Dashed horizontal lines limit the "dawn" (blue) and "dusk" (red) LT bins whose UV powers were added for the line plots shown in the bottom panel. Black arrows on top of the panel mark the collection times of the example images shown in (a–c). (e) Line plots of the total, dawn and dusk UV powers.

plasma and the slowly rotating plasma in the polar open field region (e.g., Cowley, Bunce & O'Rourke 2004; Cowley, Bunce & Prangé 2004; Cowley et al., 2005; Stallard et al., 2007; Vasyliūnas, 2016). Lacking continuous upstream solar wind monitoring, we cannot know for sure the solar wind conditions during most of Cassini's observation sequences. We therefore identify "quiet conditions" as imaging sequences where no large-scale transient brightenings (total power > 20 GW for >5 hr) were observed, indicating low magnetic reconnection activity at both dayside and nightside as such events would manifest as bifurcations at noon-dusk LTs (e.g., Badman et al., 2013; Meredith et al., 2014; Radioti et al., 2011; 2013) or as bright transient features at midnight-dawn LTs (e.g., Jackman et al., 2013; Lamy et al., 2013). Figure 1 shows an auroral keogram of one such period without transient events, covering more than two full Saturn rotations (~25 hr) with near-continuous imagery.

We notice a periodic modulation of the emitted UV auroral power, which is well explained with rotating patterns of upward and downward FACs associated with Saturn's PPO systems. In this case, the two PPO systems are aligned nearly parallel and rotating in phase—their upward and downward FAC regions overlap and enhance the associated modulations of the static main aurorae. The dawn UV power is largest roughly

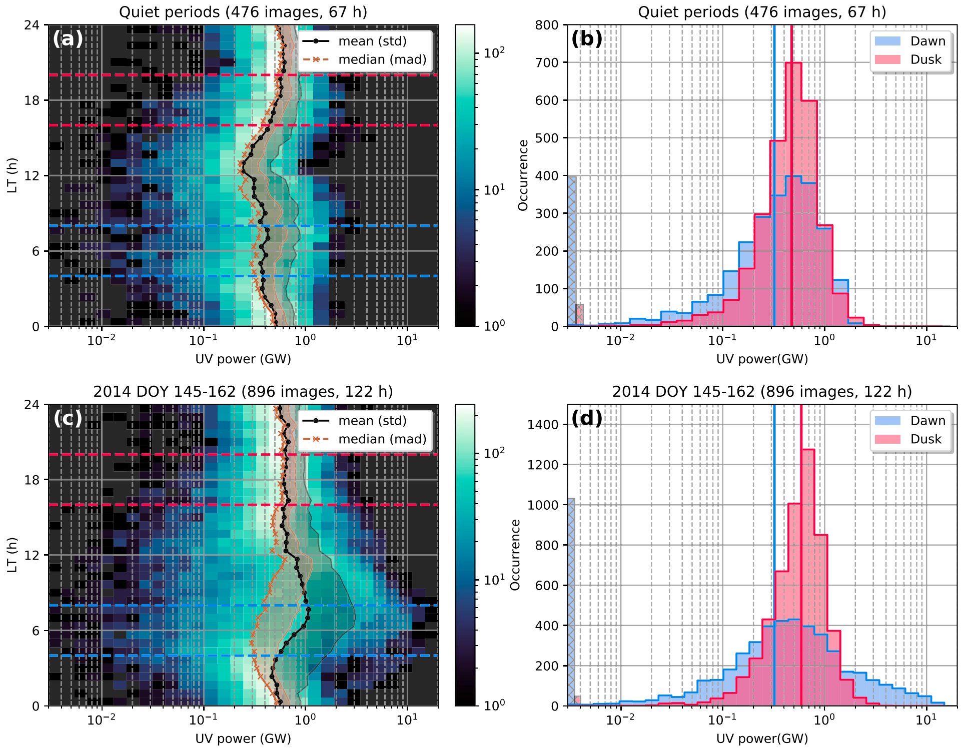

Figure 2. Ultraviolet (UV) auroral power histograms, quiet and average auroral conditions. (a) UV power histogram of five sequences with quiet auroral conditions (2014 DOY 130/147/158–159/311 and 2017 DOY 79–80, see Figure S2 in the supporting information), including 476 images with overall 67 hr of observations. Local time (LT) is on the vertical and (latitudinally integrated) UV power on the horizontal axis, the occurrence (number of observations) is shown in logarithmic color scale. Note the logarithmic UV power scaling on the horizontal axis. The mean (median) UV power per LT bin are shown in black (brown), with the standard deviation (median absolute deviation) indicated with a shaded area to the right of the graph. (b) Dawn (blue) and dusk (red) histograms, summed from all data enclosed by the blue/red dashed lines in panel (a). Hatched bars to the left show the occurrence of bins with UV powers lower than the bottom limit of the graph. Solid vertical lines mark the median UV power per LT bin at dawn/dusk. (c, d) UV power histogram of 2014 DOY 144–162 (keograms in Figures 4, S3, and S4), including 896 images with an overall exposure time of 122 hr. Same format as in panels (a) and (b).

when the expected PPO upward FAC maxima pass and weakest during opposite PPO orientations and varies by nearly a factor of 10. Consequently, the main oval seemingly disappears near dawn as the combined PPO downward FAC regions sweep over and negate the subcorotational system's upward currents (see Figure 1b). While this modulation should theoretically be of comparable strength at all LTs (Hunt et al., 2016), it is here barely discernible at dusk. This difference in modulation amplitude agrees with statistical findings (Bader et al., 2018) and might be related to a seemingly larger spread of the PPO currents at dusk than at dawn (Andrews et al., 2010).

Neither the keogram (Figure 1d) nor the summed dawn and dusk UV powers (Figure 1e) show an asymmetry as expected during periods of significant solar wind driving—this is not surprising, as the time period considered here shows rather quiet auroral conditions, probably indicating quiet solar wind conditions and low Dungey cycle activity. Surprisingly though, the duskside is noticeably brighter than the dawnside during most of the observation sequence. This can partly be explained with quasiperiodic flashes, possibly a sign of small-scale magnetodisc reconnection observed preferentially at dusk (Bader et al., 2019). These have been shown to occur near-constantly and manifest as spikes in the dusk power (Figure 1e), but they do not fully account for the underlying steady asymmetry between dawn and dusk which we observe here. At Jupiter, a similar asymmetry was observed and suggested to be related to a partial ring current in the nightside magnetosphere (Bonfond et al., 2015), but it is unclear whether a similar process could be important in Saturn's magnetosphere.

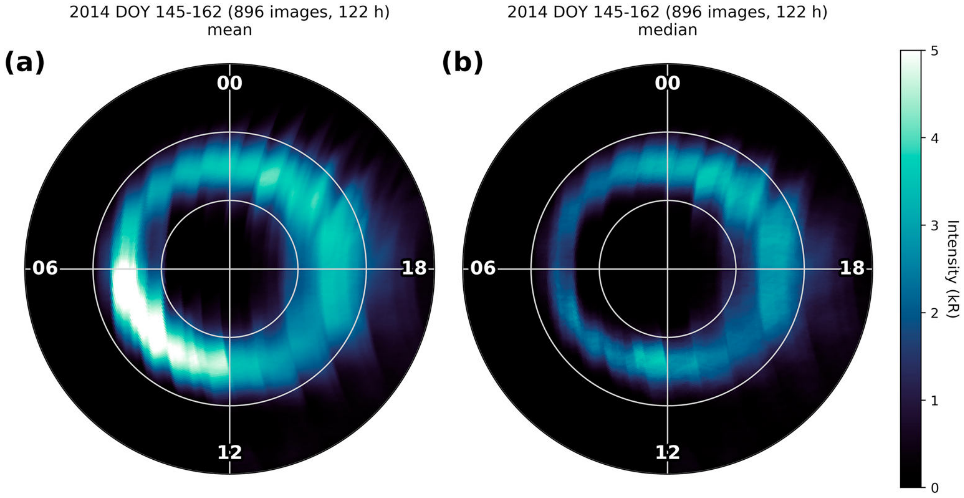

Figure 3. Comparison between Saturn's mean and median northern ultraviolet auroral brightness between 2014 DOY 145–162. The view is from above Saturn onto the planet's northern pole, with local noon to the bottom. Bold white numbers indicate local time; the northern colatitude from the pole is marked by gray concentric circles in 10° steps. The auroral brightness in kilo-Rayleigh is shown in color scale. (a) Mean and (b) median auroral brightness of all images.

The case study presented in Figure 1 is not the only quiet sequence observed. Considering only sequences with quasi-continuous coverage of at least one Saturn rotation, we find additional quiet sequences at 2014 DOY 130/147/158–159/311 (Figure S2)—including overall 476 images with 67 hr of total exposure time, corresponding to just over six Saturn rotations. A UV power-LT histogram for these images is shown in Figure 2a, with the mean and median power per LT added as line plots; the dawn and dusk slices of this histogram are compared in Figure 2b. We observe similar UV powers through all LTs, disagreeing with previously discussed UV and IR auroral intensity distributions (e.g., Badman et al., 2011; Bader et al., 2018; Carbary, 2012; Kinrade et al., 2018; Lamy et al., 2009, 2018; Nichols et al., 2016) with a brightness peak at dawn probably due to our choice of quiet periods. Centered on roughly 0.5 GW per 40 min LT bin, the powers are more variable and feature a more prominent tail toward lower powers at dawn/noon than at dusk/midnight. The occurrence of UV powers below the lower histogram limit (see Figure 2b) is much larger at dawn, indicating longer intervals with a complete absence of auroral emissions.

There appears to be a dip in the average power at noon, somewhat reminiscent of the noon discontinuity in the Jovian main emission (e.g., Radioti et al., 2008; Ray et al., 2014). The currents associated with Jupiter's main emission are thought to be internally driven by the breakdown of corotation in the magnetodisc, which is less significant at the solar wind-compressed dayside (e.g., Chané et al., 2017).

4. Typical Auroral Conditions and Periodic Magnetotail Dynamics

Figures 2c and 2d show a power histogram of all UVIS images between 2014 DOY 144–162. It includes 896 images, corresponding to ~122 hr of exposure within the ~411-hr observation window—a data set quite representative of Saturn's typical auroral dynamics, likely capturing a variety of different solar wind conditions. As each observation block covers roughly one full Saturn rotation (or PPO phase cycle) or more, we assume no significant bias in PPO phases. A keogram of the entire set is shown in Figure S3, including solar wind properties propagated from OMNI which indicate initially typical solar wind conditions, likely with average Dungey cycle activity, followed by rather quiet conditions. Note that two of the observation blocks (2014 DOY 147/158–159) were considered to show quiet auroral conditions and included in the corresponding analysis above as well as here.

Figure 2c differs from the histogram of the quiet aurora (Figure 2a) significantly only at dawn to postnoon LTs. We see a much wider spread in UV power at dawn than in quiet conditions, but do not observe a significant statistical dawn brightening (see Figure 2d). On the contrary, again the median UV power is larger at dusk than at dawn. The mean and median UV power distributions (Figure 2c) are in close agreement between noon and midnight but clearly differ near dawn—the mean maximizing here, while the median minimizes. The mean auroral power agrees very well with intensity averages of previous observations which

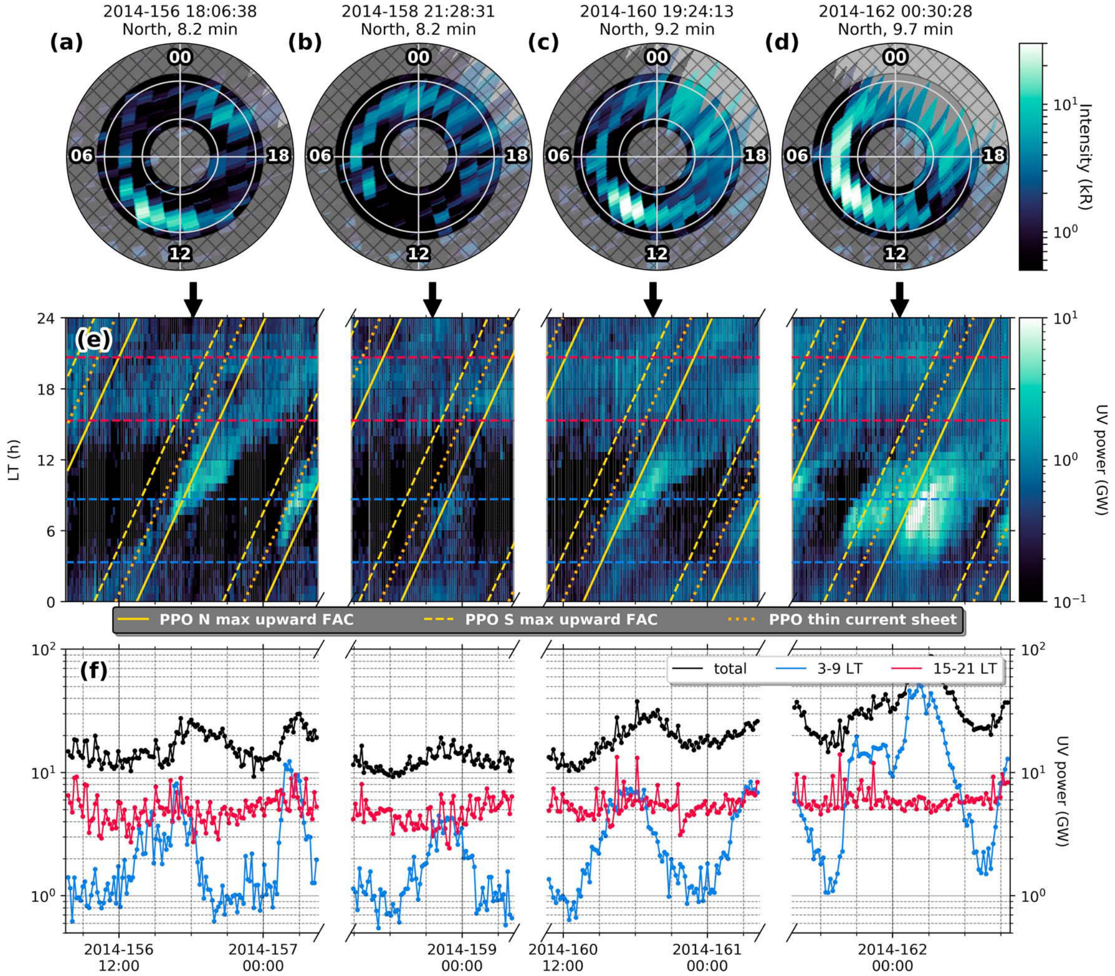

Figure 4. Ultraviolet auroral power keogram, typical auroral conditions (2014 DOY 156–162). Same format as Figure 1, but showing four observation sequences (a–d) with a broken time axis. In panel (e), orange dotted lines indicate where the planetary period oscillation-induced current sheet thinning is expected to be most pronounced, likely instigating reconnection.

all showed a distinct peak between 6 and 9 LT (e.g., Bader et al., 2018; Badman et al., 2011; Carbary, 2012; Kinrade et al., 2018; Lamy et al., 2009, 2018; Nichols et al., 2016)—but, as seen here, the mean UV intensity/power is obviously not a good representation of the typical state of the aurora. The median directly shows that in more cases than not, the dawn aurora is dimmer than the dusk aurora and not brighter; it is the few transient high-power events subcorotating through dawn which skew the mean power to unrepresentative high values at these LTs. Figure 3 compares the mean and median brightness of the actual images in this data set.

A detailed view of the 2014 DOY 156–162 keograms is shown in Figure 4 (Figure S4 shows 2014 DOY 144–149). Figures 4a–4d show an example UVIS image from each observation block—note that the observation geometry worsens toward the end, with the last images lacking coverage beyond ~20° colatitude from the pole between 18–24 LT. The integrated UV powers at these LTs are hence more uncertain as empty pixels have been filled with longitudinally averaged values of each latitudinal bin before integration.

The quiet auroral oval is overlaid with repeated powerful auroral plasma injection events (Mitchell et al., 2015) at Saturn's dawnside, which almost never rotate past noon as the perturbed source population's free energy is gradually deposited in Saturn's atmosphere, generating aurorae. The related rotating injected hot plasma populations seen in energetic neutral atom images do not stall at noon but continue rotating near rigidly with diminishing intensity back into the nightside sector where they appear to be reenergized with every pass (Carbary & Mitchell, 2017; Mitchell et al., 2009). All injections commence near dawn, indicating nightside reconnection and the consequent magnetic dipolarization (Yao et al., 2017) as a likely cause (Radioti et al., 2016)- considering the significant bendback of the magnetic field at dawn, this LT region maps well into Saturn's nightside. An auroral signature of this process may be the result of particle acceleration and precipitation during the dipolarization (Mitchell et al., 2015).

The injection events vary strongly in power, but show a regularity indicating a trigger mechanism internal to Saturn's magnetosphere. One known instigator of magnetotail reconnection is the PPO-induced modulation of the current sheet thickness (Bradley et al., 2018; Cowley & Provan, 2017; Jackman et al., 2016), which is most pronounced when the two PPO systems rotate in antiphase. This is the case in Figure 4e; the approximate location at which the current sheet is expected to be thinnest and reconnection is more likely to occur is indicated with orange dotted lines. Most of the injections observed are triggered within some 3-hr LT of these highlighted locations, suggesting the PPO current sheet thinning effect to indeed be a main influence on the occurrence of the observed large-scale disturbances.

5. Discussion and Conclusions

It is clear that Saturn's main aurorae are more dynamic than previous statistical studies may suggest. We conclude that the presently called "main aurorae" are associated with three different magnetospheric processes: the subcorotational FAC system, the two PPO FAC systems, and the occurrence of large-scale magnetotail reconnection events.

The subcorotational system is a largely or completely LT-invariant system of FACs which are likely generated by flow shears between plasma populations subcorotating at different speeds in the middle and outer magnetosphere (Cowley et al., 2004). This agrees with field line mapping of the main aurorae which places the main upward FAC sheet at an equatorial distance beyond 10 R_S, outward from the middle ring current (e.g., Belenkaya et al., 2014; Bradley et al., 2018; Talboys et al., 2011). The flow of the solar wind and the associated Dungey cycle activity (e.g., Cowley, Bunce & Prangé 2004; Jackman & Cowley, 2006) seem to have little to no impact on this system, since no significant LT asymmetries in auroral FACs (Hunt et al., 2016) and auroral brightness are observed, contrary to previous findings (e.g., Bader et al., 2018; Badman et al., 2011; Carbary, 2012; Kinrade et al., 2018; Lamy et al., 2009, 2018; Nichols et al., 2016), where observed asymmetries were likely an artifact of small data sets and averaging procedures unsuitable for determining the full variability of Saturn's auroral dynamics. This is supported by earlier studies estimating the Dungey cycle contribution to magnetic flux transport to be roughly an order of magnitude lower than the contribution arising from rotational flows in quiet solar wind conditions such that no asymmetry in auroral brightness is expected (e.g., Badman & Cowley, 2007; Badman et al., 2005). During solar wind compressions, significant asymmetries should theoretically arise (e.g., Badman & Cowley, 2007; Jackman et al., 2007) but will in reality be subsumed into the major auroral dynamics, that is, poleward extending auroral storms which occur simultaneously. The subcorotational system alone would cause a rather steady ring of upward FACs and associated auroral emissions around Saturn's poles corresponding to the region of highest flow shear, possibly with secondary emissions associated with corotation breakdown currents like Jupiter's main aurorae (Lamy et al., 2018; Stallard et al., 2007, 2008).

This subcorotational system is enhanced and reduced by the asymmetric PPO-related FACs flowing at the same latitudes (e.g., Bradley et al., 2018; Hunt et al., 2014, 2015). The slightly differing periods of the two PPO systems result in a double-sinusoidal modulation of the main oval's auroral brightness through LT, as the PPO and subcorotational FACs add up on one side of the planet but nearly negate each other on the opposite side (Bader et al., 2018)—we found this modulation to be significantly stronger at dawn than at dusk.

These two current systems combine to generate what should be considered the "main emission". Unintuitively though, the main (quasi-static and continuous) emission is often not dominant in Saturn's aurora, as it is quite dim (up to ~10 kR). It is overpowered significantly by large and bright patches which are likely a consequence of magnetic dipolarization events (e.g., Jackman et al., 2013; Jia & Kivelson, 2012; Lamy et al., 2013; Radioti et al., 2016) and which usually emerge between midnight and dawn LTs. They subcorotate and usually disperse before reaching dusk. Their occurrence seems to be partly governed by the PPO-induced thinning of the current sheet (Bradley et al., 2018; Cowley & Provan, 2017; Jackman et al., 2016); this was already observed in modeling studies (Jia & Kivelson, 2012; Zieger et al., 2010) and is likely related to similarly periodic plasma heating and ring current intensifications observed in energetic neutral atom measurements (Mitchell et al., 2009; Nichols et al., 2014). We observe such auroral plasma injection events about once per Saturn rotation, in rough agreement with direct plasmoid observations (Jackman et al., 2011, 2016) and Saturn's estimated magnetospheric refresh rate (Rymer et al., 2013).

Previous studies have further observed a clear dependence of magnetotail reconnection on solar wind conditions, as, for example, solar wind compression regions are known to trigger magnetotail reconnection and auroral storms (e.g., Badman et al., 2016; Clarke et al., 2005, 2009; Cowley et al., 2005; Crary et al., 2005; Kidder et al., 2012; Palmaerts et al., 2018), roughly about once per week (Meredith et al., 2014). Quiet solar wind conditions can lead to an expansion of the magnetotail and an accumulation of open flux as magnetotail reconnection is impeded (Badman et al., 2005, 2014; Jackman et al., 2010), and fewer or no auroral injections are observed (Gérard et al., 2006). Moreover, higher magnetopause reconnection rates cause higher flux loading, thereby indirectly promoting magnetotail reconnection events (Badman et al., 2005; Badman et al., 2014; Jackman, 2004).

These results are an important step toward a better understanding of the global dynamics of Saturn's magnetosphere and the internal and external factors at play, providing a crucial framework for future studies. Analyzing in situ data from past Saturn missions as well as modeling the system theoretically in the light of these new findings will help investigate Saturn's global plasma circulation more thoroughly, helping unravel the physics of rotating magnetospheres in general.

Acknowledgments
All Cassini data are publicly available from the NASA Planetary Data System (https://pds.jpl.nasa.gov). PPO phase data (2004–2017) can be found on the University of Leicester Research Archive (http://hdl.handle.net/2381/42436). Cassini operations are supported by NASA (managed by the Jet Propulsion Laboratory) and European Space Agency (ESA). A. B. was funded by a Lancaster University FST studentship. S. V. B., L. C. R., and J. K. were supported by STFC Grant ST/R000816/1. S. V. B. was also supported by an STFC Ernest Rutherford FellowshipST/M005534/1. Z. Y. acknowledges financial support from the Belgian Federal Science Policy Office (BELSPO) via the PRODEX Programme of ESA. T. J. B. was supported by STFC Quota StudentshipST/N504117/1. G. J. H. was supported by STFC consolidated Grant ST/000692/2.

References

Andrews, D. J., Coates, A. J., Cowley, S. W. H., Dougherty, M. K., Lamy, L., Provan, G., & Zarka, P. (2010). Magnetospheric period oscillations at Saturn: Comparison of equatorial and high-latitude magnetic field periods with north and south Saturn kilometric radiation periods. *Journal of Geophysical Research*, *115*, A12252. https://doi.org/10.1029/2010JA015666

Andrews, D. J., Cowley, S. W. H., Dougherty, M. K., & Provan, G. (2010). Magnetic field oscillations near the planetary period in Saturn's equatorial magnetosphere: Variation of amplitude and phase with radial distance and local time. *Journal of Geophysical Research*, *115*, A04212. https://doi.org/10.1029/2009JA014729

Bader, A., Badman, S. V., Kinrade, J., Cowley, S. W. H., Provan, G., & Pryor, W. R. (2018). Statistical planetary period oscillation signatures in Saturn's UV auroral intensity. *Journal of Geophysical Research: Space Physics*, *123*, 8459–8472. https://doi.org/10.1029/2018JA025855

Bader, A., Badman, S. V., Kinrade, J., Cowley, S. W. H., Provan, G., & Pryor, W. (2019). Modulations of Saturn's UV auroral oval location by planetary period oscillations. *Journal of Geophysical Research: Space Physics*, *124*, 952–970. https://doi.org/10.1029/2018JA026117

Bader, A., Badman, S. V., Yao, Z. H., Kinrade, J., & Pryor, W. R. (2019). Observations of continuous quasiperiodic auroral pulsations on Saturn in high time-resolution UV auroral imagery. *Journal of Geophysical Research: Space Physics*, *124*, 2451–2465. https://doi.org/10.1029/2018JA026320

Badman, S. V., Bunce, E. J., Clarke, J. T., Cowley, S. W. H., Gérard, J. C., Grodent, D., & Milan, S. E. (2005). Open flux estimates in Saturn's magnetosphere during the January 2004 Cassini-HST campaign, and implications for reconnection rates. *Journal of Geophysical Research*, *110*, A11216. https://doi.org/10.1029/2005JA011240

Badman, S. V., & Cowley, S. W. H. (2007). Significance of Dungey-cycle flows in Jupiter's and Saturn's magnetospheres, and their identification on closed equatorial field lines. *Annales Geophysicae*, *25*, 941–951. https://doi.org/10.5194/angeo-25-941-2007

Badman, S. V., Jackman, C. M., Nichols, J. D., Clarke, J. T., & Gérard, J. C. (2014). Open flux in Saturn's magnetosphere. *Icarus*, *231*, 137–145. https://doi.org/10.1016/j.icarus.2013.12.004

Badman, S. V., Masters, A., Hasegawa, H., Fujimoto, M., Radioti, A., Grodent, D., & Coates, A. (2013). Bursty magnetic reconnection at Saturn's magnetopause. *Geophysical Research Letters*, *40*, 1027–1031. https://doi.org/10.1002/grl.50199

Badman, S. V., Provan, G., Bunce, E. J., Mitchell, D. G., Melin, H., Cowley, S. W. H., & Dougherty, M. K. (2016). Saturn's auroral morphology and field-aligned currents during a solar wind compression. *Icarus*, *263*, 83–93. https://doi.org/10.1016/j.icarus.2014.11.014

Badman, S. V., Tao, C., Grocott, A., Kasahara, S., Melin, H., Brown, R. H., & Stallard, T. (2011). Cassini VIMS observations of latitudinal and hemispheric variations in Saturn's infrared auroral intensity. *Icarus*, *216*(2), 367–375. https://doi.org/10.1016/j.icarus.2011.09.031

Belenkaya, E. S., Cowley, S. W. H., Meredith, C. J., Nichols, J. D., Kalegaev, V. V., Alexeev, I. I., & Blokhina, M. S. (2014). Magnetospheric magnetic field modelling for the 2011 and 2012 HST Saturn aurora campaigns—Implications for auroral source regions. *Annales Geophysicae*, *32*(6), 689–704. https://doi.org/10.5194/angeo-32-689-2014

Bonfond, B., Gustin, J., Gérard, J. C., Grodent, D., Radioti, A., Palmaerts, B., & Tao, C. (2015). The far-ultraviolet main auroral emission at Jupiter—Part 1: Dawn-dusk brightness asymmetries. *Annales Geophysicae*, *33*(10), 1203–1209. https://doi.org/10.5194/angeo-33-1203-2015

Bradley, T. J., Cowley, S. W. H., Bunce, E. J., Smith, A. W., Jackman, C. M., & Provan, G. (2018). Planetary period modulation of reconnection bursts in Saturn's magnetotail. *Journal of Geophysical Research: Space Physics*, *123*, 9476–9507. https://doi.org/10.1029/2018JA025932

Bradley, T. J., Cowley, S. W. H., Provan, G., Hunt, G. J., Bunce, E. J., Wharton, S. J., & Dougherty, M. K. (2018). Field-aligned currents in Saturn's nightside magnetosphere: Subcorotation and planetary period oscillation components during northern spring. *Journal of Geophysical Research: Space Physics*, *123*, 3602–3636. https://doi.org/10.1029/2017JA024885

Brain, D. A., Halekas, J. S., Peticolas, L. M., Lin, R. P., Luhmann, J. G., Mitchell, D. L., & Réme, H. (2006). On the origin of aurorae on Mars. *Geophysical Research Letters*, *33*, L01201. https://doi.org/10.1029/2005GL024782

Carbary, J. F. (2012). The morphology of Saturn's ultraviolet aurora. *Journal of Geophysical Research*, *117*, A06210. https://doi.org/10.1029/2012JA017670

Carbary, J. F., & Mitchell, D. G. (2017). Midnight flash model of energetic neutral atom periodicities at Saturn: Midnight flash model. *Journal of Geophysical Research: Space Physics*, *122*, 7110–7117. https://doi.org/10.1002/2017JA024296

Chané, E., Saur, J., Keppens, R., & Poedts, S. (2017). How is the Jovian main auroral emission affected by the solar wind? *Journal of Geophysical Research: Space Physics*, *122*, 1960–1978. https://doi.org/10.1002/2016JA023318

Clarke, J. T., Connerney, J., Crary, F., Dougherty, M., Kurth, W., Cowley, S. W. H., & Kim, J. (2005). Morphological differences between Saturn's ultraviolet aurorae and those of Earth and Jupiter. *Nature*, *433*, 3.

Clarke, J. T., Nichols, J., Gérard, J. C., Grodent, D., Hansen, K. C., Kurth, W., & Cecconi, B. (2009). Response of Jupiter's and Saturn's auroral activity to the solar wind. *Journal of Geophysical Research*, *114*, A05210. https://doi.org/10.1029/2008JA013694

Cowley, S. W. H., Badman, S. V., Bunce, E. J., Clarke, J. T., Gérard, J. C., Grodent, D. C., & Yeoman, T. K. (2005). Reconnection in a rotation-dominated magnetosphere and its relation to Saturn's auroral dynamics. *Journal of Geophysical Research*, *110*, A02201. https://doi.org/10.1029/2004JA010796

Cowley, S. W. H., & Bunce, E. J. (2001). Origin of the main auroral oval in Jupiter's coupled magnetosphere-ionosphere system. *Planetary and Space Science*, *49*(10-11), 1067–1088. https://doi.org/10.1016/S0032-0633(00)00167-7

Cowley, S. W. H., & Bunce, E. J. (2003). Corotation-driven magnetosphere-ionosphere coupling currents in Saturn's magnetosphere and their relation to the auroras. *Annales Geophysicae*, *21*(8), 1691–1707. https://doi.org/10.5194/angeo-21-1691-2003

Cowley, S. W. H., Bunce, E. J., & O'Rourke, J. M. (2004). A simple quantitative model of plasma flows and currents in Saturn's polar ionosphere. *Journal of Geophysical Research*, *109*, A05212. https://doi.org/10.1029/2003JA010375

Cowley, S. W. H., Bunce, E. J., & Prangé, R. (2004). Saturn's polar ionospheric flows and their relation to the main auroral oval. *Annales Geophysicae*, *22*(4), 1379–1394. https://doi.org/10.5194/angeo-22-1379-2004

Cowley, S. W. H., & Provan, G. (2017). Planetary period modulations of Saturn's magnetotail current sheet during northern spring: Observations and modeling. *Journal of Geophysical Research: Space Physics*, *122*, 6049–6077. https://doi.org/10.1002/2017JA023993

Crary, F. J., Clarke, J. T., Dougherty, M. K., Hanlon, P. G., Hansen, K. C., Steinberg, J. T., & Young, D. T. (2005). Solar wind dynamic pressure and electric field as the main factors controlling Saturn's aurorae. *Nature*, *433*, 720. https://doi.org/10.1038/nature03333

Delamere, P. A., & Bagenal, F. (2010). Solar wind interaction with Jupiter's magnetosphere. *Journal of Geophysical Research*, *115*, A10201. https://doi.org/10.1029/2010JA015347

Delamere, P. A., Wilson, R. J., Eriksson, S., & Bagenal, F. (2013). Magnetic signatures of Kelvin-Helmholtz vortices on Saturn's magnetopause: Global survey. *Journal of Geophysical Research: Space Physics*, *118*, 393–404. https://doi.org/10.1029/2012JA018197

Desroche, M., Bagenal, F., Delamere, P. A., & Erkaev, N. (2013). Conditions at the magnetopause of Saturn and implications for the solar wind interaction. *Journal of Geophysical Research: Space Physics*, *118*, 3087–3095. https://doi.org/10.1002/jgra.50294

Dungey, J. W. (1961). Interplanetary magnetic field and the auroral zones. *Physical Review Letters*, *6*(2), 47–48. https://doi.org/10.1103/PhysRevLett.6.47

Esposito, L. W., Barth, C. A., Colwell, J. E., Lawrence, G. M., McClintock, W. E., Stewart, A. I. F., & Yung, Y. L. (2004). The Cassini Ultraviolet Imaging Spectrograph investigation. *Space Science Reviews*, *115*(1-4), 299–361. https://doi.org/10.1007/s11214-004-1455-8

Gérard, J. C., Bonfond, B., Gustin, J., Grodent, D., Clarke, J. T., Bisikalo, D., & Shematovich, V. (2009). Altitude of Saturn's aurora and its implications for the characteristic energy of precipitated electrons. *Geophysical Research Letters*, *36*, L02202. https://doi.org/10.1029/2008GL036554

Gérard, J. C., Grodent, D., Cowley, S. W. H., Mitchell, D. G., Kurth, W. S., Clarke, J. T., & Coates, A. J. (2006). Saturn's auroral morphology and activity during quiet magnetospheric conditions. *Journal of Geophysical Research*, *111*, A12210. https://doi.org/10.1029/2006JA011965

Gustin, J., Grodent, D., Radioti, A., Pryor, W., Lamy, L., & Ajello, J. (2017). Statistical study of Saturn's auroral electron properties with Cassini/UVIS FUV spectral images. *Icarus*, *284*, 264–283. https://doi.org/10.1016/j.icarus.2016.11.017

Gustin, J., Grodent, D., Ray, L., Bonfond, B., Bunce, E., Nichols, J., & Ozak, N. (2016). Characteristics of north Jovian aurora from STIS FUV spectral images. *Icarus*, *268*, 215–241. https://doi.org/10.1016/j.icarus.2015.12.048

Hill, T. W. (2001). The Jovian auroral oval. *Journal of Geophysical Research*, *106*(A5), 8101–8107. https://doi.org/10.1029/2000JA000302

Hunt, G. J., Cowley, S. W. H., Provan, G., Bunce, E. J., Alexeev, I. I., Belenkaya, E. S., & Coates, A. J. (2014). Field-aligned currents in Saturn's southern nightside magnetosphere: Subcorotation and planetary period oscillation components. *Journal of Geophysical Research: Space Physics*, *119*, 9847–9899. https://doi.org/10.1002/2014JA020506

Hunt, G. J., Cowley, S. W. H., Provan, G., Bunce, E. J., Alexeev, I. I., Belenkaya, E. S., & Coates, A. J. (2015). Field-aligned currents in Saturn's northern nightside magnetosphere: Evidence for interhemispheric current flow associated with planetary period oscillations. *Journal of Geophysical Research: Space Physics*, *120*, 7552–7584. https://doi.org/10.1002/2015JA021454

Hunt, G. J., Cowley, S. W. H., Provan, G., Bunce, E. J., Alexeev, I. I., Belenkaya, E. S., & Coates, A. J. (2016). Field-aligned currents in Saturn's magnetosphere: Local time dependence of southern summer currents in the dawn sector between midnight and noon. *Journal of Geophysical Research: Space Physics*, *121*, 7785–7804. https://doi.org/10.1002/2016JA022712

Isbell, J., Dessler, A. J., & Waite, J. H. (1984). Magnetospheric energization by interaction between planetary spin and the solar wind. *Journal of Geophysical Research*, *89*(A12), 10716. https://doi.org/10.1029/JA089iA12p10716

Jackman, C. M. (2004). Interplanetary magnetic field at ∼9 AU during the declining phase of the solar cycle and its implications for Saturn's magnetospheric dynamics. *Journal of Geophysical Research*, *109*, A11203. https://doi.org/10.1029/2004JA010614

Jackman, C. M., Achilleos, N., Cowley, S. W., Bunce, E. J., Radioti, A., Grodent, D., & Pryor, W. (2013). Auroral counterpart of magnetic field dipolarizations in Saturn's tail. *Planetary and Space Science*, *82-83*, 34–42. https://doi.org/10.1016/j.pss.2013.03.010

Jackman, C. M., Arridge, C. S., Slavin, J. A., Milan, S. E., Lamy, L., Dougherty, M. K., & Coates, A. J. (2010). In situ observations of the effect of a solar wind compression on Saturn's magnetotail. *Journal of Geophysical Research*, *115*, A10240. https://doi.org/10.1029/2010JA015312

Jackman, C. M., & Cowley, S. W. H. (2006). A model of the plasma flow and current in Saturn's polar ionosphere under conditions of strong Dungey cycle driving. *Annales Geophysicae*, *24*(3), 1029–1055. https://doi.org/10.5194/angeo-24-1029-2006

Jackman, C. M., Provan, G., & Cowley, S. W. H. (2016). Reconnection events in Saturn's magnetotail: Dependence of plasmoid occurrence on planetary period oscillation phase. *Journal of Geophysical Research: Space Physics*, *121*, 2922–2934. https://doi.org/10.1002/2015JA021985

Jackman, C. M., Russell, C. T., Southwood, D. J., Arridge, C. S., Achilleos, N., & Dougherty, M. K. (2007). Strong rapid dipolarizations in Saturn's magnetotail: In situ evidence of reconnection. *Geophysical Research Letters*, *34*, L11203. https://doi.org/10.1029/2007GL029764

Jackman, C. M., Slavin, J. A., & Cowley, S. W. H. (2011). Cassini observations of plasmoid structure and dynamics: Implications for the role of magnetic reconnection in magnetospheric circulation at Saturn. *Journal of Geophysical Research*, *116*, A10212. https://doi.org/10.1029/2011JA016682

Jia, X., & Kivelson, M. G. (2012). Driving Saturn's magnetospheric periodicities from the upper atmosphere/ionosphere: Magnetotail response to dual sources. *Journal of Geophysical Research*, *117*, A11219. https://doi.org/10.1029/2012JA018183

Jia, X., Kivelson, M. G., & Gombosi, T. I. (2012). Driving Saturn's magnetospheric periodicities from the upper atmosphere/ionosphere. *Journal of Geophysical Research*, *117*, A04215. https://doi.org/10.1029/2011JA017367

Kidder, A., Paty, C. S., Winglee, R. M., & Harnett, E. M. (2012). External triggering of plasmoid development at Saturn. *Journal of Geophysical Research*, *117*, A07206. https://doi.org/10.1029/2012JA017625

Kinrade, J., Badman, S. V., Provan, G., Cowley, S. W. H., Lamy, L., & Bader, A. (2018). Saturn's northern auroras and their modulation by rotating current systems during late northern spring in early 2014. *Journal of Geophysical Research: Space Physics*, *123*, 6289–6306. https://doi.org/10.1029/2018JA025426

Lamy, L., Cecconi, B., Prangé, R., Zarka, P., Nichols, J. D., & Clarke, J. T. (2009). An auroral oval at the footprint of Saturn's kilometric radio sources, colocated with the UV aurorae. *Journal of Geophysical Research*, *114*, A10212. https://doi.org/10.1029/2009JA014401

Lamy, L., Prangé, R., Pryor, W., Gustin, J., Badman, S. V., Melin, H., & Brandt, P. C. (2013). Multispectral simultaneous diagnosis of Saturn's aurorae throughout a planetary rotation. *Journal of Geophysical Research: Space Physics*, *118*, 4817–4843. https://doi.org/10.1002/jgra.50404

Lamy, L., Prangé, R., Tao, C., Kim, T., Badman, S. V., Zarka, P., & Radioti, A. (2018). Saturn's northern aurorae at solstice from HST observations coordinated with Cassini's grand finale. *Geophysical Research Letters*, *45*, 9353–9362. https://doi.org/10.1029/2018GL078211

Masters, A., Eastwood, J. P., Swisdak, M., Thomsen, M. F., Russell, C. T., Sergis, N., & Krimigis, S. M. (2012). The importance of plasma β conditions for magnetic reconnection at Saturn's magnetopause. *Geophysical Research Letters*, *39*, L08103. https://doi.org/10.1029/2012GL051372

Masters, A., Fujimoto, M., Hasegawa, H., Russell, C. T., Coates, A. J., & Dougherty, M. K. (2014). Can magnetopause reconnection drive Saturn's magnetosphere?: Saturn reconnection driving. *Geophysical Research Letters*, *41*, 1862–1868. https://doi.org/10.1002/2014GL059288

Meredith, C. J., Alexeev, I. I., Badman, S. V., Belenkaya, E. S., Cowley, S. W. H., Dougherty, M. K., & Nichols, J. D. (2014). Saturn's dayside ultraviolet auroras: Evidence for morphological dependence on the direction of the upstream interplanetary magnetic field. *Journal of Geophysical Research: Space Physics*, *119*, 1994–2008. https://doi.org/10.1002/2013JA019598

Meredith, C. J., Cowley, S. W. H., & Nichols, J. D. (2014). Survey of Saturn auroral storms observed by the Hubble Space Telescope: Implications for storm time scales: Saturn's auroral storms. *Journal of Geophysical Research: Space Physics*, *119*, 9624–9642. https://doi.org/10.1002/2014JA020601

Milan, S. E., Bunce, E. J., Cowley, S. W. H., & Jackman, C. M. (2005). Implications of rapid planetary rotation for the Dungey magnetotail of Saturn. *Journal of Geophysical Research*, *110*, A03209. https://doi.org/10.1029/2004JA010716

Milan, S. E., Lester, M., Cowley, S. W. H., Oksavik, K., Brittnacher, M., Greenwald, R. A., & Villain, J. P. (2003). Variations in the polar cap area during two substorm cycles. *Annales Geophysicae*, *21*(5), 1121–1140. https://doi.org/10.5194/angeo-21-1121-2003

Mitchell, D. G., Brandt, P. C., Carbary, J. F., Kurth, W. S., Krimigis, S. M., Paranicas, C., & Pryor, W. R. (2015). Injection, interchange, and reconnection: Energetic particle observations in Saturn's magnetosphere, *Magnetotails in the Solar System* pp. 327–343). Hoboken, NJ: John Wiley & Sons, Inc. https://doi.org/10.1002/9781118842324.ch19

Mitchell, D. G., Krimigis, S. M., Paranicas, C., Brandt, P. C., Carbary, J. F., Roelof, E. C., & Pryor, W. R. (2009). Recurrent energization of plasma in the midnight-to-dawn quadrant of Saturn's magnetosphere, and its relationship to auroral UV and radio emissions. *Planetary and Space Science*, *57*(14-15), 1732–1742. https://doi.org/10.1016/j.pss.2009.04.002

Nichols, J. D., Badman, V. S., Baines, K. H., Brown, R. H., Bunce, E. J., Clarke, J. T., & Stallard, T. S. (2014). Dynamic auroral storms on Saturn as observed by the Hubble Space Telescope. *Geophysical Research Letters*, *41*, 3323–3330. https://doi.org/10.1002/2014GL060186

Nichols, J. D., Badman, S. V., Bunce, E. J., Clarke, J. T., Cowley, S. W. H., Hunt, G. J., & Provan, G. (2016). Saturn's northern auroras as observed using the Hubble Space Telescope. *Icarus*, *263*, 17–31. https://doi.org/10.1016/j.icarus.2015.09.008

Palmaerts, B., Radioti, A., Grodent, D., Yao, Z. H., Bradley, T. J., Roussos, E., & Pryor, W. R. (2018). Auroral storm and polar arcs at Saturn—Final Cassini/UVIS auroral observations. *Geophysical Research Letters*, *45*, 6832–6842. https://doi.org/10.1029/2018GL078094

Provan, G., Andrews, D. J., Cecconi, B., Cowley, S. W. H., Dougherty, M. K., Lamy, L., & Zarka, P. M. (2011). Magnetospheric period magnetic field oscillations at Saturn: Equatorial phase "jitter" produced by superposition of southern and northern period oscillations. *Journal of Geophysical Research*, *116*, A04225. https://doi.org/10.1029/2010JA016213

Provan, G., Cowley, S. W. H., Bradley, T. J., Bunce, E. J., Hunt, G. J., & Dougherty, M. K. (2018). Planetary period oscillations in Saturn's magnetosphere: Cassini magnetic field observations over the northern summer solstice interval. *Journal of Geophysical Research: Space Physics*, *123*, 3859–3899. https://doi.org/10.1029/2018JA025237

Provan, G., Cowley, S. W. H., Lamy, L., Bunce, E. J., Hunt, G. J., Zarka, P., & Dougherty, M. K. (2016). Planetary period oscillations in Saturn's magnetosphere: Coalescence and reversal of northern and southern periods in late northern spring. *Journal of Geophysical Research: Space Physics*, *121*, 9829–9862. https://doi.org/10.1002/2016JA023056

Provan, G., Cowley, S. W. H., Sandhu, J., Andrews, D. J., & Dougherty, M. K. (2013). Planetary period magnetic field oscillations in Saturn's magnetosphere: Postequinox abrupt nonmonotonic transitions to northern system dominance. *Journal of Geophysical Research: Space Physics*, *118*, 3243–3264. https://doi.org/10.1002/jgra.50186

Radioti, A., Gérard, J. C., Grodent, D., Bonfond, B., Krupp, N., & Woch, J. (2008). Discontinuity in Jupiter's main auroral oval. *Journal of Geophysical Research*, *113*, A01215. https://doi.org/10.1029/2007JA012610

Radioti, A., Grodent, D., Gérard, J. C., Bonfond, B., Gustin, J., Pryor, W., & Arridge, C. S. (2013). Auroral signatures of multiple magnetopause reconnection at Saturn. *Geophysical Research Letters*, *40*, 4498–4502. https://doi.org/10.1002/grl.50889

Radioti, A., Grodent, D., Gérard, J. C., Milan, S. E., Bonfond, B., Gustin, J., & Pryor, W. (2011). Bifurcations of the main auroral ring at Saturn: Ionospheric signatures of consecutive reconnection events at the magnetopause. *Journal of Geophysical Research*, *116*, A11209. https://doi.org/10.1029/2011JA016661

Radioti, A., Grodent, D., Jia, X., Gérard, J. C., Bonfond, B., Pryor, W., & Jackman, C. (2016). A multi-scale magnetotail reconnection event at Saturn and associated flows: Cassini/UVIS observations. *Icarus*, *263*, 75–82. https://doi.org/10.1016/j.icarus.2014.12.016

Ray, L. C., Achilleos, N. A., Vogt, M. F., & Yates, J. N. (2014). Local time variations in Jupiter's magnetosphere-ionosphere coupling system. *Journal of Geophysical Research: Space Physics*, *119*, 4740–4751. https://doi.org/10.1002/2014JA019941

Rymer, A. M., Mitchell, D. G., Hill, T. W., Kronberg, E. A., Krupp, N., & Jackman, C. M. (2013). Saturn's magnetospheric refresh rate. *Geophysical Research Letters*, *40*, 2479–2483. https://doi.org/10.1002/grl.50530

Sandel, B. R., & Broadfoot, A. L. (1981). Morphology of Saturn's aurora. *Nature*, *292*(5825), 679–682. https://doi.org/10.1038/292679a0

Sandel, B. R., Shemansky, D. E., Broadfoot, A. L., Holberg, J. B., Smith, G. R., Mcconnell, J. C., & Linick, S. (1982). Extreme ultraviolet observations from the Voyager 2 encounter with Saturn. *Science*, *215*(4532), 548–553. https://doi.org/10.1126/science.215.4532.548

Southwood, D. J., & Cowley, S. W. H. (2014). The origin of Saturn's magnetic periodicities: Northern and southern current systems. *Journal of Geophysical Research: Space Physics*, *119*, 1563–1571. https://doi.org/10.1002/2013JA019632

Southwood, D. J., & Kivelson, M. G. (2001). A new perspective concerning the influence of the solar wind on the Jovian magnetosphere. *Journal of Geophysical Research*, *106*(A4), 6123–6130. https://doi.org/10.1029/2000JA000236

Southwood, D. J., & Kivelson, M. G. (2007). Saturnian magnetospheric dynamics: Elucidation of a camshaft model. *Journal of Geophysical Research*, *112*, A12222. https://doi.org/10.1029/2007JA012254

Stallard, T., Miller, S., Melin, H., Lystrup, M., Cowley, S. W. H., Bunce, E. J., & Dougherty, M. (2008). Jovian-like aurorae on Saturn. *Nature*, *453*(7198), 1083–1085. https://doi.org/10.1038/nature07077

Stallard, T., Smith, C., Miller, S., Melin, H., Lystrup, M., Aylward, A., & Dougherty, M. (2007). Saturn's auroral/polar H_3^+ infrared emission: II. A comparison with plasma flow models. *Icarus*, *191*(2), 678–690. https://doi.org/10.1016/j.icarus.2007.05.016

Talboys, D. L., Bunce, E. J., Cowley, S. W. H., Arridge, C. S., Coates, A. J., & Dougherty, M. K. (2011). Statistical characteristics of field-aligned currents in Saturn's nightside magnetosphere. *Journal of Geophysical Research*, *116*, A04213. https://doi.org/10.1029/2010JA016102

Vasyliūnas, V. M. (1983). Plasma distribution and flow, *Physics of the Jovian magnetosphere* pp. 395–453). Cambridge, UK: Cambridge University Press.

Vasyliūnas, V. M. (2016). Physical origin of pickup currents. *Annales Geophysicae*, *34*(1), 153–156. https://doi.org/10.5194/angeo-34-153-2016

Walach, M. T., Milan, S. E., Murphy, K. R., Carter, J. A., Hubert, B. A., & Grocott, A. (2017). Comparative study of large-scale auroral signatures of substorms, steady magnetospheric convection events, and sawtooth events. *Journal of Geophysical Research: Space Physics*, *122*, 6357–6373. https://doi.org/10.1002/2017JA023991

Yao, Z. H., Grodent, D., Ray, L. C., Rae, I. J., Coates, A. J., Pu, Z. Y., & Dunn, W. R. (2017). Two fundamentally different drivers of dipolarizations at Saturn. *Journal of Geophysical Research: Space Physics*, *122*, 4348–4356. https://doi.org/10.1002/2017JA024060

Zieger, B., Hansen, K. C., Gombosi, T. I., & De Zeeuw, D. L. (2010). Periodic plasma escape from the mass-loaded Kronian magnetosphere. *Journal of Geophysical Research*, *115*, A08208. https://doi.org/10.1029/2009JA014951

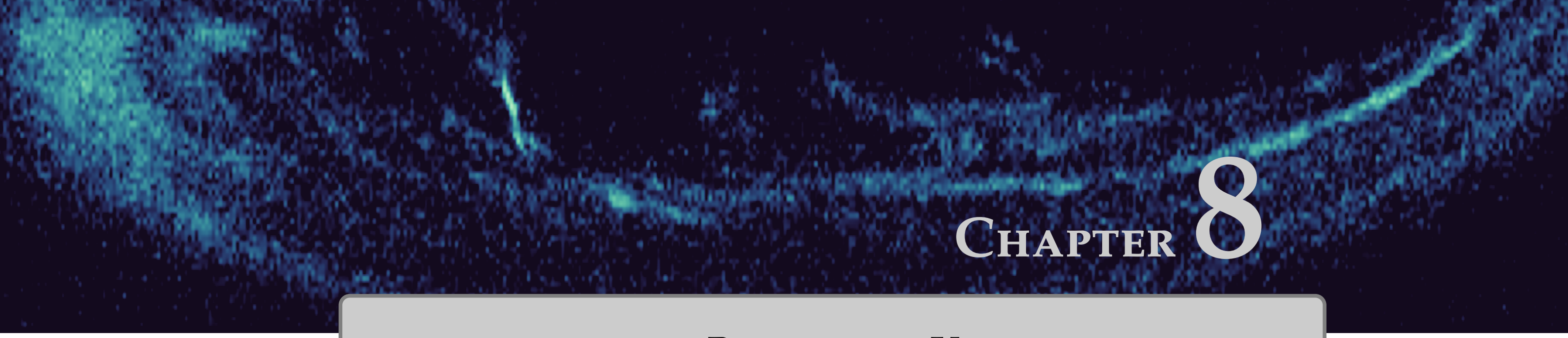

CHAPTER 8

PUBLICATION V

Energetic particle signatures above Saturn's aurorae

A. BADER, S. V. BADMAN, L. C. RAY, C. PARANICAS, C. T. S. LORCH, G. CLARK, M. ANDRÉ,
D. G. MITCHELL, D. A. CONSTABLE, J. KINRADE, G. J. HUNT AND W. R. PRYOR (2020)

Journal of Geophysical Research: Space Physics, *125*, e2019JA027403
doi:10.1029/2019JA027403

AUTHOR CONTRIBUTION STATEMENT AB conceived the study, performed the data reduction and analysis and authored the initial draft. SVB and LCR provided guidance and expertise in magnetospheric physics. CP and DGM provided technical support for MIMI data. CTSL supported the data analysis. GC, MA and DAC provided expertise on wave-particle interaction. JK provided various theoretical support. GJH provided expertise on FACs. WRP provided technical support for UVIS data. All authors contributed to the interpretation of the results and were involved in review and editing of the paper until publication.

This authorship statement was approved by all collaborating research groups.

Supplementary information for this publication can be found in appendix B.

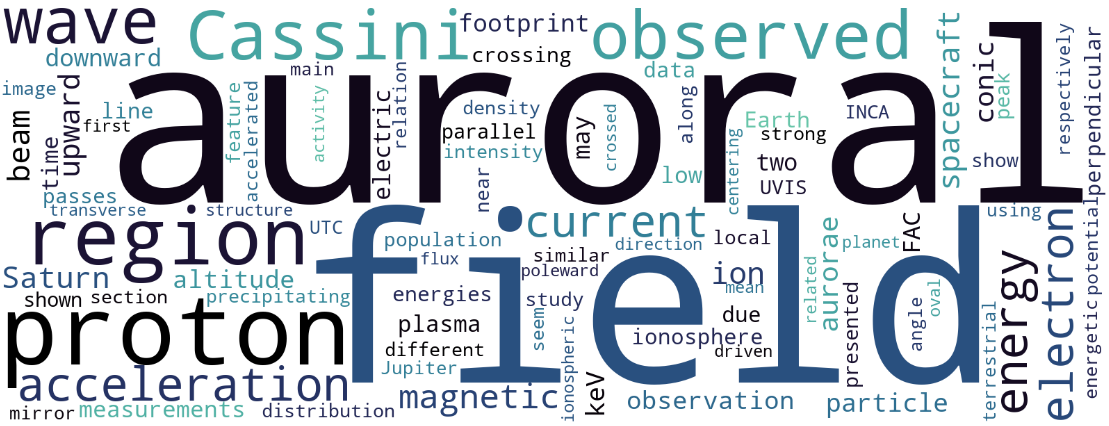

JGR Space Physics

RESEARCH ARTICLE
10.1029/2019JA027403

Key Points:
- Low-altitude orbits of Cassini reveal energetic proton and related plasma wave signatures within/above Saturn's auroral acceleration region
- Observations of proton conics in downward current regions indicate strong parallel electric potentials and transverse heating
- Observed energies are much higher at Saturn than above the terrestrial aurorae, but the acceleration mechanisms may be of a similar nature

Supporting Information:
- Supporting Information S1

Correspondence to:
A. Bader,
a.bader@lancaster.ac.uk

Citation:
Bader, A., Badman, S. V., Ray, L. C., Paranicas, C., Lorch, C. T. S., Clark, G., et al. (2020). Energetic particle signatures above Saturn's aurorae. *Journal of Geophysical Research: Space Physics*, *125*, e2019JA027403. https://doi.org/10.1029/2019JA027403

Received 12 SEP 2019
Accepted 9 DEC 2019
Accepted article online 22 DEC 2019

Energetic Particle Signatures Above Saturn's Aurorae

A. Bader[1], S. V. Badman[1], L. C. Ray[1], C. P. Paranicas[2], C. T. S. Lorch[1], G. Clark[2], M. André[3], D. G. Mitchell[2], D. A. Constable[1], J. Kinrade[1], G. J. Hunt[4], and W. Pryor[5]

[1]Department of Physics, Lancaster University, Lancaster, UK, [2]The Johns Hopkins University Applied Physics Laboratory, Laurel, MD, USA, [3]Swedish Institute of Space Physics, Uppsala, Sweden, [4]Blackett Laboratory, Imperial College London, London, UK, [5]Science Department, Central Arizona College, Coolidge, AZ, USA

Abstract Near the end of its mission, NASA's Cassini spacecraft performed several low-altitude passes across Saturn's auroral region. We present ultraviolet auroral imagery and various coincident particle and field measurements of two such passes, providing important information about the structure and dynamics of Saturn's auroral acceleration region. In upward field-aligned current regions, upward proton beams are observed to reach energies of several tens of keV; the associated precipitating electron populations are found to have mean energies of about 10 keV. With no significant wave activity being apparent, these findings indicate strong parallel potentials responsible for auroral acceleration, about 100 times stronger than at Earth. This is further supported by observations of proton conics in downward field-aligned current regions above the acceleration region, which feature a lower energy cutoff above ~50 keV—indicating energetic proton populations trapped by strong parallel potentials while being transversely energized until they can overcome the trapping potential, likely through wave-particle interactions. A spacecraft pass through a downward current region at an altitude near the acceleration region reveals plasma wave features, which may be driving the transverse proton acceleration generating the conics. Overall, the signatures observed resemble those related to the terrestrial and Jovian aurorae, the particle energies and potentials at Saturn appearing to be significantly higher than at Earth and comparable to those at Jupiter.

Plain Language Summary NASA's Cassini spacecraft orbited closer to Saturn than ever before during the last stage of its mission, the "Grand Finale". This allowed the onboard instruments to measure charged particles and plasma waves directly above the auroral region while simultaneously providing high-resolution imagery of the ultraviolet aurorae. Based on observations of highly energetic ions streaming away from the planet in regions of low plasma wave activity, we infer the existence of strong electric fields which act to accelerate electrons down into the atmosphere, driving the bright auroral emissions. Our estimates of the average energy of the precipitating electrons support this finding. Charged ions sometimes seem to be energized by plasma waves above the aurorae before they can escape, but the exact process in which this happens is not fully understood. Most signatures presented here resemble those observed in relation to Earth's aurorae, suggesting that the mechanisms acting at both planets are quite similar although Saturn's acceleration mechanism is significantly stronger.

1. Introduction

In the final year of its mission, NASA's Cassini spacecraft performed a set of orbits bringing it closer to Saturn than ever before. This presented a unique opportunity to combine remote sensing of Saturn's aurorae in unprecedented spatial resolution with in situ measurements of particles and fields advancing our understanding of the auroral acceleration process which has so far been investigated mostly at Earth and Jupiter.

Earth's brightest aurorae are generated by monoenergetic precipitating electron populations (e.g., Evans, 1968; McIlwain, 1960), which are accelerated into the ionosphere by quasistatic electric fields along the magnetic field lines connecting the magnetosphere and ionosphere (e.g., Carlson et al., 1998; Ergun et al., 1998; Knight, 1973; McFadden et al., 1999). On adjacent field lines where no auroral emissions are observed, electrons were found to be accelerated in the opposite direction—away from the planet and out of the ionosphere (e.g., Marklund et al., 2001).

These downward and upward beaming electrons are accompanied by ion beams and conics, respectively, the latter being generated when ions are energized perpendicular to the magnetic field. As these are driven away from the planet by the mirror force their pitch angle decreases and the accelerated population forms conics in velocity space as it travels out along the field lines of the nonuniform planetary magnetic field (e.g., André, 1997, and references therein). The energy for this acceleration process is provided either by the free energy of the anisotropic beam-like electron distribution— with plasma waves acting as an intermediary to facilitate the energy transfer— or by direct interaction with plasma waves moving toward the ionosphere from where they were generated (see, e.g., Hamrin et al., 2002; Shen et al., 2018). At low altitudes (∼1,000 km), lower hybrid waves seem to be of importance (e.g., Chang, 1993; Kintner et al., 1992; Vago et al., 1992, and references therein), while at higher altitudes (several thousand km), broadband electromagnetic waves heat the local ion population through cyclotron resonance (e.g., André et al., 1990, Ball & André, 1991, Kintner et al., 1979; Klumpar, 1979, Garbe et al., 1992, Okuda & Ashour-Abdalla, 1981). In multicomponent plasma including heavier ion species, the proton population may also couple with waves at frequencies below the proton gyrofrequency (Le Quau et al., 1993; Rauch et al., 1993). The accelerated ion beam and conic fluxes were shown to vary with solar illumination (Peterson et al., 2006).

While Earth's aurorae are largely solar wind driven (e.g., Milan et al., 2003; Walach et al., 2017), aurorae observed at the gas giants are powered internally due to their rapid rotation and significant internal plasma sources—Jupiter's aurorae are formed almost entirely due to the breakdown of plasma corotation in the magnetodisc (e.g., Cowley & Bunce, 2001; Hill, 1979, 2001; Southwood & Kivelson, 2001), and the static signatures within Saturn's much more dynamic aurorae seem to be related to similar processes occurring in the outer magnetosphere (e.g., Bader et al., 2019; Cowley et al., 2004a, 2004b; Milan et al., 2005). Prior to the arrival of NASA's Juno spacecraft at Jupiter, the wave-particle interaction processes responsible for auroral acceleration at the giant planets were nevertheless assumed to be similar to what is observed in the terrestrial magnetosphere. However, the first passes through Jupiter's auroral region did not reveal a powerful acceleration region and strong field-aligned currents (FACs) as expected (Cowley et al., 2017; Ray et al., 2010; 2012) but weaker FACs of a filamentary nature (Kotsiaros et al., 2019) and signatures of aurorae powered by stochastic/broadband acceleration processes substantially different from those at Earth (Allegrini et al., 2017; Mauk et al., 2017b, 2017a). Juno also observed ion conics on auroral field lines (Clark et al., 2017b), which may be the result of field-aligned electron beams and the associated broadband whistler waves (Tetrick et al., 2017) similar to the those observed at Earth although at much higher energies. Contrary to the initial lack of such observations, later spacecraft passes indicated the presence of strong parallel electric fields, coherent particle acceleration, and inverted-V structures (Clark et al., 2017a, 2018; Ebert et al., 2017; Mauk et al., 2018; Paranicas et al., 2018). Juno magnetometer measurements as well as recent theoretical work further suggest that Alfvén waves may play an important role for auroral particle acceleration (Gershman et al., 2019; Saur et al., 2018).

This study applies insights gained from previous studies on terrestrial and Jovian auroral acceleration to recent measurements from the Cassini spacecraft at Saturn. FACs in Saturn's auroral regions have previously been investigated in detail based on magnetometer data (e.g., Bunce et al., 2008; Cowley et al., 2008; Hunt et al., 2014, 2015, 2016, 2018; Talboys et al., 2009, 2009, 2011), but Cassini's orbit greatly limited our ability to characterize the acceleration region in more detail before the last low spacecraft passes across the auroral region. However, some observations suggest the presence of energetic upward electron (Saur et al., 2006) and ion beams (Badman et al., 2012; Mitchell et al., 2009) at auroral latitudes. Mitchell et al. (2009) also observed ion conics similar to those found in relation to the terrestrial and, later on, Jovian aurorae and concluded that the driving mechanisms may be closely related, although Cassini's position was far above the acceleration region ($>5\,R_S$), and no auroral imagery was available for these observations. More evidence for wave-particle interactions similar to terrestrial processes has been found by Menietti et al. (2011), who investigated the relation between ion cyclotron harmonics and electron beams observed at the same time. Their modeling suggests that this process can produce significant ion heating as previously investigated for Earth's auroral region (Singh et al., 1981). However, the height and structure of Saturn's auroral acceleration region remains a matter of ongoing research—so far based on the analyses of Saturn Kilometric Radiation (e.g., Lamy et al., 2011, 2018; Menietti et al., 2011) and modeling efforts (e.g., Ray et al., 2013).

We describe our data processing methods in section 2 before presenting two auroral passes with their coincident auroral imagery and measurements of fields and particles in section 3. We conclude and summarize this study in section 4.

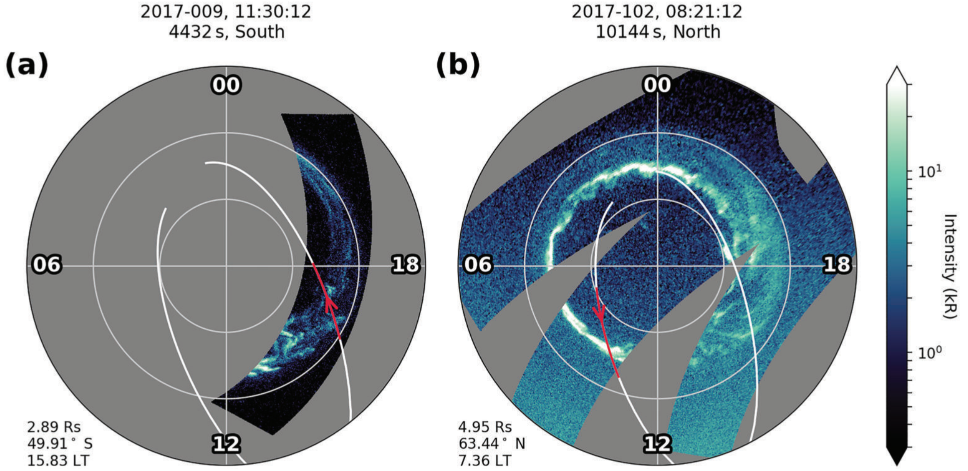

Figure 1. Polar projection of two Cassini UVIS images of Saturn's aurorae from (a) 2017-009 (southern hemisphere) and (b) 2017-102 (northern hemisphere), seen from above the north pole with noon toward the bottom. The auroral intensity is shown in logarithmic color scale. Cassini's magnetically mapped footprint (Burton et al., 2010, internal field model with Bunce et al., 2008, ring current contribution) is overlaid in white and highlighted in red to mark the corresponding image exposure. The spacecraft's radial distance, latitude, and local time position at the start of the exposure is indicated on the bottom left of each panel; the start, duration, and hemisphere of each exposure on top.

2. Data and Method

2.1. Auroral Imagery

Our study analyzes two auroral passes with imagery of Saturn's ultraviolet (UV) aurorae from Cassini's Ultraviolet Imaging Spectrograph (UVIS; Esposito et al., 2004). In order to obtain an auroral image, the slit of the far-UV (FUV, 110–190 nm) detector is moved across the auroral region. The slit consists of 64 pixels, resulting in an instantaneous field of view of 64 × 1.5 mrad. Using Cassini SPICE pointing information from the NASA Planetary Data System, each pixel is projected onto a planetocentric polar grid with resolution $0.1° \times 0.05°$ (lon × lat) at an altitude of 1,100 km above Saturn's 1-bar level (defined by $R_{\text{SEQ}} = 60,268$ km and $R_{\text{SPO}} = 54,364$ km as Saturn's equatorial and polar radii)—the altitude where aurorae are thought to be generated (Gérard et al., 2009). The estimated total unabsorbed H_2 auroral emission intensity (70–170 nm) is obtained from the UVIS FUV intensity by multiplying the intensity observed in the 155- to 162-nm band by a factor 8.1 as this minimizes dayglow and hydrocarbon absorption effects (Gustin et al., 2016, 2017). The two projected images used in this study are shown in Figure 1.

2.2. Magnetic Field and FACs

Magnetic field data were obtained using the Cassini magnetometer (Dougherty et al., 2004) and is presented in Kronocentric radial-theta-phi ($r - \theta - \phi$) coordinates, with the latest internal field model (Dougherty et al., 2018) subtracted. Hereby θ and ϕ denote the southward and eastward components, respectively. We determine the FAC density in order to provide context for the particle and fields measurements presented in the following sections and to compare it with the associated auroral intensities. Due to the close alignment between Saturn's magnetic dipole and rotational axes, applying Ampère's law lets us determine the equatorward directed height-integrated Pedersen current in the ionosphere I_P directly from the azimuthal field component B_ϕ measured in the magnetosphere. The azimuthal field just above the ionosphere $B_{\phi i}$ is determined from the field measured at the spacecraft location using

$$B_{\phi i} = B_\phi \frac{\rho}{\rho_i}, \tag{1}$$

where ρ and ρ_i are the perpendicular distance of Cassini and its magnetic footprint from Saturn's spin axis, respectively. The horizontal equatorward height-integrated Pedersen current is then given by

$$I_P = \pm \frac{\rho_i B_{\phi i}}{\mu_0} = \pm \frac{\rho B_\phi}{\mu_0}, \tag{2}$$

with μ_0 as the permeability of free space and the negative sign applying in the northern hemisphere. The so derived I_P is in this study approximated with a cubic spline with as many knots as are required to keep the residual sum of squares below $N \cdot (0.05\ \mathrm{MA/rad})^2$ with N as the number of data points. Due to current continuity, I_P is then equal to the net FAC flowing into the ionosphere between Saturn's pole and Cassini's ionospheric footprint—changes in I_P along Cassini's moving ionospheric footprint hence relate directly to the FAC density at the ionospheric latitudes crossed. The FAC density just above the ionosphere $j_\parallel$ is hence given by

$$j_\parallel = \frac{\Delta I_P}{R_i^2(\theta_i)\sin(\theta_i)\Delta\theta_i}, \tag{3}$$

with $R_i(\theta_i)$ as the distance between the center of Saturn and the upper edge of the ionosphere at colatitude θ_i, assumed to be located 1,100 km above Saturn's 1-bar level. $\Delta\theta_i$ denotes the absolute colatitudinal width of the region across which the observed change in ionospheric Pedersen current ΔI_P occurred (e.g., Bunce et al., 2008; Badman et al., 2012; Hunt et al., 2014; Talboys et al., 2009, 2011).

2.3. Particle and Field Measurements

All particle data presented here were measured by detectors of Cassini's Magnetosphere Imaging Instrument (Krimigis et al., 2004). The Low Energy Magnetospheric Measurements System (LEMMS) is a two-ended telescope measuring high-energy ions and electrons; in this study we present electron count rates from Channels C2–C5 (41–300 keV). The lowest energy Channels C0 and C1 are not shown due to sunlight contamination. All these channels are situated in the same side of the telescope (low energy telescope) and hence have the same pointing direction. LEMMS was built to rotate back and forth to increase the coverage of magnetic pitch angles, but this mechanism stopped working in 2005 such that the viewing direction only changes with the spacecraft attitude. During auroral observations with UVIS such as presented here, the LEMMS low energy telescope points perpendicular to the local magnetic field.

The Ion and Neutral Camera (INCA) observes ions and energetic neutral atoms in a field of view of 120°×90° in eight energy bands between 5 and 360 keV. In this study, we use INCA to obtain partial proton pitch angle distributions around the field-aligned direction. We note that the data presented here were obtained while INCA operated in neutral mode; this may lead to decreased proton fluxes in the 5- to 24-keV bands and striations along the long axis of the instrument due to ions being slightly focused by the deflection plate system. However, measurements are not expected to be significantly affected otherwise, as a low resistance path developed in the deflection plate system in 2015 and charged particles can hence pass near unhindered regardless of the detector's observation mode.

The Charge-Energy-Mass Spectrometer (CHEMS) is an ion mass spectrometer used to determine the energy, charge, and mass of ions between 3 and 220 keV/e. It is composed of three telescopes arranged in a fan shape; due to the pointing of the spacecraft during auroral observations with UVIS, all three of them are directed perpendicular to the local magnetic field in all observations shown here. We present proton energy spectrograms combined from the three sensors.

Lastly, the Cassini Radio and Plasma Wave Science instrument (RPWS, Gurnett et al., 2004) provided electric and magnetic field spectrograms through a wide range of frequencies. In this study we present low rate full resolution data from the low and medium frequency receivers for oscillations perpendicular to the magnetic field (parallel to the spacecraft x axis). Key parameter electric field spectrograms covering the full frequency range are shown in Supporting Information S1.

3. Results and Discussion

3.1. Dim Auroral Patches at Southern Dusk: 2017-009

On 2017-009, Cassini crossed the southern auroral oval near local dusk at an altitude of about 3 R_S. Figure 2 shows the path of Cassini's magnetic footprint across the auroral zone and the coincident measurements recorded by its magnetometer.

The crossing occurred in a poleward direction, such that Cassini left the closed magnetosphere and entered the polar cap region during the time period shown. Figure 2b shows the intensity of the UV aurorae at Cassini's ionospheric footprint, averaged in a 1°×0.5° (lon×lat) box to account for possible mapping uncertainty of the model used (Dougherty et al., 2018 internal field model with Bunce et al., 2008, ring current contribution) and timing uncertainty between the auroral observation and the actual spacecraft pass (<30 min). The dusk aurorae did not form a clear ring of main emission at this time, so instead of a single strong inten-

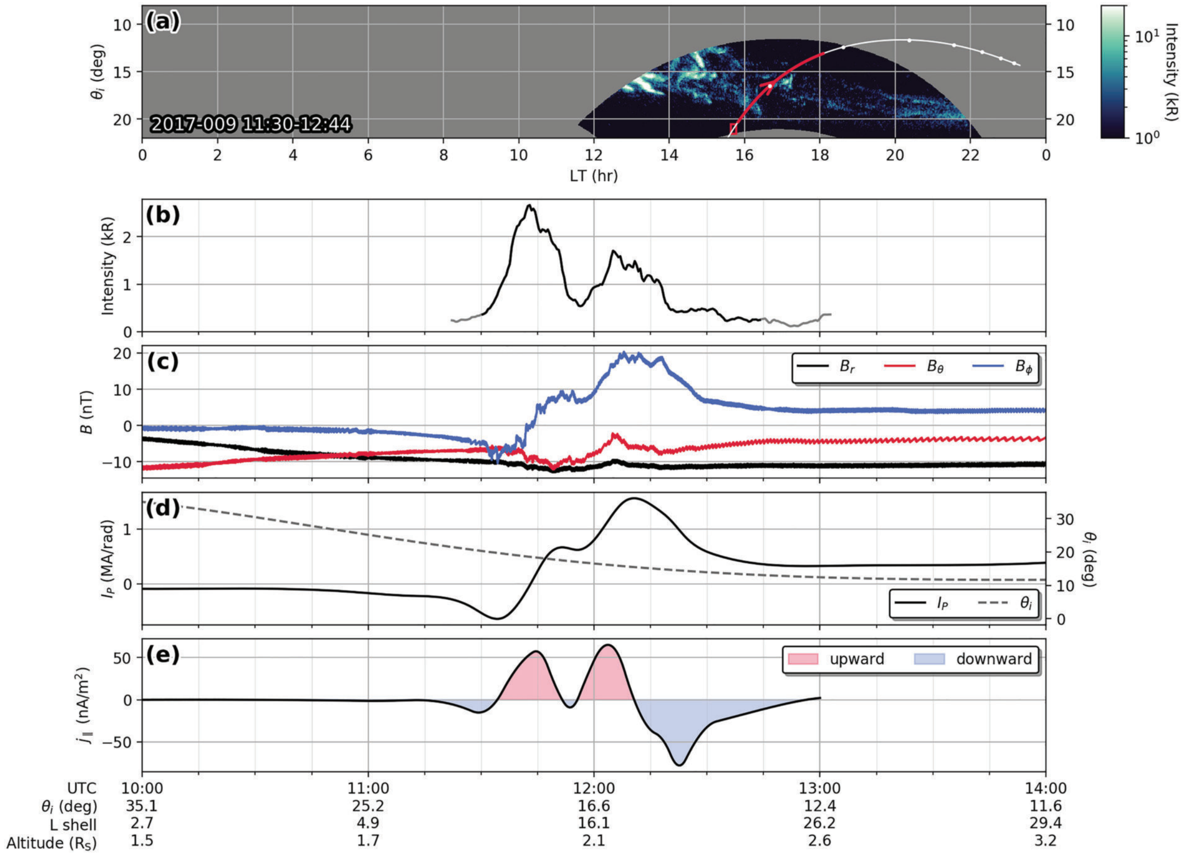

Figure 2. Magnetometer data and derived auroral currents of the 2017-009 crossing. (a) Local time-colatitude (LT-θ_i) projected UVIS image in logarithmic color scale, with Cassini's magnetically mapped footprint shown in white and highlighted in red during the exposure of the image. White dots on the trajectory are at full hours UTC. (b) Auroral intensity at Cassini's footprint through time, averaged within a small box as shown in (a). The graph is gray for times outside the exposure of the image. (c) Magnetic field data in Kronocentric radial-theta-phi coordinates after subtraction of an internal field model (Dougherty et al., 2018). (d) Height-integrated ionospheric Pedersen current, derived from B_ϕ using equation (2) and smoothed; colatitude of the magnetically mapped spacecraft footprint. (e) Field-aligned current density just above the ionosphere, calculated using equation (3). Red and blue shaded sections correspond to upward and downward currents, respectively. The horizontal axis is labeled with time stamp, colatitude of the spacecraft footprint, spacecraft L shell, and spacecraft altitude over Saturn's 1 bar surface.

sity peak, we observe two brightenings over the course of the crossing. The UVIS image obtained soon after the one shown in Figure 1a (see Supporting Information S1) indicates that these structures are relatively long-lived and not related to the short-lived auroral flashes frequently observed near dusk (Bader et al., 2019). While the first and brighter peak reaches nearly 3 kR as Cassini's footprint moves directly through a dim auroral patch, the second intensity peak falls short of 2 kR and is associated with Cassini cutting the edge of a second, slightly brighter auroral patch. We note that the intensity of the observed patches may vary between their observation with UVIS and the crossing of the spacecraft footprint.

The ionospheric Pedersen current I_P (Figure 2d), derived from smoothed magnetic field measurements as described in section 2, is initially close to zero but shows two strong increases during the crossing. The associated peaks in (upward) FAC density (Figure 2e, red) line up remarkably well with the two auroral intensity peaks observed. On both sides of the auroral oval, there seem to be downward current regions—a quite weak one at the equatorward edge and a stronger one at the poleward edge. Additionally, a downward current region may be located between the two auroral patches.

During the time of the crossing, the INCA instrument observed the proton environment; Figure 3a shows its observations along the field from roughly 11:20–12:45 UTC. The sensor was directed downward such as to measure field-aligned particles flowing up from the ionosphere. In the 13- to 90-keV energy range, we observe a broadband antiplanetward field-aligned proton beam maximizing in intensity just as Cassini begins to cross the first auroral patch (first upward FAC peak in Figure 3b). As the upward current den-

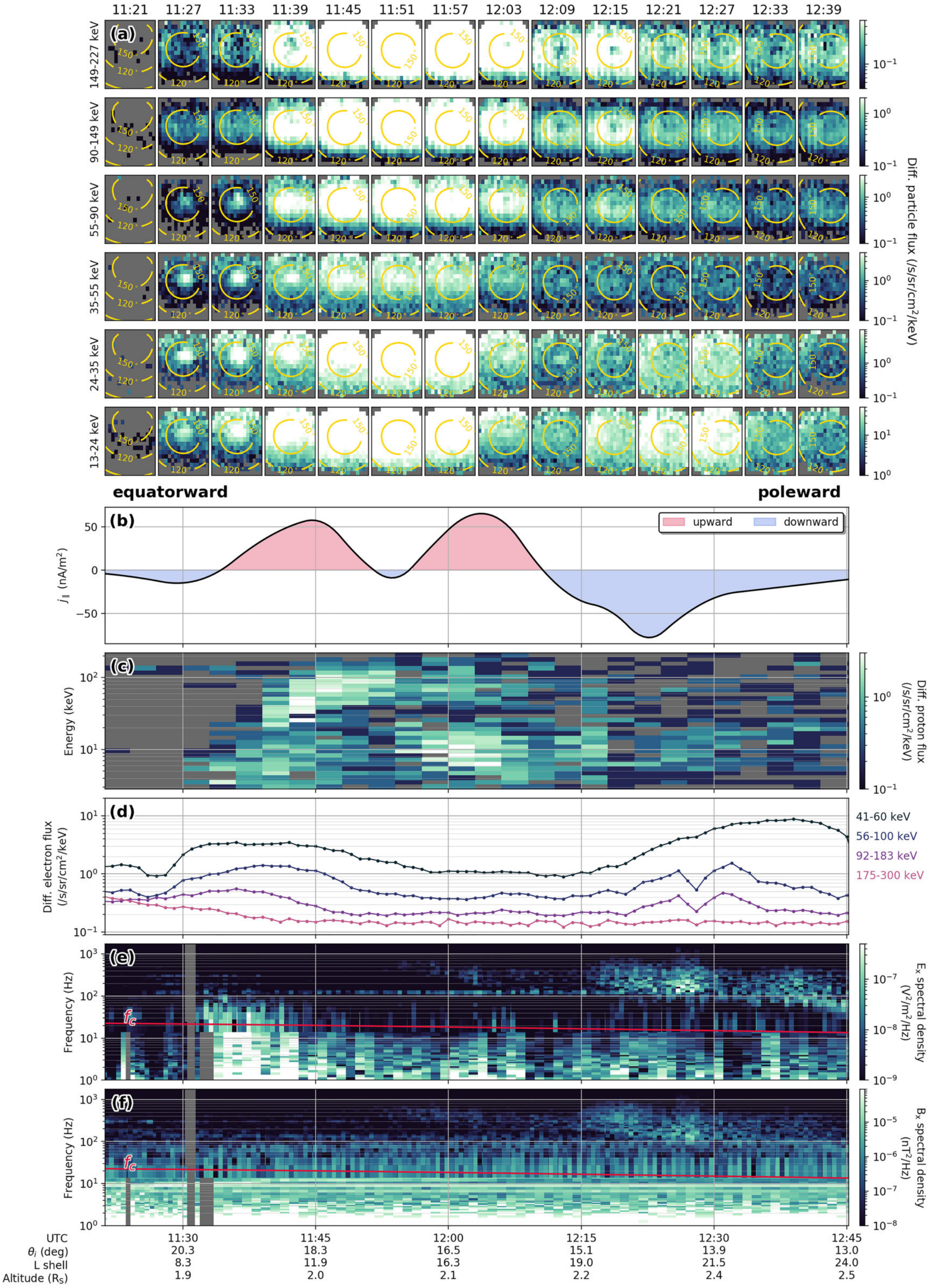

Figure 3. Overview of Cassini particle and wave measurements from 2017-009. (a) Cassini INCA proton observations, each panel showing the differential proton flux at a certain time and within a certain energy range. Magnetic pitch angle contours are overlain in yellow; note that Cassini was in the southern hemisphere and 180° pitch angle (~ center of each subpanel) corresponds to the upward direction. (b) Inferred field-aligned currents at Cassini's ionospheric footprint. (c) Cassini CHEMS proton flux spectrogram ⊥ to B and (d) Cassini LEMMS electron flux measurements ⊥ to B. (e) Cassini RPWS electric and (f) magnetic field spectrogram; the local proton gyrofrequency f_c is indicated with a red line.

sity begins to decrease, the INCA detector is suddenly flooded with protons at all energies. The following scans are characterized by a near complete saturation of the detector, apart from the 35- to 55-keV energy range where some faint signatures of an upward proton beam are still visible. A top-to-bottom gradient in intensity visible between ∼11:45 and 12:00 UTC is a signature of uneven sensor saturation and not a feature of the observed proton distribution. During the crossing of the second patch (second upward FAC peak in Figure 3b), we again observe a faint proton beam in the 24- to 55-keV energy range. Both before and after the episode of detector saturation, the distributions observed in the 90- to 227-keV range appear to show a depression of proton flux in the field-aligned direction. This is likely to be a signature of the loss cone but may also be a proton conic which cannot be completely resolved by the detector due to the large fluxes observed here. This is followed by a short proton flux enhancement at 13–35 keV before the ambient polar cap plasma is reached. To better understand these features, we compare this INCA data to CHEMS and LEMMS measurements of energetic proton and electron fluxes perpendicular to the magnetic field, respectively, as well as RPWS instrument electric and magnetic field spectrograms, shown in panels 3c–3f.

Between ∼11:30 and 11:45 UTC, enhanced wave activity near and below the proton gyrofrequency, f_c, coincides with upward proton beams as Cassini moves into the first auroral patch (panels 3e and 3f). The observed plasma waves could be electrostatic ion cyclotron (EIC) waves, perhaps coinciding with ion acoustic waves at lower frequencies; EIC waves can be generated by unstable electron or ion beam distributions such as typically observed in the auroral acceleration region (e.g., André, 1986; Kindel & Kennel, 1971; Kaufmann & Kintner, 1982). At Earth, they are generally observed in the main upward current region together with upgoing ion beams (e.g., André et al., 1987; Cattell et al., 1991; Kintner et al., 1979) just as in these measurements at Saturn. Assuming that all of the power spectral density at the proton gyrofrequency is due to left-handed waves, that is, waves in resonance with the proton gyration, we can use the relation

$$\frac{dW}{dt} = S_E \frac{q^2}{2m}, \tag{4}$$

to estimate the theoretical transverse heating rate dW/dt of the local proton population (e.g., André et al., 1998; Chang et al., 1986). Hereby S_E denotes the electric field spectral density at the proton gyrofrequency and q and m the charge and mass of a proton, respectively. We estimate $dW/dt \approx 23$ eV/s, making it seem unlikely that the observed proton beams which reach energies of tens of keV are driven by these waves—particles of these energies are not expected to remain in the relatively small acceleration region for a sufficient length of time in upward FAC regions. It is hence more probable that the plasma waves are instead themselves driven by the unstable electron/proton beam distributions.

As the crossing of the first auroral patch is completed and Cassini's footprint moves into a downward return current region (see also Figure 2e), accelerated protons become visible in both the INCA and CHEMS detectors. INCA (observing $\| B$, Figure 3a) is saturated on most channels, while CHEMS (observing $\perp B$, Figure 3c) measures first a highly energetic (∼100 keV) and later on a colder (∼10 keV) transversely accelerated proton population, suggesting a powerful energization process taking place on the field lines crossed. At Earth, one such process is the “pressure cooker” mechanism where plasma waves in a wide frequency range can transversely heat ions (e.g., André, 1997; Chang, 1993; Gorney et al., 1985). However, the energized ion population is trapped by the electric field structures which accelerate electrons upward to carry the downward current; the heated ions can hence only move upward along the field line once the mirror force is large enough to overcome the static potential drop. Ion conics and beams driven this way therefore feature a characteristic low energy cutoff if observed above the acceleration region. During the sequence examined here, we only note some very weak extremely low frequency (ELF) wave activity at ∼12:00 UTC (∼200–900 Hz) which may be related to the heated protons. We do not observe a low energy cutoff in the proton measurements, which may either be explained with the cutoff being below the lowest proton energies of a few keV observable with INCA and CHEMS or by Cassini traversing through the acceleration region instead of passing above it. It is worth mentioning that signatures in this frequency range may also be an effect of static structures such as FAC sheets or of dispersive Alfvén waves being Doppler-shifted due to the spacecraft motion (e.g., Gurnett et al., 1984; Stasiewicz et al., 2000).

After a second upward current region, again coincident with now weak upward proton beams and some weak EIC wave activity at the proton gyrofrequency at ∼12:05 UTC, both auroral features have been

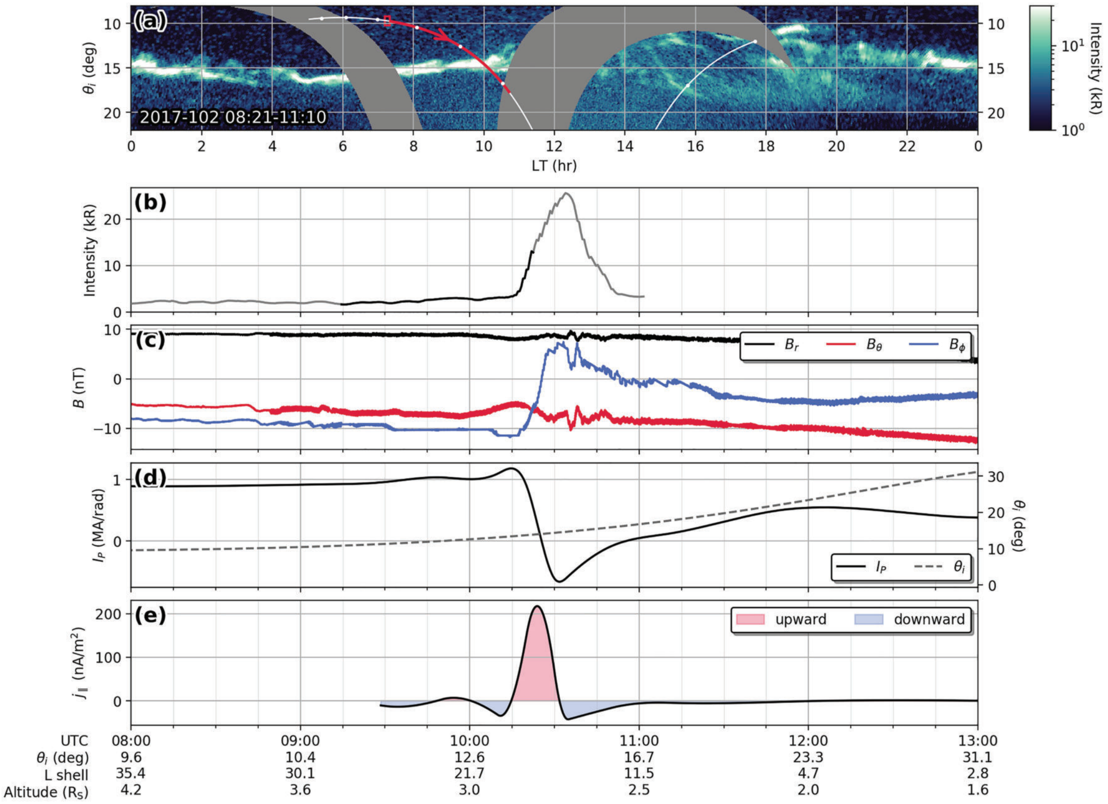

Figure 4. Magnetometer data and derived auroral currents of the 2017-102 crossing, same format as Figure 2. The black section in (b) corresponds to the UVIS scan across the aurorae which covers the subspacecraft region, of the three scans overall included in this exposure.

crossed. Just poleward of the auroral oval, Cassini then encountered broadband electromagnetic ELF waves (~12:15–12:30 UTC) at ~100–500 Hz. These occur together with proton flux intensifications in the lower two of INCA's energy bins (13–35 keV), indicating again the “pressure cooker” energization process taking place as ELF waves transversely energize the protons (e.g., Temerin, 1986). We note that the perpendicular electron fluxes in the 56- to 300-keV energy range drop shortly (see Figure 3d) just as the ELF waves are most intense, indicating that these may be driven by the free energy in the anisotropic electron distribution.

It may appear puzzling that panels 3a, 3c and 3d do not show periods of increased/decreased electron and ion fluxes in phase with one another. However, it is not expected that they should—the data are from three different instruments observing different parts of the velocity distribution and/or different particle species, their fields of view not overlapping at all. Differences between electrons and protons $\perp B$ (panels 3c and 3d) may, for example, arise due to parallel electric fields trapping protons while further accelerating electrons, leading to increased proton and decreased electron fluxes $\perp B$. Proton observations $\|B$ and $\perp B$ (Figure 3a/3c) show signatures at different energies moving at different angles to the magnetic field, so it is likely that populations of different origins are being observed which further complicates matters and limits the applicability of a simple comparison between the respective panels.

3.2. Crossing the Bright Auroral Arc at Northern Dawn: 2017-102

Figures 4 and 5 show observations from a crossing of the northern aurorae between local dawn and noon on 2017-102, in the same format as Figures 2 and 3. The aurorae are again relatively patchy near dusk, but where Cassini crosses the main oval, there is a bright arc of emission (Figure 4a). The thin band of the main auroral oval is located at slightly different latitudes throughout local time, as the oval is not centered on Saturn's northern pole but slightly displaced toward midnight and dawn (e.g., Bader et al., 2019; Nichols et al., 2016). In this example, the crossing is in the equatorward direction. The auroral intensity along Cassini's footprint (Figure 4b) forms a clear peak reaching a brightness of more than 20 kR, coinciding rather well with a similarly clear peak in the upward FAC (Figure 4e) as derived from magnetic field data (Figure 4c).

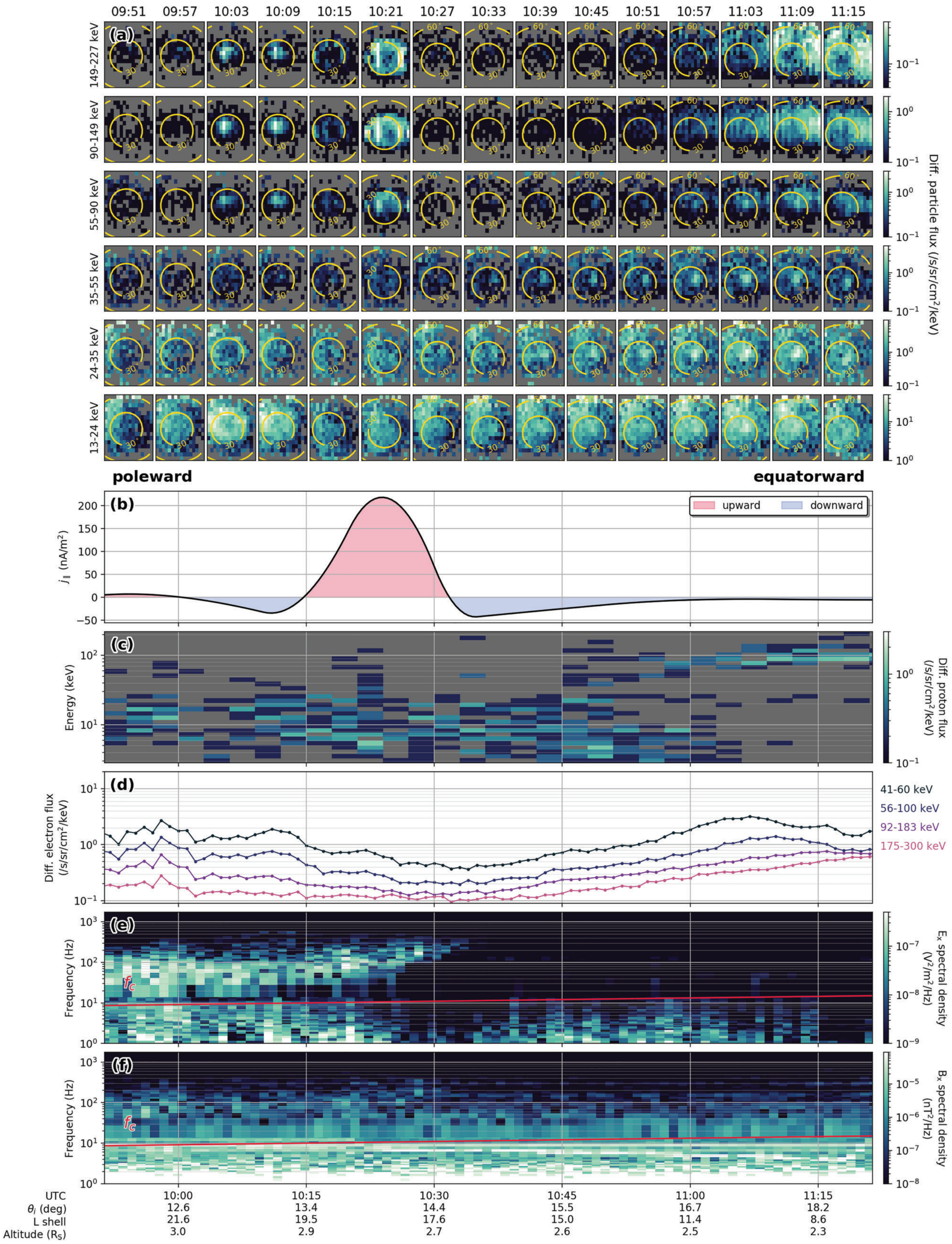

Figure 5. Overview of Cassini particle and wave measurements from 2017-102, same format as Figure 3.

The peak FAC reaches more than 200 nA/m^2, more than twice the average current density typically observed during Cassini's F-ring orbits (Hunt et al., 2018).

The particle data collected by the INCA detector (see Figure 5a) show only few similarities to the auroral pass presented in the previous section—the plasma seems rather ambient, except for the occurrence of faint proton beams at 13–55 keV equatorward of the auroral oval which may be accompanied by high-energy proton conics near the end of the observation window. Poleward of the aurorae, between ~10:05 and 10:25 UTC, the 55- to 227-keV energy range is dominated by a proton beam which seems to develop into a conic feature as Cassini moves into the main upward current region. This conic is entirely located outside the loss cone (~5) and disappears as the auroral brightness peak is encountered. No conclusive features are visible in the LEMMS energetic proton and electron flux measurements, again obtained perpendicular to the magnetic field (see panels 5c and 5d).

We now focus on the proton beam/conic just poleward of the main auroral arc, which exhibits a clear low energy cutoff above 50 keV throughout its observation—indicating that it may have been created through the “pressure cooker” process in a strong static electric field. The high energy of this feature may suggest that the electric field structure may be U-shaped and not coupled to the ionosphere (Hwang et al., 2009a, 2009b). We note that the ion conic at 10:21 UTC exhibits some vertical striping; this is an effect of the INCA detector running in neutral mode as mentioned in section 2.3. Due to the similarity in energy, it may seem reasonable to assume that the same proton population or acceleration structure is observed both as a beam and as a conic. Over the course of the observation of this feature, Cassini moved from an altitude of ~3 to ~2.8 R_S, which could explain the gradual development from a beam feature into a conic feature due to the increase in magnetic field strength. To verify this, we use the most recent magnetic field model of Saturn (Dougherty et al., 2018) and trace the magnetic field line in both directions to determine the conic's mirror altitude and its expected change in pitch angle over the radial distance covered by Cassini during the observation. This is done assuming conservation of the first adiabatic invariant and purely transverse acceleration at the source location such that

$$\frac{B_{s/c}}{B} = \frac{\sin^2(\alpha_{s/c})}{\sin^2(\alpha)}, \tag{5}$$

holds, as done recently, for example, at Jupiter (Clark et al., 2017b). $B_{s/c}$ and $\alpha_{s/c}$ are hereby the total magnetic field strength and the conic angle measured at the spacecraft, respectively, and B and α the same properties at another location along the field line.

We find the mirror altitude of the transversely accelerated protons—the altitude at/above which the transverse energization takes place—by solving for $\alpha = 90°$, starting with a cone angle of $\alpha_{s/c} \approx 30°$ at Cassini's location at 10:21 UTC. With this basic approach, the transverse acceleration of this proton conic is determined to take place at an altitude of ~2.4 R_S, far above the ionosphere. Tracing the field line outward, the conic observed at 10:21 UTC is expected to be collapsed to ~20 cone angle at ~3 R_S, Cassini's altitude during the first observation of this signature at 10:03 UTC. This opening angle is barely resolvable with INCA; the evolution of this feature may hence occur both due to Cassini moving closer toward the acceleration region and due to a latitudinal structure being crossed, similar to observations at Earth (e.g., Andersson et al., 2002). However, we note that the conic observed at 10:21 UTC may alternatively be a result of transverse acceleration of upward proton beams in an upward current region (“elevated conic”) unrelated to the proton beams observed shortly before (collapsed “pressure cooker” conic).

The lower energy cutoff of this proton beam can provide us with an estimate of the parallel potential drop trapping the protons in the acceleration region. For trapping to occur, the magnetic mirror force acting to drive the protons into regions of lower field strength has to at least be balanced by the downward force due to the electric field $E_\parallel$,

$$\mu \frac{\mathrm{dB}}{\mathrm{dz}} = qE_\parallel, \tag{6}$$

where μ is the magnetic moment, $\frac{\mathrm{dB}}{\mathrm{dz}}$ the gradient of the magnetic field strength along the field line, and q the charge of a proton. The electric field strength is then given by

$$E_{\|}(\mathrm{V/m}) = \frac{\varepsilon_{\perp}(\mathrm{eV})}{B} \cdot \frac{\mathrm{dB}}{\mathrm{dz}}, \tag{7}$$

with $\varepsilon_{\perp}$ as the perpendicular energy—the magnetic moment μ is directly related to $\varepsilon_{\perp}$. In order to trap protons up to 50 keV, a parallel electric field of ~0.74 mV/m is required at the inferred mirror location of the observed conic; roughly an order of magnitude higher than similar fields at Earth (Gorney et al., 1985).

The appearance of faint upward proton beams at ~24–55 keV and signatures of accelerated protons above ~90 keV after the auroral crossing is likely the result of Cassini moving closer toward the ionosphere while still being close to the auroral region. However, these features are relatively weak and significantly equatorward of the main upward current region; they may hence be related a second upward current sheet which is observed in magnetic field measurements (Hunt et al., 2014, 2018).

3.3. Mean Auroral Electron Energy

In the previous section we have presented auroral observations closely coincident with Cassini's crossing of the related FACs which were derived using magnetic field measurements; combining these parameters allows us to infer the mean energy of the precipitating electrons. Knight (1973) theory describes the relation between the field-aligned voltage and the FAC carried by precipitating electrons, and building on that a relationship between the energy flux incident on the upper ionosphere and energy of electrons precipitating through a steady-state parallel potential drop was first formulated by Lundin and Sandahl (1978). This has been applied to Jupiter's and Saturn's FAC systems in several previous studies which provide more detailed discussions of this topic (e.g., Cowley & Bunce, 2001; Cowley et al., 2003; Gustin, 2004, 2016, 2017; Ray et al., 2010, 2013; Tao et al., 2014). The initially rather cumbersome relations can be approximated with a linear relation if the mirror ratio R_x (ratio of the magnetic field strengths in the ionosphere and at the top of the acceleration region) is much larger than the ratio between the energy of the potential drop, $e\phi$, and the average thermal energy of the electron distribution at the top of the acceleration region, $k_B T_e$, that is, $1 \ll \frac{e\phi}{k_B T_e} \ll R_x$ (Lyons, 1980). Assuming the top of the auroral acceleration region to be located at altitude of ~2.4 R_S as estimated in the previous section, we obtain a mirror ratio of only $R_x \approx$ 30–40—limiting the full applicability of this approximation but indicating that it should serve to provide a rough estimate (e.g., Ray et al., 2009). As such, the relation between the precipitating energy flux E_f, the FAC density $j_{\|}$, and the mean electron energy $\langle W \rangle$ in the planet's ionosphere is given by

$$\langle W \rangle = e\phi = e\frac{E_f}{j_{\|}}. \tag{8}$$

The precipitating energy flux is obtained from the auroral brightness using a conversion factor of 1 mW/m^2 per 10 kR (e.g., Gérard & Singh, 1982; Grodent et al., 2001; Waite et al., 1983) and shown in Figure 6a/6d for the two auroral passes investigated in this study. Before deriving the mean electron energy, we cross-correlate the precipitating energy flux with the FAC current density which was derived from magnetic field measurements (see section 2). This is done to account for a possible motion of the auroral emissions between the time at which they were observed by UVIS and the time at which the spacecraft footprint passed over; as well as for uncertainties in the magnetic mapping of the spacecraft footprint and in the spacecraft pointing and subsequently the projection of UVIS images. We find E_f and $j_{\|}$ to correlate best if one of the two data sets is shifted by 165 s (2017-009) and 540 s (2017-102), respectively.

The original and shifted FAC densities are displayed in Figure 6b/6e. We compare E_f and $j_{\|}$ whenever $j_{\|}$ increases above 20% of its maximum value observed during the crossing of the aurorae; the 20% limit is indicated with a horizontal red line, and the time spans considered are shaded in red. Figure 6c/6f shows $\langle W \rangle$ within the intervals investigated. In all three passes, the mean electron energy seems to increase toward the edges of the auroral arcs crossed. This may be a physical feature but may also be an effect of the limited spatial resolution of UVIS and the filtering employed when determining the auroral brightness at the ionospheric footprint of the spacecraft, artificially broadening the auroral arc and consequently the width of the peaks observed in E_f.

We determine a mean electron energy for the center of each of the three auroral passes when E_f and $j_{\|}$ reach their peak values; we obtain values of ~4 and ~2.5 keV for the two auroral patches on 2017-009 and ~12 keV for the crossing of the bright arc on 2017-102. These values fit well into the 1- to 11- and 7- to 17-keV ranges statistically determined by Gustin et al. (2017) using the Lyα/H$_2$ method and the hydrocarbon/color ratio

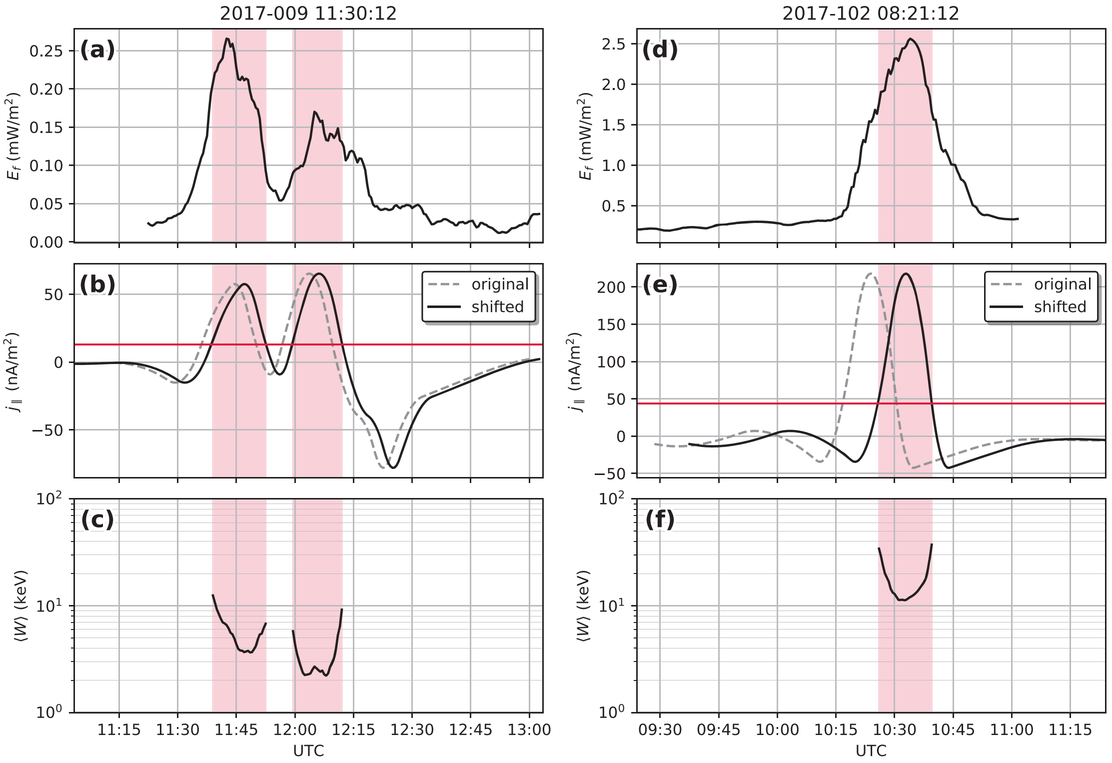

Figure 6. Estimation of the mean energy of precipitating auroral electrons. (a, d) Energy flux E_f derived from the auroral intensity at the magnetically mapped spacecraft footprint. (b, e) FAC density $j_\parallel$ inferred from magnetometer measurements (gray-dashed) and shifted for maximum correlation with the energy flux (black). All data points above the red horizontal line (20% of the maximum value) are considered for deriving the mean energy, the corresponding time spans shaded red. (c, f) Mean electron energy in the red shaded sections. Note the logarithmic scale.

method, respectively. Their LT distribution of statistical mean electron energies shows values of 10–20 keV near the northern prenoon aurorae and 1–10 keV near the southern predusk aurorae in good agreement with the two case studies presented here.

4. Conclusions and Summary

The two auroral passes presented above involve a number of different processes all occurring in the vicinity of auroral field lines. Figure 7 attempts to put our observations into context, using an idealized sketch of neighboring upward and downward current regions.

On 2017-102, Cassini observed a high-energy proton conic with a lower energy cutoff, likely associated with a high-altitude crossing of a downward current region poleward of the main oval. No proton features could be observed as the main upward current region was traversed, but a weak proton beam equatorward of the auroral oval increased in intensity with decreasing spacecraft altitude.

Cassini's poleward pass on 2017-009 began with observations of intense antiplanetward proton beams in the main upward current region, accompanied by low-frequency electric field perturbations. Subsequently, a downward current region was crossed at an altitude of ~2.2 R_S, which roughly corresponds to the inferred source altitude of the proton conics observed on the 2017-102 pass. Large increases in parallel and perpendicular proton fluxes at all energies seem to confirm that a “pressure cooker”-like source region was crossed, although only some wave activity below the proton cyclotron frequency and in the ELF frequency range could be observed. A subsequent upward current region was identified from magnetic field data as Cassini crossed a second auroral patch, coinciding with weak proton beams and followed by a second downward current region at the poleward edge of the aurorae where strong ELF wave activity was found to modify the local electron and proton distributions.

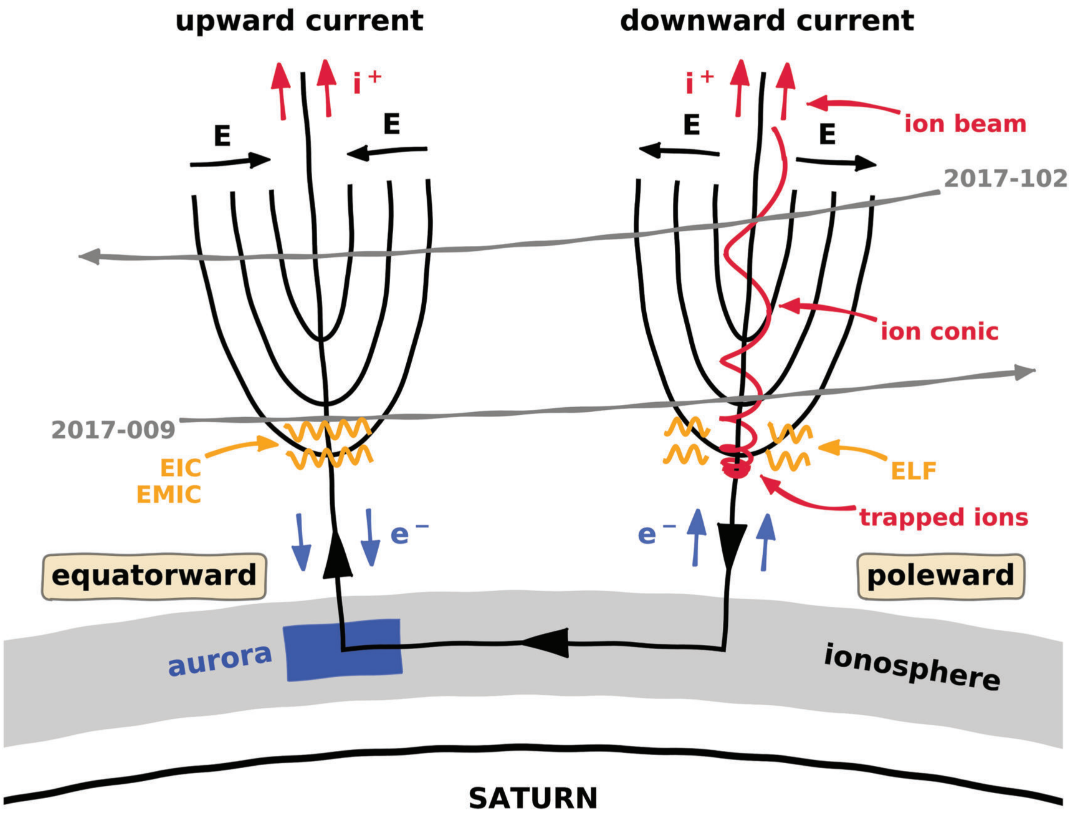

Figure 7. Conceptual sketch of neighboring upward and downward current regions, with possible trajectories of Cassini during the two auroral passes presented in this study. Based on Carlson et al. (1998) and Marklund et al. (2001).

We find that the auroral acceleration region at Saturn appears to be located at an altitude below ~2.4 R_S and the two events we analyzed in this study may correspond to one spacecraft pass above and one pass through it. The processes observed in the vicinity of the acceleration region seem to be similar to those occurring the terrestrial and Jovian auroral acceleration region, as is evidenced by the close agreement of particle beam structures and wave types observed.

Accelerated upward proton beams in upward current regions reach energies of up to ~90 keV, with the associated precipitating electrons exhibiting mean energies of order 10 keV. These energies are consistent with findings by Mitchell et al. (2009) and similar to those found at Jupiter (e.g., Clark et al., 2017a, 2017b) but about a hundred times more energetic than at Earth (e.g., Carlson et al., 1998; Gorney et al., 1985). The acceleration seems to be of a broadband nature, but it is not clear whether it is driven by Alfvén waves like at Jupiter (Gershman et al., 2019; Saur et al., 2018) or by static electric potentials similar to Earth's (e.g., Carlson et al., 1998; Ergun et al., 1998; Evans, 1968; Knight, 1973). As we do not find any evidence of wave activity of sufficient magnitude to produce the accelerated proton populations observed, we suggest that strong parallel electric potentials may be responsible for the acceleration of particles along auroral field lines. How these potentials are generated and maintained and how they vary spatially and temporally are crucial questions in auroral physics and the topic of ongoing research both at Earth and the outer planets.

Proton conics observed above the acceleration region imply perpendicular proton acceleration to take place in downward current regions. The lower energy cutoff of the signature at some ~50 keV supports our reasoning for the existence of strong parallel fields, which in downward current regions act to trap ions until these reach sufficiently high energies allowing them to escape. The perpendicular energization may occur through various wave-particle interaction processes, but a detailed investigation cannot be performed as the responsible acceleration process and the resulting accelerated particles can usually not be observed by a single spacecraft at the same time. The exact workings of perpendicular heating are, however, the topic of intensive research in the terrestrial auroral regions.

Acknowledgments
Cassini operations are supported by NASA (managed by the Jet Propulsion Laboratory) and European Space Agency (ESA). All data used in this study is available on NASA's Planetary Data System (PDS) (https://pds.jpl.nasa.gov/). A. B. was funded by a Lancaster University FST studentship. S. V. B., L. C. R., D. A. C., and J. K. were supported by STFC Grant ST/R000816/1. S. V. B. was also supported by an STFC Ernest Rutherford FellowshipST/M005534/1. G. J. H. was supported by STFC Grant ST/N000692/1.

References

Allegrini, F., Bagenal, F., Bolton, S., Connerney, J., Clark, G., Ebert, R. W., & Zink, J. L. (2017). Electron beams and loss cones in the auroral regions of Jupiter: Jupiter auroral electrons. *Geophysical Research Letters*, *44*, 7131–7139. https://doi.org/10.1002/2017GL073180

Andersson, L., Ergun, R. E., Newman, D. L., McFadden, J. P., Carlson, C. W., & Su, Y. J. (2002). Characteristics of parallel electric fields in the downward current region of the aurora. *Physics of Plasmas*, *9*(8), 3600–3609. https://doi.org/10.1063/1.1490134

André, M. (1986). Electrostatic ion waves generated by ion loss-cone distributions in the magnetosphere. *Annales Geophysicae*, *4*, 241–246.

André, M. (1997). Waves and wave-particle interactions in the auroral region. *Journal of Atmospheric and Solar-Terrestrial Physics*, *59*(14), 1687–1712. https://doi.org/10.1016/S1364-6826(96)00173-3

André, M., Crew, G. B., Peterson, W. K., Persoon, A. M., Pollock, C. J., & Engebretson, M. J. (1990). Ion heating by broadband low-frequency waves in the cusp/cleft. *Journal of Geophysical Research*, *95*(A12), 20,809–20,823. https://doi.org/10.1029/JA095iA12p20809

André, M., Koskinen, H., Gustafsson, G., & Lundin, R. (1987). Ion waves and upgoing ion beams observed by the Viking satellite. *Geophysical Research Letters*, *14*(4), 463–466. https://doi.org/10.1029/GL014i004p00463

André, M., Norqvist, P., Andersson, L., Eliasson, L., Eriksson, A. I., Blomberg, L., & Waldemark, J. (1998). Ion energization mechanisms at 1700 km in the auroral region. *Journal of Geophysical Research*, *103*, 4199–4222. https://doi.org/10.1029/97JA00855

Bader, A., Badman, S. V., Cowley, S. W. H., Yao, Z. H., Ray, L. C., Kinrade, J., & Pryor, W. R. (2019). The dynamics of Saturn's main aurorae. *Geophysical Research Letters*, *46*, 10,283–10,294. https://doi.org/10.1029/2019GL084620

Bader, A., Badman, S. V., Kinrade, J., Cowley, S. W. H., Provan, G., & Pryor, W. (2019). Modulations of Saturn's UV auroral oval location by planetary period oscillations. *Journal of Geophysical Research: Space Physics*, *124*, 952–970. https://doi.org/10.1029/2018JA026117

Bader, A., Badman, S. V., Yao, Z. H., Kinrade, J., & Pryor, W. R. (2019). Observations of continuous quasiperiodic auroral pulsations on Saturn in high time-resolution UV auroral imagery. *Journal of Geophysical Research: Space Physics*, *124*, 2451–2465. https://doi.org/10.1029/2018JA026320

Badman, S. V., Achilleos, N., Arridge, C. S., Baines, K. H., Brown, R. H., Bunce, E. J., & Tao, C. (2012). Cassini observations of ion and electron beams at Saturn and their relationship to infrared auroral arcs. *Journal of Geophysical Research*, *117*, A01211. https://doi.org/10.1029/2011JA017222

Ball, L., & André, M. (1991). What parts of broadband spectra are responsible for ion conic production? *Geophysical Research Letters*, *18*(9), 1683–1686. https://doi.org/10.1029/91GL00169

Bunce, E. J., Arridge, C. S., Clarke, J. T., Coates, A. J., Cowley, S. W. H., Dougherty, M. K., & Talboys, D. L. (2008). Origin of Saturn's aurora: Simultaneous observations by Cassini and the Hubble Space Telescope. *Journal of Geophysical Research*, *113*, A09209. https://doi.org/10.1029/2008JA013257

Bunce, E. J., Arridge, C. S., Cowley, S. W. H., & Dougherty, M. K. (2008). Magnetic field structure of Saturn's dayside magnetosphere and its mapping to the ionosphere: Results from ring current modeling. *Journal of Geophysical Research*, *113*, A02207. https://doi.org/10.1029/2007JA012538

Burton, M. E., Dougherty, M. K., & Russell, C. T. (2010). Saturn's internal planetary magnetic field. *Geophysical Research Letters*, *37*, L24105. https://doi.org/10.1029/2010GL045148

Carlson, C. W., McFadden, J. P., Ergun, R. E., Temerin, M., Peria, W., Mozer, F. S., & Pfaff, R. (1998). FAST observations in the downward auroral current region: Energetic upgoing electron beams, parallel potential drops, and ion heating. *Geophysical Research Letters*, *25*, 2017–2020. https://doi.org/10.1029/98GL00851

Carlson, C. W., Pfaff, R. F., & Watzin, J. G. (1998). The Fast Auroral SnapshoT (FAST) Mission. *Geophysical Research Letters*, *25*(12), 2013–2016. https://doi.org/10.1029/98GL01592

Cattell, C. A., Mozer, F. S., Roth, I., Anderson, R. R., Elphic, R. C., Lennartsson, W., & Ungstrup, E. (1991). ISEE 1 observations of electrostatic ion cyclotron waves in association with ion beams on auroral field lines from ∼2.5 to 4.5 R_E. *Journal of Geophysical Research*, *96*(A7), 11,421–11,439. https://doi.org/10.1029/91JA00378

Chang, T. (1993). Lower-hybrid collapse, caviton turbulence, and charged particle energization in the topside auroral ionosphere and magnetosphere. *Physics of Fluids B: Plasma Physics*, *5*(7), 2646–2656. https://doi.org/10.1063/1.860702

Chang, T., Crew, G. B., Hershkowitz, N., Jasperse, J. R., Retterer, J. M., & Winningham, J. D. (1986). Transverse acceleration of oxygen ions by electromagnetic ion cyclotron resonance with broad band left-hand polarized waves. *Geophysical Research Letters*, *13*(7), 636–639. https://doi.org/10.1029/GL013i007p00636

Clark, G., Mauk, B. H., Haggerty, D., Paranicas, C., Kollmann, P., Rymer, A., & Valek, P. (2017a). Energetic particle signatures of magnetic field-aligned potentials over Jupiter's polar regions: Jovian polar acceleration region. *Geophysical Research Letters*, *44*, 8703–8711. https://doi.org/10.1002/2017GL074366

Clark, G., Mauk, B. H., Paranicas, C., Haggerty, D., Kollmann, P., Rymer, A., & Valek, P. (2017b). Observation and interpretation of energetic ion conics in Jupiter's polar magnetosphere. *Geophysical Research Letters*, *44*, 4419–4425. https://doi.org/10.1002/2016GL072325

Clark, G., Tao, C., Mauk, B. H., Nichols, J., Saur, J., Bunce, E. J., & Valek, P. (2018). Precipitating electron energy flux and characteristic energies in Jupiter's main auroral region as measured by Juno/JEDI. *Journal of Geophysical Research: Space Physics*, *123*, 7554–7567. https://doi.org/10.1029/2018JA025639

Cowley, S. W. H., Arridge, C. S., Bunce, E. J., Clarke, J. T., Coates, A. J., Dougherty, M. K., & Talboys, D. L. (2008). Auroral current systems in Saturn's magnetosphere: Comparison of theoretical models with Cassini and HST observations. *Annales Geophysicae*, *26*(9), 2613–2630. https://doi.org/10.5194/angeo-26-2613-2008

Cowley, S. W. H., & Bunce, E. J. (2001). Origin of the main auroral oval in Jupiter's coupled magnetosphere-ionosphere system. *Planetary and Space Science*, *49*, 1067–1088. https://doi.org/10.1016/S0032-0633(00)00167-7

Cowley, S. W. H., Bunce, E. J., & Nichols, J. D. (2003). Origins of Jupiter's main oval auroral emissions. *Journal of Geophysical Research*, *108*(A4), 8002. https://doi.org/10.1029/2002JA009329

Cowley, S. W. H., Bunce, E. J., & O'Rourke, J. M. (2004a). A simple quantitative model of plasma flows and currents in Saturn's polar ionosphere. *Journal of Geophysical Research*, *109*, A05212. https://doi.org/10.1029/2003JA010375

Cowley, S. W. H., Bunce, E. J., & Prang, R. (2004b). Saturn's polar ionospheric flows and their relation to the main auroral oval. *Annales Geophysicae*, *22*(4), 1379–1394. https://doi.org/10.5194/angeo-22-1379-2004

Cowley, S. W. H., Provan, G., Bunce, E. J., & Nichols, J. D. (2017). Magnetosphere-ionosphere coupling at Jupiter: Expectations for Juno Perijove 1 from a steady state axisymmetric physical model. *Geophysical Research Letters*, *44*, 4497–4505. https://doi.org/10.1002/2017GL073129

Dougherty, M. K., Cao, H., Khurana, K. K., Hunt, G. J., Provan, G., Kellock, S., & Southwood, D. J. (2018). Saturn's magnetic field revealed by the Cassini Grand Finale. *Science*, *362*, 6410. https://doi.org/10.1126/science.aat5434

Dougherty, M. K., Kellock, S., Southwood, D. J., Balogh, A., Smith, E. J., Tsurutani, B. T., & Cowley, S. W. H. (2004). The Cassini magnetic field investigation. *Space Science Reviews*, *114*(1-4), 331–383. https://doi.org/10.1007/978-1-4020-2774-1_4

Ebert, R. W., Allegrini, F., Bagenal, F., Bolton, S. J., Connerney, J. E. P., Clark, G., & Wilson, R. J. (2017). Spatial distribution and properties of 0.1-100 keV electrons in Jupiter's polar auroral region: Electrons over Jupiter's poles. *Geophysical Research Letters*, *44*, 9199–9207. https://doi.org/10.1002/2017GL075106

Ergun, R. E., Carlson, C. W., McFadden, J. P., Mozer, F. S., Delory, G. T., Peria, W., & Kistler, L. (1998). FAST satellite observations of electric field structures in the auroral zone. *Geophysical Research Letters*, *25*(12), 2025–2028. https://doi.org/10.1029/98GL00635

Esposito, L. W., Barth, C. A., Colwell, J. E., Lawrence, G. M., McClintock, W. E., Stewart, A. I. F., & Yung, Y. L. (2004). The Cassini ultraviolet imaging spectrograph investigation. *Space Science Reviews*, *115*(1-4), 299–361. https://doi.org/10.1007/s11214-004-1455-8

Evans, D. S. (1968). The observations of a near monoenergetic flux of auroral electrons. *Journal of Geophysical Research*, *73*(7), 2315–2323. https://doi.org/10.1029/JA073i007p02315

Garbe, G. P., Arnold, R. L., Moore, T. E., Kintner, P. M., & Vago, J. L. (1992). Observations of transverse ion acceleration in the topside auroral ionosphere. *Journal of Geophysical Research*, *97*(A2), 1257–1269. https://doi.org/10.1029/91JA02127

Gershman, D. J., Connerney, J. E. P., Kotsiaros, S., DiBraccio, G. A., Martos, Y. M., Vimas, A. F., & Bolton, S. J. (2019). Alfvénic fluctuations associated with Jupiter's auroral emissions. *Geophysical Research Letters*, *46*, 7157–7165. https://doi.org/10.1029/2019GL082951

Gorney, D. J., Chiu, Y. T., & Croley, D. R. (1985). Trapping of ion conics by downward parallel electric fields. *Journal of Geophysical Research*, *90*(A5), 4205–4210. https://doi.org/10.1029/JA090iA05p04205

Gérard, J. C., Bonfond, B., Gustin, J., Grodent, D., Clarke, J. T., Bisikalo, D., & Shematovich, V. (2009). Altitude of Saturn's aurora and its implications for the characteristic energy of precipitated electrons. *Geophysical Research Letters*, *36*, L02202. https://doi.org/10.1029/2008GL036554

Gérard, J. C., & Singh, V. (1982). A model of energy deposition of energetic electrons and EUV emission in the Jovian and Saturnian atmospheres and implications. *Journal of Geophysical Research*, *87*(A6), 4525–4532. https://doi.org/10.1029/JA087iA06p04525

Grodent, D., Waite, J. H., & Grard, J. C. (2001). A self-consistent model of the Jovian auroral thermal structure. *Journal of Geophysical Research*, *106*(A7), 12,933–12,952. https://doi.org/10.1029/2000JA900129

Gurnett, D. A., Huff, R. L., Menietti, J. D., Burch, J. L., Winningham, J. D., & Shawhan, S. D. (1984). Correlated low-frequency electric and magnetic noise along the auroral field lines. *Journal of Geophysical Research*, *89*(A10), 8971. https://doi.org/10.1029/JA089iA10p08971

Gurnett, D. A., Kurth, W. S., Kirchner, D. L., Hospodarsky, G. B., Averkamp, T. F., Zarka, P., & Pedersen, A. (2004). The Cassini radio and plasma wave investigation. *Space Science Reviews*, *114*(1-4), 395–463. https://doi.org/10.1007/978-1-4020-2774-1_6

Gustin, J. (2004). Energy-flux relationship in the FUV Jovian aurora deduced from HST-STIS spectral observations. *Journal of Geophysical Research*, *109*, A10205. https://doi.org/10.1029/2003JA010365

Gustin, J., Grodent, D., Radioti, A., Pryor, W., Lamy, L., & Ajello, J. (2017). Statistical study of Saturn's auroral electron properties with Cassini/UVIS FUV spectral images. *Icarus*, *284*, 264–283. https://doi.org/10.1016/j.icarus.2016.11.017

Gustin, J., Grodent, D., Ray, L., Bonfond, B., Bunce, E., Nichols, J., & Ozak, N. (2016). Characteristics of North Jovian aurora from STIS FUV spectral images. *Icarus*, *268*, 215–241. https://doi.org/10.1016/j.icarus.2015.12.048

Hamrin, M., Norqvist, P., Hellstrom, T., André, M., & Eriksson, A. I. (2002). A statistical study of ion energization at 1700 km in the auroral region. *Annales Geophysicae*, *20*, 1943–1958. https://doi.org/10.5194/angeo-20-1943-2002

Hill, T. (1979). Inertial limit on corotation. *Journal of Geophysical Research*, *84*(A11), 6554. https://doi.org/10.1029/JA084iA11p06554

Hill, T. W. (2001). The Jovian auroral oval. *Journal of Geophysical Research*, *106*(A5), 8101–8107. https://doi.org/10.1029/2000JA000302

Hunt, G. J., Cowley, S. W. H., Provan, G., Bunce, E. J., Alexeev, I. I., Belenkaya, E. S., & Coates, A. J. (2014). Field-aligned currents in Saturn's southern nightside magnetosphere: Subcorotation and planetary period oscillation components. *Journal of Geophysical Research: Space Physics*, *119*, 9847–9899. https://doi.org/10.1002/2014JA020506

Hunt, G. J., Cowley, S. W. H., Provan, G., Bunce, E. J., Alexeev, I. I., Belenkaya, E. S., & Coates, A. J. (2015). Field-aligned currents in Saturn's northern nightside magnetosphere: Evidence for interhemispheric current flow associated with planetary period oscillations. *Journal of Geophysical Research: Space Physics*, *120*, 7552–7584. https://doi.org/10.1002/2015JA021454

Hunt, G. J., Cowley, S. W. H., Provan, G., Bunce, E. J., Alexeev, I. I., Belenkaya, E. S., & Coates, A. J. (2016). Field-aligned currents in Saturn's magnetosphere: Local time dependence of southern summer currents in the dawn sector between midnight and noon. *Journal of Geophysical Research: Space Physics*, *121*, 7785–7804. https://doi.org/10.1002/2016JA022712

Hunt, G. J., Provan, G., Bunce, E. J., Cowley, S. W. H., Dougherty, M. K., & Southwood, D. J. (2018). Field-aligned currents in Saturn's magnetosphere: Observations from the F-ring orbits. *Journal of Geophysical Research: Space Physics*, *123*, 3806–3821. https://doi.org/10.1029/2017JA025067

Hwang, K. J., Lynch, K. A., Newman, D. L., & Carlson, C. W. (2009a). FAST observations of downward current regions: Effect of ionospheric constraints on parallel signatures. *Journal of Geophysical Research*, *114*, A02219. https://doi.org/10.1029/2008JA013080

Hwang, K. J., Lynch, K. A., Newman, D. L., & Carlson, C. W. (2009b). FAST observations of downward current regions: Effect of magnetospheric conditions on the parallel potential drop. *Journal of Geophysical Research*, *114*, A02218. https://doi.org/10.1029/2008JA013079

Kaufmann, R. L., & Kintner, P. M. (1982). Upgoing ion beams: 1. Microscopic analysis. *Journal of Geophysical Research*, *87*(A12), 10487. https://doi.org/10.1029/JA087iA12p10487

Kindel, J. M., & Kennel, C. F. (1971). Topside current instabilities. *Journal of Geophysical Research*, *76*(13), 3055–3078. https://doi.org/10.1029/JA076i013p03055

Kintner, P. M., Kelley, M. C., Sharp, R. D., Ghielmetti, A. G., Temerin, M., Cattell, C., & Fennell, J. F. (1979). Simultaneous observations of energetic (keV) upstreaming and electrostatic hydrogen cyclotron waves. *Journal of Geophysical Research*, *84*(A12), 7201–7212. https://doi.org/10.1029/JA084iA12p07201

Kintner, P. M., Vago, J., Chesney, S., Arnoldy, R. L., Lynch, K. A., Pollock, C. J., & Moore, T. E. (1992). Localized lower hybrid acceleration of ionospheric plasma. *Physical Review Letters*, *68*(16), 2448–2451. https://doi.org/10.1103/PhysRevLett.68.2448

Klumpar, D. M. (1979). Transversely accelerated ions: An ionospheric source of hot magnetospheric ions. *Journal of Geophysical Research*, *84*(A8), 4229–4237. https://doi.org/10.1029/JA084iA08p04229

Knight, S. (1973). Parallel electric fields. *Planetary and Space Science*, *21*(5), 741–750. https://doi.org/10.1016/0032-0633(73)90093-7

Kotsiaros, S., Connerney, J. E. P., Clark, G., Allegrini, F., Gladstone, G. R., Kurth, W. S., & Levin, S. M. (2019). Birkeland currents in Jupiter's magnetosphere observed by the polar-orbiting Juno spacecraft. *Nature Astronomy*, *3*, 904–909. https://doi.org/10.1038/s41550-019-0819-7

Krimigis, S. M., Mitchell, D. G., Hamilton, D. C., Livi, S., Dandouras, J., Jaskulek, S., & Williams, D. J. (2004). Magnetosphere Imaging Instrument (MIMI) on the Cassini Mission to Saturn/Titan. *Space Science Reviews*, *114*(1-4), 233–329. https://doi.org/10.1007/978-1-4020-2774-1_3

Lamy, L., Cecconi, B., Zarka, P., Canu, P., Schippers, P., Kurth, W. S., & Louarn, P. (2011). Emission and propagation of Saturn kilometric radiation: Magnetoionic modes, beaming pattern, and polarization state. *Journal of Geophysical Research*, *116*, A04212. https://doi.org/10.1029/2010JA016195

Lamy, L., Zarka, P., Cecconi, B., Prang, R., Kurth, W. S., Hospodarsky, G., & Hunt, G. J. (2018). The low-frequency source of Saturn's kilometric radiation. *Science*, *362*(6410), eaat2027. https://doi.org/10.1126/science.aat2027

Le Quau, D., Roux, A., Rauch, J. L., Lefeuvre, F., & Bosqued, J. M. (1993). Heating of protons by resonant absorption in a multicomponent plasma: 2. Theoretical model. *Journal of Geophysical Research*, *98*(A8), 13,363–13,375. https://doi.org/10.1029/91JA02186

Lundin, R., & Sandahl, I. (1978). Some characteristics of the parallel electric field acceleration of electrons over discrete auroral arcs as observed from two rocket flights. ESA SP-135 125.

Lyons, L. (1980). Generation of large-scale regions of auroral currents, electric potentials, and precipitation by the divergence of the convection electric field. *Journal of Geophysical Research*, *85*(A1), 17–24. https://doi.org/10.1029/JA085iA01p00017

Marklund, G. T., Ivchenko, N., Karlsson, T., Fazakerley, A., & Dunlop, M. (2001). Temporal evolution of the electric field accelerating electrons away from the auroral ionosphere. *Nature*, *414*, 724–727.

Mauk, B. H., Haggerty, D. K., Paranicas, C., Clark, G., Kollmann, P., Rymer, A. M., & Valek, P. (2017a). Discrete and broadband electron acceleration in Jupiter's powerful aurora. *Nature*, *549*(7670), 66–69. https://doi.org/10.1038/nature23648

Mauk, B. H., Haggerty, D. K., Paranicas, C., Clark, G., Kollmann, P., Rymer, A. M., & Valek, P. (2017b). Juno observations of energetic charged particles over Jupiter's polar regions: Analysis of monodirectional and bidirectional electron beams: Jovian polar energetic particle beams. *Geophysical Research Letters*, *44*, 4410–4418. https://doi.org/10.1002/2016GL072286

Mauk, B. H., Haggerty, D. K., Paranicas, C., Clark, G., Kollmann, P., Rymer, A. M., & Valek, P. (2018). Diverse electron and ion acceleration characteristics observed over Jupiter's main aurora. *Geophysical Research Letters*, *45*, 1277–1285. https://doi.org/10.1002/2017GL076901

McFadden, J. P., Carlson, C. W., & Ergun, R. E. (1999). Microstructure of the auroral acceleration region as observed by FAST. *Journal of Geophysical Research*, *104*(A7), 14,453–14,480. https://doi.org/10.1029/1998JA900167

McIlwain, C. E. (1960). Direct measurement of particles producing visible auroras. *Journal of Geophysical Research*, *65*(9), 2727–2747. https://doi.org/10.1029/JZ065i009p02727

Menietti, J. D., Mutel, R. L., Schippers, P., Ye, S. Y., Gurnett, D. A., & Lamy, L. (2011). Analysis of Saturn kilometric radiation near a source center. *Journal of Geophysical Research*, *116*, A12222. https://doi.org/10.1029/2011JA017056

Menietti, J. D., Schippers, P., Santolk, O., Gurnett, D. A., Crary, F., & Coates, A. J. (2011). Ion cyclotron harmonics in the Saturn downward current auroral region. *Journal of Geophysical Research*, *116*, A12234. https://doi.org/10.1029/2011JA017102

Milan, S. E., Bunce, E. J., Cowley, S. W. H., & Jackman, C. M. (2005). Implications of rapid planetary rotation for the Dungey magnetotail of Saturn. *Journal of Geophysical Research*, *110*, A03209. https://doi.org/10.1029/2004JA010716

Milan, S. E., Lester, M., Cowley, S. W. H., Oksavik, K., Brittnacher, M., Greenwald, R. A., & Villain, J. P. (2003). Variations in the polar cap area during two substorm cycles. *Annales Geophysicae*, *21*(5), 1121–1140. https://doi.org/10.5194/angeo-21-1121-2003

Mitchell, D. G., Kurth, W. S., Hospodarsky, G. B., Krupp, N., Saur, J., Mauk, B. H., & Hamilton, D. C. (2009). Ion conics and electron beams associated with auroral processes on Saturn. *Journal of Geophysical Research*, *114*, A02212. https://doi.org/10.1029/2008JA013621

Nichols, J. D., Badman, S. V., Bunce, E. J., Clarke, J. T., Cowley, S. W. H., Hunt, G. J., & Provan, G. (2016). Saturn's northern auroras as observed using the Hubble Space Telescope. *Icarus*, *263*, 17–31. https://doi.org/10.1016/j.icarus.2015.09.008

Okuda, H., & Ashour-Abdalla, M. (1981). Formation of a conical distribution and intense ion heating in the presence of hydrogen cyclotron waves. *Geophysical Research Letters*, *8*(7), 811–814. https://doi.org/10.1029/GL008i007p00811

Paranicas, C., Mauk, B. H., Haggerty, D. K., Clark, G., Kollmann, P., Rymer, A. M., & Bolton, S. J. (2018). Intervals of intense energetic electron beams over Jupiter's poles. *Journal of Geophysical Research: Space Physics*, *123*, 1989–1999. https://doi.org/10.1002/2017JA025106

Peterson, W. K., Collin, H. L., Lennartsson, O. W., & Yau, A. W. (2006). Quiet time solar illumination effects on the fluxes and characteristic energies of ionospheric outflow. *Journal of Geophysical Research: Space Physics*, *111*, A11S05. https://doi.org/10.1029/2005JA011596

Rauch, J. L., Lefeuvre, F., Le Quau, D., Roux, A., Bosqued, J. M., & Berthelier, J. J. (1993). Heating of proton conics by resonant absorption in a multicomponent plasma: 1. Experimental evidence. *Journal of Geophysical Research*, *98*(A8), 13,347–13,361. https://doi.org/10.1029/92JA02255

Ray, L. C., Ergun, R. E., Delamere, P. A., & Bagenal, F. (2010). Magnetosphere-ionosphere coupling at Jupiter: Effect of field-aligned potentials on angular momentum transport. *Journal of Geophysical Research*, *115*, A09211. https://doi.org/10.1029/2010JA015423

Ray, L. C., Galand, M., Delamere, P. A., & Fleshman, B. L. (2013). Current-voltage relation for the Saturnian system. *Journal of Geophysical Research: Space Physics*, *118*, 3214–3222. https://doi.org/10.1002/jgra.50330

Ray, L. C., Galand, M., Moore, L. E., & Fleshman, B. (2012). Characterizing the limitations to the coupling between Saturn's ionosphere and middle magnetosphere. *Journal of Geophysical Research*, *117*, A07210. https://doi.org/10.1029/2012JA017735

Ray, L. C., Su, Y. J., Ergun, R. E., Delamere, P. A., & Bagenal, F. (2009). Current-voltage relation of a centrifugally confined plasma. *Journal of Geophysical Research*, *114*, A04214. https://doi.org/10.1029/2008JA013969

Saur, J., Janser, S., Schreiner, A., Clark, G., Mauk, B. H., Kollmann, P., & Kotsiaros, S. (2018). Wave particle interaction of Alfvén waves in Jupiter's magnetosphere: Auroral and magnetospheric particle acceleration. *Journal of Geophysical Research: Space Physics*, *123*, 9560–9573. https://doi.org/10.1029/2018JA025948

Saur, J., Mauk, B. H., Mitchell, D. G., Krupp, N., Khurana, K. K., Livi, S., & Dougherty, M. K. (2006). Anti-planetward auroral electron beams at Saturn. *Nature*, *439*(7077), 699–702. https://doi.org/10.1038/nature04401

Shen, Y., Knudsen, D. J., Burchill, J. K., Howarth, A. D., Yau, A. W., Miles, D. M., & Cogger, L. (2018). Low-altitude ion heating, downflowing ions, and BBELF waves in the return curent region. *Journal of Geophysical Research: Space Physics*, *123*, 3087–3110. https://doi.org/10.1002/2017JA024955

Singh, N., Schunk, R. W., & Sojka, J. J. (1981). Energization of ionospheric ions by electrostatic hydrogen cyclotron waves. *Geophysical Research Letters*, *8*(12), 1249–1252. https://doi.org/10.1029/GL008i012p01249

Southwood, D. J., & Kivelson, M. G. (2001). A new perspective concerning the influence of the solar wind on the Jovian magnetosphere. *Journal of Geophysical Research*, *106*(A4), 6123–6130. https://doi.org/10.1029/2000JA000236

Stasiewicz, K., Khotyaintsev, Y., Berthomier, M., & Wahlund, J. E. (2000). Identification of widespread turbulence of dispersive Alfvén waves. *Geophysical Research Letters*, *27*(2), 173–176. https://doi.org/10.1029/1999GL010696

Talboys, D. L., Arridge, C. S., Bunce, E. J., Coates, A. J., Cowley, S. W. H., & Dougherty, M. K. (2009). Characterization of auroral current systems in Saturn's magnetosphere: High-latitude Cassini observations. *Journal of Geophysical Research*, *114*, A06220. https://doi.org/10.1029/2008JA013846

Talboys, D. L., Arridge, C. S., Bunce, E. J., Coates, A. J., Cowley, S. W. H., Dougherty, M. K., & Khurana, K. K. (2009). Signatures of field-aligned currents in Saturn's nightside magnetosphere. *Geophysical Research Letters*, *36*, L19107. https://doi.org/10.1029/2009GL039867

Talboys, D. L., Bunce, E. J., Cowley, S. W. H., Arridge, C. S., Coates, A. J., & Dougherty, M. K. (2011). Statistical characteristics of field-aligned currents in Saturn's nightside magnetosphere. *Journal of Geophysical Research*, *116*, A04213. https://doi.org/10.1029/2010JA016102

Tao, C., Lamy, L., & Prang, R. (2014). The brightness ratio of H Lyman-α/H $_2$ bands in FUV auroral emissions: A diagnosis for the energy of precipitating electrons and associated magnetospheric acceleration processes applied to Saturn. *Geophysical Research Letters*, *41*, 6644–6651. https://doi.org/10.1002/2014GL061329

Temerin, M. (1986). Evidence for a large bulk ion conic heating region. *Geophysical Research Letters*, *13*(10), 1059–1062. https://doi.org/10.1029/GL013i010p01059

Tetrick, S. S., Gurnett, D. A., Kurth, W. S., Imai, M., Hospodarsky, G. B., Bolton, S. J., & Mauk, B. H. (2017). Plasma waves in Jupiter's high-latitude regions: Observations from the Juno spacecraft: Jupiter's high-latitude plasma waves. *Geophysical Research Letters*, *44*, 4447–4454. https://doi.org/10.1002/2017GL073073

Vago, J. L., Kintner, P. M., Chesney, S. W., Arnoldy, R. L., Lynch, K. A., Moore, T. E., & Pollock, C. J. (1992). Transverse ion acceleration by localized lower hybrid waves in the topside auroral ionosphere. *Journal of Geophysical Research*, *97*(A11), 16935. https://doi.org/10.1029/92JA01526

Waite, J. H., Cravens, T. E., Kozyra, J., Nagy, A. F., Atreya, S. K., & Chen, R. H. (1983). Electron precipitation and related aeronomy of the Jovian thermosphere and ionosphere. *Journal of Geophysical Research*, *88*(A8), 6143–6163. https://doi.org/10.1029/JA088iA08p06143

Walach, M. T., Milan, S. E., Murphy, K. R., Carter, J. A., Hubert, B. A., & Grocott, A. (2017). Comparative study of large-scale auroral signatures of substorms, steady magnetospheric convection events, and sawtooth events. *Journal of Geophysical Research: Space Physics*, *122*, 6357–6373. https://doi.org/10.1002/2017JA023991

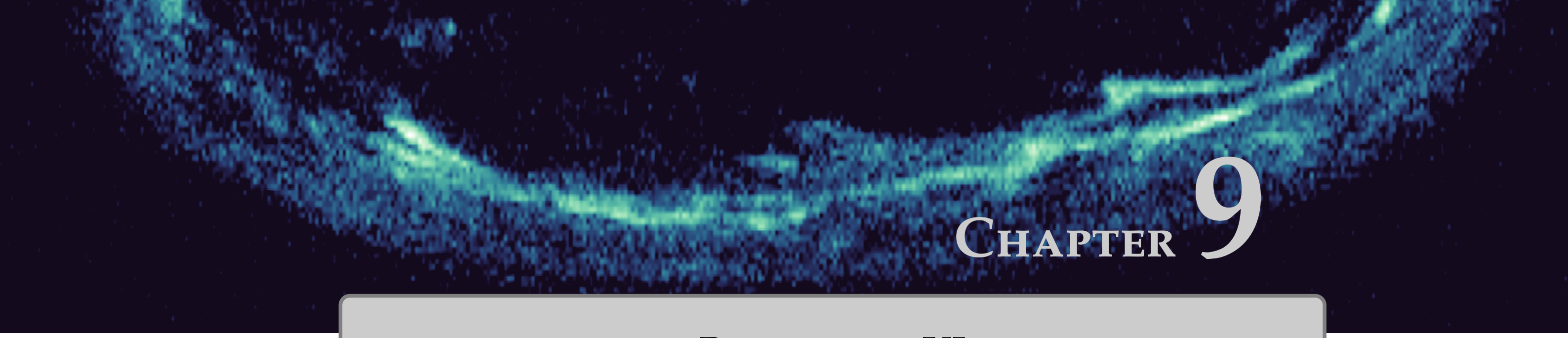

CHAPTER 9

PUBLICATION VI

The morphology of Saturn's aurorae observed during the Cassini Grand Finale

A. BADER, S. W. H. COWLEY, S. V. BADMAN, L. C. RAY, J. KINRADE, B. PALMAERTS AND
W. R. PRYOR (2020)

Geophysical Research Letters, *47*, e2019GL085800

doi:10.1029/2019GL085800

AUTHOR CONTRIBUTION STATEMENT AB conceived the study, performed the data reduction and analysis and authored the initial draft. SWHC, SVB and LCR provided guidance and expertise in all matters. JK and BP provided theoretical support concerning auroral morphology. WRP provided technical support for UVIS data. All authors contributed to the interpretation of the results and were involved in review and editing of the paper until publication.

This authorship statement was approved by all collaborating research groups.

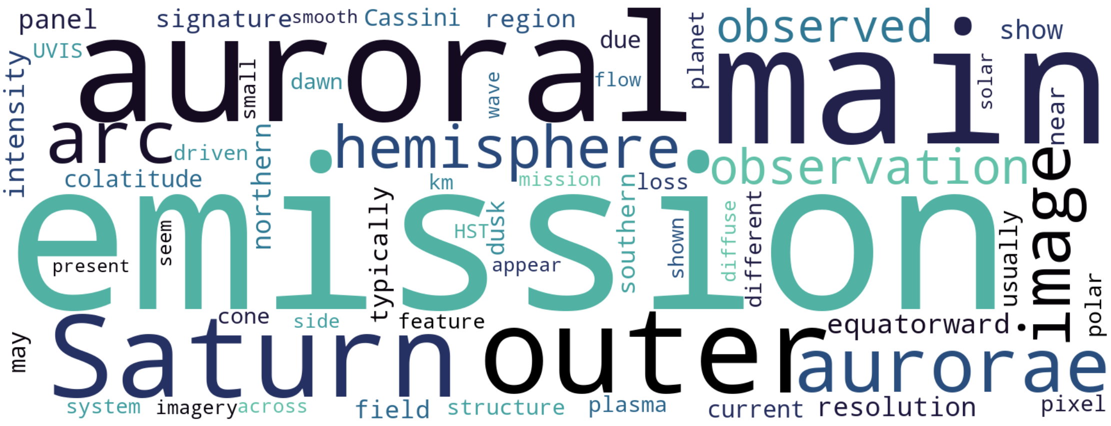

Geophysical Research Letters

RESEARCH LETTER

10.1029/2019GL085800

Key Points:
- We present observations of Saturn's ultraviolet aurorae in unprecedented resolution, revealing previously unseen small-scale features
- The main aurorae can be smooth or rippled, likely depending on magnetospheric conditions, and multiple parallel arcs are observed near dusk
- An outer emission is, although variable in brightness, always present and suggested to be driven by hot electrons from the ring current

Correspondence to:
A. Bader,
a.bader@lancaster.ac.uk

Citation:
Bader, A., Cowley, S. W. H., Badman, S. V., Ray, L. C., Kinrade, J., Palmaerts, B., & Pryor, W. R.. (2020), The morphology of Saturn's aurorae observed during the Cassini Grand Finale. *Geophysical Research Letters*, *47*, e2019GL085800. https://doi.org/10.1029/2019GL085800

Received 14 OCT 2019
Accepted 13 DEC 2019
Accepted article online 24 DEC 2019

The Morphology of Saturn's Aurorae Observed During the Cassini Grand Finale

A. Bader[1], S. W. H. Cowley[2], S. V. Badman[1], L. C. Ray[1], J. Kinrade[1], B. Palmaerts[3], and W. R. Pryor[4]

[1]Department of Physics, Lancaster University, Lancaster, UK, [2]Department of Physics and Astronomy, University of Leicester, Leicester, UK, [3]Laboratoire de Physique Atmosphérique et Planétaire, Space sciences, Technologies and Astrophysics Research (STAR) Institute, Université de Liége, Liége, Belgium, [4]Science Department, Central Arizona College, Coolidge, AZ, USA

Abstract Cassini's mission exploring the Saturn system ended with the Grand Finale, a series of orbits bringing the spacecraft closer to the planet than ever before and providing unique opportunities for observations of the ultraviolet aurorae. This study presents a selection of high-resolution imagery showing the aurorae's small-scale structure in unprecedented detail. We find the main arc to vary between a smooth and a rippled structure, likely indicating quiet and disturbed magnetospheric conditions, respectively. It is usually accompanied by a diffuse and dim outer emission on its equatorward side which appears to be driven by wave scattering of hot electrons from the inner ring current into the loss cone. The duskside is characterized by highly dynamic structures which may be signatures of radial plasma injections. This image set will be the only high-resolution data for the foreseeable future and hence forms an important basis for future auroral research on Saturn.

Plain Language Summary At the end of its mission, the Cassini spacecraft performed a set of orbits bringing it closer to Saturn than ever before. By passing over the planet's polar regions at such low altitude, its ultraviolet camera could observe Saturn's aurorae in unprecedented resolution. The observations show for the first time the detailed structure of the main auroral arc which varies between a smooth and a rippled shape, likely depending on how quiet or disturbed the plasma near Saturn is. We further find a host of small arcs and blobs near dusk whose origins are not readily explained with the current understanding of how Saturn's aurorae are driven. Diffuse features surrounding the brightest auroral emissions are attributed to hot electrons from the equatorial plane which are scattered such that they can reach Saturn's atmosphere. These observations are of unique quality and invaluable for future auroral studies.

1. Introduction

Saturn's ultraviolet (UV) aurorae consist of various morphological components located around the planet's poles. Some of these are rather static and long-lived, while others are more transient, indicating explosive energy release somewhere along the associated magnetic field lines.

The overall auroral morphology is typically dominated by the so-called "main auroral oval" or "main emission." Located at typically 15–20° colatitude from either pole (e.g., Carbary, 2012; Bader, Badman, Kinrade, et al., 2019), equatorward of Saturn's polar hexagon in the north (Pryor et al., 2019), the relatively circular bright band of main UV emission around the pole is colocated with the infrared main aurorae (e.g., Melin, et al., 2011; Badman, Achilleos, et al., 2011; Badman, Tao, et al., 2011) and expected to map to equatorial distances beyond the middle ring current (e.g., Belenkaya et al., 2014). The exact mechanism causing the acceleration of electrons into Saturn's polar ionospheres and thus generating the aurorae is unclear, but it is presumed that azimuthal flow shears between plasma populations subcorotating at different angular velocities in the outer magnetosphere may provide the required electric fields driving the observed auroral field-aligned currents (FACs) (e.g., Cowley, Bunce, & O'Rourke, 2004; Stallard et al., 2007; Talboys et al., 2009; Hunt et al., 2014; Bradley et al., 2018).

The auroral brightness varies with local time (LT), which may partly be due to the interaction of Saturn's magnetosphere with the solar wind flow. Both a static flow shear between the solar wind and magnetospheric plasma populations (e.g., Cowley, Bunce & Prangé, 2004) and viscous interaction through Kelvin-Helmholtz waves (e.g., Delamere & Bagenal, 2010; Delamere et al., 2013) could cause asymmetries arising between the dawn and dusk aurorae. Further dynamic asymmetries are known to be imposed by the rotating patterns of FACs caused by the two planetary period oscillation (PPO) current systems (e.g., Hunt et al., 2014; Bader et al., 2018) and frequent auroral plasma injections due to magnetotail reconnection (e.g., Mitchell et al., 2009; Radioti et al., 2016; Bader, Badman, Cowley, et al., 2019).

The main emission usually does not assume a fully closed circular shape but consists of multiple structures subcorotating with the planet (e.g., Grodent et al., 2005). It is not centered on Saturn's magnetic/spin pole, but slightly displaced toward the midnight-dawn direction due to the compression of the dayside magnetosphere by the solar wind and the dawn-dusk differences in auroral morphology; the location of the oval is modulated about this average position by the rotating PPO current systems (e.g., Nichols et al., 2008, 2016; Bader, Badman, Kinrade, et al., 2019). Due to the significant quadrupole moment of Saturn's internal magnetic field, effectively an offset of the internal dipole field toward the northern hemisphere, the southern oval is typically larger than the northern one (e.g., Carbary, 2012; Bader, Badman, Kinrade, et al., 2019).

The structure of the main emission is highly variable. The dawnside generally features a thin well-defined arc, while the aurorae cover a wider swath in latitude postnoon. In either of those regions the arc can include interesting substructures such as “auroral beads,” which are multiple detached and consecutive auroral spots located along the main emission which may be related to shear flow-ballooning instabilities (Radioti et al., 2019). Similar small isolated features are sometimes observed in the dayside aurora; Grodent et al. (2011) termed this the “bunch of grapes” configuration and proposed FACs driven by nonuniform plasma flow in the equatorial plane and vortices triggered by magnetopause Kelvin-Helmholtz waves as possible drivers.

Equatorward of the main aurorae a semipermanent band of emission can often be observed, the so-called “outer emission.” While first observed in Hubble Space Telescope (HST) imagery near Saturn's limb (Grodent et al., 2005, 2010), the outer emission is typically too faint to exceed the HST's detection threshold on the dayside. Nevertheless, outer emission signatures were tentatively identified in some images of the most recent HST observation campaign (Lamy et al., 2018). Cassini's Ultraviolet Imaging Spectrograph (UVIS) however provided many more observations (visible in, e.g., Radioti et al., 2017), which will here be exploited to further investigate this signature. It is believed to be caused by hot electrons between 7 and 10 R_S (Schippers et al., 2008) which may reach the ionosphere through pitch angle scattering by plasma waves (Grodent et al., 2010; Grodent, 2015; Tripathi et al., 2018).

In this study a selection of auroral imagery from Cassini's Grand Finale mission is presented. The orbit geometry of the spacecraft during this mission phase allowed the UVIS instrument to obtain imagery of unprecedented resolution, revealing previously unseen details of Saturn's aurorae and the high complexity of this dynamic system. Section 2 summarizes the processing methods used to obtain clean auroral imagery from the raw observation data, while sections 3 and 4 show and discuss different aspects of the observed morphology and signatures. We conclude this study in section 5 by summarizing our findings.

2. Data and Methods

The far-ultraviolet channel of Cassini's UVIS instrument performed observations at wavelengths between 110 and 190 nm in up to 1,024 spectral bins (Esposito et al., 2004). Its 64 spatial pixels are arranged in a single line to provide an instantaneous field of view of 64×1.5 mrad. To obtain a two-dimensional image of Saturn's auroral region, this slit was moved across the region of interest by slewing the spacecraft at a slow rate while accumulating the exposure. Depending on Cassini's distance from Saturn and the viewing geometry, repeated slews across different sections of the polar region may be necessary to construct a full auroral image. The image resulting from this process is more appropriately termed a “pseudo-image,” as different pixels in the final product have been imaged at different points in time. With exposure times sometimes reaching up to more than 2 hr, this is especially important to keep in mind when the dynamics of the auroral emissions are investigated.

Each pixel is projected onto a planetocentric polar grid with resolution 0.1° × 0.05° (longitude × latitude) using Cassini SPICE pointing information from the NASA Planetary Data System. The projection altitude is chosen to be 1,100 km above Saturn's 1-bar pressure level (defined by $R_{\mathrm{SEQ}} = 60,268$ km and $R_{\mathrm{SPO}} = 54,364$ km as Saturn's equatorial and polar radii), corresponding to the approximate altitude at which Saturn's aurorae are thought to be generated (Gérard et al., 2009). Finally, we obtain the estimated total unabsorbed H_2 auroral emission intensity in the 70–170 nm spectral range from the observed intensity in the UVIS FUV range by multiplying the intensity measured in the 155- to 162-nm band by a factor 8.1, as this minimizes hydrocarbon absorption effects (Gustin et al., 2016, 2017). Some dayglow usually remains in sunlit regions, but it can be removed as described in Bader, Badman, Yao, et al. (2019) if needed. Dayglow removal was only performed for the images shown in Figure 4 below.

Most images presented in this study were obtained from radial distances between 2 and 5 R_S, such that one UVIS pixel at the planet measures approximately 120–300 km across. This is at least comparable to three UVIS images from 2008 where a resolution of ~200 km/pixel could be achieved (Grodent et al., 2011) and represents about a tenfold increase in resolution compared to most other UVIS images which were obtained from distances between 20 and 50 R_S. The HST for comparison offers a theoretical resolution of ~150 km/pixel, but only values of >500 km/pixel can realistically be achieved due to the presence of leaking sunlight, a relatively wide point spread function, and the long exposure times required due to the high detection threshold (Grodent et al., 2011). Furthermore, the usually oblique viewing geometry from Earth orbit largely limits observations to Saturn's dayside and can lead to significant pixel stretching and limb-brightening close to the terminator region (Grodent et al., 2005).

3. Dawn-Dusk Asymmetries of the Main Aurorae

The first set of images, presented in Figure 1, shows six near-complete views of the northern and southern polar auroral regions. As has already been observed in the earliest HST campaigns imaging Saturn's aurorae before the arrival of Cassini (Gérard et al., 2004, 2005), there typically is a distinct morphological difference between the dawn and dusk emissions. The region poleward of the relatively circumpolar band of variable main emission is typically dark and featureless, unlike in infrared observations where a complete infilling of the polar cap can be observed (Stallard et al., 2008). Exceptions are small patches slightly poleward of the main oval on, for example, 2017-080/232 (Figure 1a/1d); these may be related to similar “polar dawn spots” in Jupiter's auroral emissions which appear to be signatures of internally driven magnetotail reconnection (Radioti et al., 2008, 2010). The region equatorward of the brightest aurorae often features a typically dimmer band of diffuse emission, the outer aurorae, which will be considered in more detail in the following section.

The dawnside is usually characterized by a narrow arc which, while essentially always present, shows significant variations in latitude and intensity. The latitudinal variation is thought to be controlled by the amount of open flux contained in the polar cap, by periodic displacements due to PPO FACs and by solar activity (e.g., Badman et al., 2005, 2014; Cowley et al., 2005; Bader, Badman, Kinrade, et al., 2019); the variation in intensity is less understood but seems to be influenced by solar wind conditions and PPO current systems overlaid with different transient signatures resulting from dynamic events in the magnetosphere (e.g., Bader, Badman, Cowley, et al., 2019). This auroral arc is thought to correspond to the layer of upward FAC seen in in situ field data in the same LT sector, which is located about 1° equatorward of the open-closed field line boundary and may be related to a subcorotation flow shear modulated by conductivity gradients (Hunt et al., 2014; Bradley et al., 2018).

Figure 2 shows high-resolution views of the predawn aurorae in both hemispheres, with Figure 2c presenting the highest-resolved image of Saturn's UV aurorae obtained to date where one pixel on the planet measures ~100 km across. Next to the main auroral arc an outer emission is discernible in all images, suggesting that it is continuously present but often too weak to be observed with HST or UVIS depending on the dayglow intensity and observation geometry. Both the main arc and the outer emission show an interesting substructure, which appears to be quite variable. While, for example, Figures 2a/2c/2f are characterized by a rather smooth and largely featureless main arc, Figures 2b/2d/2e show patchy or wavy substructure which may indicate disturbed magnetospheric conditions. Even the usually rather smooth outer emission shows patchy features in Figure 2a/2e. Another interesting feature is an apparent bifurcation of the main arc in Figure 2c, similar to observations of the terrestrial aurorae.

Figures 2g–2j show selected latitudinal intensity profiles of these auroral images. The main auroral arc is clearly distinguishable in most cases, being brighter than surrounding emissions by about an order of magnitude in the northern hemisphere (Figures 2g/2i) but only of comparable intensity in the south

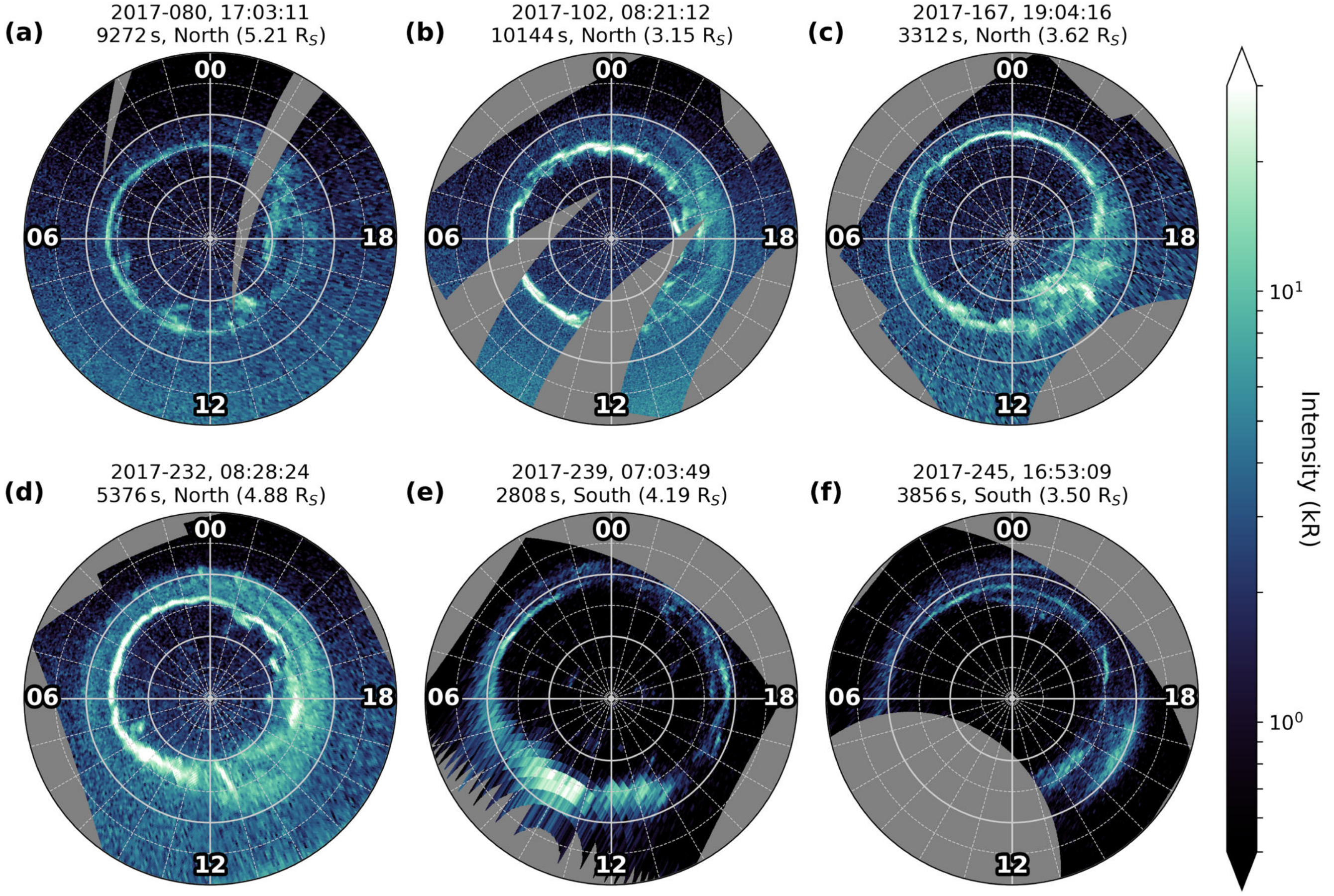

Figure 1. Selection of (nearly) full views of the (a–d) northern and (e–f) southern auroral oval obtained during Cassini's Grand Finale mission phase. The view is from above the north pole, down onto the northern or "through" the planet into the southern polar region; local noon (12 LT) is at the bottom and dawn (6 LT) at the left. Gray concentric rings mark colatitude from the pole in steps of 5°, radial lines mark local time in steps of 1 hr. The images are sorted by the time of their observation; start time, exposure time, observed hemisphere, and radial distance of Cassini from Saturn's surface are given at the top of each panel. The differences in background brightness (dayglow) between the northern and southern hemispheres are a seasonal effect; 2017 was a year of northern summer and southern winter.

(Figures 2h/2j). The width of the main arc (clearly discernible in the northern hemisphere, at ~18–19° in the southern) is typically found to be just below 1° in colatitude, or ~1,000 km in the emission layer, both in the northern and southern hemispheres.

Signatures on the duskside are of a fundamentally different nature. Instead of a defined arc, scattered patches, bifurcations, and other small-scale structures indicate disturbed magnetospheric conditions thought to be controlled by the interplay between dayside reconnection activity and Vasyliūnas cycle outflow down the magnetotail. Figure 3 shows a number of high-resolution slews across the dusk aurorae (except for Figure 3c all from the southern hemisphere) with selected colatitudinal intensity profiles shown in Figures 3i–3l. The emissions are structured at least down to the smallest resolvable scale of UVIS (here ~150 km for images from the southern hemisphere); one example is a very fine arc protruding somewhat poleward in Figure 3f (near ~ 18 LT and ~ 14° colatitude), whose full width at half maximum is ~ 0.2°, or ~200 km (see inset in Figure 3j).

Only a few similarities can be discerned among this set of images, highlighting the great temporal variability of the system, and a clear separation of the main emission and the outer emission is not usually evident. While, for example, Figures 3f–3h allow the identification of a thin main arc and a dimmer, discrete outer emission on its equatorward side, emissions in the remaining images cannot easily be classified into any of

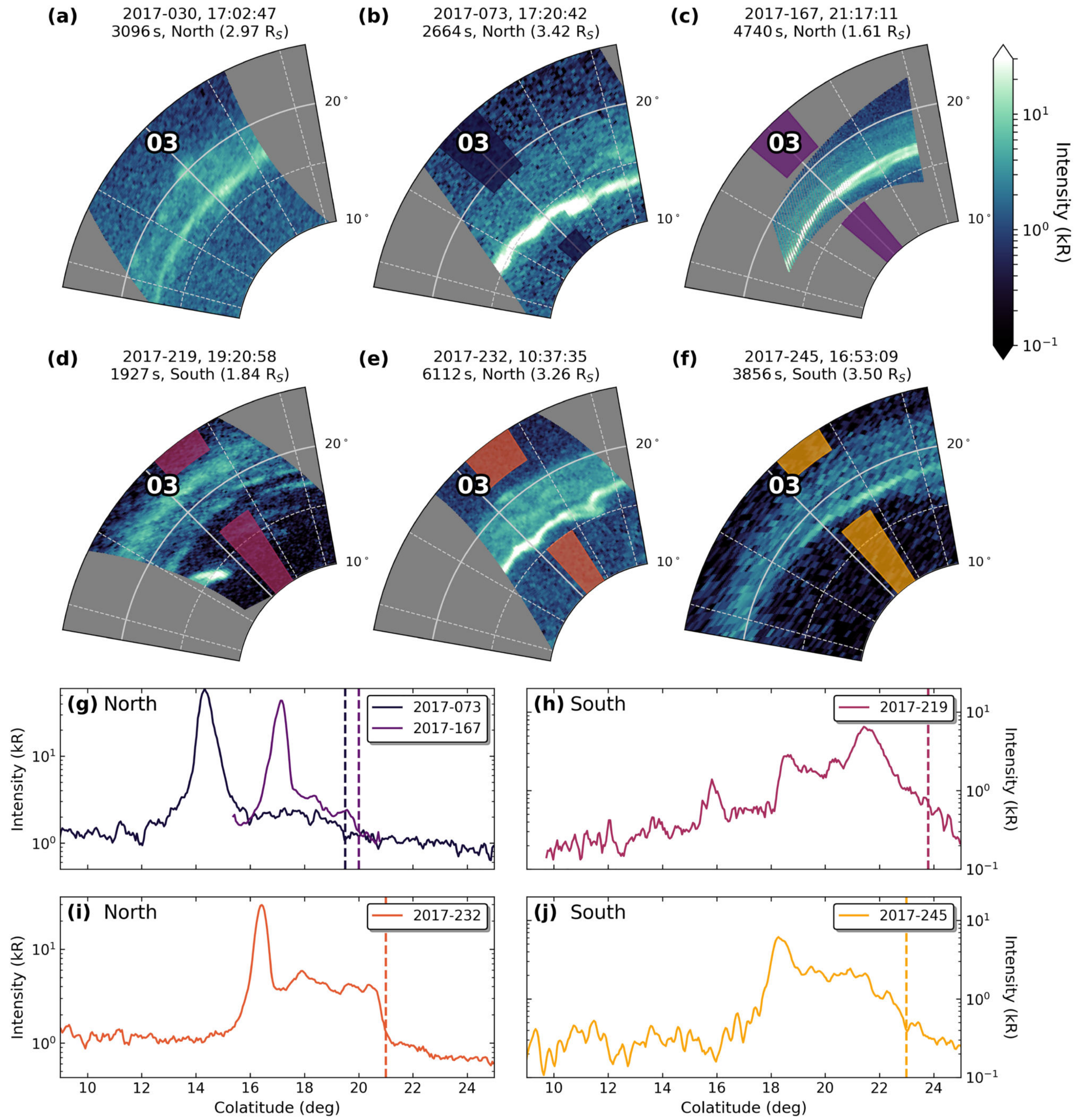

Figure 2. Selection of high-resolution imagery of Saturn's predawn main auroral arc in the (a–c, e) northern and (d, f) southern hemispheres. The view is the same as in Figure 1, but now only showing part of the polar region between roughly ~1–5 LT and 10–25° colatitude. (g–j) Latitudinal intensity profiles of panels b–f. Shown is the intensity versus colatitude averaged within within the accordingly colored regions in panels b–f. Vertical dashed lines indicate the approximate equatorward boundary of the outer emission.

the existing groups of recurrent signatures identified and investigated in previous works (e.g., Badman et al., 2015; Grodent, 2015).

Several images show single or multiple parallel arcs with various inclination across the “auroral oval.” Both 2017-219 and 2017-252 exhibit four parallel arcs oriented in the near-azimuthal direction, separated by about 1–2° colatitude each (see Figures 3c/3i and 3h/3l, respectively) and slightly more equatorward at their leading edge. While it is unclear whether one of the parallel arcs on 2017-219 corresponds to the main emission, the arcs' appearance equatorward of the main emission on 2017-252 and their extent reaching the

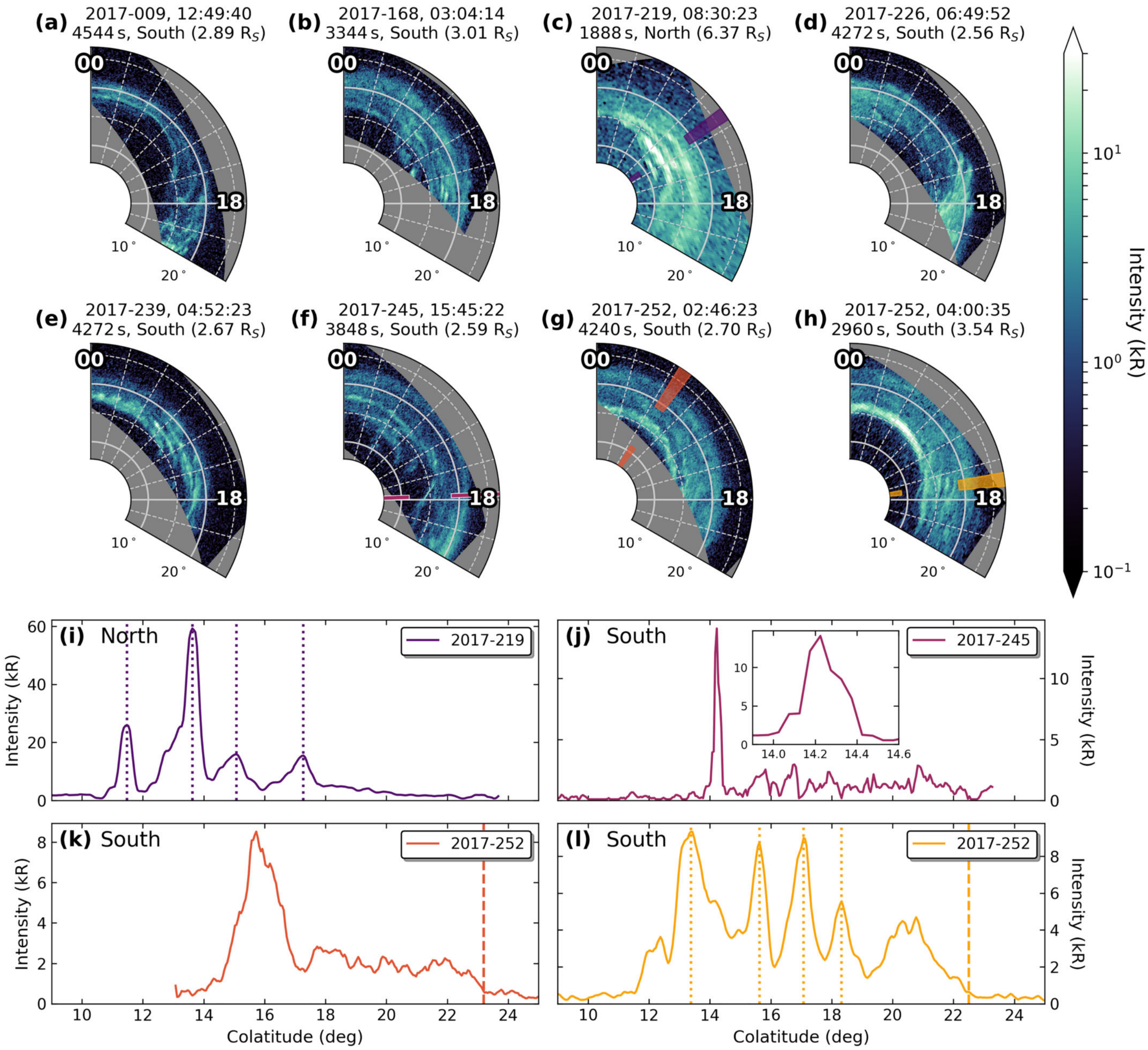

Figure 3. Selection of high-resolution imagery of Saturn's dusk auroral region in the (c) northern and (a, b, d–h) southern hemisphere. The view is the same as in Figure 1, but now only showing part of the polar region between 16 and 24 LT and between 7° and 27° colatitude. (i–l) Intensity versus colatitude averaged within (i, k, l) 40 min LT (10° longitude) or (j) 1 min LT (0.25° longitude) around the colored lines in panels c and f–h. (i, l) Parallel arcs are highlighted with dotted vertical lines. (j) An inset shows the thin intensity peak in more detail.

equatorward edge of the diffuse emission suggests a source region in the middle magnetosphere. It is thus unlikely that they are driven by solar wind interaction at the magnetopause and related to the corresponding bifurcations observed in previous studies (e.g., Radioti et al., 2011, 2013; Badman et al., 2013).

In Figures 3a/3b/3d–3f, sheared arcs of comparable size are visible, extending to later LTs with increasing colatitude. Auroral emissions are expected to rotate faster at larger colatitudes, as they are located on magnetic field lines which map into the magnetodisc closer to the planet where plasma rotates with a larger angular velocity (e.g., McAndrews et al., 2009; Thomsen et al., 2010; Wilson et al., 2017). An example of this differential rotation is visible when considering the fine arc in Figure 3f (near ~ 18 LT and ~ 14° colatitude). While the arc is still rather diagonal in this image, the exposure taken directly after this image (shown in

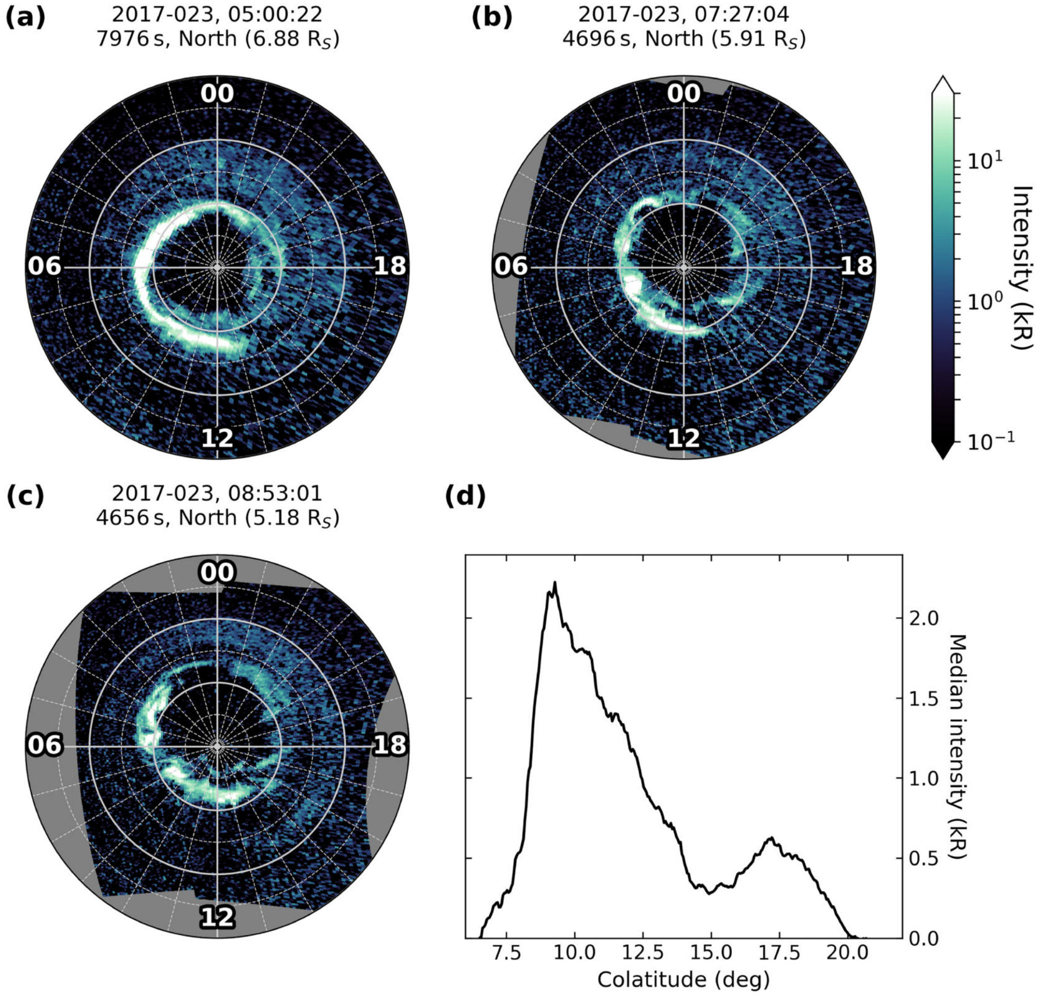

Figure 4. Observations of Saturn's outer auroral emission with the main aurorae contracted far poleward. (a–c) Images from 2017-023 with the dayglow subtracted, showing a dim and wide incomplete ring of outer emission. View is again the same as in Figure 1. (d) Average brightness per colatitude of images in panels a–c combined for all LTs. A secondary peak between 15° and 20° marks the outer emission, near fully detached from the main emission.

Figure 1f) shows it to be oriented in the near-azimuthal direction. Extending this evolution backward, it seems quite possible that this arc may have had a radial orientation initially and undergone some shearing before the first of the two images was obtained.

We propose that these sheared and azimuthal arcs, sometimes parallel to one another, may be auroral signatures of radial interchange injections. These would, similar to large-scale plasma injections triggered by magnetotail reconnection (e.g., Mitchell et al., 2009; Bader, Badman, Cowley, et al., 2019), set up localized FAC systems linking to the ionosphere and cause enhanced particle precipitation, although on a much smaller scale. Additionally to their orientation and evolution, the small width of the sheared arcs appears to be comparable to the azimuthal width of injections in the equatorial plane of roughly 2–4° longitude (e.g., Chen & Hill, 2008; Thomsen et al., 2015; Paranicas et al., 2016). However, the available auroral imagery seems to indicate a preference for these auroral features to appear near dusk while in situ observations of fresh interchange injections were shown to slightly favor the nightside (e.g., Chen & Hill, 2008; Azari et al., 2019). This is somewhat surprising as the LT preference of interchange injections and their auroral signature should be the same, but may well be a result of bias in Cassini's auroral and in situ data relating to, e.g., season or solar wind activity or the overall sparsity of observations.

4. The Outer Emission

Nearly all images presented up to this point have in common the presence of an outer emission. It usually seems to be more prominent on the nightside, although this may be due to its low brightness which is comparable to the intensity of dayglow on the Sun-facing side of the planet. The outer emission is typically more pronounced and spatially separated from the main emission in the southern hemisphere, whereas it forms no more than a dim, diffuse band just equatorward of the main emission in the northern hemisphere.

In general, the outer emission appears circular and centered on the spin pole in both hemispheres as visible in Figures 1 and 3. Considering the latitudinal intensity profiles shown in Figures 2g–2j, 3k, and 3l it usually has a clearly defined outer edge at ~19–21° in the northern hemisphere and ~22–24° in the southern hemisphere (indicated with dashed vertical lines), the clear difference in northern and southern colatitudes being due to the quadrupole asymmetry of Saturn's internal magnetic field. These outer boundaries map to a radial distance of ~6–7 R_S in the magnetic equator plane, corresponding to the inner edge of the region of hot ion/electron plasma as determined in equatorial data (Schippers et al., 2008; Kellett et al., 2010, 2011; Carbary et al., 2018; Carbary, 2019). The "diffuse" emission observed here and in previous studies is consistent with wave-driven precipitation from this hot plasma population (Grodent et al., 2010; Tripathi et al., 2018), similar to the diffuse outer emission in Jupiter's aurorae (Radioti et al., 2009).

The poleward boundary of the outer emission typically appears to be colocated with the main aurorae. To verify whether this is true, we consider Figure 4; a quite extreme example of poleward contracted main aurorae in the northern hemisphere. The mean brightness per colatitude (all images combined to reduce noise) is shown in Figure 4d. The outer emission, albeit very dim, seems to still occupy all latitudes between the main emission and its typical equatorward boundary at ~ 20° colatitude. There is however a dip in intensity between the main and the outer emission, similar to some observations in the southern hemisphere where the outer emission is most intense near its equatorward edge and becomes dimmer closer to the main emission (see, e.g., Figures 1f and 2d/2h). This suggests that the driving mechanism of the outer emission operates throughout the ring current but is most efficient near its planetward boundary.

It seems that the outer emission is typically weaker in the northern hemisphere than in the southern hemisphere; considering the intensity profiles shown in Figures 2g–2j and 3i–3l, the northern outer emission reaches up to 4 kR only in exceptional cases (Figure 2i), whereas larger intensities are observed frequently in the south (Figures 1f, 2d/2h, and 3h/3l). This implies that the wave diffusion responsible is "weak"; that is, the loss cone is not filled. Weak diffusion corresponds to pitch angle scattering per bounce which is less than the angular width of the loss cone, so that only the outer part of the loss cone gets filled. With the loss cone being smaller in the north than in the south as a result of the higher magnetic field strength in the north, arising from the significant quadrupole asymmetry, more particles precipitate in the south. An equivalent effect is found in the South Atlantic Anomaly on Earth (e.g., Vampola & Gorney, 1983). If the pitch angle scattering becomes "strong," meaning scattering by at least the loss cone angle in each bounce, then the loss cone will be "full" in both hemispheres, resulting in an isotropized distribution with identical precipitating flux in both hemispheres.

5. Conclusions

In this study we presented a selection of auroral images from Cassini's Grand Finale orbits, providing auroral observations of unprecedented spatial resolution in both hemispheres, and put them into context with previous results obtained in auroral studies. The data presented here reveal the amazing small-scale structure and dynamics of Saturn's UV aurorae which were usually not resolvable during earlier mission phases, and remains hidden with the limited capabilities of the HST.

Close views of the main auroral oval at predawn LTs reveal that the main arc's structure is highly variable; it can be smooth or rippled and at times bifurcated. It is yet to be investigated in detail what controls this changeable behavior, but it seems reasonable to suggest that disturbed magnetospheric conditions are associated with more rippled configurations as an effect of disturbed plasma flows and density gradients in the equatorial magnetodisc.

The dusk emission was shown to be highly complex, every image exhibiting very different signatures. Recurring behavior could not readily be observed for the most part, although several observations of multiple parallel arcs with different inclination across the auroral oval were found. Their orientation and size seem to indicate they are signatures of radial interchange injections, evolving into a sheared and eventually azimuthal configuration due to the differential rotation of the magnetosphere.

Virtually all imagery obtained during the Grand Finale shows an outer emission to be present, a diffuse ring of dim aurorae just equatorward of the main emission. Based on its location and circular shape, we presume that it is driven by hot electrons from the inner ring current which are scattered into the loss cone by wave activity. The interhemispheric difference in intensity and latitudinal position, owing to the significant quadrupole moment of Saturn's internal magnetic field, indicates the wave diffusion to be weak such that only a part of the loss cone is filled.

After being in orbit around Saturn for more than 13 years, these are the last auroral images from the Cassini spacecraft. They reveal previously unseen detail of Saturn's UV aurorae and perhaps prompt more questions about their origins than they can help answer—highlighting ever more the need for capable missions to planets in the outer solar system and, especially in the absence of such missions to the Saturn system anytime soon, the need for comparative planetology.

Acknowledgments

All Cassini data are publicly available from the NASA Planetary Data System (https://pds.jpl.nasa.gov). Cassini operations are supported by NASA (managed by the Jet Propulsion Laboratory) and European Space Agency (ESA). A. B. was funded by a Lancaster University FST studentship. S. W. H. C. was supported by STFC Grant ST/N000749/1. S. V. B., L. C. R., and J. K. were supported by STFC Grant ST/R000816/1. S. V. B. was also supported by an STFC Ernest Rutherford FellowshipST/M005534/1. B. P. acknowledges financial support from the Belgian Federal Science Policy Office (BELSPO) via the PRODEX Programme of ESA.

References

Azari, A. R., Jia, X., Liemohn, M. W., Hospodarsky, G. B., Provan, G., Ye, S., et al. (2019). Are Saturn's interchange injections organized by rotational longitude. *Journal of Geophysical Research: Space Physics*, *124*, 1806–1822. https://doi.org/10.1029/2018JA026196

Bader, A., Badman, S. V., Cowley, S. W. H., Yao, Z. H., Ray, L. C., Kinrade, J., et al. (2019). The Dynamics of Saturn's Main Aurorae. *Geophysical Research Letters*, *46*, 10283–10294. https://doi.org/10.1029/2019GL084620

Bader, A., Badman, S. V., Kinrade, J., Cowley, S. W. H., Provan, G., & Pryor, W. (2019). Modulations of Saturn's UV auroral oval location by planetary period oscillations. *Journal of Geophysical Research: Space Physics*, *124*, 952–970. https://doi.org/10.1029/2018JA026117

Bader, A., Badman, S. V., Kinrade, J., Cowley, S. W. H., Provan, G., & Pryor, W. R. (2018). Statistical planetary period oscillation signatures in Saturn's UV auroral intensity. *Journal of Geophysical Research: Space Physics*, *123*, 8459–8472. https://doi.org/10.1029/2018JA025855

Bader, A., Badman, S. V., Yao, Z. H., Kinrade, J., & Pryor, W. R. (2019). Observations of Continuous Quasiperiodic Auroral Pulsations on Saturn in High Time-Resolution UV Auroral Imagery. *Journal of Geophysical Research: Space Physics*, *124*, 2451–2465. https://doi.org/10.1029/2018JA026320

Badman, S. V., Achilleos, N., Baines, K. H., Brown, R. H., Bunce, E. J., Dougherty, M. K., et al. (2011). Location of Saturn's northern infrared aurora determined from Cassini VIMS images. *Geophysical Research Letters*, *38*, L03102. https://doi.org/10.1029/2010GL046193

Badman, S. V., Branduardi-Raymont, G., Galand, M., Hess, S. L. G., Krupp, N., Lamy, L., et al. (2015). Auroral Processes at the Giant Planets: Energy Deposition, Emission Mechanisms, Morphology and Spectra. *Space Science Reviews*, *187*(1-4), 99–179. https://doi.org/10.1007/s11214-014-0042-x

Badman, S. V., Bunce, E. J., Clarke, J. T., Cowley, S. W. H., Gérard, J.-C., Gro-dent, D., & Milan, S. E. (2005). Open flux estimates in Saturn's magnetosphere during the January 2004 Cassini-HST campaign, and implications for reconnection rates. *Journal of Geophysical Research*, *110*, A11216. https://doi.org/10.1029/2005JA011240

Badman, S. V., Jackman, C. M., Nichols, J. D., Clarke, J. T., & Gérard, J.-C. (2014). Open flux in Saturn's magnetosphere. *Icarus*, *231*, 137–145. https://doi.org/10.1016/j.icarus.2013.12.004

Badman, S. V., Masters, A., Hasegawa, H., Fujimoto, M., Radioti, A., Grodent, D., et al. (2013). Bursty magnetic reconnection at Saturn's magnetopause. *Geophysical Research Letters*, *40*(6), 1027–1031. https://doi.org/10.1002/grl.50199

Badman, S. V., Tao, C., Grocott, A., Kasahara, S., Melin, H., Brown, R. H., et al. (2011). Cassini VIMS observations of latitudinal and hemispheric variations in Saturn's infrared auroral intensity. *Icarus*, *216*(2), 367–375. https://doi.org/10.1016/j.icarus.2011.09.031

Belenkaya, E. S., Cowley, S. W. H., Meredith, C. J., Nichols, J. D., Kalegaev, V. V., Alexeev, I. I., et al. (2014). Magnetospheric magnetic field modelling for the 2011 and 2012 HST Saturn aurora campaigns—Implications for auroral source regions. *Annales Geophysicae*, *32*(6), 689–704. https://doi.org/10.5194/angeo-32-689-2014

Bradley, T. J., Cowley, S. W. H., Provan, G., Hunt, G. J., Bunce, E. J., Wharton, S. J., et al. (2018). Field-aligned currents in Saturn's nightside magnetosphere: Subcorotation and planetary period oscillation components during northern spring. *Journal of Geophysical Research: Space Physics*, *123*, 3602–3636. https://doi.org/10.1029/2017JA024885

Carbary, J. F. (2012). The morphology of Saturn's ultraviolet aurora. *Journal of Geophysical Research: Space Physics*, *117*, A06210. https://doi.org/10.1029/2012JA017670

Carbary, J. F. (2019). A New Ring Current Model for Saturn. *Journal of Geophysical Research: Space Physics*, *124*, 3378–3389. https://doi.org/10.1029/2019JA026560

Carbary, J. F., Hamilton, D. C., & Mitchell, D. G. (2018). Global Maps of Energetic Ions in Saturn's Magnetosphere. *Journal of Geophysical Research: Space Physics*, *123*, 8557–8571. https://doi.org/10.1029/2018JA025814

Chen, Y., & Hill, T. W. (2008). Statistical analysis of injection/dispersion events in Saturn's inner magnetosphere. *Journal of Geophysical Research: Space Physics*, *113*, A07215. https://doi.org/10.1029/2008JA013166

Cowley, S. W. H., Badman, S. V., Bunce, E. J., Clarke, J. T., Gérard, J.-C., Grodent, D. C., et al. (2005). Reconnection in a rotation-dominated magnetosphere and its relation to Saturn's auroral dynamics. *Journal of Geophysical Research*, *110*, A02201. https://doi.org/10.1029/2004JA010796

Cowley, S. W. H., Bunce, E. J., & O'Rourke, J. M. (2004). A simple quantitative model of plasma flows and currents in Saturn's polar ionosphere. *Journal of Geophysical Research*, *109*, A05212. https://doi.org/10.1029/2003JA010375

Cowley, S. W. H., Bunce, E. J., & Prangé, R. (2004). Saturn's polar ionospheric flows and their relation to the main auroral oval. *Annales Geophysicae*, *22*(4), 1379–1394. https://doi.org/10.5194/angeo-22-1379-2004

Delamere, P. A., & Bagenal, F. (2010). Solar wind interaction with Jupiter's magnetosphere. *Journal of Geophysical Research: Space Physics*, *115*, A10201. https://doi.org/10.1029/2010JA015347

Delamere, P. A., Wilson, R. J., Eriksson, S., & Bagenal, F. (2013). Mag- netic signatures of Kelvin-Helmholtz vortices on Saturn's magnetopause: Global survey. *Journal of Geophysical Research: Space Physics*, *118*, 393–404. https://doi.org/10.1029/2012JA018197

Esposito, L. W., Barth, C. A., Colwell, J. E., Lawrence, G. M., McClintock, W. E., Stewart, A. I. F., et al. (2004). The Cassini Ultraviolet Imaging Spectrograph investigation. *Space Science Reviews*, *115*(1-4), 299–361. https://doi.org/10.1007/s11214-004-1455-8

Gérard, J.-C., Bonfond, B., Gustin, J., Grodent, D., Clarke, J. T., Bisikalo, D., & Shematovich, V. (2009, January). Altitude of Saturn's aurora and its implications for the characteristic energy of precipitated electrons. *Geophysical Research Letters*, *36*, L02202. https://doi.org/10.1029/2008GL036554

Gérard, J.-C., Bunce, E. J., Grodent, D., Cowley, S. W. H., Clarke, J. T., & Badman, S. V. (2005). Signature of Saturn's auroral cusp: Simultane- ous Hubble Space Telescope FUV observations and upstream solar wind monitoring. *Journal of Geophysical Research*, *110*, A11201. https://doi.org/10.1029/2005JA011094

Gérard, J.-C., Grodent, D. C., Gustin, J., Saglam, A., Clarke, J. T., & Trauger, J. T. (2004). Characteristics of Saturn's FUV aurora observed with the Space Telescope Imaging Spectrograph. *Journal of Geophysical Research*, *109*, A09207. https://doi.org/10.1029/2004JA010513

Grodent, D. (2015). A Brief Review of Ultraviolet Auroral Emissions on Giant Planets. *Space Science Reviews*, *187*(1-4), 23–50. https://doi.org/10.1007/s11214-014-0052-8

Grodent, D., Gérard, J.-C., Cowley, S. W. H., Bunce, E. J., & Clarke, J. T. (2005). Variable morphology of Saturn's southern ultraviolet aurora. *Journal of Geophysical Research*, *110*, A07215. https://doi.org/10.1029/2004JA010983

Grodent, D., Gustin, J., Gérard, J.-C., Radioti, A., Bonfond, B., & Pryor, W. R. (2011). Small-scale structures in Saturn's ultraviolet aurora. *Journal of Geophysical Research: Space Physics*, *116*, A09225. https://doi.org/10.1029/2011JA016818

Grodent, D., Radioti, A., Bonfond, B., & Gérard, J.-C. (2010). On the ori- gin of Saturn's outer auroral emission. *Journal of Geophysical Research: Space Physics*, *115*, A08219. https://doi.org/10.1029/2009JA014901

Gustin, J., Grodent, D., Radioti, A., Pryor, W., Lamy, L., & Ajello, J. (2017). Statistical study of Saturn's auroral electron properties with Cassini/UVIS FUV spectral images. *Icarus*, *284*, 264–283. https://doi.org/10.1016/j.icarus.2016.11.017

Gustin, J., Grodent, D., Ray, L., Bonfond, B., Bunce, E., Nichols, J., & Ozak, N. (2016). Characteristics of north jovian aurora from STIS FUV spectral images. *Icarus*, *268*, 215–241. https://doi.org/10.1016/j.icarus.2015.12.048

Hunt, G. J., Cowley, S. W. H., Provan, G., Bunce, E. J., Alexeev, I. I., Belenkaya, E. S., et al. (2014). Field-aligned currents in Saturn's southern nightside magnetosphere: Subcorotation and planetary period oscillation components. *Journal of Geophysical Research: Space Physics*, *119*(12), 9847–9899. https://doi.org/10.1002/2014JA020506

Kellett, S., Arridge, C. S., Bunce, E. J., Coates, A. J., Cowley, S. W. H., Dougherty, M. K., et al. (2010). Nature of the ring current in Saturn's dayside magnetosphere. *Journal of Geophysical Research: Space Physics*, *115*, A08201. https://doi.org/10.1029/2009JA015146

Kellett, S., Arridge, C. S., Bunce, E. J., Coates, A. J., Cowley, S. W. H., Dougherty, M. K., et al. (2011). Saturn's ring current: Local time dependence and temporal variability. *Journal of Geophysical Research: Space Physics*, *116*, A05220. https://doi.org/10.1029/2010JA016216

Lamy, L., Prangé, R., Tao, C., Kim, T., Badman, S. V., Zarka, P., et al. (2018). Saturn's Northern Aurorae at Solstice From HST Observations Coordinated With Cassini's Grand Finale. *Geophysical Research Letters*, *45*, 9353–9362. https://doi.org/10.1029/2018GL078211

McAndrews, H., Thomsen, M., Arridge, C., Jackman, C., Wilson, R., Hender-son, M., et al. (2009). Plasma in Saturn's nightside magnetosphere and the implications for global circulation. *Plane- tary and Space Science*, *57*(14-15), 1714–1722. https://doi.org/10.1016/j.pss.2009.03.003

Melin, H., Stallard, T., Miller, S., Gustin, J., Galand, M., Badman, S. V., et al. (2011). Simultaneous Cassini VIMS and UVIS observations of Saturn's southern aurora: Comparing emissions from H, H 2 and H 3 + at a high spatial resolution. *Geophysical Research Letters*, *38*, L15203. https://doi.org/10.1029/2011GL048457

Mitchell, D. G., Krimigis, S. M., Paranicas, C., Brandt, P. C., Carbary, J. F., Roelof, E. C., et al. (2009). Recurrent energization of plasma in the midnight-to-dawn quadrant of Saturn's magnetosphere, and its relationship to auroral UV and radio emissions. *Planetary and Space Science*, *57*(14-15), 1732–1742. https://doi.org/10.1016/j.pss.2009.04.002

Nichols, J. D., Badman, S. V., Bunce, E. J., Clarke, J. T., Cowley, S. W. H., Hunt, G. J., & Provan, G. (2016). Saturn's northern auroras as observed using the Hubble Space Telescope. *Icarus*, *263*, 17–31. https://doi.org/10.1016/j.icarus.2015.09.008

Nichols, J. D., Clarke, J. T., Cowley, S. W. H., Duval, J., Farmer, A. J., Gérard, J. C., et al. (2008). Oscillation of Saturn's southern auroral oval. *Journal of Geophysical Research: Space Physics*, *113*, A11205. https://doi.org/10.1029/2008JA013444

Paranicas, C., Thomsen, M., Achilleos, N., Andriopoulou, M., Badman, S., Hospodarsky, G., et al. (2016). Effects of radial motion on interchange injections at Saturn. *Icarus*, *264*, 342–351. https://doi.org/10.1016/j.icarus.2015.10.002

Pryor, W. R., Esposito, L. W., Jouchoux, A., West, R. A., Grodent, D., Gérard, J., et al. (2019). Cassini UVIS Detection of Saturn's North Polar Hexagon in the Grand Finale Orbits. *Journal of Geophys- ical Research: Planets*, *124*, 1979–1988. https://doi.org/10.1029/2019JE005922

Radioti, A., Grodent, D., Gérard, J.-C., & Bonfond, B. (2010). Auroral sig- natures of flow bursts released during magnetotail reconnection at Jupiter. *Journal of Geophysical Research: Space Physics*, *115*, A07214. https://doi.org/10.1029/2009JA014844

Radioti, A., Grodent, D., Gérard, J.-C., Bonfond, B., & Clarke, J. T. (2008). Auroral polar dawn spots: Signatures of internally driven reconnection processes at Jupiter's magnetotail. *Geophysical Research Letters*, *35*, L03104. https://doi.org/10.1029/2007GL032460

Radioti, A., Grodent, D., Gérard, J.-C., Bonfond, B., Gustin, J., Pryor, W., et al. (2013). Auroral signatures of multiple magnetopause reconnection at Saturn. *Geophysical Research Letters*, *40*, 4498–4502. https://doi.org/10.1002/grl.50889

Radioti, A., Grodent, D., Gérard, J.-C., Milan, S. E., Bonfond, B., Gustin, J., & Pryor, W. (2011). Bifurcations of the main auroral ring at Saturn: ionospheric signatures of consecutive reconnection events at the magnetopause. *Journal of Geophysical Research: Space Physics*, *116*, A11209. https://doi.org/10.1029/2011JA016661

Radioti, A., Grodent, D., Jia, X., Gérard, J.-C., Bonfond, B., Pryor, W., et al. (2016). A multi-scale magnetotail reconnection event at Saturn and associated flows: Cassini/UVIS observations. *Icarus*, *263*, 75–82. https://doi.org/10.1016/j.icarus.2014.12.016

Radioti, A., Grodent, D., Yao, Z. H., Gérard, J.-C., Badman, S. V., Pryor, W., & Bonfond, B. (2017). Dawn Auroral Breakup at Saturn Initiated by Auroral Arcs: UVIS/Cassini Beginning of Grand Finale Phase. *Journal of Geophysical Research: Space Physics*, *122*, 12,111–12,119. https://doi.org/10.1002/2017JA024653

Radioti, A., Tomás, A. T., Grodent, D., Gérard, J.-C., Gustin, J., Bonford, B., et al. (2009). Equatorward diffuse auroral emissions at Jupiter: Simultaneous HST and Galileo observations. *Geophysical Research Letters*, *36*, L07101. https://doi.org/10.1029/2009GL037857

Radioti, A., Yao, Z., Grodent, D., Palmaerts, B., Roussos, E., Dialynas, K., et al. (2019). Auroral Beads at Saturn and the Driving Mechanism: *Cassini* Proximal Orbits. *The Astrophysical Journal*, *885*(1), L16. https://doi.org/10.3847/2041-8213/ab4e20

Schippers, P., Blanc, M., André, N., Dandouras, I., Lewis, G. R., Gilbert, L. K., et al. (2008). Multi-instrument analysis of electron populations in Saturn's magnetosphere. *Journal of Geophysical Research: Space Physics*, *113*, A07208. https://doi.org/10.1029/2008JA013098

Stallard, T., Miller, S., Lystrup, M., Achilleos, N., Bunce, E. J., Arridge, C. S., et al. (2008). Complex structure within Saturn's infrared aurora. *Nature*, *456*, 214–217. https://doi.org/10.1038/nature07440

Stallard, T., Miller, S., Melin, H., Lystrup, M., Dougherty, M., & Achilleos, N. (2007). Saturn's auroral/polar H+3 infrared emission: I. General morphology and ion velocity structure. *Icarus*, *189*(1), 1–13. https://doi.org/10.1016/j.icarus.2006.12.027

Talboys, D. L., Arridge, C. S., Bunce, E. J., Coates, A. J., Cowley, S. W. H., Dougherty, M. K., & Khurana, K. K. (2009). Signatures of field-aligned currents in Saturn's nightside magnetosphere. *Geophysical Research Letters*, *36*, L19107. https://doi.org/10.1029/2009GL039867

Thomsen, M. F., Mitchell, D. G., Jia, X., Jackman, C. M., Hospodarsky, G., & Coates, A. J. (2015). Plasmapause formation at Saturn: Plasmapause Formation at Saturn. *Journal of Geophysical Research: Space Physics*, *120*(4), 2571–2583. https://doi.org/10.1002/2015JA021008

Thomsen, M. F., Reisenfeld, D. B., Delapp, D. M., Tokar, R. L., Young, D. T., Crary, F. J., et al. (2010). Survey of ion plasma parameters in Saturn's magnetosphere. *Journal of Geophysical Research: Space Physics*, *115*, A10220. https://doi.org/10.1029/2010JA015267

Tripathi, A. K., Singhal, R. P., & Singh, O. N. (2018). The Generation of Saturn's Aurora at Lower Latitudes by Electrostatic Waves. *Journal of Geophysical Research: Space Physics*, *123*, 3565–3579. https://doi.org/10.1002/2017JA024804

Vampola, A. L., & Gorney, D. J. (1983). Electron energy deposition in the middle atmosphere. *Journal of Geophysical Research*, *88*, A86267. https://doi.org/10.1029/JA088iA08p06267

Wilson, R. J., Bagenal, F., & Persoon, A. M. (2017). Survey of thermal plasma ions in Saturn's magnetosphere utilizing a forward model. *Journal of Geophysical Research: Space Physics*, *122*, 7256–7278. https://doi.org/10.1002/2017JA024117

Chapter 10

Discussion and Conclusions

In this thesis a detailed investigation of the dynamics of Saturn's UV auroral emissions has been presented. This last chapter serves to summarize and discuss the insights gained and to identify unanswered questions of interest for future research concerning gas giant aurorae.

10.1 The Different Drivers of Saturn's Main Aurorae

Following the terminology of the Jovian main aurorae, the brightest and seemingly steady aurorae on Saturn are typically referred to by the same name since the first spatially resolved observations from the HST were obtained – inherently implying close similarities in the origin of the Jovian and Kronian aurorae. However, thorough inspection of the aurorae typically encircling both planets' poles reveals striking differences between the two systems.

The Jovian main aurorae firmly rotate with the planet while largely maintaining their brightness and are thought to be driven by corotation breakdown currents in the middle to outer magnetosphere. At first sight, Saturn's aurorae appear to be a similar quasistatic band of emissions with an increased average intensity near dawn as a likely sign of more significant solar wind driving compared to Jupiter. This concept was probed in **Publication IV** (chapter 7) in which long-term observations of Saturn's northern aurorae were investigated in order to separate and identify different drivers of the main aurorae using the temporal intensity variations observed.

A major finding of this study is that the main emission is not dominated by a steady system of FACs driven by corotation breakdown or flow shears between the rotating magnetosphere and the antisunward solar wind flow. While a faint signature which may be related to such processes could be observed during quiet magnetospheric conditions, the bulk of the observable aurorae seems to be attributable to bright signatures of magnetotail reconnection which regularly appear near midnight and subcorotate with the planet – hence causing a statistical intensification of the aurorae near dawn.

The transient magnetospheric disturbances causing such auroral signatures may be driven either by continued internal plasma loading requiring the shedding of plasma through Vasyliūnas cycle reconnection, or by passing solar wind compressions leading to the closure of open flux through Dungey cycle reconnection. The balance between drivers internal and external to Saturn's magnetosphere is currently not well understood and a topic of ongoing research.

In absence of magnetotail reconnection events, a flow shear-driven main emission is usually identifiable at dawn while the dusk side typically doesn't feature one such. High-resolution imagery presented in **Publication VI** (chapter 9) showed that the main arc can be smooth, rippled or bifurcated, possibly indicating laminar or perturbed plasma flow in the source region depending on quiet or disturbed magnetospheric conditions.

The most static component of Saturn's aurorae is probably the outer emission which was also observed in more detail in **Publication VI**. It turns out to be nearly always present, albeit often very dim, and to extend to ~ 20° (~ 23°) colatitude in the northern (southern) hemisphere regardless of the compression state of the magnetosphere. It seems therefore realistic to relate this emission to the inner ring current, where hot electrons may be scattered into the loss cone such that they reach the upper atmosphere to drive aurorae. Future research could investigate the relationship between the intensity of the outer aurorae and the state of the ring current using for example in situ particle and magnetometer observations or remote sensing of ENAs.

10.2 Planetary Period Oscillations as a Near Omnipresent Modulation

PPOs are observed in all observations collected within Saturn's magnetosphere, and the aurorae are no exception. **Publication I** (chapter 4) and **Publication II** (chapter 5) statistically investigated the effect of these magnetospheric modulations on the auroral intensity and location and observed clear dependencies in agreement with the generally accepted model of PPO fields and currents described in sections 2.2 and 3.7.

The auroral intensity is observed to maximize (minimize) where the PPO upward (downward) FACs are predicted to be located; the modulation is significantly stronger for the local PPO system but also observed interhemispherically (i.e., the intensity modulation of the northern aurorae due to the northern PPO system is stronger than the one due to the southern PPO system and vice versa). Both the latitudinal location and the fitted center of the auroral oval are periodically displaced by the PPO FACs as is predicted, further solidifying the accuracy of the currently accepted PPOs model. It is also shown that the displacements are larger when the two PPO systems rotate in antiphase than they are in phase with one another, indicating again that both PPO systems affect not only their local hemisphere but also the opposite one.

However, it is also worth pointing out the limitations of **Publication I** in particular. From the results of **Publication IV**, we now know that the auroral brightness is for the main part determined by transient signatures of magnetotail reconnection events and not by a Jupiter-like quasistatic main emission modulated by PPO FACs as previously thought. The phasing of these reconnection events hereby appears to be partly controlled by the PPO-dependent thinning and thickening of the equatorial current sheet, as was investigated in previous works and also observed in **Publication IV**. This means that the PPO dependence determined in **Publication I**, in which all auroral imagery obtained by the UVIS instrument were binned by PPO phase, is likely to be dominated by the occurrence of magnetotail reconnection events and not by direct modulation of the auroral brightness by the PPO FACs.

Nevertheless, a case study of continuous auroral observations spanning more than two Saturn rotations published in **Publication IV** does indeed show the expected dimming and brightening of a quasistatic auroral oval in perfect sync with the modelled PPO systems. In this case, no transient intensifications related to magnetotail reconnection were observed, and the two PPO systems were aligned in phase with one another to reveal this strikingly clear intensity modulation showing a thin half ring of aurorae near the PPO upward FACs and an absence of emissions near the PPO downward FACs.

10.3 Transient Small-Scale Structures

The previous paragraphs concerned the general morphology of Saturn's aurora and how it is determined by the large-scale dynamics within Saturn's magnetosphere. There are also many small transient auroral signatures which indicate dynamics on a smaller scale, such as dayside cusp spots and post-noon bifurcations. **Publication III** (chapter 6) identified a new type of such transient events: short-lived auroral flashes (~ 10 min lifetime) which exhibit a ~ 1 h quasiperiodicity and were found to occur throughout the UVIS dataset. Single events have been identified in HST data as well, but a full investigation of these data is yet to be performed.

These transient flashes are predominantly observed on the duskside, but can occur at all LTs. Their characteristic periodicity and LT preference is very similar to previous observations of such periodicities in energetic electron, magnetic field and auroral hiss measurements. A case study shown in **Publication III** presents an HST observation of one such auroral flash together with in situ particle and field measurements obtained by Cassini along the same magnetic field line to clearly reveal their close relationship.

It is concluded that these periodic intensifications of the aurora and related in situ parameters occur on closed field lines, suggesting a driver internal to Saturn's magnetosphere. The most likely cause is small-scale magnetodisc reconnection which was recently discovered based on Cassini data. Combined with the greatly increased number of possible magnetodisc reconnection sites near dusk suggested in previous studies, the ~ 1 h quasiperiodic features observed here may be a sign of a near-continuous "drizzle" of small reconnection events which may contribute significantly to plasma circulation in Saturn's magnetosphere. Further investigations of HST auroral imagery with respect to transient flashes would be very useful to explore their temporal evolution and relation to in situ signatures in more detail.

The true complexity of Saturn's dusk aurorae was only fully revealed by UVIS observations obtained during Cassini's Grand Finale which were summarized in **Publication VI**. Every orbit provided one or two high resolution slews of the southern dusk aurorae, and no two of them look even remotely the same (the interested reader may have noticed that unprojected versions of these beautiful images were used as chapter heading backgrounds in this thesis). We observe thin parallel arcs, blobs and patches drawn out by the differential rotation of Saturn, which may be related to radial injection events in the middle magnetosphere. However, our understanding of these features is poor at best and unlikely to improve significantly since the very limited set of Cassini's high-resolution auroral imagery will not be expanded with additional observations in the foreseeable future.

10.4 ON AURORAL ACCELERATION AT SATURN

With the arrival of the JUNO spacecraft at Jupiter in 2016, a first understanding of the auroral acceleration process at the gas giants could be formed based on observations during low spacecraft passes above the Jovian aurorae. Surprisingly, the energetic electrons causing Jupiter's bright aurorae do not appear to be accelerated into the atmosphere by parallel electric fields like at Earth, but may instead be driven by wave-particle interactions. Similar data could not be obtained at Saturn until CASSINI's Grand Finale, when the spacecraft orbit was changed to a low enough altitude to come close to where the auroral acceleration region is expected to be located.

Publication V (chapter 8) summarizes CASSINI's observations from two low-altitude passes above Saturn's auroral region. Upward and downward FAC regions were identified based on magnetometer measurements to provide context for the particle and wave features which were observed. Upward FAC regions were characterized by broadband upward ion beams with energies up to tens of keV and precipitating electrons with $\sim 10\,\text{keV}$, while downward current regions featured energetic ion conics indicating the presence of strong parallel electric fields. Different wave signatures were observed in both upward and downward FAC regions in conjunction with the described particle features, highlighting the importance of wave-particle interaction to the acceleration processes at play.

These observations are similar to those of JUNO in that both suggest that monoenergetic electron beams driven by parallel electric fields do not seem to be the main acceleration mechanism for auroral electrons. Furthermore, the auroral particle energies observed in both systems are in a similar range, and at that ~ 100 times larger than at Earth. We may hence assume that the many JUNO observations from above the Jovian aurorae may be well suited to complement the scant measurements obtained by CASSINI to further our understanding of auroral acceleration above Saturn's aurorae. Despite the sparsity of data, much of it is left unexplored and remains for future investigations.

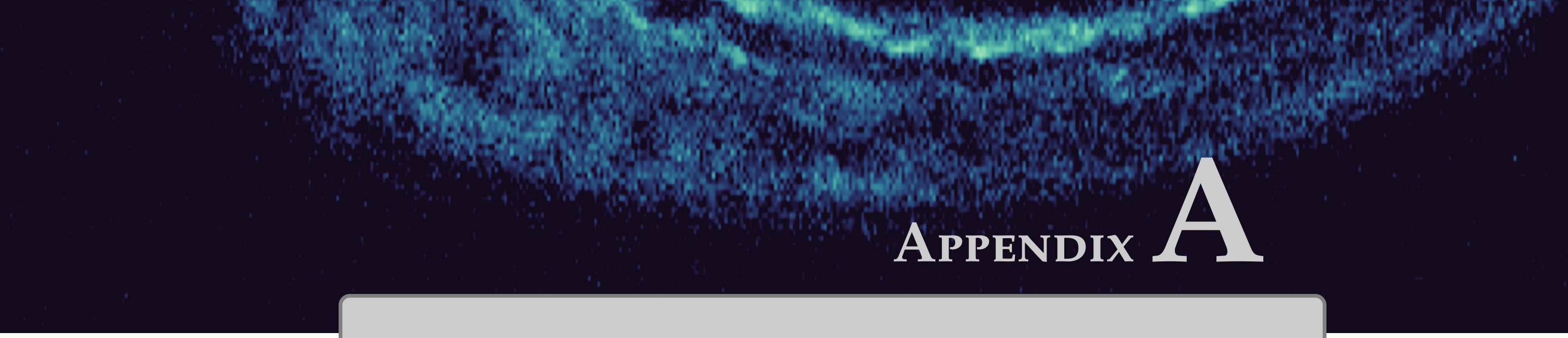

Appendix A

Radiance Conversions

A.1 The Rayleigh and Radiant Flux

The brightness unit used in auroral physics is the **Rayleigh**, named after the fourth Lord Rayleigh, R.J. Strutt, 1875-1947, who made first measurements of night airglow [*Rayleigh*, 1930]. It describes the **column emission rate** I, assuming an isotropic source with no self absorption and a column of unspecified length [*Hunten et al.*, 1956], and is defined as

$$1\,\mathrm{R} = 10^{10}\,\frac{\mathrm{Photons}}{\mathrm{s\,m^2\,column}} \tag{A.1}$$

in SI units [*Baker and Romick*, 1976]. We can convert the **column emission rate** I into the **radiance** L by using [*Baker and Romick*, 1976]

$$L\left[\frac{\mathrm{Photons}}{\mathrm{s\,m^2\,sr}}\right] = \frac{10^{10}}{4\pi}\cdot I\,[\mathrm{R}], \tag{A.2}$$

and for the in auroral physics usually preferred *Kilorayleigh*, kR, obviously

$$L\left[\frac{\mathrm{Photons}}{\mathrm{s\,m^2\,sr}}\right] = \frac{10^{13}}{4\pi}\cdot I\,[\mathrm{kR}]. \tag{A.3}$$

The **radiant flux** Φ is obtained by integrating over the full 4π sr solid angle, and the apparent emitting surface area A seen from the detector in m^2,

$$\Phi\left[\frac{\mathrm{Photons}}{\mathrm{s}}\right] = L\left[\frac{\mathrm{Photons}}{\mathrm{s\,m^2\,sr}}\right]\cdot 4\pi\,\mathrm{sr}\cdot A\,\left[\mathrm{m}^2\right]. \tag{A.4}$$

Note that the radiant flux is only meaningful in combination with spectral information, i.e. the mean energy of the emitted photons. Therefore, multiplying by the mean H_2 photon energy of $1.6\cdot 10^{-18}\,\frac{\mathrm{J}}{\mathrm{Photon}}$ [*Kurth et al.*, 2016] gives the radiant flux, often also named “auroral power”, in SI units,

$$\Phi\,[\mathrm{W}] = 1.6\cdot 10^{-18}\,\frac{\mathrm{J}}{\mathrm{Photon}}\cdot\Phi\left[\frac{\mathrm{Photons}}{\mathrm{s}}\right]. \tag{A.5}$$

A.2 Emitting Surface Area

Unprojected HST Images

The emission area for an HST pixel is equal to the perpendicular area this pixel covers at the distance of Saturn. This area is

$$A\,[\mathrm{m}^2] = r^2 \cdot \sin(\alpha_1) \cdot \sin(\alpha_2) \tag{A.6}$$

with r as the distance between HST and Saturn and $\alpha_{1/2}$ as the angular FOV of a pixel. For the STIS sensor with a FOV of $25 \times 25\,\mathrm{arcsec}^2$ and 1024 pixels across in each direction, we find

$$\alpha_{1/2} = 25/1024\,\mathrm{arcsec} \tag{A.7}$$

such that

$$A\,[\mathrm{m}^2] = (r\,[\mathrm{m}] \cdot \sin(25/1024\,\mathrm{arcsec}))^2 \tag{A.8}$$

or

$$A\,[\mathrm{m}^2] = \left(r\,[\mathrm{km}] \cdot 10^3 \cdot \sin(25/1024\,\mathrm{arcsec})\right)^2 . \tag{A.9}$$

Projected HST and UVIS Images

The radiant flux can also be determined from an image which has already been projected onto a longitude-latitude grid. However, care has to be taken when the radiance L is integrated over the emitting surface.

As shown in Figure A.1, instrument pixel footprints on the planetary surface are skewed depending on the angle under which the emission “surface”, the ionospheric layer in which auroras are generated, is being observed. The absolute surface area of one longitude-latitude grid bin is therefore not equal to the corresponding apparent emitting surface seen from the spacecraft based on which the column emission rate has been determined. With small grid bin sizes, each grid bin can be approximated by a flat plane such that its apparent emitting surface A_{app} and absolute surface A_{abs} are related

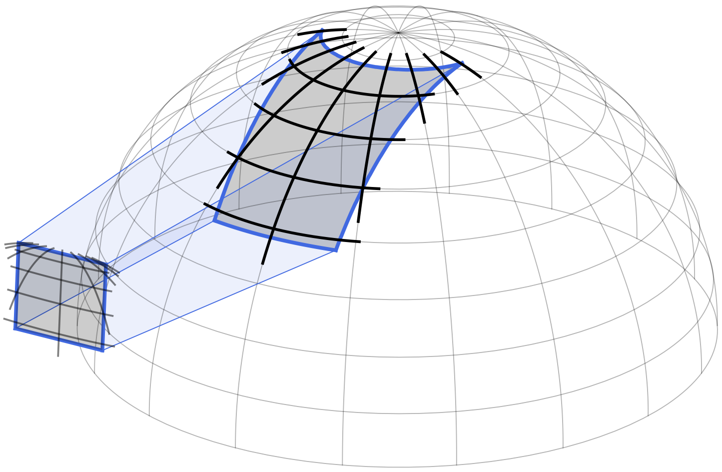

FIGURE A.1: *Example FOV of an observational instrument pixel projected on the surface of the planet, not to scale. The longitude-latitude grid drawn on the planet is also shown in the instrument plane.*

through

$$A_{\mathrm{app}} = \sin \varepsilon \cdot A_{\mathrm{abs}} \tag{A.10}$$

with ε as the elevation angle of the observing instrument above the horizon as seen from the grid bin location.

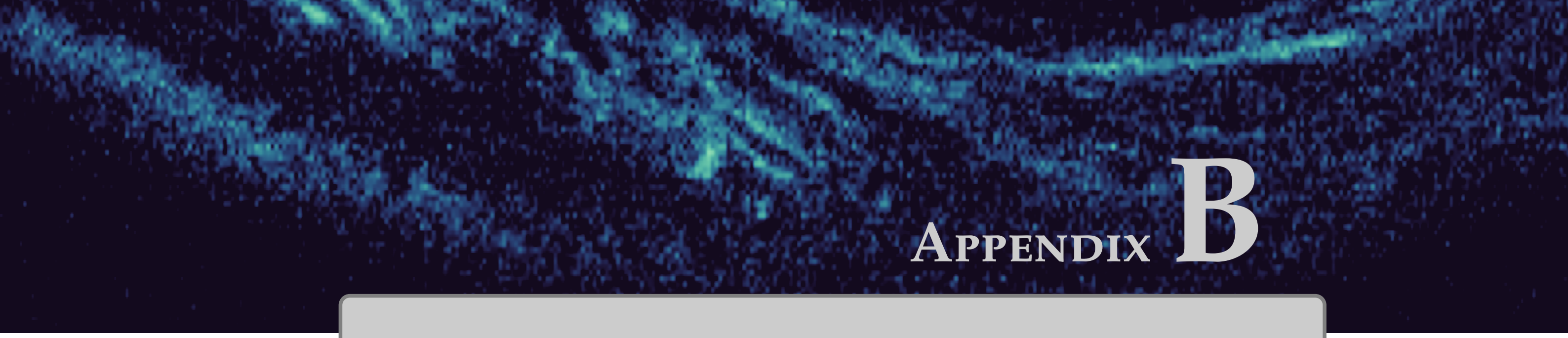

Appendix B

Supplementary Information

This section collects all supplementary information published together with the research articles presented in chapters 4 to 9, edited for convenience and readability.

Supporting Information for "Modulations of Saturn's UV auroral location by planetary period oscillations"

A. Bader[1], S. V. Badman[1], J. Kinrade[1], S. W. H. Cowley[2], G. Provan[2], W. R. Pryor[3]

[1]Department of Physics, Lancaster University, Lancaster, UK
[2]Department of Physics and Astronomy, University of Leicester, Leicester, UK
[3]Science Department, Central Arizona College, Coolidge, Arizona, USA

Contents

1. Figures S1 to S8

Figures S1 to S8

Corresponding author: Alexander Bader, `a.bader@lancaster.ac.uk`

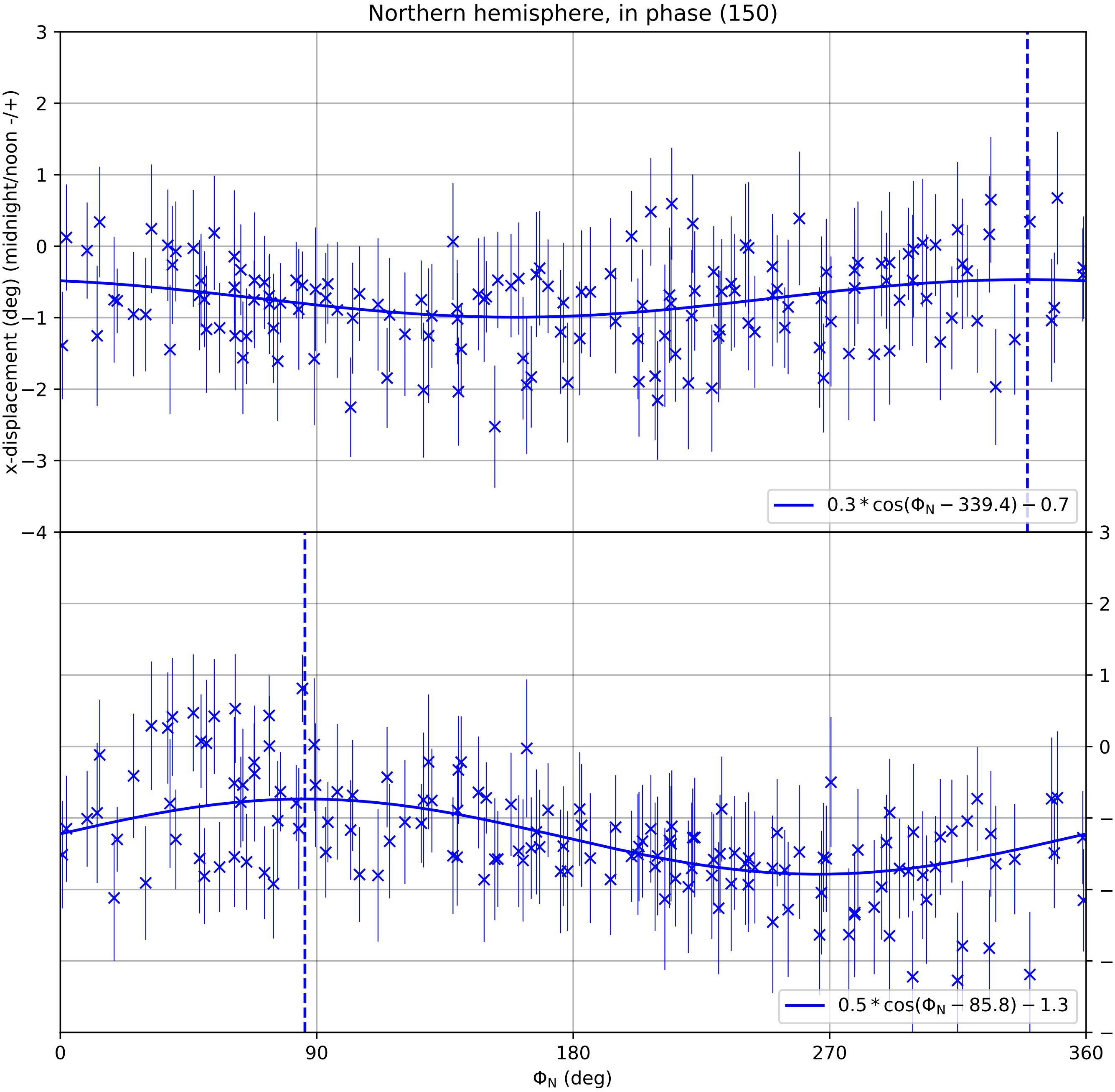

Figure S1. Sine fits to the x and y displacements of the northern hemisphere, *in phase* images. Same format as Figure 9.

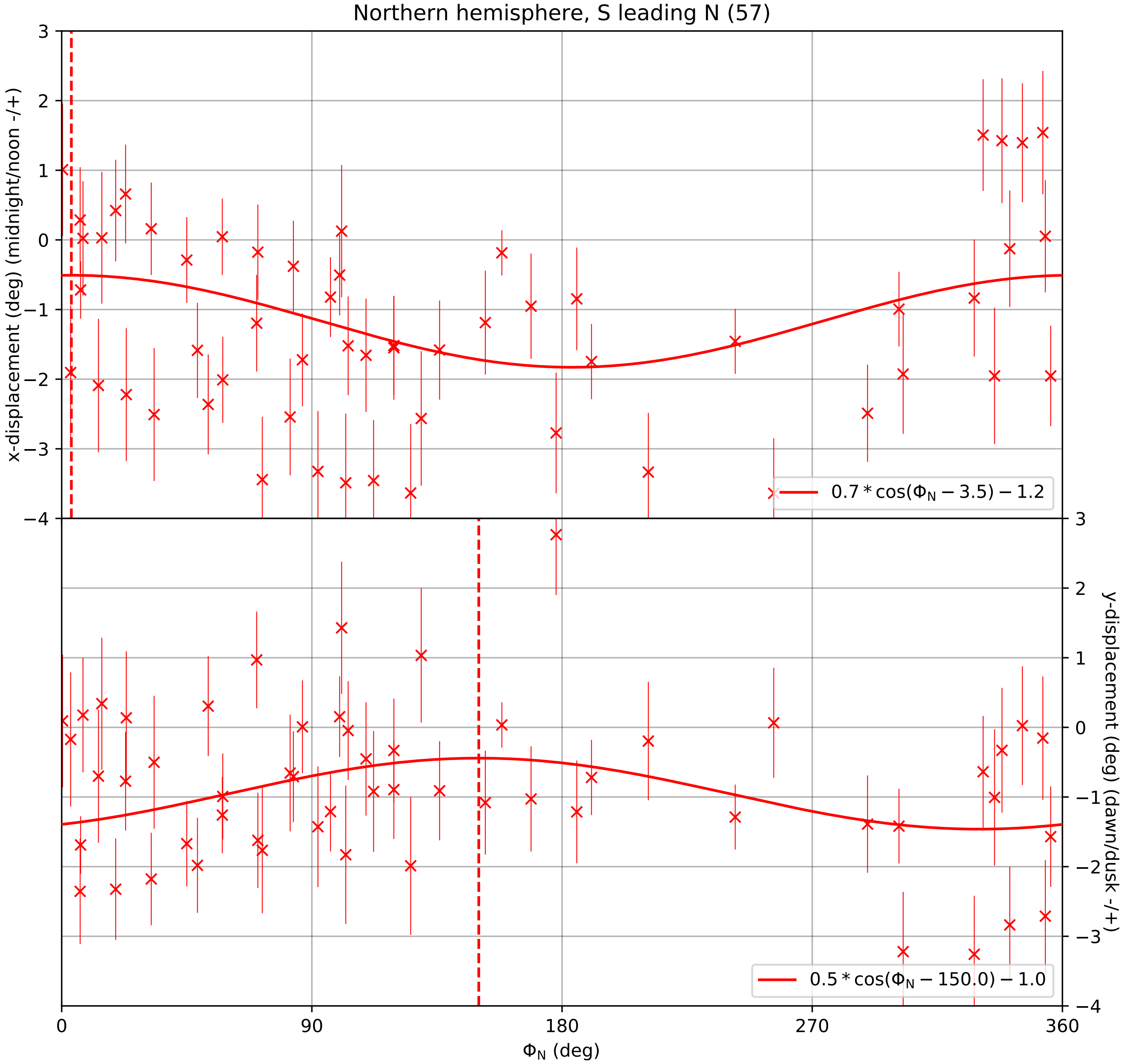

Figure S2. Sine fits to the x and y displacements of the northern hemisphere, *S leading N* images. Same format as Figure 9.

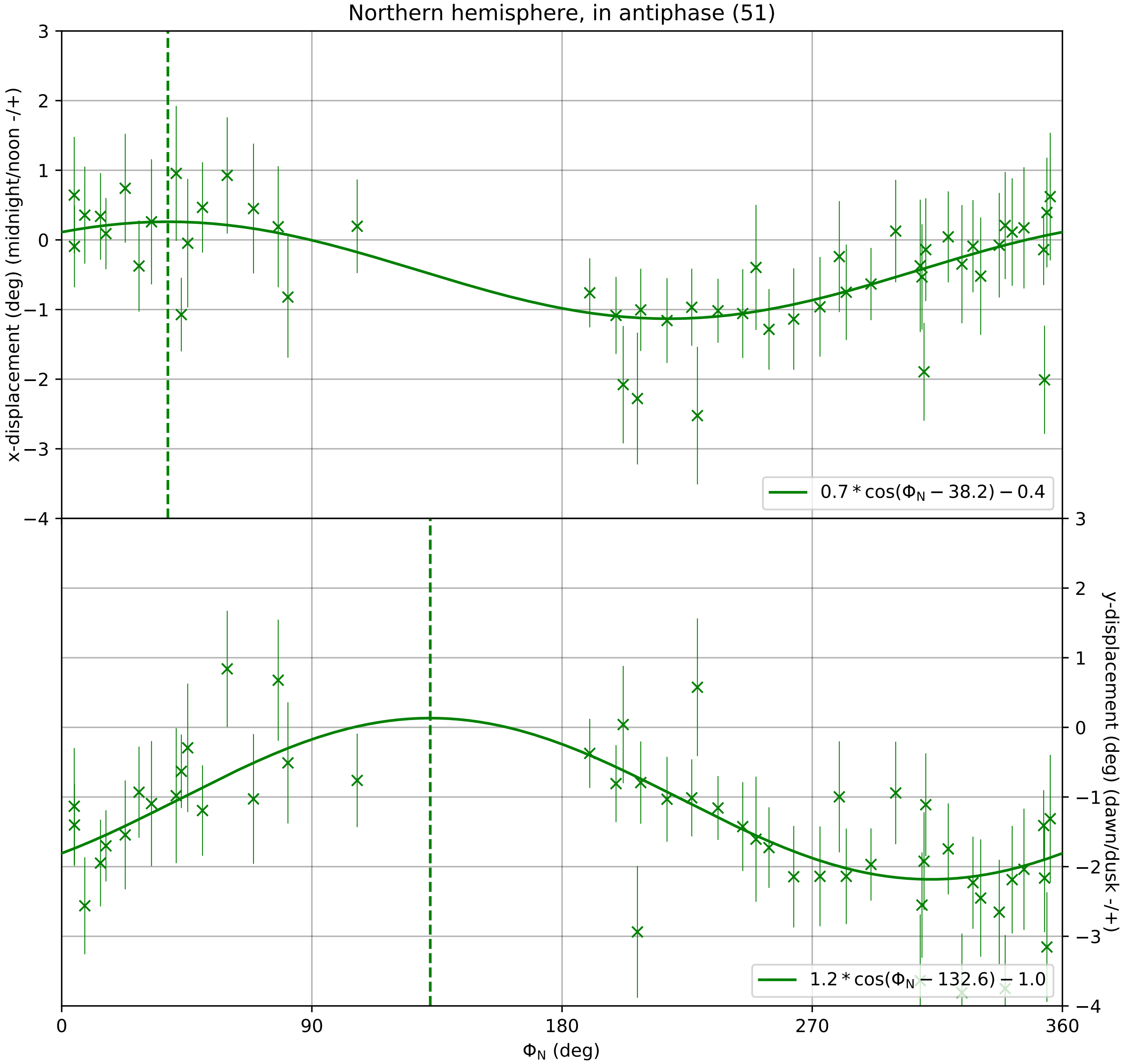

Figure S3. Sine fits to the x and y displacements of the northern hemisphere, *in antiphase* images. Same format as Figure 9.

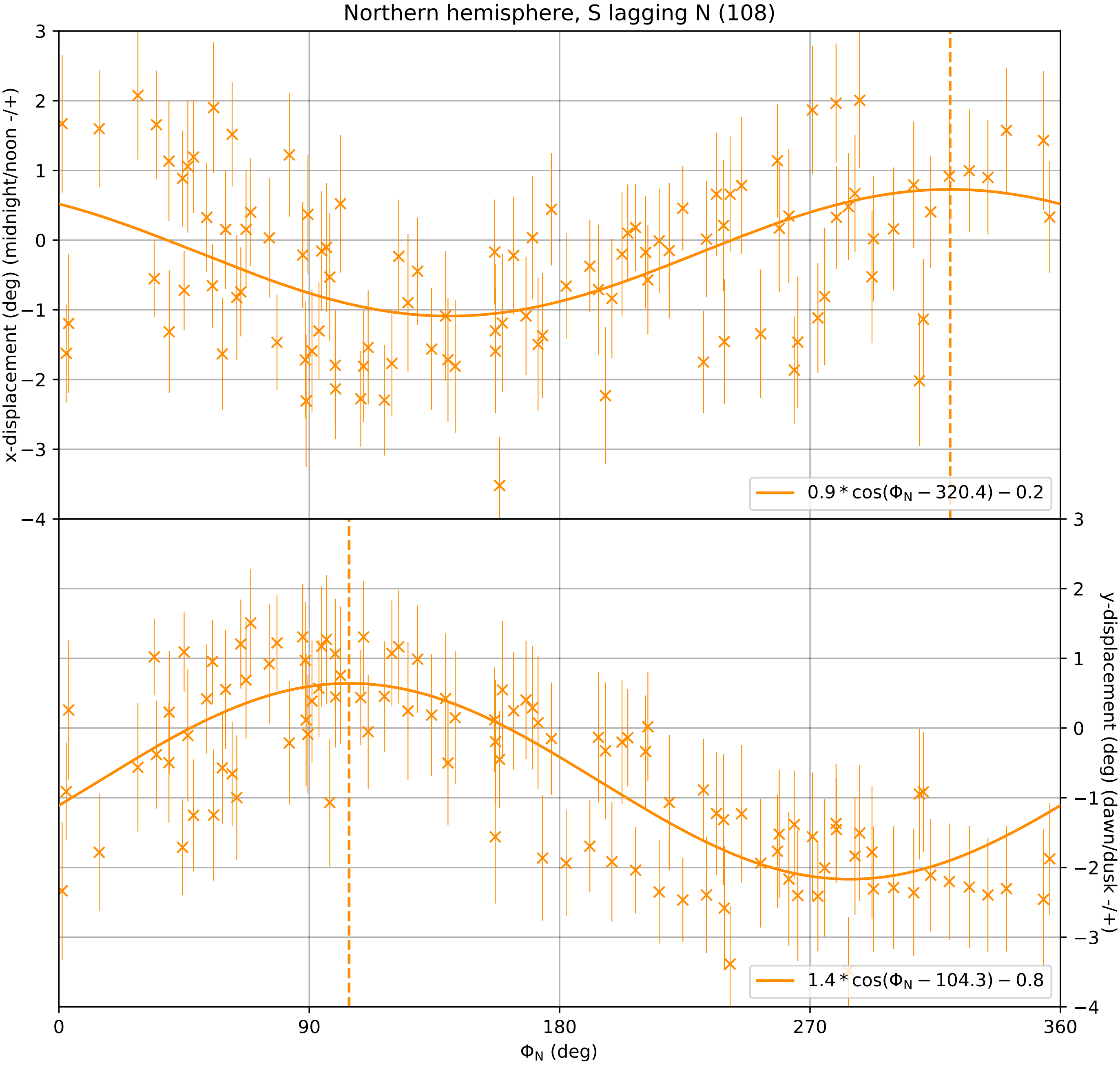

Figure S4. Sine fits to the x and y displacements of the northern hemisphere, *S lagging N* images. Same format as Figure 9.

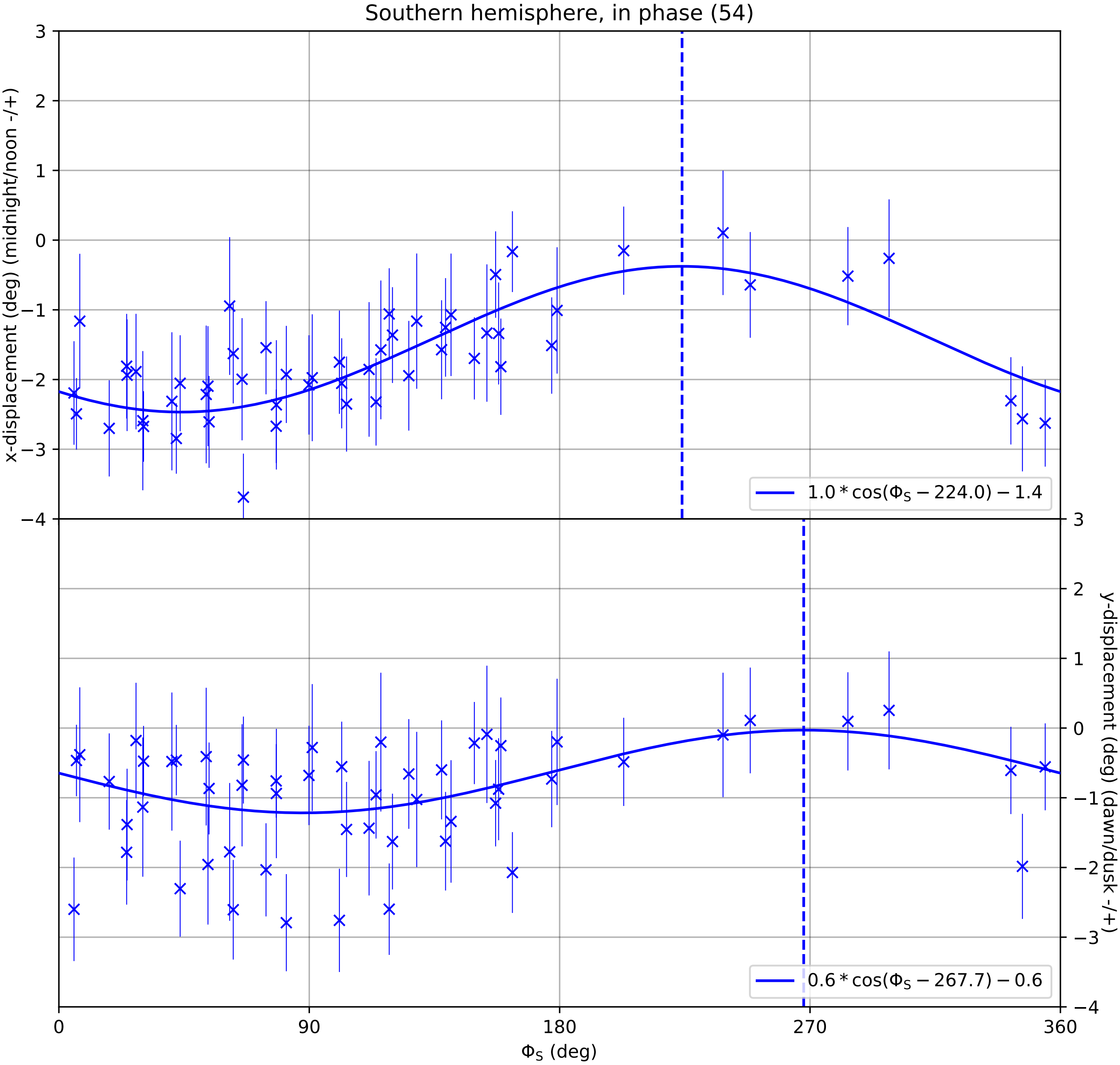

Figure S5. Sine fits to the x and y displacements of the southern hemisphere, *in phase* images. Same format as Figure 9.

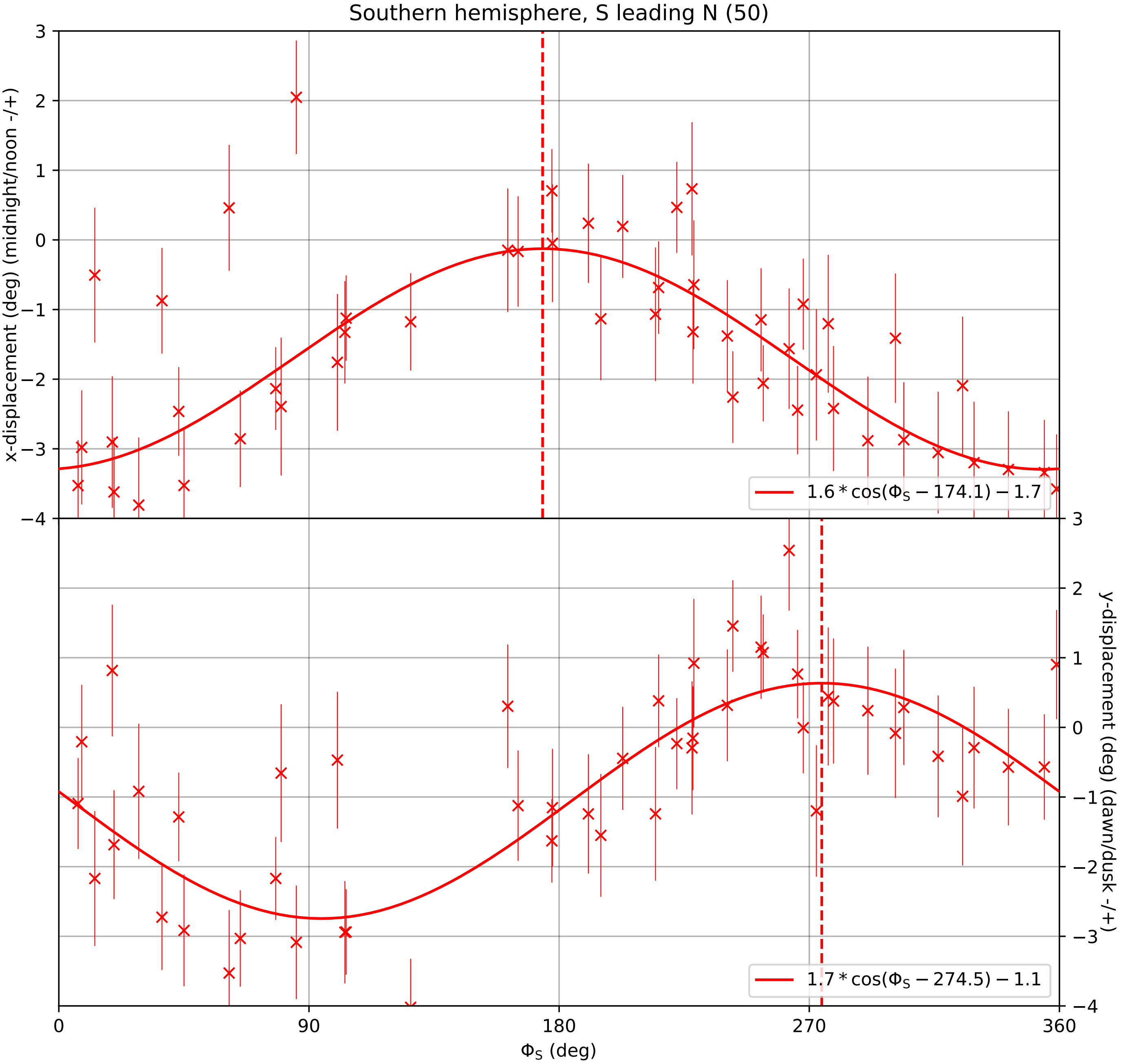

Figure S6. Sine fits to the x and y displacements of the southern hemisphere, *S leading N* images. Same format as Figure 9.

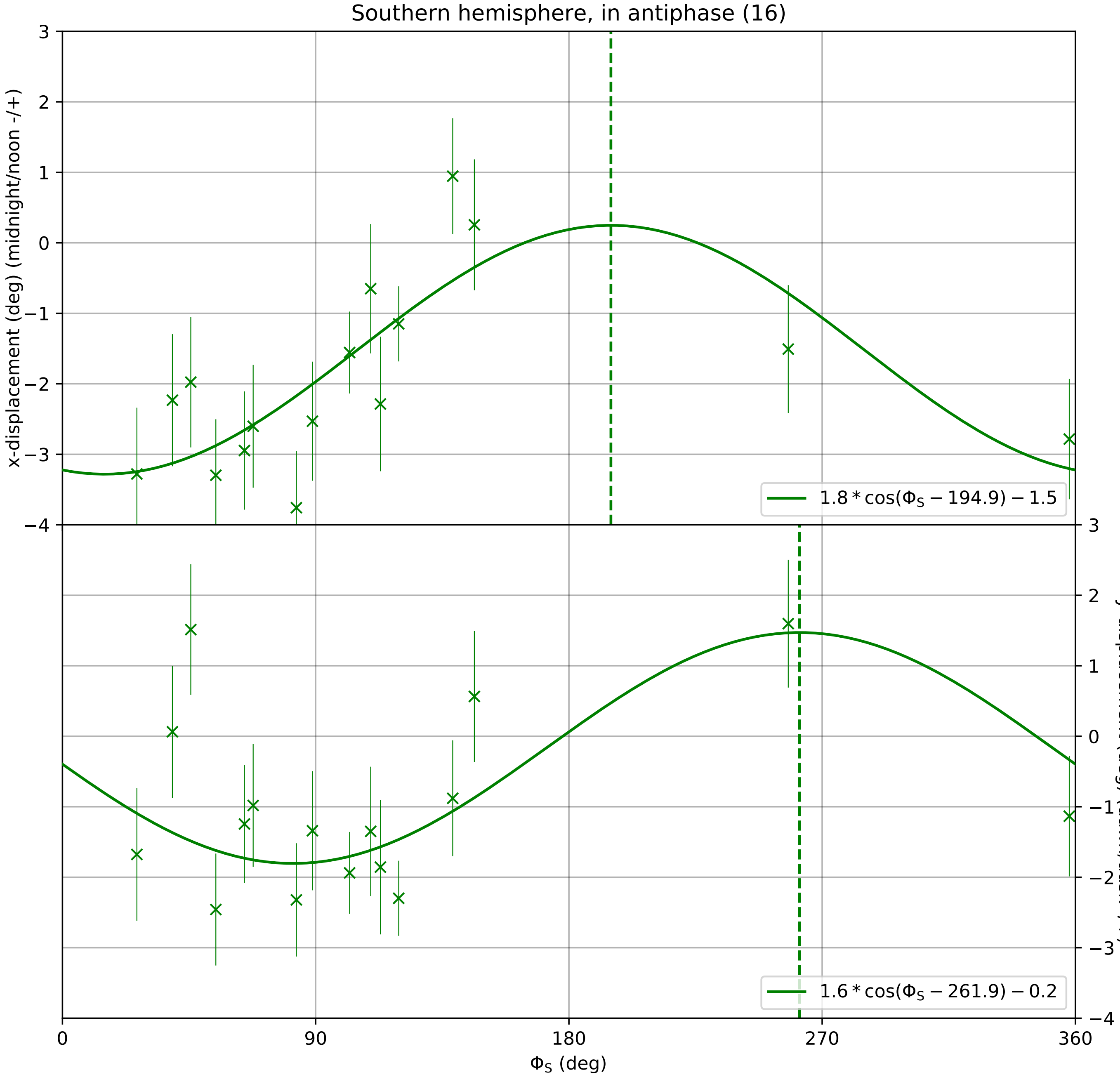

Figure S7. Sine fits to the x and y displacements of the southern hemisphere, *in antiphase* images. Same format as Figure 9.

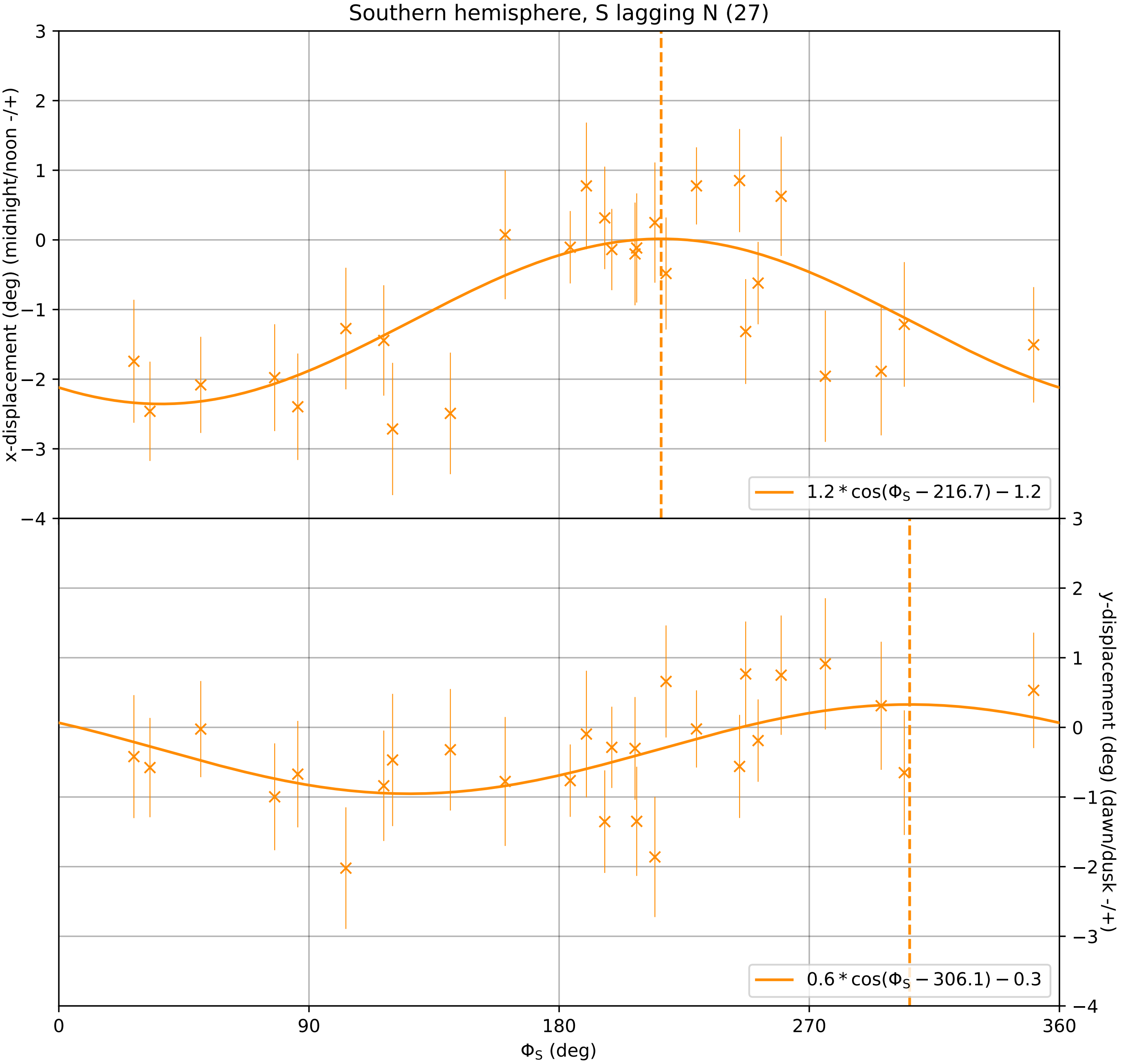

Figure S8. Sine fits to the x and y displacements of the southern hemisphere, *S lagging N* images. Same format as Figure 9.

Supporting Information for "Observations of continuous quasiperiodic auroral pulsations on Saturn in high time-resolution UV auroral imagery"

A. Bader[1], S. V. Badman[1], Z.H. Yao[2], J. Kinrade[1], W. R. Pryor[3]

[1]Department of Physics, Lancaster University, Lancaster, UK
[2]Laboratoire de Physique Atmosphérique et Planétaire, Space sciences, Technologies and Astrophysics Research (STAR) Institute, Université de Liège, Liège, Belgium
[3]Science Department, Central Arizona College, Coolidge, Arizona, USA

Contents

List of all auroral flashes

List of all auroral flashes identified in the UVIS dataset used in this study. Given for each observation are the timestamp, the approximate local time (LT) location, the observed UV power of the flash above the auroral background and the hemisphere the flash was observed on. If the LT location could not be clearly identified by the algorithm described in this study, the value "nan" is given in the table.

UTC time	LT location (h)	UV power (GW)	Hemisphere
2008-109T12:03	nan	6.34	North
2008-109T13:07	14.33	14.25	North
2008-129T09:29	2.33	10.86	North
2008-129T10:46	16.33	27.53	North
2008-129T11:50	15.00	6.62	North
2008-129T13:01	17.67	10.78	North
2008-195T10:18	17.00	7.31	North
2008-201T04:31	5.00	9.74	North
2008-201T05:05	9.67	11.53	North
2008-201T05:39	nan	9.67	North
2008-201T07:41	8.33	5.20	North
2008-201T12:31	3.00	3.90	North
2014-079T02:03	nan	5.39	North
2014-079T02:52	13.00	9.27	North
2014-079T03:51	13.00	17.73	North
2014-087T10:58	nan	5.54	North
2014-087T11:33	13.00	15.93	North
2014-087T12:30	16.33	30.98	North
2014-087T13:25	15.67	46.71	North
2014-087T14:16	14.33	35.12	North
2014-087T15:12	15.67	24.02	North
2014-087T16:11	15.00	49.17	North
2014-087T16:53	15.00	18.56	North
2014-087T17:59	19.00	9.23	North
2014-130T05:24	19.00	5.99	North
2014-130T08:12	17.00	10.02	North

Corresponding author: Alexander Bader, `a.bader@lancaster.ac.uk`

2014-130T10:06	16.33	3.91	North
2014-130T10:48	15.67	4.74	North
2014-130T12:17	17.00	5.33	North
2014-130T13:59	16.33	6.17	North
2014-145T05:46	nan	5.12	North
2014-145T06:34	22.33	10.05	North
2014-145T07:37	nan	5.61	North
2014-145T08:22	19.67	8.37	North
2014-145T09:22	nan	8.69	North
2014-145T11:06	nan	7.84	North
2014-145T12:16	17.67	16.45	North
2014-145T13:06	16.33	13.06	North
2014-145T14:04	19.00	13.67	North
2014-145T14:48	18.33	20.96	North
2014-145T15:58	19.67	8.13	North
2014-145T16:48	19.67	10.66	North
2014-145T17:35	20.33	9.20	North
2014-145T18:22	19.67	6.44	North
2014-145T19:10	9.00	8.29	North
2014-145T20:13	22.33	6.31	North
2014-145T21:26	nan	5.21	North
2014-145T22:21	16.33	9.03	North
2014-147T09:01	nan	3.82	North
2014-147T09:56	nan	3.06	North
2014-147T10:58	nan	5.75	North
2014-147T11:59	nan	4.07	North
2014-147T14:38	nan	3.19	North
2014-147T15:25	nan	4.19	North
2014-147T16:21	nan	6.56	North
2014-147T17:36	13.67	10.54	North
2014-147T18:21	15.67	14.69	North
2014-147T19:12	15.67	3.68	North
2014-147T21:08	17.67	2.50	North
2014-149T04:57	nan	8.96	North
2014-149T05:36	8.33	44.40	North
2014-149T06:26	nan	7.42	North
2014-149T08:05	8.33	22.39	North
2014-149T10:14	nan	10.54	North
2014-149T11:15	nan	6.31	North
2014-149T12:22	14.33	11.51	North
2014-149T13:20	nan	6.11	North
2014-149T14:16	nan	7.58	North
2014-149T15:27	13.67	8.22	North
2014-149T16:23	15.00	6.87	North
2014-149T17:17	13.67	8.73	North
2014-149T18:05	15.00	9.90	North
2014-149T19:03	13.67	7.83	North
2014-149T19:58	14.33	12.53	North
2014-149T20:47	13.00	19.64	North
2014-149T21:40	13.67	10.72	North
2014-150T17:40	16.33	11.83	North
2014-150T18:16	nan	9.37	North
2014-150T18:46	nan	7.94	North
2014-150T19:43	nan	9.87	North
2014-150T20:35	18.33	13.41	North

2014-150T21:19	nan	14.54	North
2014-151T17:53	nan	6.85	North
2014-151T18:50	10.33	11.09	North
2014-151T19:36	17.67	8.61	North
2014-151T21:15	17.00	12.08	North
2014-152T17:30	11.00	5.98	North
2014-152T19:46	17.00	7.47	North
2014-152T20:34	nan	7.36	North
2014-153T18:13	19.67	16.05	North
2014-153T18:57	19.67	16.32	North
2014-153T20:14	21.00	7.46	North
2014-153T21:05	19.00	13.76	North
2014-153T21:46	nan	3.38	North
2014-153T22:30	21.00	7.81	North
2014-153T23:22	15.00	13.62	North
2014-154T18:35	16.33	8.86	North
2014-154T19:42	14.33	9.23	North
2014-154T20:24	nan	8.73	North
2014-154T21:14	8.33	13.74	North
2014-154T23:16	nan	7.18	North
2014-156T08:23	nan	3.43	North
2014-156T09:14	17.67	4.77	North
2014-156T10:04	1.67	6.31	North
2014-156T10:57	nan	2.77	North
2014-156T11:59	nan	4.28	North
2014-156T15:07	17.00	4.22	North
2014-156T17:04	15.67	6.75	North
2014-156T17:55	nan	4.16	North
2014-156T20:35	14.33	5.12	North
2014-156T22:56	nan	5.32	North
2014-157T02:14	nan	5.26	North
2014-157T02:53	nan	4.52	North
2014-158T21:15	15.00	5.32	North
2014-158T22:18	nan	4.59	North
2014-158T23:13	17.67	4.84	North
2014-159T00:38	nan	3.31	North
2014-159T02:01	13.00	4.76	North
2014-160T14:47	17.00	4.89	North
2014-160T16:27	18.33	12.34	North
2014-160T18:09	18.33	11.80	North
2014-160T19:52	19.00	4.68	North
2014-161T03:21	nan	3.68	North
2014-161T18:57	17.67	6.00	North
2014-161T19:35	16.33	8.94	North
2014-161T21:22	21.00	7.43	North
2014-161T22:26	17.00	12.02	North
2014-161T23:24	nan	7.52	North
2014-162T01:24	7.00	13.97	North
2014-162T02:28	nan	15.88	North
2014-162T03:17	8.33	15.14	North
2014-162T05:04	9.67	4.51	North
2014-162T08:22	17.67	6.39	North
2014-162T09:16	21.67	5.48	North
2014-248T12:28	nan	11.69	North
2014-248T13:08	nan	13.81	North

2014-248T14:10	13.67	34.43	North
2014-248T15:01	14.33	33.70	North
2014-248T16:00	nan	34.71	North
2014-248T16:49	4.33	19.54	North
2014-248T18:19	nan	5.68	North
2014-248T18:55	nan	12.19	North
2014-248T19:41	9.67	26.48	North
2014-248T20:25	10.33	53.17	North
2014-256T06:48	6.33	24.12	North
2014-256T07:53	5.00	16.91	North
2014-256T08:59	nan	11.80	North
2014-256T10:27	8.33	12.05	North
2014-256T11:55	9.00	15.90	North
2014-256T12:55	9.00	28.23	North
2014-256T13:44	nan	7.81	North
2014-289T17:15	17.00	10.66	North
2014-289T18:04	nan	3.86	North
2014-289T19:48	12.33	7.15	North
2014-289T21:01	19.00	9.44	North
2014-289T22:22	11.67	12.73	North
2014-289T23:28	13.67	16.59	North
2014-290T00:43	16.33	16.66	North
2014-290T01:42	15.00	20.13	North
2014-290T02:39	13.67	8.28	North
2014-290T04:17	nan	3.88	North
2014-290T05:04	nan	3.20	North
2014-311T03:12	13.67	4.94	North
2014-311T04:17	nan	8.42	North
2014-311T06:11	18.33	9.64	North
2014-311T07:15	19.00	6.06	North
2014-311T10:34	20.33	4.93	North
2014-311T11:35	7.67	6.60	North
2014-327T13:16	23.67	20.89	North
2014-327T14:06	9.00	9.83	North
2014-327T14:59	nan	9.09	North
2014-327T15:45	nan	10.42	North
2014-327T16:29	nan	5.14	North
2014-331T20:56	nan	6.00	North
2014-331T22:00	nan	9.74	North
2014-331T22:46	nan	7.39	North
2014-332T00:21	6.33	5.82	North
2014-332T01:12	5.00	19.43	North
2014-332T02:46	9.00	10.39	North
2014-332T03:35	11.67	15.01	North
2014-332T04:35	13.67	14.97	North
2014-332T05:32	9.00	8.12	North
2014-332T06:14	nan	7.95	North
2014-332T07:19	14.33	20.49	North
2014-332T08:18	nan	10.99	North
2014-335T05:36	11.67	5.41	North
2014-335T06:38	nan	2.99	North
2014-335T07:41	15.67	5.37	North
2016-177T04:51	14.33	6.77	North
2016-177T05:46	13.00	8.16	North
2016-250T23:59	9.00	5.98	North

2016-251T00:39	8.33	7.69	North
2016-251T03:40	nan	6.15	North
2016-251T05:11	17.67	6.50	North
2016-273T18:18	13.67	5.00	North
2016-274T15:43	18.33	3.19	North
2016-275T13:29	17.00	3.64	North
2016-276T00:05	17.67	4.37	North
2016-303T03:57	nan	10.30	North
2016-303T08:56	10.33	4.25	North
2017-014T20:38	23.00	5.65	North
2017-079T07:40	18.33	13.16	North
2017-079T08:57	19.67	10.21	North
2017-079T14:29	19.67	5.70	North
2017-079T15:19	19.00	7.12	North
2017-079T17:28	3.67	3.70	North
2017-079T21:57	15.00	5.55	North
2017-079T23:50	17.00	3.77	North
2017-080T00:37	15.00	4.26	North
2017-080T02:27	19.67	3.37	North
2017-092T16:45	21.00	9.34	North
2017-092T18:01	22.33	5.22	North
2017-092T18:46	0.33	7.67	North
2017-092T20:45	19.00	6.17	North

Figures S1 to S35

Keograms of all sequences used in this study. (a) Keogram similar to the one shown in Figure 3a, with the PPO upward current maxima marked with white lines as in Figure 3b. (b) Total UV power (black) and background UV power (red) as in Figure 3a. (c) The difference between the total and background UV powers in panel (b), with a boxcar average overlaid in red similar to Figure 3c.

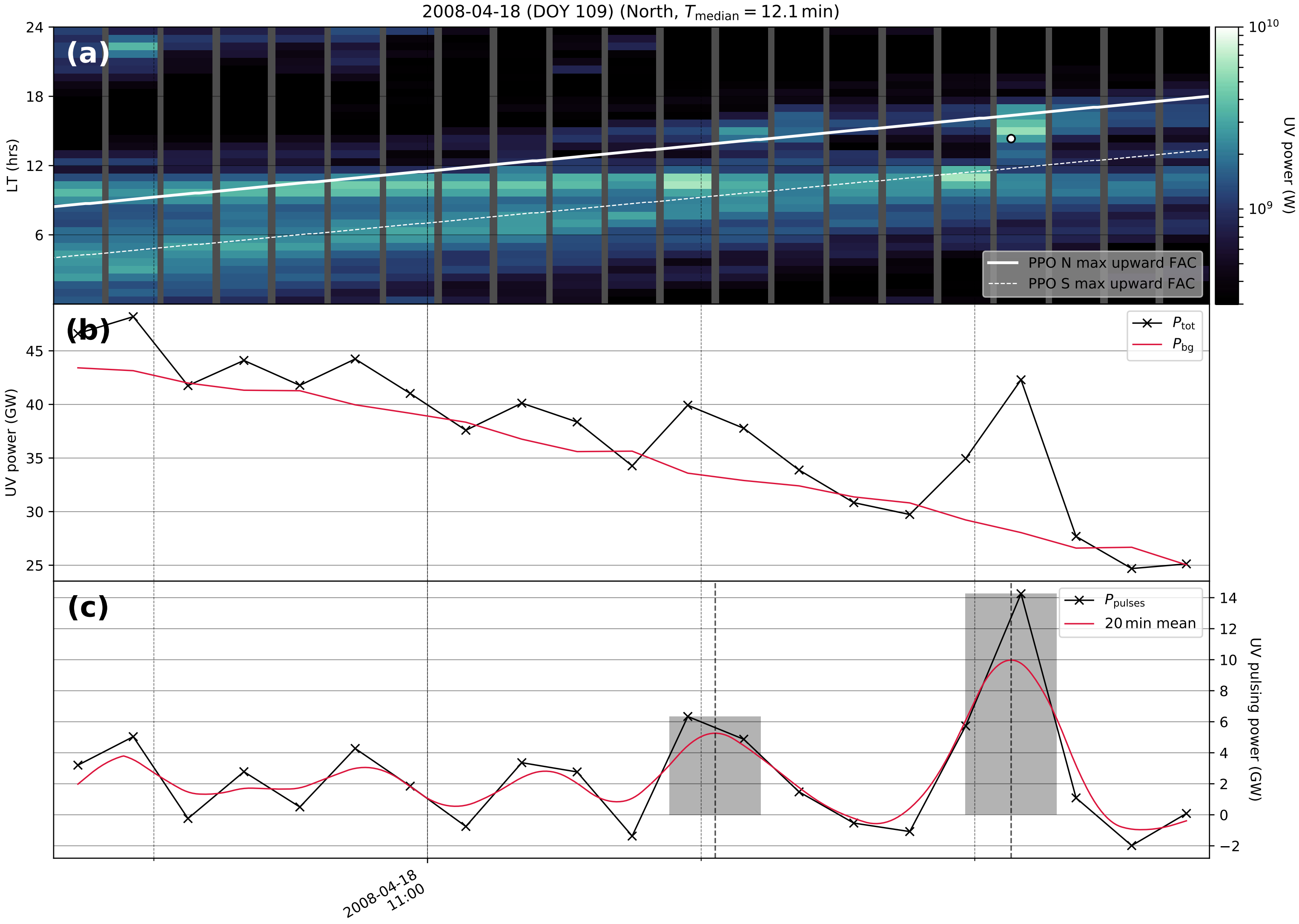
2008-04-18 (DOY 109) (North, $T_{\text{median}} = 12.1\,\text{min}$)
(a)
LT (hrs)
24
18
12
6
UV power (W)
10^{10}
10^{9}
PPO N max upward FAC
PPO S max upward FAC
(b)
UV power (GW)
45
40
35
30
25
P_{tot}
P_{bg}
(c)
UV pulsing power (GW)
14
12
10
8
6
4
2
0
−2
P_{pulses}
20 min mean
2008-04-18 11:00

Figure S1.

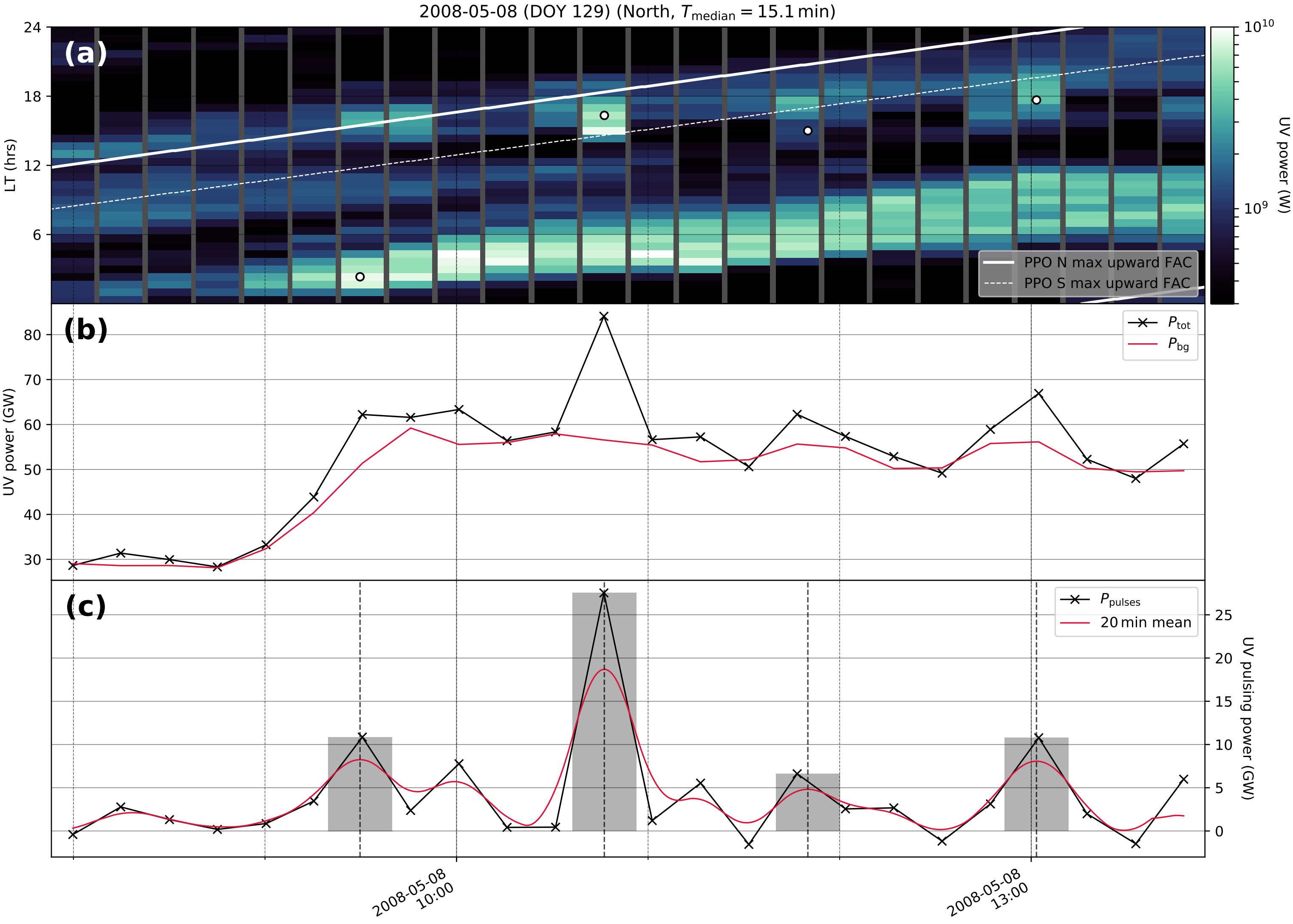
2008-05-08 (DOY 129) (North, $T_{\mathrm{median}} = 15.1\,\mathrm{min}$)
(a)
LT (hrs)
24
18
12
6
UV power (W)
10^{10}
10^{9}
PPO N max upward FAC
PPO S max upward FAC
(b)
UV power (GW)
80
70
60
50
40
30
P_{tot}
P_{bg}
(c)
UV pulsing power (GW)
25
20
15
10
5
0
P_{pulses}
20 min mean
2008-05-08 10:00
2008-05-08 13:00

Figure S2.

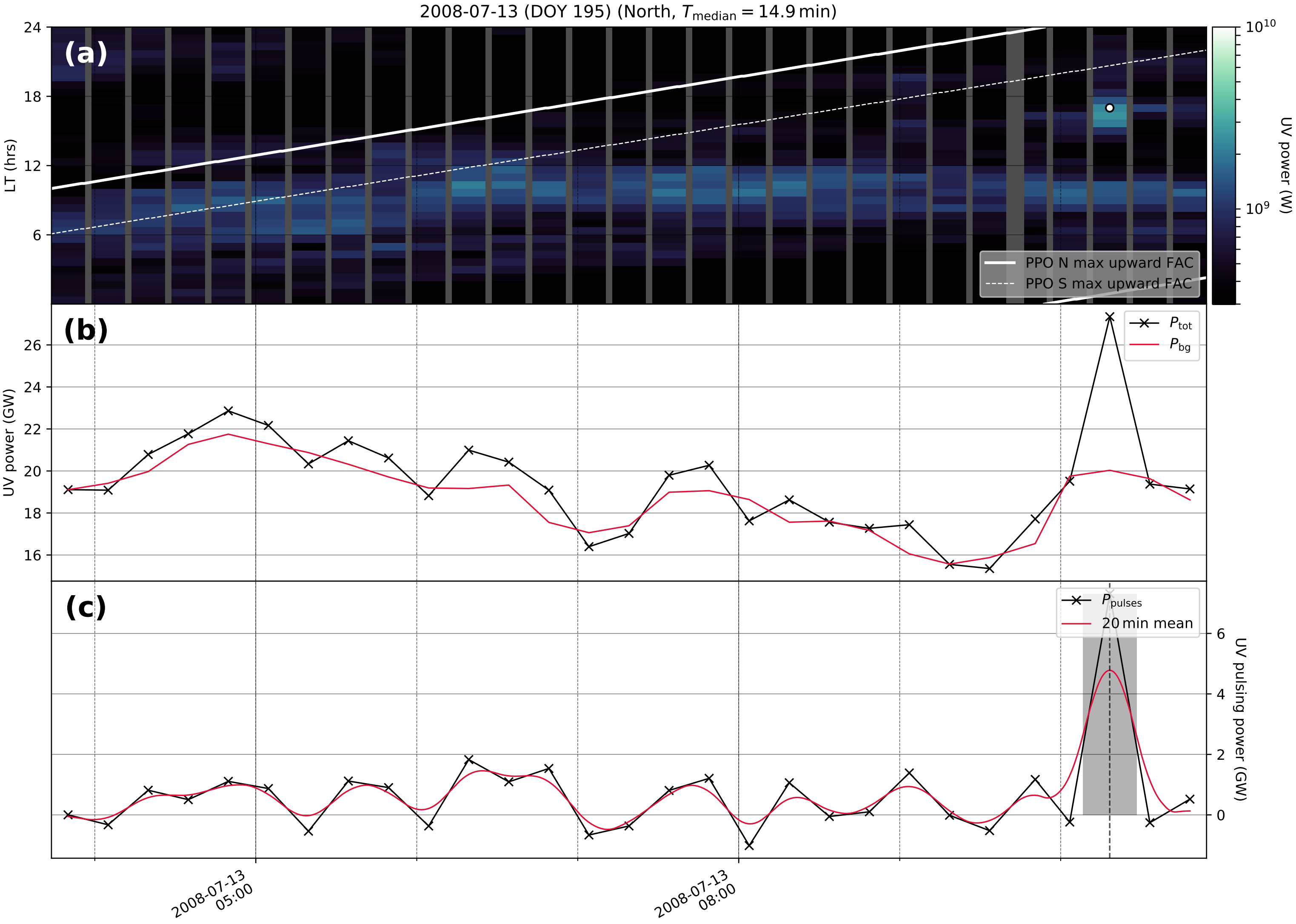
2008-07-13 (DOY 195) (North, $T_{\mathrm{median}} = 14.9$ min)
(a)
(b)
(c)
LT (hrs)
24
18
12
6
UV power (W)
10^{10}
10^{9}
PPO N max upward FAC
PPO S max upward FAC
UV power (GW)
26
24
22
20
18
16
P_{tot}
P_{bg}
P_{pulses}
20 min mean
UV pulsing power (GW)
6
4
2
0
2008-07-13 05:00
2008-07-13 08:00

Figure S3.

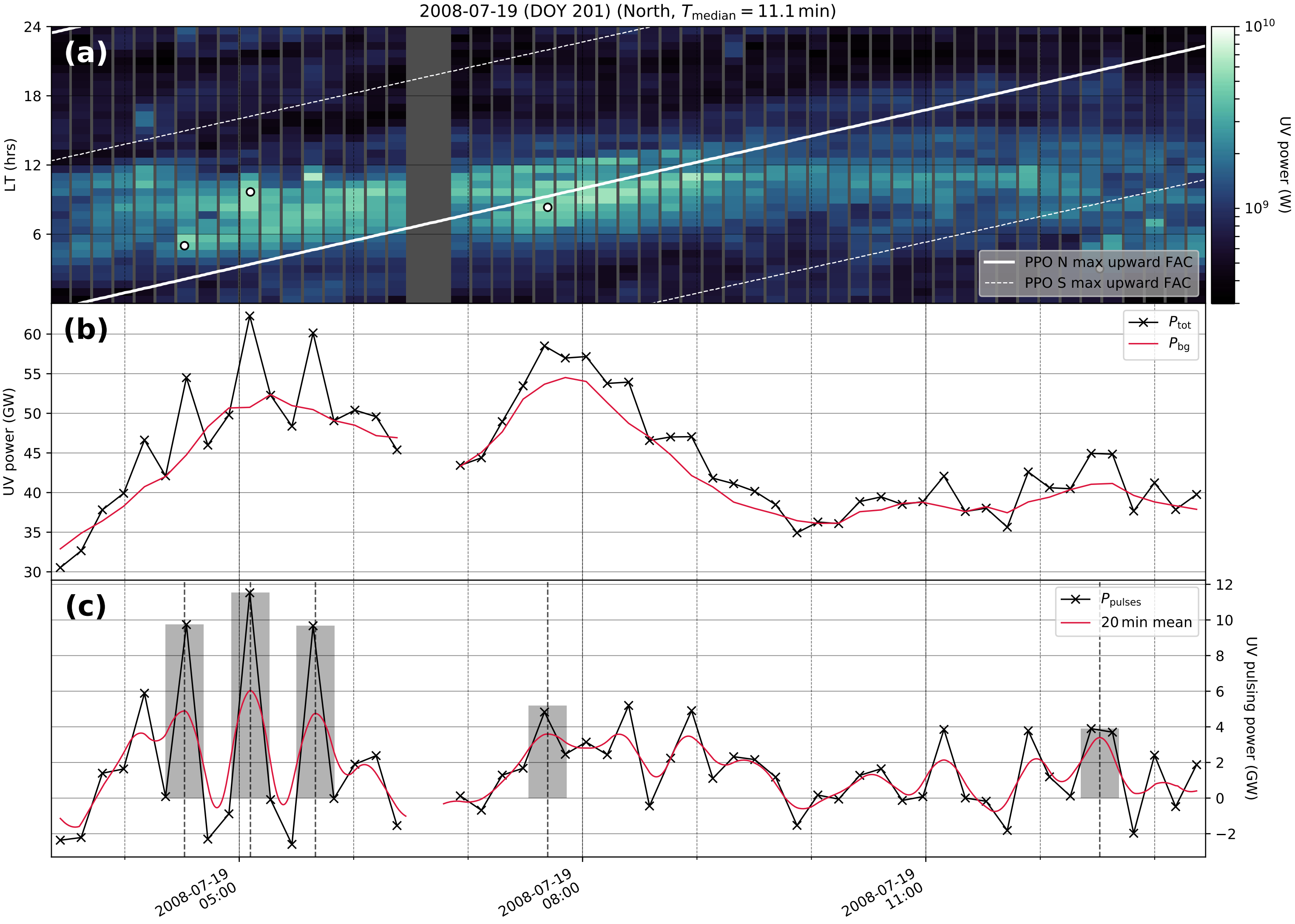
2008-07-19 (DOY 201) (North, $T_{\mathrm{median}} = 11.1$ min)
(a)
LT (hrs)
24
18
12
6
PPO N max upward FAC
PPO S max upward FAC
UV power (W)
10^{10}
10^{9}
(b)
UV power (GW)
60
55
50
45
40
35
30
P_{tot}
P_{bg}
(c)
P_{pulses}
20 min mean
UV pulsing power (GW)
12
10
8
6
4
2
0
−2
2008-07-19 05:00
2008-07-19 08:00
2008-07-19 11:00

Figure S4.

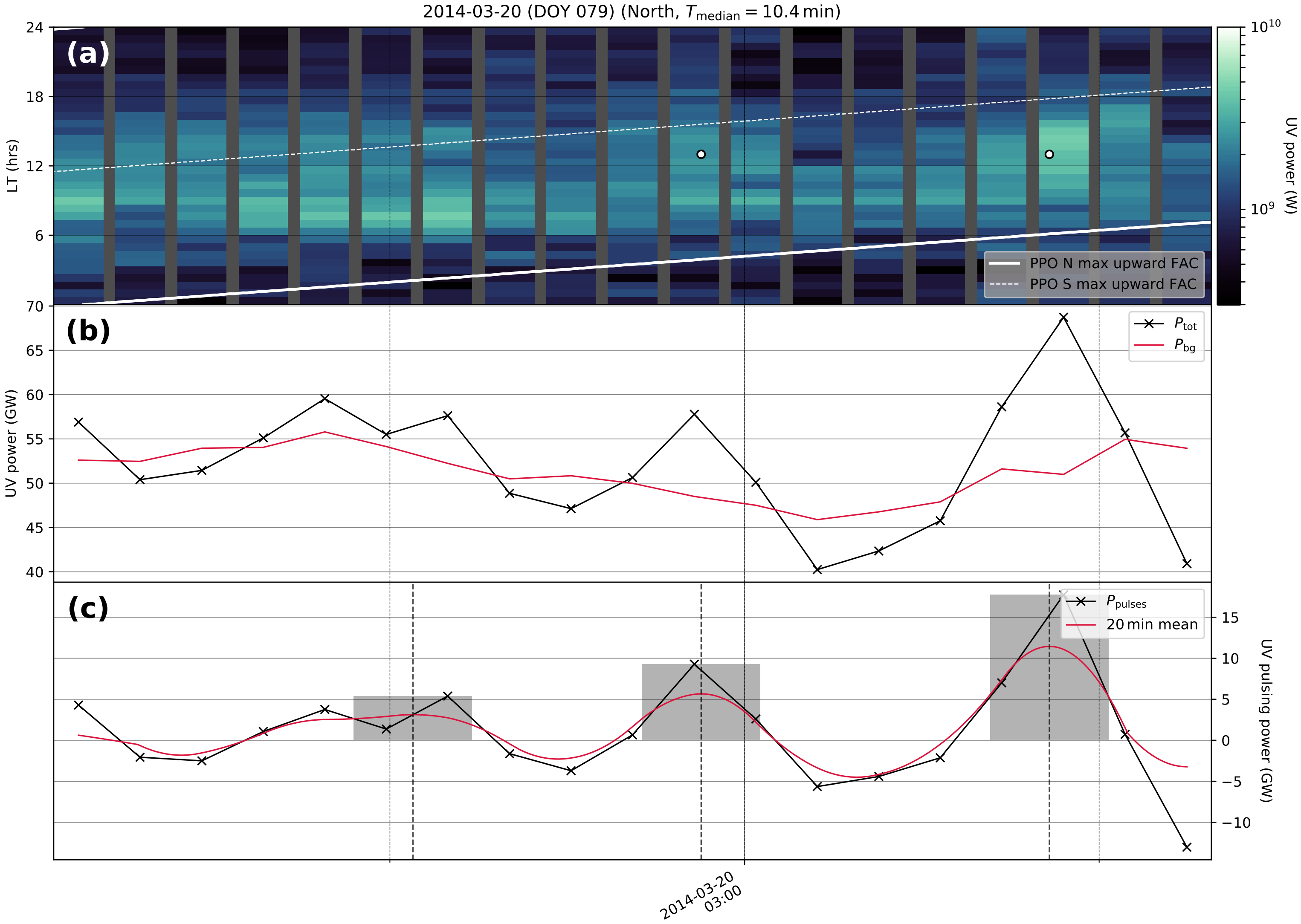
2014-03-20 (DOY 079) (North, $T_{median} = 10.4$ min)
(a)
LT (hrs)
24
18
12
6
70
UV power (W)
10^{10}
10^{9}
PPO N max upward FAC
PPO S max upward FAC
(b)
UV power (GW)
70
65
60
55
50
45
40
P_{tot}
P_{bg}
(c)
P_{pulses}
20 min mean
UV pulsing power (GW)
15
10
5
0
−5
−10
2014-03-20
03:00

Figure S5.

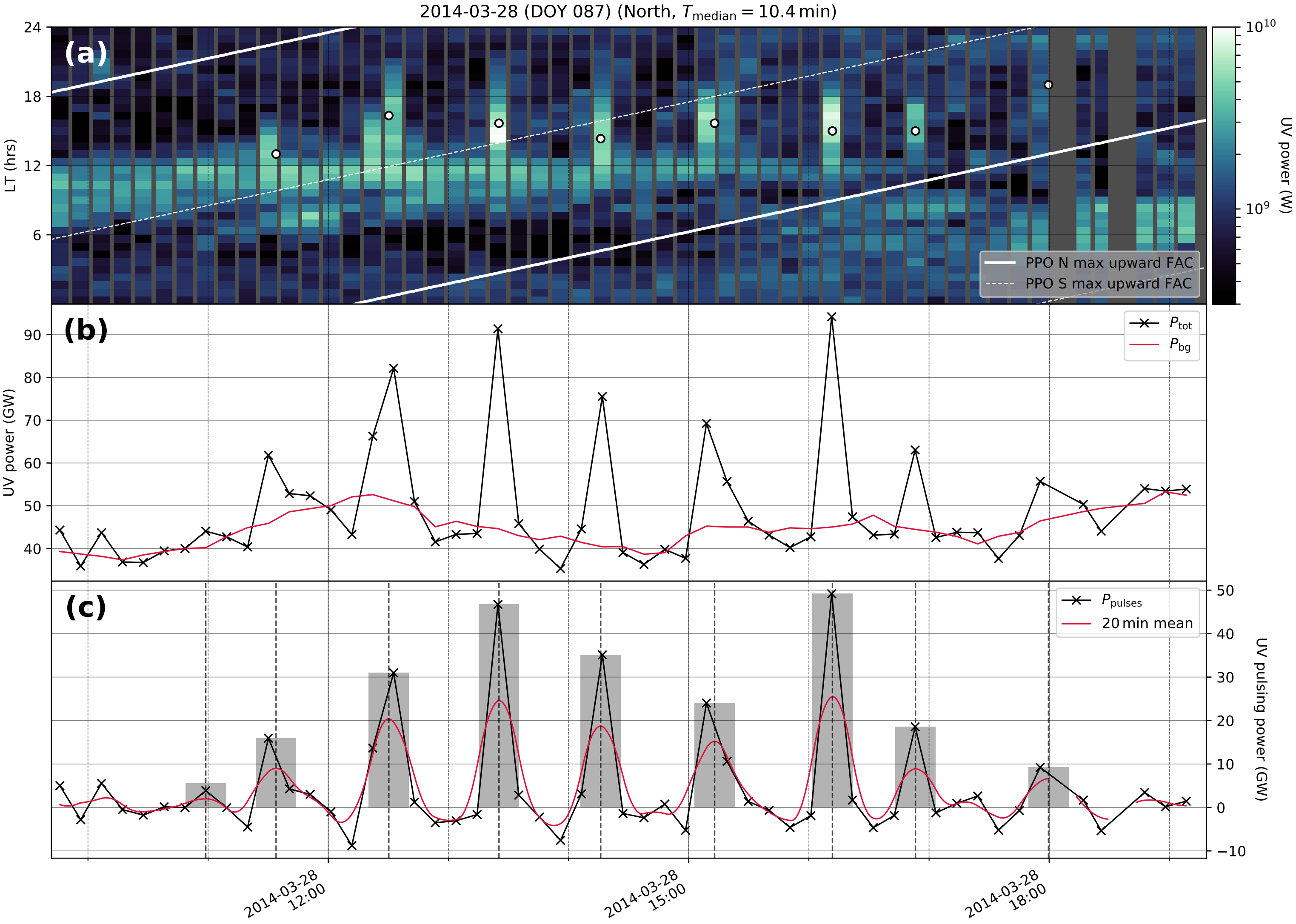
2014-03-28 (DOY 087) (North, $T_{\mathrm{median}} = 10.4$ min)
(a)
(b)
(c)
LT (hrs)
24
18
12
6
UV power (W)
10^{10}
10^{9}
PPO N max upward FAC
PPO S max upward FAC
UV power (GW)
90
80
70
60
50
40
P_{tot}
P_{bg}
P_{pulses}
20 min mean
UV pulsing power (GW)
50
40
30
20
10
0
−10
2014-03-28 12:00
2014-03-28 15:00
2014-03-28 18:00

Figure S6.

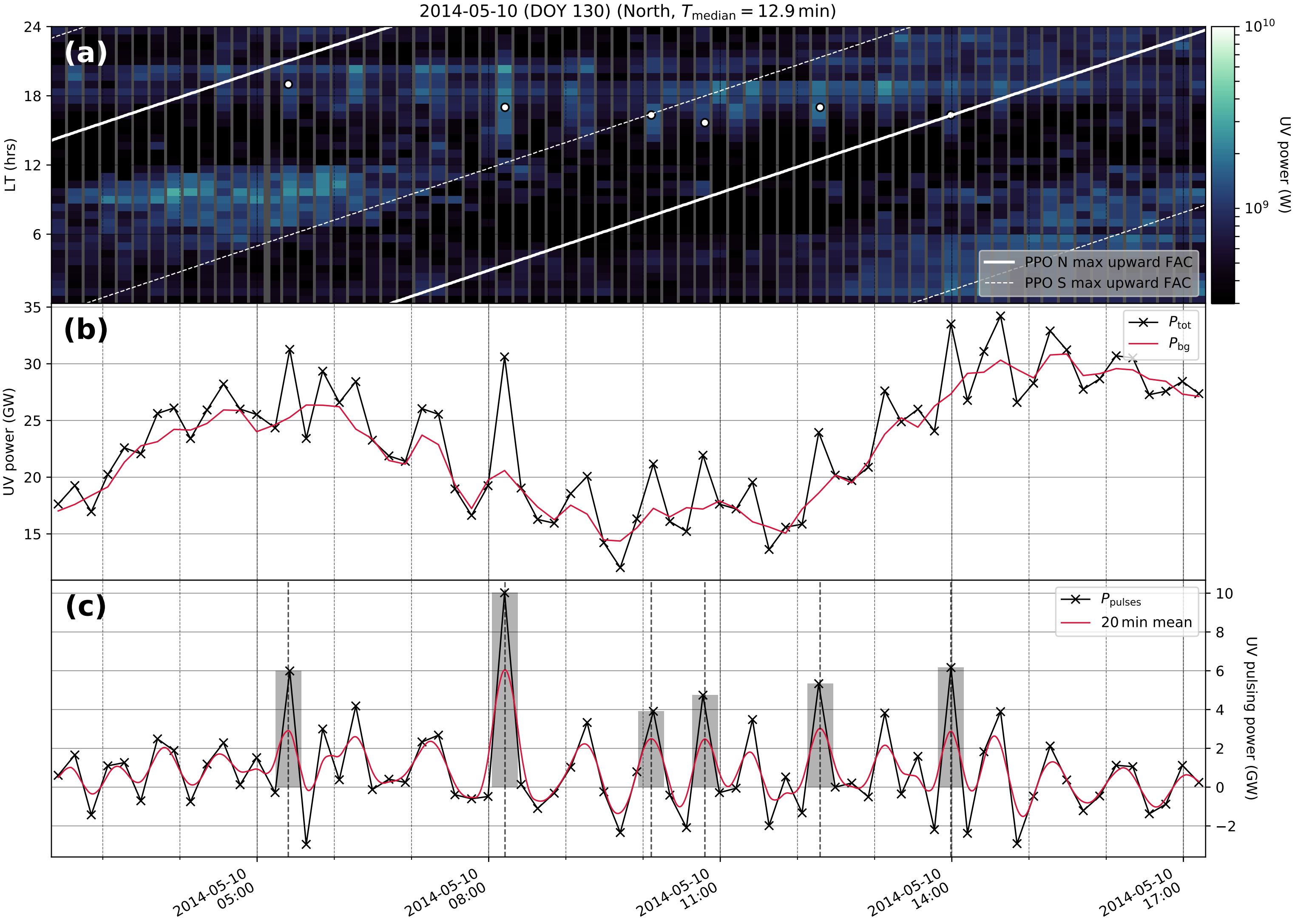
2014-05-10 (DOY 130) (North, $T_{median} = 12.9$ min)
(a)
(b)
(c)
LT (hrs)
24
18
12
6
UV power (W)
10^{10}
10^9
PPO N max upward FAC
PPO S max upward FAC
UV power (GW)
35
30
25
20
15
P_{tot}
P_{bg}
P_{pulses}
20 min mean
UV pulsing power (GW)
10
8
6
4
2
0
−2
2014-05-10 05:00
2014-05-10 08:00
2014-05-10 11:00
2014-05-10 14:00
2014-05-10 17:00

Figure S7.

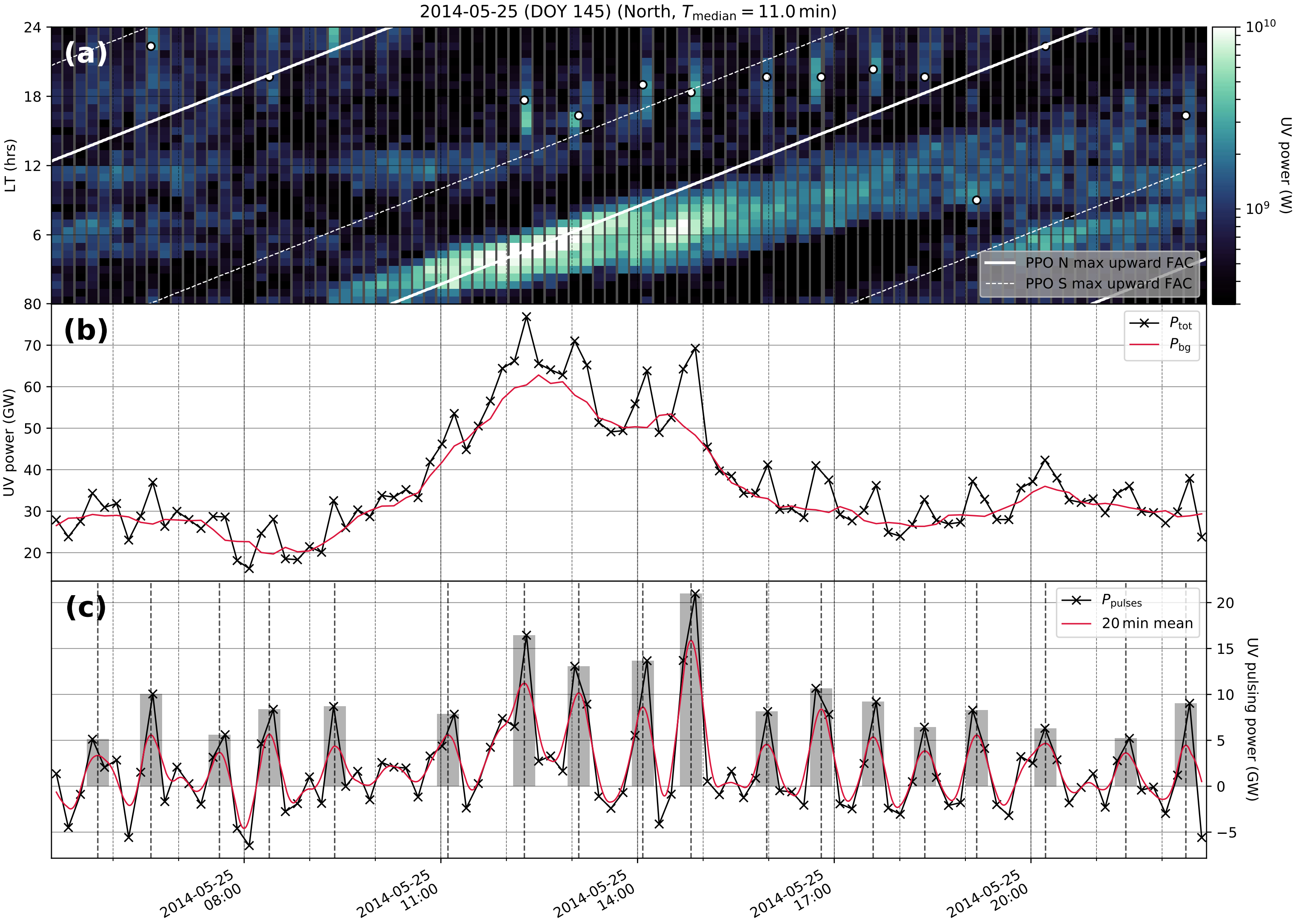
2014-05-25 (DOY 145) (North, $T_{median} = 11.0$ min)
(a)
LT (hrs)
24
18
12
6
0
PPO N max upward FAC
PPO S max upward FAC
UV power (W)
10^{10}
10^{9}
(b)
UV power (GW)
80
70
60
50
40
30
20
P_{tot}
P_{bg}
(c)
P_{pulses}
20 min mean
UV pulsing power (GW)
20
15
10
5
0
−5
2014-05-25 08:00
2014-05-25 11:00
2014-05-25 14:00
2014-05-25 17:00
2014-05-25 20:00

Figure S8.

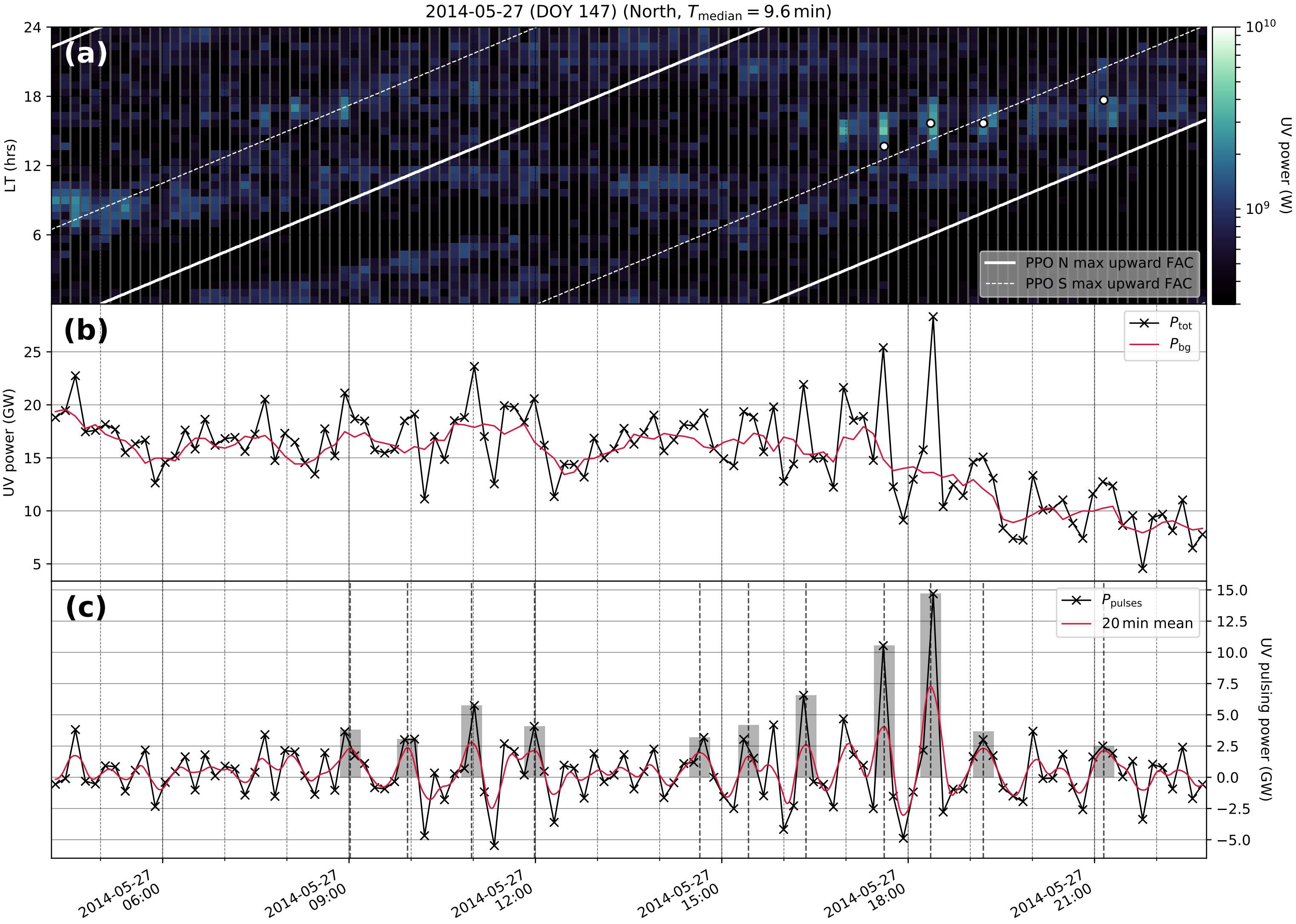
2014-05-27 (DOY 147) (North, $T_{\mathrm{median}} = 9.6\,\mathrm{min}$)
(a)
(b)
(c)
LT (hrs)
24
18
12
6
UV power (W)
10^{10}
10^{9}
PPO N max upward FAC
PPO S max upward FAC
UV power (GW)
25
20
15
10
5
P_{tot}
P_{bg}
P_{pulses}
20 min mean
UV pulsing power (GW)
15.0
12.5
10.0
7.5
5.0
2.5
0.0
−2.5
−5.0
2014-05-27 06:00
2014-05-27 09:00
2014-05-27 12:00
2014-05-27 15:00
2014-05-27 18:00
2014-05-27 21:00

Figure S9.

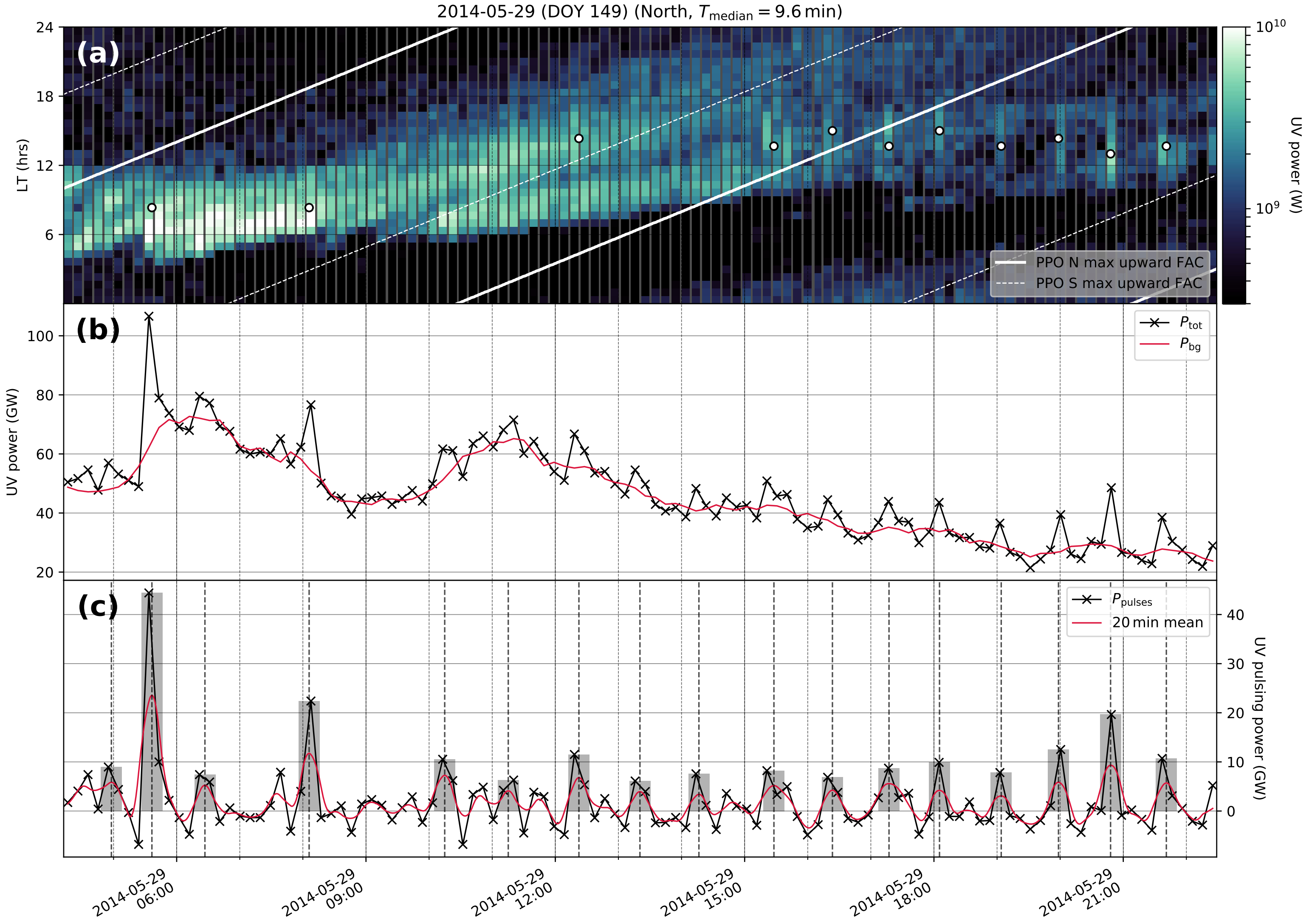
2014-05-29 (DOY 149) (North, $T_{\mathrm{median}} = 9.6\,\mathrm{min}$)
(a)
(b)
(c)
LT (hrs)
24
18
12
6
UV power (W)
10^{10}
10^{9}
PPO N max upward FAC
PPO S max upward FAC
UV power (GW)
100
80
60
40
20
P_{tot}
P_{bg}
P_{pulses}
20 min mean
UV pulsing power (GW)
40
30
20
10
0
2014-05-29 06:00
2014-05-29 09:00
2014-05-29 12:00
2014-05-29 15:00
2014-05-29 18:00
2014-05-29 21:00

Figure S10.

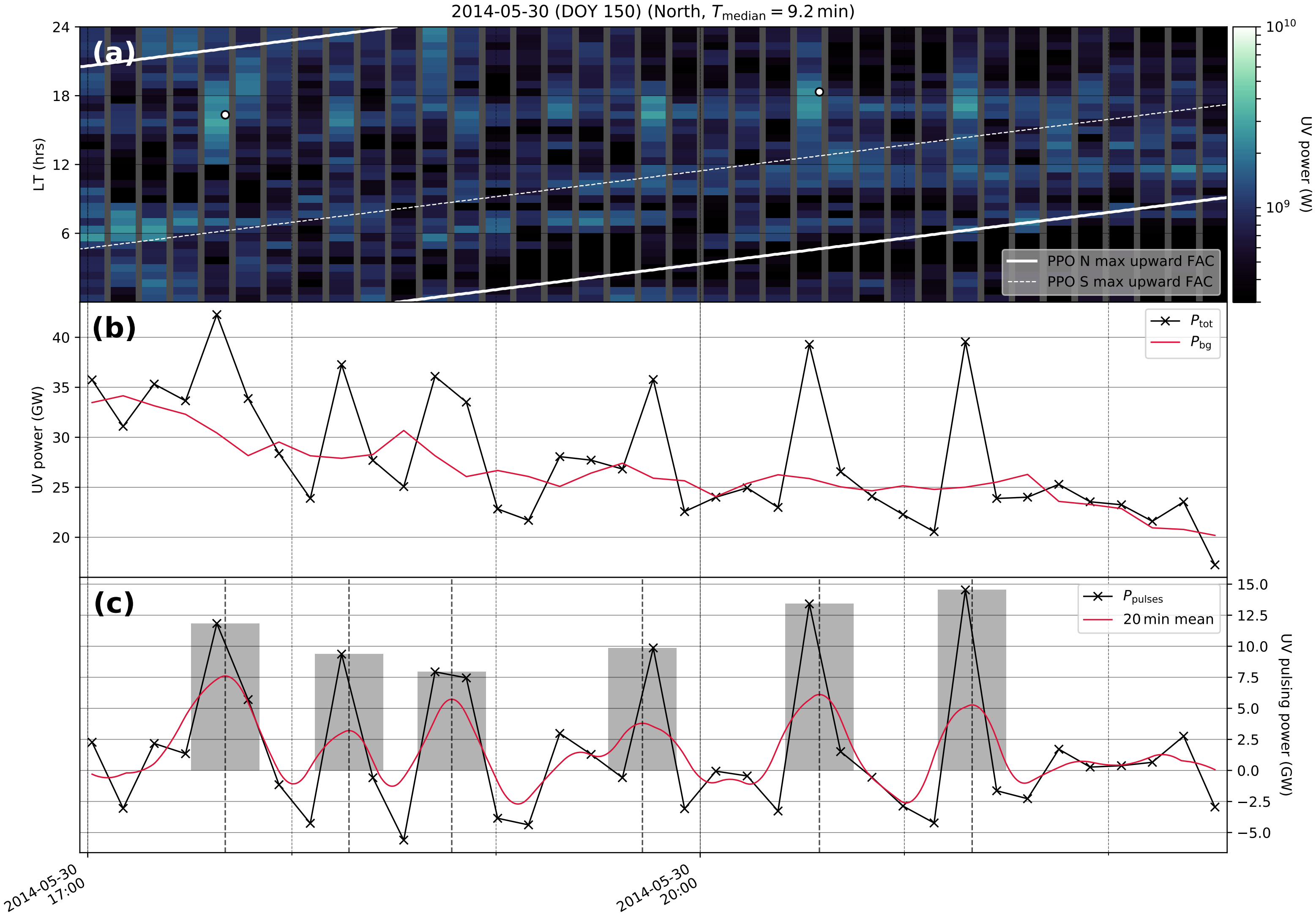
2014-05-30 (DOY 150) (North, $T_{\text{median}} = 9.2$ min)
(a)
LT (hrs)
24
18
12
6
UV power (W)
10^{10}
10^9
PPO N max upward FAC
PPO S max upward FAC
(b)
UV power (GW)
40
35
30
25
20
P_{tot}
P_{bg}
(c)
P_{pulses}
20 min mean
UV pulsing power (GW)
15.0
12.5
10.0
7.5
5.0
2.5
0.0
−2.5
−5.0
2014-05-30 17:00
2014-05-30 20:00

Figure S11.

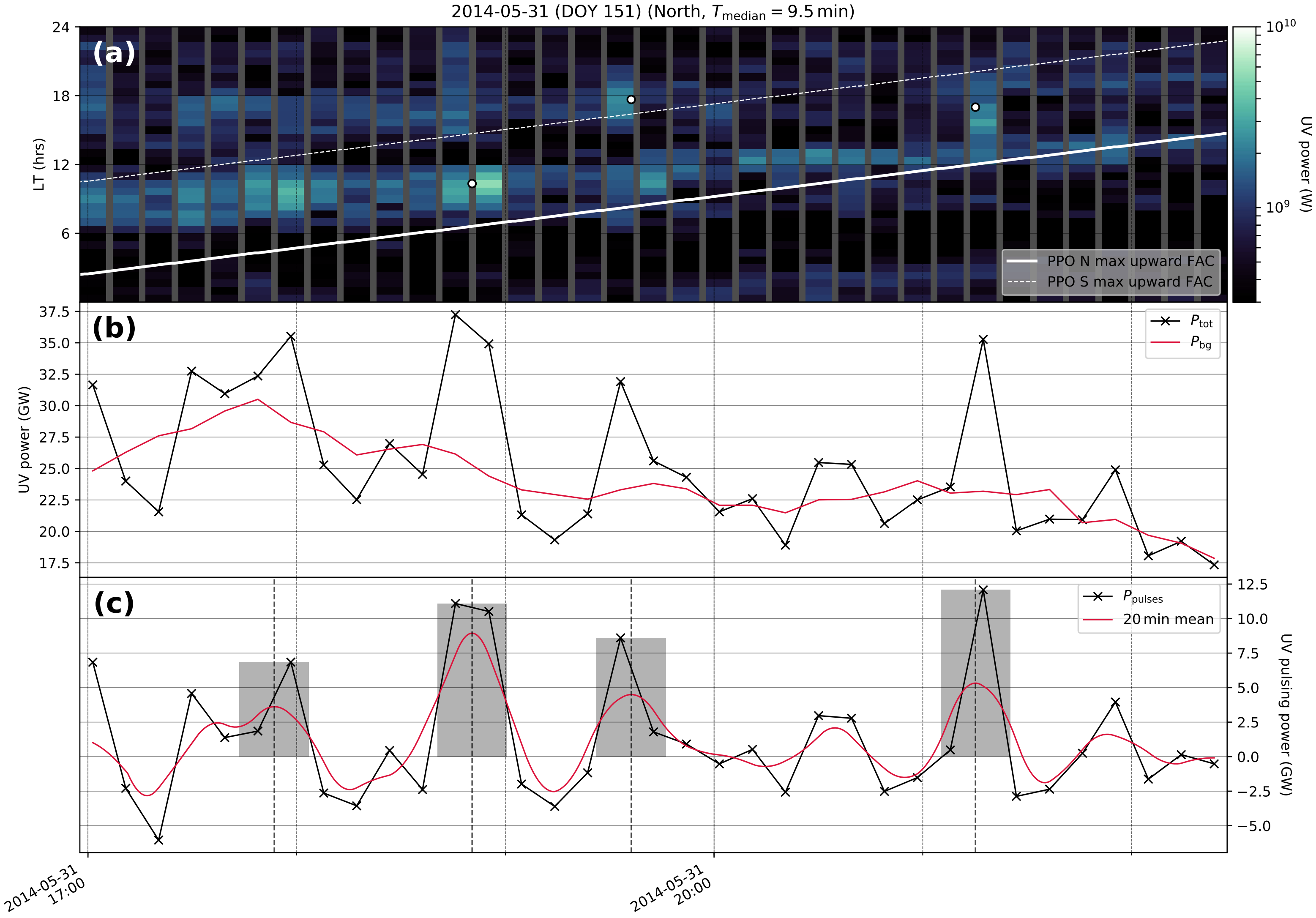
2014-05-31 (DOY 151) (North, T_{median} = 9.5 min)
(a)
LT (hrs)
24
18
12
6
PPO N max upward FAC
PPO S max upward FAC
UV power (W)
10^{10}
10^{9}
(b)
UV power (GW)
37.5
35.0
32.5
30.0
27.5
25.0
22.5
20.0
17.5
P_{tot}
P_{bg}
(c)
UV pulsing power (GW)
12.5
10.0
7.5
5.0
2.5
0.0
−2.5
−5.0
P_{pulses}
20 min mean
2014-05-31 17:00
2014-05-31 20:00

Figure S12.

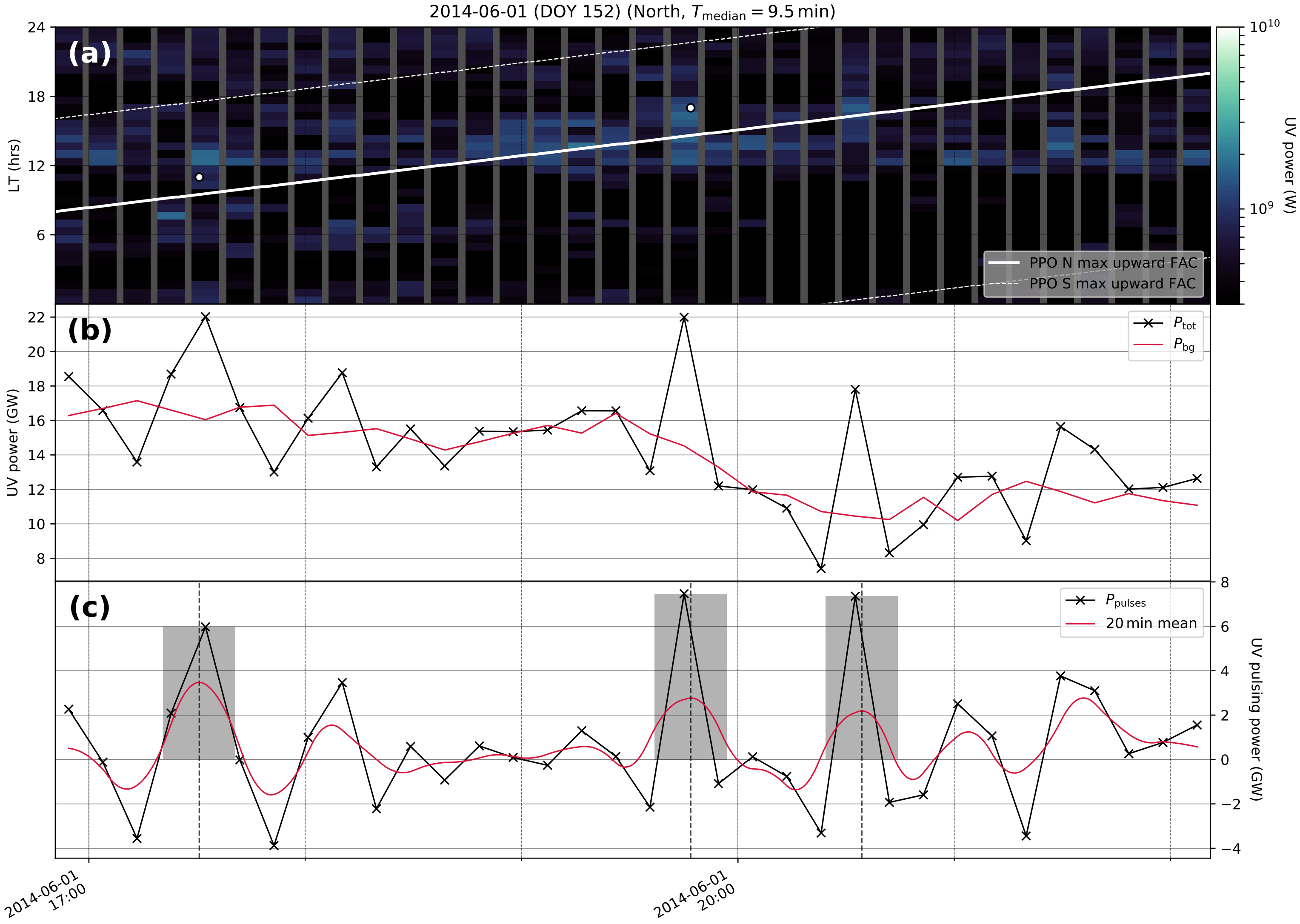
2014-06-01 (DOY 152) (North, T_{median} = 9.5 min)
(a)
(b)
(c)
LT (hrs)
24
18
12
6
UV power (W)
10^{10}
10^9
PPO N max upward FAC
PPO S max upward FAC
UV power (GW)
22
20
18
16
14
12
10
8
P_{tot}
P_{bg}
P_{pulses}
20 min mean
UV pulsing power (GW)
8
6
4
2
0
−2
−4
2014-06-01 17:00
2014-06-01 20:00

Figure S13.

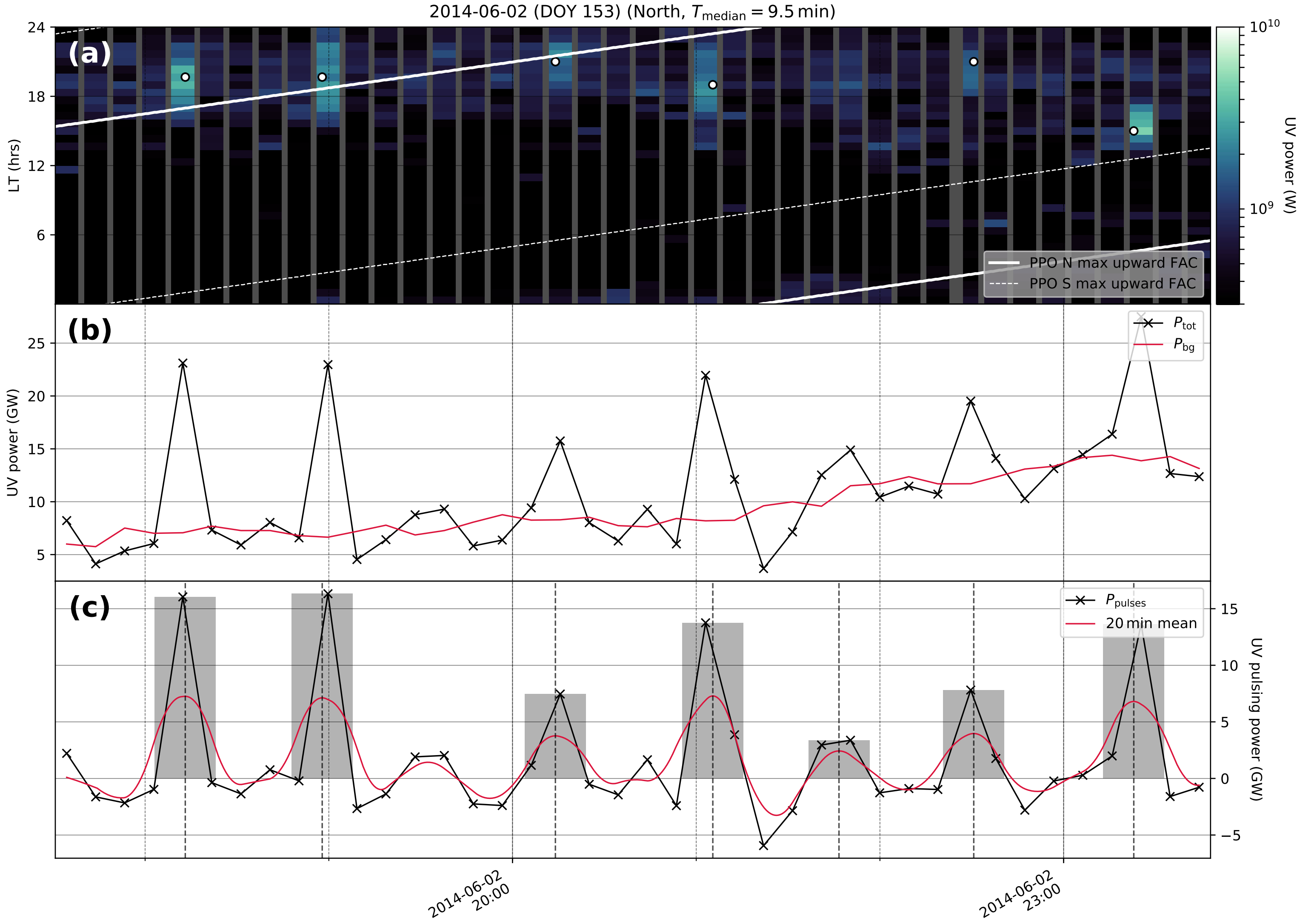
2014-06-02 (DOY 153) (North, $T_{\mathrm{median}} = 9.5\,\mathrm{min}$)
(a)
(b)
(c)
LT (hrs)
24
18
12
6
PPO N max upward FAC
PPO S max upward FAC
UV power (W)
10^{10}
10^{9}
UV power (GW)
25
20
15
10
5
P_{tot}
P_{bg}
P_{pulses}
20 min mean
UV pulsing power (GW)
15
10
5
0
−5
2014-06-02 20:00
2014-06-02 23:00

Figure S14.

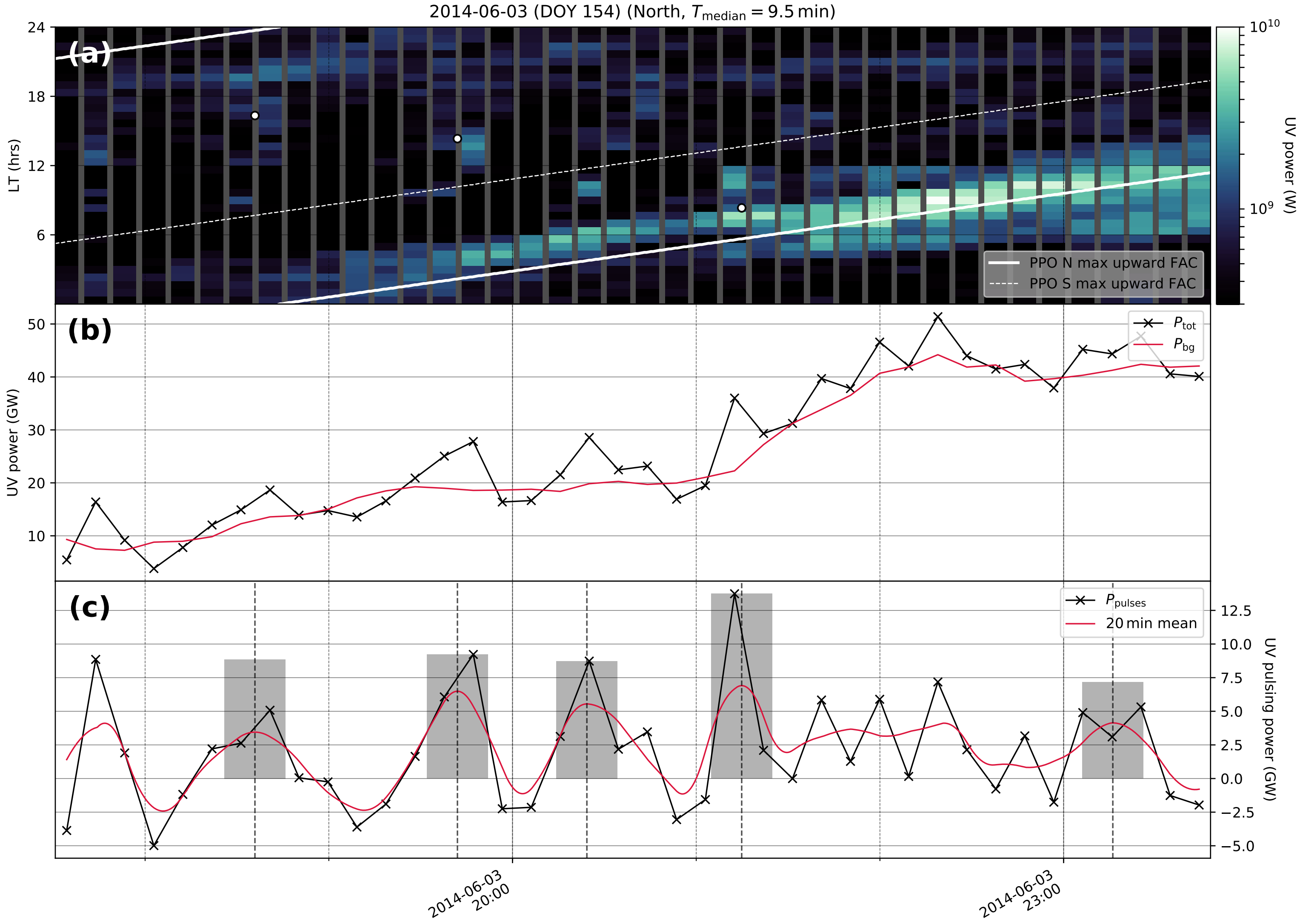
2014-06-03 (DOY 154) (North, $T_{\mathrm{median}} = 9.5\,\mathrm{min}$)
(a)
LT (hrs)
24
18
12
6
PPO N max upward FAC
PPO S max upward FAC
10^{10}
10^{9}
UV power (W)
(b)
UV power (GW)
50
40
30
20
10
P_{tot}
P_{bg}
(c)
P_{pulses}
20 min mean
UV pulsing power (GW)
12.5
10.0
7.5
5.0
2.5
0.0
−2.5
−5.0
2014-06-03 20:00
2014-06-03 23:00

Figure S15.

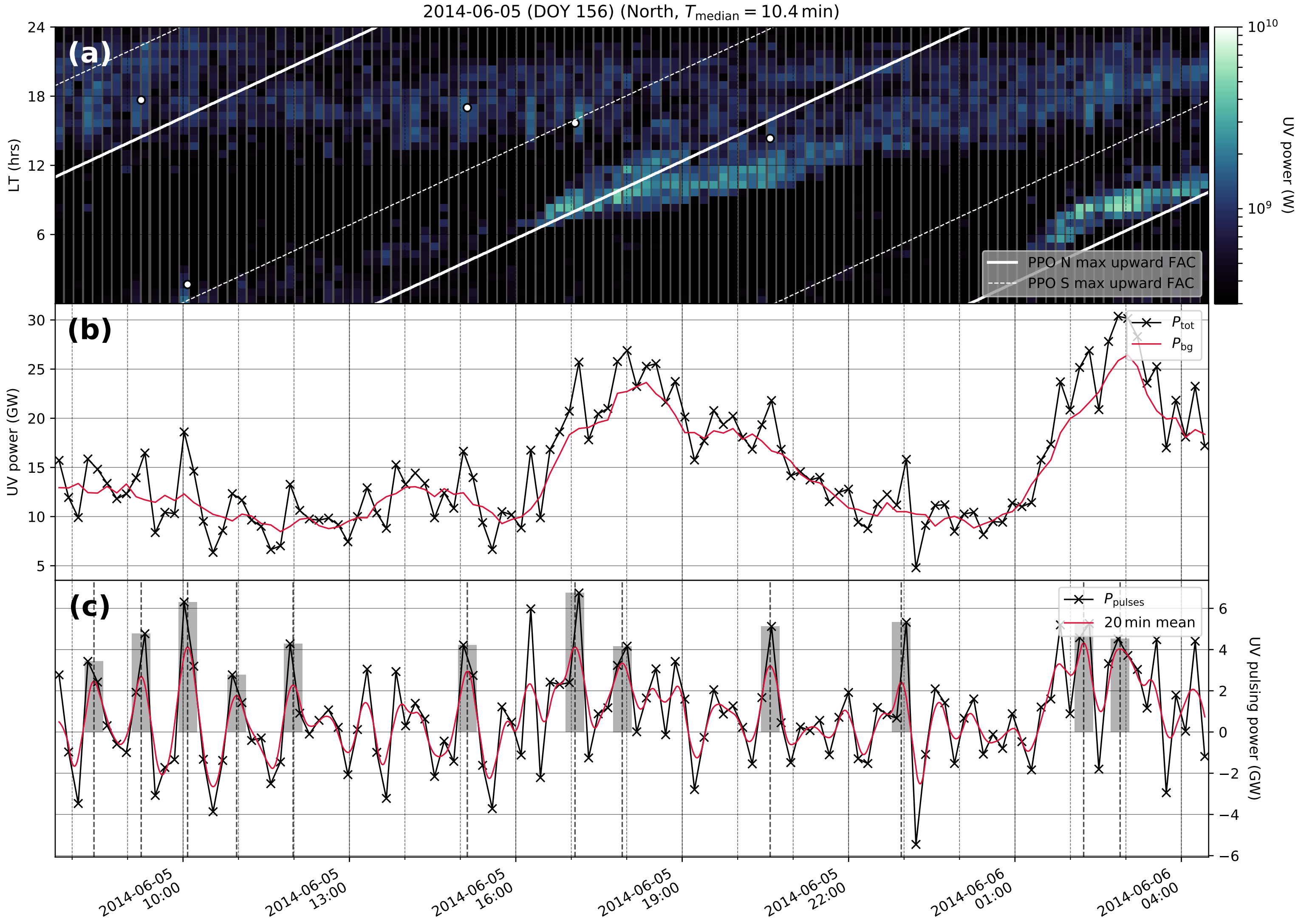
2014-06-05 (DOY 156) (North, $T_{\text{median}} = 10.4$ min)
(a)
LT (hrs)
24
18
12
6
PPO N max upward FAC
PPO S max upward FAC
10^{10}
10^9
UV power (W)
(b)
UV power (GW)
30
25
20
15
10
5
P_{tot}
P_{bg}
(c)
P_{pulses}
20 min mean
UV pulsing power (GW)
6
4
2
0
−2
−4
−6
2014-06-05 10:00
2014-06-05 13:00
2014-06-05 16:00
2014-06-05 19:00
2014-06-05 22:00
2014-06-06 01:00
2014-06-06 04:00

Figure S16.

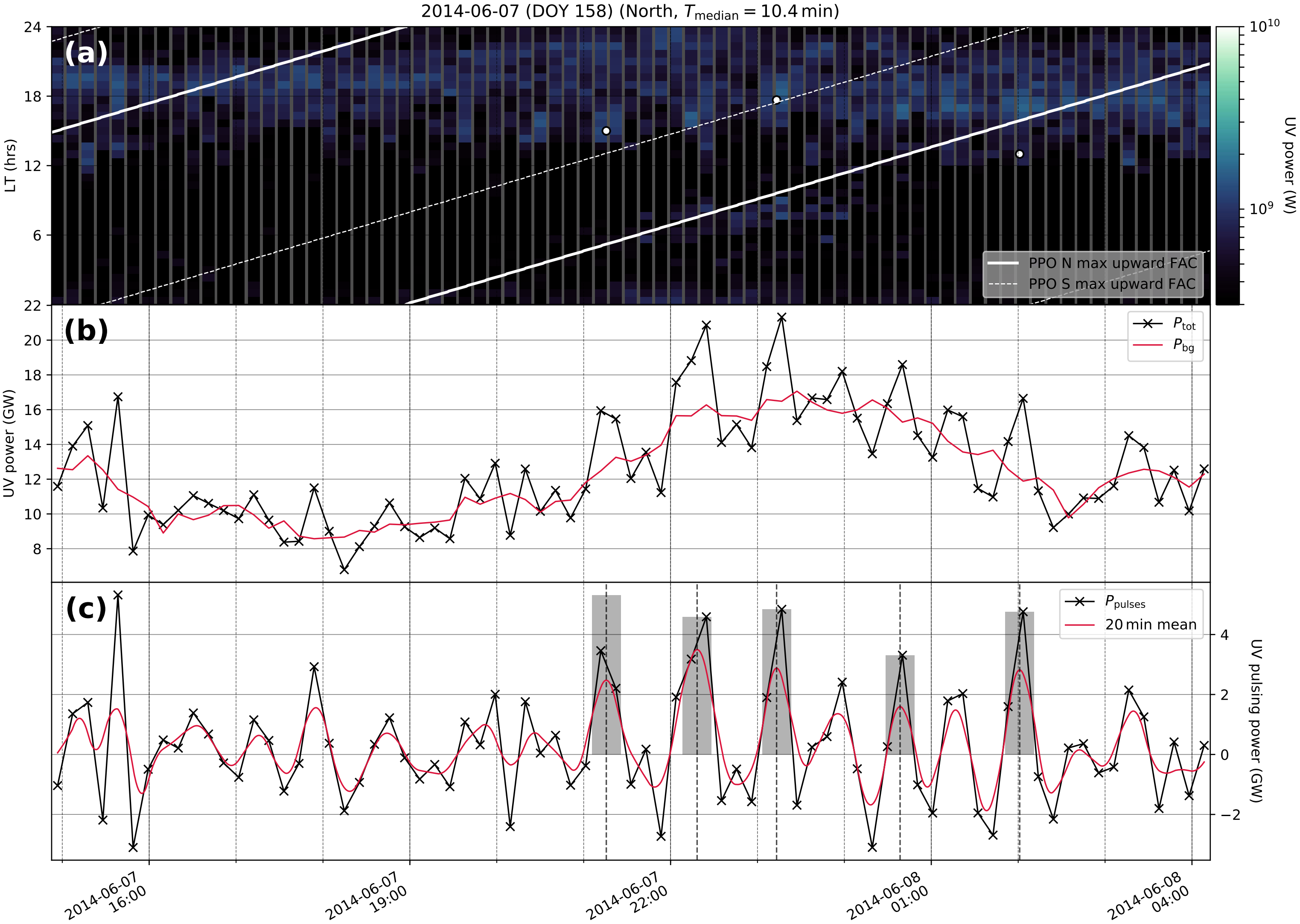
2014-06-07 (DOY 158) (North, $T_{median} = 10.4$ min)
(a)
(b)
(c)
LT (hrs)
24
18
12
6
22
UV power (W)
10^{10}
10^{9}
PPO N max upward FAC
PPO S max upward FAC
UV power (GW)
20
18
16
14
12
10
8
P_{tot}
P_{bg}
P_{pulses}
20 min mean
UV pulsing power (GW)
4
2
0
−2
2014-06-07 16:00
2014-06-07 19:00
2014-06-07 22:00
2014-06-08 01:00
2014-06-08 04:00

Figure S17.

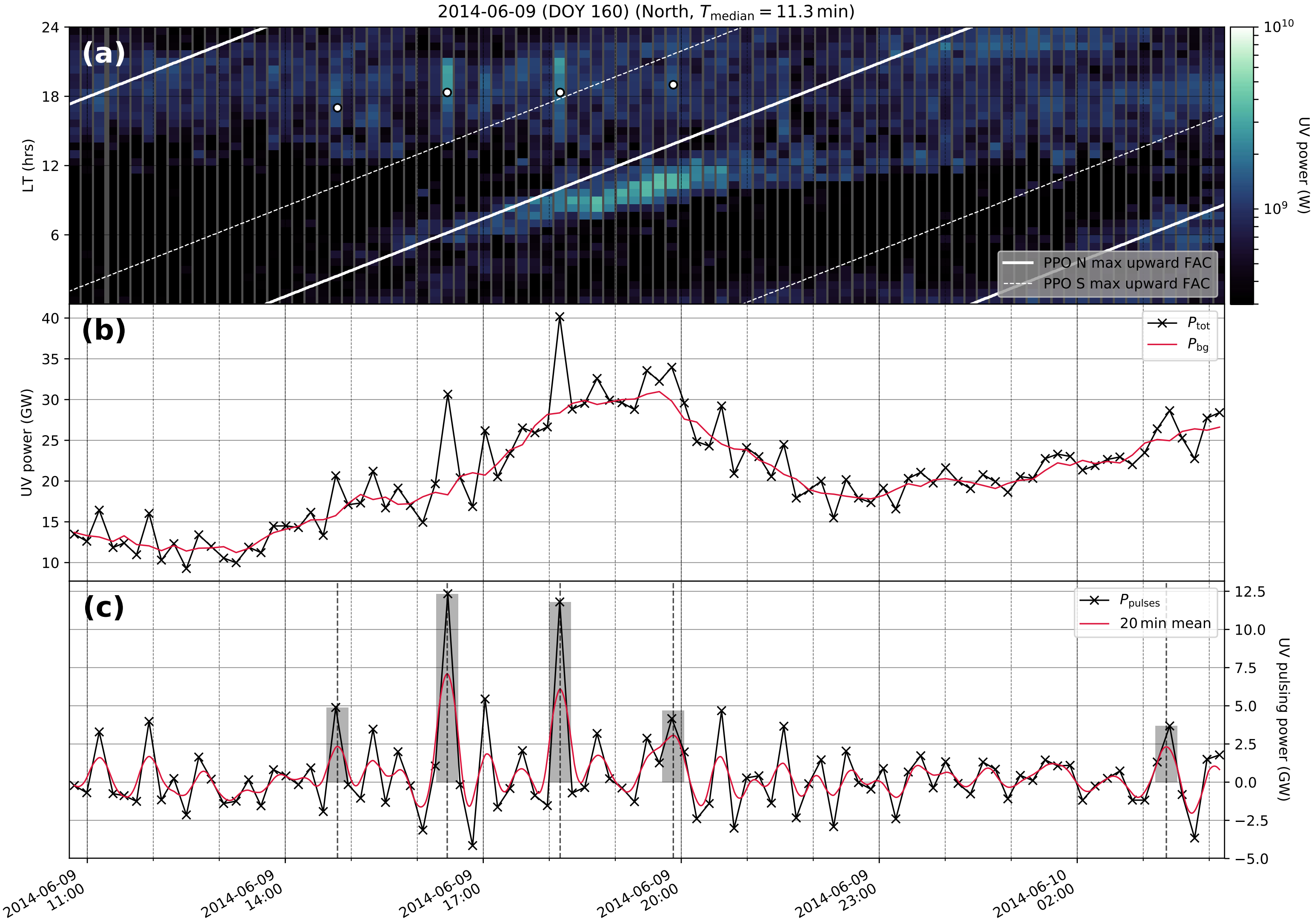
2014-06-09 (DOY 160) (North, $T_{\mathrm{median}} = 11.3$ min)
(a)
LT (hrs)
24
18
12
6
PPO N max upward FAC
PPO S max upward FAC
UV power (W)
10^{10}
10^{9}
(b)
UV power (GW)
40
35
30
25
20
15
10
P_{tot}
P_{bg}
(c)
UV pulsing power (GW)
12.5
10.0
7.5
5.0
2.5
0.0
−2.5
−5.0
P_{pulses}
20 min mean
2014-06-09 11:00
2014-06-09 14:00
2014-06-09 17:00
2014-06-09 20:00
2014-06-09 23:00
2014-06-10 02:00

Figure S18.

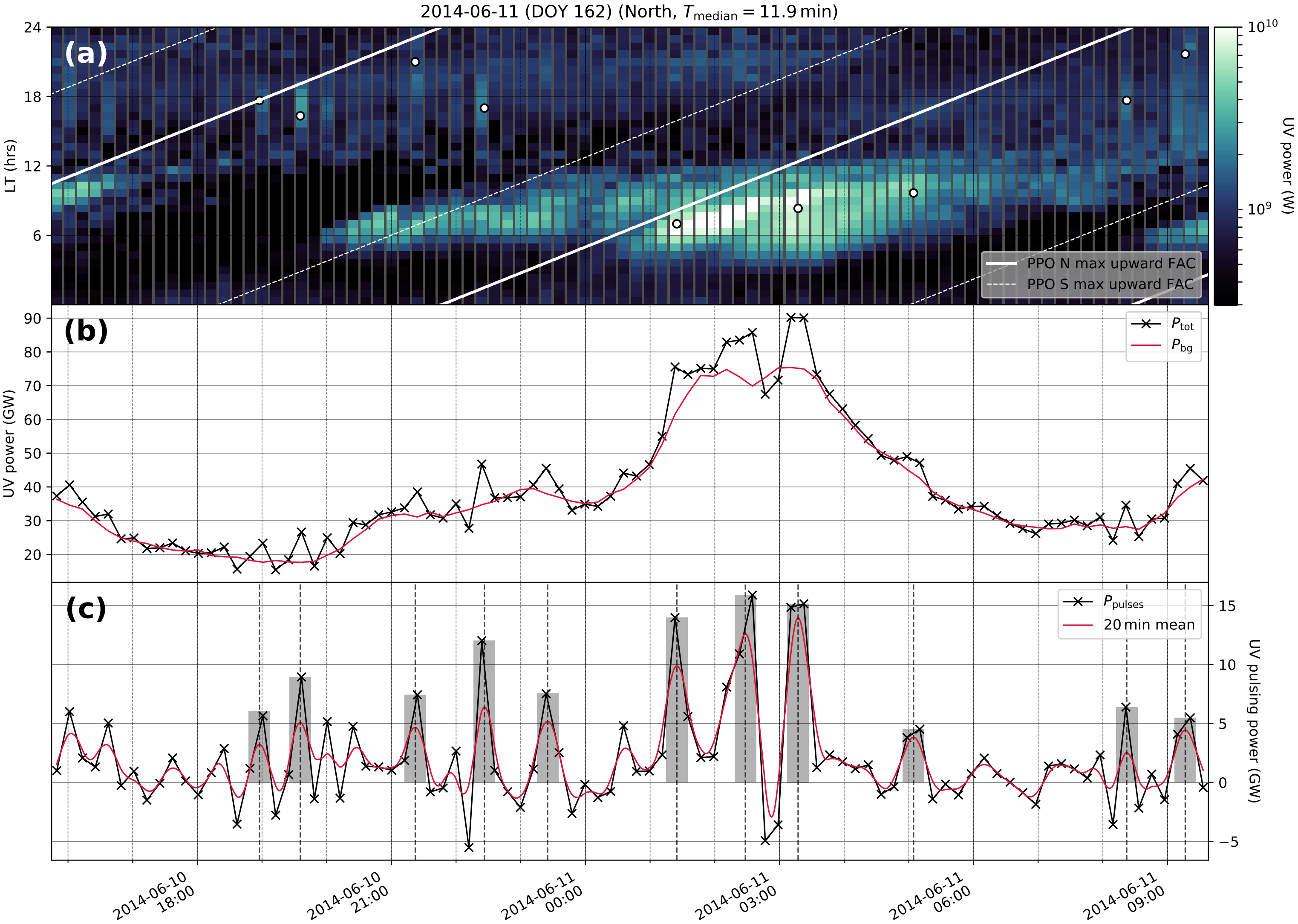
2014-06-11 (DOY 162) (North, $T_{\mathrm{median}} = 11.9$ min)
(a)
(b)
(c)
LT (hrs)
24
18
12
6
UV power (W)
10^{10}
10^{9}
PPO N max upward FAC
PPO S max upward FAC
UV power (GW)
90
80
70
60
50
40
30
20
P_{tot}
P_{bg}
P_{pulses}
20 min mean
UV pulsing power (GW)
15
10
5
0
−5
2014-06-10 18:00
2014-06-10 21:00
2014-06-11 00:00
2014-06-11 03:00
2014-06-11 06:00
2014-06-11 09:00

Figure S19.

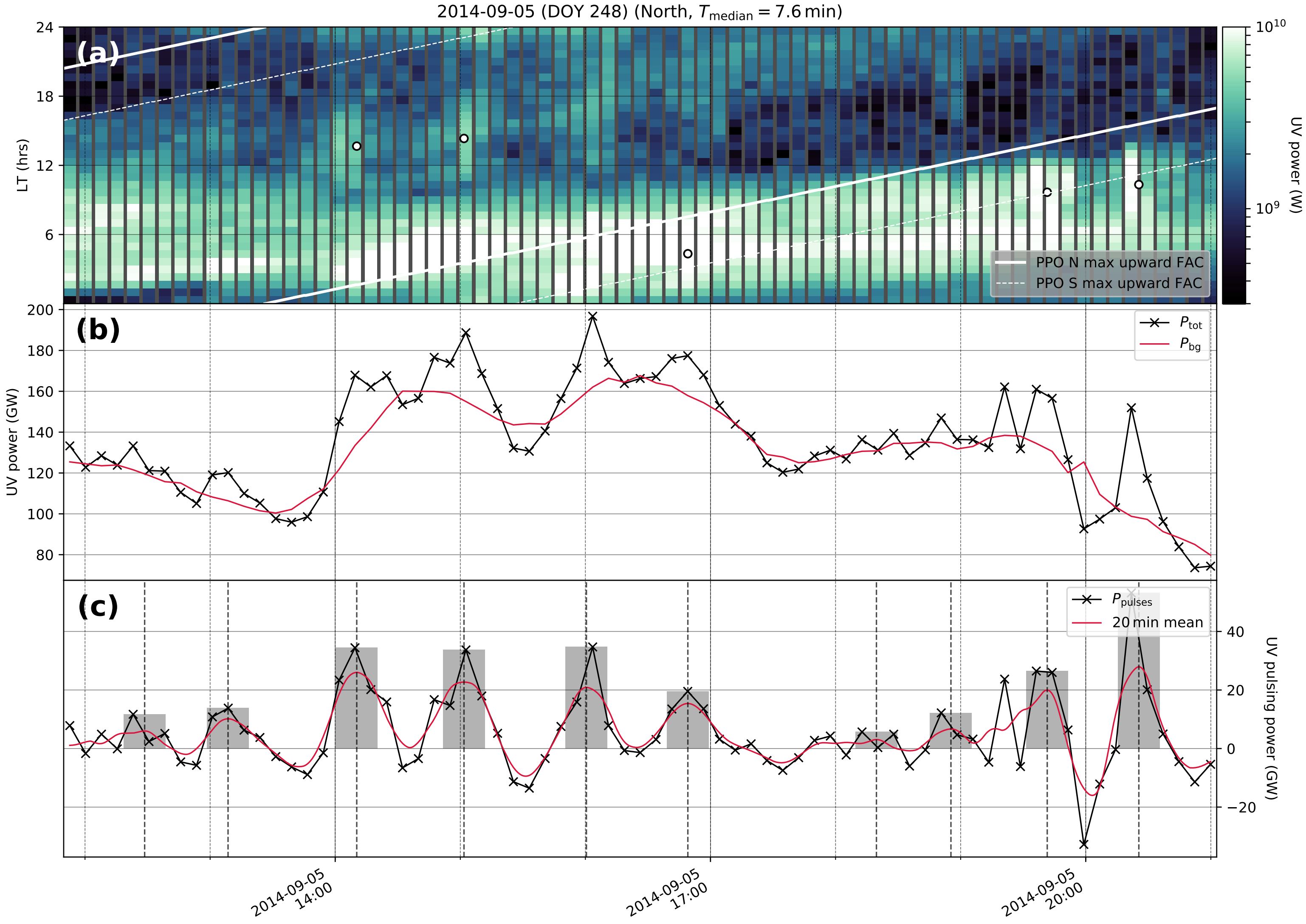
2014-09-05 (DOY 248) (North, $T_{\text{median}} = 7.6\,\text{min}$)
(a)
LT (hrs)
24
18
12
6
UV power (W)
10^{10}
10^{9}
PPO N max upward FAC
PPO S max upward FAC
(b)
UV power (GW)
200
180
160
140
120
100
80
P_{tot}
P_{bg}
(c)
P_{pulses}
20 min mean
UV pulsing power (GW)
40
20
0
−20
2014-09-05 14:00
2014-09-05 17:00
2014-09-05 20:00

Figure S20.

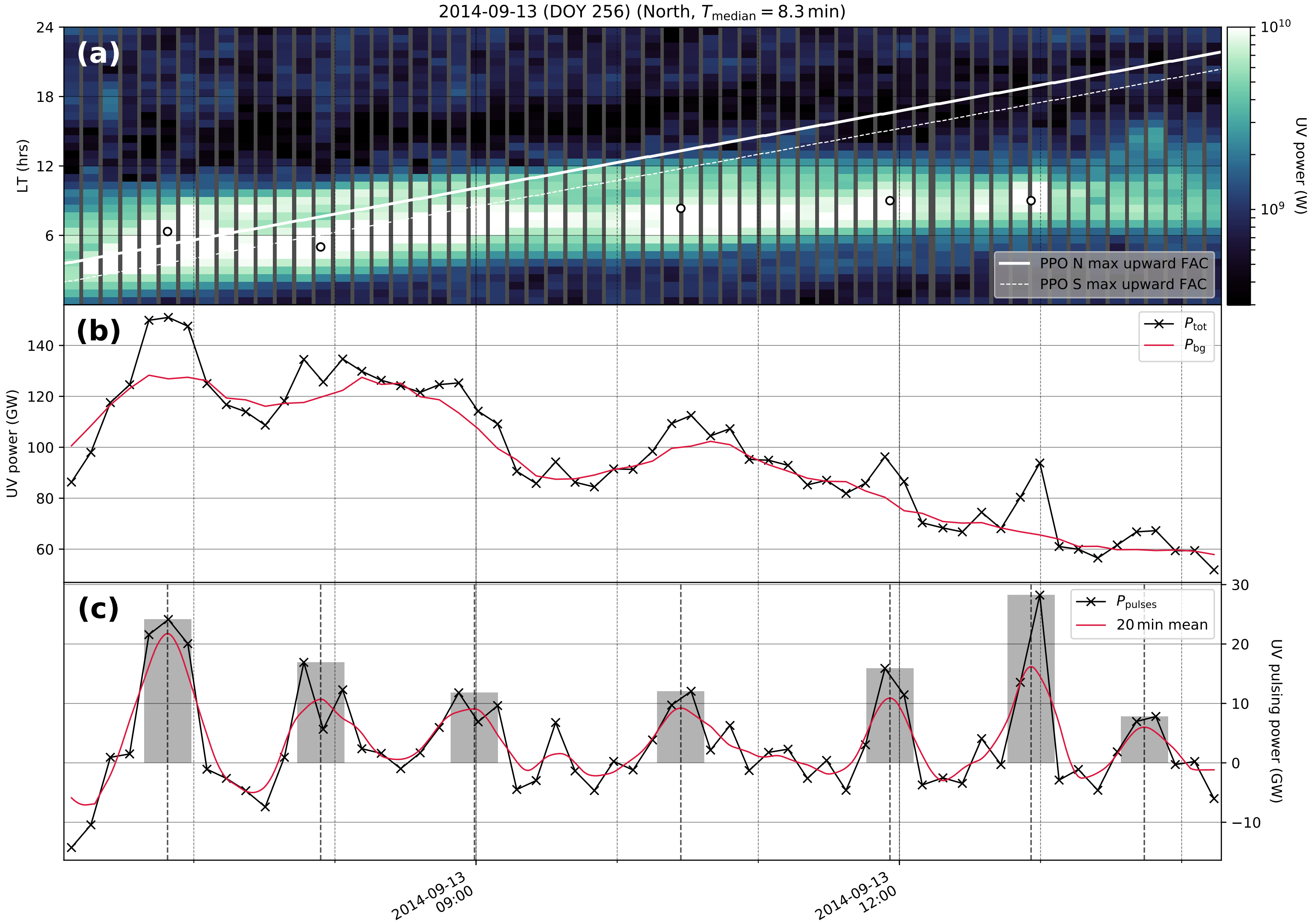
2014-09-13 (DOY 256) (North, T_{median} = 8.3 min)
(a)
LT (hrs)
24
18
12
6
PPO N max upward FAC
PPO S max upward FAC
UV power (W)
10^{10}
10^{9}
(b)
UV power (GW)
140
120
100
80
60
P_{tot}
P_{bg}
(c)
P_{pulses}
20 min mean
UV pulsing power (GW)
30
20
10
0
−10
2014-09-13 09:00
2014-09-13 12:00

Figure S21.

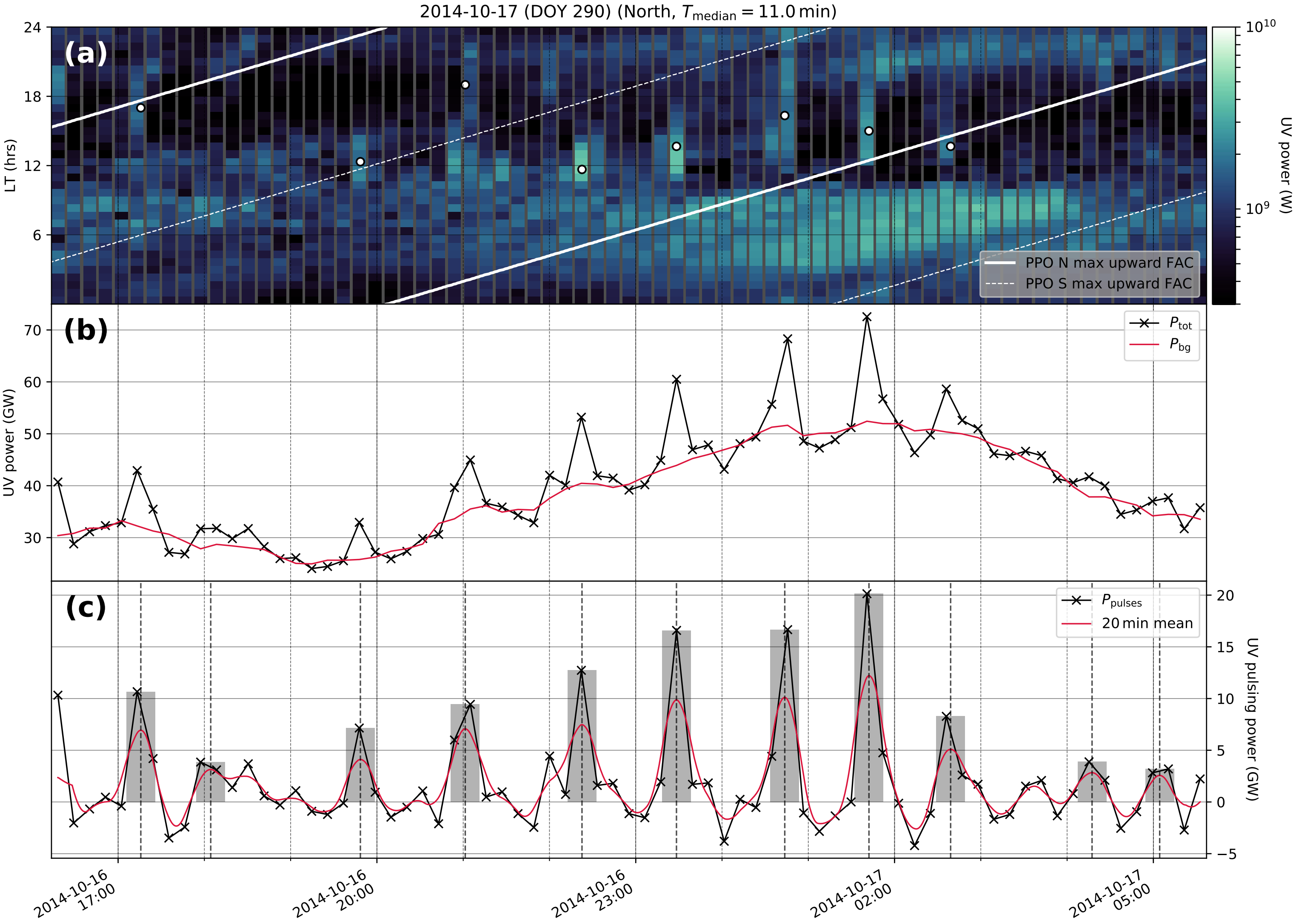
2014-10-17 (DOY 290) (North, $T_{\mathrm{median}} = 11.0\,\mathrm{min}$)
(a)
(b)
(c)
LT (hrs)
24
18
12
6
UV power (W)
10^{10}
10^{9}
PPO N max upward FAC
PPO S max upward FAC
UV power (GW)
70
60
50
40
30
P_{tot}
P_{bg}
P_{pulses}
20 min mean
UV pulsing power (GW)
20
15
10
5
0
−5
2014-10-16 17:00
2014-10-16 20:00
2014-10-16 23:00
2014-10-17 02:00
2014-10-17 05:00

Figure S22.

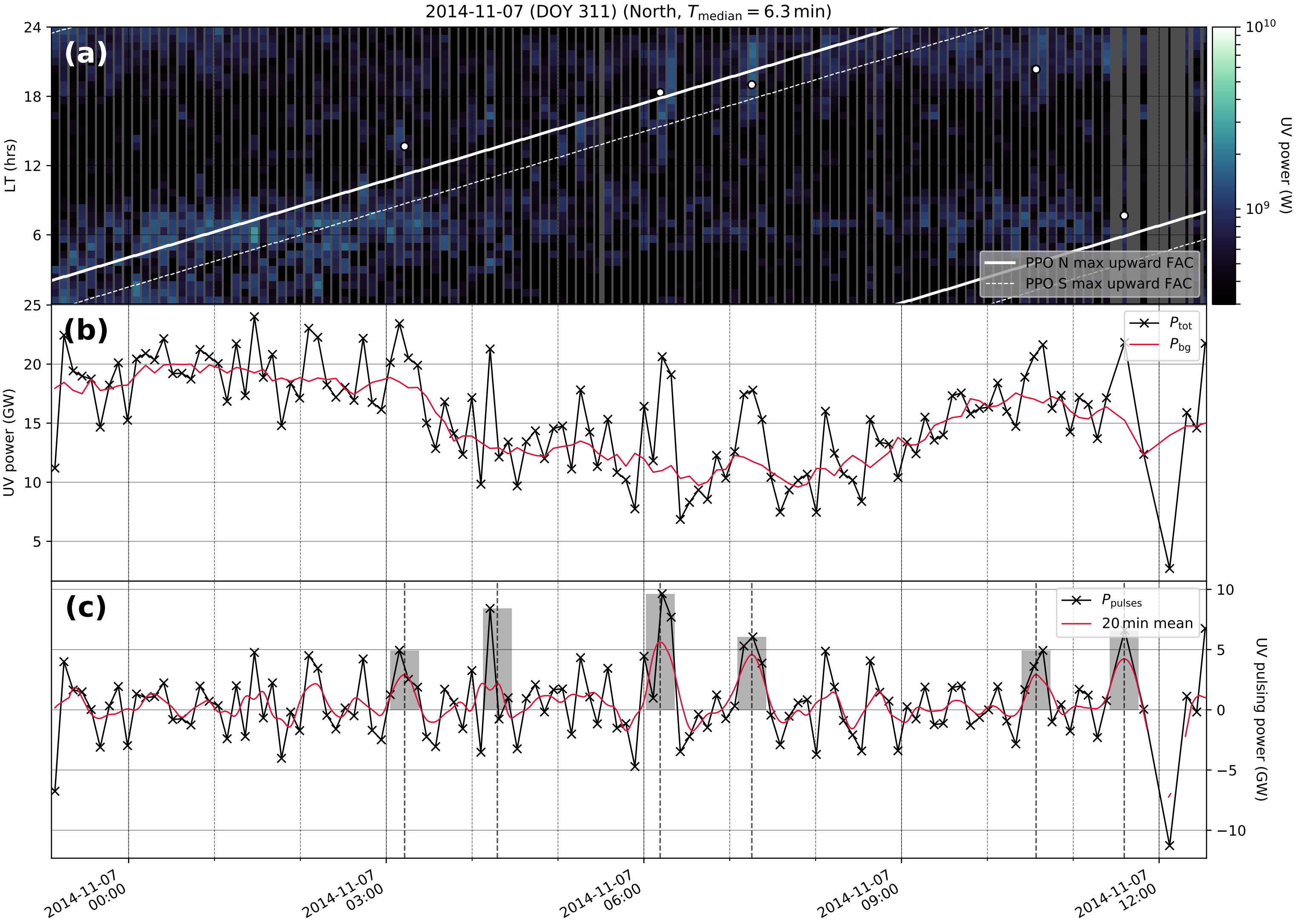
2014-11-07 (DOY 311) (North, T_{median} = 6.3 min)
(a)
(b)
(c)
LT (hrs)
24
18
12
6
25
UV power (W)
10^{10}
10^{9}
PPO N max upward FAC
PPO S max upward FAC
UV power (GW)
20
15
10
5
P_{tot}
P_{bg}
P_{pulses}
20 min mean
UV pulsing power (GW)
10
5
0
−5
−10
2014-11-07 00:00
2014-11-07 03:00
2014-11-07 06:00
2014-11-07 09:00
2014-11-07 12:00

Figure S23.

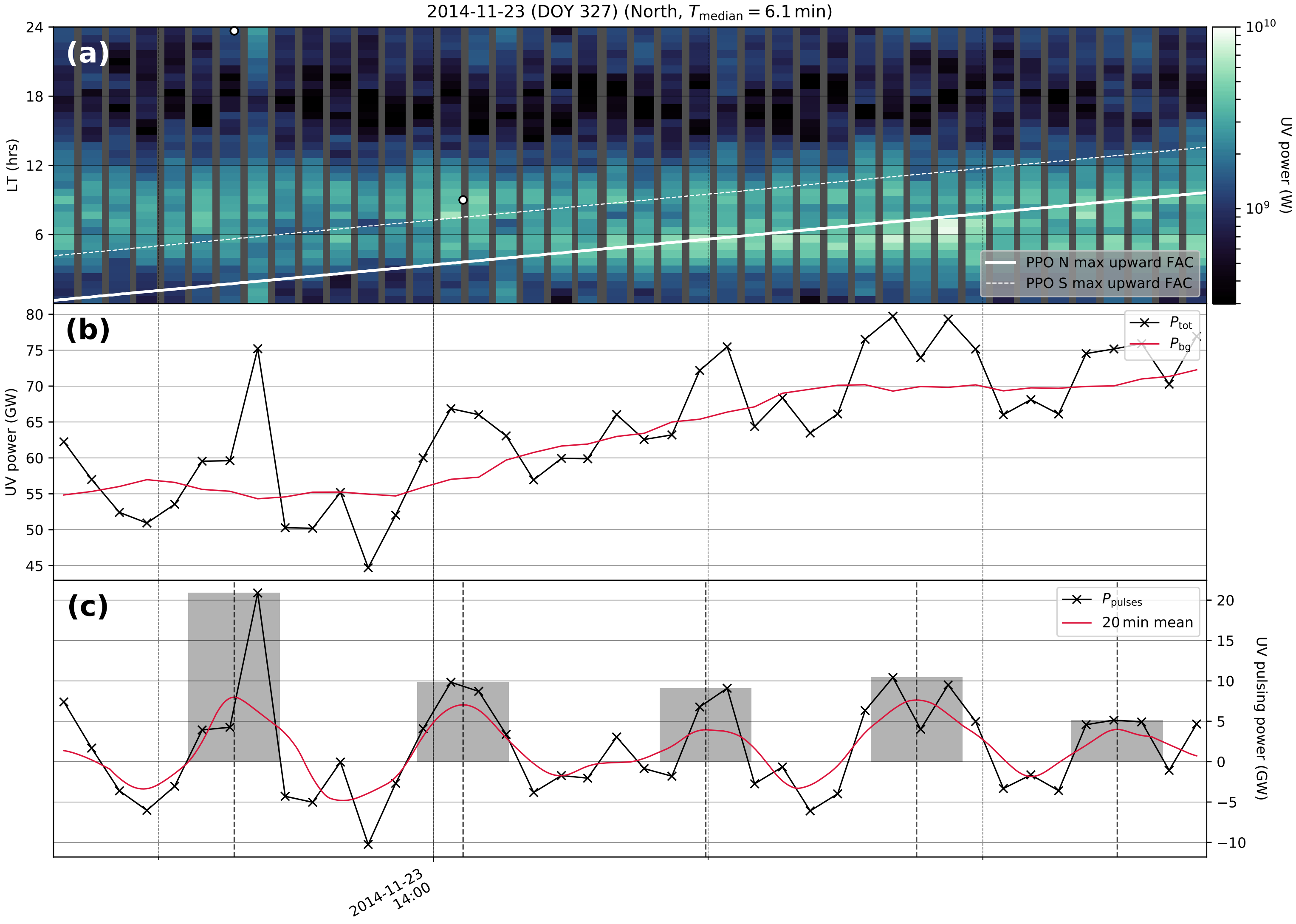
2014-11-23 (DOY 327) (North, $T_{\mathrm{median}} = 6.1$ min)
(a)
LT (hrs)
24
18
12
6
PPO N max upward FAC
PPO S max upward FAC
UV power (W)
10^{10}
10^{9}
(b)
UV power (GW)
80
75
70
65
60
55
50
45
P_{tot}
P_{bg}
(c)
P_{pulses}
20 min mean
UV pulsing power (GW)
20
15
10
5
0
−5
−10
2014-11-23
14:00

Figure S24.

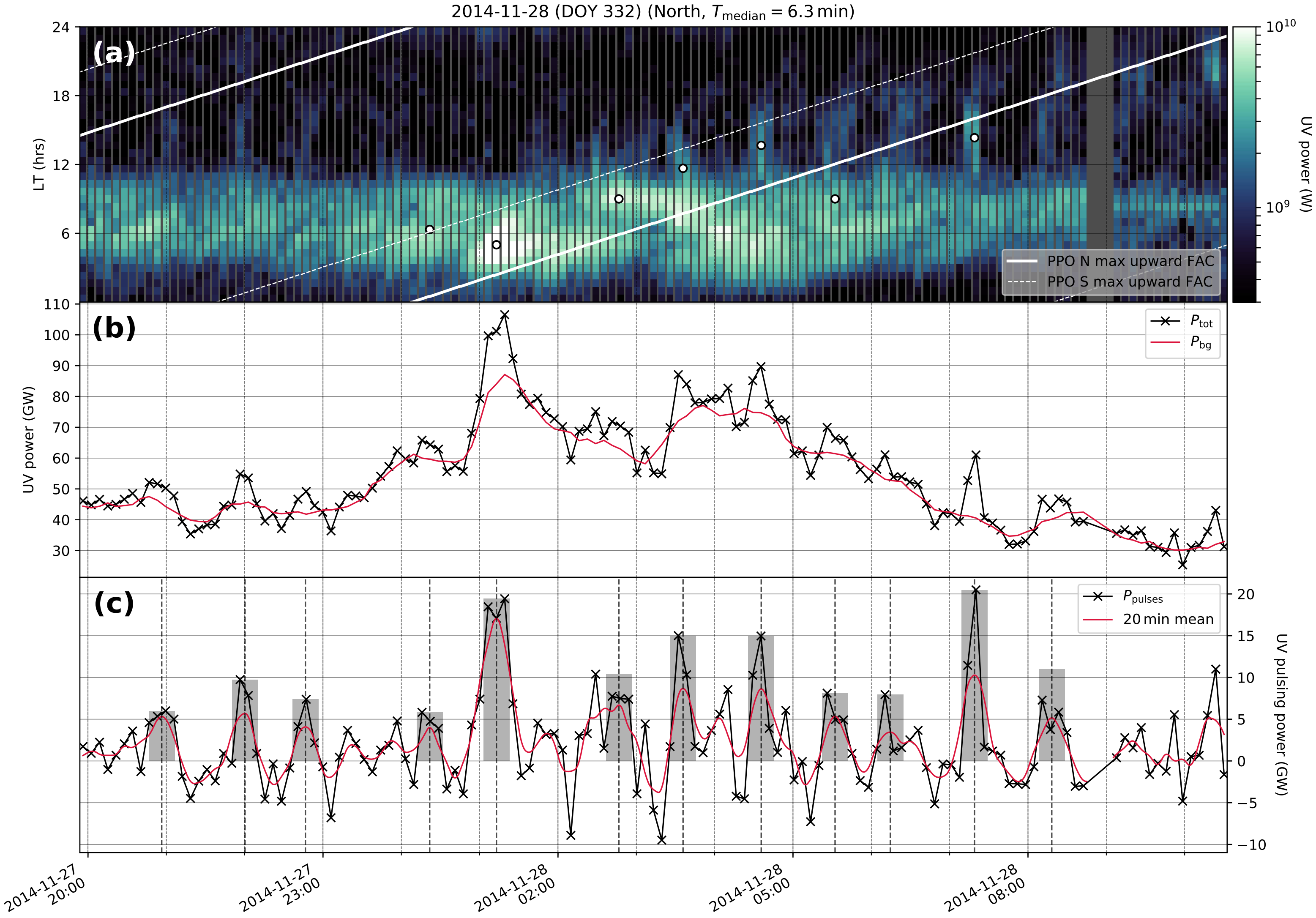
2014-11-28 (DOY 332) (North, $T_{\mathrm{median}} = 6.3\,\mathrm{min}$)
(a)
LT (hrs)
24
18
12
6
UV power (W)
10^{10}
10^{9}
PPO N max upward FAC
PPO S max upward FAC
(b)
UV power (GW)
110
100
90
80
70
60
50
40
30
P_{tot}
P_{bg}
(c)
P_{pulses}
20 min mean
UV pulsing power (GW)
20
15
10
5
0
−5
−10
2014-11-27 20:00
2014-11-27 23:00
2014-11-28 02:00
2014-11-28 05:00
2014-11-28 08:00

Figure S25.

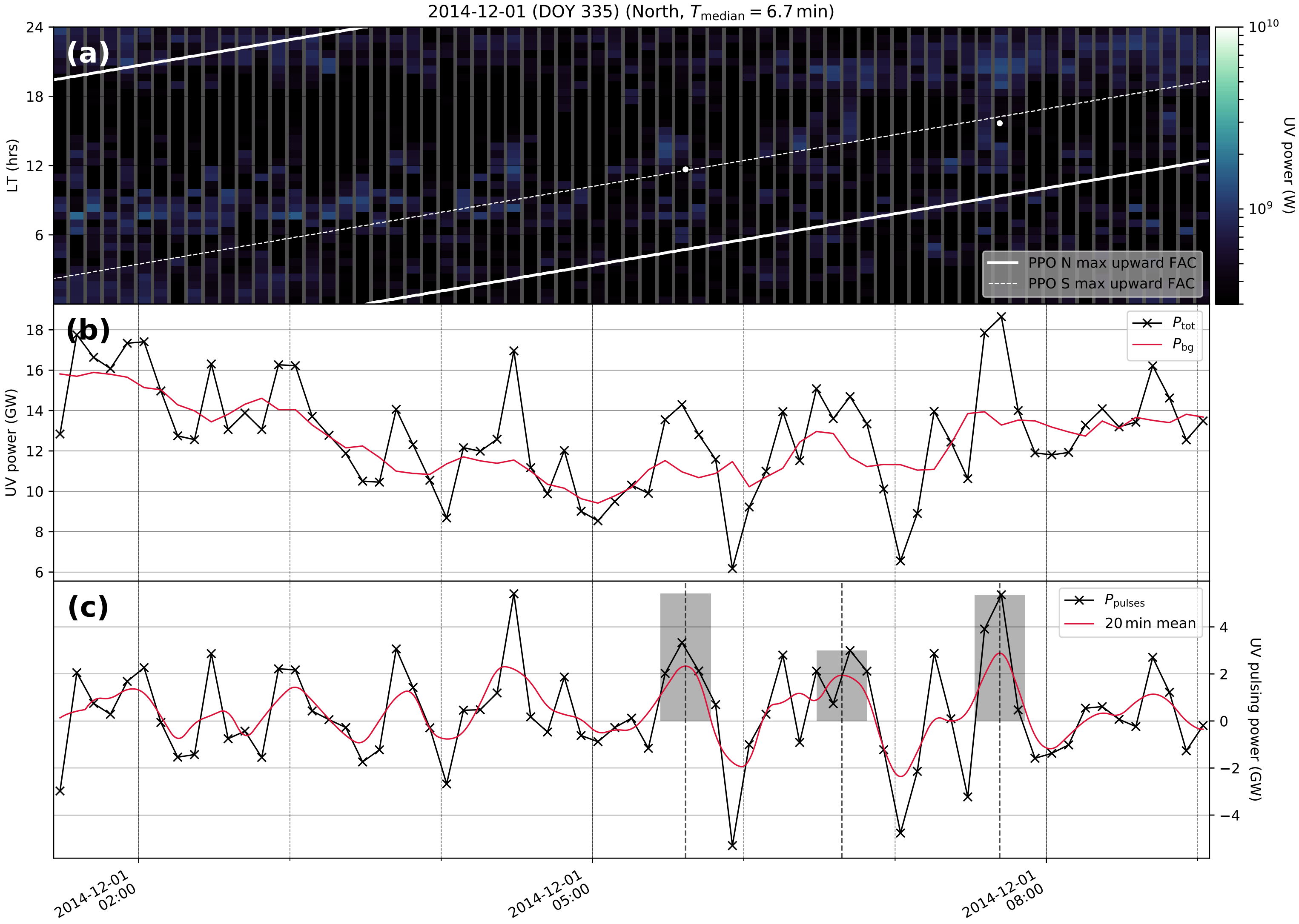
2014-12-01 (DOY 335) (North, T_{median} = 6.7 min)
(a)
(b)
(c)
LT (hrs)
24
18
12
6
UV power (W)
10^{10}
10^{9}
PPO N max upward FAC
PPO S max upward FAC
UV power (GW)
18
16
14
12
10
8
6
P_{tot}
P_{bg}
P_{pulses}
20 min mean
UV pulsing power (GW)
4
2
0
−2
−4
2014-12-01 02:00
2014-12-01 05:00
2014-12-01 08:00

Figure S26.

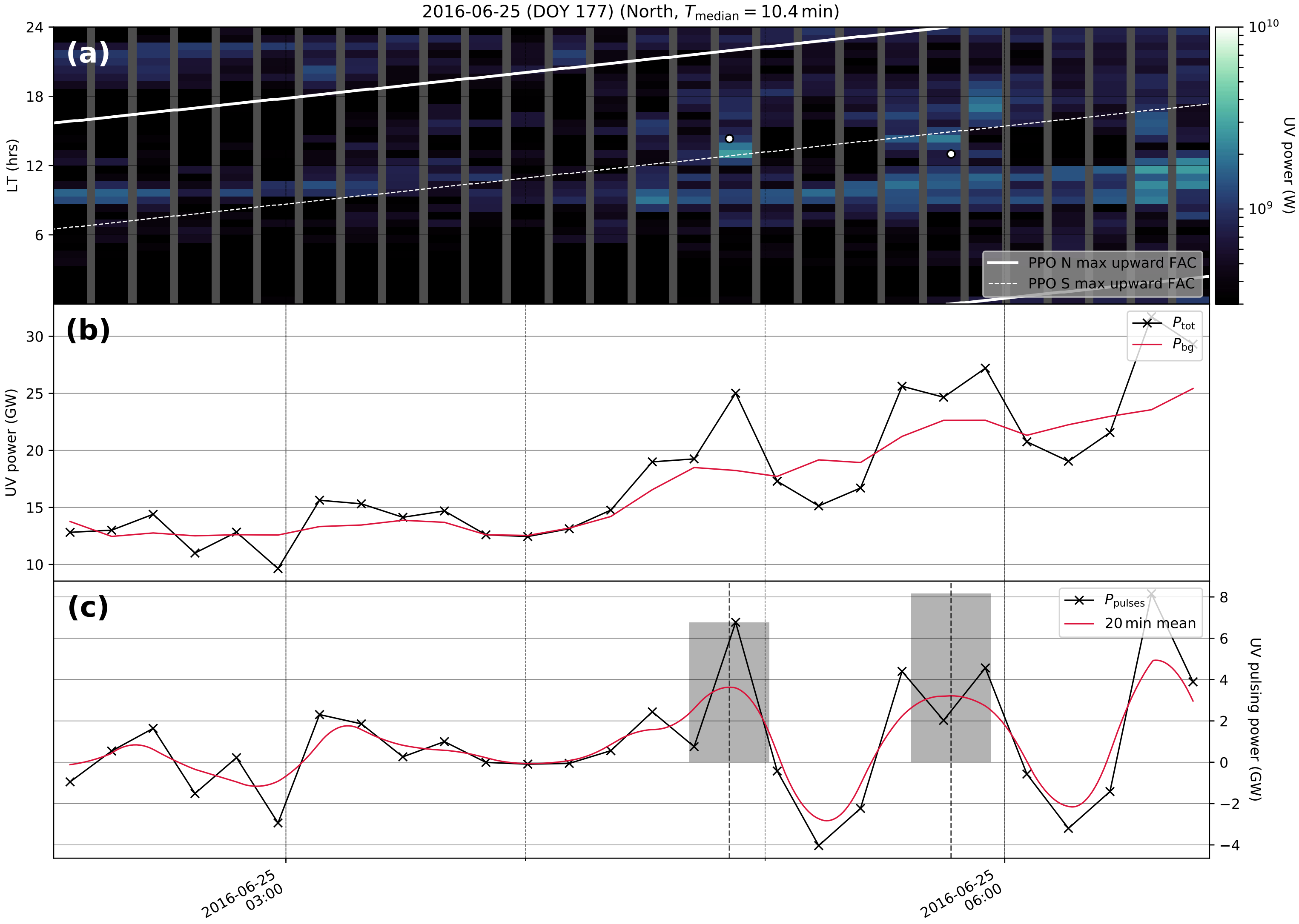
2016-06-25 (DOY 177) (North, $T_{\rm median} = 10.4$ min)
(a)
(b)
(c)
LT (hrs)
24
18
12
6
UV power (W)
10^{10}
10^{9}
PPO N max upward FAC
PPO S max upward FAC
UV power (GW)
30
25
20
15
10
$P_{\rm tot}$
$P_{\rm bg}$
$P_{\rm pulses}$
20 min mean
UV pulsing power (GW)
8
6
4
2
0
−2
−4
2016-06-25 03:00
2016-06-25 06:00

Figure S27.

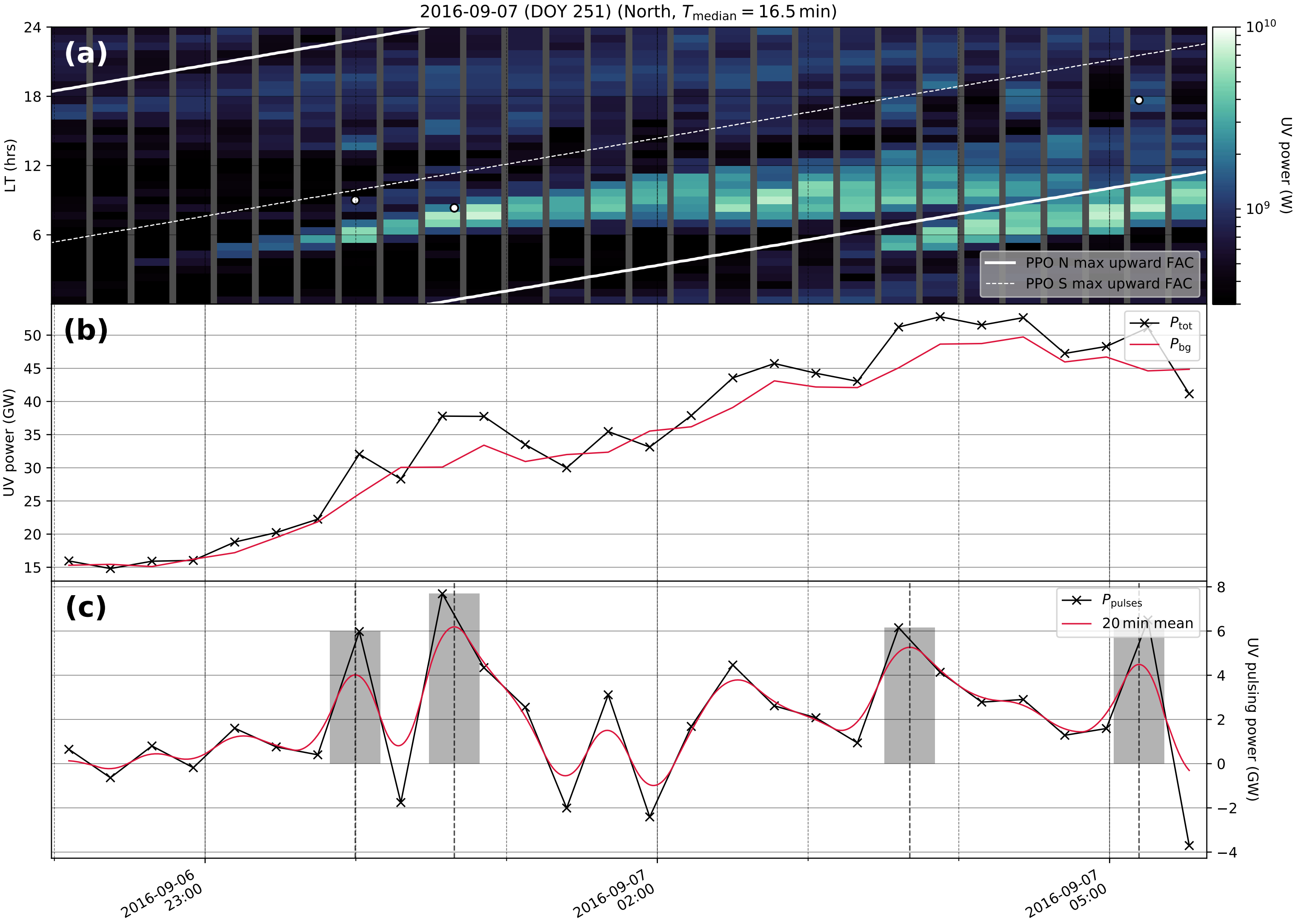
2016-09-07 (DOY 251) (North, T_{median} = 16.5 min)
(a)
LT (hrs)
24
18
12
6
UV power (W)
10^{10}
10^{9}
PPO N max upward FAC
PPO S max upward FAC
(b)
UV power (GW)
50
45
40
35
30
25
20
15
P_{tot}
P_{bg}
(c)
P_{pulses}
20 min mean
UV pulsing power (GW)
8
6
4
2
0
−2
−4
2016-09-06 23:00
2016-09-07 02:00
2016-09-07 05:00

Figure S28.

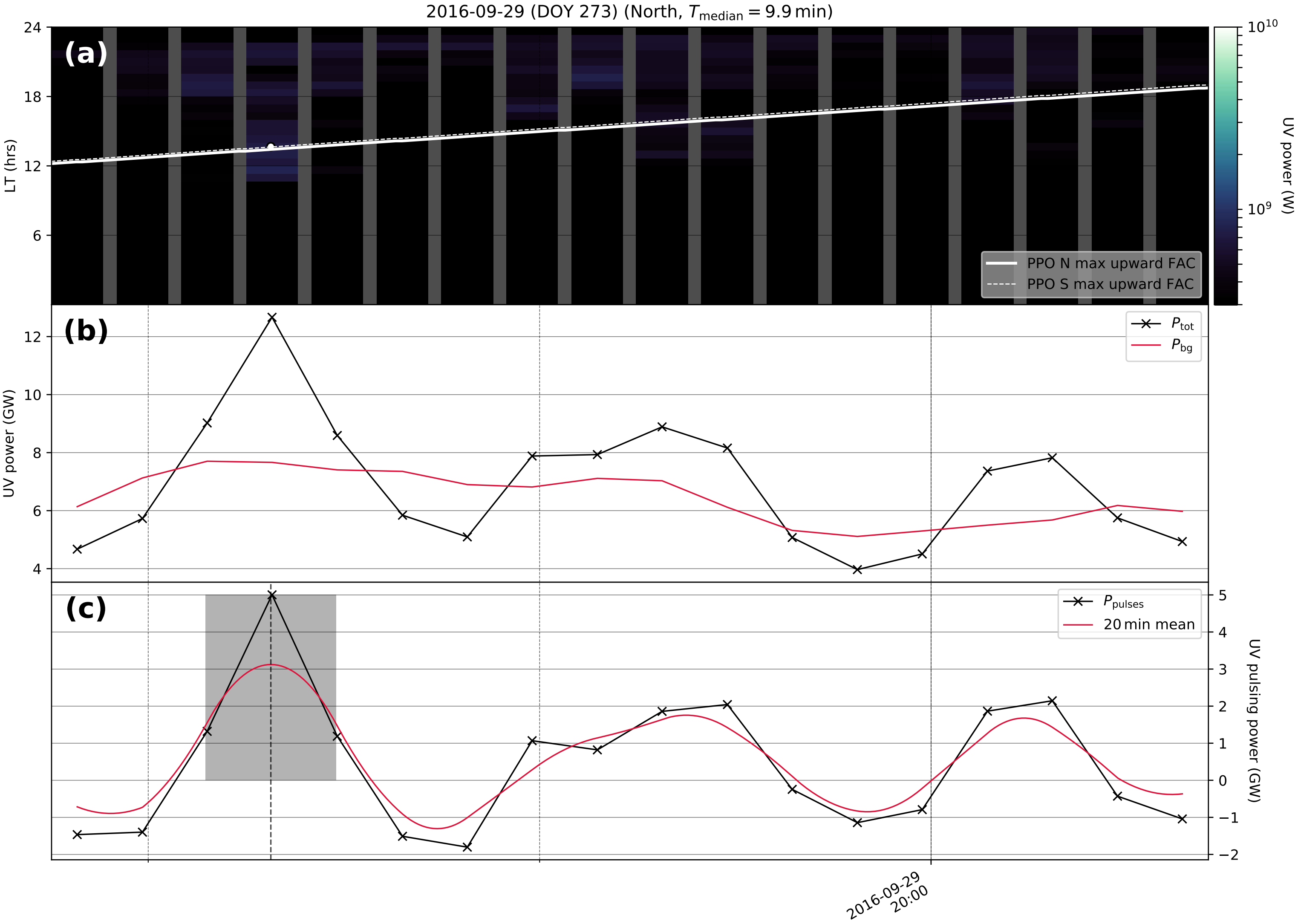
2016-09-29 (DOY 273) (North, $T_{\mathrm{median}} = 9.9$ min)
(a)
(b)
(c)
LT (hrs)
24
18
12
6
PPO N max upward FAC
PPO S max upward FAC
UV power (W)
10^{10}
10^{9}
UV power (GW)
12
10
8
6
4
P_{tot}
P_{bg}
P_{pulses}
20 min mean
UV pulsing power (GW)
5
4
3
2
1
0
−1
−2
2016-09-29
20:00

Figure S29.

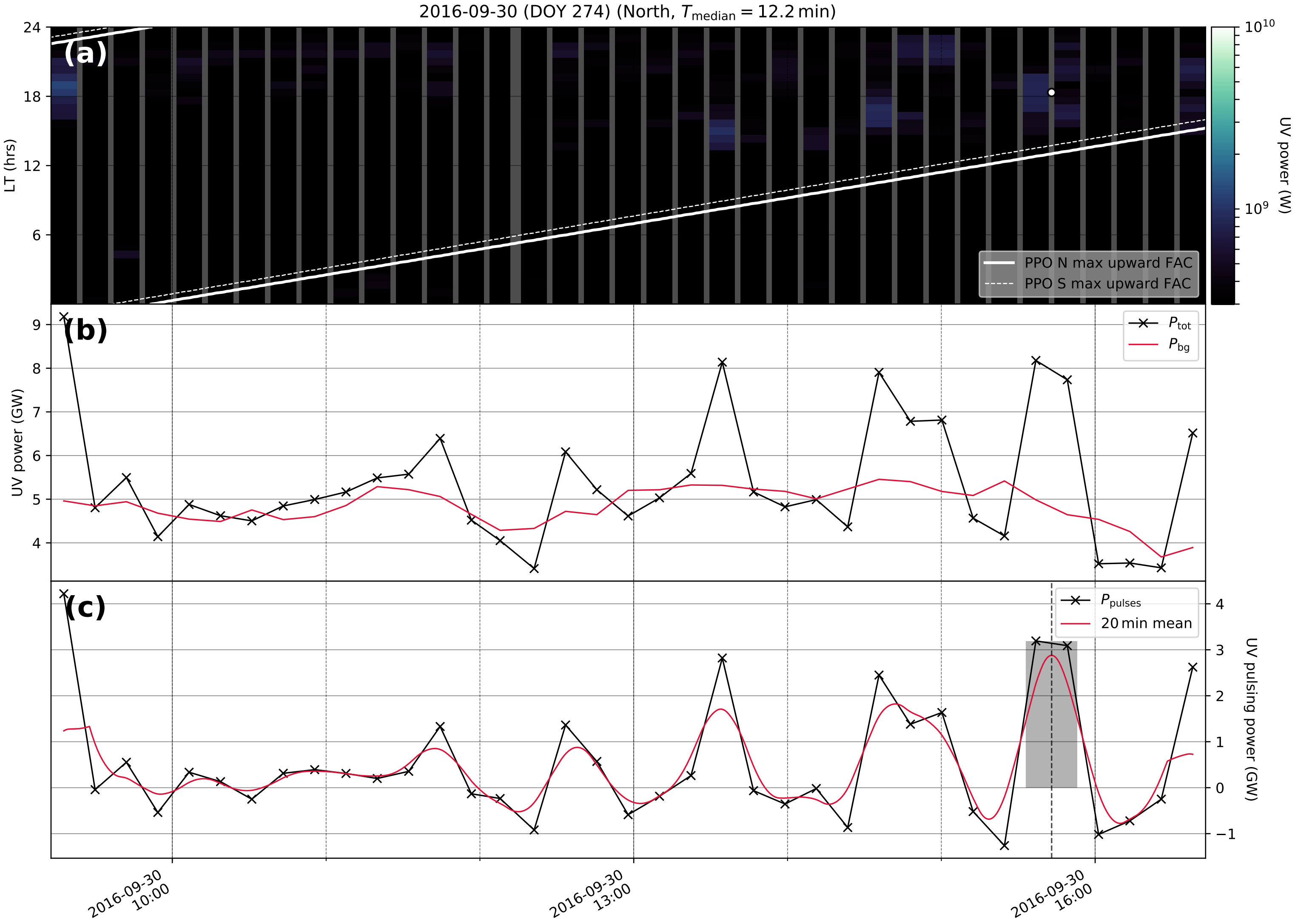
2016-09-30 (DOY 274) (North, $T_{\text{median}} = 12.2\,\text{min}$)
(a)
(b)
(c)
LT (hrs)
24
18
12
6
10^{10}
10^{9}
UV power (W)
PPO N max upward FAC
PPO S max upward FAC
UV power (GW)
9
8
7
6
5
4
P_{tot}
P_{bg}
P_{pulses}
20 min mean
UV pulsing power (GW)
4
3
2
1
0
−1
2016-09-30 10:00
2016-09-30 13:00
2016-09-30 16:00

Figure S30.

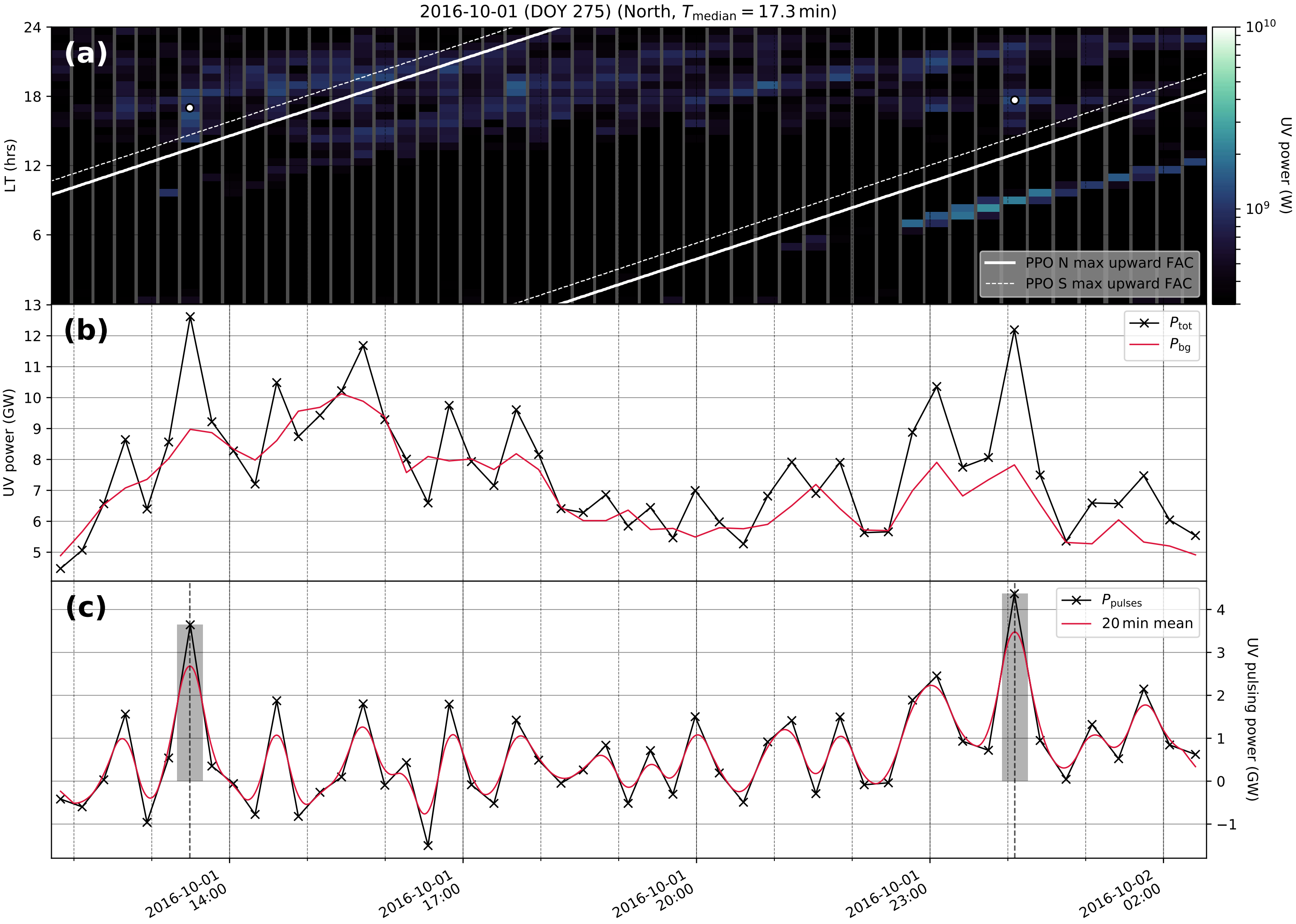
2016-10-01 (DOY 275) (North, $T_{median} = 17.3$ min)
(a)
(b)
(c)
LT (hrs)
24
18
12
6
13
UV power (W)
10^{10}
10^{9}
PPO N max upward FAC
PPO S max upward FAC
UV power (GW)
P_{tot}
P_{bg}
P_{pulses}
20 min mean
UV pulsing power (GW)
2016-10-01 14:00
2016-10-01 17:00
2016-10-01 20:00
2016-10-01 23:00
2016-10-02 02:00

Figure S31.

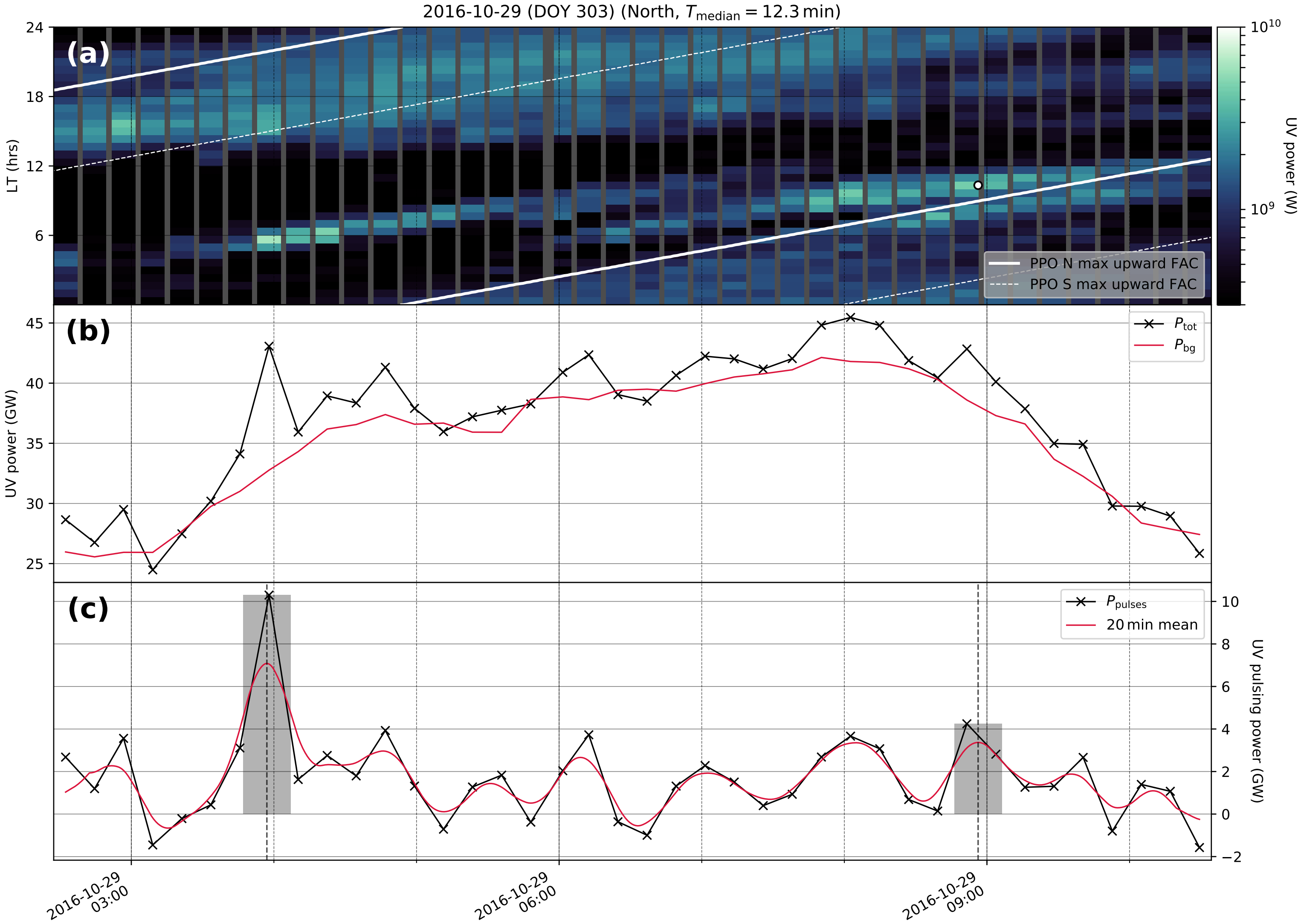
2016-10-29 (DOY 303) (North, $T_{\mathrm{median}} = 12.3$ min)
(a)
(b)
(c)
LT (hrs)
24
18
12
6
PPO N max upward FAC
PPO S max upward FAC
UV power (W)
10^{10}
10^{9}
UV power (GW)
45
40
35
30
25
P_{tot}
P_{bg}
P_{pulses}
20 min mean
UV pulsing power (GW)
10
8
6
4
2
0
−2
2016-10-29 03:00
2016-10-29 06:00
2016-10-29 09:00

Figure S32.

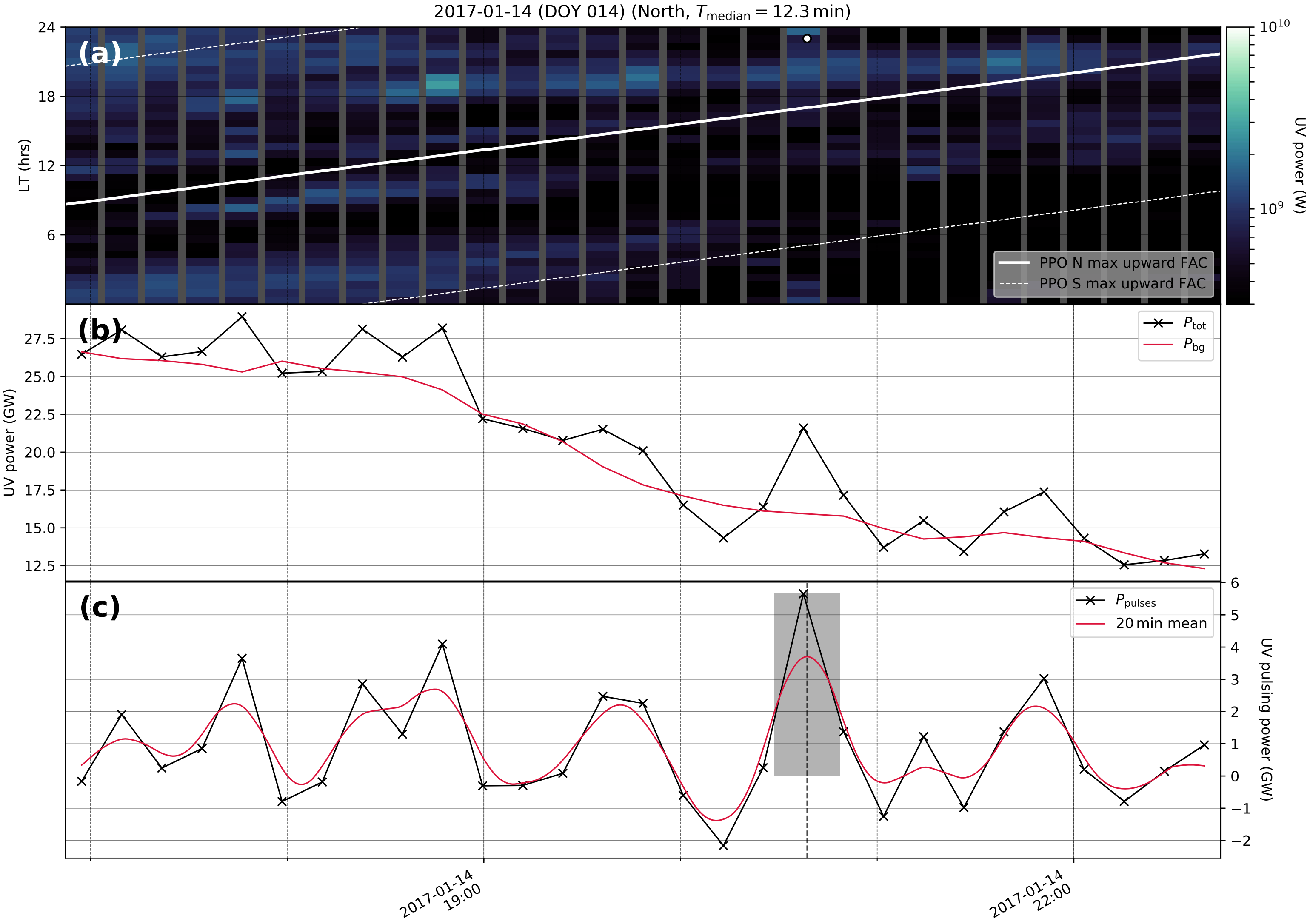
2017-01-14 (DOY 014) (North, $T_{\mathrm{median}} = 12.3\,\mathrm{min}$)
(a)
LT (hrs)
24
18
12
6
PPO N max upward FAC
PPO S max upward FAC
UV power (W)
10^{10}
10^{9}
(b)
UV power (GW)
27.5
25.0
22.5
20.0
17.5
15.0
12.5
P_{tot}
P_{bg}
(c)
P_{pulses}
20 min mean
UV pulsing power (GW)
6
5
4
3
2
1
0
−1
−2
2017-01-14 19:00
2017-01-14 22:00

Figure S33.

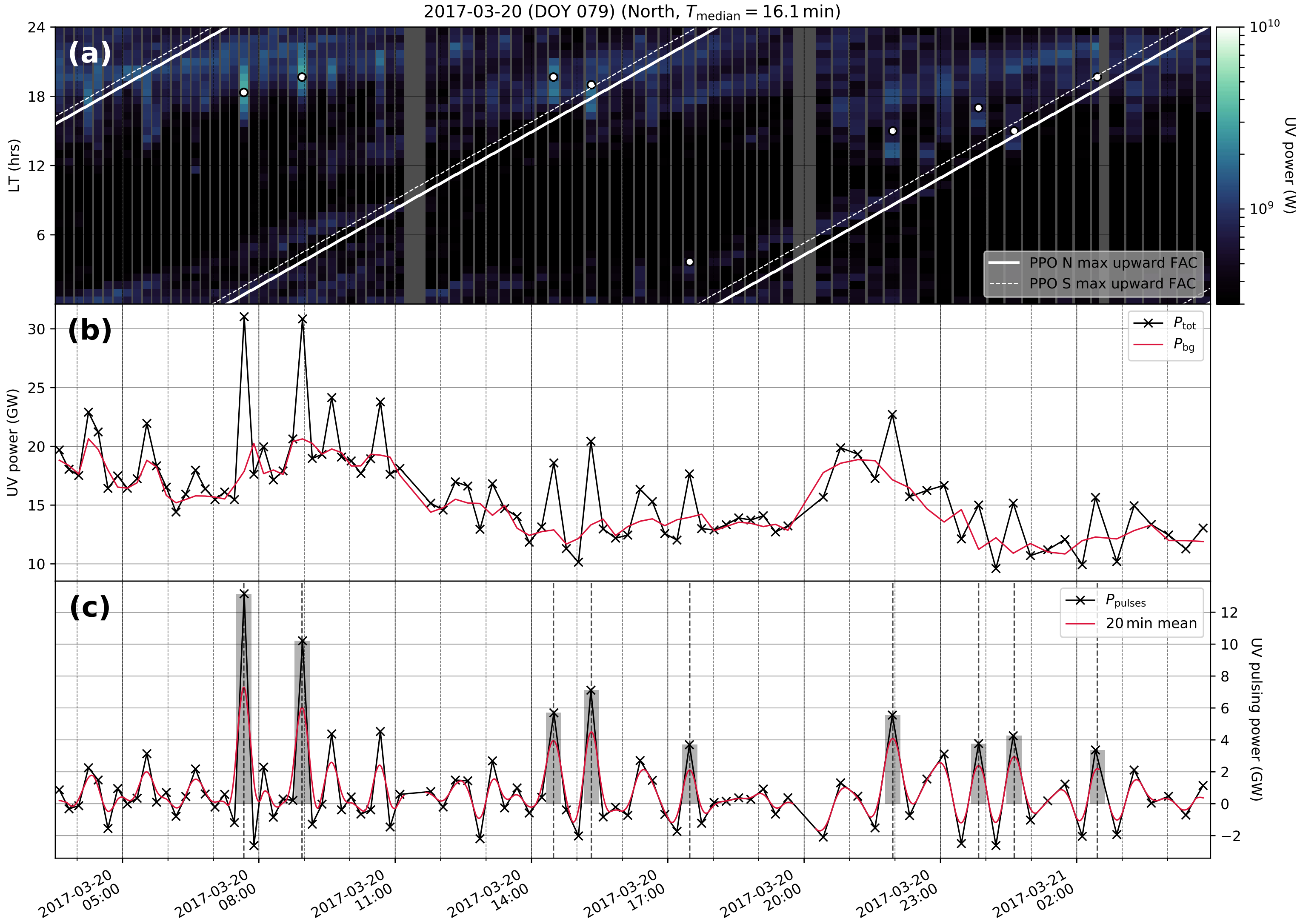
2017-03-20 (DOY 079) (North, $T_{\mathrm{median}} = 16.1$ min)
(a)
(b)
(c)
LT (hrs)
24
18
12
6
UV power (W)
10^{10}
10^{9}
PPO N max upward FAC
PPO S max upward FAC
UV power (GW)
30
25
20
15
10
P_{tot}
P_{bg}
P_{pulses}
20 min mean
UV pulsing power (GW)
12
10
8
6
4
2
0
−2
2017-03-20 05:00
2017-03-20 08:00
2017-03-20 11:00
2017-03-20 14:00
2017-03-20 17:00
2017-03-20 20:00
2017-03-20 23:00
2017-03-21 02:00

Figure S34.

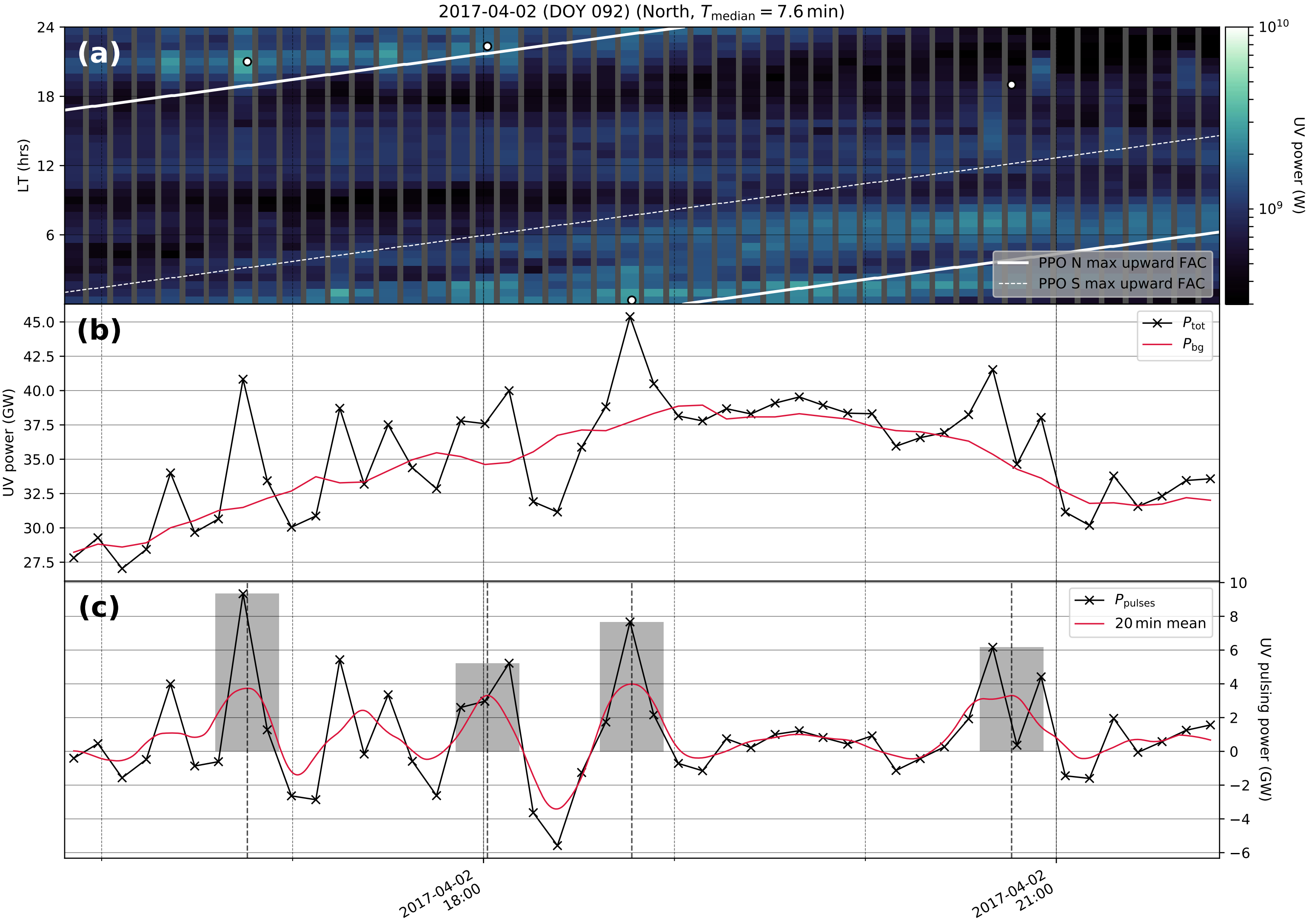
2017-04-02 (DOY 092) (North, T_{median} = 7.6 min)
(a)
LT (hrs)
24
18
12
6
PPO N max upward FAC
PPO S max upward FAC
UV power (W)
10^{10}
10^{9}
(b)
UV power (GW)
45.0
42.5
40.0
37.5
35.0
32.5
30.0
27.5
P_{tot}
P_{bg}
(c)
P_{pulses}
20 min mean
UV pulsing power (GW)
10
8
6
4
2
0
−2
−4
−6
2017-04-02 18:00
2017-04-02 21:00

Figure S35.

Supporting Information for "The dynamics of Saturns main aurorae"

A. Bader[1], S. V. Badman[1], S. W. H. Cowley[2], Z. H. Yao[3], L. C. Ray[1], J. Kinrade[1], E. J. Bunce[2], G. Provan[2], T. J. Bradley[2], C. Tao[4,5], G. J. Hunt[6], W. R. Pryor[7]

[1]Department of Physics, Lancaster University, Lancaster, UK
[2]Department of Physics and Astronomy, University of Leicester, Leicester, UK
[3]Laboratoire de Physique Atmosphérique et Planétaire, Space sciences, Technologies and Astrophysics Research (STAR) Institute, Université de Liège, Liège, Belgium
[4]National Institute of Information and Communications Technology, Koganei, Japan
[5]Department of Geophysics, Tohoku University, Sendai, Japan
[6]Blackett Laboratory, Imperial College London, London, UK
[7]Science Department, Central Arizona College, Coolidge, Arizona, USA

Contents

Corresponding author: Alexander Bader, `a.bader@lancaster.ac.uk`

Text S1: Integration of auroral powers

The brightness unit generally used in auroral physics is the Rayleigh (R) and physically describes the column emission rate I of an isotropic source with no self-absorption over a column of unspecified length (Hunten, Roach, & Chamberlain, 1956). The conversion from a column emission rate in kilo-Rayleigh (kR) to a radiance L is given by (Baker & Romick, 1976)

$$L\left[\frac{\text{Photons}}{\text{s}\,\text{m}^2\,\text{sr}}\right] = \frac{10^{13}}{4\pi} \cdot I\,[\text{kR}]. \tag{1}$$

The radiant flux Φ can then be determined by integrating over the full 4π solid angle and the apparent emitting surface area A_{app} as seen from the detector,

$$\Phi\left[\frac{\text{Photons}}{\text{s}}\right] = L\left[\frac{\text{Photons}}{\text{s}\,\text{m}^2\,\text{sr}}\right] \cdot 4\pi\,\text{sr} \cdot A_{\text{app}}\,\left[\text{m}^2\right]. \tag{2}$$

This value is only meaningful in combination with spectral information, i.e. the mean energy of the emitted photons. Multiplying by the mean H_2 photon energy of $1.6 \cdot 10^{-18}\,\frac{\text{J}}{\text{Photon}}$ (Kurth et al., 2016) gives the radiant flux, often also named "auroral power", in SI units,

$$\Phi\;[\text{W}] = 1.6 \cdot 10^{-18}\,\frac{\text{J}}{\text{Photon}} \cdot \Phi\left[\frac{\text{Photons}}{\text{s}}\right]. \tag{3}$$

However, care has to be taken when the auroral power Φ is integrated from polar projections of the auroral intensity. As is quite obvious in some projected UVIS images, instrument pixel footprints are skewed depending on the angle under which the emission "surface", the ionospheric layer in which aurorae are generated, is being observed. The physical surface area of one longitude-latitude grid bin is hence not equal to the corresponding apparent emitting surface seen from the spacecraft based on which the column emission rate has been determined, but changes with the observation angle. With small grid bin sizes, each grid bin can be approximated by a flat plane such that its apparent emitting surface area A_{app} from Eq. 2 and the absolute surface area A_{abs} are related through

$$A_{\text{app}} = \sin\varepsilon \cdot A_{\text{abs}} \tag{4}$$

with ε as the elevation angle of Cassini above the horizon as seen from the grid bin location.

Figures S1-S4.

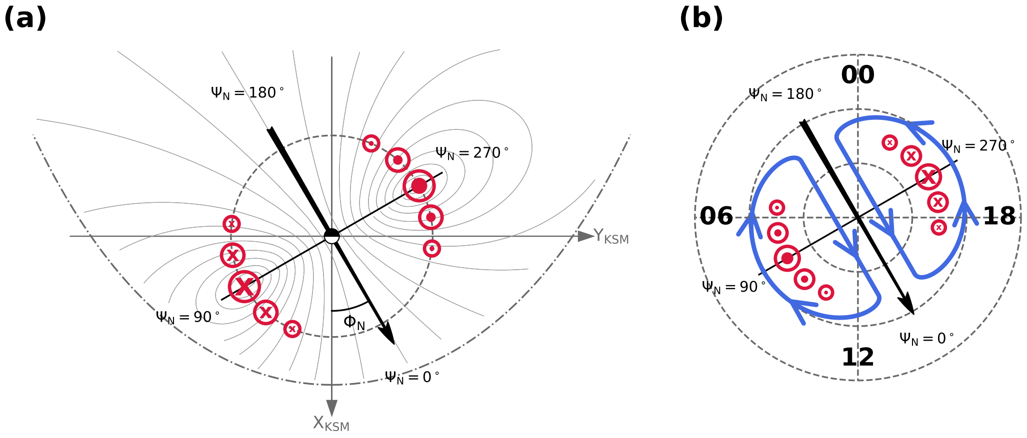

Figure S1. Sketch showing the northern planetary period oscillation (PPO) system as seen from above the northern hemisphere. (a) Saturn's equatorial magnetosphere, with noon toward the bottom and dusk toward the right. The magnetopause is indicated with a grey dash-dotted line, following the model of Arridge et al. (2006) with $p_{\mathrm{dyn}} = 0.05\,\mathrm{nPa}$. The inner grey dashed circle marks the approximate location where the main PPO-related field-aligned currents (FACs) pass through the equatorial plane. At the instant shown, the northern PPO phase is $\Phi_{\mathrm{N}}(t) = 30^\circ$, a black arrow marking the orientation of the associated equatorial model perturbation dipole. The magnetic perturbation field lines of the northern PPO system are shown as solid grey lines (Provan et al., 2009). The principal meridians of the PPO phase function are shown by the black arrow and its perpendicular, the phase values Ψ_{N} increasing clockwise as indicated. The direction of FACs passing the equatorial plane due to the perturbation field is marked in red, with circled crosses indicating a flow into and circled dots a flow out of the plane of the figure. (b) The corresponding view of Saturn's northern ionosphere as seen from above the north pole, again with noon towards the bottom. Bold numbers around the edge of the panel indicate the local time, dashed circles mark the northern colatitude from the pole in 10° steps. The orientation of the model perturbation dipole and the PPO principal meridians are marked in black as in panel (a). Ionospheric upward (downward) FAC regions at auroral latitudes are indicated with red circled dots (crosses). Blue lines and arrows sketch the driving neutral atmospheric and ionospheric flows in the northern hemisphere (e.g., Hunt et al., 2014; Jia et al., 2012).

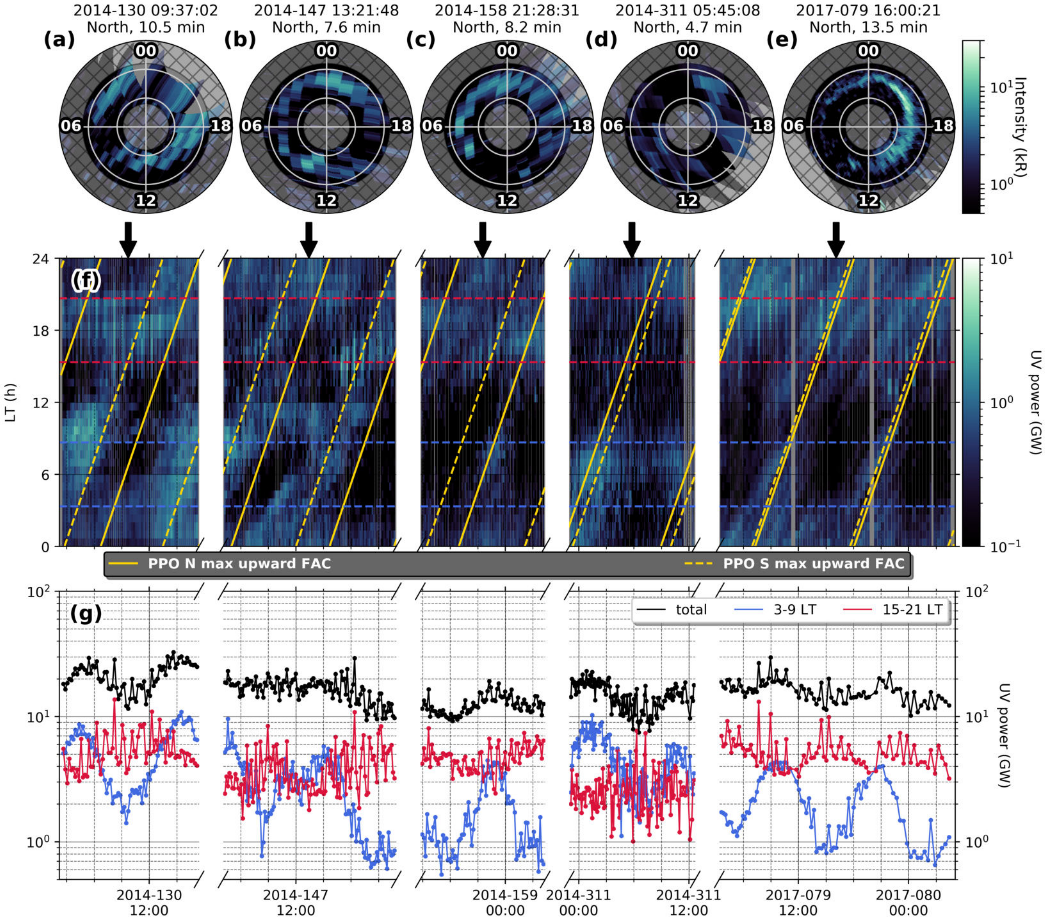

Figure S2. UV power keograms of all observation sequences with quiet auroral conditions. Same format as Fig. 1, but showing five observation sequences (including 2017 DOY 79-80 from Fig. 1) with a broken time axis.

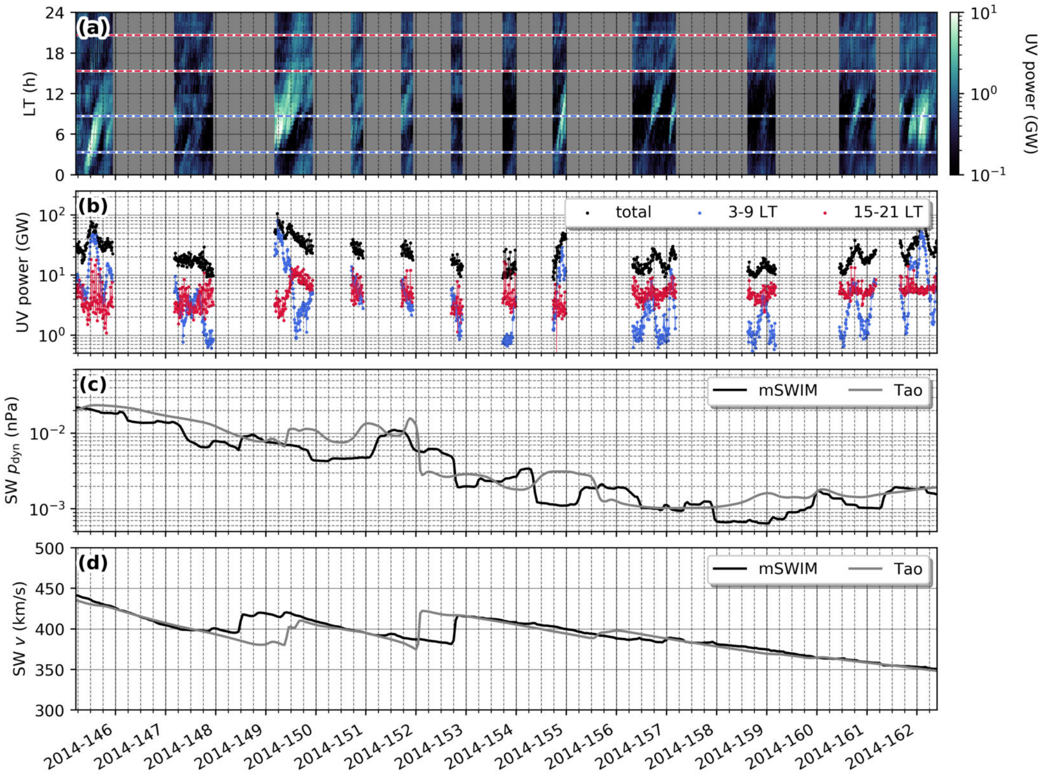

Figure S3. UVIS observation summary of Saturn's ultraviolet (UV) aurora between 2014 DOY 145-162. (a) Keogram of UV emitted power integrated in 36 local time bins between 8 – 22° northern colatitude, same format as Fig. 1d. (b) Summed UV power of the whole LT range (black), the dawn (blue) and dusk region (red) as marked with dashed lines in (a). (c) Solar wind dynamic pressure, propagated from OMNI using the Tao et al. (2005) and the mSWIM (Zieger & Hansen, 2008) models. The Earth-Saturn opposition angle was < 30° during the period shown. (d) Solar wind radial velocity from the same propagation.

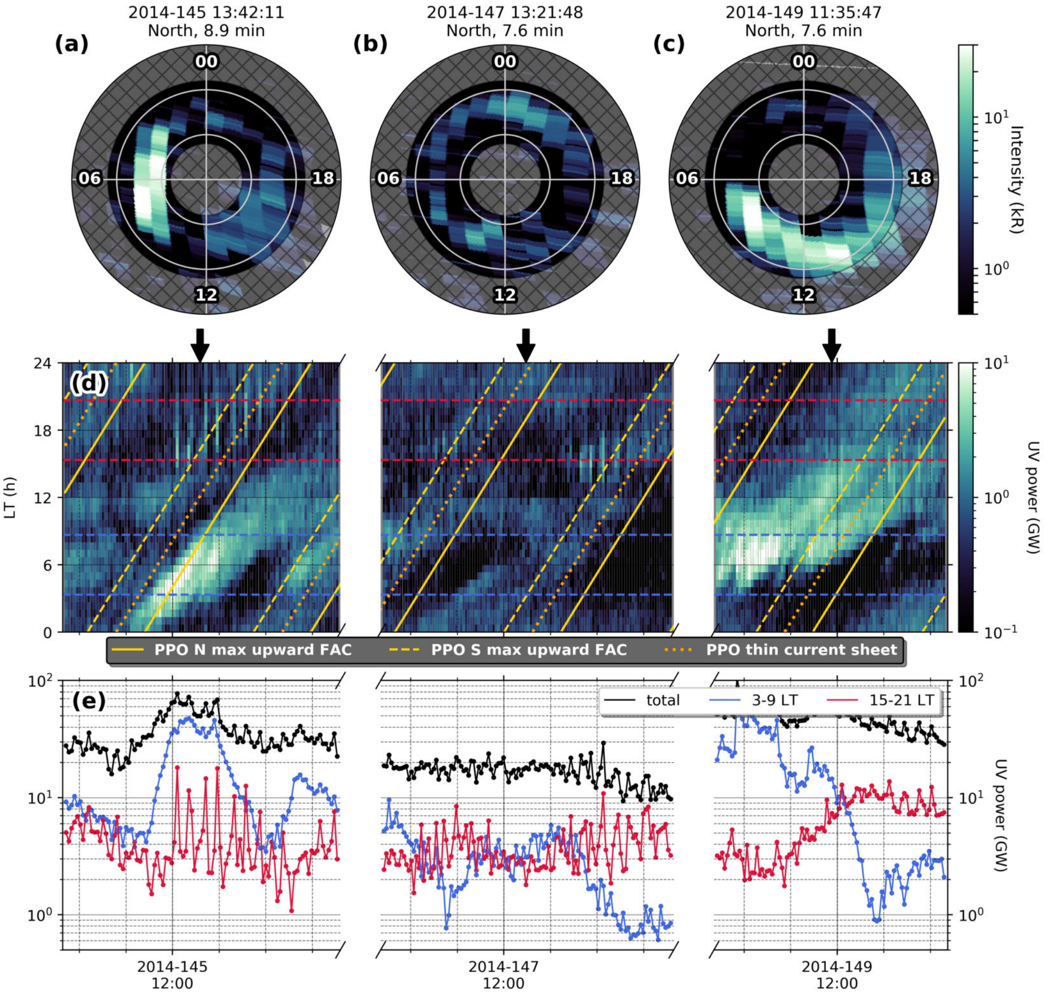

Figure S4. UV power keogram, average auroral conditions (2014 DOY 145-149). Same format as Fig. 3, note the broken time axis.

References

Arridge, C. S., Achilleos, N., Dougherty, M. K., Khurana, K. K., & Russell, C. T. (2006, November). Modeling the size and shape of Saturn's magnetopause with variable dynamic pressure. *Journal of Geophysical Research*, *111*(A11227). Retrieved 2018-04-20TZ, from `http://doi.wiley.com/10.1029/2005JA011574` doi: 10.1029/2005JA011574

Baker, D. J., & Romick, G. J. (1976, August). The Rayleigh: Interpretation of the unit in terms of column emission rate or apparent radiance expressed in SI units. *Applied Optics*, *15*(8), 1966. Retrieved 2018-10-09TZ, from `https://www.osapublishing.org/abstract.cfm?URI=ao-15-8-1966` doi: 10.1364/AO.15.001966

Hunt, G. J., Cowley, S. W. H., Provan, G., Bunce, E. J., Alexeev, I. I., Belenkaya, E. S., ... Coates, A. J. (2014, December). Field-aligned currents in Saturn's southern nightside magnetosphere: Subcorotation and planetary period oscillation components. *Journal of Geophysical Research: Space Physics*, *119*(12), 9847–9899. Retrieved 2018-04-20TZ, from `http://doi.wiley.com/10.1002/2014JA020506` doi: 10.1002/2014JA020506

Hunten, D. M., Roach, F. E., & Chamberlain, J. W. (1956). A photometric unit for the airglow and aurora. *Journal of Atmospheric and Terrestrial Physics*, *8*, 345–346.

Jia, X., Kivelson, M. G., & Gombosi, T. I. (2012, April). Driving Saturn's magnetospheric periodicities from the upper atmosphere/ionosphere. *Journal of Geophysical Research: Space Physics*, *117*(A04215). Retrieved 2018-04-20TZ, from `http://doi.wiley.com/10.1029/2011JA017367` doi: 10.1029/2011JA017367

Kurth, W., Hospodarsky, G., Gurnett, D., Lamy, L., Dougherty, M., Nichols, J., ... Crary, F. (2016, January). Saturn kilometric radiation intensities during the Saturn auroral campaign of 2013. *Icarus*, *263*, 2–9. Retrieved 2018-05-15TZ, from `http://linkinghub.elsevier.com/retrieve/pii/S0019103515000093` doi: 10.1016/j.icarus.2015.01.003

Provan, G., Cowley, S. W. H., & Nichols, J. D. (2009, April). Phase relation of oscillations near the planetary period of Saturn's auroral oval and the equatorial magnetospheric magnetic field. *Journal of Geophysical Research: Space Physics*, *114*(A04205). Retrieved 2018-04-20TZ, from `http://doi.wiley.com/10.1029/2008JA013988` doi: 10.1029/2008JA013988

Tao, C., Kataoka, R., Fukunishi, H., Takahashi, Y., & Yokoyama, T. (2005). Magnetic field variations in the Jovian magnetotail induced by solar wind dynamic pressure enhancements. *Journal of Geophysical Research*, *110*(A11208). Retrieved 2018-06-18TZ, from `http://doi.wiley.com/10.1029/2004JA010959` doi: 10.1029/2004JA010959

Zieger, B., & Hansen, K. C. (2008, August). Statistical validation of a solar wind propagation model from 1 to 10 AU. *Journal of Geophysical Research: Space Physics*, *113*(A08107). Retrieved 2018-06-07TZ, from `http://doi.wiley.com/10.1029/2008JA013046` doi: 10.1029/2008JA013046

Supporting Information for "Energetic particle signatures above Saturn's aurorae"

A. Bader[1], S. V. Badman[1], L. C. Ray[1], C. Paranicas[2], C. T. S. Lorch[1], G. Clark[2], M. André[3], D. G. Mitchell[2], D. Constable[1], J. Kinrade[1], G. J. Hunt[4], W. R. Pryor[5]

[1]Department of Physics, Lancaster University, Lancaster, UK
[2]Johns Hopkins University Applied Physics Laboratory, Laurel, MD, USA
[3]Swedish Institute of Space Physics, Uppsala, Sweden
[4]Blackett Laboratory, Imperial College London, London, UK
[5]Science Department, Central Arizona College, Coolidge, AZ, USA

Contents

Figures S1 to S3

Corresponding author: Alexander Bader, `a.bader@lancaster.ac.uk`

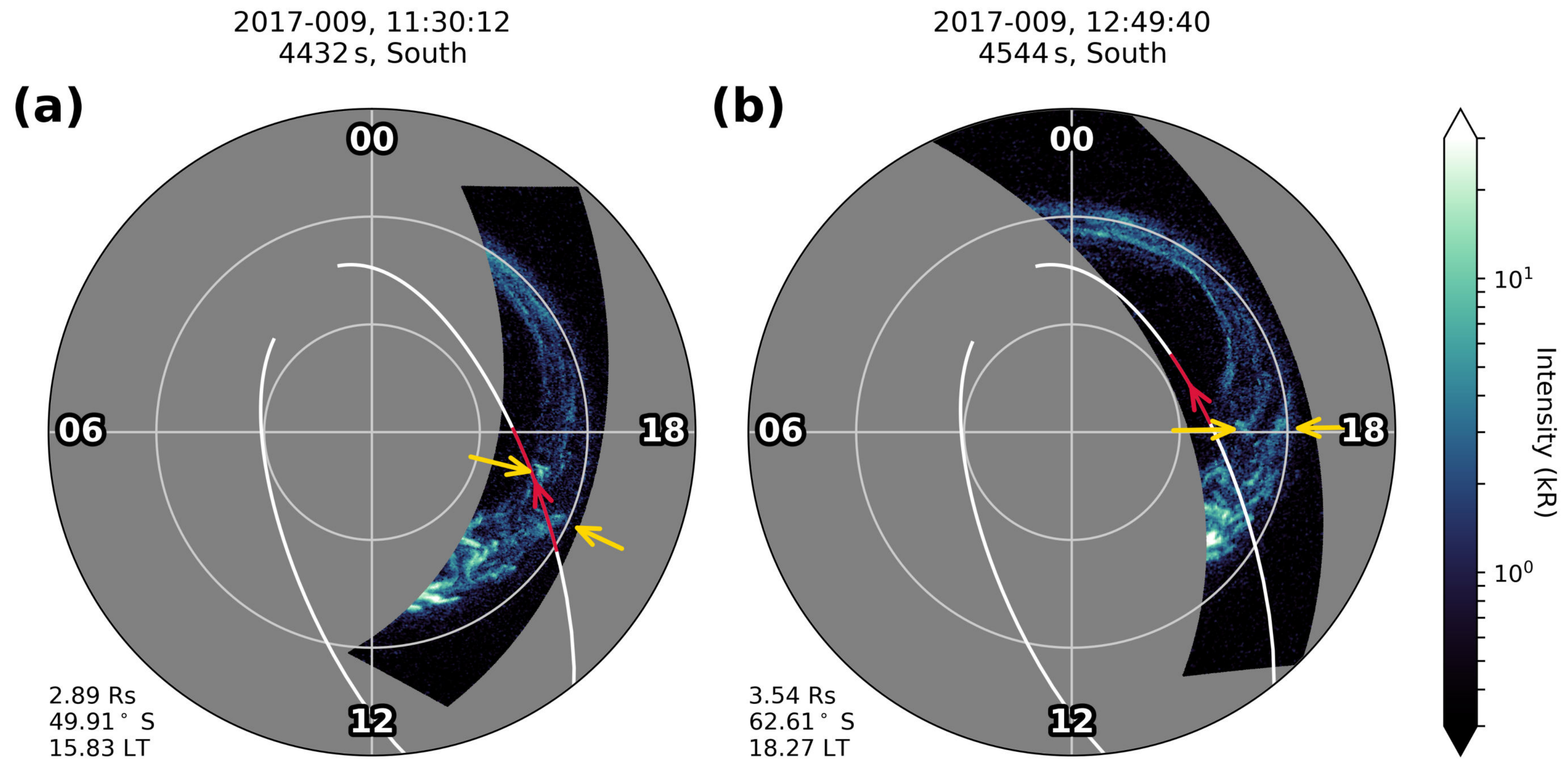

Figure S1. Cassini UVIS auroral imagery from 2017-009, same format as Figure 1. Yellow arrows mark the two patches which were crossed, both are long-lived and still visible in the second image.

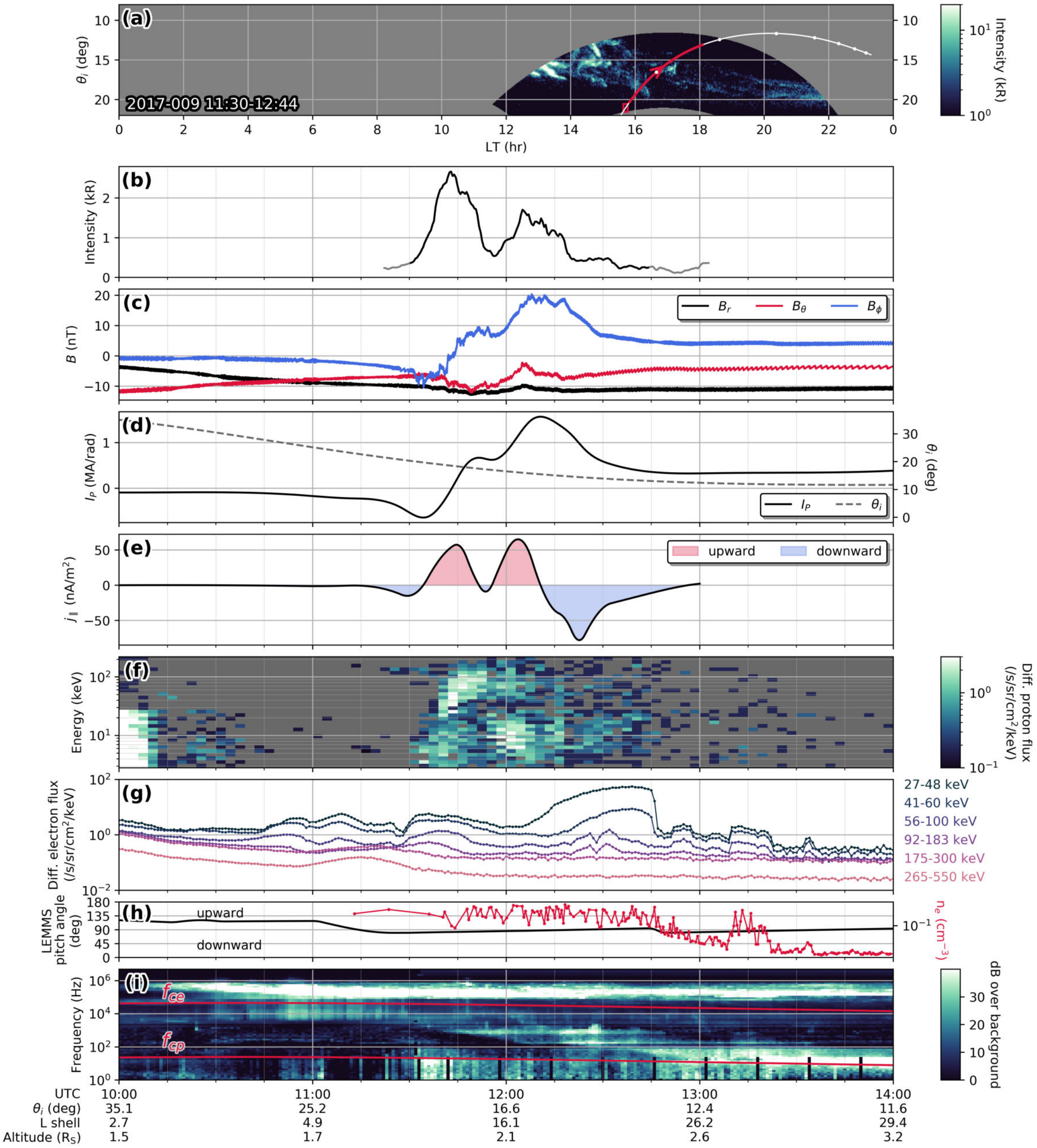

Figure S2. Data summary of the 2017-009 crossing, similar format to Figures 2 and 3 but in a longer time window. (g) shows more energy bins of the LEMMS electron detectors. (h) shows the pitch angle of LEMMS and the electron density inferred from RPWS Langmuir-probe measurements. (i) shows the full electric field spectrogram, albeit at lower time resolution than the data presented in Figure 3. The proton gyrofrequency f_{cp} and the electron gyrofrequency f_{ce} are marked in red.

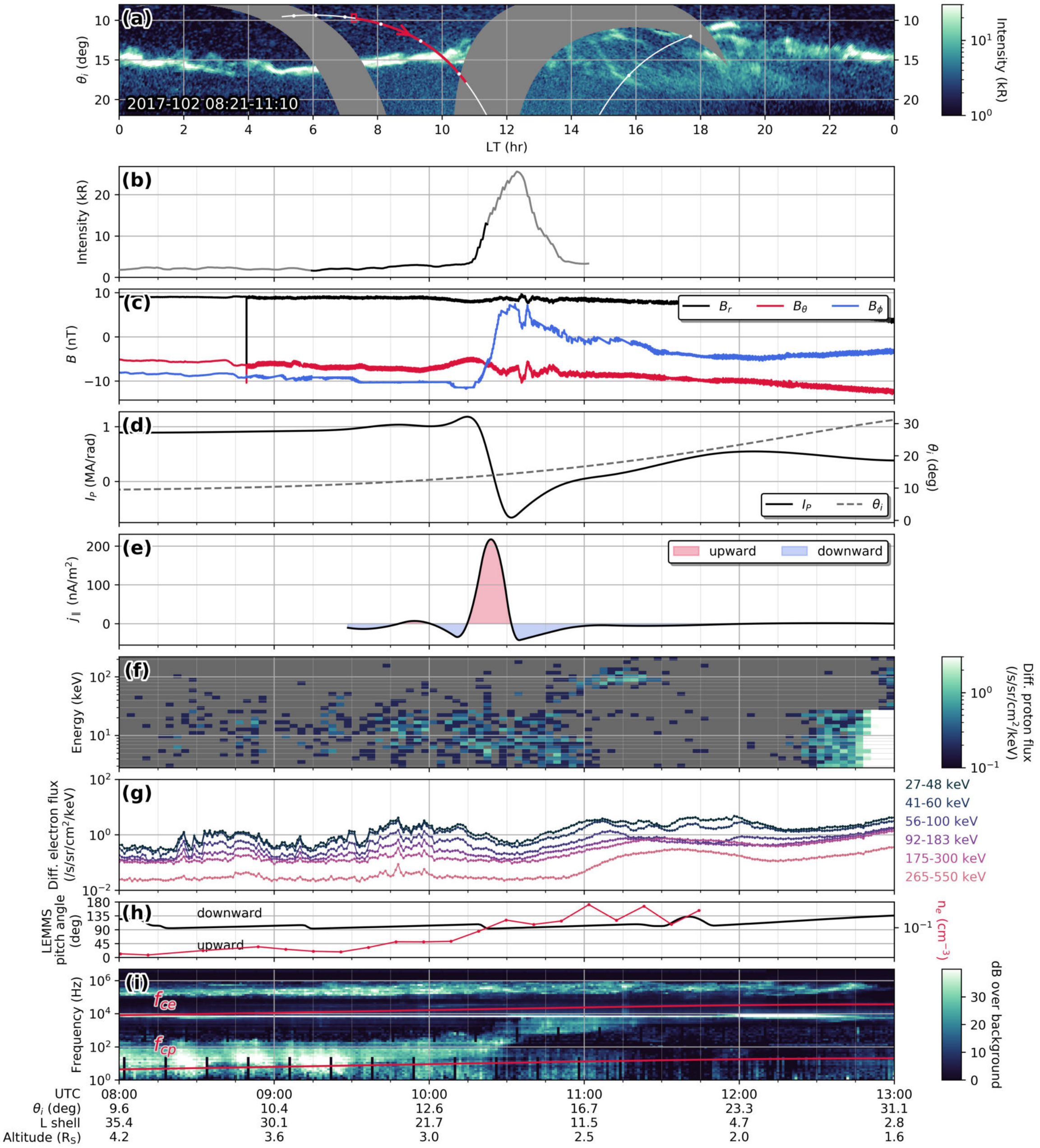

Figure S3. Data summary of the 2017-009 crossing, same format as Figure S2.

References

Achilleos, N., C. S. Arridge, C. Bertucci, C. M. Jackman, M. K. Dougherty, K. K. Khurana, and C. T. Russell, Large-scale dynamics of Saturn's magnetopause: Observations by Cassini, *Journal of Geophysical Research: Space Physics*, *113*(A11209), doi:10.1029/2008JA013265, 2008.

Acuña, M. H., N. F. Ness, and J. E. P. Connerney, The magnetic field of Saturn: Further studies of the Pioneer 11 observations, *Journal of Geophysical Research*, *85*(A11), 5675–5678, doi:10.1029/JA085iA11p05675, 1980.

Allegrini, F., F. Bagenal, S. Bolton, J. Connerney, G. Clark, R. W. Ebert, T. K. Kim, W. S. Kurth, S. Levin, P. Louarn, B. Mauk, D. J. McComas, C. Pollock, D. Ranquist, M. Reno, J. R. Szalay, M. F. Thomsen, P. Valek, S. Weidner, R. J. Wilson, and J. L. Zink, Electron beams and loss cones in the auroral regions of Jupiter: Jupiter Auroral Electrons, *Geophysical Research Letters*, *44*(14), 7131–7139, doi:10.1002/2017GL073180, 2017.

Andersson, L., R. E. Ergun, D. L. Newman, J. P. McFadden, C. W. Carlson, and Y.-J. Su, Characteristics of parallel electric fields in the downward current region of the aurora, *Physics of Plasmas*, *9*(8), 3600–3609, doi:10.1063/1.1490134, 2002.

Andrews, D. J., E. J. Bunce, S. W. H. Cowley, M. K. Dougherty, G. Provan, and D. J. Southwood, Planetary period oscillations in Saturn's magnetosphere: Phase relation of equatorial magnetic field oscillations and Saturn kilometric radiation modulation, *Journal of Geophysical Research: Space Physics*, *113*(A09205), doi:10.1029/2007JA012937, 2008.

Andrews, D. J., A. J. Coates, S. W. H. Cowley, M. K. Dougherty, L. Lamy, G. Provan, and P. Zarka, Magnetospheric period oscillations at Saturn: Comparison of equatorial and high-latitude magnetic field periods with north and south Saturn kilometric radiation periods, *Journal of Geophysical Research: Space Physics*, *115*(A12252), doi:10.1029/2010JA015666, 2010a.

Andrews, D. J., S. W. H. Cowley, M. K. Dougherty, and G. Provan, Magnetic field oscillations near the planetary period in Saturn's equatorial magnetosphere: Variation of amplitude and phase with radial distance and local time, *Journal of Geophysical Research: Space Physics*, *115*(A04212), doi:10.1029/2009JA014729, 2010b.

Andrews, D. J., S. W. H. Cowley, M. K. Dougherty, L. Lamy, G. Provan, and D. J. Southwood, Planetary period oscillations in Saturn's magnetosphere: Evolution of magnetic oscillation properties from southern summer to post-equinox, *Journal of Geophysical Research: Space Physics*, *117*(A04224), doi:10.1029/2011JA017444, 2012.

André, M., Electrostatic ion waves generated by ion loss-cone distributions in the magnetosphere, *Annales Geophysicae*, *4*, 241–246, 1986.

André, M., Waves and wave-particle interactions in the auroral region, *Journal of Atmospheric and Solar-Terrestrial Physics*, *59*(14), 1687–1712, doi:10.1016/S1364-6826(96)00173-3, 1997.

André, M., H. Koskinen, G. Gustafsson, and R. Lundin, Ion waves and upgoing ion beams observed by the Viking satellite, *Geophysical Research Letters*, *14*(4), 463–466, doi:10.1029/GL014i004p00463, 1987.

André, M., G. B. Crew, W. K. Peterson, A. M. Persoon, C. J. Pollock, and M. J. Engebretson, Ion heating by broadband low-frequency waves in the cusp/cleft, *Journal of Geophysical Research*, *95*(A12), 20809–20823, doi:10.1029/JA095iA12p20809, 1990.

André, M., P. Norqvist, L. Andersson, L. Eliasson, A. I. Eriksson, L. Blomberg, R. E. Erlandson, and J. Waldemark, Ion energization mechanisms at 1700 km in the auroral region, *Journal of Geophysical Research: Space Physics*, *103*(A3), 4199–4222, doi:10.1029/97JA00855, 1998.

Arridge, C. S., N. Achilleos, M. K. Dougherty, K. K. Khurana, and C. T. Russell, Modeling the size and shape of Saturn's magnetopause with variable dynamic pressure, *Journal of Geophysical Research*, *111*(A11227), doi:10.1029/2005JA011574, 2006.

Arridge, C. S., K. K. Khurana, C. T. Russell, D. J. Southwood, N. Achilleos, M. K. Dougherty, A. J. Coates, and H. K. Leinweber, Warping of Saturn's magnetospheric and magnetotail current sheets, *Journal of Geophysical Research: Space Physics*, *113*(A08217), doi:10.1029/2007JA012963, 2008a.

Arridge, C. S., C. T. Russell, K. K. Khurana, N. Achilleos, S. W. H. Cowley, M. K. Dougherty, D. J. Southwood, and E. J. Bunce, Saturn's magnetodisc current sheet, *Journal of Geophysical Research: Space Physics*, *113*(A04214), doi:10.1029/2007JA012540, 2008b.

Arridge, C. S., N. André, K. K. Khurana, C. T. Russell, S. W. H. Cowley, G. Provan, D. J. Andrews, C. M. Jackman, A. J. Coates, E. C. Sittler, M. K. Dougherty, and D. T. Young, Periodic motion of Saturn's nightside plasma sheet, *Journal of Geophysical Research: Space Physics*, *116*(A11205), doi:10.1029/2011JA016827, 2011.

Azari, A. R., X. Jia, M. W. Liemohn, G. B. Hospodarsky, G. Provan, S. Ye, S. W. H. Cowley, C. Paranicas, N. Sergis, A. M. Rymer, M. F. Thomsen, and D. G. Mitchell, Are Saturn's Interchange Injections Organized by Rotational Longitude?, *Journal of Geophysical Research: Space Physics*, *124*(3), 1806–1822, doi:10.1029/2018JA026196, 2019.

Bader, A., S. V. Badman, J. Kinrade, S. W. H. Cowley, G. Provan, and W. R. Pryor, Statistical planetary period oscillation signatures in Saturn's UV auroral intensity, *Journal of Geophysical Research: Space Physics*, *123*, 8459–8472, doi:10.1029/2018JA025855, 2018.

Bader, A., S. V. Badman, S. W. H. Cowley, Z. H. Yao, L. C. Ray, J. Kinrade, E. J. Bunce, G. Provan, T. J. Bradley, C. Tao, G. J. Hunt, and W. R. Pryor, The Dynamics of Saturn's Main Aurorae, *Geophysical Research Letters*, *46*(17-18), 10283–10294, doi:10.1029/2019GL084620, 2019a.

Bader, A., S. V. Badman, J. Kinrade, S. W. H. Cowley, G. Provan, and W. Pryor, Modulations of Saturn's UV auroral oval location by planetary period oscillations, *Journal of Geophysical Research: Space Physics*, *124*(2), 952–970, doi:10.1029/2018JA026117, 2019b.

Bader, A., S. V. Badman, Z. H. Yao, J. Kinrade, and W. R. Pryor, Observations of Continuous Quasiperiodic Auroral Pulsations on Saturn in High Time-Resolution UV Auroral Imagery, *Journal of Geophysical Research: Space Physics*, *124*, 2451–2465, doi:10.1029/2018JA026320, 2019c.

Bader, A., S. V. Badman, L. C. Ray, C. P. Paranicas, C. T. S. Lorch, G. Clark, M. André, D. G. Mitchell, D. A. Constable, J. Kinrade, G. J. Hunt, and W. Pryor, Energetic Particle Signatures Above Saturn's Aurorae, *Journal of Geophysical Research: Space Physics*, *125*(1), e2019JA027403, doi:10.1029/2019JA027403, 2020a.

Bader, A., S. W. H. Cowley, S. V. Badman, L. C. Ray, J. Kinrade, B. Palmaerts, and W. R. Pryor, The Morphology of Saturn's Aurorae Observed During the Cassini Grand Finale, *Geophysical Research Letters*, *47*(2), e2019GL085800, doi:10.1029/2019GL085800, 2020b.

Badman, S. V., and S. W. H. Cowley, Significance of Dungey-cycle flows in Jupiter's and Saturn's magnetospheres, and their identification on closed equatorial field lines, *Annales Geophysicae*, *25*(4), 941–951, doi:10.5194/angeo-25-941-2007, 2007.

Badman, S. V., E. J. Bunce, J. T. Clarke, S. W. H. Cowley, J.-C. Gérard, D. Grodent, and S. E. Milan, Open flux estimates in Saturn's magnetosphere during the January 2004 Cassini-HST campaign, and implications for reconnection rates, *Journal of Geophysical Research*, *110*(A11216), doi:10.1029/2005JA011240, 2005.

Badman, S. V., S. W. H. Cowley, J.-C. Gérard, and D. Grodent, A statistical analysis of the location and width of Saturn's southern auroras, *Annales Geophysicae*, *24*(12), 3533–3545, doi:10.5194/angeo-24-3533-2006, 2006.

Badman, S. V., N. Achilleos, K. H. Baines, R. H. Brown, E. J. Bunce, M. K. Dougherty, H. Melin, J. D. Nichols, and T. Stallard, Location of Saturn's northern infrared aurora determined from Cassini VIMS images, *Geophysical Research Letters*, *38*(L03102), doi:10.1029/2010GL046193, 2011a.

Badman, S. V., C. Tao, A. Grocott, S. Kasahara, H. Melin, R. H. Brown, K. H. Baines, M. Fujimoto, and T. Stallard, Cassini VIMS observations of latitudinal and hemispheric variations in Saturn's infrared auroral intensity, *Icarus*, *216*(2), 367–375, doi:10.1016/j.icarus.2011.09.031, 2011b.

Badman, S. V., N. Achilleos, C. S. Arridge, K. H. Baines, R. H. Brown, E. J. Bunce, A. J. Coates, S. W. H. Cowley, M. K. Dougherty, M. Fujimoto, G. Hospodarsky, S. Kasahara,

T. Kimura, H. Melin, D. G. Mitchell, T. Stallard, and C. Tao, Cassini observations of ion and electron beams at Saturn and their relationship to infrared auroral arcs, *Journal of Geophysical Research: Space Physics*, *117*(A01211), doi:10.1029/2011JA017222, 2012a.

Badman, S. V., D. J. Andrews, S. W. H. Cowley, L. Lamy, G. Provan, C. Tao, S. Kasahara, T. Kimura, M. Fujimoto, H. Melin, T. Stallard, R. H. Brown, and K. H. Baines, Rotational modulation and local time dependence of Saturn's infrared H3+ auroral intensity, *Journal of Geophysical Research: Space Physics*, *117*(A09228), doi:10.1029/2012JA017990, 2012b.

Badman, S. V., A. Masters, H. Hasegawa, M. Fujimoto, A. Radioti, D. Grodent, N. Sergis, M. K. Dougherty, and A. Coates, Bursty magnetic reconnection at Saturn's magnetopause, *Geophysical Research Letters*, *40*(6), 1027–1031, doi:10.1002/grl.50199, 2013.

Badman, S. V., C. M. Jackman, J. D. Nichols, J. T. Clarke, and J.-C. Gérard, Open flux in Saturn's magnetosphere, *Icarus*, *231*, 137–145, doi:10.1016/j.icarus.2013.12.004, 2014.

Badman, S. V., G. Branduardi-Raymont, M. Galand, S. L. G. Hess, N. Krupp, L. Lamy, H. Melin, and C. Tao, Auroral Processes at the Giant Planets: Energy Deposition, Emission Mechanisms, Morphology and Spectra, *Space Science Reviews*, *187*(1-4), 99–179, doi:10.1007/s11214-014-0042-x, 2015.

Badman, S. V., G. Provan, E. Bunce, D. Mitchell, H. Melin, S. W. H. Cowley, A. Radioti, W. S. Kurth, W. R. Pryor, J. D. Nichols, S. L. Jinks, T. S. Stallard, R. H. Brown, K. H. Baines, and M. K. Dougherty, Saturn's auroral morphology and field-aligned currents during a solar wind compression, *Icarus*, *263*, 83–93, doi:10.1016/j.icarus.2014.11.014, 2016.

Bagenal, F., The magnetosphere of Jupiter: Coupling the equator to the poles, *Journal of Atmospheric and Solar-Terrestrial Physics*, *69*(3), 387–402, doi:10.1016/j.jastp.2006.08.012, 2007.

Bagenal, F., and P. A. Delamere, Flow of mass and energy in the magnetospheres of Jupiter and Saturn, *Journal of Geophysical Research: Space Physics*, *116*(A05209), doi:10.1029/2010JA016294, 2011.

Baker, D. J., and G. J. Romick, The Rayleigh: Interpretation of the unit in terms of column emission rate or apparent radiance expressed in SI units, *Applied Optics*, *15*(8), 1966, doi:10.1364/AO.15.001966, 1976.

Ball, L., and M. André, What parts of broadband spectra are responsible for ion conic production?, *Geophysical Research Letters*, *18*(9), 1683–1686, doi:10.1029/91GL00169, 1991.

Belenkaya, E. S., I. I. Alexeev, M. S. Blokhina, S. W. H. Cowley, S. V. Badman, V. V. Kalegaev, and M. S. Grigoryan, IMF dependence of the open-closed field line boundary in Saturn's ionosphere, and its relation to the UV auroral oval observed by the Hubble Space Telescope, *Annales Geophysicae*, *25*(5), 1215–1226, doi:10.5194/angeo-25-1215-2007, 2007.

Belenkaya, E. S., S. W. H. Cowley, J. D. Nichols, M. S. Blokhina, and V. V. Kalegaev, Magnetospheric mapping of the dayside UV auroral oval at Saturn using simultaneous HST images, Cassini IMF data, and a global magnetic field model, *Annales Geophysicae*, *29*(7), 1233–1246, doi:10.5194/angeo-29-1233-2011, 2011.

Belenkaya, E. S., S. W. H. Cowley, C. J. Meredith, J. D. Nichols, V. V. Kalegaev, I. I. Alexeev, O. G. Barinov, W. O. Barinova, and M. S. Blokhina, Magnetospheric magnetic field modelling for the 2011 and 2012 HST Saturn aurora campaigns - implications for auroral source regions, *Annales Geophysicae*, *32*(6), 689–704, doi:10.5194/angeo-32-689-2014, 2014.

Blanc, M., D. J. Andrews, A. J. Coates, D. C. Hamilton, C. M. Jackman, X. Jia, A. Kotova, M. Morooka, H. T. Smith, and J. H. Westlake, Saturn Plasma Sources and Associated Transport Processes, *Space Science Reviews*, *192*(1-4), 237–283, doi:10.1007/s11214-015-0172-9, 2015.

Bonfond, B., J. Gustin, J.-C. Gérard, D. Grodent, A. Radioti, B. Palmaerts, S. V. Badman, K. K. Khurana, and C. Tao, The far-ultraviolet main auroral emission at Jupiter - Part 1: Dawn-dusk brightness asymmetries, *Annales Geophysicae*, *33*(10), 1203–1209, doi:10.5194/angeo-33-1203-2015, 2015.

Bradley, T. J., S. W. H. Cowley, E. J. Bunce, A. W. Smith, C. M. Jackman, and G. Provan, Planetary Period Modulation of Reconnection Bursts in Saturn's Magnetotail, *Journal of Geophysical Research: Space Physics*, *123*(11), 9476–9507, doi:10.1029/2018JA025932, 2018a.

Bradley, T. J., S. W. H. Cowley, G. Provan, G. J. Hunt, E. J. Bunce, S. J. Wharton, I. I. Alexeev, E. S. Belenkaya, V. V. Kalegaev, and M. K. Dougherty, Field-aligned currents in Saturn's nightside magnetosphere: Subcorotation and planetary period oscillation components during northern spring, *Journal of Geophysical Research: Space Physics*, *123*, 3602–3636, doi:10.1029/2017JA024885, 2018b.

Brain, D. A., J. S. Halekas, L. M. Peticolas, R. P. Lin, J. G. Luhmann, D. L. Mitchell, G. T. Delory, S. W. Bougher, M. H. Acuña, and H. Rème, On the origin of aurorae on Mars, *Geophysical Research Letters*, *33*(L01201), doi:10.1029/2005GL024782, 2006.

Brandt, P. C., K. K. Khurana, D. G. Mitchell, N. Sergis, K. Dialynas, J. F. Carbary, E. C. Roelof, C. P. Paranicas, S. M. Krimigis, and B. H. Mauk, Saturn's periodic magnetic field perturbations caused by a rotating partial ring current, *Geophysical Research Letters*, *37*(L22103), doi:10.1029/2010GL045285, 2010.

Brice, N. M., and G. A. Ioannidis, The magnetospheres of Jupiter and Earth, *Icarus*, *13*(2), 173–183, doi:10.1016/0019-1035(70)90048-5, 1970.

Brooks, E. L., C. Fernandez, and D. H. Pontius, Saturn's Multiple, Variable Periodicities: A Dual-Flywheel Model of Thermosphere-Ionosphere-Magnetosphere Coupling, *Journal of Geophysical Research: Space Physics*, *124*(10), 7820–7836, doi:10.1029/2019JA026870, 2019.

Brown, R. H., K. H. Baines, G. Bellucci, J.-P. Bibring, B. J. Buratti, F. Capaccioni, P. Cerroni, R. N. Clark, A. Coradini, D. P. Cruikshank, P. Drossart, V. Formisano, R. Jaumann, Y. Langevin, D. L. Matson, T. B. Mccord, V. Mennella, E. Miller, R. M. Nelson, P. D. Nicholson, B. Sicardy, and C. Sotin, The Cassini Visual and Infrared Mapping Spectrometer (VIMS) Investigation, *Space Science Reviews*, *115*(1-4), 111–168, doi:10.1007/s11214-004-1453-x, 2004.

Bunce, E. J., S. W. H. Cowley, and S. E. Milan, Interplanetary magnetic field control of Saturn's polar cusp aurora, *Annales Geophysicae*, *23*(4), 1405–1431, doi:10.5194/angeo-23-1405-2005, 2005a.

Bunce, E. J., S. W. H. Cowley, D. M. Wright, A. J. Coates, M. K. Dougherty, N. Krupp, W. S. Kurth, and A. M. Rymer, In situ observations of a solar wind compression-induced hot plasma injection in Saturn's tail, *Geophysical Research Letters*, *32*(L20S04), doi:10.1029/2005GL022888, 2005b.

Bunce, E. J., S. W. H. Cowley, I. I. Alexeev, C. S. Arridge, M. K. Dougherty, J. D. Nichols, and C. T. Russell, Cassini observations of the variation of Saturn's ring current parameters with system size, *Journal of Geophysical Research: Space Physics*, *112*(A10202), doi:10.1029/2007JA012275, 2007.

Bunce, E. J., C. S. Arridge, J. T. Clarke, A. J. Coates, S. W. H. Cowley, M. K. Dougherty, J.-C. Gérard, D. Grodent, K. C. Hansen, J. D. Nichols, D. J. Southwood, and D. L. Talboys, Origin of Saturn's aurora: Simultaneous observations by Cassini and the Hubble Space Telescope, *Journal of Geophysical Research: Space Physics*, *113*(A09209), doi:10.1029/2008JA013257, 2008a.

Bunce, E. J., C. S. Arridge, S. W. H. Cowley, and M. K. Dougherty, Magnetic field structure of Saturn's dayside magnetosphere and its mapping to the ionosphere: Results from ring current modeling, *Journal of Geophysical Research: Space Physics*, *113*(A02207), doi:10.1029/2007JA012538, 2008b.

Burton, M. E., M. K. Dougherty, and C. T. Russell, Saturn's internal planetary magnetic field, *Geophysical Research Letters*, *37*(L24105), doi:10.1029/2010GL045148, 2010.

Cao, H., C. T. Russell, U. R. Christensen, M. K. Dougherty, and M. E. Burton, Saturn's very axisymmetric magnetic field: No detectable secular variation or tilt, *Earth and Planetary Science Letters*, *304*(1-2), 22–28, doi:10.1016/j.epsl.2011.02.035, 2011.

Carbary, J. F., The morphology of Saturn's ultraviolet aurora, *Journal of Geophysical Research: Space Physics*, *117*(A06210), doi:10.1029/2012JA017670, 2012.

Carbary, J. F., Longitude dependences of Saturn's ultraviolet aurora, *Geophysical Research Letters*, *40*(10), 1902–1906, doi:10.1002/grl.50430, 2013.

Carbary, J. F., Update on Saturn's energetic electron periodicities, *Journal of Geophysical Research: Space Physics*, *122*(1), 156–165, doi:10.1002/2016JA023405, 2017.

Carbary, J. F., A New Ring Current Model for Saturn, *Journal of Geophysical Research: Space Physics*, *124*(5), 3378–3389, doi:10.1029/2019JA026560, 2019.

Carbary, J. F., and D. G. Mitchell, Periodicities in Saturn's magnetosphere, *Reviews of Geophysics*, *51*(1), 1–30, doi:10.1002/rog.20006, 2013.

Carbary, J. F., and D. G. Mitchell, Midnight flash model of energetic neutral atom periodicities at Saturn: Midnight Flash Model, *Journal of Geophysical Research: Space Physics*, *122*(7), 7110–7117, doi:10.1002/2017JA024296, 2017.

Carbary, J. F., D. G. Mitchell, P. Brandt, C. Paranicas, and S. M. Krimigis, ENA periodicities at Saturn, *Geophysical Research Letters*, *35*(L07102), doi:10.1029/2008GL033230, 2008a.

Carbary, J. F., D. G. Mitchell, P. Brandt, E. C. Roelof, and S. M. Krimigis, Statistical morphology of ENA emissions at Saturn, *Journal of Geophysical Research: Space Physics*, *113*(A05210), doi:10.1029/2007JA012873, 2008b.

Carbary, J. F., D. G. Mitchell, P. Brandt, E. C. Roelof, and S. M. Krimigis, Track analysis of energetic neutral atom blobs at Saturn, *Journal of Geophysical Research: Space Physics*, *113*(A01209), doi:10.1029/2007JA012708, 2008c.

Carbary, J. F., D. G. Mitchell, P. C. Brandt, S. M. Krimigis, and D. A. Gurnett, ENA periodicities and their phase relations to SKR emissions at Saturn, *Geophysical Research Letters*, *38*(L16106), doi:10.1029/2011GL048418, 2011.

Carbary, J. F., N. Achilleos, and C. S. Arridge, Statistical ring current of Saturn, *Journal of Geophysical Research: Space Physics*, *117*(A06223), doi:10.1029/2011JA017472, 2012.

Carbary, J. F., W. S. Kurth, and D. G. Mitchell, Short periodicities in low-frequency plasma waves at Saturn, *Journal of Geophysical Research: Space Physics*, *121*(7), 6562–6572, doi:10.1002/2016JA022732, 2016.

Carbary, J. F., D. C. Hamilton, and D. G. Mitchell, Global Maps of Energetic Ions in Saturn's Magnetosphere, *Journal of Geophysical Research: Space Physics*, *123*(10), 8557–8571, doi:10.1029/2018JA025814, 2018.

Carlson, C. W., J. P. McFadden, R. E. Ergun, M. Temerin, W. Peria, F. S. Mozer, D. M. Klumpar, E. G. Shelley, W. K. Peterson, E. Moebius, R. Elphic, R. Strangeway, C. Cattell, and R. Pfaff, FAST observations in the downward auroral current region: Energetic upgoing electron beams, parallel potential drops, and ion heating, *Geophysical Research Letters*, *25*(12), 2017–2020, doi:10.1029/98GL00851, 1998a.

Carlson, C. W., R. F. Pfaff, and J. G. Watzin, The Fast Auroral SnapshoT (FAST) Mission, *Geophysical Research Letters*, *25*(12), 2013–2016, doi:10.1029/98GL01592, 1998b.

Cassidy, T., and R. Johnson, Collisional spreading of Enceladus' neutral cloud, *Icarus*, *209*(2), 696–703, doi:10.1016/j.icarus.2010.04.010, 2010.

Cattell, C. A., F. S. Mozer, I. Roth, R. R. Anderson, R. C. Elphic, W. Lennartsson, and E. Ungstrup, ISEE 1 observations of electrostatic ion cyclotron waves in association with ion beams on auroral field lines from ~2.5 to 4.5 R_E, *Journal of Geophysical Research*, *96*(A7), 11421–11439, doi:10.1029/91JA00378, 1991.

Chancia, R., M. Hedman, S. Cowley, G. Provan, and S.-Y. Ye, Seasonal structures in Saturn's dusty Roche Division correspond to periodicities of the planet's magnetosphere, *Icarus*, *330*, 230–255, doi:10.1016/j.icarus.2019.04.012, 2019.

Chang, T., Lower-hybrid collapse, caviton turbulence, and charged particle energization in the topside auroral ionosphere and magnetosphere, *Physics of Fluids B: Plasma Physics*, *5*(7), 2646–2656, doi:10.1063/1.860702, 1993.

Chang, T., G. B. Crew, N. Hershkowitz, J. R. Jasperse, J. M. Retterer, and J. D. Winningham, Transverse acceleration of oxygen ions by electromagnetic ion cyclotron resonance with broad band left-hand polarized waves, *Geophysical Research Letters*, *13*(7), 636–639, doi:10.1029/GL013i007p00636, 1986.

Chané, E., J. Saur, R. Keppens, and S. Poedts, How is the Jovian main auroral emission affected by the solar wind?, *Journal of Geophysical Research: Space Physics*, *122*, 1960–1978, doi:10.1002/2016JA023318, 2017.

Chen, Y., and T. W. Hill, Statistical analysis of injection/dispersion events in Saturn's inner magnetosphere, *Journal of Geophysical Research: Space Physics*, *113*(A07215), doi:10.1029/2008JA013166, 2008.

Clark, G., B. H. Mauk, D. Haggerty, C. Paranicas, P. Kollmann, A. Rymer, E. J. Bunce, S. W. H. Cowley, D. G. Mitchell, G. Provan, R. W. Ebert, F. Allegrini, F. Bagenal, S. Bolton, J. Connerney, S. Kotsiaros, W. S. Kurth, S. Levin, D. J. McComas, J. Saur, and P. Valek, Energetic particle signatures of magnetic field-aligned potentials over Jupiter's polar regions, *Geophysical Research Letters*, *44*(17), 8703–8711, doi:10.1002/2017GL074366, 2017a.

Clark, G., B. H. Mauk, C. Paranicas, D. Haggerty, P. Kollmann, A. Rymer, L. Brown, S. Jaskulek, C. Schlemm, C. Kim, J. Peachey, D. LaVallee, F. Allegrini, F. Bagenal, S. Bolton, J. Connerney, R. W. Ebert, G. Hospodarsky, S. Levin, W. S. Kurth, D. J. McComas, D. G. Mitchell, D. Ranquist, and P. Valek, Observation and interpretation of energetic ion conics in Jupiter's polar magnetosphere, *Geophysical Research Letters*, *44*(10), 4419–4425, doi:10.1002/2016GL072325, 2017b.

Clark, G., C. Tao, B. H. Mauk, J. Nichols, J. Saur, E. J. Bunce, F. Allegrini, R. Gladstone, F. Bagenal, S. Bolton, B. Bonfond, J. Connerney, R. W. Ebert, D. J. Gershman, D. Haggerty, T. Kimura, P. Kollmann, S. Kotsiaros, W. S. Kurth, S. Levin, D. J. McComas, G. Murakami, C. Paranicas, A. Rymer, and P. Valek, Precipitating Electron Energy Flux and Characteristic Energies in Jupiter's Main Auroral Region as Measured by Juno/JEDI, *Journal of Geophysical Research: Space Physics*, *123*(9), 7554–7567, doi:10.1029/2018JA025639, 2018.

Clarke, J. T., J. Ajello, G. Ballester, L. Ben Jaffel, J. Connerney, J.-C. Gérard, G. R. Gladstone, D. Grodent, W. Pryor, J. Trauger, and J. H. Waite, Ultraviolet emissions from the magnetic footprints of Io, Ganymede and Europa on Jupiter, *Nature*, *415*(6875), 997–1000, doi:10.1038/415997a, 2002.

Clarke, J. T., J. Connerney, F. Crary, M. Dougherty, W. Kurth, S. W. H. Cowley, E. J. Bunce, T. Hill, and J. Kim, Morphological differences between Saturn's ultraviolet aurorae and those of Earth and Jupiter, *Nature*, *433*, 3, doi:10.1038/nature03331, 2005.

Clarke, J. T., J. Nichols, J.-C. Gérard, D. Grodent, K. C. Hansen, W. Kurth, G. R. Gladstone, J. Duval, S. Wannawichian, E. Bunce, S. W. H. Cowley, F. Crary, M. Dougherty, L. Lamy, D. Mitchell, W. Pryor, K. Retherford, T. Stallard, B. Zieger, P. Zarka, and B. Cecconi, Response of Jupiter's and Saturn's auroral activity to the solar wind, *Journal of Geophysical Research: Space Physics*, *114*(A05210), doi:10.1029/2008JA013694, 2009.

Clarke, K. E., D. J. Andrews, C. S. Arridge, A. J. Coates, and S. W. H. Cowley, Magnetopause oscillations near the planetary period at Saturn: Occurrence, phase, and amplitude, *Journal of Geophysical Research: Space Physics*, *115*(A08209), doi:10.1029/2009JA014745, 2010a.

Clarke, K. E., D. J. Andrews, A. J. Coates, S. W. H. Cowley, and A. Masters, Magnetospheric period oscillations of Saturn's bow shock, *Journal of Geophysical Research: Space Physics*, *115*(A05202), doi:10.1029/2009JA015164, 2010b.

Connerney, J. E. P., M. H. Acuña, and N. F. Ness, Saturn's ring current and inner magnetosphere, *Nature*, *292*(5825), 724–726, doi:10.1038/292724a0, 1981.

Connerney, J. E. P., N. F. Ness, and M. H. Acuña, Zonal harmonic model of Saturn's magnetic field from Voyager 1 and 2 observations, *Nature*, *298*, doi:10.1038/298044a0, 1982.

Cowley, S. W. H., and E. J. Bunce, Origin of the main auroral oval in Jupiter's coupled magnetosphere–ionosphere system, *Planetary and Space Science*, *49*(10-11), 1067–1088, doi:10.1016/S0032-0633(00)00167-7, 2001.

Cowley, S. W. H., and E. J. Bunce, Corotation-driven magnetosphere-ionosphere coupling currents in Saturn's magnetosphere and their relation to the auroras, *Annales Geophysicae*, *21*(8), 1691–1707, doi:10.5194/angeo-21-1691-2003, 2003.

Cowley, S. W. H., and G. Provan, Planetary period modulations of Saturn's magnetotail current sheet during northern spring: Observations and modeling, *Journal of Geophysical Research: Space Physics*, *122*(6), 6049–6077, doi:10.1002/2017JA023993, 2017.

Cowley, S. W. H., E. J. Bunce, and J. D. Nichols, Origins of Jupiter's main oval auroral emissions, *Journal of Geophysical Research*, *108*(A4), 8002, doi:10.1029/2002JA009329, 2003.

Cowley, S. W. H., E. J. Bunce, and J. M. O'Rourke, A simple quantitative model of plasma flows and currents in Saturn's polar ionosphere, *Journal of Geophysical Research*, *109*(A05212), doi:10.1029/2003JA010375, 2004a.

Cowley, S. W. H., E. J. Bunce, and R. Prangé, Saturn's polar ionospheric flows and their relation to the main auroral oval, *Annales Geophysicae*, *22*(4), 1379–1394, doi:10.5194/angeo-22-1379-2004, 2004b.

Cowley, S. W. H., S. V. Badman, E. J. Bunce, J. T. Clarke, J.-C. Gérard, D. C. Grodent, C. M. Jackman, S. E. Milan, and T. K. Yeoman, Reconnection in a rotation-dominated magnetosphere and its relation to Saturn's auroral dynamics, *Journal of Geophysical Research*, *110*(A02201), doi:10.1029/2004JA010796, 2005.

Cowley, S. W. H., C. S. Arridge, E. J. Bunce, J. T. Clarke, A. J. Coates, M. K. Dougherty, J.-C. Gérard, D. Grodent, J. D. Nichols, and D. L. Talboys, Auroral current systems in Saturn's magnetosphere: comparison of theoretical models with Cassini and HST observations, *Annales Geophysicae*, *26*(9), 2613–2630, doi:10.5194/angeo-26-2613-2008, 2008.

Cowley, S. W. H., G. Provan, E. J. Bunce, and J. D. Nichols, Magnetosphere-ionosphere coupling at Jupiter: Expectations for Juno Perijove 1 from a steady state axisymmetric physical model, *Geophysical Research Letters*, *44*(10), 4497–4505, doi:10.1002/2017GL073129, 2017.

Cowling, T. G., The magnetic field of sunspots, *Monthly Notices of the Royal Astronomical Society*, *94*(1), 39–48, doi:10.1093/mnras/94.1.39, 1933.

Crary, F. J., J. T. Clarke, M. K. Dougherty, P. G. Hanlon, K. C. Hansen, J. T. Steinberg, B. L. Barraclough, A. J. Coates, J.-C. Gérard, D. Grodent, W. S. Kurth, D. G. Mitchell, A. M. Rymer, and D. T. Young, Solar wind dynamic pressure and electric field as the main factors controlling Saturn's aurorae, *Nature*, *433*, 720, doi:10.1038/nature03333, 2005.

Delamere, P. A., and F. Bagenal, Solar wind interaction with Jupiter's magnetosphere, *Journal of Geophysical Research: Space Physics*, *115*(A10201), doi:10.1029/2010JA015347, 2010.

Delamere, P. A., R. J. Wilson, S. Eriksson, and F. Bagenal, Magnetic signatures of Kelvin-Helmholtz vortices on Saturn's magnetopause: Global survey, *Journal of Geophysical Research: Space Physics*, *118*(1), 393–404, doi:10.1029/2012JA018197, 2013.

Delamere, P. A., A. Otto, X. Ma, F. Bagenal, and R. J. Wilson, Magnetic flux circulation in the rotationally driven giant magnetospheres, *Journal of Geophysical Research: Space Physics*, *120*(6), 4229–4245, doi:10.1002/2015JA021036, 2015.

Desch, M. D., and M. L. Kaiser, Voyager measurement of the rotation period of Saturn's magnetic field, *Geophysical Research Letters*, *8*(3), 253–256, doi:10.1029/GL008i003p00253, 1981.

Desroche, M., F. Bagenal, P. A. Delamere, and N. Erkaev, Conditions at the magnetopause of Saturn and implications for the solar wind interaction, *Journal of Geophysical Research: Space Physics*, *118*(6), 3087–3095, doi:10.1002/jgra.50294, 2013.

Dialynas, K., S. M. Krimigis, D. G. Mitchell, R. B. Decker, and E. C. Roelof, The bubble-like shape of the heliosphere observed by Voyager and Cassini, *Nature Astronomy*, *1*(5), doi:10.1038/s41550-017-0115, 2017.

Dougherty, M. K., S. Kellock, D. J. Southwood, A. Balogh, E. J. Smith, B. T. Tsurutani, B. Gerlach, K.-H. Glassmeier, F. Gleim, C. T. Russell, G. Erdos, F. M. Neubauer, and

S. W. H. Cowley, The Cassini Magnetic Field Investigation, *Space Science Reviews*, *114*(1-4), 331–383, doi:10.1007/s11214-004-1432-2, 2004.

Dougherty, M. K., K. K. Khurana, F. M. Neubauer, C. T. Russell, J. Saur, J. S. Leisner, and M. E. Burton, Identification of a Dynamic Atmosphere at Enceladus with the Cassini Magnetometer, *Science*, *311*(5766), 1406–1409, doi:10.1126/science.1120985, 2006.

Dougherty, M. K., H. Cao, K. K. Khurana, G. J. Hunt, G. Provan, S. Kellock, M. E. Burton, T. A. Burk, E. J. Bunce, S. W. H. Cowley, M. G. Kivelson, C. T. Russell, and D. J. Southwood, Saturn's magnetic field revealed by the Cassini Grand Finale, *Science*, *362*(6410), doi:10.1126/science.aat5434, 2018.

Dungey, J. W., Interplanetary magnetic field and the auroral zones, *Physical Review Letters*, *6*(2), 47–48, doi:10.1103/PhysRevLett.6.47, 1961.

Dyudina, U. A., A. P. Ingersoll, S. P. Ewald, and D. Wellington, Saturn's aurora observed by the Cassini camera at visible wavelengths, *Icarus*, *263*, 32–43, doi:10.1016/j.icarus.2015.05.022, 2016.

Ebert, R. W., F. Allegrini, F. Bagenal, S. J. Bolton, J. E. P. Connerney, G. Clark, G. R. Gladstone, V. Hue, W. S Kurth, S. Levin, P. Louarn, B. H. Mauk, D. J. McComas, C. Paranicas, M. Reno, J. Saur, J. R. Szalay, M. F. Thomsen, P. Valek, S. Weidner, and R. J. Wilson, Spatial Distribution and Properties of 0.1-100 keV Electrons in Jupiter's Polar Auroral Region, *Geophysical Research Letters*, *44*(18), 9199–9207, doi:10.1002/2017GL075106, 2017.

Elachi, C., M. D. Allison, L. Borgarelli, P. Encrenaz, E. Im, M. A. Janssen, W. T. K. Johnson, R. L. Kirk, R. D. Lorenz, J. I. Lunine, D. O. Muhleman, S. J. Ostro, G. Picardi, F. Posa, C. G. Rapley, L. E. Roth, R. Seu, L. A. Soderblom, S. Vetrella, S. D. Wall, C. A. Wood, and H. A. Zebker, Radar: The Cassini Titan Radar Mapper, *Space Science Reviews*, *115*(1-4), 71–110, doi:10.1007/s11214-004-1438-9, 2004.

Elliott, S. S., D. A. Gurnett, W. S. Kurth, G. Clark, B. H. Mauk, S. J. Bolton, J. E. P. Connerney, and S. M. Levin, Pitch Angle Scattering of Upgoing Electron Beams in

Jupiter's Polar Regions by Whistler Mode Waves, *Geophysical Research Letters*, *45*(3), 1246–1252, doi:10.1002/2017GL076878, 2018.

Ergun, R. E., C. W. Carlson, J. P. McFadden, F. S. Mozer, G. T. Delory, W. Peria, C. C. Chaston, M. Temerin, R. Elphic, R. Strangeway, R. Pfaff, C. A. Cattell, D. Klumpar, E. Shelley, W. Peterson, E. Moebius, and L. Kistler, FAST satellite observations of electric field structures in the auroral zone, *Geophysical Research Letters*, *25*(12), 2025–2028, doi:10.1029/98GL00635, 1998.

Espinosa, S. A., and M. K. Dougherty, Periodic perturbations in Saturn's magnetic field, *Geophysical Research Letters*, *27*(17), 2785–2788, doi:10.1029/2000GL000048, 2000.

Espinosa, S. A., D. J. Southwood, and M. K. Dougherty, Reanalysis of Saturn's magnetospheric field data view of spin-periodic perturbations, *Journal of Geophysical Research: Space Physics*, *108*(A2), 1085, doi:10.1029/2001JA005083, 2003.

Esposito, L. W., C. A. Barth, J. E. Colwell, G. M. Lawrence, W. E. McClintock, A. I. F. Stewart, H. U. Keller, A. Korth, H. Lauche, M. C. Festou, A. L. Lane, C. J. Hansen, J. N. Maki, R. A. West, H. Jahn, R. Reulke, K. Warlich, D. E. Shemansky, and Y. L. Yung, The Cassini Ultraviolet Imaging Spectrograph investigation, *Space Science Reviews*, *115*(1-4), 299–361, doi:10.1007/s11214-004-1455-8, 2004.

Evans, D. S., The observations of a near monoenergetic flux of auroral electrons, *Journal of Geophysical Research*, *73*(7), 2315–2323, doi:10.1029/JA073i007p02315, 1968.

Fillius, W., and W. H. Ip, Trapped radiation belts of Saturn: First look, *Science*, *207*, 425–431, doi:10.1126/science.207.4429.425, 1980.

Flasar, F. M., V. G. Kunde, M. M. Abbas, R. K. Achterberg, P. Ade, A. Barucci, B. Bézard, G. L. Bjoraker, J. C. Brasunas, S. Calcutt, R. Carlson, C. J. Césarsky, B. J. Conrath, A. Coradini, R. Courtin, A. Coustenis, S. Edberg, S. Edgington, C. Ferrari, T. Fouchet, D. Gautier, P. J. Gierasch, K. Grossman, P. Irwin, D. E. Jennings, E. Lellouch, A. A. Mamoutkine, A. Marten, J. P. Meyer, C. A. Nixon, G. S. Orton, T. C. Owen, J. C. Pearl, R. Prangé, F. Raulin, P. L. Read, P. N. Romani, R. E. Samuelson, M. E. Segura, M. R.

Showalter, A. A. Simon-Miller, M. D. Smith, J. R. Spencer, L. J. Spilker, and F. W. Taylor, Exploring the Saturn System in the Thermal Infrared: The Composite Infrared Spectrometer, *Space Science Reviews*, *115*(1-4), 169–297, doi:10.1007/s11214-004-1454-9, 2004.

Fuselier, S. A., H. U. Frey, K. J. Trattner, S. B. Mende, and J. L. Burch, Cusp aurora dependence on interplanetary magnetic field B_z, *Journal of Geophysical Research*, *107*(A7), 1111, doi:10.1029/2001JA900165, 2002.

Galand, M., L. Moore, I. Mueller-Wodarg, M. Mendillo, and S. Miller, Response of Saturn's auroral ionosphere to electron precipitation: Electron density, electron temperature, and electrical conductivity, *Journal of Geophysical Research: Space Physics*, *116*(A09306), doi:10.1029/2010JA016412, 2011.

Galopeau, P., P. Zarka, and D. Le Quéau, Theoretical model of Saturn's kilometric radiation spectrum, *Journal of Geophysical Research*, *94*(A7), 8739, doi:10.1029/JA094iA07p08739, 1989.

Galopeau, P. H. M., and A. Lecacheux, Variations of Saturn's radio rotation period measured at kilometer wavelengths, *Journal of Geophysical Research: Space Physics*, *105*(A6), 13089–13101, doi:10.1029/1999JA005089, 2000.

Garbe, G. P., R. L. Arnold, T. E. Moore, P. M. Kintner, and J. L. Vago, Observations of transverse ion acceleration in the topside auroral ionosphere, *Journal of Geophysical Research*, *97*(A2), 1257–1269, doi:10.1029/91JA02127, 1992.

Gershman, D. J., J. E. P. Connerney, S. Kotsiaros, G. A. DiBraccio, Y. M. Martos, A. F. -Viñas, V. Hue, G. Clark, F. Bagenal, S. Levin, and S. J. Bolton, Alfvénic Fluctuations Associated With Jupiter's Auroral Emissions, *Geophysical Research Letters*, *46*(13), 7157–7165, doi:10/ggmbr5, 2019.

Giampieri, G., M. K. Dougherty, E. J. Smith, and C. T. Russell, A regular period for Saturn's magnetic field that may track its internal rotation, *Nature*, *441*(7089), 62–64, doi:10.1038/nature04750, 2006.

Gkioulidou, M., C.-P. Wang, L. R. Lyons, and R. A. Wolf, Formation of the Harang reversal and its dependence on plasma sheet conditions: Rice convection model simulations, *Journal of Geophysical Research: Space Physics*, *114*(A07204), doi:10.1029/2008JA013955, 2009.

Gold, T., Motions in the magnetosphere of the Earth, *Journal of Geophysical Research*, *64*(9), 1219–1224, doi:10.1029/JZ064i009p01219, 1959.

Gombosi, T. I., T. P. Armstrong, C. S. Arridge, K. K. Khurana, S. M. Krimigis, N. Krupp, A. M. Persoon, and M. F. Thomsen, Saturn's Magnetospheric Configuration, in *Saturn from Cassini-Huygens*, edited by M. K. Dougherty, L. W. Esposito, and S. M. Krimigis, pp. 203–255, Springer Netherlands, Dordrecht, doi:10.1007/978-1-4020-9217-6_9, 2009.

Gorney, D. J., Y. T. Chiu, and D. R. Croley, Trapping of ion conics by downward parallel electric fields, *Journal of Geophysical Research*, *90*(A5), 4205–4210, doi:10.1029/JA090iA05p04205, 1985.

Grodent, D., A Brief Review of Ultraviolet Auroral Emissions on Giant Planets, *Space Science Reviews*, *187*(1-4), 23–50, doi:10.1007/s11214-014-0052-8, 2015.

Grodent, D., J. H. Waite, and J.-C. Gérard, A self-consistent model of the Jovian auroral thermal structure, *Journal of Geophysical Research: Space Physics*, *106*(A7), 12933–12952, doi:10.1029/2000JA900129, 2001.

Grodent, D., J.-C. Gérard, S. W. H. Cowley, E. J. Bunce, and J. T. Clarke, Variable morphology of Saturn's southern ultraviolet aurora, *Journal of Geophysical Research*, *110*(A07215), doi:10.1029/2004JA010983, 2005.

Grodent, D., A. Radioti, B. Bonfond, and J.-C. Gérard, On the origin of Saturn's outer auroral emission, *Journal of Geophysical Research: Space Physics*, *115*(A08219), doi:10.1029/2009JA014901, 2010.

Grodent, D., J. Gustin, J.-C. Gérard, A. Radioti, B. Bonfond, and W. R. Pryor, Small-scale structures in Saturn's ultraviolet aurora, *Journal of Geophysical Research: Space Physics*, *116*(A09225), doi:10.1029/2011JA016818, 2011.

Guo, R. L., Z. H. Yao, N. Sergis, Y. Wei, D. Mitchell, E. Roussos, B. Palmaerts, W. R. Dunn, A. Radioti, L. C. Ray, A. J. Coates, D. Grodent, C. S. Arridge, P. Kollmann, N. Krupp, J. H. Waite, M. K. Dougherty, J. L. Burch, and W. X. Wan, Reconnection Acceleration in Saturn's Dayside Magnetodisk: A Multicase Study with *Cassini*, *The Astrophysical Journal*, *868*(2), L23, doi:10.3847/2041-8213/aaedab, 2018a.

Guo, R. L., Z. H. Yao, Y. Wei, L. C. Ray, I. J. Rae, C. S. Arridge, A. J. Coates, P. A. Delamere, N. Sergis, P. Kollmann, D. Grodent, W. R. Dunn, J. H. Waite, J. L. Burch, Z. Y. Pu, B. Palmaerts, and M. K. Dougherty, Rotationally driven magnetic reconnection in Saturn's dayside, *Nature Astronomy*, *2*(8), 640–645, doi:10.1038/s41550-018-0461-9, 2018b.

Gurnett, D. A., Radio and Plasma Wave Observations at Saturn from Cassini's Approach and First Orbit, *Science*, *307*(5713), 1255–1259, doi:10.1126/science.1105356, 2005.

Gurnett, D. A., S. D. Shawhan, and R. R. Shaw, Auroral hiss, *Z* mode radiation, and auroral kilometric radiation in the polar magnetosphere: DE 1 observations, *Journal of Geophysical Research*, *88*(A1), 329, doi:10/fmx3dr, 1983.

Gurnett, D. A., R. L. Huff, J. D. Menietti, J. L. Burch, J. D. Winningham, and S. D. Shawhan, Correlated low-frequency electric and magnetic noise along the auroral field lines, *Journal of Geophysical Research*, *89*(A10), 8971, doi:10.1029/JA089iA10p08971, 1984.

Gurnett, D. A., W. S. Kurth, D. L. Kirchner, G. B. Hospodarsky, T. F. Averkamp, P. Zarka, A. Lecacheux, R. Manning, A. Roux, P. Canu, N. Cornilleau-Wehrlin, P. Galopeau, A. Meyer, R. Boström, G. Gustafsson, J.-E. Wahlund, L. Åhlen, H. O. Rucker, H. P. Ladreiter, W. Macher, L. J. C. Woolliscroft, H. Alleyne, M. L. Kaiser, M. D. Desch, W. M. Farrell, C. C. Harvey, P. Louarn, P. J. Kellogg, K. Goetz, and A. Pedersen, The Cassini Radio and Plasma Wave Investigation, *Space Science Reviews*, *114*(1-4), 395–463, doi:10.1007/s11214-004-1434-0, 2004.

Gurnett, D. A., A. Lecacheux, W. S. Kurth, A. M. Persoon, J. B. Groene, L. Lamy, P. Zarka, and J. F. Carbary, Discovery of a north-south asymmetry in Saturn's radio rotation period, *Geophysical Research Letters*, *36*(16), doi:10.1029/2009GL039621, 2009a.

Gurnett, D. A., A. M. Persoon, J. B. Groene, A. J. Kopf, G. B. Hospodarsky, and W. S. Kurth, A north-south difference in the rotation rate of auroral hiss at Saturn: Comparison to Saturn's kilometric radio emission, *Geophysical Research Letters*, *36*(L21108), doi:10.1029/2009GL040774, 2009b.

Gurnett, D. A., J. B. Groene, A. M. Persoon, J. D. Menietti, S.-Y. Ye, W. S. Kurth, R. J. MacDowall, and A. Lecacheux, The reversal of the rotational modulation rates of the north and south components of Saturn kilometric radiation near equinox, *Geophysical Research Letters*, *37*(L24101), doi:10.1029/2010GL045796, 2010.

Gustin, J., Energy-flux relationship in the FUV Jovian aurora deduced from HST-STIS spectral observations, *Journal of Geophysical Research*, *109*(A10205), doi:10.1029/2003JA010365, 2004.

Gustin, J., J.-C. Gérard, W. Pryor, P. Feldman, D. Grodent, and G. Holsclaw, Characteristics of Saturn's polar atmosphere and auroral electrons derived from HST/STIS, FUSE and Cassini/UVIS spectra, *Icarus*, *200*(1), 176–187, doi:10.1016/j.icarus.2008.11.013, 2009.

Gustin, J., B. Bonfond, D. Grodent, and J.-C. Gérard, Conversion from HST ACS and STIS auroral counts into brightness, precipitated power, and radiated power for H2 giant planets, *Journal of Geophysical Research: Space Physics*, *117*(A07316), doi:10.1029/2012JA017607, 2012.

Gustin, J., J.-C. Gérard, D. Grodent, G. Gladstone, J. Clarke, W. Pryor, V. Dols, B. Bonfond, A. Radioti, L. Lamy, and J. Ajello, Effects of methane on giant planet's UV emissions and implications for the auroral characteristics, *Journal of Molecular Spectroscopy*, *291*, 108–117, doi:10.1016/j.jms.2013.03.010, 2013.

Gustin, J., D. Grodent, L. Ray, B. Bonfond, E. Bunce, J. Nichols, and N. Ozak, Characteristics of north jovian aurora from STIS FUV spectral images, *Icarus*, *268*, 215–241, doi:10.1016/j.icarus.2015.12.048, 2016.

Gustin, J., D. Grodent, A. Radioti, W. Pryor, L. Lamy, and J. Ajello, Statistical study of Saturn's auroral electron properties with Cassini/UVIS FUV spectral images, *Icarus*, *284*, 264–283, doi:10.1016/j.icarus.2016.11.017, 2017.

Gérard, J.-C., and V. Singh, A model of energy deposition of energetic electrons and EUV emission in the Jovian and Saturnian atmospheres and implications, *Journal of Geophysical Research*, *87*(A6), 4525–4532, doi:10.1029/JA087iA06p04525, 1982.

Gérard, J.-C., D. C. Grodent, J. Gustin, A. Saglam, J. T. Clarke, and J. T. Trauger, Characteristics of Saturn's FUV aurora observed with the Space Telescope Imaging Spectrograph, *Journal of Geophysical Research*, *109*(A09207), doi:10.1029/2004JA010513, 2004.

Gérard, J.-C., E. J. Bunce, D. Grodent, S. W. H. Cowley, J. T. Clarke, and S. V. Badman, Signature of Saturn's auroral cusp: Simultaneous Hubble Space Telescope FUV observations and upstream solar wind monitoring, *Journal of Geophysical Research*, *110*(A11201), doi:10.1029/2005JA011094, 2005.

Gérard, J.-C., D. Grodent, S. W. H. Cowley, D. G. Mitchell, W. S. Kurth, J. T. Clarke, E. J. Bunce, J. D. Nichols, M. K. Dougherty, F. J. Crary, and A. J. Coates, Saturn's auroral morphology and activity during quiet magnetospheric conditions, *Journal of Geophysical Research*, *111*(A12210), doi:10.1029/2006JA011965, 2006.

Gérard, J.-C., B. Bonfond, J. Gustin, D. Grodent, J. T. Clarke, D. Bisikalo, and V. Shematovich, Altitude of Saturn's aurora and its implications for the characteristic energy of precipitated electrons, *Geophysical Research Letters*, *36*(L02202), doi:10.1029/2008GL036554, 2009.

Hamrin, M., P. Norqvist, and M. André, A statistical study of wave properties and electron density at 1700 km in the auroral region, *Journal of Geophysical Research: Space Physics*, *107*(A8), 1204, doi:10.1029/2001JA900144, 2002a.

Hamrin, M., P. Norqvist, T. Hellstrom, M. André, and A. I. Eriksson, A statistical study of ion energization at 1700 km in the auroral region, *Annales Geophysicae*, *20*, 1943–1958, doi:10.5194/angeo-20-1943-2002, 2002b.

Hansen, C. J., L. W. Esposito, A. I. F. Stewart, J. Colwell, A. Hendrix, W. R. Pryor, D. E. Shemansky, and R. West, Enceladus' Water Vapor Plume, *Science*, *311*(5766), 1422–1425, doi:10.1126/science.1121254, 2006.

Hansen, C. J., D. E. Shemansky, L. W. Esposito, A. I. F. Stewart, B. R. Lewis, J. E. Colwell, A. R. Hendrix, R. A. West, J. H. Waite, B. Teolis, and B. A. Magee, The composition and structure of the Enceladus plume, *Geophysical Research Letters*, *38*(L11202), doi:10.1029/2011GL047415, 2011.

Hedman, M. M., C. M. Gosmeyer, P. D. Nicholson, C. Sotin, R. H. Brown, R. N. Clark, K. H. Baines, B. J. Buratti, and M. R. Showalter, An observed correlation between plume activity and tidal stresses on Enceladus, *Nature*, *500*(7461), 182–184, doi:10.1038/nature12371, 2013.

Hedman, M. M., D. Dhingra, P. D. Nicholson, C. J. Hansen, G. Portyankina, S. Ye, and Y. Dong, Spatial variations in the dust-to-gas ratio of Enceladus' plume, *Icarus*, *305*, 123–138, doi:10.1016/j.icarus.2018.01.006, 2018.

Hill, T., Inertial limit on corotation, *Journal of Geophysical Research*, *84*(A11), 6554, doi:10.1029/JA084iA11p06554, 1979.

Hill, T. W., The Jovian auroral oval, *Journal of Geophysical Research: Space Physics*, *106*(A5), 8101–8107, doi:10.1029/2000JA000302, 2001.

Hill, T. W., A. M. Rymer, J. L. Burch, F. J. Crary, D. T. Young, M. F. Thomsen, D. Delapp, N. André, A. J. Coates, and G. R. Lewis, Evidence for rotationally driven plasma transport in Saturn's magnetosphere, *Geophysical Research Letters*, *32*(L14S10), doi:10.1029/2005GL022620, 2005.

Hunt, G. J., S. W. H. Cowley, G. Provan, E. J. Bunce, I. I. Alexeev, E. S. Belenkaya, V. V. Kalegaev, M. K. Dougherty, and A. J. Coates, Field-aligned currents in Saturn's southern nightside magnetosphere: Subcorotation and planetary period oscillation components, *Journal of Geophysical Research: Space Physics*, *119*(12), 9847–9899, doi:10.1002/2014JA020506, 2014.

Hunt, G. J., S. W. H. Cowley, G. Provan, E. J. Bunce, I. I. Alexeev, E. S. Belenkaya, V. V. Kalegaev, M. K. Dougherty, and A. J. Coates, Field-aligned currents in Saturn's northern nightside magnetosphere: Evidence for interhemispheric current flow associated with planetary period oscillations, *Journal of Geophysical Research: Space Physics*, *120*(9), 7552–7584, doi:10.1002/2015JA021454, 2015.

Hunt, G. J., S. W. H. Cowley, G. Provan, E. J. Bunce, I. I. Alexeev, E. S. Belenkaya, V. V. Kalegaev, M. K. Dougherty, and A. J. Coates, Field-aligned currents in Saturn's magnetosphere: Local time dependence of southern summer currents in the dawn sector between midnight and noon, *Journal of Geophysical Research: Space Physics*, *121*(8), 7785–7804, doi:10.1002/2016JA022712, 2016.

Hunt, G. J., G. Provan, E. J. Bunce, S. W. H. Cowley, M. K. Dougherty, and D. J. Southwood, Field-Aligned Currents in Saturn's Magnetosphere: Observations From the F-Ring Orbits, *Journal of Geophysical Research: Space Physics*, *123*(5), 3806–3821, doi:10/gdtcd5, 2018a.

Hunt, G. J., G. Provan, S. W. H. Cowley, M. K. Dougherty, and D. J. Southwood, Saturn's Planetary Period Oscillations During the Closest Approach of Cassini's Ring-Grazing Orbits, *Geophysical Research Letters*, *45*(10), 4692–4700, doi:10/gdjzb4, 2018b.

Hunten, D. M., F. E. Roach, and J. W. Chamberlain, A photometric unit for the airglow and aurora, *Journal of Atmospheric and Terrestrial Physics*, *8*, 345–346, doi:10.1016/0021-9169(56)90111-8, 1956.

Hwang, K.-J., K. A. Lynch, D. L. Newman, and C. W. Carlson, FAST observations of downward current regions: Effect of ionospheric constraints on parallel signatures, *Journal of Geophysical Research: Space Physics*, *114*(A02219), doi:10.1029/2008JA013080, 2009a.

Hwang, K.-J., K. A. Lynch, D. L. Newman, and C. W. Carlson, FAST observations of downward current regions: Effect of magnetospheric conditions on the parallel potential drop, *Journal of Geophysical Research: Space Physics*, *114*(A02218), doi:10.1029/2008JA013079, 2009b.

Ingersoll, A. P., and S. P. Ewald, Total particulate mass in Enceladus plumes and mass of Saturn's E ring inferred from Cassini ISS images, *Icarus*, *216*(2), 492–506, doi:10.1016/j.icarus.2011.09.018, 2011.

Isbell, J., A. J. Dessler, and J. H. Waite, Magnetospheric energization by interaction between planetary spin and the solar wind, *Journal of Geophysical Research*, *89*(A12), 10716, doi:10.1029/JA089iA12p10716, 1984.

Jackman, C. M., Interplanetary magnetic field at ~9 AU during the declining phase of the solar cycle and its implications for Saturn's magnetospheric dynamics, *Journal of Geophysical Research*, *109*(A11203), doi:10.1029/2004JA010614, 2004.

Jackman, C. M., and S. W. H. Cowley, A model of the plasma flow and current in Saturn's polar ionosphere under conditions of strong Dungey cycle driving, *Annales Geophysicae*, *24*(3), 1029–1055, doi:10.5194/angeo-24-1029-2006, 2006.

Jackman, C. M., C. T. Russell, D. J. Southwood, C. S. Arridge, N. Achilleos, and M. K. Dougherty, Strong rapid dipolarizations in Saturn's magnetotail: In situ evidence of reconnection, *Geophysical Research Letters*, *34*(L11203), doi:10.1029/2007GL029764, 2007.

Jackman, C. M., C. S. Arridge, N. Krupp, E. J. Bunce, D. G. Mitchell, H. J. McAndrews, M. K. Dougherty, C. T. Russell, N. Achilleos, G. H. Jones, and A. J. Coates, A multi-instrument view of tail reconnection at Saturn, *Journal of Geophysical Research: Space Physics*, *113*(A11213), doi:10.1029/2008JA013592, 2008a.

Jackman, C. M., R. J. Forsyth, and M. K. Dougherty, The overall configuration of the interplanetary magnetic field upstream of Saturn as revealed by Cassini observations, *Journal of Geophysical Research: Space Physics*, *113*(A08114), doi:10.1029/2008JA013083, 2008b.

Jackman, C. M., C. S. Arridge, J. A. Slavin, S. E. Milan, L. Lamy, M. K. Dougherty, and A. J. Coates, In situ observations of the effect of a solar wind compression on Saturn's magnetotail, *Journal of Geophysical Research: Space Physics*, *115*(A10240), doi:10.1029/2010JA015312, 2010.

Jackman, C. M., J. A. Slavin, and S. W. H. Cowley, Cassini observations of plasmoid structure and dynamics: Implications for the role of magnetic reconnection in magnetospheric circulation at Saturn, *Journal of Geophysical Research: Space Physics*, *116*(A10212), doi:10.1029/2011JA016682, 2011.

Jackman, C. M., N. Achilleos, S. W. Cowley, E. J. Bunce, A. Radioti, D. Grodent, S. V. Badman, M. K. Dougherty, and W. Pryor, Auroral counterpart of magnetic field dipolarizations in Saturn's tail, *Planetary and Space Science*, *82-83*, 34–42, doi:10.1016/j.pss.2013.03.010, 2013.

Jackman, C. M., G. Provan, and S. W. H. Cowley, Reconnection events in Saturn's magnetotail: Dependence of plasmoid occurrence on planetary period oscillation phase, *Journal of Geophysical Research: Space Physics*, *121*(4), 2922–2934, doi:10.1002/2015JA021985, 2016.

Jasinski, J. M., C. S. Arridge, L. Lamy, J. S. Leisner, M. F. Thomsen, D. G. Mitchell, A. J. Coates, A. Radioti, G. H. Jones, E. Roussos, N. Krupp, D. Grodent, M. K. Dougherty, and J. H. Waite, Cusp observation at Saturn's high-latitude magnetosphere by the Cassini spacecraft, *Geophysical Research Letters*, *41*(5), 1382–1388, doi:10.1002/2014GL059319, 2014.

Jasinski, J. M., C. S. Arridge, A. Bader, A. W. Smith, M. Felici, J. Kinrade, A. J. Coates, G. H. Jones, T. A. Nordheim, L. Gilbert, A. R. Azari, S. V. Badman, G. Provan, N. Sergis, and N. Murphy, Saturn's Open-Closed Field Line Boundary: A Cassini Electron Survey at Saturn's Magnetosphere, *Journal of Geophysical Research: Space Physics*, *124*(12), 10018–10035, doi:10.1029/2019JA027090, 2019.

Jia, X., and M. G. Kivelson, Driving Saturn's magnetospheric periodicities from the upper atmosphere/ionosphere: Magnetotail response to dual sources, *Journal of Geophysical Research: Space Physics*, *117*(A11219), doi:10.1029/2012JA018183, 2012.

Jia, X., M. G. Kivelson, and T. I. Gombosi, Driving Saturn's magnetospheric periodicities from the upper atmosphere/ionosphere, *Journal of Geophysical Research: Space Physics*, *117*(A04215), doi:10.1029/2011JA017367, 2012.

Johnson, R. E., H. T. Smith, O. J. Tucker, M. Liu, M. H. Burger, E. C. Sittler, and R. L. Tokar, The Enceladus and OH Tori at Saturn, *The Astrophysical Journal*, *644*(2), L137–L139, doi:10.1086/505750, 2006.

Jurac, S., and J. D. Richardson, A self-consistent model of plasma and neutrals at Saturn: Neutral cloud morphology, *Journal of Geophysical Research: Space Physics*, *110*(A09220), doi:10.1029/2004JA010635, 2005.

Kaminker, V., P. A. Delamere, C. S. Ng, T. Dennis, A. Otto, and X. Ma, Local time dependence of turbulent magnetic fields in Saturn's magnetodisc, *Journal of Geophysical Research: Space Physics*, *122*(4), 3972–3984, doi:10.1002/2016JA023834, 2017.

Kaufmann, R. L., and P. M. Kintner, Upgoing ion beams: 1. Microscopic analysis, *Journal of Geophysical Research*, *87*(A12), 10487, doi:10.1029/JA087iA12p10487, 1982.

Kellett, S., C. S. Arridge, E. J. Bunce, A. J. Coates, S. W. H. Cowley, M. K. Dougherty, A. M. Persoon, N. Sergis, and R. J. Wilson, Nature of the ring current in Saturn's dayside magnetosphere, *Journal of Geophysical Research: Space Physics*, *115*(A08201), doi:10.1029/2009JA015146, 2010.

Kellett, S., C. S. Arridge, E. J. Bunce, A. J. Coates, S. W. H. Cowley, M. K. Dougherty, A. M. Persoon, N. Sergis, and R. J. Wilson, Saturn's ring current: Local time dependence and temporal variability, *Journal of Geophysical Research: Space Physics*, *116*(A05220), doi:10.1029/2010JA016216, 2011.

Kennelly, T. J., J. S. Leisner, G. B. Hospodarsky, and D. A. Gurnett, Ordering of injection events within Saturnian SLS longitude and local time, *Journal of Geophysical Research: Space Physics*, *118*(2), 832–838, doi:10.1002/jgra.50152, 2013.

Kidder, A., C. S. Paty, R. M. Winglee, and E. M. Harnett, External triggering of plasmoid development at Saturn, *Journal of Geophysical Research: Space Physics*, *117*(A07206), doi:10.1029/2012JA017625, 2012.

Kindel, J. M., and C. F. Kennel, Topside current instabilities, *Journal of Geophysical Research*, *76*(13), 3055–3078, doi:10.1029/JA076i013p03055, 1971.

Kinrade, J., S. V. Badman, E. J. Bunce, C. Tao, G. Provan, S. W. H. Cowley, A. Grocott, R. L. Gray, D. Grodent, T. Kimura, J. D. Nichols, C. S. Arridge, A. Radioti, J. T. Clarke, F. J. Crary, W. R. Pryor, H. Melin, K. H. Baines, and M. K. Dougherty, An isolated, bright cusp aurora at Saturn, *Journal of Geophysical Research: Space Physics*, *122*(6), 6121–6138, doi:10.1002/2016JA023792, 2017.

Kinrade, J., S. V. Badman, G. Provan, S. W. H. Cowley, L. Lamy, and A. Bader, Saturn's Northern Auroras and Their Modulation by Rotating Current Systems During Late Northern Spring in Early 2014, *Journal of Geophysical Research: Space Physics*, *123*(8), 6289–6306, doi:10.1029/2018JA025426, 2018.

Kinrade, J., S. V. Badman, C. Paranicas, D. G. Mitchell, C. S. Arridge, R. L. Gray, A. Bader, G. Provan, S. W. H. Cowley, C. J. Martin, and N. Achilleos, Tracking Counterpart Signatures in Saturn's Auroras and ENA Imagery During Large-Scale Plasma Injection Events, *Journal of Geophysical Research: Space Physics*, *125*(2), e2019JA027542, doi:10.1029/2019JA027542, 2020.

Kintner, P. M., M. C. Kelley, R. D. Sharp, A. G. Ghielmetti, M. Temerin, C. Cattell, P. F. Mizera, and J. F. Fennell, Simultaneous observations of energetic (keV) upstreaming and electrostatic hydrogen cyclotron waves, *Journal of Geophysical Research*, *84*(A12), 7201–7212, doi:10.1029/JA084iA12p07201, 1979.

Kintner, P. M., J. Vago, S. Chesney, R. L. Arnoldy, K. A. Lynch, C. J. Pollock, and T. E. Moore, Localized lower hybrid acceleration of ionospheric plasma, *Physical Review Letters*, *68*(16), 2448–2451, doi:10.1103/PhysRevLett.68.2448, 1992.

Kivelson, M., Moon–magnetosphere interactions: a tutorial, *Advances in Space Research*, *33*(11), 2061–2077, doi:10.1016/j.asr.2003.08.042, 2004.

Kivelson, M. G., and X. Jia, Control of periodic variations in Saturn's magnetosphere by compressional waves, *Journal of Geophysical Research: Space Physics*, *119*(10), 8030–8045, doi:10.1002/2014JA020258, 2014.

Kivelson, M. G., and D. J. Southwood, Dynamical consequences of two modes of centrifugal instability in Jupiter's outer magnetosphere, *Journal of Geophysical Research*, *110*(A12209), doi:10.1029/2005JA011176, 2005.

Kleindienst, G., K.-H. Glassmeier, S. Simon, M. K. Dougherty, and N. Krupp, Quasiperiodic ULF-pulsations in Saturn's magnetosphere, *Annales Geophysicae*, *27*(2), 885–894, doi:10.5194/angeo-27-885-2009, 2009.

Kliore, A. J., J. D. Anderson, J. W. Armstrong, S. W. Asmar, C. L. Hamilton, N. J. Rappaport, H. D. Wahlquist, R. Ambrosini, F. M. Flasar, R. G. French, L. Iess, E. A. Marouf, and A. F. Nagy, Cassini Radio Science, *Space Science Reviews*, *115*(1-4), 1–70, doi:10.1007/s11214-004-1436-y, 2004.

Klumpar, D. M., Transversely accelerated ions: An ionospheric source of hot magnetospheric ions, *Journal of Geophysical Research: Space Physics*, *84*(A8), 4229–4237, doi:10.1029/JA084iA08p04229, 1979.

Knight, S., Parallel electric fields, *Planetary and Space Science*, *21*(5), 741–750, doi:10.1016/0032-0633(73)90093-7, 1973.

Kollmann, P., E. Roussos, C. Paranicas, N. Krupp, and D. Haggerty, Processes forming and sustaining Saturn's proton radiation belts, *Icarus*, *222*(1), 323–341, doi:10.1016/j.icarus.2012.10.033, 2013.

Kopf, A. J., D. A. Gurnett, J. D. Menietti, P. Schippers, C. S. Arridge, G. B. Hospodarsky, W. S. Kurth, S. Grimald, N. André, A. J. Coates, and M. K. Dougherty, Electron beams as the source of whistler-mode auroral hiss at Saturn, *Geophysical Research Letters*, *37*(L09102), doi:10.1029/2010GL042980, 2010.

Kotsiaros, S., J. E. P. Connerney, G. Clark, F. Allegrini, G. R. Gladstone, W. S. Kurth, B. H. Mauk, J. Saur, E. J. Bunce, D. J. Gershman, Y. M. Martos, T. K. Greathouse, S. J. Bolton, and S. M. Levin, Birkeland currents in Jupiter's magnetosphere observed by the polar-orbiting Juno spacecraft, *Nature Astronomy*, doi:10.1038/s41550-019-0819-7, 2019.

Krimigis, S. M., J. F. Carbary, E. P. Keath, T. P. Armstrong, L. J. Lanzerotti, and G. Gloeckler, General characteristics of hot plasma and energetic particles in the Saturnian magnetosphere: Results from the Voyager spacecraft, *Journal of Geophysical Research: Space Physics*, *88*(A11), 8871–8892, doi:10.1029/JA088iA11p08871, 1983.

Krimigis, S. M., D. G. Mitchell, D. C. Hamilton, S. Livi, J. Dandouras, S. Jaskulek, T. P. Armstrong, J. D. Boldt, A. F. Cheng, G. Gloeckler, J. R. Hayes, K. C. Hsieh, W.-H. Ip, E. P. Keath, E. Kirsch, N. Krupp, L. J. Lanzerotti, R. Lundgren, B. H. Mauk, R. W. McEntire, E. C. Roelof, C. E. Schlemm, B. E. Tossman, B. Wilken, and D. J. Williams, Magnetosphere Imaging Instrument (MIMI) on the Cassini Mission to Saturn/Titan, *Space Science Reviews*, *114*(1-4), 233–329, doi:10.1007/s11214-004-1410-8, 2004.

Krimigis, S. M., N. Sergis, D. G. Mitchell, D. C. Hamilton, and N. Krupp, A dynamic, rotating ring current around Saturn, *Nature*, *450*(7172), 1050–1053, doi:10.1038/nature06425, 2007.

Krimigis, S. M., R. B. Decker, E. C. Roelof, M. E. Hill, C. O. Bostrom, K. Dialynas, G. Gloeckler, D. C. Hamilton, E. P. Keath, and L. J. Lanzerotti, Energetic charged particle measurements from Voyager 2 at the heliopause and beyond, *Nature Astronomy*, doi:10.1038/s41550-019-0927-4, 2019.

Krupp, N., E. Roussos, A. Lagg, J. Woch, A. Müller, S. Krimigis, D. Mitchell, E. Roelof, C. Paranicas, J. Carbary, G. Jones, D. Hamilton, S. Livi, T. Armstrong, M. Dougherty, and N. Sergis, Energetic particles in Saturn's magnetosphere during the Cassini nominal mission (July 2004–July 2008), *Planetary and Space Science*, *57*(14-15), 1754–1768, doi:10.1016/j.pss.2009.06.010, 2009.

Krupp, N., P. Kollmann, D. G. Mitchell, M. Thomsen, X. Jia, A. Masters, and P. Zarka, Global Configuration and Seasonal Variations of Saturn's Magnetosphere, in *Saturn in the 21st Century*, edited by K. H. Baines, F. M. Flasar, N. Krupp, and T. Stallard, 1 ed., pp. 126–165, Cambridge University Press, doi:10.1017/9781316227220.006, 2018.

Kurth, W. S., T. F. Averkamp, D. A. Gurnett, J. B. Groene, and A. Lecacheux, An update to a Saturnian longitude system based on kilometric radio emissions, *Journal of Geophysical Research: Space Physics*, *113*(A05222), doi:10.1029/2007JA012861, 2008.

Kurth, W. S., G. B. Hospodarsky, D. A. Gurnett, L. Lamy, M. K. Dougherty, J. Nichols, E. J. Bunce, W. Pryor, K. Baines, T. Stallard, H. Melin, and F. J. Crary, Saturn kilometric radiation intensities during the Saturn auroral campaign of 2013, *Icarus*, *263*, 2–9, doi:10.1016/j.icarus.2015.01.003, 2016.

Lallo, M. D., Experience with the Hubble Space Telescope: 20 years of an archetype, *Optical Engineering*, *51*(1), 011011, doi:10.1117/1.OE.51.1.011011, 2012.

Lamy, L., Variability of southern and northern periodicities of Saturn Kilometric Radiation, in *Planetary Radio Emissions VII*, edited by H. O. Rucker, W. S. Kurth, P. Louarn, and G. Fischer, pp. 39–50, Austrian Academy of Sciences Press, Vienna, 2011.

Lamy, L., P. Zarka, B. Cecconi, R. Prangé, W. S. Kurth, and D. A. Gurnett, Saturn kilometric radiation: Average and statistical properties, *Journal of Geophysical Research: Space Physics*, *113*(A07201), doi:10.1029/2007JA012900, 2008.

Lamy, L., B. Cecconi, R. Prangé, P. Zarka, J. D. Nichols, and J. T. Clarke, An auroral oval at the footprint of Saturn's kilometric radio sources, colocated with the UV aurorae, *Journal of Geophysical Research: Space Physics*, *114*(A10212), doi:10.1029/2009JA014401, 2009.

Lamy, L., B. Cecconi, P. Zarka, P. Canu, P. Schippers, W. S. Kurth, R. L. Mutel, D. A. Gurnett, D. Menietti, and P. Louarn, Emission and propagation of Saturn kilometric radiation: Magnetoionic modes, beaming pattern, and polarization state, *Journal of Geophysical Research: Space Physics*, *116*(A04212), doi:10.1029/2010JA016195, 2011.

Lamy, L., R. Prangé, W. Pryor, J. Gustin, S. V. Badman, H. Melin, T. Stallard, D. Mitchell, and P. C. Brandt, Multispectral simultaneous diagnosis of Saturn's aurorae throughout a planetary rotation, *Journal of Geophysical Research: Space Physics*, *118*(8), 4817–4843, doi:10.1002/jgra.50404, 2013.

Lamy, L., R. Prangé, C. Tao, T. Kim, S. V. Badman, P. Zarka, B. Cecconi, W. S. Kurth, W. Pryor, E. Bunce, and A. Radioti, Saturn's Northern Aurorae at Solstice From HST Observations Coordinated With Cassini's Grand Finale, *Geophysical Research Letters*, *45*(18), 9353–9362, doi:10.1029/2018GL078211, 2018a.

Lamy, L., P. Zarka, B. Cecconi, R. Prangé, W. S. Kurth, G. Hospodarsky, A. Persoon, M. Morooka, J.-E. Wahlund, and G. J. Hunt, The low-frequency source of Saturn's kilometric radiation, *Science*, *362*(6410), eaat2027, doi:10.1126/science.aat2027, 2018b.

Le Quéau, D., A. Roux, J. L. Rauch, F. Lefeuvre, and J. M. Bosqued, Heating of protons by resonant absorption in a multicomponent plasma: 2. Theoretical model, *Journal of Geophysical Research: Space Physics*, *98*(A8), 13363–13375, doi:10.1029/91JA02186, 1993.

Livi, R., J. Goldstein, J. L. Burch, F. Crary, A. M. Rymer, D. G. Mitchell, and A. M. Persoon, Multi-instrument analysis of plasma parameters in Saturn's equatorial, inner magnetosphere using corrections for corrections for spacecraft potential and penetrating background radiation, *Journal of Geophysical Research: Space Physics*, *119*(5), 3683–3707, doi:10.1002/2013JA019616, 2014.

Louarn, P., F. Allegrini, D. J. McComas, P. W. Valek, W. S. Kurth, N. André, F. Bagenal, S. Bolton, J. Connerney, R. W. Ebert, M. Imai, S. Levin, J. R. Szalay, S. Weidner, R. J. Wilson, and J. L. Zink, Generation of the Jovian hectometric radiation: First lessons from Juno: Juno Observations in a HOM Radio Source, *Geophysical Research Letters*, *44*(10), 4439–4446, doi:10.1002/2017GL072923, 2017.

Lundin, R., and I. Sandahl, Some characteristics of the parallel electric field acceleration of electrons over discrete auroral arcs as observed from two rocket flights, *ESA SP-135*, p. 125, 1978.

Lyons, L., Generation of large-scale regions of auroral currents, electric potentials, and precipitation by the divergence of the convection electric field, *Journal of Geophysical Research: Space Physics*, *85*(A1), 17–24, doi:10.1029/JA085iA01p00017, 1980.

Maggs, J. E., Coherent Generation of VLF Hiss, *Journal of Geophysical Research*, *81*(10), 1707–1724, doi:10/bps6f8, 1976.

Marklund, G. T., N. Ivchenko, T. Karlsson, A. Fazakerley, and M. Dunlop, Temporal evolution of the electric field accelerating electrons away from the auroral ionosphere, *Nature*, *414*, 724–727, doi:10.1038/414724a, 2001.

Martin, C. J., and C. S. Arridge, Current Density in Saturn's Equatorial Current Sheet: Cassini Magnetometer Observations, *Journal of Geophysical Research: Space Physics*, *124*(1), 279–292, doi:10.1029/2018JA025970, 2019.

Masters, A., N. Achilleos, C. Bertucci, M. Dougherty, S. Kanani, C. Arridge, H. McAndrews, and A. Coates, Surface waves on Saturn's dawn flank magnetopause driven by the Kelvin–Helmholtz instability, *Planetary and Space Science*, *57*(14-15), 1769–1778, doi:10.1016/j.pss.2009.02.010, 2009.

Masters, A., J. P. Eastwood, M. Swisdak, M. F. Thomsen, C. T. Russell, N. Sergis, F. J. Crary, M. K. Dougherty, A. J. Coates, and S. M. Krimigis, The importance of plasma β conditions for magnetic reconnection at Saturn's magnetopause, *Geophysical Research Letters*, *39*(L08103), doi:10.1029/2012GL051372, 2012.

Masters, A., M. Fujimoto, H. Hasegawa, C. T. Russell, A. J. Coates, and M. K. Dougherty, Can magnetopause reconnection drive Saturn's magnetosphere?, *Geophysical Research Letters*, *41*(6), 1862–1868, doi:10.1002/2014GL059288, 2014.

Mauk, B. H., J. Saur, D. G. Mitchell, E. C. Roelof, P. C. Brandt, T. P. Armstrong, D. C. Hamilton, S. M. Krimigis, N. Krupp, S. A. Livi, J. W. Manweiler, and C. P. Paranicas, Energetic particle injections in Saturn's magnetosphere, *Geophysical Research Letters*, *32*(L14S05), doi:10.1029/2005GL022485, 2005.

Mauk, B. H., D. K. Haggerty, C. Paranicas, G. Clark, P. Kollmann, A. M. Rymer, S. J. Bolton, S. M. Levin, A. Adriani, F. Allegrini, F. Bagenal, B. Bonfond, J. E. P. Connerney, G. R. Gladstone, W. S. Kurth, D. J. McComas, and P. Valek, Discrete and broadband electron acceleration in Jupiter's powerful aurora, *Nature*, *549*(7670), 66–69, doi:10.1038/nature23648, 2017a.

Mauk, B. H., D. K. Haggerty, C. Paranicas, G. Clark, P. Kollmann, A. M. Rymer, D. G. Mitchell, S. J. Bolton, S. M. Levin, A. Adriani, F. Allegrini, F. Bagenal, J. E. P. Connerney,

G. R. Gladstone, W. S. Kurth, D. J. McComas, D. Ranquist, J. R. Szalay, and P. Valek, Juno observations of energetic charged particles over Jupiter's polar regions: Analysis of monodirectional and bidirectional electron beams, *Geophysical Research Letters*, *44*(10), 4410–4418, doi:10.1002/2016GL072286, 2017b.

Mauk, B. H., D. K. Haggerty, C. Paranicas, G. Clark, P. Kollmann, A. M. Rymer, J. M. Peachey, S. J. Bolton, S. M. Levin, A. Adriani, F. Allegrini, F. Bagenal, B. Bonfond, J. E. P. Connerney, R. W. Ebert, G. R. Gladstone, W. S. Kurth, D. J. McComas, D. Ranquist, and P. Valek, Diverse Electron and Ion Acceleration Characteristics Observed Over Jupiter's Main Aurora, *Geophysical Research Letters*, *45*(3), 1277–1285, doi:10.1002/2017GL076901, 2018.

McAndrews, H., M. Thomsen, C. Arridge, C. Jackman, R. Wilson, M. Henderson, R. Tokar, K. Khurana, E. Sittler, A. Coates, and M. Dougherty, Plasma in Saturn's nightside magnetosphere and the implications for global circulation, *Planetary and Space Science*, *57*(14-15), 1714–1722, doi:10.1016/j.pss.2009.03.003, 2009.

McFadden, J. P., C. W. Carlson, and R. E. Ergun, Microstructure of the auroral acceleration region as observed by FAST, *Journal of Geophysical Research: Space Physics*, *104*(A7), 14453–14480, doi:10.1029/1998JA900167, 1999.

McIlwain, C. E., Direct measurement of particles producing visible auroras, *Journal of Geophysical Research*, *65*(9), 2727–2747, doi:10.1029/JZ065i009p02727, 1960.

Melin, H., T. Stallard, S. Miller, J. Gustin, M. Galand, S. V. Badman, W. R. Pryor, J. O'Donoghue, R. H. Brown, and K. H. Baines, Simultaneous Cassini VIMS and UVIS observations of Saturn's southern aurora: Comparing emissions from H, H_2 and H_3^+ at a high spatial resolution, *Geophysical Research Letters*, *38*(L15203), doi:10.1029/2011GL048457, 2011.

Melin, H., S. Badman, T. Stallard, S. Cowley, U. Dyudina, J. Nichols, G. Provan, J. O'Donoghue, W. Pryor, K. Baines, S. Miller, J. Gustin, A. Radioti, C. Tao, C. Meredith, J. Blake, and R. Johnson, Simultaneous multi-scale and multi-instrument observations of Saturn's aurorae during the 2013 observing campaign, *Icarus*, *263*, 56–74, doi:10.1016/j.icarus.2015.08.021, 2016.

Menietti, J. D., R. L. Mutel, P. Schippers, S.-Y. Ye, D. A. Gurnett, and L. Lamy, Analysis of Saturn kilometric radiation near a source center, *Journal of Geophysical Research: Space Physics*, *116*(A12222), doi:10.1029/2011JA017056, 2011a.

Menietti, J. D., P. Schippers, O. Santolík, D. A. Gurnett, F. Crary, and A. J. Coates, Ion cyclotron harmonics in the Saturn downward current auroral region, *Journal of Geophysical Research: Space Physics*, *116*(A12234), doi:10.1029/2011JA017102, 2011b.

Meredith, C. J., S. W. H. Cowley, K. C. Hansen, J. D. Nichols, and T. K. Yeoman, Simultaneous conjugate observations of small-scale structures in Saturn's dayside ultraviolet auroras: Implications for physical origins, *Journal of Geophysical Research: Space Physics*, *118*(5), 2244–2266, doi:10.1002/jgra.50270, 2013.

Meredith, C. J., I. I. Alexeev, S. V. Badman, E. S. Belenkaya, S. W. H. Cowley, M. K. Dougherty, V. V. Kalegaev, G. R. Lewis, and J. D. Nichols, Saturn's dayside ultraviolet auroras: Evidence for morphological dependence on the direction of the upstream interplanetary magnetic field, *Journal of Geophysical Research: Space Physics*, *119*(3), 1994–2008, doi:10.1002/2013JA019598, 2014a.

Meredith, C. J., S. W. H. Cowley, and J. D. Nichols, Survey of Saturn auroral storms observed by the Hubble Space Telescope: Implications for storm time scales, *Journal of Geophysical Research: Space Physics*, *119*(12), 9624–9642, doi:10.1002/2014JA020601, 2014b.

Milan, S. E., M. Lester, S. W. H. Cowley, and M. Brittnacher, Dayside convection and auroral morphology during an interval of northward interplanetary magnetic field, *Annales Geophysicae*, *18*(4), 436–444, doi:10.1007/s00585-000-0436-9, 2000.

Milan, S. E., M. Lester, S. W. H. Cowley, K. Oksavik, M. Brittnacher, R. A. Greenwald, G. Sofko, and J.-P. Villain, Variations in the polar cap area during two substorm cycles, *Annales Geophysicae*, *21*(5), 1121–1140, doi:10.5194/angeo-21-1121-2003, 2003.

Milan, S. E., E. J. Bunce, S. W. H. Cowley, and C. M. Jackman, Implications of rapid planetary rotation for the Dungey magnetotail of Saturn, *Journal of Geophysical Research*, *110*(A03209), doi:10.1029/2004JA010716, 2005.

Miller, S., T. Stallard, J. Tennyson, and H. Melin, Cooling by $H_3{}^+$ Emission, *The Journal of Physical Chemistry A*, *117*(39), 9770–9777, doi:10.1021/jp312468b, 2013.

Mitchell, C. J., C. C. Porco, and J. W. Weiss, Tracking the geysers of Enceladus into Saturn's E-ring, *The Astronomical Journal*, *149*(5), 156, doi:10.1088/0004-6256/149/5/156, 2015a.

Mitchell, D. G., S. M. Krimigis, C. Paranicas, P. C. Brandt, J. F. Carbary, E. C. Roelof, W. S. Kurth, D. A. Gurnett, J. T. Clarke, J. D. Nichols, J.-C. Gérard, D. C. Grodent, M. K. Dougherty, and W. R. Pryor, Recurrent energization of plasma in the midnight-to-dawn quadrant of Saturn's magnetosphere, and its relationship to auroral UV and radio emissions, *Planetary and Space Science*, *57*(14-15), 1732–1742, doi:10.1016/j.pss.2009.04.002, 2009a.

Mitchell, D. G., W. S. Kurth, G. B. Hospodarsky, N. Krupp, J. Saur, B. H. Mauk, J. F. Carbary, S. M. Krimigis, M. K. Dougherty, and D. C. Hamilton, Ion conics and electron beams associated with auroral processes on Saturn, *Journal of Geophysical Research: Space Physics*, *114*(A02212), doi:10.1029/2008JA013621, 2009b.

Mitchell, D. G., P. C. Brandt, J. F. Carbary, W. S. Kurth, S. M. Krimigis, C. Paranicas, N. Krupp, D. C. Hamilton, B. H. Mauk, G. B. Hospodarsky, M. K. Dougherty, and W. R. Pryor, Injection, Interchange, and Reconnection: Energetic Particle Observations in Saturn's Magnetosphere, in *Magnetotails in the Solar System*, edited by A. Keiling, C. M. Jackman, and P. A. Delamere, no. 207 in Geophysical Monograph Series, pp. 327–343, John Wiley & Sons, Inc, Hoboken, NJ, doi:10.1002/9781118842324.ch19, 2015b.

Mitchell, D. G., J. F. Carbary, E. J. Bunce, A. Radioti, S. V. Badman, W. R. Pryor, G. B. Hospodarsky, and W. S. Kurth, Recurrent pulsations in Saturn's high latitude magnetosphere, *Icarus*, *263*, 94–100, doi:10.1016/j.icarus.2014.10.028, 2016.

Ness, N. F., M. H. Acuña, R. P. Lepping, J. E. P. Connerney, K. W. Behannon, L. F. Burlaga, and F. M. Neubauer, Magnetic Field Studies by Voyager 1: Preliminary Results at Saturn, *Science*, *212*(4491), 211–217, doi:10.1126/science.212.4491.211, 1981.

Ness, N. F., M. H. Acuña, K. W. Behannon, L. F. Burlaga, J. E. P. Connerney, R. P. Lepping, and F. M. Neubauer, Magnetic Field Studies by Voyager 2: Preliminary Results at Saturn, *Science*, *215*(4532), 558–563, doi:10.1126/science.215.4532.558, 1982.

Nichols, J. D., J. T. Clarke, S. W. H. Cowley, J. Duval, A. J. Farmer, J.-C. Gérard, D. Grodent, and S. Wannawichian, Oscillation of Saturn's southern auroral oval, *Journal of Geophysical Research: Space Physics*, *113*(A11205), doi:10.1029/2008JA013444, 2008.

Nichols, J. D., B. Cecconi, J. T. Clarke, S. W. H. Cowley, J.-C. Gérard, A. Grocott, D. Grodent, L. Lamy, and P. Zarka, Variation of Saturn's UV aurora with SKR phase, *Geophysical Research Letters*, *37*(L15102), doi:10.1029/2010GL044057, 2010a.

Nichols, J. D., S. W. H. Cowley, and L. Lamy, Dawn-dusk oscillation of Saturn's conjugate auroral ovals, *Geophysical Research Letters*, *37*(L24101), doi:10.1029/2010GL045818, 2010b.

Nichols, J. D., S. V.Badman, K. H. Baines, R. H. Brown, E. J. Bunce, J. T. Clarke, S. W. H. Cowley, F. J. Crary, M. K. Dougherty, J.-C. Gérard, A. Grocott, D. Grodent, W. S. Kurth, H. Melin, D. G. Mitchell, W. R. Pryor, and T. S. Stallard, Dynamic auroral storms on Saturn as observed by the Hubble Space Telescope, *Geophysical Research Letters*, *41*(10), 3323–3330, doi:10.1002/2014GL060186, 2014.

Nichols, J. D., S. V. Badman, E. J. Bunce, J. T. Clarke, S. W. H. Cowley, G. J. Hunt, and G. Provan, Saturn's northern auroras as observed using the Hubble Space Telescope, *Icarus*, *263*, 17–31, doi:10.1016/j.icarus.2015.09.008, 2016.

Nichols, J. D., S. V. Badman, F. Bagenal, S. J. Bolton, B. Bonfond, E. J. Bunce, J. T. Clarke, J. E. P. Connerney, S. W. H. Cowley, R. W. Ebert, M. Fujimoto, J.-C. Gérard, G. R. Gladstone, D. Grodent, T. Kimura, W. S. Kurth, B. H. Mauk, G. Murakami, D. J. McComas, G. S. Orton, A. Radioti, T. S. Stallard, C. Tao, P. W. Valek, R. J.

Wilson, A. Yamazaki, and I. Yoshikawa, Response of Jupiter's auroras to conditions in the interplanetary medium as measured by the Hubble Space Telescope and Juno, *Geophysical Research Letters*, *44*(15), 7643–7652, doi:10.1002/2017GL073029, 2017.

Okuda, H., and M. Ashour-Abdalla, Formation of a conical distribution and intense ion heating in the presence of hydrogen cyclotron waves, *Geophysical Research Letters*, *8*(7), 811–814, doi:10.1029/GL008i007p00811, 1981.

Palmaerts, B., A. Radioti, E. Roussos, D. Grodent, J.-C. Gérard, N. Krupp, and D. G. Mitchell, Pulsations of the polar cusp aurora at Saturn, *Journal of Geophysical Research: Space Physics*, *121*(12), 11,952–11,963, doi:10.1002/2016JA023497, 2016a.

Palmaerts, B., E. Roussos, N. Krupp, W. Kurth, D. Mitchell, and J. Yates, Statistical analysis and multi-instrument overview of the quasi-periodic 1-hour pulsations in Saturn's outer magnetosphere, *Icarus*, *271*, 1–18, doi:10.1016/j.icarus.2016.01.025, 2016b.

Palmaerts, B., A. Radioti, D. Grodent, Z. H. Yao, T. J. Bradley, E. Roussos, L. Lamy, E. J. Bunce, S. W. H. Cowley, N. Krupp, W. S. Kurth, J.-C. Gérard, and W. R. Pryor, Auroral storm and polar arcs at Saturn — Final Cassini/UVIS auroral observations, *Geophysical Research Letters*, *45*(14), 6832–6842, doi:10.1029/2018GL078094, 2018.

Paranicas, C., D. G. Mitchell, E. C. Roelof, P. C. Brandt, D. J. Williams, S. M. Krimigis, and B. H. Mauk, Periodic intensity variations in global ENA images of Saturn, *Geophysical Research Letters*, *32*(21), doi:10.1029/2005GL023656, 2005.

Paranicas, C., D. G. Mitchell, E. C. Roelof, B. H. Mauk, S. M. Krimigis, P. C. Brandt, M. Kusterer, F. S. Turner, J. Vandegriff, and N. Krupp, Energetic electrons injected into Saturn's neutral gas cloud, *Geophysical Research Letters*, *34*(2), L02109, doi:10.1029/2006GL028676, 2007.

Paranicas, C., M. Thomsen, N. Achilleos, M. Andriopoulou, S. Badman, G. Hospodarsky, C. Jackman, X. Jia, T. Kennelly, K. Khurana, P. Kollmann, N. Krupp, P. Louarn, E. Roussos, and N. Sergis, Effects of radial motion on interchange injections at Saturn, *Icarus*, *264*, 342–351, doi:10.1016/j.icarus.2015.10.002, 2016.

Paranicas, C., B. H. Mauk, D. K. Haggerty, G. Clark, P. Kollmann, A. M. Rymer, B. Bonfond, W. R. Dunn, R. W. Ebert, G. R. Gladstone, E. Roussos, N. Krupp, F. Bagenal, S. M. Levin, J. E. P. Connerney, and S. J. Bolton, Intervals of Intense Energetic Electron Beams Over Jupiter's Poles, *Journal of Geophysical Research: Space Physics*, doi:10.1002/2017JA025106, 2018.

Parker, E. N., Sweet's mechanism for merging magnetic fields in conducting fluids, *Journal of Geophysical Research*, *62*(4), 509–520, doi:10.1029/JZ062i004p00509, 1957.

Parker, E. N., Dynamics of the Interplanetary Gas and Magnetic Fields, *The Astrophysical Journal*, *128*, 664, doi:10.1086/146579, 1958.

Paschmann, G., S. Haaland, and R. Treumann, *Auroral Plasma Physics*, Springer Netherlands, Dordrecht, 2003.

Patthoff, D. A., S. A. Kattenhorn, and C. Cooper, Implications of nonsynchronous rotation on the deformational history and ice shell properties in the south polar terrain of Enceladus, *Icarus*, *321*, 445–457, doi:10.1016/j.icarus.2018.11.028, 2019.

Persoon, A. M., D. A. Gurnett, W. S. Kurth, and J. B. Groene, A simple scale height model of the electron density in Saturn's plasma disk, *Geophysical Research Letters*, *33*(L18106), doi:10.1029/2006GL027090, 2006.

Persoon, A. M., D. A. Gurnett, J. S. Leisner, W. S. Kurth, J. B. Groene, and J. B. Faden, The plasma density distribution in the inner region of Saturn's magnetosphere, *Journal of Geophysical Research: Space Physics*, *118*(6), 2970–2974, doi:10.1002/jgra.50182, 2013.

Peterson, W. K., H. L. Collin, O. W. Lennartsson, and A. W. Yau, Quiet time solar illumination effects on the fluxes and characteristic energies of ionospheric outflow, *Journal of Geophysical Research: Space Physics*, *111*(A11S05), doi:10.1029/2005JA011596, 2006.

Pilkington, N. M., N. Achilleos, C. S. Arridge, P. Guio, A. Masters, L. C. Ray, N. Sergis, M. F. Thomsen, A. J. Coates, and M. K. Dougherty, Internally driven large-scale changes in the size of Saturn's magnetosphere, *Journal of Geophysical Research: Space Physics*, *120*(9), 7289–7306, doi:10.1002/2015JA021290, 2015.

Pontius, D. H., and T. W. Hill, Plasma mass loading from the extended neutral gas torus of Enceladus as inferred from the observed plasma corotation lag, *Geophysical Research Letters*, *36*(L23103), doi:10.1029/2009GL041030, 2009.

Porco, C. C., R. A. West, S. Squyres, A. McEwen, P. Thomas, C. D. Murray, A. Delgenio, A. P. Ingersoll, T. V. Johnson, G. Neukum, J. Veverka, L. Dones, A. Brahic, J. A. Burns, V. Haemmerle, B. Knowles, D. Dawson, T. Roatsch, K. Beurle, and W. Owen, Cassini Imaging Science: Instrument Characteristics and Anticipated Scientific Investigations at Saturn, *Space Science Reviews*, *115*(1-4), 363–497, doi:10.1007/s11214-004-1456-7, 2004.

Porco, C. C., P. Helfenstein, P. C. Thomas, A. P. Ingersoll, J. Wisdom, R. West, G. Neukum, T. Denk, R. Wagner, T. Roatsch, S. Kieffer, E. Turtle, A. McEwen, T. V. Johnson, J. Rathbun, J. Veverka, D. Wilson, J. Perry, J. Spitale, A. Brahic, J. A. Burns, A. D. DelGenio, L. Dones, C. D. Murray, and S. Squyres, Cassini Observes the Active South Pole of Enceladus, *Science*, *311*(5766), 1393–1401, doi:10.1126/science.1123013, 2006.

Porco, C. C., D. DiNino, and F. Nimmo, How the geysers, tidal stresses, and thermal emission across the south polar terrain of Enceladus are related, *The Astronomical Journal*, *148*(3), 45, doi:10.1088/0004-6256/148/3/45, 2014.

Provan, G., D. J. Andrews, C. S. Arridge, A. J. Coates, S. W. H. Cowley, S. E. Milan, M. K. Dougherty, and D. M. Wright, Polarization and phase of planetary-period magnetic field oscillations on high-latitude field lines in Saturn's magnetosphere, *Journal of Geophysical Research: Space Physics*, *114*(A02225), doi:10.1029/2008JA013782, 2009a.

Provan, G., S. W. H. Cowley, and J. D. Nichols, Phase relation of oscillations near the planetary period of Saturn's auroral oval and the equatorial magnetospheric magnetic field, *Journal of Geophysical Research: Space Physics*, *114*(A04205), doi:10.1029/2008JA013988, 2009b.

Provan, G., D. J. Andrews, B. Cecconi, S. W. H. Cowley, M. K. Dougherty, L. Lamy, and P. M. Zarka, Magnetospheric period magnetic field oscillations at Saturn: Equatorial phase "jitter" produced by superposition of southern and northern period oscillations, *Journal of Geophysical Research: Space Physics*, *116*(A04225), doi:10.1029/2010JA016213, 2011.

Provan, G., D. J. Andrews, C. S. Arridge, A. J. Coates, S. W. H. Cowley, G. Cox, M. K. Dougherty, and C. M. Jackman, Dual periodicities in planetary-period magnetic field oscillations in Saturn's tail, *Journal of Geophysical Research: Space Physics*, *117*(A01209), doi:10.1029/2011JA017104, 2012.

Provan, G., S. W. H. Cowley, J. Sandhu, D. J. Andrews, and M. K. Dougherty, Planetary period magnetic field oscillations in Saturn's magnetosphere: Postequinox abrupt nonmonotonic transitions to northern system dominance, *Journal of Geophysical Research: Space Physics*, *118*(6), 3243–3264, doi:10.1002/jgra.50186, 2013.

Provan, G., L. Lamy, S. W. H. Cowley, and M. K. Dougherty, Planetary period oscillations in Saturn's magnetosphere: Comparison of magnetic oscillations and SKR modulations in the postequinox interval, *Journal of Geophysical Research: Space Physics*, *119*(9), 7380–7401, doi:10.1002/2014JA020011, 2014.

Provan, G., C. Tao, S. W. H. Cowley, M. K. Dougherty, and A. J. Coates, Planetary period oscillations in Saturn's magnetosphere: Examining the relationship between abrupt changes in behavior and solar wind-induced magnetospheric compressions and expansions, *Journal of Geophysical Research: Space Physics*, *120*(11), 9524–9544, doi:10.1002/2015JA021642, 2015.

Provan, G., S. W. H. Cowley, L. Lamy, E. J. Bunce, G. J. Hunt, P. Zarka, and M. K. Dougherty, Planetary period oscillations in Saturn's magnetosphere: Coalescence and reversal of northern and southern periods in late northern spring, *Journal of Geophysical Research: Space Physics*, *121*(10), 9829–9862, doi:10.1002/2016JA023056, 2016.

Provan, G., S. W. H. Cowley, T. J. Bradley, E. J. Bunce, G. J. Hunt, and M. K. Dougherty, Planetary period oscillations in Saturn's magnetosphere: Cassini magnetic field observations over the northern summer solstice interval, *Journal of Geophysical Research: Space Physics*, *123*, 3859–3899, doi:10.1029/2018JA025237, 2018.

Pryor, W. R., A. M. Rymer, D. G. Mitchell, T. W. Hill, D. T. Young, J. Saur, G. H. Jones, S. Jacobsen, S. W. H. Cowley, B. H. Mauk, A. J. Coates, J. Gustin, D. Grodent, J.-C. Gérard, L. Lamy, J. D. Nichols, S. M. Krimigis, L. W. Esposito, M. K. Dougherty, A. J. Jouchoux, A. I. F. Stewart, W. E. McClintock, G. M. Holsclaw, J. M. Ajello, J. E. Colwell, A. R. Hendrix, F. J. Crary, J. T. Clarke, and X. Zhou, The auroral footprint of Enceladus on Saturn, *Nature*, *472*(7343), 331–333, doi:10.1038/nature09928, 2011.

Pryor, W. R., L. W. Esposito, A. Jouchoux, R. A. West, D. Grodent, J. Gérard, A. Radioti, L. Lamy, and T. Koskinen, Cassini UVIS Detection of Saturn's North Polar Hexagon in the Grand Finale Orbits, *Journal of Geophysical Research: Planets*, *124*, 1979–1988, doi:10.1029/2019JE005922, 2019.

Prölss, G. W., *Physics of the Earth's Space Environment*, Springer, Berlin, Heidelberg, 2004.

Radioti, A., D. Grodent, J.-C. Gérard, B. Bonfond, and J. T. Clarke, Auroral polar dawn spots: Signatures of internally driven reconnection processes at Jupiter's magnetotail, *Geophysical Research Letters*, *35*(L03104), doi:10.1029/2007GL032460, 2008a.

Radioti, A., J.-C. Gérard, D. Grodent, B. Bonfond, N. Krupp, and J. Woch, Discontinuity in Jupiter's main auroral oval, *Journal of Geophysical Research: Space Physics*, *113*(A01215), doi:10.1029/2007JA012610, 2008b.

Radioti, A., D. Grodent, J.-C. Gérard, E. Roussos, C. Paranicas, B. Bonfond, D. G. Mitchell, N. Krupp, S. Krimigis, and J. T. Clarke, Transient auroral features at Saturn: Signatures of energetic particle injections in the magnetosphere, *Journal of Geophysical Research: Space Physics*, *114*(A03201), doi:10.1029/2008JA013632, 2009a.

Radioti, A., A. T. Tomás, D. Grodent, J.-C. Gérard, J. Gustin, B. Bonford, N. Krupp, J. Woch, and J. D. Menietti, Equatorward diffuse auroral emissions at Jupiter: Simultaneous HST and Galileo observations, *Geophysical Research Letters*, *36*(L07101), doi:10.1029/2009GL037857, 2009b.

Radioti, A., D. Grodent, J.-C. Gérard, and B. Bonfond, Auroral signatures of flow bursts released during magnetotail reconnection at Jupiter, *Journal of Geophysical Research: Space Physics*, *115*(A07214), doi:10.1029/2009JA014844, 2010.

Radioti, A., D. Grodent, J.-C. Gérard, S. E. Milan, B. Bonfond, J. Gustin, and W. Pryor, Bifurcations of the main auroral ring at Saturn: ionospheric signatures of consecutive reconnection events at the magnetopause, *Journal of Geophysical Research: Space Physics*, *116*(A11209), doi:10.1029/2011JA016661, 2011.

Radioti, A., D. Grodent, J.-C. Gérard, B. Bonfond, J. Gustin, W. Pryor, J. M. Jasinski, and C. S. Arridge, Auroral signatures of multiple magnetopause reconnection at Saturn, *Geophysical Research Letters*, *40*(17), 4498–4502, doi:10.1002/grl.50889, 2013.

Radioti, A., D. Grodent, X. Jia, J.-C. Gérard, B. Bonfond, W. Pryor, J. Gustin, D. Mitchell, and C. Jackman, A multi-scale magnetotail reconnection event at Saturn and associated flows: Cassini/UVIS observations, *Icarus*, *263*, 75–82, doi:10.1016/j.icarus.2014.12.016, 2016.

Radioti, A., D. Grodent, J.-C. Gérard, D. J. Southwood, E. Chané, B. Bonfond, and W. Pryor, Stagnation of Saturn's auroral emission at noon, *Journal of Geophysical Research: Space Physics*, *122*(6), 6078–6087, doi:10.1002/2016JA023820, 2017a.

Radioti, A., D. Grodent, Z. H. Yao, J.-C. Gérard, S. V. Badman, W. Pryor, and B. Bonfond, Dawn Auroral Breakup at Saturn Initiated by Auroral Arcs: UVIS/Cassini Beginning of Grand Finale Phase, *Journal of Geophysical Research: Space Physics*, *122*(12), 12,111–12,119, doi:10.1002/2017JA024653, 2017b.

Radioti, A., Z. Yao, D. Grodent, B. Palmaerts, E. Roussos, K. Dialynas, D. Mitchell, Z. Pu, S. V. Badman, J.-C. Gérard, W. Pryor, and B. Bonfond, Auroral Beads at Saturn and the Driving Mechanism: *Cassini* Proximal Orbits, *The Astrophysical Journal*, *885*(1), L16, doi:10.3847/2041-8213/ab4e20, 2019.

Rauch, J. L., F. Lefeuvre, D. Le Quéau, A. Roux, J. M. Bosqued, and J. J. Berthelier, Heating of proton conics by resonant absorption in a multicomponent plasma: 1.

Experimental evidence, *Journal of Geophysical Research: Space Physics*, *98*(A8), 13347–13361, doi:10.1029/92JA02255, 1993.

Ray, L. C., Magnetospheric and Atmospheric Controls of Giant Planet Auroral Currents, in *Electric Currents in Geospace and Beyond*, edited by A. Keiling, O. Marghitu, and M. Wheatland, Geophysical Monograph Series, pp. 359–369, John Wiley & Sons, Inc., Hoboken, NJ, USA, doi:10.1002/9781119324522.ch21, 2018.

Ray, L. C., and R. E. Ergun, Auroral Signatures of Ionosphere-Magnetosphere Coupling at Jupiter and Saturn, in *Geophysical Monograph Series*, vol. 197, edited by A. Keiling, E. Donovan, F. Bagenal, and T. Karlsson, pp. 205–214, American Geophysical Union, Washington, D. C., doi:10.1029/2011GM001172, 2012.

Ray, L. C., Y.-J. Su, R. E. Ergun, P. A. Delamere, and F. Bagenal, Current-voltage relation of a centrifugally confined plasma, *Journal of Geophysical Research: Space Physics*, *114*(A04214), doi:10.1029/2008JA013969, 2009.

Ray, L. C., R. E. Ergun, P. A. Delamere, and F. Bagenal, Magnetosphere-ionosphere coupling at Jupiter: Effect of field-aligned potentials on angular momentum transport, *Journal of Geophysical Research: Space Physics*, *115*(A09211), doi:10.1029/2010JA015423, 2010.

Ray, L. C., M. Galand, L. E. Moore, and B. Fleshman, Characterizing the limitations to the coupling between Saturn's ionosphere and middle magnetosphere, *Journal of Geophysical Research: Space Physics*, *117*(A07210), doi:10.1029/2012JA017735, 2012.

Ray, L. C., M. Galand, P. A. Delamere, and B. L. Fleshman, Current-voltage relation for the Saturnian system, *Journal of Geophysical Research: Space Physics*, *118*(6), 3214–3222, doi:10.1002/jgra.50330, 2013.

Ray, L. C., N. A. Achilleos, M. F. Vogt, and J. N. Yates, Local time variations in Jupiter's magnetosphere-ionosphere coupling system, *Journal of Geophysical Research: Space Physics*, *119*(6), 4740–4751, doi:10.1002/2014JA019941, 2014.

Rayleigh, L., Absolute Intensity of the Aurora Line in the Night Sky, and the Number of Atomic Transitions Required to Maintain It, *Proceedings of the Royal Society A: Mathematical, Physical and Engineering Sciences*, *129*(811), 458–467, doi:10.1098/rspa.1930.0167, 1930.

Roelof, E. C., Energetic neutral atom image of a storm-time ring current, *Geophysical Research Letters*, *14*(6), 652–655, doi:10/css8v3, 1987.

Roussos, E., N. Krupp, T. P. Armstrong, C. Paranicas, D. G. Mitchell, S. M. Krimigis, G. H. Jones, K. Dialynas, N. Sergis, and D. C. Hamilton, Discovery of a transient radiation belt at Saturn, *Geophysical Research Letters*, *35*(L22106), doi:10.1029/2008GL035767, 2008.

Roussos, E., N. Krupp, C. P. Paranicas, P. Kollmann, D. G. Mitchell, S. M. Krimigis, T. P. Armstrong, D. R. Went, M. K. Dougherty, and G. H. Jones, Long- and short-term variability of Saturn's ionic radiation belts, *Journal of Geophysical Research: Space Physics*, *116*(A02217), doi:10.1029/2010JA015954, 2011.

Roussos, E., N. Krupp, D. Mitchell, C. Paranicas, S. Krimigis, M. Andriopoulou, B. Palmaerts, W. Kurth, S. Badman, A. Masters, and M. Dougherty, Quasi-periodic injections of relativistic electrons in Saturn's outer magnetosphere, *Icarus*, *263*, 101–116, doi:10.1016/j.icarus.2015.04.017, 2016.

Roussos, E., P. Kollmann, N. Krupp, A. Kotova, L. Regoli, C. Paranicas, D. G. Mitchell, S. M. Krimigis, D. Hamilton, P. Brandt, J. Carbary, S. Christon, K. Dialynas, I. Dandouras, M. E. Hill, W. H. Ip, G. H. Jones, S. Livi, B. H. Mauk, B. Palmaerts, E. C. Roelof, A. Rymer, N. Sergis, and H. T. Smith, A radiation belt of energetic protons located between Saturn and its rings, *Science*, *362*(47), eaat1962, doi:10.1126/science.aat1962, 2018.

Russell, C. T., J. S. Leisner, C. S. Arridge, M. K. Dougherty, and X. Blanco-Cano, Nature of magnetic fluctuations in Saturn's middle magnetosphere, *Journal of Geophysical Research*, *111*(A12205), doi:10.1029/2006JA011921, 2006.

Rymer, A. M., D. G. Mitchell, T. W. Hill, E. A. Kronberg, N. Krupp, and C. M. Jackman, Saturn's magnetospheric refresh rate, *Geophysical Research Letters*, *40*(11), 2479–2483, doi:10.1002/grl.50530, 2013.

Sandel, B. R., and A. L. Broadfoot, Morphology of Saturn's aurora, *Nature*, *292*(5825), 679–682, doi:10.1038/292679a0, 1981.

Sandel, B. R., D. E. Shemansky, A. L. Broadfoot, J. B. Holberg, G. R. Smith, J. C. Mcconnell, D. F. Strobel, S. K. Atreya, T. M. Donahue, H. W. Moos, D. M. Hunten, R. B. Pomphrey, and S. Linick, Extreme Ultraviolet Observations from the Voyager 2 Encounter with Saturn, *Science*, *215*(4532), 548–553, doi:10.1126/science.215.4532.548, 1982.

Saur, J., B. H. Mauk, D. G. Mitchell, N. Krupp, K. K. Khurana, S. Livi, S. M. Krimigis, P. T. Newell, D. J. Williams, P. C. Brandt, A. Lagg, E. Roussos, and M. K. Dougherty, Anti-planetward auroral electron beams at Saturn, *Nature*, *439*(7077), 699–702, doi:10.1038/nature04401, 2006.

Saur, J., N. Schilling, F. M. Neubauer, D. F. Strobel, S. Simon, M. K. Dougherty, C. T. Russell, and R. T. Pappalardo, Evidence for temporal variability of Enceladus' gas jets: Modeling of Cassini observations, *Geophysical Research Letters*, *35*(L20105), doi:10.1029/2008GL035811, 2008.

Saur, J., S. Janser, A. Schreiner, G. Clark, B. H. Mauk, P. Kollmann, R. W. Ebert, F. Allegrini, J. R. Szalay, and S. Kotsiaros, Wave-Particle Interaction of Alfvén Waves in Jupiter's Magnetosphere: Auroral and Magnetospheric Particle Acceleration, *Journal of Geophysical Research: Space Physics*, *123*(11), 9560–9573, doi:10.1029/2018JA025948, 2018.

Schippers, P., M. Blanc, N. André, I. Dandouras, G. R. Lewis, L. K. Gilbert, A. M. Persoon, N. Krupp, D. A. Gurnett, A. J. Coates, S. M. Krimigis, D. T. Young, and M. K. Dougherty, Multi-instrument analysis of electron populations in Saturn's magnetosphere, *Journal of Geophysical Research: Space Physics*, *113*(A07208), doi:10.1029/2008JA013098, 2008.

Sergis, N., S. M. Krimigis, E. C. Roelof, C. S. Arridge, A. M. Rymer, D. G. Mitchell, D. C. Hamilton, N. Krupp, M. F. Thomsen, M. K. Dougherty, A. J. Coates, and D. T. Young, Particle pressure, inertial force, and ring current density profiles in the magnetosphere of Saturn, based on Cassini measurements, *Geophysical Research Letters*, *37*(L02102), doi:10.1029/2009GL041920, 2010.

Sergis, N., E. J. Bunce, J. F. Carbary, S. W. H. Cowley, X. Jia, D. C. Hamilton, S. M. Krimigis, D. G. Mitchell, and M. K. Dougherty, The Ring Current of Saturn, in *Electric Currents in Geospace and Beyond*, edited by A. Keiling, O. Marghitu, and M. Wheatland, Geophysical Monograph Series, pp. 139–154, John Wiley & Sons, Inc., Hoboken, NJ, USA, doi:10.1002/9781119324522.ch9, 2018.

Shen, Y., D. J. Knudsen, J. K. Burchill, A. D. Howarth, A. W. Yau, D. M. Miles, H. G. James, G. W. Perry, and L. Cogger, Low-Altitude Ion Heating, Downflowing Ions, and BBELF Waves in the Return Current Region, *Journal of Geophysical Research: Space Physics*, *123*(4), 3087–3110, doi:10.1002/2017JA024955, 2018.

Singh, N., R. W. Schunk, and J. J. Sojka, Energization of ionospheric ions by electrostatic hydrogen cyclotron waves, *Geophysical Research Letters*, *8*(12), 1249–1252, doi:10.1029/GL008i012p01249, 1981.

Smith, A. W., C. M. Jackman, and M. F. Thomsen, Magnetic reconnection in Saturn's magnetotail: A comprehensive magnetic field survey, *Journal of Geophysical Research: Space Physics*, *121*(4), 2984–3005, doi:10.1002/2015JA022005, 2016.

Smith, A. W., C. M. Jackman, M. F. Thomsen, L. Lamy, and N. Sergis, Multi-instrument Investigation of the Location of Saturn's Magnetotail X-Line, *Journal of Geophysical Research: Space Physics*, *123*(7), 5494–5505, doi:10.1029/2018JA025532, 2018.

Smith, C. G. A., A Saturnian cam current system driven by asymmetric thermospheric heating, *Monthly Notices of the Royal Astronomical Society*, *410*(4), 2315–2328, doi:10.1111/j.1365-2966.2010.17602.x, 2011.

Smith, C. G. A., On the nature and location of the proposed twin vortex systems in Saturn's polar upper atmosphere, *Journal of Geophysical Research: Space Physics*, *119*(7), 5964–5977, doi:10.1002/2014JA019934, 2014.

Smith, E. J., L. Davis, D. E. Jones, P. J. Coleman, D. S. Colburn, P. Dyal, and C. P. Sonett, Saturn's magnetosphere and its interaction with the solar wind, *Journal of Geophysical Research*, *85*(A11), 5655–5674, doi:10.1029/JA085iA11p05655, 1980a.

Smith, E. J., L. Davis, D. E. Jones, P. J. Coleman, D. S. Colburn, P. Dyal, and C. P. Sonett, Saturn's magnetic field and magnetosphere, *Science*, *207*(4429), 407–410, doi:10.1126/science.207.4429.407, 1980b.

Smith, H. T., R. E. Johnson, M. E. Perry, D. G. Mitchell, R. L. McNutt, and D. T. Young, Enceladus plume variability and the neutral gas densities in Saturn's magnetosphere, *Journal of Geophysical Research: Space Physics*, *115*(A10252), doi:10.1029/2009JA015184, 2010.

Snodgrass, H. B., and R. K. Ulrich, Rotation of Doppler features in the solar photosphere, *The Astrophysical Journal*, *351*, 309–316, doi:10.1086/168467, 1990.

Sorba, A. M., N. A. Achilleos, P. Guio, C. S. Arridge, N. Sergis, and M. K. Dougherty, The Periodic Flapping and Breathing of Saturn's Magnetodisk During Equinox, *Journal of Geophysical Research: Space Physics*, *123*(10), 8292–8316, doi:10.1029/2018JA025764, 2018.

Southwood, D. J., and E. Chané, High-latitude circulation in giant planet magnetospheres, *Journal of Geophysical Research: Space Physics*, *121*(6), 5394–5403, doi:10.1002/2015JA022310, 2016.

Southwood, D. J., and S. W. H. Cowley, The origin of Saturn's magnetic periodicities: Northern and southern current systems, *Journal of Geophysical Research: Space Physics*, *119*(3), 1563–1571, doi:10.1002/2013JA019632, 2014.

Southwood, D. J., and M. G. Kivelson, Magnetospheric interchange instability, *Journal of Geophysical Research*, *92*(A1), 109–116, doi:10.1029/JA092iA01p00109, 1987.

Southwood, D. J., and M. G. Kivelson, A new perspective concerning the influence of the solar wind on the Jovian magnetosphere, *Journal of Geophysical Research: Space Physics*, *106*(A4), 6123–6130, doi:10.1029/2000JA000236, 2001.

Southwood, D. J., and M. G. Kivelson, Saturnian magnetospheric dynamics: Elucidation of a camshaft model, *Journal of Geophysical Research: Space Physics*, *112*(A12222), doi:10.1029/2007JA012254, 2007.

Southwood, D. J., and M. G. Kivelson, The source of Saturn's periodic radio emission, *Journal of Geophysical Research: Space Physics*, *114*(A09201), doi:10.1029/2008JA013800, 2009.

Spahn, F., J. Schmidt, N. Albers, M. Hörning, M. Makuch, M. Seiß, S. Kempf, R. Srama, V. Dikarev, S. Helfert, G. Moragas-Klostermeyer, A. V. Krivov, M. Sremčević, A. J. Tuzzolino, T. Economou, and E. Grün, Cassini Dust Measurements at Enceladus and Implications for the Origin of the E Ring, *Science*, *311*(5766), 1416–1418, doi:10.1126/science.1121375, 2006.

Srama, R., T. J. Ahrens, N. Altobelli, S. Auer, J. G. Bradley, M. Burton, V. V. Dikarev, T. Economou, H. Fechtig, M. Görlich, M. Grande, A. Graps, E. Grün, O. Havnes, S. Helfert, M. Horanyi, E. Igenbergs, E. K. Jessberger, T. V. Johnson, S. Kempf, A. V. Krivov, H. Krüger, A. Mocker-Ahlreep, G. Moragas-Klostermeyer, P. Lamy, M. Landgraf, D. Linkert, G. Linkert, F. Lura, J. a. M. McDonnell, D. Möhlmann, G. E. Morfill, M. Müller, M. Roy, G. Schäfer, G. Schlotzhauer, G. H. Schwehm, F. Spahn, M. Stübig, J. Svestka, V. Tschernjawski, A. J. Tuzzolino, R. Wäsch, and H. A. Zook, The Cassini Cosmic Dust Analyzer, *Space Science Reviews*, *114*(1-4), 465–518, doi:10.1007/s11214-004-1435-z, 2004.

Stallard, T., S. Miller, L. M. Trafton, T. R. Geballe, and R. D. Joseph, Ion winds in Saturn's southern auroral/polar region, *Icarus*, *167*(1), 204–211, doi:10.1016/j.icarus.2003.09.006, 2004.

Stallard, T., S. Miller, H. Melin, M. Lystrup, M. Dougherty, and N. Achilleos, Saturn's auroral/polar H+3 infrared emission: I. General morphology and ion velocity structure, *Icarus*, *189*(1), 1–13, doi:10.1016/j.icarus.2006.12.027, 2007a.

Stallard, T., C. Smith, S. Miller, H. Melin, M. Lystrup, A. Aylward, N. Achilleos, and

M. Dougherty, Saturn's auroral/polar H+3 infrared emission: II. A comparison with plasma flow models, *Icarus*, *191*(2), 678–690, doi:10.1016/j.icarus.2007.05.016, 2007b.

Stallard, T., S. Miller, M. Lystrup, N. Achilleos, E. J. Bunce, C. S. Arridge, M. K. Dougherty, S. W. H. Cowley, S. V. Badman, D. L. Talboys, R. H. Brown, K. H. Baines, B. J. Buratti, R. N. Clark, C. Sotin, P. D. Nicholson, and P. Drossart, Complex structure within Saturn's infrared aurora, *Nature*, *456*, 214–217, doi:10.1038/nature07440, 2008a.

Stallard, T., S. Miller, H. Melin, M. Lystrup, S. W. H. Cowley, E. J. Bunce, N. Achilleos, and M. Dougherty, Jovian-like aurorae on Saturn, *Nature*, *453*(7198), 1083–1085, doi:10.1038/nature07077, 2008b.

Stallard, T., S. V. Badman, U. Dyudina, D. Grodent, and L. Lamy, Saturn's Aurorae, in *Saturn in the 21st Century*, edited by K. H. Baines, F. M. Flasar, N. Krupp, and T. Stallard, 1 ed., pp. 166–195, Cambridge University Press, doi:10.1017/9781316227220.007, 2018.

Stasiewicz, K., Y. Khotyaintsev, M. Berthomier, and J. E. Wahlund, Identification of widespread turbulence of dispersive Alfvén waves, *Geophysical Research Letters*, *27*(2), 173–176, doi:10.1029/1999GL010696, 2000.

Stevenson, D. J., Saturn's Luminosity and Magnetism, *Science*, *208*(4445), 746–748, doi:10.1126/science.208.4445.746, 1980.

Stevenson, D. J., Reducing the non-axisymmetry of a planetary dynamo and an application to saturn, *Geophysical & Astrophysical Fluid Dynamics*, *21*(1-2), 113–127, doi:10.1080/03091928208209008, 1982.

Sweet, P. A., The neutral point theory of solar flares, *Symposium - International Astronomical Union*, *6*, 123–134, doi:10.1017/S0074180900237704, 1958.

Talboys, D. L., C. S. Arridge, E. J. Bunce, A. J. Coates, S. W. H. Cowley, and M. K. Dougherty, Characterization of auroral current systems in Saturn's magnetosphere: High-latitude Cassini observations, *Journal of Geophysical Research: Space Physics*, *114*(A06220), doi:10.1029/2008JA013846, 2009a.

Talboys, D. L., C. S. Arridge, E. J. Bunce, A. J. Coates, S. W. H. Cowley, M. K. Dougherty, and K. K. Khurana, Signatures of field-aligned currents in Saturn's nightside magnetosphere, *Geophysical Research Letters*, *36*(L19107), doi:10.1029/2009GL039867, 2009b.

Talboys, D. L., E. J. Bunce, S. W. H. Cowley, C. S. Arridge, A. J. Coates, and M. K. Dougherty, Statistical characteristics of field-aligned currents in Saturn's nightside magnetosphere, *Journal of Geophysical Research: Space Physics*, *116*(A04213), doi:10.1029/2010JA016102, 2011.

Tao, C., S. V. Badman, and M. Fujimoto, UV and IR auroral emission model for the outer planets: Jupiter and Saturn comparison, *Icarus*, *213*(2), 581–592, doi:10.1016/j.icarus.2011.04.001, 2011.

Tao, C., L. Lamy, and R. Prangé, The brightness ratio of H Lyman- α /H $_2$ bands in FUV auroral emissions: A diagnosis for the energy of precipitating electrons and associated magnetospheric acceleration processes applied to Saturn, *Geophysical Research Letters*, *41*(19), 6644–6651, doi:10.1002/2014GL061329, 2014.

Temerin, M., Evidence for a large bulk ion conic heating region, *Geophysical Research Letters*, *13*(10), 1059–1062, doi:10.1029/GL013i010p01059, 1986.

Tetrick, S. S., D. A. Gurnett, W. S. Kurth, M. Imai, G. B. Hospodarsky, S. J. Bolton, J. E. P. Connerney, S. M. Levin, and B. H. Mauk, Plasma waves in Jupiter's high-latitude regions: Observations from the Juno spacecraft, *Geophysical Research Letters*, *44*(10), 4447–4454, doi:10.1002/2017GL073073, 2017.

Thomas, N., F. Bagenal, T. W. Hill, and J. K. Wilson, The Io neutral clouds and plasma torus, in *Jupiter: The Planet, Satellites and Magnetosphere*, edited by F. Bagenal, T. E. Dowling, and W. B. McKinnon, pp. 561–591, Cambridge University Press, New York, 2004.

Thomsen, M. F., Saturn's magnetospheric dynamics, *Geophysical Research Letters*, *40*(20), 5337–5344, doi:10.1002/2013GL057967, 2013.

Thomsen, M. F., D. B. Reisenfeld, D. M. Delapp, R. L. Tokar, D. T. Young, F. J. Crary, E. C. Sittler, M. A. McGraw, and J. D. Williams, Survey of ion plasma parameters in Saturn's magnetosphere, *Journal of Geophysical Research: Space Physics*, *115*(A10220), doi:10.1029/2010JA015267, 2010.

Thomsen, M. F., C. M. Jackman, R. L. Tokar, and R. J. Wilson, Plasma flows in Saturn's nightside magnetosphere, *Journal of Geophysical Research: Space Physics*, *119*(6), 4521–4535, doi:10.1002/2014JA019912, 2014.

Thomsen, M. F., C. M. Jackman, D. G. Mitchell, G. Hospodarsky, W. S. Kurth, and K. C. Hansen, Sustained lobe reconnection in Saturn's magnetotail, *Journal of Geophysical Research: Space Physics*, *120*(12), 10,257–10,274, doi:10.1002/2015JA021768, 2015a.

Thomsen, M. F., D. G. Mitchell, X. Jia, C. M. Jackman, G. Hospodarsky, and A. J. Coates, Plasmapause formation at Saturn, *Journal of Geophysical Research: Space Physics*, *120*(4), 2571–2583, doi:10.1002/2015JA021008, 2015b.

Thomsen, M. F., C. M. Jackman, S. W. H. Cowley, X. Jia, M. G. Kivelson, and G. Provan, Evidence for periodic variations in the thickness of Saturn's nightside plasma sheet, *Journal of Geophysical Research: Space Physics*, *122*(1), 280–292, doi:10.1002/2016JA023368, 2017.

Tripathi, A. K., R. P. Singhal, and O. N. Singh, The Generation of Saturn's Aurora at Lower Latitudes by Electrostatic Waves, *Journal of Geophysical Research: Space Physics*, *123*(5), 3565–3579, doi:10.1002/2017JA024804, 2018.

Vago, J. L., P. M. Kintner, S. W. Chesney, R. L. Arnoldy, K. A. Lynch, T. E. Moore, and C. J. Pollock, Transverse ion acceleration by localized lower hybrid waves in the topside auroral ionosphere, *Journal of Geophysical Research*, *97*(A11), 16935, doi:10.1029/92JA01526, 1992.

Vampola, A. L., and D. J. Gorney, Electron energy deposition in the middle atmosphere, *Journal of Geophysical Research*, *88*(A8), 6267, doi:10.1029/JA088iA08p06267, 1983.

Vasyliūnas, V. M., Plasma distribution and flow, in *Physics of the Jovian Magnetosphere*, edited by A. J. Dessler, pp. 395–453, Cambridge University Press, Cambridge, UK, 1983.

Vasyliūnas, V. M., Physical origin of pickup currents, *Annales Geophysicae*, *34*(1), 153–156, doi:10.5194/angeo-34-153-2016, 2016.

von Papen, M., and J. Saur, Longitudinal and local time asymmetries of magnetospheric turbulence in Saturn's plasma sheet, *Journal of Geophysical Research: Space Physics*, *121*(5), 4119–4134, doi:10.1002/2016JA022427, 2016.

Wahlund, J.-E., P. Louarn, T. Chust, H. de Feraudy, A. Roux, B. Holback, B. Cabrit, A. I. Eriksson, P. M. Kintner, M. C. Kelley, J. Bonnell, and S. Chesney, Observations of ion acoustic fluctuations in the auroral topside ionosphere by the FREJA S/C, *Geophysical Research Letters*, *21*(17), 1835–1838, doi:10/crrkdx, 1994.

Waite, J. H., T. E. Cravens, J. Kozyra, A. F. Nagy, S. K. Atreya, and R. H. Chen, Electron precipitation and related aeronomy of the Jovian thermosphere and ionosphere, *Journal of Geophysical Research*, *88*(A8), 6143–6163, doi:10.1029/JA088iA08p06143, 1983.

Waite, J. H., W. S. Lewis, W. T. Kasprzak, V. G. Anicich, B. P. Block, T. E. Cravens, G. G. Fletcher, W.-H. Ip, J. G. Luhmann, R. L. McNutt, H. B. Niemann, J. K. Parejko, J. E. Richards, R. L. Thorpe, E. M. Walter, and R. V. Yelle, The Cassini Ion and Neutral Mass Spectrometer (INMS) Investigation, *Space Science Reviews*, *114*(1-4), 113–231, doi:10.1007/s11214-004-1408-2, 2004.

Waite, J. H., M. R. Combi, W.-H. Ip, T. E. Cravens, R. L. McNutt, W. Kasprzak, R. Yelle, J. Luhmann, H. Niemann, D. Gell, B. Magee, G. Fletcher, J. Lunine, and W.-L. Tseng, Cassini Ion and Neutral Mass Spectrometer: Enceladus Plume Composition and Structure, *Science*, *311*(5766), 1419–1422, doi:10.1126/science.1121290, 2006.

Walach, M.-T., S. E. Milan, K. R. Murphy, J. A. Carter, B. A. Hubert, and A. Grocott, Comparative study of large-scale auroral signatures of substorms, steady magnetospheric convection events, and sawtooth events, *Journal of Geophysical Research: Space Physics*, *122*(6), 6357–6373, doi:10.1002/2017JA023991, 2017.

Wilson, R. J., R. L. Tokar, and M. G. Henderson, Thermal ion flow in Saturn's inner magnetosphere measured by the Cassini plasma spectrometer: A signature of the Enceladus torus?, *Geophysical Research Letters*, *36*(L23104), doi:10.1029/2009GL040225, 2009.

Wilson, R. J., F. Bagenal, and A. M. Persoon, Survey of thermal plasma ions in Saturn's magnetosphere utilizing a forward model, *Journal of Geophysical Research: Space Physics*, *122*(7), 7256–7278, doi:10.1002/2017JA024117, 2017.

Woodfield, E. E., R. B. Horne, S. A. Glauert, J. D. Menietti, Y. Y. Shprits, and W. S. Kurth, Formation of electron radiation belts at Saturn by Z-mode wave acceleration, *Nature Communications*, *9*(5062), doi:10.1038/s41467-018-07549-4, 2018.

Woodgate, B., R. Kimble, C. Bowers, S. Kraemer, M. Kaiser, A. Danks, J. Grady, J. Loiacono, M. Brumfield, L. Feinberg, T. Gull, S. Heap, S. Maran, D. Lindler, D. Hood, W. Meyer, C. VanHouten, V. Argabright, S. Franka, R. Bybee, D. Dorn, M. Bottema, R. Woodruff, D. Michika, J. Sullivan, J. Hetlinger, C. Ludtke, R. Stocker, A. Delamere, D. Rose, I. Becker, H. Garner, J. Timothy, M. Blouke, C. Joseph, G. Hartig, R. Green, E. Jenkins, J. Linsky, J. Hutchings, H. Moos, A. Boggess, F. Roesler, and D. Weistrop, The Space Telescope Imaging Spectrograph Design, *Publications of the Astronomical Society of the Pacific*, *110*(752), 1183–1204, doi:10.1086/316243, 1998.

Wu, C., Kinetic cyclotron and synchrotron maser instabilities: Radio emission processes by direct amplification of radiation, *Space Science Reviews*, *41*(3-4), doi:10/bwcbqj, 1985.

Yao, Z. H., D. Grodent, L. C. Ray, I. J. Rae, A. J. Coates, Z. Y. Pu, A. T. Lui, A. Radioti, J. H. Waite, G. H. Jones, R. L. Guo, and W. R. Dunn, Two fundamentally different drivers of dipolarizations at Saturn, *Journal of Geophysical Research: Space Physics*, *122*(4), 4348–4356, doi:10.1002/2017JA024060, 2017a.

Yao, Z. H., A. Radioti, I. J. Rae, J. Liu, D. Grodent, L. C. Ray, S. V. Badman, A. J. Coates, J.-C. Gérard, J. H. Waite, J. N. Yates, Q. Q. Shi, Y. Wei, B. Bonfond, M. K. Dougherty, E. Roussos, N. Sergis, and B. Palmaerts, Mechanisms of Saturn's Near-Noon Transient

Aurora: In Situ Evidence From Cassini Measurements, *Geophysical Research Letters*, *44*(22), 11,217–11,228, doi:10.1002/2017GL075108, 2017b.

Yates, J. N., D. J. Southwood, M. K. Dougherty, A. H. Sulaiman, A. Masters, S. W. H. Cowley, M. G. Kivelson, C. H. K. Chen, G. Provan, D. G. Mitchell, G. B. Hospodarsky, N. Achilleos, A. M. Sorba, and A. J. Coates, Saturn's quasiperiodic magnetohydrodynamic waves, *Geophysical Research Letters*, *43*(21), 11,102–11,111, doi:10.1002/2016GL071069, 2016.

Ye, S.-Y., G. Fischer, W. S. Kurth, J. D. Menietti, and D. A. Gurnett, Rotational modulation of Saturn's radio emissions after equinox, *Journal of Geophysical Research: Space Physics*, *121*(12), 11,714–11,728, doi:10.1002/2016JA023281, 2016.

Young, D. T., J. J. Berthelier, M. Blanc, J. L. Burch, A. J. Coates, R. Goldstein, M. Grande, T. W. Hill, R. E. Johnson, V. Kelha, D. J. McComas, E. C. Sittler, K. R. Svenes, K. Szegö, P. Tanskanen, K. Ahola, D. Anderson, S. Bakshi, R. A. Baragiola, B. L. Barraclough, R. K. Black, S. Bolton, T. Booker, R. Bowman, P. Casey, F. J. Crary, D. Delapp, G. Dirks, N. Eaker, H. Funsten, J. D. Furman, J. T. Gosling, H. Hannula, C. Holmlund, H. Huomo, J. M. Illiano, P. Jensen, M. A. Johnson, D. R. Linder, T. Luntama, S. Maurice, K. P. McCabe, K. Mursula, B. T. Narheim, J. E. Nordholt, A. Preece, J. Rudzki, A. Ruitberg, K. Smith, S. Szalai, M. F. Thomsen, K. Viherkanto, J. Vilppola, T. Vollmer, T. E. Wahl, M. Wüest, T. Ylikorpi, and C. Zinsmeyer, Cassini Plasma Spectrometer Investigation, *Space Science Reviews*, *114*(1-4), 1–112, doi:10.1007/s11214-004-1406-4, 2004.

Zarka, P., Auroral radio emissions at the outer planets: Observations and theories, *Journal of Geophysical Research: Planets*, *103*(E9), 20159–20194, doi:10/c4qd56, 1998.

Zarka, P., L. Lamy, B. Cecconi, R. Prangé, and H. O. Rucker, Modulation of Saturn's radio clock by solar wind speed, *Nature*, *450*(7167), 265–267, doi:10.1038/nature06237, 2007.

Zieger, B., and K. C. Hansen, Statistical validation of a solar wind propagation model from 1 to 10 AU, *Journal of Geophysical Research: Space Physics*, *113*(A08107), doi:10.1029/2008JA013046, 2008.